**Department of Exploration Geophysics**

# Multispectral analysis of high spatial resolution 256-channel radiometrics for soil and regolith mapping

**Kirsty A Beckett**

**This thesis is presented for the Degree of**
**Doctor of Philosophy**
**of**
**Curtin University of Technology**

**August 2007**

**Declaration**

To the best of my knowledge and belief this thesis contains no material previously published by any other person except where due acknowledgement has been made.

This thesis contains no material which has been accepted for the award of any other degree or diploma in any university.

Signature:……..

Date:……

This page has been intentionally left blank.

# Abstract

Over the past decade studies into the application of radiometrics for soil and regolith mapping have met with mixed response. While the use of radiometric data for regolith mapping has been generally well received, radiometric methods have not commonly been adopted to assist and improve soil mapping. This thesis contributes to the development of radiometric techniques as soil and regolith mapping tools by examining soil characteristics and radiometric response using non-standard radiometric methods. This is accomplished through the development of new data processing methodologies, which extracts additional information from standard radiometric data that is unattainable using standard processing methods, and development of a new interpretation approach to soil and regolith mapping employing the multispectral processed radiometric data.

The new multispectral processing methodology resolves seven gamma ray peaks from standard 256-channel NaI radiometric data to produce new radiometric uranium ternary, thorium ternary and uranium ratio imagery. Changes in the gamma ray relationships, identified through the new imagery, identify changes in soil and/or environmental conditions that are absent or difficult to identify in the standard radiometric imagery.

With the isolation of non-standard thorium channels $^{228}$Ac (900 keV) and $^{228}$Ac (1600 keV), case studies in this thesis demonstrate how the difference of 1.9 years (half-life) between thorium $^{228}$Ac and $^{232}$Th decay daughter products can be mapped through the interpretation of thorium energy using ternary imagery [red: $^{208}$Tl (1764 keV), green: $^{228}$Ac (900 keV), blue: $^{228}$Ac (1600 keV)]. Energy peak differences may be be linked to local variations in soil chemistry, soil movement, and water movement.

Additionally, through the isolation of non-standard uranium channels $^{214}$Bi (1120 keV) and $^{214}$Bi (1253 keV), preferential attenuation of lower energy gamma-rays from $^{214}$Bi decay events are exploited to map variations in soil density and/or porosity. These variations are illustrated through the interpretation of uranium

energy using ternary imagery [red: $^{214}$Bi (1764 keV), green: $^{214}$Bi (1120 keV), blue: $^{214}$Bi (1253 keV)] and uranium peak energy ratio [$^{214}$Bi 1120 keV / $^{214}$Bi 1764 keV] pseudo colour imagery.

Case studies examined in this thesis explore the characteristics of 256-channel radiometric spectrum from different resolution datasets from different Western Australian soil types, provide recommendations for acquiring radiometric data for soil mapping in different agricultural environments, demonstrate how high resolution 256-channel radiometric data can be used to model soil properties in three-dimensions, and illustrate how three-dimension soil models can be used to separate surface waterlogging influences from rising groundwater induced waterlogging.

# Contents

## Chapter 4: Development of a new multispectral processing methodology



## Chapter 5: Mapping methodology using multispectral processing



## Chapter 6: Case Studies

## Appendices



## References

# List of Figures

# List of Tables

# Acknowledgements

This work was supported by the Co-operative Research Centre for Landscape, Environment and Mineral Exploration (CRC LEME), the Co-operative Research Centre for Plant Based Solutions to Dryland Salinity, and Curtin University of Technology, Bentley, Western Australia. In-kind support was also received from Greg Street and Simon Abbott at GeoAg Pty Ltd for the acquistion of soil samples in the Waroona area. Thanks to the following for access to their radiometric data:

- A. Bissett for access to the Moyagee dataset.
- C. Green formerly of Water Corporation, Western Australia for access to the Yaragadee dataset.
- D. Chester formerly of Harvey Water and J. Anning at Geoforce Pty Ltd for access to the Waroona ground dataset.
- R. George at the Department of Agriculture and Food, Government of Western Australia for access to the Elashgin dataset and supply of soil sample information at Elashgin.

Thanks also to my supervisory panel: Dr Jayson Meyers, Dr Anton Kepic, and Dr Bruce Hartley from Curtin University of Technology, and Dr Richard George from the Department of Agriculture and Food, Government of Western Australia.

# Reference declaration

“Every reasonable effort has been made to acknowledge the owners of copyright material. I would be pleased to hear from any copyright owner who has been omitted or incorrectly acknowledged."

# Executive summary

Studies over the past decade into the application of radiometrics for soil and regolith mapping have met with mixed response. While the use of radiometric data for regolith mapping has been generally well received, radiometric methods have not commonly been adopted to assist and improve soil mapping. This thesis contributes to the development of radiometric techniques as soil and regolith mapping tools by examining soil characteristics and radiometric response using non-standard radiometric methods. This is accomplished through the development of a new data processing methodology and interpretation approach to soil and regolith mapping. Case studies examined in this thesis explore the 256-channel radiometric spectrum from different resolution datasets and show how the new multispectral processed data improves soil and regolith mapping.

## Multispectral processing

The new multispectral processing methodology extracts additional information from standard radiometric data that was unattainable using standard processing methods by resolving seven gamma ray peaks from standard 256-channel NaI radiometric data:

1. $^{40}$K full energy peak at 1461 keV [potassium],
2. $^{214}$Bi full energy peak at 1764 keV [uranium],
3. $^{208}$Tl full energy peak at 2614 keV [thorium],
4. combined $^{228}$Ac full energy peaks at 908 keV, 960 keV and 966 keV [thorium],
5. $^{214}$Bi full energy peak at 1120 keV [uranium],
6. combined $^{228}$Ac full energy peaks at 1590-1640 keV [thorium], and
7. $^{214}$Bi single escape energies at 1253 keV from pair-production reaction at 1764 keV [uranium] with influences from $^{40}$K 1461 keV Compton edge.

These channels were subsequently combined to produce a new series of radiometric imagery, including:

- thorium ternary (red: $^{208}$Tl, green: $^{228}$Ac (900 keV), blue: $^{228}$Ac(1600 keV)) imagery,

- uranium ternary [red: $^{214}$Bi (1764 keV), green: $^{214}$Bi (1120 keV), blue: $^{214}$Bi (1253 keV)] imagery, and
- uranium ratio [$^{214}$Bi 1120 keV / $^{214}$Bi 1764 keV] pseudo colour imagery.

Case studies examined in this thesis were used to demonstrate how the new imagery highlights soil properties characterised by changes in radiometric response, which were difficult to identify in standard processed radiometric imagery. Relationships between the identified gamma ray emissions were also explored through the case studies, with respect to their application for mapping soil or regolith, and local environmental condition. The case studies demonstrate that changes in the gamma ray relationships identified through the new imagery show changes in soil characteristics and/or local environmental conditions.

In particular, the physical interaction of gamma rays with and radionuclide behaviour in the environment were believed to indicate soil characteristics or local environmental conditions. These relationships were resolved through the analysis of the following new radiometric imagery.

Thorium ternary imagery. $^{232}$Th decay daughter product $^{228}$Ac is produced at least 1.9 years (half-life) before the production of $^{208}$Tl, the standard source of gamma ray energy used to measure $^{232}$Th concentration. Consequently, the separation of these daughter products, highlighted through the thorium ternary imagery, may be linked to local variations in soil chemistry, soil movement, and water movement.

Uranium ternary imagery. Decay energy from all three uranium channels are derived from the same $^{214}$Bi decay reaction. Preferential attenuation of the lower energies may be due to soil characteristics, such as increased density or decreased porosity. However, potassium energies can contaminate the $^{214}$Bi 1253 keV (blue) channel. While this does not detract from the use of the imagery for identifying changes in soil characteristics, caution should be applied when using the imagery to directly attribute cause from uranium response alone.

Uranium ratio pseudo colour imagery. As described above, both 1120 keV and 1764 keV energy gamma rays are emitted at the same time, such that variations in the energy may indicate changes in soil characteristics such as density or porosity.

The preferential attenuation of the lower 1120 keV energy is more clearly defined through the ratio of $^{214}$Bi 1120 keV to $^{214}$Bi 1764 keV.

## Interpretation

The relationship between radiometric response and soil type is nonlinear. Consequently, soil type is derived through interpretation of the radiometric response with respect to: surrounding radiometric responses, patterns expressed through radiometric imagery, geomorphology of the landscape, and *a priori* knowledge of soil type across survey areas, including soil formation history. This can often amount to a considerable volume of information that cannot be readily digested by an interpreter. As the new processing methodology developed in this thesis produced more radiometric channels, with variable confidence levels, an alternate radiometric classification and interpretation approach was developed.

The classification methodology developed in this thesis provided greater control over the significance of changes in radiometric response when determining soil boundaries, while utilising the data sorting advantages of classification. The classification methodology is divided into four parts:

1. Preliminary investigation. Establish the survey resolution required for the mapping purpose and collate available soil information.
2. Soil texture distribution. Classify radiometric data, collect and integrate field survey data, and create a three-dimensional soil texture map.
3. Soil unit definition. Integrate soil knowledge and cluster radiometric classes to form units.
4. Soil type definition (optional). Integrate chemical and structural soil data and simplify soil textural changes.

This classification methodology, applied throughout the case studies examined in this thesis, is flexible and suitable for a range of mapping applications and producing a range of map products, including: soil texture maps, water infiltration rates and waterlogging potential, water retention and repellence, drainage management, and soil type.

## Case Studies

The Case Studies section of this thesis is designed to:

- address the issues arising from the analysis of the 256-channel radiometric data,
- compare the imagery produced through the multispectral processing methodology with standard processed imagery, and
- examine the application of the multispectral processing methodology with respect to soil and regolith mapping applications.

## Case Study 1

Case Study 1 provides a background to the imagery, geological, and environmental settings for the four study areas: Yaragadee, Elashgin, Moyagee, and Waroona. It defines uncommon and new terminology used in the thesis, and conveys observations made from careful inspection of the 256-channel data.

Five radiometric datasets from four study areas in Western Australia are studied during this project:

- low resolution airborne data from Yaragadee in the Tuart Forrest National Park in the south-west of Western Australia,
- high resolution airborne data from Elashgin in the northern wheatbelt district, northeast of Perth,
- high resolution airborne data from Moyagee in the salt lake district of central Western Australia, south of Cue, and
- high resolution ground and airborne data from Waroona in the intensive agricultural region in south-west of Western Australia.

## Case Study 2

Case Study 2 examines the strong correlation between the thorium and uranium channels exhibited in the standard processed Elashgin high resolution radiometric dataset. In spite of conforming to industry standards, the ternary imagery from this

dataset is dominated by red and cyan/aqua green tones, which are indicators of strong thorium and uranium correlation.

Extensive investigation of the recorded 256-channel gamma ray spectral response, before and after processing, clarifies how a $^{228}$Ac (thorium) response at approximately 1610 keV, situated between the standard uranium and potassium windows, contributes counts to the standard uranium window. Although the $^{228}$Ac response is a daughter product of the thorium-232 decay series and should be removed through the stripping process, the ratio of the $^{208}$Tl (standard thorium) peak to the $^{228}$Ac response changes spatially across the dataset. With low uranium counts in the Elashgin dataset, the $^{228}$Ac to $^{208}$Tl variation is sufficient to influence the stripping process, such that residual $^{228}$Ac energy incorporated into the uranium channel. This significantly increases the uranium count rate, thereby increasing the correlation between uranium and thorium channels.

Using the multispectral processing methodology, a more appropriate the window width of 1700 keV – 1860 keV is used to encompass the uranium peak. The reduced window width successfully excludes the $^{228}$Ac (thorium) energies from the uranium channel, illustrated by the return of the full colour range to the Elashgin multispectral processed ternary imagery. In future, thorium and uranium correlation in standard processed data can be alleviated by incorporating the reduced window width into the standard processing calibration routine and using the reduced uranium window width during processing.

## Case Study 3

In Case Study 3, data quality, data resolution, and cost differences between airborne and ground acquisition high resolution systems with similar acquisition specifications are compared for soil or regolith mapping applications. The surveys were conducted using a line spacing of 25 m, with airborne data acquired at an altitude of 30 m.

Comparison of the data footprint shows that the increased overlap in the airborne data serves to produce more coherent, continuous images of surface radiometric

response. Comparison of eleven line profiles, examining data resolution, interpreted changes in soil type, ground ternary imagery, airborne ternary imagery, and aerial photography, shows both platforms produce comparable imagery, suitable for identifying changes in radionuclide distribution. The ground platform data displays an accuracy of ±7 m; comparable to 1:10,000 scale imaged products and interpretations. The airborne platform data displays an accuracy of ±50 m; comparable to 1:25,000 scale image products and interpretations.

Cost comparisons of the airborne and ground platforms show the ground platform to be the most cost effective option for small surveys close to Perth requiring less than 500 line kilometres or 1,250 Ha (12,500,000 $m^2$) at 25 m line spacing. For surveys greater than 500 line kilometres the airborne platform is the more cost effective option. The ground platform is preferred for broad acre farming and non-agricultural, non residential land use areas only when the survey area covers less than 1,000 line kilometres and is located more than 200 km from an airport. Nevertheless, due to the logistical constraints associated with airborne surveys that can limit the surveyable area in intensive agriculture regions, the ground platform is the preferred option for any size survey in intensive agriculture areas.

## Case Study 4

In Case Study 4, soil maps are produced for seven selected 25 Ha (250 000 $m^2$) areas in Elashgin, Western Australia. The maps are produced by integrating information from available soil maps, aerial photography, and radiometric data. The radiometric data is presented as low resolution (200 m line spaced, 20 m flying height) and high resolution (25 m line spaced, 20 m flying height) ternary imagery (red: potassium, blue: uranium, and green: thorium), as well as high resolution thorium ternary imagery, uranium ternary imagery, and uranium ratio imagery, produced using the multispectral processing methodology developed during the study.

Comparison of the low and high resolution radiometric imagery shows that, where the contrast between the soil unit radiometric responses is weak, high resolution radiometric data is able to resolve boundaries between soil units. The same

boundaries can only be inferred from the lower resolution data. Additionally, the comparison shows that where the radiometric response is strong, the high resolution data serves to refine the boundary location. These results imply that when interpreting soil boundaries from radiometric data, high resolution radiometric data is required to resolve soil boundaries when the contrast between the radiometric responses of soil units is low, or where the overall radiometric intensity of the soil is low.

Comparison of radiometric imagery with aerial photography and available soil maps confirmed that high resolution airborne radiometric data could resolve features approximately 50 m wide, providing that the extent of the characteristic radiometric response was in excess of 100 m. Features smaller than these dimensions were occasionally resolved when the acquisition path was directly over the top of the feature and there was a high radiometric response contrast between the feature and the background. Subsequently, although the prescribed scale for the high resolution data was believed to be 1:25,000, in locations where there were strong contrasts between the radiometric responses of the soil units, the data was considered to be suitable for mapping at scales of 1:2,500 or “paddock-scale”.

In addition, comparison of the standard radiometric and multispectral processed images in this case study showed that additional spatial patterns, beyond those exhibited by the standard ternary radiometric image, were resolved in the alternative multispectral processed radiometric imagery: thorium ternary, uranium ternary, and uranium ratio. Through interpretation, the additional patterns were used to resolve additional soil unit boundaries and to provide additional environmental condition and soil characteristic information in each mapping study.

## Case Study 5

In the Waroona irrigation area soils change rapidly, in less than a metre, from sandy well drained materials that rarely become waterlogged to heavy clay soils with good water holding characteristics that become waterlogged in high rainfall. This rapid variation in soil texture results in variably waterlogged and dehydrated soils that are

difficult to manage. By isolating soil textures, farmers can alter their paddock layouts and irrigation patterns to better suit the individual soils, and thereby improve the efficiency of water and nutrient applications, crop production, and pasture growth.

In Case Study 5, a ground radiometric survey from Waroona is used to define three-dimensional variations in soil texture, down to ~40 cm. The soil units are broken into three vertical units:

- horizon A (approximately 0 cm to 10 cm),
- horizon B (approximately 10cm to 20 cm), and
- horizon C (approximately 20 cm to 40 cm).

(Note that the horizon names A, B, and C do not represent Australian standard soil horizons.)

During classification, the data is subjected to a series of classification, cluster, and verification analysis procedures, incorporating field observations designed to ensure non-unique radiometric signatures are correctly grouped with spatially and texturally related classes. Following classification, the resulting soil texture model is used to create a map of potential soil waterlogging. As a stand alone map product and without calibration, the potential waterlogging map provides a general guide to where waterlogging is expected to occur as a result of vertical infiltration constraints.

## Case Study 6

Total waterlogging potential reflects the horizontal and vertical movement of water, and the potential for waterlogging to occur as a function of changing soil texture. Case Study 6 expands on the methodology developed in Case Study 5 to calculate the total waterlogging potential as a result of incident rainfall for Elashgin, Western Australia.

A full three-dimensional soil model derived for Elashgin is calculated using the methodology developed in this thesis. The vertical and horizontal waterlogging

potentials are subsequently calculated and summed, with the aid of a digital terrain model, to resolve total waterlogging potential.

From the total waterlogging potential map, areas relating to surface water recharge, discharge, and waterlogging are identified, independent of groundwater movement. Although the waterlogging potential is not calibrated, the results facilitate the separation of complex surface water and groundwater relationships in observed waterlogging, assisting in the selection of appropriate land management or surface water management controls for areas prone to waterlogging.

## Recommendations for future studies

1. The hull removal method developed here and used in the multispectral processing methodology as a surrogate for the Compton continuum and bremsstrahlung energies has limited application. As demonstrated in the Yaragadee data, when using the multispectral processing methodology a significant proportion of the Compton continuum remains in the data if the continuum does not continually decrease.

   While the use of the hull removal facilitated the identification of additional gamma ray peaks from 256-channel sodium-iodide (NaI) data for the purposes of this study, it is not a replacement for standard radiometric processing as the technique does not resolve equivalent ground concentrations. To further study the additional peaks and their relationship to each other as well as soil characteristics and local environmental condition, it is recommended that a new processing methodology be developed to isolate only the seven gamma ray peaks discussed in this study. By isolating only these peaks of interest, alternate approaches to modelling Compton continuum and bremsstrahlung energies can be employed to ensure noise levels within the data are minimal.

2. The artificial increase in uranium and thorium correlation as a result of standard processing presents a significant problem for the general application of radiometric data. Multispectral processing during this study offered a means of identifying potential correlation problems and provided alternate radiometric imagery. However, it could not

replicate calibrated, equivalent ground concentrations of potassium, thorium, and uranium required from radiometric surveys.

Modification of the standard radiometric acquisition, processing, and calibration system to use the reduced standard uranium window of 1700 – 1860 keV is recommended to prevent artificial uranium and thorium correlation. However, the conditions under which the $^{228}$Ac 1590 – 1640 keV peak forms remains unresolved. Additional study into the formation of the $^{228}$Ac 1590 – 1640 keV peak is recommended to improve the predictability of the disruptive energies and reduce artificial uranium and thorium correlation within standard processed radiometric data.

3. Radon corrections were omitted from the multispectral processing. This was done to ensure the radon correction routines did not unduly influence the correlation between the derived uranium peaks. It is recommended that a radon removal routine is introduced to the multispectral processing to reduce the noise fraction within the uranium channels.

4. The relationships established between radiometric response, soil and environment in this thesis are exclusively for characterisation of soils in the study areas. To confidently apply these relationships outside the study areas and facilitate the production of standard soil and regolith maps at 1:50,000 scales or higher resolution, robust examination and cataloguing of the multispectral radiometric response of Australian soil and regolith types is required.

   It is recommended that these additional studies be conducted under controlled conditions, with known soil compositions, moisture profiles, and porosities. Additional sensors should be used to monitor these conditions during experimentation. During these additional studies, it is also recommended that higher energy resolution spectrometers be used in conjunction with the standard NaI survey spectrometers, to verify the positioning of and relationships between the multispectral peaks.

5. Although there was substantial reference literature available on the behaviour of radionuclides under different soil conditions, literature on spatial variability relative to

radionuclide behaviour was scarce. To further the application of high resolution radiometric data for soil mapping applications, it is recommended that controlled spatial experiments be performed to catalogue the radiometric response of changing surface and subsurface water content, acidity, texture, and soil boundary mixing.

# Chapter 1 - Introduction

The following introduction establishes the focus of the thesis and provides an overview of the thesis content.

## 1.1 Background

Over the past decade, the spatial application of gamma ray spectrometry or radiometric surveying has been a research focus for soil and regolith mapping applications. In general, radiometric data acquired in conjunction with airborne magnetic data for mineral exploration has been studied and used to map geomorphological differences in the landscape (eg Bierwirth *et al.*, 1996; George, 1998; Pracilio *et al.*, 1998; Lawrie *et al.*, 2000). These studies have contributed to the development of current radiometric interpretation methodology, which is used to map geological, regolith, or soil characteristics from the variability in three main radiometric products: ground percentage potassium (%K), equivalent ground concentration thorium (Th ppm), and equivalent ground concentration uranium (U ppm) (IAEA, 2003).

Conventional soil and regolith mapping techniques rely on aerial photographs, satellite remote sensing, and/or soil pit cross-sections to chart soil or regolith patterns. Anthropogenic changes to the landscape, such as tree clearing and cropping, mask or remove visual indicators that are used to isolate soil or regolith units, especially in aerial photography. This restricts the effectiveness of conventional soil and regolith mapping techniques in agricultural areas.

Airborne radiometric surveying, on the other hand, combines the advantage of fast data acquisition and continuous spatial coverage with the ability to measure changes within the top 40 cm of the ground; irrespective of normal vegetation cover. These characteristics have been utilised in radiometric surveying for mineral exploration to

map weathering effects and mineral alteration throughout Australia. However, acceptance of radiometric surveying for soil mapping has been less forthcoming. This is partly due to attempts to introduce a new paradigm in soil mapping with less reliance on fieldwork and over-reliance on computer generated interpretation (Spies and Woodgate, 2005).

Criticism of the radiometric interpretation methodology as a tool for assisting soil mapping has emerged from a number of sources, although no definitive criticism has been published. Failure of the technique to be accepted as a tool to assist soil mapping suggests to this author a general misunderstanding and apprehension in both academic and commercial sectors in the use of radiometric surveying. Differing opinions on what constitutes a soil map have added to the general confusion. The most significant misunderstanding surrounding the application of radiometric surveying for soil mapping is the fact that not all characteristics that are diagnostic of a soil type (Isbell, 1997) are reflected in radiometric data, and not all the characteristics of the radiometric data represent changes in soil type. While this situation is not unique to radiometric data (the same argument can be applied to aerial photography) it has been a cause of significant confusion.

Of all the characteristics used to describe soil, generally only soil texture, one of the most important soil properties (Kiss *et al.*, 1988), directly influences radiometric response (Talibudeen, 1964; Taylor *et al.*, 2002). Consequently, *a priori* knowledge of the soil type and its properties in relation to a radiometric response and radiometric interpretation skills are required to draw meaningful information from the data. Over the past decade the most common approach to soil mapping with radiometric data has involved data classification through automated systems that separate spatial groups or decision tree analysis (Anderson-Mayes, 1999; Calleja, 2001; Taylor *et al.*, 2002). While some of these studies may have erred in the implied application of their results, or neglected to document what *a priori* information was integrated into their conclusions, the simplicity of the classification approach has lead to the use of classified radiometric data as a soil map; which clearly it is not. The subsequent

disparity between comparable classified radiometric "soil maps" and conventional soil maps have led to increased uncertainty over the benefits of radiometric surveying for soil mapping amongst those unfamiliar with the technique.

From an academic perspective, there is merit in questioning the appropriateness of the standard radiometric processing methodology for soil mapping. In environments where chemical activity, leaching, or degassing are taking place, gaseous and mobile daughter products may be separated from their primary source element, producing disequilibrium in the decay series (IAEA, 2003). The standard radiometric data processing methodology (IAEA, 2003) was designed to calculate the equivalent ground concentrations of potassium, thorium, and uranium within rocks where the environment is relatively stable, the chemical activity, leaching, and degassing are minimal, and the radionuclide decay series is in equilibrium. However, in the top 40 cm of soil and in the plant root zone, the environment is very dynamic and chemical activity, leaching, and soil degassing occur continually (Leeper and Uren, 1993). This dynamic environment leads to disequilibrium in the uranium decay chain, and to some extent the thorium decay chain, resulting in erroneous calculations of uranium and thorium equivalent ground concentrations using the standard radiometric processing methodology. Accordingly, soil units defined by uranium or thorium concentration alone are inherently erroneous.

The influence of recently introduced spectral smoothing techniques (Hovgaard and Grasty, 1997; Green *et al.*, 1988; Lee *et al.*, 1990; Minty and Hovgaard, 2001) on radiometric spectral response also bears careful consideration for soil mapping applications. Spectral smoothing techniques were introduced to standard processing to reduce noise in survey data. While the benefits to the improved signal to noise ratio are without question, it is noted that the techniques are capable of introducing false anomalies into the data where spectral shape is not well represented in a dataset (IAEA, 2003). In surveys where there is a significant difference between local soil radiometric response and neighbouring outcropping or sub-cropping geology, anthropogenic sources, or other soil types, there is a risk of introducing false

anomalies or falsely magnifying smaller data peaks. As subtle changes in the radiometric response are as important for defining soil units and describing changes in soil characteristics as strong radiometric response, these false anomalies will inaccurately represent soil characteristics.

These limitations do not prevent radiometric data from being used for soil mapping applications. However, there is clearly room for alternative approaches to data analysis that facilitate the production of soil maps.

## 1.2 Thesis overview

The aim of this thesis was to improve the way radiometric data is used to aid soil mapping. To achieve this aim, a new method of data processing/analysis was explored using the decay spectrum from 256-channel sodium-iodide (NaI) radiometric data.

This thesis:

- Reviews the behaviour of radionuclides and radioelements in soil as a function of their physical and chemical properties, soil characteristics, and local environmental setting.
- Reviews the historical development of radiometric surveying as a soil mapping technique.
- Establishes a new multispectral data analysis/processing methodology for data acquired using 256-channel spectrometers combined with NaI detectors.
- Develops a new radiometric classification and interpretation approach to accommodate the characteristics of the multispectral processed data.
- Applies the new processing and interpretation techniques to study areas in Western Australia and documents the appropriateness of this new approach.

## 1.3 Thesis layout

This thesis is composed of seven chapters on radiometric theory, data processing analysis, and interpretation. Chapter 1 is this introduction.

In Chapters 2 to 5 the practice of using radiometric data for soil mapping is reviewed and a new approach to radiometric data analysis is presented. Chapter 2 provides a brief review of the history and development of radiometric surveying from the discovery of natural radioactivity to the development of gamma ray spectrometers, and modern applications for radionuclides and radiometric surveying. This chapter also reviews the behaviour and properties of dominant, naturally occurring, radioactive elements (radioelements) potassium, thorium, and uranium.

Chapter 3 reviews the behaviour of radionuclides in soil. It looks at the role of pedology in radiometric interpretation and how the relative abundance of radionuclides is influenced by:

- particle size redistribution,
- leaching,
- frequency and intensity of wet and dry localised cycles,
- Eh/pH conditions,
- organic matter content, and
- sesquioxide and carbonate content.

Chapter 4 presents the methodology behind the new multispectral data analysis technique. The chapter examines the source of the gamma rays isolated through the multispectral analysis, and then describes the relationships between the multispectral channels and their significance to soil mapping applications.

Chapter 5 describes a methodology to aid soil mapping using the new multispectral data analysis technique. The methodology defines the roles of classification techniques, decision tree style analyses, and *a priori* knowledge in the interpretation

process to enhance latent radiometric responses that can be used to characterise soil properties and local environmental condition.

Chapter 6 consists of six independent case studies produced to demonstrate the enhanced soil and regolith mapping capabilities that emerge from the radiometric processing and interpretation methodology developed in this thesis. The case studies explore issues, problems, solutions, and new approaches to the interpretation of radiometric data for soil and regolith mapping applications. A detailed overview is provided below.

Case Study 1: Introduction to the study areas.

This section introduces the study areas and general data available for use in the studies. The section also briefly discusses problems identified during the general processing and subsequent inspection of the data, and the benefits arising from the multispectral processing.

Case Study 2: Artificial correlation between uranium and thorium in Western Australian radiometric data.

This case study addresses the apparent, strong correlation between uranium and thorium identified in the Elashgin high-resolution airborne radiometric dataset, and its link to standard radiometric processing. The study concludes with a method to reduce the correlation

Case Study 3: Comparison of high-resolution NaI 256-channel radiometric airborne and ground data.

This case study compares the data quality, data resolution, and cost differences between the airborne and ground high resolution data acquired at Waroona in Western Australia for mapping soil or regolith at 1:50,000 scale or less. The study also examines the survey logistics associated with the different survey styles, and reviews subsequent problems that arise including survey timing, local community co-ordination, and noise issues.

Case Study 4: Improving image resolution and radiometric interpretation using multispectral processing.

This case study illustrates through the interpretation of seven, small case studies how characteristics of radiometric data can be used to differentiate landscape, soil characteristics, and local environmental conditions. The study also highlights the advantages of the multispectral radiometric imagery in radiometric interpretation.

Case Study 5: Mapping soil textural changes in Waroona, Western Australia.

This case study applies the radiometric methodology described in Chapter 5 to assist in the production of the local soil maps for the Waroona community.

Case Study 6: Mapping local recharge and discharge locations from soil textural changes.

This case study expands on the concept of identifying areas of potential waterlogging through the radiometric interpretation of soil texture. The study uses digital terrain information to incorporate longitudinal water movement and identify potential waterlogging.

Chapter 7 concludes the thesis, highlighting the advantages of the alternate multispectral radiometric processing technique for mapping soil and regolith.

## 1.4 Data and terminology employed in this project

Throughout this thesis terminology and abbreviations related to radiometric data types, acquisition, and image processing are used. Wherever possible a full descriptor of the radiometric information has been used. However, to improve the flow of the text, particularly during the case studies, irregular abbreviations are employed. The following list of terms provides a breakdown of the more irregular terminology employed in this thesis.

For further descriptions of the geophysical terms used in this thesis refer to Sheriff (2002), for soil terms refer to Leeper and Uren (1993), and for regolith terminology refer to Taylor and Eggleton (2001).

### 1.4.1 Unusual radiometric terminology specific to this thesis

**K1** or **potassium1** – The radiometric channel derived from the $^{40}$K full energy peak at 1461 keV using the multispectral processing methodology defined in this thesis (refer to Chapter 4). This channel is considered to be the equivalent of the potassium or K channel in standard radiometric processing.

**Ternary** – This term is applied to any standard radiometric image presented as red-green-blue (RGB) image, created using potassium data in the red colour channel, thorium in the green colour channel, and uranium data in the blue colour channel. Derivations of ternary images include uranium ternary and thorium ternary images, where only uranium or thorium data is used to create the image, and variations in colour reflect non-linear differences in peak response.

**Th1** or **thorium1** – The radiometric channel derived from the $^{208}$Tl full energy peak at 2614 keV using the multispectral processing methodology defined in Chapter 4 of this thesis. This channel is considered to be the equivalent of the thorium, T, or Th channel in standard radiometric processing.

**Th2** or **thorium2** – The radiometric channel derived from the combined $^{228}$Ac full energy peaks at 1590-1640 keV using the multispectral processing methodology defined in Chapter 4 of this thesis.

**Th3** or **thorium3** – The radiometric channel derived from the combined $^{228}$Ac full energy peaks at 908 keV, 960 keV and 966 keV using the multispectral processing methodology defined in Chapter 4 of this thesis.

**Thorium ternary** – This term is applied to the derived ternary imagery created from the results of the multispectral processing, where Th1 data in represented by the red colour channel, Th2 data in the blue colour channel, and Th3 in the green colour channel.

**U1** or **uranium1** – The radiometric channel derived from the $^{214}$Bi full energy peak at 1764 keV using the multispectral processing methodology defined in Chapter 4 of this thesis. This channel is considered to be the equivalent of the uranium or U channel in standard radiometric processing.

**U2** or **uranium2** – The radiometric channel derived from the $^{214}$Bi single escape energies at 1253 keV from pair-production reaction at 1764 keV with influences from $^{40}$K 1461 keV Compton edge using the multispectral processing methodology defined in Chapter 4 of this thesis.

**U3** or **uranium3** – The radiometric channel derived from the $^{214}$Bi full energy peak at 1120 keV using the multispectral processing methodology defined in Chapter 4 of this thesis.

**Uranium ratio** – The value derived from the division of multispectral processing results U3 channel by U1 channel, usually presented as a grey scale image. For the significance of the ratio refer to Chapter 4.

**Uranium ternary** – This term is applied to the derived ternary imagery created from the results of the multispectral processing, where U1 data is represented by the red colour channel, U2 data is the blue colour channel, and U3 is the green colour channel.

### 1.4.2 Clarification of “high-resolution”

The term “high-resolution” in radiometric surveying is loosely applied in Australia to any data set with a line spacing of less than 400 m. It should be recognised that the resolving capability of these “high-resolution” data, which includes line spacing varying from 20 m to 200 m, are considerably different, and have a significant impact on their ability to map spatial variation. As a result, in this project the line spacing of the data is used to differentiate regolith mapping and soil mapping capability, where regolith mapping pertains to use of radiometric data with a line spacing of 50 m or greater (an approximate equivalent of 1:50,000 scale mapping or greater) and soil mapping pertains to use of radiometric data with a line spacing of 50 m or less. Consequently, the methodology established for soil mapping is considered to be similar for regolith mapping, and thus regolith mapping techniques are not discussed separately.

# Chapter 2 - A brief history of natural radionuclides and gamma ray detection

This chapter summarises the history of radionuclide studies, including the adoption of gamma-ray scintillators for studying radionuclide behaviour, and events in recent history that have influenced the way radiometric data is acquired and processed.

## 2.1 Establishing radioactivity

After Becquerel discovered radioactivity in uranium in 1896, Pierre and Marie Curie observed the strongly radioactive elements polonium and radium occurring naturally in uranium ores (Encyclopaedia Britannica, 2000 ed., s.v. “atom”). Marie Curie applied the term radioactivity to the release of ionising energy by unstable isotopes or radionuclides in order to increase their stability. In 1899, Rutherford observed there was more than one type of radiation. Then in 1900, Villard identified the third type of radiation, the gamma ray. Gamma radiation was later described by Rutherford in 1903 as zero mass, zero charge ionising energy. The zero mass, zero charge energy of the gamma ray allows the radiation to travel through 30 cm of rock, up to 50 cm of soil, several hundred metres of air or across the galaxy before dissipating. Rutherford's later research demonstrated that released gamma ray energies were characteristic of particular radionuclides. These properties were utilised to develop gamma ray scintillometers that defined and measured the amount of radioactive parent materials present in soils and rocks.

By the 1940s, interest in radioactivity had switched from characterising radiation to understanding natural background radioactivity (Marsden and Watson-Munro, 1944; Trener and Scaramucci, 1948) and the relationship between mineral grain size and radioactivity (Sizou and Hoogteijling, 1947; Hoogteijling and Sizou, 1948). Natural radionuclides were observed to originate from bedrock geology, and were subject to local landform processes and mobilised under different conditions, altering their chemical and radioactive characteristics. Initial measurements of radioactivity and radionuclides were based on geochemical analysis, providing the foundations for

later development of Geiger-Muller counters, which measured total gamma-ray activity, and then scintillometers, which identified radioelements by the intensity of individual, measurable gamma-ray energies.

Between 1950 and 1990, baseline studies of radiometric decay employed the latest in both geochemical and scintillation technologies to establish inventories of natural radionuclides in geology, vegetation, and soil (Kiss *et al.*, 1988). Improvements in scintillation technologies, which enabled specific radioelements to be identified, spawned studies comparing scintillation results with standard geochemical techniques (de Lange, 1959; Purvis and Buckmeier, 1969), including evaluation of airborne counting and scintillation systems (Darnley and Fleet, 1968; Darnley and Grasty, 1971). These studies validated the scintillation technologies as a comparable method for identifying and measuring radionuclides, although precision of the scintillometers remained a limitation, much of which was dependent on the efficiency of the crystal sensors employed. More significantly, the cost of identifying and measuring radioactivity was significantly lowered with the introduction of scintillometers, expanding the field and number of radioactivity studies.

## 2.2 Behaviour and properties of radionuclides

Studies into soil processes and the role of radionuclides in the natural environment began in the 1940s. Early studies by Sizou and Hoogteijling (1947) demonstrated an inverse correlation between mineral grain size and radioactivity. Common radioactive elements observed in soil included tritium, carbon-14, potassium-40, rubidium-87, thorium and uranium. Several studies investigated the movement of the parent radionuclides and their daughter products through soil, and their chemical reactivity, with individual studies focusing on weathering processes and groundwater interactions (eg Miller and Reitemeier, 1957; Talibudeen, 1964; Foote, 1968; Somasiri, Yee and Huang, 1971; Baranov and Morozova, 1973; Martz and de Jong, 1987).

With increasing awareness of the health effects of high radioactivity, attention diverted to radionuclide interaction in agriculture. Russian work in the 1960s linked

radioactivity with the ability of soils to grow crops (Talibudeen, 1964). Other studies carefully monitored the influence of various radionuclides on crop growth, natural vegetation and potential food contamination (eg Marchesi Sociats, 1948; Gulyakin and Yudintseva, 1960; Mahon and Mathewes, 1983).

Consequently, by the end of the 1980s there existed a wealth of information on the nature and behaviour of radionuclides in the natural environment. Summarising, pedological processes altering the relative abundances of radionuclides in the soil are, in order of importance (after Talibudeen, 1964):

1. particle size distribution from erosion/deposition processes;
2. leaching;
3. frequency and intensity of wet and dry localised cycles;
4. Eh/pH conditions;
5. organic matter content; and
6. sesquioxide and carbonate content.

Potassium, thorium, and uranium decay series radioactive elements (radioelements) dominate natural gamma ray contributions from radionuclides. Identification of other radioelements is dependent on the efficiency and energy sensitivity of the detector. The properties of the radionuclide families pertinent to this thesis, potassium, thorium, and uranium, are summarised in Tables 2.1 to 2.3.

**Table 2.1. Behaviour and properties of radionuclide $^{40}K$ (after IAEA, 2003).**

| **Potassium, $^{40}K$** | | | | | |
|---|---|---|---|---|---|
| **Radionuclides** | **Daughter** | **Parent** | **Decay mode** | **Gamma energy** | **Convert %** |
| | $^{40}Ar$ | $^{40}K$ | electron capture | 1.461 MeV | 11 |
| **Crustal abundance** | 2.5% wt | | | | |
| **Common mineral associations** | Alkali-feldspars and micas | | | | |
| **Mobility** | Highly mobile | | | | |
| **Decay observations** | Abundance of total K measured directly from 1.461 MeV decay | | | | |
| **Weathering history** | Released during intermediate to late stage weathering | | | | |
| | Erosion and transportation of K in feldspar and mica grains | | | | |
| | Depletion of K can indicate leaching | | | | |
| | Elevated K associated with potassic clays (illite) or adsorption in swelling clays (montmorillonite) | | | | |
| | Can be associated with precipitation of sylvite salts in evaporative basins | | | | |
| **Agricultural notes** | Often added as a fertilizer | | | | |
| | Absorbed by plants and returned to soil after death | | | | |
| | Plant available K not equal to total $^{40}K$. | | | | |

**Table 2.2. Behaviour and properties of radionuclide $^{238}U$ (after IAEA, 2003).**

**Uranium, $^{238}U$**

The yellow boxes highlight potentially mobile nuclides as a result of soil and environmental conditions.

| Nuclide | Half-life | Major radiation energies (MeV) and intensities* | | |
|---|---|---|---|---|
| | | α | β | γ |
| $^{238}U$ | $4.468 \times 10^9$y | 4.15 (23%)<br>4.19 (77%) | – | – |
| $^{234}Th$ | 24.1d | – | ~0.103 (19%)<br>0.191 (81%) | 0.063 (3.5%)<br>0.093 (4%) |
| $^{234}Pa$ | 1.18m | – | 2.29 (98%) | 0.765 (0.30%)<br>1.001 (0.60%) |
| 99.86% / 0.14% | | | | |
| $^{234}Pa$ | 6.7h | – | 0.53 (66%)<br>1.13 (13%) | 0.10 (50%)<br>0.70 (24%)<br>0.90 (70%) |
| $^{234}U$ | $2.48 \times 10^5$y | 4.72 (28%)<br>4.77 (72%) | – | 0.053 (0.2%) |
| $^{230}Th$ | $7.52 \times 10^4$y | 4.62 (24%)<br>4.68 (76%) | – | 0.068 (0.6%)<br>0.142 (0.07%) |
| $^{226}Ra$ | 1602y | 4.60 (5.5%)<br>4.78 (94.5%) | – | 0.186 (4%) |
| $^{222}Rn$ | 3.825d | 5.49 (~100%) | – | 0.510 (0.07%) |
| $^{218}Po$ | 3.05m | 6.11 (100%) | 0.33 (100%) | – |
| 99.98% / 0.02% | | | | |
| $^{214}Pb$ | 26.8m | – | 1.03 (6%) | 0.295 (19%)<br>0.352 (36%) |
| $^{218}At$ | 2s | 6.65 (6%)<br>6.70 (94%) | 0.67 (94%) | – |
| $^{214}Bi$ | 19.7m | 5.61 (100%) | 3.26 (100%) | 0.609 (47%)<br>1.120 (17%)<br>1.764 (17%) |
| 99.96% / 0.04% | | | | |
| $^{214}Po$ | 164μs | 7.83 (100%) | – | 0.799 (0.014%) |
| $^{210}Tl$ | 1.32m | – | 2.3 (100%) | 0.296 (80%)<br>0.795 (100%)<br>1.31 (21%) |
| $^{210}Pb$ | ~22y | 3.7 ($1.8 \times 10^{-8}$%) | 0.017 (85%)<br>0.064 (15%) | 0.047 (4%) |
| $^{210}Bi$ | 5.02d | 4.93 (60%)<br>4.89 (34%)<br>4.59 (5%) | 1.155 (100%) | – |
| ~100% / ~.00001% | | | | |
| $^{210}Po$ | 138.3d | 5.30 (100%) | – | 0.803 (0.0011%) |
| $^{206}Tl$ | 4.19m | – | 1.520 (100%) | – |
| $^{206}Pb$ | Stable | – | – | – |

*Intensities refer to percentage of disintegration of the nuclide itself, not to the original parent series.

**Table 2.2. cont'd. Behaviour and properties of radionuclide $^{238}U$ (after IAEA, 2003).**

| **Uranium, $^{238}U$** | |
|---|---|
| **Crustal abundance** | 3 ppm |
| **Common mineral associations** | Uranitite (pitchblende), Betafite, Huttonite, Uranospherite, Thorite, Uranothorite, Thorianite, Uranothorianite, Carnotite, U carbonate. |
| | Common accessory minerals: Zircon, Xenotime, Monozite, Allanite, Apatite, Sphene. |
| | Igneous rocks, granites, pegmatite and hydrothermal veins. |
| **Mobility** | Variable, dependant on oxidation/reduction conditions |
| **Decay observations** | Under oxidising conditions hexavalent U forms $UO_2^+$ i.e. autunite $Ca(UO_2)2PO_4.10H_2O$ or carnotite $Cu(UO_2)2PO_4.12H_2O$ |
| | Strongly chelated in organic matter. |
| | $^{226}Ra$ very mobile and easily transported in water. |
| | Gaseous member $^{222}Rn$ highly mobile. $^{222}Rn$ diffuses to atmosphere, but is retained in soils with larger pore spaces i.e. loamy soils. |
| | $^{234}U$ preferentially leached over $^{238}U$. |
| | Highly mobile decay elements $^{226}Ra$ and $^{222}Rn$ and preferential leaching of $^{234}U$ result in disequilibrium conditions in soil. Difficult to re-establish equilibrium. |
| | Chemical fractionation between $^{238}U$ and $^{230}Th$, $^{230}Th$ and $^{226}Ra$ during magmatic processes results in disequilibrium in some volcanic rocks. |
| **Weathering history** | Variable dependant on mineralogy, maybe released early in weathering. |
| | If locked in resistate minerals, released during late stage weathering. |
| | Higher adsorption by swelling clays (montmorillonite) than non-expanding kaolin clays |
| **Agricultural notes** | U added to soil in some superphosphate fertilizers, and accumulates in soil. |
| | Trace amounts adsorbed by plants and consumed by animals, but usually excreted by animals without harm. |

**Table 2.3. Behaviour and properties of NaI detectable radionuclide $^{232}$Th (after IAEA, 2003).**

**Thorium, $^{232}$Th**

The yellow boxes highlight potentially mobile nuclides as a result of soil and environmental conditions.

| Nuclide | Half-life | Major radiation energies (MeV) and intensities* | | |
|---|---|---|---|---|
| | | α | β | γ |
| $^{232}$Th | $1.39 \times 10^{10}$y | 3.95 (24%)<br>4.01 (76%) | – | – |
| ↓ | | | | |
| $^{228}$Ra | 5.75y | – | 0.055 (100%) | – |
| ↓ | | | | |
| $^{228}$Ac | 6.13h | – | 2.11 (100%) | 0.34 (15%)<br>0.908 (25%)<br>0.96 (20%) |
| ↓ | | | | |
| $^{228}$Th | 1.913y | 5.34 (28%<br>5.42 (71%) | – | 0.084 (1.6%)<br>0.214 (0.3%) |
| ↓ | | | | |
| $^{224}$Ra | 3.64d | 5.45 (5.5%)<br>5.68 (94.5%) | – | 0.241 (3.7%) |
| ↓ | | | | |
| $^{220}$Rn | 55.6s | 6.30 (~100%) | – | 0.55 (0.07%) |
| ↓ | | | | |
| $^{216}$Po | 0.145s | 6.78 (100%) | – | – |
| ↓ | | | | |
| $^{212}$Pb | 10.64h | – | 0.580 | 0.239 (47%)<br>0.300 (3.2%) |
| ↓ | | | | |
| $^{212}$Bi | 60.5m | 6.05 (70%)<br>6.09 (30%) | 2.25 (100%) | 0.040 (2%)<br>0.727 (7%)<br>1.620 (1.8%) |
| 64.0% ↓ 36.0% | | | | |
| $^{212}$Po | 304ns | 8.78 (100%) | – | – |
| ↓ | | | | |
| $^{208}$Tl | 3.1m | – | 1.80 (100%) | 0.511 (23%)<br>0.583 (86%)<br>0.860 (12%)<br>2.614 (100%) |
| ↓ | | | | |
| $^{208}$Pb | Stable | – | – | – |

*Intensities refer to percentage of disintegration of the nuclide itself, not to the original parent series.

**Table 2.3. cont'd. Behaviour and properties of NaI detectable radionuclide $^{232}$Th (after IAEA, 2003).**

| **Thorium, $^{232}$Th** | |
|---|---|
| **Crustal abundance** | 12 ppm |
| **Common mineral associations** | Huttonite, Thorite, Uranothorite, Cheralite, Thorianite, Uranothorianite. |
| | Resistate accessory minerals include Monazite, Zircon, Apatite, Epidote, Xenotime, Allanite, Sphene |
| | Th scavenged by iron-rich pisoliths |
| **Mobility** | Low to negligible |
| | Solubility is enhanced by humic acids |
| **Decay observations** | Gaseous member $^{220}$Rn highly mobile. $^{220}$Rn diffuses to atmosphere, but is retained in soils with larger pore spaces i.e. loamy soils. |
| | Diffusion of $^{220}$Rn causes disequilibrium, however equilibrium is re-established in around 40 years in a closed system. |
| **Weathering history** | Released only in the late stages of weathering |
| **Agricultural notes** | Best radionuclide for discriminating soil texture |

## 2.3 Modern applications of radionuclides

With the advent of the desktop computer in the late 1980s, studies of radionuclides progressed to integrate digital terrain and landscape interpretations. These studies identified spatial patterns in radionuclide distributions from airborne surveys. These patterns were indicative of landscape formation processes, expanding the understanding of geological history, soil, and regolith processes (eg Martz and de Jong, 1987; Martz and de Jong, 1988; Kiss *et al.*, 1988). Scintillators became the dominant method for measuring radioactivity and identifying radionuclides. The progression to geographic information systems (GIS) for interpretation in the 1990s increased demand for spatial data, data that could provide landscape formation understanding. Airborne radiometric data previously acquired for mineral exploration provided a cheap source of spatial data. Consequently, airborne radiometric data has been regularly investigated as a means of improving regolith and soil maps, with differences of opinion as to the success of the technology (eg Wilford, 1992; Cook *et al.*, 1996b; Bierwirth, 1996; Wilford *et al*., 1997).

The first airborne surveys were conducted in the late 1960s using total radiation counters (Darnley and Fleet, 1968). The system was capable of covering large areas of land quickly. This enabled elevated radioactive anomalies to be rapidly located. These attributes were desirable to the uranium exploration industry. With aid from mineral explorers, improvements in radiation detection and identification technologies were rapidly implemented in airborne systems. However, demand for uranium and uranium products declined following nuclear accidents at Three Mile Island in 1979 and Chernobyl in 1986, and with the end of the Cold War and abundant fissile material obtainable from decommissioned nuclear warheads. Exploration funding dried up and further development laboured. Airborne radiometric systems developed in the 1980s are still used today.

## 2.4 Concluding remarks

In spite of the strong knowledge base for radionuclide behaviour in the environment, recent publications employing radiometrics for soil mapping have failed to incorporate this information. In the author's opinion, this has resulted in a misunderstanding of the relationship between radionuclides, radiometric response, and the natural environment, and contributed to the mistrust of radiometric interpretation results in the wider community.

Problems associated with interpreting soil properties as a function of radiometric response are often related to the low resolution of the data. The quality and resolution of airborne data is highly dependent on the acquisition system and the survey design, while the significance of the interpretation result is dependent on the knowledge of the interpreter, and the quality and resolution of data. Therefore, it is hardly surprising that data acquired to provide a regional understanding of the mineral potential for an area does not produce good soil mapping results.

Radiometric data acquired especially for soil mapping purposes is becoming more common. In Chapter 6, Case Study 3, the resolution capabilities of comparable high resolution radiometric airborne and ground data is assessed. A new methodology for

interpreting this high resolution radiometric data for soil mapping applications is subsequently developed in Chapter 6, Case Study 5.

# Chapter 3 - Radiometric expression in soils

This chapter reviews radiometric interpretation as applied to soil mapping, and the impacts of soil and landscape processes on the distribution of radionuclides in the landscape.

## 3.1 Introduction

'Radiometric data' is a colloquial term used to describe gamma ray spectrometry data acquired for assessing spatial distribution of radionuclides. The methodology employed to interpret radiometric data is similar to that used in other spatial geosciences, such as aerial photo geology or remote sensing. However, where aerial photos and remote sensing data are interpreted to define current geological setting from which geologic history is inferred, radiometric data reflects a complex combination of radioactive source geology and soil radionuclides concentrated through past and present, regional and local landscape processes. Consequently, the interpretation of radiometric data for soil mapping applications requires knowledge of landscape processes as well as an understanding of radiometric expression as a function of changing soil characteristics and local environmental conditions.

## 3.2 Radiometric interpretation methodology

### 3.2.1 Interpretation of soil units from radiometric data

Radiometric surveying is a non-invasive, fast method for identifying and quantifying radionuclide concentration and distribution in the landscape. The technique does not require extensive laboratory analysis, and hence the cost is lower than equivalent standard field surveying and mapping methods (Pracilio *et al*., 2003).

Radiometric response is closely associated with soil texture (Talibudeen, 1964), and can be used to identify and/or differentiate landscape processes. The influence of other soil characteristics, such as soil pH, Eh and structure, on radionuclide distribution is more difficult to identify unless they have a direct influence on the radiometric response. However, as most local soils are defined by changes in soil

texture, radiometric data provides an efficient means of mapping the spatial distribution of soil. And while soil type is not characterised by a unique radiometric response, soil units with similar geochemical and local environmental conditions can be isolated by similar, localised radiometric thorium, potassium, and uranium responses (IAEA, 2003). Changes between radiometric responses are then used to identify instantaneous and gradational boundaries between soil units.

In order to determine the significance of the soil units and the soil characteristics and local environmental conditions responsible for the soil unit, the spatial distribution, and radiometric response of the soil units is compared with:

- Radiometric signatures from surrounding units, to provide an indication of the uniqueness of the signature.
- The geometry of the surrounding units, to ascertain if the unit belongs to an identifiable spatial pattern. If so, the spatial pattern may be indicative of a landscape process, or may otherwise establish a spatial relationship with neighbouring soil units with a similar distribution pattern.
- The geomorphology of the surrounding landscape, to determine the landscape and environmental setting of the unit.
- *A priori* knowledge including soil type and formation history in the area and soil samples, to determine whether the soil unit conforms to or conflicts with the accepted landscape history.

Where appropriate, soil units may then be grouped to form soil types to complete the radiometric interpretation process.

Field verification is often performed to ensure that the predicted/interpreted distribution of soil properties is accurate. The degree of verification, the number of samples, and the properties measured depend on the desired outcome of the interpretation, the resolution of the data, and the desired accuracy of the interpretation. For the interpretation methodology presented in Chapter 6, Case Study 5, field verification was completed by taking soil texture measurements in 5 to 10 locations within each soil unit at 10 cm intervals to a depth of 40 cm. Field samples taken from within the same soil unit should express similar textural characteristics, soil horizons and be located in similar environmental settings.

Where the samples do not conform to the predicted results, within acceptable limits, the original interpretation should be revisited to resolve the discrepancy. However, the 'acceptable limits' are also subject to interpretation, reflecting the desired accuracy of the final results.

### 3.2.2 Separation of uniform radiometric signatures

Soil units are generally characterised by somewhat uniform radiometric signatures. Two approaches for isolating uniform radiometric signatures are demonstrated in the literature: the classical approach and the classification approach. The classical approach is a manual interpretation process, through which the interpreter manually delineates the bounds of each unit with pen and paper or electronically using a GIS or digitising tablet (eg Wilford, 1992; Wilford, 1995). The classification approach employs neural network or automated classification algorithms (eg Anderson-Mayes, 1999). Each technique has its own merits, with the strength of the approach lying in the experience of the interpreter.

Using the classical approach, the interpreter directly inputs *a priori* knowledge into the classification when identifying radiometric units. The process of identifying the units and interpretation of the significance of the units often merge during the process, with the interpreter marking only those boundaries they consider significant to the interpretation. This can produce a faster interpretation. However, the classical approach can produce poor results if the interpreter does not consider all of the available ancillary data. This is often the case when interpreting large, complex datasets. Otherwise, the classical approach can be extremely time consuming when a large volume of ancillary data is available.

Neural network and automated classification systems employ computer algorithms to identify regions of similarity from a series of datasets according to the limitations and variables supplied by the user. When operated correctly, these classifiers assist the interpreter by rapidly identifying the boundaries between similar radiometric units without interpretation bias. However, if the classification limitations and variables are incorrectly configured, the resulting classification will represent groups of variables other than the targeted response. Soil units derived from the

classification approach require more stringent attention during interpretation to ensure that the identified boundaries reflect the desired interpretation targets.

Chapter 6, case study 5 demonstrates the application of the classification approach for soil mapping.

### 3.2.3 Spatial patterns in radiometrics

Relationships between radiometric concentration, geology, and landscape processes are very complex, but are reflected in the data's spatial distribution and patterns (Martz and de Jong, 1990). In particular, similar spatial patterns recognised for interpreting landscape processes from aerial photography (Drury, 1993) are reflected in radiometric imagery and represent the same landscape processes. Common patterns recognised in radiometrics include gradational changes, dendritic branching, linear units, speckling, and oval units. The following descriptions provide a guide to interpreting some of the spatial patterns regularly observed in radiometric imagery.

Gradational changes generally correlate with slopes in the landscape. Outcrop and sub-outcrop supply fresh radionuclides to the soil, such that, at these locations, radionuclide concentration is elevated. Physical weathering and mixing of soil down slope dilutes the concentration of radionuclides, while increased water availability down slope induces chemical weathering. As a result, radionuclides are leached from the base of the slope. These weathering influences combine to create the high upslope, low down slope concentration patterns.

Dendritic branching patterns are usually related to current or palaeo-drainage. Soils and water are transported towards and along channels, highlighting the drainage pattern. Alternatively, in palaeo-drainage settings, increased water content in the channels contributes to an altered chemical weathering profile, modifying the soil properties and radionuclide distribution. At the edge of the channel, physical soil mixing dominates, creating an intermediate soil unit between channel soils and local soils.

Linear patterns are usually the result of outcropping or subsurface linear geological units or anthropogenic structures. Linear geological units include fracture and fault systems with associated local alteration halos, dolerite dykes, quartz sills, and other confined intrusions. The boundaries of these units are defined, but may grade towards the edge as a result of soil mixing or alteration. Alteration halos often produce multiple concentric soil units around the original geological features as a result of chemical speciation in the original bedrock. Anthropogenic sources, including roads, railways, and canals, are usually highlighted as a result of the introduction of foreign materials with incongruent radiometric signatures.

Speckle patterns in radiometric imagery (Figure 3.1) result from poor signal strength, low spatial resolution, or fluctuating ground concentration. Where the speckle is not a function of poor signal and/or spatial resolution, speckle induced by fluctuating radioactivity may indicate increased radionuclide mobility, an indicator of changing soil Eh/pH or vegetation conditions. Fluctuating radioactivity may also highlight water movement, signifying leaching or variable deposition from groundwater discharge. On a regional scale, speckle in imagery may result from differences in soil moisture content, changes in micro-topography, or increased soil organic matter content.

To define soil units in speckled imagery, the combined flux of individual potassium, thorium, and uranium channels are used to establish textures in radiometric imagery. Soil unit boundaries are subsequently located at the edge of these texture units, rather than around the smaller uniform responses comprising the texture, as illustrated in Figure 3.1.

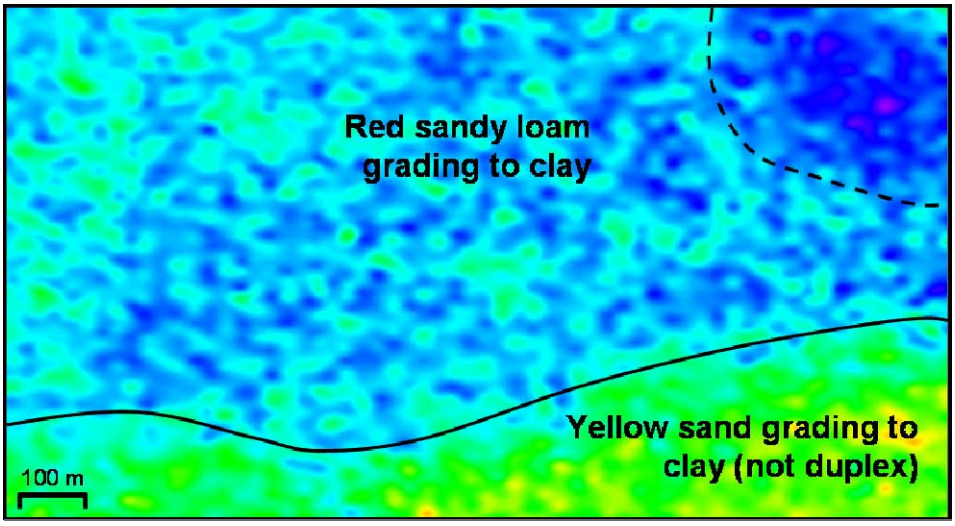


**Figure 3.1. Speckle patterns used to define soil units. The speckled pattern results from fluctuating ground concentrations of $^{40}$K. Soil units are subsequently defined by fluctuating colour and spatial association. In this example, the soil unit - yellow sand grading to clay, is defined by a cluster of green and yellow speckles. The red sandy loam grading to clay soil unit is defined by blue to green speckles. This soil unit may also be subdivided into a blue to green speckled unit and pruple to light blue speckled unit to highlight increasing clay content within the soil horizon. Airborne radiometric data from Elashgin, Western Australia.**

Circular shapes are usually indicative of local sinks or deposition areas, such as exposed lakes beds or playas. These local topographic lows accumulate water and fine materials, creating unique, chemically active environments with distinct, separable radiometric signatures after water has evaporated. In addition, radionuclides transported in solution to the area are precipitated through evaporation then adsorbed to clays and other fines, contributing to the increased radiometric response.

### 3.2.4 Establishing soil type from radiometrics

The *Australian Soil Classification* (ASC) (Isbell, 1997) is the Australian standard for classifying soil types. The aim of the ASC is to identify and name soils according to an orderly system of defined classes that facilitates communication about soils in an accurate and consistent manner. The ASC groups soils according to soil evolution, focusing on the soil B horizon, such that soil groups have similar physical and chemical properties.

On a regional scale, the ASC provides information for determining possible land uses, land management requirements, and land use limitation factors. However at local scales, physical and chemical soil characteristics that are important for local land management are not well represented by ASC units. As a consequence, local soil classification schemes are often developed for individual catchments. Soil texture plays an important role in these local soil classification schemes, with links to soil erosion potential, water holding characteristics, and nutrient holding capability (Leeper and Uren, 1993). Considering changes in soil texture are readily reflected in radiometric response, there is potential for high resolution radiometric data to play an important role in local land management where standard ASC soil maps cannot.

However, where soil type is the desirable outcome from the interpretation of radiometric data, careful consideration must be made to the physical and chemical properties that differentiate the units. Unless substantial supporting information is available, or the soil type can be differentiated by soil texture alone, the interpretation of ASC soil type from radiometric data is not recommended.

## 3.3 Radionuclides and their relationship to soil and landscape processes

The link between radionuclides, their movement, and local environmental conditions are well established (Talibudeen, 1964). Landscape processes, including erosion/deposition (particle re-distribution), leaching, and wet and drying cycles, are influenced by, and in turn, influence soil characteristics such as redox state and sesquioxide, carbonate, and organic matter content. The cumulative effect of these processes is to change the mobility and distribution of radionuclides in the landscape. Consequently, while the origin of the radionuclides are dependent on the geology of the region, landscape processes control radionuclide redistribution throughout the landscape.

Radionuclide distribution can be observed at different scales. From a highly localised perspective, within the top 50 cm of soil, variations in radionuclide concentrations are predominantly controlled by vegetation (O'Dea and Dowdall, 1999). On a local scale, pedological processes control radionuclide concentrations

and distribution (Martz and de Jong, 1990). On a regional scale, regional geology and landscape processes govern radionuclide distribution (Hariss and Adams, 1965).

In the following sections, landscape processes that can be interpreted from radiometric data at local scales are reviewed with respect to their influence on radionuclides, followed by a review of soil characteristics that control nuclide chemical mobility.

### 3.3.1 Erosion

Erosion encompasses the physical and chemical weathering of rock. As demonstrated in Table 3.1, the initial rock radionuclide content is highly variable. Physical and chemical weathering processes wear away rock, breaking the rock down into smaller and smaller rocks, and eventually grains whose radionuclide content is representative of its parent source.

However, the initial increase in surface area of fragmented rock surrounding the parent source increases the volume of gamma rays reaching the sensor. This results in an apparent increase in radiometric concentration surrounding the solid outcrop.

**Table 3.1. Radioelement content of Australian rocks (from IAEA, 2003 after Dickson and Scott, 1997).**

| Rock Type | | K (%) | U (ppm) | Th (ppm) |
|---|---|---|---|---|
| Intrusives | Granitoids | 0.3-4.5 (2.4) | 0.4-7.8 (3.3) | 2.3-45 (16) |
| | Gneissic rock | 2.4-3.8 (2.4) | 2.1-3.6 (2.5) | 18-55 (15) |
| | Pegmatite | 2.6-5.5 (3.7) | 0.3-1 (0.7) | 0.3-9.6 (2) |
| | Aplites | 0.6-4 (2.4) | 1-8 (3.3) | 3-20 (7) |
| | Quartz-feldspar porphyry | 1-5 (2.9) | 1.3-2.9 (1.7) | 6-14 (13) |
| | Intermediate intrusives | 0.7-5.6(2.7) | 0.1-1.2 (0.8) | 0.8-6.1 (2.4) |
| | Mafic intrusives | 0.1-0.8 (0.4) | 0.0-1.1 (0.3) | 0.0-3.1 (1.2) |
| Extrusives | Felsic volcanics | 2.0-4.4 (3.7) | 1.4-13 (2.4) | 13-28 (17) |
| | Intermediate volcanics | 1.8-4.1 (2.7) | 0.9-5.6 (2.3) | 1.5-15 (9) |
| | Low-K andesites | 0.7-0.9 (0.8) | 1.0-2.5 (1.6) | 3-8 (5) |
| | Mafic volcanics | 0.3-1.3 (0.9) | 0.3-1.3 (0.7) | 2.0-5.0 (3.0) |
| | Ultramafic volcanics | 0.2-0.9 (0.4) | 0.3-0.9 (0.6) | 0.0-4.0 (1.2) |
| Sedimentary rocks | Archean shales | 0.4-1.6 (0.9) | 0.3-1.3 (0.9) | 1-5 (2.7) |
| | Other shales | 0.1-4.0 (2.6) | 1.6-3.8 (2.6) | 10-55 (19) |
| | Arenites | 0.0-5.5 (1.8) | 0.7-5.1 (2.3) | 4-22 (12) |
| | Carbonates | 0.0-0.5 (0.2) | 0.4-2.9 (1.6) | 0-2.9 (1.4) |

### 3.3.2 Deposition

Deposition involves the redistribution of materials. As one of the strongest controls on radionuclide distribution and concentration, deposition includes the physical movement, sorting, and deposition of material eroded by physical or chemical means. The degree of sorting is subsequently dependent on the depositional environment.

In general, erosion/deposition processes separate larger fragments of resistive minerals from smaller less resistive minerals and can chemically precipitate new minerals. As radionuclides are generally bound to resistive materials, the sorting process separates radionuclide-bearing minerals from radionuclide poor materials. The result is a differential radiometric response across the sorting grades.

With colluvial deposits, gravitational forces control the sorting process. Larger, heavier fractions are preferentially transported down slope along the steepest gradient. Consequently, the direction of movement, the flow path, is highlighted by differential response from the coarse fraction of minerals. In Figure 3.2, K-feldspars dominate the coarse scree fraction. As these minerals move preferentially down slope, the $^{40}$K radionuclide in the K-feldspars highlights the current flow path.

Water movement is the main deposition control in alluvial environments. As the flow rate decreases, heavier particles suspended in water are preferentially deposited. The result is a deposition of coarse grains along the base of the stream, with finer fractions deposited along the edge of the steam and in overbank deposits. Movement of the stream with time produces a complex accumulation of interbanded coarse and fine fractions across the alluvial plane, with soil properties varying rapidly, vertically and horizontally.

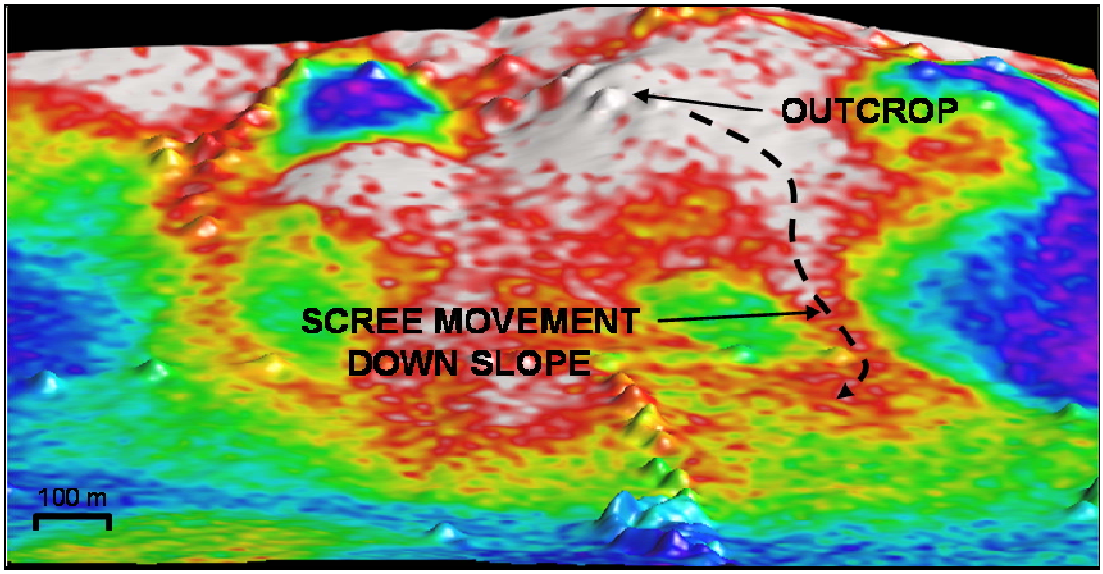


**Figure 3.2. Radiometric response used to trace soil/regolith movement. Potassium-40 radionuclide pseudocolour image (white high, purple low) draped over digital terrain data, from Elashgin, Western Australia. The $^{40}$K response is derived from K-feldspar in granitic bedrock. Material eroded and transported down the scree slope from the bedrock is highlighted by the increased $^{40}$K response.**

Radionuclides are introduced to these complex systems bound to particles during deposition. The initial sorting of the grains during deposition can separate different radionuclides. However, following successive depositional events, the finer soil fractions adsorb local radionuclides, resulting in a range of different radionuclide distributions and concentrations across the alluvial plane. As a result, the differential

radiometric signatures can assist in separating different age and style of deposit (Wilford *et al.*, 1997).

Aeolian deposits are wind-blown sediments. The wind is a very efficient mechanism for sorting grain size, operating over much larger distances than colluvial or alluvial processes. Fine fractions are preferentially carried further than coarse fractions and may be dispersed and deposited hundreds of kilometres apart. Identification of these deposits is performed with respect to local soil signatures. In particular, sand dunes and reworked sands, illustrated in Figure 3.3, are identifiable by their low radionuclide concentrations due to high quartz concentration. Other aeolian deposits, such as the parna deposits in Eastern Australia, are distinguished by their relative high radiometric response.

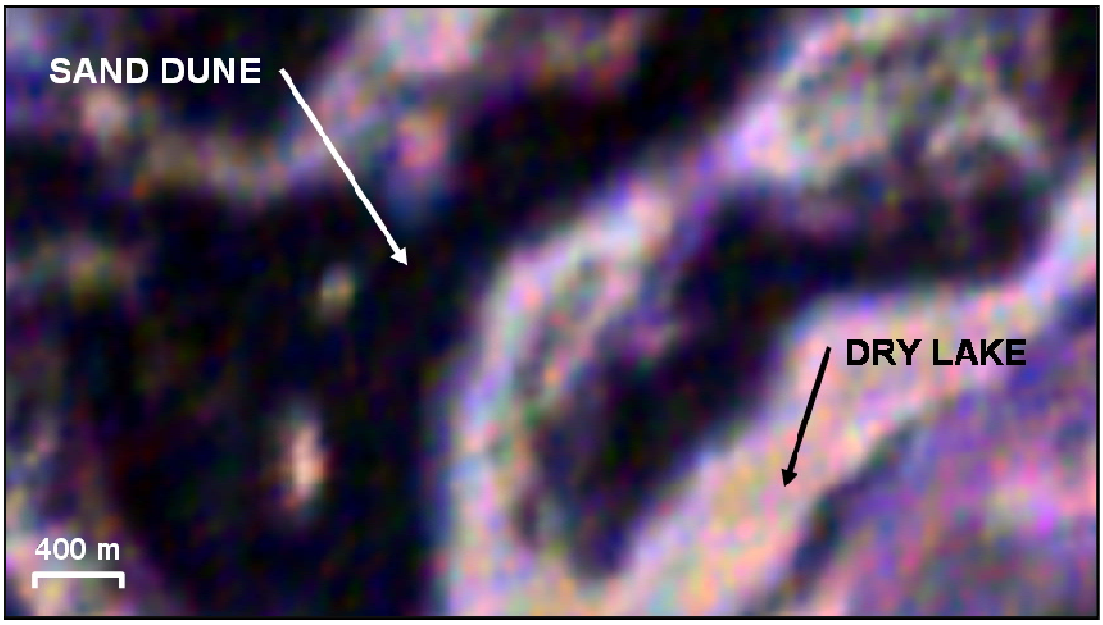


**Figure 3.3. Wind sorted materials with different radiometric response. Ternary radiometric image, potassium [red], uranium [blue], and thorium [green], from Moyagee, Western Australia. Sand dunes on a salt lake near Cue in Western Australia resulting from accumulation of wind blown quartz grains are highlighted by their low (black) radiometric response. Radiometric response from finer grained materials in the salt lakes, such as developing and accumulated clays, produces the pink tones in the image.**

### 3.3.3 Leaching

Water removes or leaches soluble minerals and clays as it percolates through the soil profile. Thus, the degree of leaching depends on the water chemistry, physical structure of the soil and the chemical reactivity of its radionuclides.

In permeable soils, radionuclides that form soluble complexes or adsorb to fine soil fractions are readily leached from the surface and deposited further down the soil profile. Alternatively, leached radionuclides may be transported with the water and precipitated as the result of a change in soil chemistry or discharged with groundwater to the surface. Either way, leached soils are identified by localised, low radionuclide concentration.

On a regional scale, hydrothermal alterations as a result of geological processes also facilitate localised leaching. During hydrothermal alteration the mineral assemblage of the bedrock is changed due to the actions of water under high temperatures. As a result, the local distribution of radionuclides is modified in accordance with the hydrothermal alteration, increasing radionuclide concentration with the precipitation of potassium clays or feldspars, or decreasing the radionuclide concentration. The altered areas generally contain less resistive minerals than the surrounding bedrock, and can provide preferential pathways for groundwater movement. Movement of water along these pathways subsequently encourages weathering and leaching. Conversely, the altered geology can also weather to form nutrient poor clays with lower permeability, blocking groundwater movement and encouraging waterlogging, groundwater discharge, and subsequently an increase in radionuclide concentration.

Leaching is the primary cause of disequilibrium in radionuclide decay. For a decay series to be in equilibrium, each immediate parent radionuclide must generate sufficient daughter nuclides to preserve the decay series parent:daughter ratio. With the removal of all or some of the daughters from the system, the parent:daughter ratio is modified and the system is said to be in disequilibrium until the parent can produce sufficient daughter products again to restore the balance.

Identification of disequilibrium is particularly important when calculating parent radionuclide concentrations based on the concentration of daughter radionuclides. For example, the concentration of elements $^{238}U$ and $^{232}Th$ are routinely determined from daughter products $^{214}Bi$ and $^{208}Tl$, respectively. If daughter products $^{214}Bi$ or $^{208}Tl$ are separated from the parent radionuclides $^{238}U$ or $^{232}Th$, standard radionuclide calibrations (refer to Appendix A) will underestimate the parent concentration where

the parent resides, and incorrectly locate the parent to the location of the daughter radionuclides.

The uranium decay series (Table 2.2) contains a number of mobile daughter products. Under normal soil conditions, mobile daughter products are often leached from the surface and away from parent source, such that uranium disequilibrium is common in the top of the soil profile.

The mobile daughter products are leached through various mechanisms. Uranium decay daughter radionuclides $^{238}U$, $^{234}U$, and $^{226}Ra$ may form soluble complexes under normal soil conditions and adsorb to fine fractions in the soil. Conversely, $^{238}U$ and $^{234}U$ may form insoluble compounds, then along with $^{230}Th$, these daughters accumulate as a fine fraction in the soil. During leaching, the fine daughter-bearing soil fraction may be physically transported down the soil profile with the moving water. Alternatively, soluble radionuclides may desorb from the fine fraction into the water column to be transported with the moving water. The gaseous uranium decay daughter product $^{222}Rn$ may also be displaced down the soil profile during leaching. Consequently, the distribution of uranium daughter products in the top 50 cm can vary considerably, and is highly dependent on soil conditions.

The thorium decay series (Table 2.3) also contains mobile members. Soluble radionuclides $^{228}Ra$ and $^{224}Ra$ and gaseous $^{220}Rn$ may be leached from the surface, adsorbed to fine fractions, or dissolved in the water column. These mobile thorium radionuclides have relatively short half lives: $^{228}Ra$ with 5.75 years, $^{224}Ra$ with 3.64 days and $^{220}Rn$ with 55.6 seconds. However, unlike mobile radionuclides in the uranium series, parents of the leached components in the thorium series generally have a half-life greater than their daughters. As a result, equilibrium is more rapidly re-established. However, under some conditions it can take up to 45 years to re-establish equilibrium (Adams and Gasparini, 1970), so disequilibrium cannot be discounted.

Potassium-40 does not produce daughter radionuclides, decaying directly to the stable isotope $^{40}Ar$, so is not subject to disequilibrium conditions. However potassium itself is a mobile element. Figure 3.4 highlights the mobility of potassium

relative to other major mineral constituents. Potassium has greater mobility than uranium or thorium minerals, and consequently is generally leached before uranium or thorium.

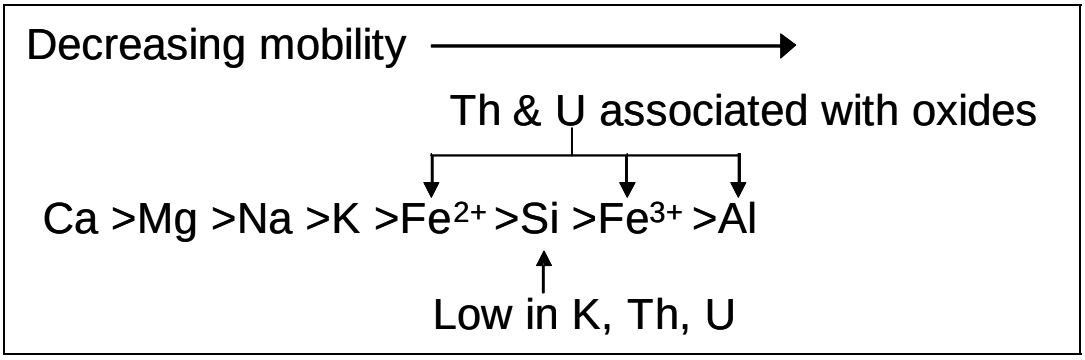


**Figure 3.4. Relative mobility of major mineral constituents and their gamma-ray response (from Wilford *et al.*, 1997).**

Nevertheless, changes in environmental conditions and soil characteristics can change the mobility order (Wilford *et al.*, 1997). Tetravalent thorium and tetravalent uranium share a similar ionic radius, and often occur together in minerals (Talibudeen, 1964). However, uranium complexes are generally more mobile than thorium, thus uranium is removed before the thorium making thorium a relatively immobile element. Consequently, IAEA (2003) suggests that ratios of thorium to uranium greater than 5:1 indicate leaching.

### 3.3.4 Frequency and intensity of wet and dry cycles

Local variations in topography and aspect create a variety of micro-climates within a catchment. Within these micro-climates, the frequency and intensity of wet and dry cycles vary. As the interaction of water with the local geology and vegetation regulates weathering and plant growth, these micro-climates result in different weathering styles, vegetation type, and vegetation growth across the catchment. In turn, the style of weathering and vegetation growth influences the distribution of radionuclides.

During wet cycles, when the supply of fresh minerals to the soil is limited, chemical weathering dominates. Chemical weathering causes solid geology beneath the soil horizons to decompose under anaerobic conditions, resulting in the formation of clay

minerals at depth. Extensive wet periods encourage leaching, transporting daughter products away from the surface and prevent decay series equilibrium from re-establishing. The transported radionuclides then accumulate at depth, adsorbed to clay 'sinks' above the decomposing bedrock.

Wet cycles also encourage vegetation growth. As $^{40}K$ is an essential nutrient in plant growth, during intensive vegetative growth increased amounts of potassium are absorbed from the root zone and stored within the plant. Following the death of the plant, the potassium is returned to the top soil. Thus $^{40}K$ is leached and then returned to the soil.

Dry cycles encourage physical weathering. Physical weathering encompasses physical erosion and deposition processes that transport soils from local topographic highs to local lows, mixing soils, and adding new minerals and radionuclides from exposed, eroded bedrock.

Radionuclides are less chemically mobile under dry conditions. However, under prolonged dry conditions, radionuclides can be remobilised from subsurface sinks to the surface via groundwater and the capillary fringe. Where radionuclide-bearing groundwater discharges, evaporation precipitates dissolved solids containing radionuclides. Common radionuclide-bearing deposits formed in this manner include calcium carbonate cements bearing carnotite (uranium) and potassic salts.

Climate also influences soil temperature. Chemical reactions increase with increasing temperature, while the solubility of gas decreases (Leeper and Uren, 1993). However, with increased temperatures, gaseous radionuclides $^{222}Rn$ and $^{220}Rn$ are released from the soil; although soils with larger pore spaces are more likely to retain radon gas (Talibudeen, 1964). As the soils cool, emission rates decline.

As the gas leaves the soil, atmospheric conditions and micro-topography control its distribution. Calm night conditions and temperature inversions result in pools of radon gas accumulating in local topographic lows (Minty, 1998). These pools can cause spurious, high uranium results when measured in the early morning; although

the response is not associated the ground uranium concentration. Light winds mix the radon pools with the atmosphere, adding to the natural background radioactivity.

## 3.4 Chemical mobility of radionuclides

### 3.4.1 Eh/pH conditions

Soil oxidation-reduction potential (Eh) and hydrogen potential (pH) conditions control the stability of mineral or chemical species. Eh is a measure of soil electron activity. pH is a measure of the activity of hydrogen ions in the soil. Soil pH varies between 2 (very acidic) and 14 (very alkaline). Under various Eh/pH conditions, radionuclides change ionic state, forming different chemical complexes, chelates, and ions that ultimately control radionuclide solubility and mobility in soil.

Oxidising and reducing conditions, or redox condition, are regulated by oxygen levels in the soil. Soil pore spaces contain oxygen, encouraging oxidising conditions. During periods of sustained waterlogging, oxygen in the soil is depleted through biological activity, and reducing conditions are produced. These reducing conditions lead to sulphication and acidification in soils.

Uranium is very sensitive to Eh/pH condition. For example, under oxidising conditions, uranium is readily weathered to form soluble uranyl compounds $(UO_2)^{2+}$ (Garrels and Christ, 1964). Uranyl compounds are readily transported in water, and so readily leached from soil. When uranyl ions encounter reducing agents, such as organic matter, uranium changes to $U^{4+}$, precipitating uraninite. However, the speciation of uranium is complex and dependent on the presence of other elements, such as Si, C, and Fe.

Hydrogen sulphide $H_2S$ is an acidic reducing agent common in waterlogged environments. While uranium is generally precipitated under these conditions, radium is mobilised.

Potassium, although highly soluble as an ion, is relatively stable as a compound. Strong reducing conditions are required to mobilise potassium ions from potassium-

bearing rocks. This is generally accomplished via plant roots, which generate reducing agents to absorb the ions. The ions are then returned to soil on the death of the plant.

### 3.4.2 Organic matter

Organic matter plays a pivotal role in the formation of soils. The chemicals generated, consumed, rejected, and re-circulated by vegetation change the chemical properties of soil. These interactions are as equally important to radionuclide distribution as to any other elements in the soil. In general, the presence of organic matter reduces the mobility of radionuclides (O'Dea and Dowdall, 1999). However, under different Eh/pH conditions radionuclide solubility can be changed, increasing mobility.

Organic matter acts as a reducing agent in most soils. In the presence of organic matter, uranium forms insoluble $U^{4+}$ compounds, which accumulate in the organic matter. However, should the organic matter produce $CH_4$ or $H_2S$ acids, the uranium will be preferentially adsorbed onto silicate and oxide surfaces (Hem, 1985), while radium will be mobilised and potentially leached away from the organic matter.

As mentioned previously, thorium and potassium in rocks are relatively insoluble. Concentrated chemicals released at the root-soil interface are required to mobilise these radionuclides (Langmuir and Herman, 1980). Subsequently, thorium can be mobilised from rock and locked in the root zone until the death of the plant; while potassium is stored in the plant and remobilised to the topsoil following the death of the plant.

### 3.4.3 Sesquioxide and carbonate content

Sesquioxides, weathered clays including $Al_2O_3$ and carbonates are common components of soil. Potassium ions readily adsorb to the surface of sesquioxides. Although with changing soil conditions, potassium can be released from the clay surface and remobilised.

Thorium is receptive to sesquioxide and carbonate content, with both materials adsorbing and accumulating thorium. This results in an increase in thorium in upper soil horizons or wherever sesquioxides and carbonates reside.

Uranium is also accumulated by sesquioxides. In carbonate rich soils, uranyl-carbonate anions are more mobile than radium, which can induce uranium disequilibrium in carbonate rich soils.

## 3.5 Conclusions

'Radiometric data' is a colloquial term used to describe gamma ray spectrometry data acquired for assessing spatial distribution of radiometrics. The interpretation of radiometric data for soil mapping employs similar interpretation skills used in other spatial geosciences, such as aerial photography or remote sensing. However, the significance of a radiometric response is not based on the concentration of potassium, thorium, and uranium alone, but is determined with respect to:

- the surrounding radiometric responses,
- the patterns expressed through the radiometric imagery,
- the geomorphology of the landscape, and
- *a priori* knowledge including soil formation history in the area and soil samples.

The links between radionuclides, their movement, and local environmental conditions are well established (Talibudeen, 1964). Landscape processes including erosion/deposition (particle re-distribution), leaching, and wet and drying cycles are influenced by and in turn influence soil characteristics such as redox state and sesquioxide, carbonate, and organic matter content. The cumulative effect of these processes results in changes to the mobility, distribution, and final concentration of radionuclides in the landscape. Thus changes in soil characteristics and local environmental conditions can be expressed as a function of the distribution and concentration of radionuclides, as subsequently reflected in radiometric imagery.

# Chapter 4 - Development of a new multispectral processing methodology

This chapter develops a multispectral processing methodology to improve data analysis of 256-channel data, and explores the significance and relationships between the modified channels with respect to improving soil mapping.

## 4.1 Background

The Exploranium 256-channel NaI (sodium-iodide) gamma ray spectrometry system is the most common radiometric system used in Australia. Single 4 litre NaI crystals are used to measure radiometric response from ground based systems, while a combination of 4 litre packs, usually totalling 32 litres, are used for measuring the response in airborne platforms. As similar spectrometry systems are used for ground and airborne acquisition, the same data calibration and processing methods are employed. These methods are summarised in Appendix A.

The systems are generally programmed to measure gamma ray emission energies between 0 MeV and 3 MeV at 1 second intervals. Gamma ray response is grouped by energy increments of around 11.7 keV, or 256-channels for the full spectrum. The total number of gamma rays recorded in each channel is referred to as the channel count. A typical raw spectrum derived from the 256-channel count is shown in Figure 4.1.

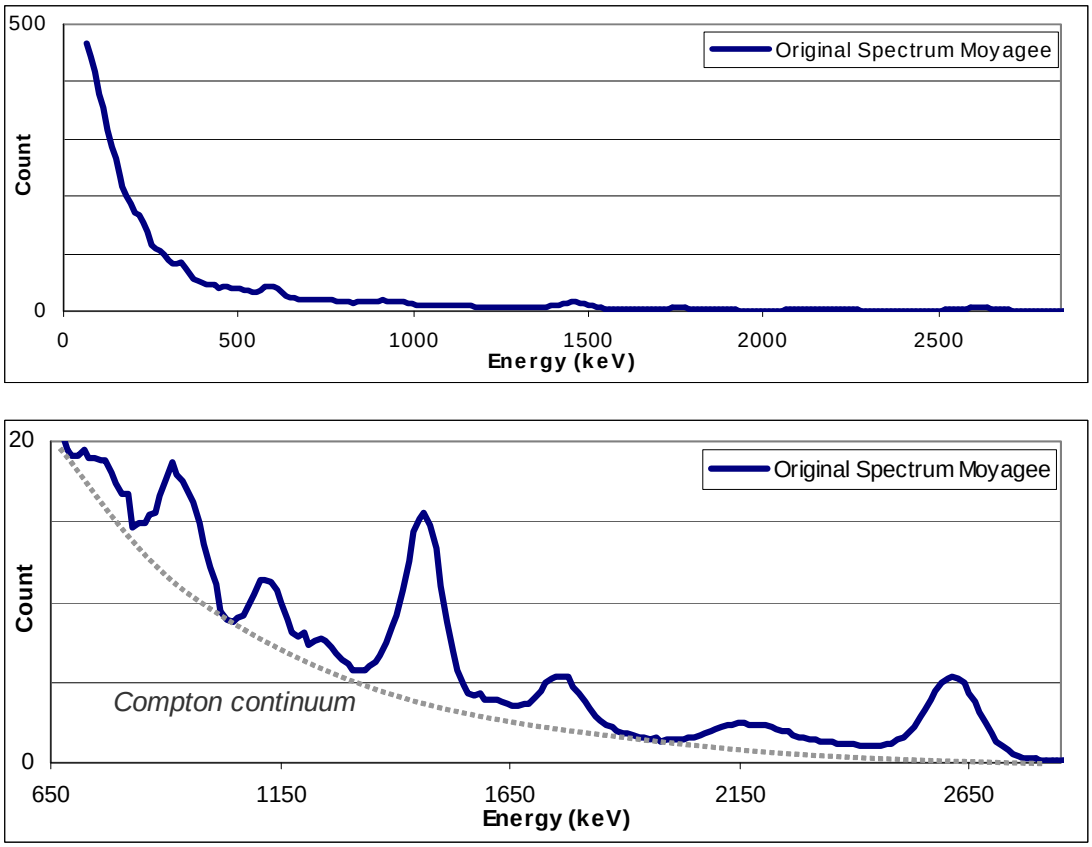


**Figure 4.1. Typical spectrum for 256-channel gamma ray spectrometer (top) and the same spectrum at a different scale to highlight significant content of the spectrum (bottom).**

The general, decreasing slope of the spectrum is the Compton continuum. It is a product of the Compton scattering of the gamma radiation before detection. Compton scattering occurs when individual gamma ray emissions interact with electrons causing the gamma ray to transfer energy to the electron and alter its trajectory. Multiple interactions lead to multiple scattering events, reducing the energy of the gamma ray with each interaction. The cumulative result of the scattering process, the Compton continuum, as observed in the 256-channel spectrum, is as a non-linear ramp of decreasing energy and counts.

At the lower energies, the spectrum is marked by a sharp increase in counts. The increase is a combination of the Compton continuum and bremsstrahlung. The bremsstrahlung results from x-radiation produced when an electrically charged particle is slowed down by the electric field of an atomic nucleus, and is associated with the decay of $^{40}$K. For more information on basic radioactivity refer to Appendix A.

The shape of the Compton continuum and bremsstrahlung are influenced by the properties of the radioactive source and the materials between the source and the detector. However, to isolate the full, non-scattered energy emissions and better characterise the source of the radioactivity, the Compton continuum and bremsstrahlung must be separated from the spectrum.

In controlled gamma ray measurements, the radioactive background can be calibrated and removed from the sample spectra, thereby isolating the spectrum of the source. However, in a radiometric survey, the sampled spectra are a composite of a continually moving sensor with an ever changing source and background. This produces a significant number of unknown factors.

The number of unknowns, including: background, source, source-to-receiver geometry, and finite sampling period (usually 1 second), limit the methods suitable to remove the unwanted energies. At present, the standard processing methodology, described in Appendix A, is the most robust method available. This method enables a full energy peak from each of the potassium-40, thorium-232, and uranium-238 decay series to be resolved; and through calibration, converted into equivalent ground concentrations. Thus, in using radiometric data to map soils, past studies have examined how radionuclide concentration defines soil and soil units.

There are a range of pedological and geomorphological processes that influence radionuclide concentration and distribution, as discussed in Chapter 3, and by extension, a number of ways through which different decay products interact with the environment. While disequilibrium conditions are the most recognised influence of the environment on the decay series, how this condition may be used to identify soil properties has not been explored. In addition, while the response of gamma rays to physical interactions with matter has been studied (Adams and Dams, 1970), how these interactions may be used to passively map changing soil characteristics and local environmental conditions is an emerging field of study (Cruvinel and Balogun, 2006).

However, to use the interaction of gamma rays as a tool to map soil characteristics or local environmental conditions, or at least changes to these characteristics and

conditions, characteristics of the gamma ray interactions must be captured in the radiometric data. Moreover, for the technique to be financially viable for mapping applications, the response must be captured in available 256-channel radiometric data. Thus a new approach to analysing the 256-channel data was developed, with the objective of isolating emission peaks that may lead to the characterisation of gamma ray interaction.

## 4.2 Multispectral analysis

### 4.2.1 Hull removal

A significant proportion of the total 256-channel response is derived from the Compton scatter of gamma rays and bremsstrahlung. When trying to separate individual gamma ray peak responses from the 256-channel spectrum these energies act as a source of coherent noise, and must be removed from the individual 256-channel spectrum readings to create a peak spectrum.

It is possible to model the Compton continuum and bremsstrahlung of a spectrum using inversion techniques, using the spectrum of major contributing radionuclides potassium, thorium, and uranium (Minty, 1998). However, the computation time for a standard survey of over 50,000 sample points is excessive and due to the absence of calibration data, the results would still contain some error. Instead, a simple hull removal technique was developed here.

The hull was derived by calculating a decreasing negative gradient based on the local minima of the spectrum, as illustrated in Figure 4.2. Although this represented only a generalisation of the Compton continuum and bremsstrahlung contribution, the hull removed the most significant proportion of the Compton continuum and bremsstrahlung from the 256-channel spectrum, enabling direct gamma ray emission peaks to be resolved with the smallest fraction of noise. Mathematically, this hull could have been represented by the first derivative of the data. However, spurious values in the data significantly distorted the shape of the curve when testing this approach. The Matlab code used to separate the hull response from the peak response is presented in Appendix B.

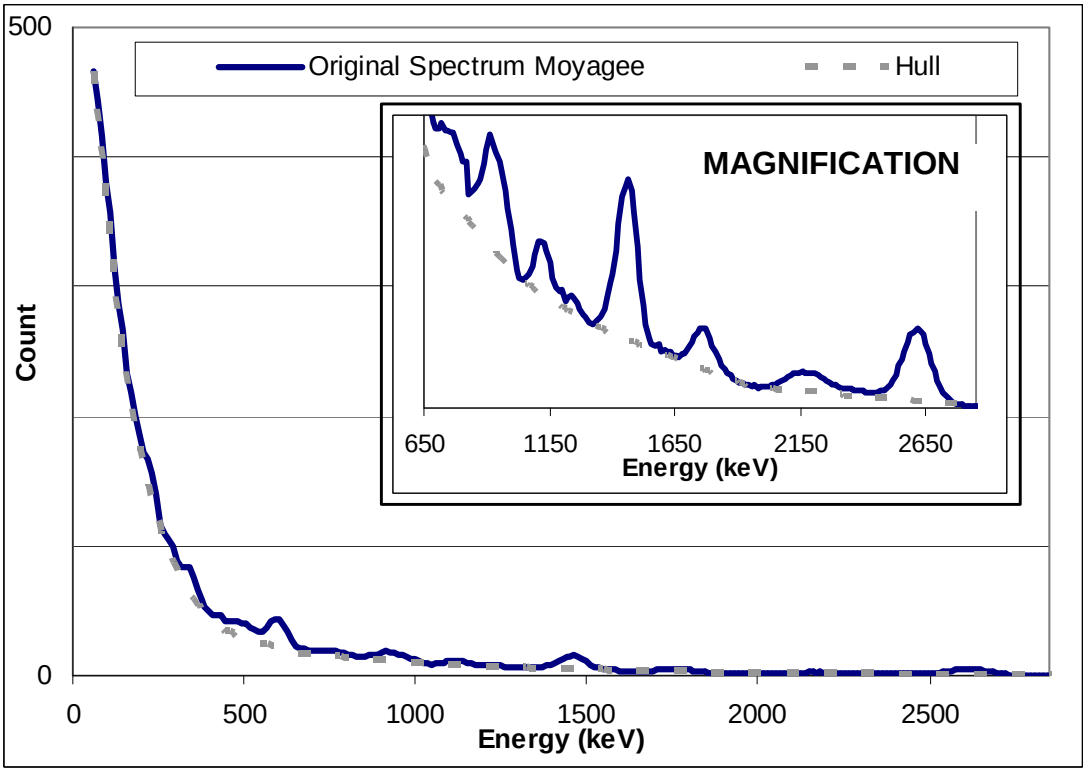


**Figure 4.2. Hull (shown in grey dashed line) derived from a sample of 256-channel radiometric data. The insert provides a magnification of the image for higher radiometric energies.**

The proportion of the continuum removed by the hull is dependent on the energy resolution of the spectrum. The energy resolution is a measure of detector's ability to distinguish between two gamma rays of slightly differing energy (IAEA, 2003). As the resolution of the standard radiometric system is less than 100%, occasionally incoming radiation will be incorrectly recorded, producing an artificially higher count in one channel and an artificially lower count in the neighbouring channel. Depending on where in the spectrum the error occurs, the artificially lower count may form an erroneous local minimum. When data is processed using the hull program, the erroneous minima increases the gradient of the hull, thereby increasing the proportion of the continuum retained in the channel data, as illustrated in Figure 4.3.

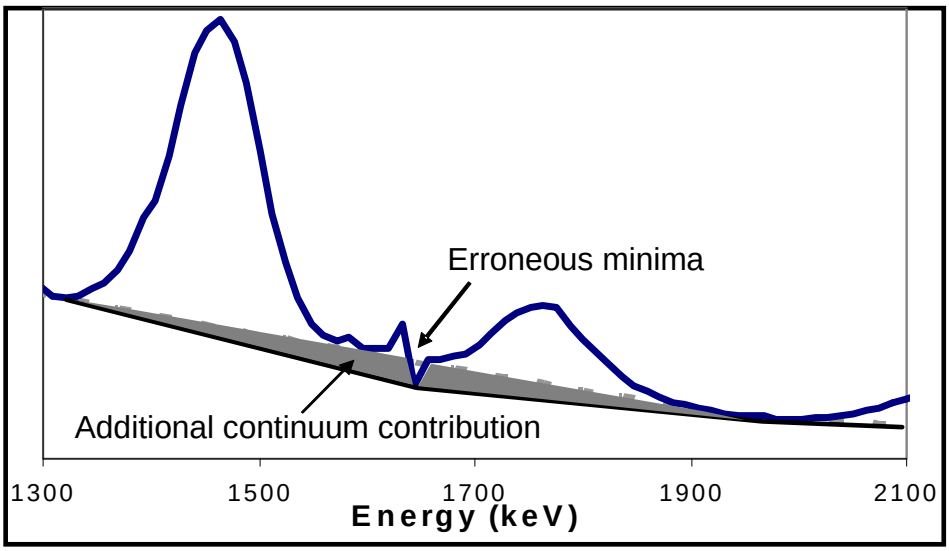


**Figure 4.3. The effect of erroneous data on the hull removal process. Erroneous data as a result of detector energy resolution can increase the contribution from the Compton continuum in the hull removal process. This increases the gradient of the hull, thereby increasing the proportion of continuum retained in the channel data.**

As the hull removal process is applied to each survey sample spectra independently, and the location of the erroneous data is random, so the random increase in Compton continuum is relatively insignificant. However, in data that is particularly noisy, the cumulative effect of these small errors is a nonlinear increase in average radiometric channel counts, as illustrated in Figure 4.4. When the channel counts from the peaks are compared during interpretation, the increased Compton contribution in the noisy data can change the interpretation of the data. However, the application of a spectral smoothing filter, as regularly used in standard 256-channel processing, reduces spectral noise thereby reducing erroneous Compton contribution to the peak spectra.

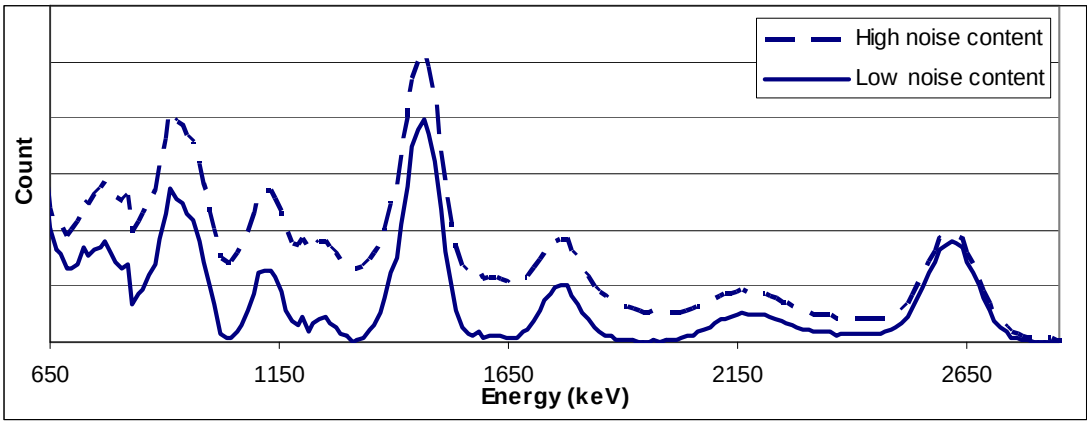


**Figure 4.4. Difference in average peak spectrum response between data with high and low noise content following hull removal. The cumulative effect of small errors generated during the hull removal process by data with high noise content is a nonlinear increase in average radiometric channel counts.**

### 4.2.2 Peak spectrum

As a result of hull removal, a number of spectral peaks were visible in the 256-channel data (Figure 4.5). The source of the peaks was determined using reference standards, such as *Scintillation spectrometry*, *Gamma ray spectrum catalogue* (Heath, 1964) for sodium-iodide crystals. The peaks are all the products of the decay of naturally occurring radioelements potassium-40, thorium-232, and uranium-238.

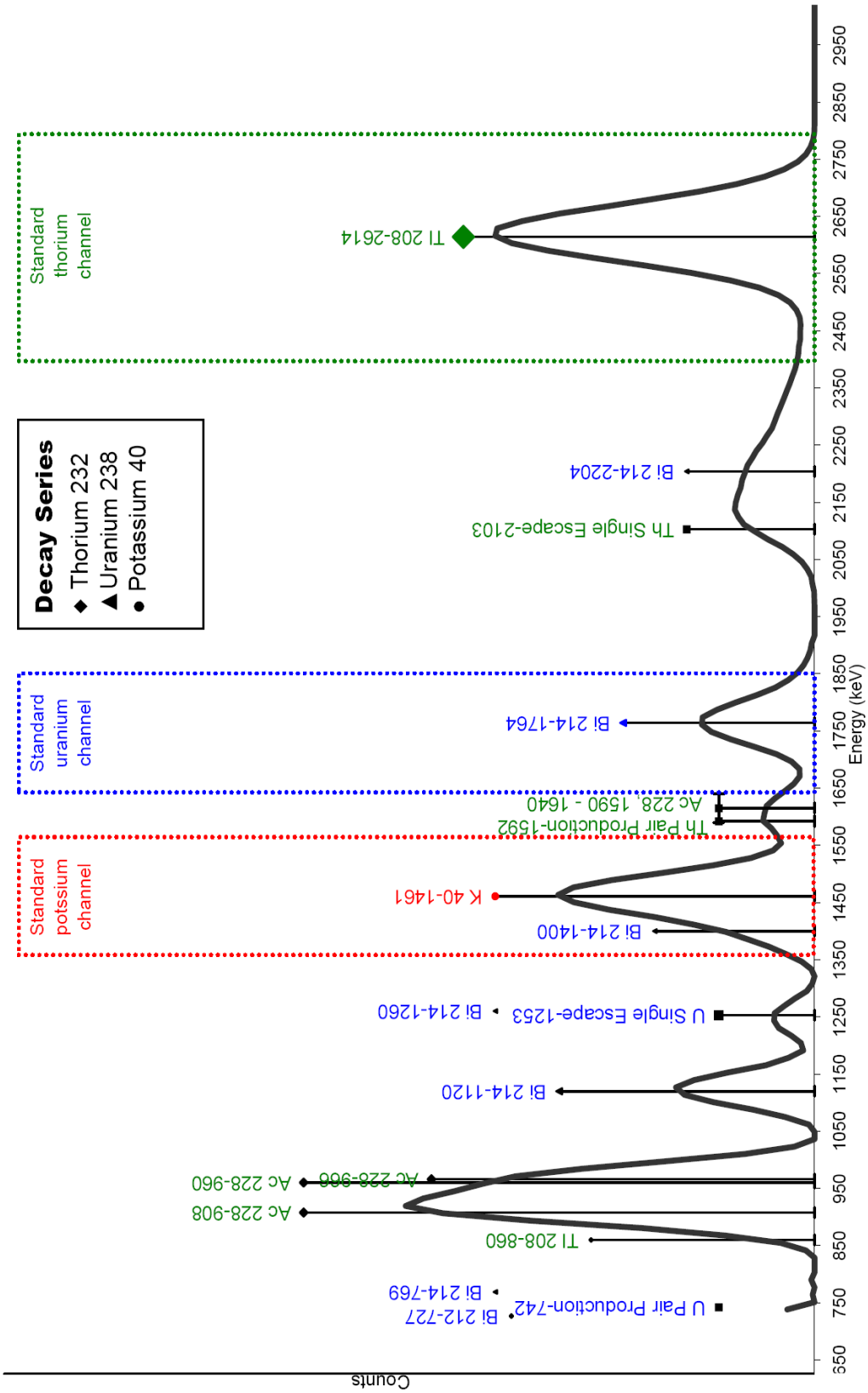


**Figure 4.5. Spectral peaks and their inferred source derived from 256-channel NaI radiometric data using the hull removal process.**

## 4.3 Multispectral analysis peaks

To test the veracity of the results, the hull removal process was applied to four data sets from Western Australia: airborne data from Yaragadee, Elashgin, and Moyagee, and ground data from Waroona. The acquisition specifications for the data sets and individual data spectra results before and after hull removal are presented in Chapter 6, Case Study 1. An average peak spectrum for the four data sets was calculated by summing the sampled spectra and dividing by the number of spectra. The average peak spectrum standardised to the $^{208}$Tl peak is shown in Figure 4.6.

In the Elashgin, Moyagee and Waroona datasets, channels 0 to 8, the equivalent of energies 0 keV to ~50 keV contained abnormal results, and were removed from the processing before application of the hull removal process. Channels 0 to 22, representing up to approximately 250 keV were not available for the Yaragadee dataset.

In the energy range <600 keV, the peaks were difficult to separate due to the close proximity of daughter product gamma ray energies, intermittent atmospheric radon gas emission energies, and Gaussian distribution of the peaks produced as an artefact of the detector response. Consequently, these complex areas were omitted from further analysis.

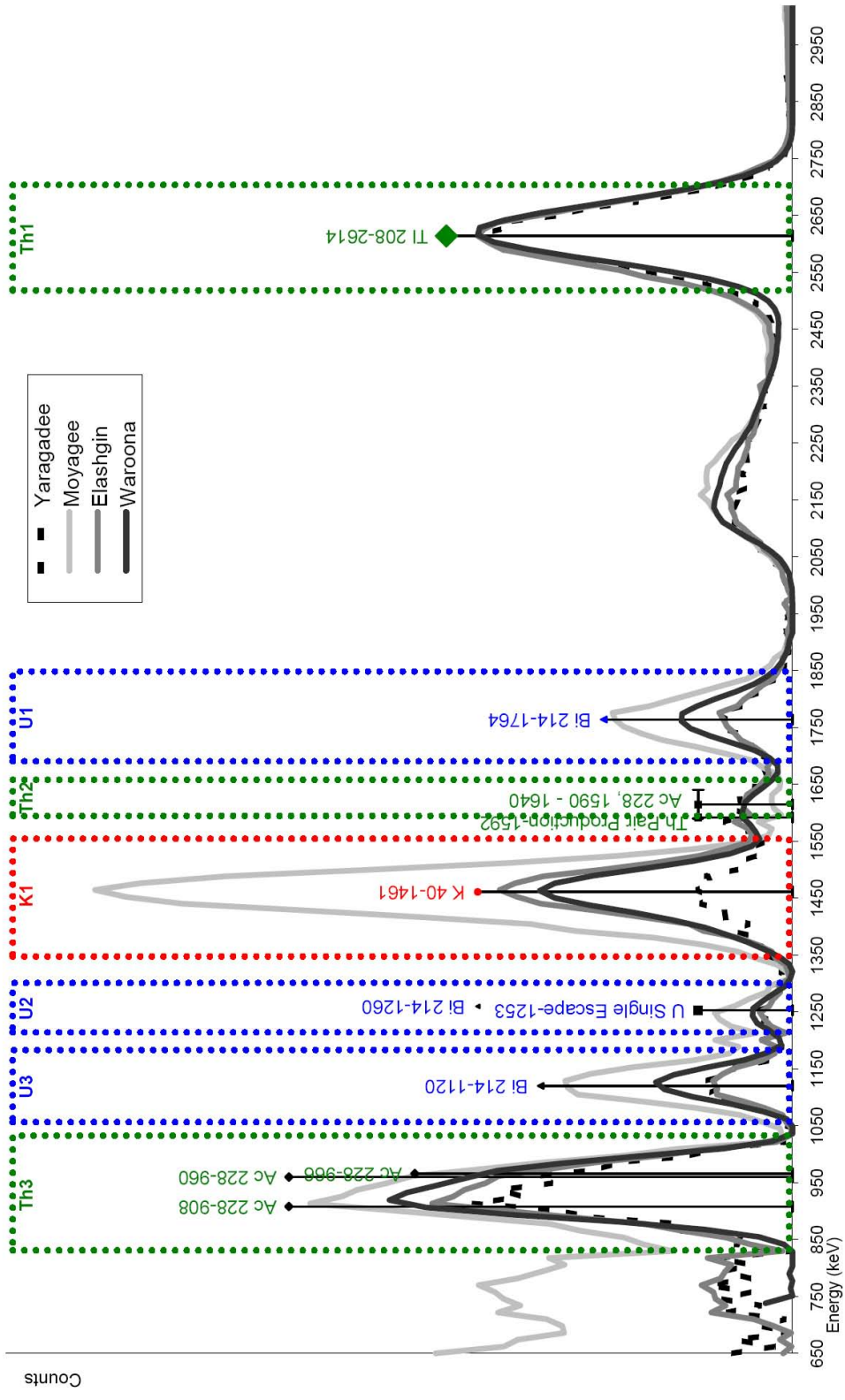


**Figure 4.6. Multispectral analysis peaks. Results from the hull removal process for the Yaragadee, Elashgin, Moyagee, and Waroona data sets shown as average peak spectrum standardised to the $^{208}$Tl peak, with their inferred source. Optimal peak energy windows are illustrated for thorium channels: th1, th2, and th3; uranium channels: u1, u2, and u3; and potassium channel: k1.**

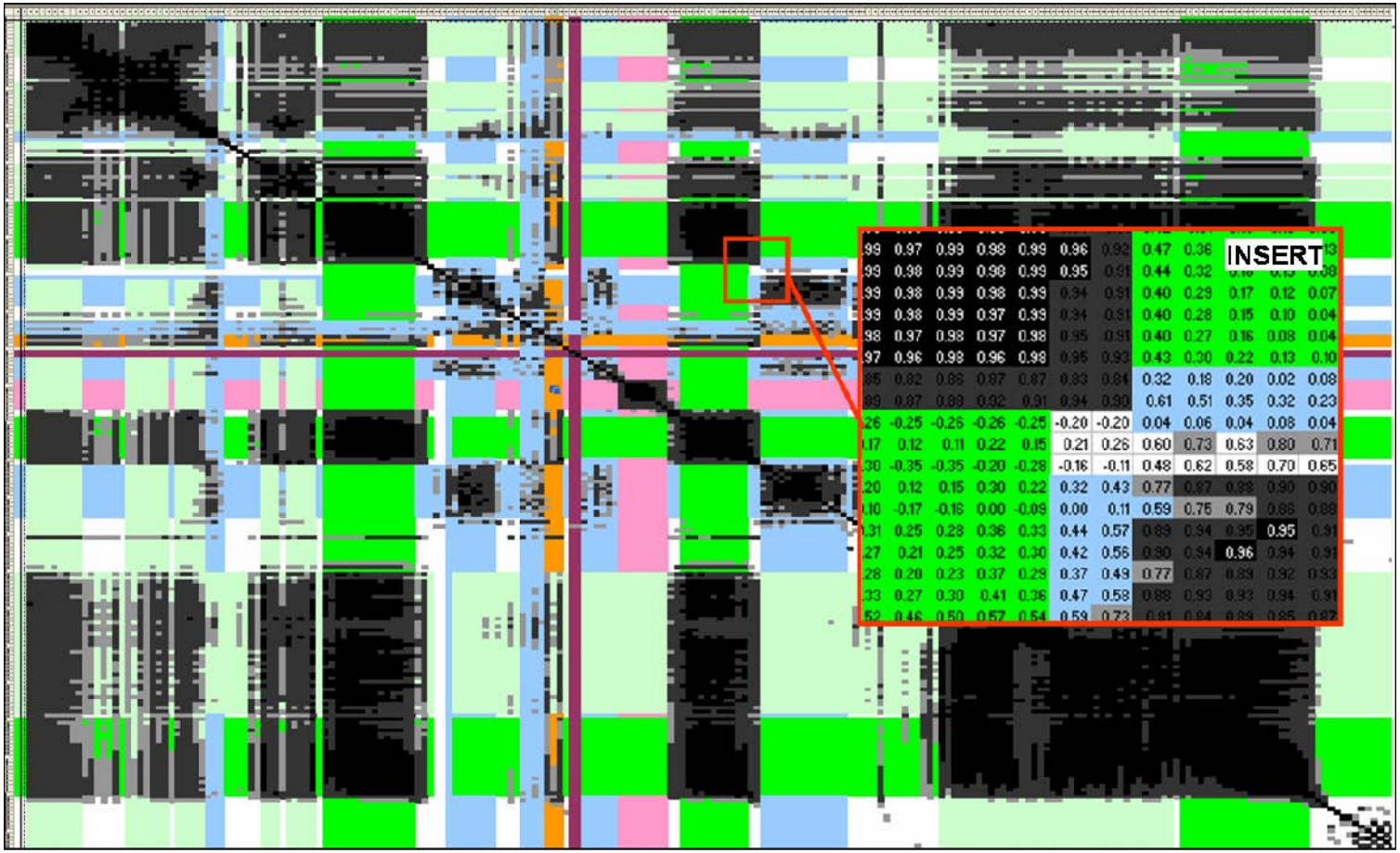


**Figure 4.7. Correlation matrix generated from 256-channel NaI radiometric data. In this example, the x and y axis contain the channels 1 to 256. The matrix is colour coded to highlight different trends between channels: green shades highlight thorium related emission energies, blue shades highlight uranium related emission energies, and pink shades highlight the potassium energies (accounting for energy resolution capability). Correlation values between the energies are subsequently overprinted in a separate colour code: 0.7-0.8 with a grey background, 0.8-0.9 with a dark grey background, and >0.9 with a black background with white font. An insert is provided to magnify the matrix content.**

In the energy range above 600 keV, seven distinct gamma ray energy peaks were resolved across all four datasets, as illustrated in Figure 4.6. Correlating to potassium, thorium, and uranium decay series emissions, the peaks include:

- $^{40}$K full energy peak at 1461 keV [potassium],
- $^{214}$Bi full energy peak at 1764 keV [uranium],
- $^{208}$Tl full energy peak at 2614 keV [thorium],
- combined $^{228}$Ac full energy peaks at 908 keV, 960 keV and 966 keV [thorium],
- $^{214}$Bi full energy peak at 1120 keV [uranium],
- combined $^{228}$Ac full energy peaks at 1590-1640 keV [thorium], and
- $^{214}$Bi single escape energies at 1253 keV from pair-production reaction at 1764 keV [uranium] with influences from $^{40}$K 1461 keV Compton edge.

During the initial identification of the source of the emission, primary consideration was given to decay conversion probability, which is the probability that a specific daughter product will be generated from the parent nuclide. Correlation coefficients generated from the 256-channel data (Figure 4.7) confirmed the relationships between the thorium and uranium peaks. Correlation greater than 0.7 between channels was established only where energies were predicted to relate to thorium or uranium decay series gamma ray emissions, allowing for Gaussian scattering. Potassium, which has emission energy of 1.460 MeV and no daughter products, showed little correlation with other channels, except where the potassium was known to occur with uranium naturally in the environment, and in such cases the correlation remained below 0.8.

As mentioned previously, the sodium-iodide detector has limited resolution and is not totally efficient. This results in a scattering of incoming energy away from its true energy in a Gaussian distribution. To improve the statistics of the peak data, the channels at either side of the energy peak were aggregated, creating peak energy windows. The peak energy windows are illustrated in Figure 4.6.

For the seven peaks identified, peak energy windows were created to incorporate 90% of the predicted Gaussian scattered energies, based on the observed shape of the peak. The observed peak shape was used in preference to the mathematically predicted Gaussian distribution range, which is used to determine the peak energy windows in the standard processing methodology, as the peak shapes were observed

to change slightly from dataset to dataset. The window widths used to define the peak counts for each area are listed in Table 4.1. The peak counts were then gridded using a minimum curvature algorithm to facilitate spatial analysis. Examples of such images are presented in Chapter 6, Case Study 1.

**Table 4.1. Window widths used to establish peak data channels in the Yaragadee, Elashgin, Moyagee and Waroona datasets.**

| | Energy (keV) | | | | |
|---|---|---|---|---|---|
| **Peak** | **Yaragadee** | **Elashgin** | **Moyagee** | **Waroona** | **Optimal Window** |
| Th3 | 866-1009 | 854-1009 | 878-997 | 868-977 | 867-1003 |
| U3 | 1081-1165 | 1081-1165 | 1081-1165 | 1075-1165 | 1081-1165 |
| U2 | 1237-1285 | 1225-1285 | 1225-1285 | 1204-1295 | 1225-1285 |
| K1 | 1416-1524 | 1416-1524 | 1416-1524 | 1399-1515 | 1416-1524 |
| Th2 | 1608-1644 | 1608-1644 | 1608-1644 | 1567-1671 | 1608-1644 |
| U1 | 1716-1824 | 1716-1824 | 1716-1836 | 1722-1826 | 1716-1825 |
| Th1 | 2542-2698 | 2530-2698 | 2554-2698 | 2551-2694 | 2547-2698 |

## 4.4 Physical significance of the multispectral peaks

The physical and chemical environment surrounding a radioactive source can change the way the source and its decay products behave in the environment. In addition, the physical location of the source in the soil profile, the soil moisture content, soil density and many other factors influence the gamma ray emission response as detected at the surface. The following sections describe the physical relationships that exist between the identified gamma ray emissions, with respect to their application for mapping soil/regolith characteristics and local environmental conditions. Spatial relationships between the seven peak channels in light of these observations are explored in Chapter 6.

### 4.4.1 Uranium peaks

Three of the peaks isolated by the multispectral analysis are related to the uranium-238 decay series:

- $^{214}$Bi full energy peak at 1764 keV [uranium];
- $^{214}$Bi full energy peak at 1120 keV [uranium]; and
- $^{214}$Bi single escape energies at 1253 keV from pair-production reaction at 1764 keV [uranium] with influences from $^{40}$K 1461 keV Compton edge.

Gamma ray emissions of 1120 keV and 1764 keV are produced from the same decay reaction and have the same probability of emission during decay. Thus they should produce equal intensities, a 1:1 ratio. However, the lower 1120 keV energy is more susceptible to backscattering and normal Compton scatter than the stronger 1764 keV energy. The probability for scatter to occur is correlated to the density and thickness of the absorber (Adams and Dams, 1970). In natural settings, the absorber is soil and/or bedrock. Consequently, as density or thickness of the soil and/or bedrock increases, the probability of scatter increases. Thus changes in the 1120:1764 ratio may indicate changes in soil thickness and/or density.

The single escape energies at 1253 keV from pair-production reaction at 1764 keV are generated within the acquisition crystal and are consequently considered a systematic artefact. However, the spatial distribution of the single escape energy, as shown in Chapter 6, Case Studies and illustrated in Figure 4.8, demonstrates the response is not entirely random, but is proportional to the intensity of the incoming energy.

However, the 1253 keV window is also influenced by scatter from the $^{40}$K 1461 keV peak. As the intensity of scatter is proportional to the intensity of the original energy, $^{40}$K will contribute to the 1253 keV window when the intensity of the $^{40}$K channel is high.

As a result, the 1253 keV window represents a combination of high ground concentrations of uranium 1764 keV and potassium 1461 keV. While these characteristics are, in general, not representative of soil characteristics or local environmental conditions, the data does make an interesting contribution to contrast

and colour range when incorporated with the uranium 1120 keV and 1764 keV windows in a ternary image, as illustrated in Figure 4.8.

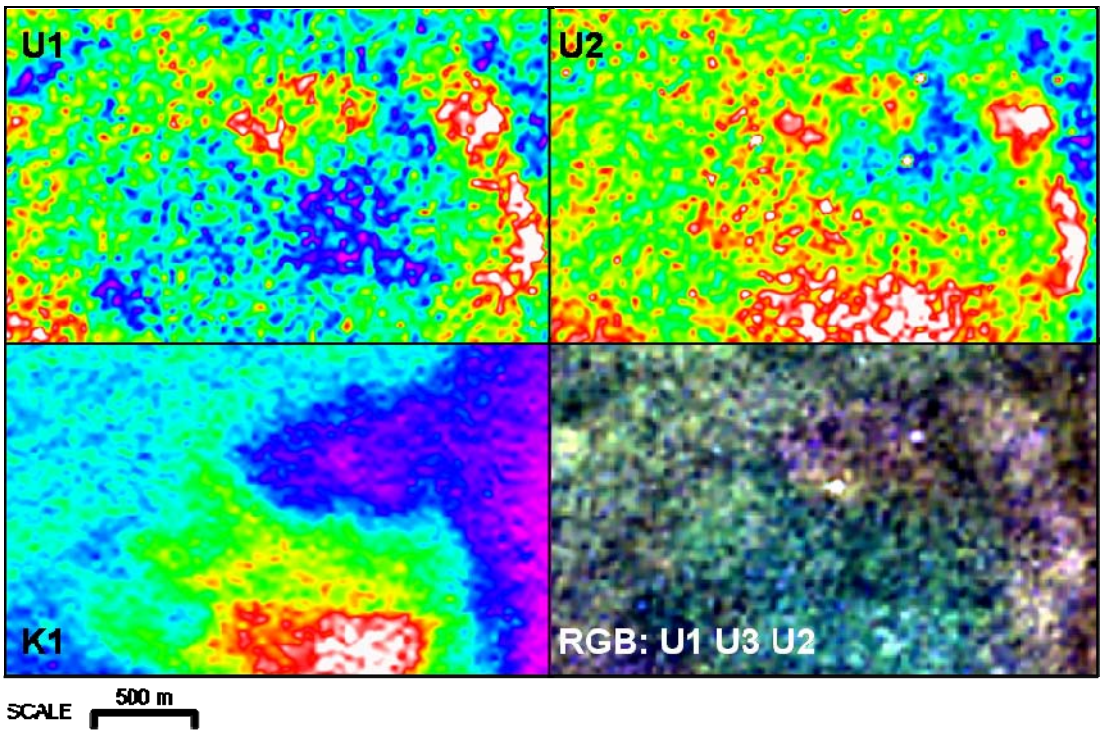


**Figure 4.8. Estimating changes in soil properties using the 1120 keV to 1764 keV uranium ratio. Attenuation differences in the spatial patterns between 1764 keV (U1) and 1120 keV (U2) gamma ray emissions are possibly related to physical characteristics of the soil, such as soil thickness and/or density. Caution must be applied, however, as the 1120 keV channel (U2) can be contaminated by scattered energy from potassium decay (K1). Nevertheless, the uranium channels presented as a ternary image (RGB: U1 U3 U2) provide interesting spatial patterns for interpreting changes in soil characteristics or local environmental conditions. Data from Elashgin, Western Australia.**

**(U1) Pseudocolour image (white high, purple low) of $^{214}$Bi full energy peak at 1764 keV.**

**(U2) Pseudocolour image (white high, purple low) of $^{214}$Bi single escape energies at 1253 keV.**

**(K1) Pseudocolour image (white high, purple low) of $^{40}$K full energy peak at 1461 keV.**

**(RGB: U1 U3 U2) Uranium ternary image: $^{214}$Bi full energy peak at 1764 keV [red], $^{214}$Bi single escape energies at 1253 keV [blue], $^{214}$Bi full energy peak at 1120 keV [green].**

### 4.4.2 Thorium peaks

Three of the peaks isolated by the multispectral analysis are related to the thorium-232 decay series:

- $^{208}$Tl full energy peak at 2614 keV [thorium];
- combined $^{228}$Ac full energy peaks at 908 keV, 960 keV and 966 keV [thorium]; and
- combined $^{228}$Ac full energy peaks at 1590-1640 keV [thorium].

Full energy peak $^{208}$Tl is produced towards the end of the thorium-232 decay series and is used to determine the equivalent ground concentration of thorium in standard radiometric processing. The $^{228}$Ac is produced earlier in the thorium-232 decay series, approximately 1.9 years before the formation of $^{208}$Tl. Because the age difference and the half life of the daughter products in between the thorium peaks are relatively small, it is assumed that the two decay energies are in equilibrium. However, as illustrated in Figure 4.9, the spatial distribution and intensity patterns are not necessarily identical.

Instead, the distribution of $^{228}$Ac appears to vary under different soil characteristics and local environmental conditions. While the reasons for the difference have not been fully investigated in this project, it is possible that the loss of gaseous intermediate daughter product $^{220}$Rn or reactivity of other intermediary daughter products with the soil may induce disequilibrium conditions. Even if the difference observed between the $^{228}$Ac and $^{208}$Tl peaks is only a function of the displacement of $^{208}$Tl further up or down the soil profile, the change in the peak response ratio provides a link to changing soil characteristics or local environmental conditions.

It was difficult to establish a direct relationship between the combined $^{228}$Ac full energy peaks at 1590-1640 keV and soil characteristics and local environmental conditions, as the relationships between this channel and others multispectral channels differed for each Case Study. This observation has implications for standard processing, as discussed in the following section. However for the purposes of identifying changes in soil and moisture conditions, the combined $^{228}$Ac full energy peaks at 1590-1640 keV contributed to the formation of the thorium ternary image, illustrated in Figure 4.9c.

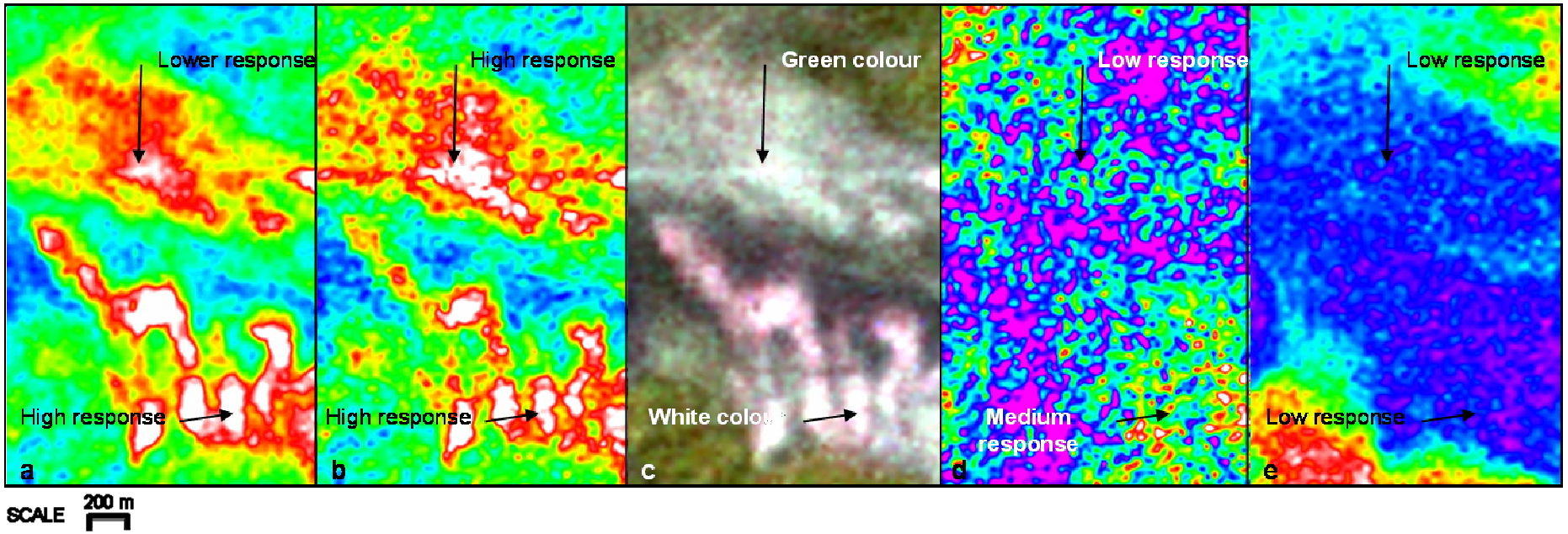


**Figure 4.9. Spatial patterns in selected multispectral channels. In (a) $^{208}$Tl response in the anomaly to the north is lower than the anomaly to the south, while in (b) $^{228}$Ac responses are approximately the same. As a result, in the combined thorium ternary image (c) the bodies are clearly differentiated by colour and texture. Images (d) and (e) demonstrate the differences in the thorium anomalies are not a result of contamination from other radiometric sources such as uranium (d) or potassium (e). Data from Elashgin, Western Australia**

**a) Pseudocolour image (white high, purple low) of full energy peak $^{208}$Tl.**

**b) Pseudocolour image (white high, purple low) of combined full energy peaks of $^{228}$Ac 908 keV, 960 keV, and 966 keV.**

**c) Thorium ternary image: $^{208}$Tl 2614 keV [red], $^{228}$Ac 1590-1640 keV [blue], and combined $^{228}$Ac 908 keV, 960 keV and 966 keV [green].**

**d) Pseudocolour image (white high, purple low) of uranium 1765 keV.**

**e) Pseudocolour image (white high, purple low) of potassium 1461 keV.**

## 4.5 Implications to standard processing

### 4.5.1 Separation of $^{228}$Th from thorium-232

In standard processing, the contribution of Compton scatter and daughter decay emission from the thorium-232 decay series in the potassium and uranium channels is calculated as a percentage of the $^{208}$Tl 2614 keV count rate from a known concentration of thorium-232 decay in equilibrium and subtracted from the total channel count. However, as illustrated in Figure 4.10, the relative contribution of thorium to the potassium and uranium windows would change if the $^{228}$Th daughter product was separate from $^{232}$Th.

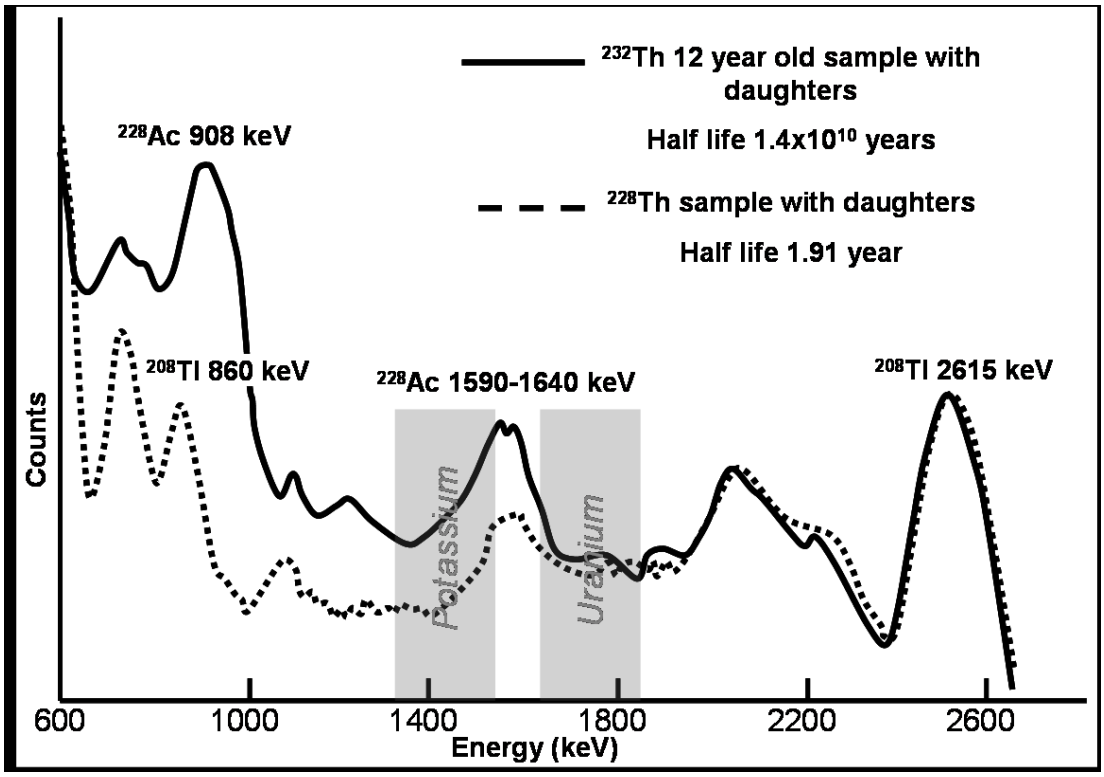


**Figure 4.10. Gamma ray response of $^{232}$Th and daughter product $^{228}$Th for a NaI spectrometer. The fraction of thorium within the potassium and uranium channels relative to $^{208}$Tl 2615 keV is different for the two thorium decay sequences.**

The most probable scenario for the separation of these elements is as a result of increased solubility of the intermediate daughter product $^{228}$Ra. With a half life of 5.75 years, it is possible for the $^{228}$Ra to be dissolved or adsorbed to fine fractions in the soil and leached through the soil profile (refer to Chapter 3). The deposited $^{228}$Ra will decay to $^{228}$Ac (the half life of $^{228}$Ac is 6.13 hours). However, once the $^{228}$Ra

source is exhausted, detectable gamma radiation in the area of deposition would be confined to the $^{228}$Th decay series for the remainder of the cycle.

Hence, by varying the solubility of $^{228}$Ra, soil characteristics and local environmental conditions influence thorium gamma ray response. And as a result, the count rate for the $^{208}$Tl 2615 keV window will not always accurately represent thorium content in the uranium and potassium windows. This will, in turn, produce inaccuracies in the calculation of equivalent potassium and uranium concentrations using standard processing techniques.

However, by using the $^{208}$Tl full energy peak at 2614 keV and combined $^{228}$Ac full energy peaks at 908 keV, 960 keV and 966 keV multispectral channels, it was possible to differentiate $^{208}$Tl and $^{228}$Ac distributions. If it is assumed that the lower $^{228}$Ac to $^{208}$Tl ratio is indicative of $^{228}$Th separation, it is possible to infer and monitor soil chemical and physical mobility and identify potential radiometric disequilibrium conditions.

### 4.5.2 Influence of $^{228}$Ac combined full energy peaks at 1590-1640 keV

The full energy peaks from the available 256-channel data demonstrated irregularities in the Gaussian distribution widths, predominantly in the uranium channel. The change in distribution width was particularly problematic for the uranium channel, as reduced distribution resulted in the inclusion of neighbouring $^{228}$Ac 1590-1640 keV peak energies in the uranium channel, as illustrated in Figure 4.11.

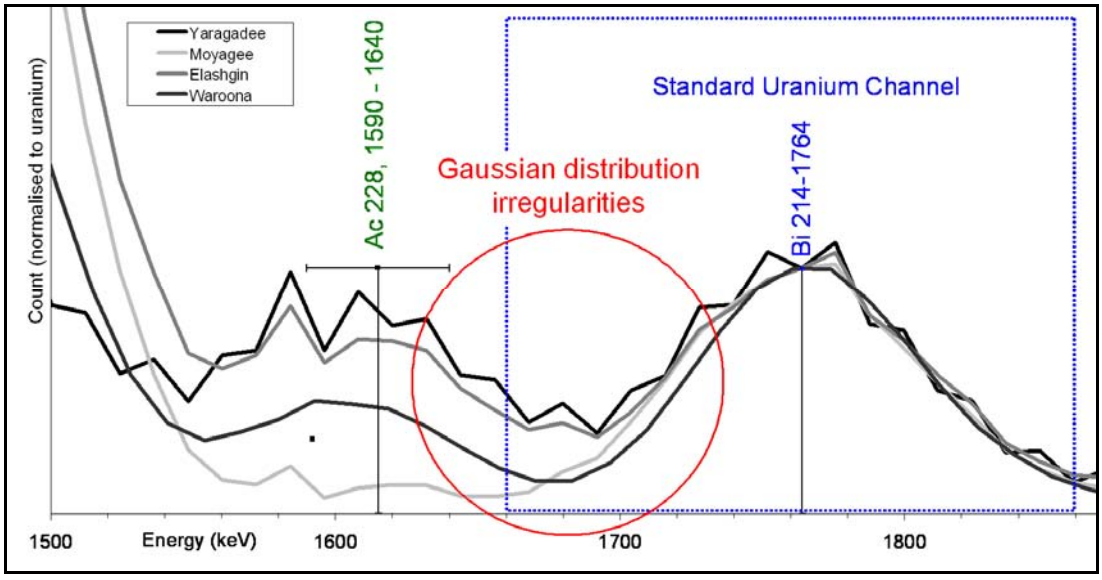


**Figure 4.11. Average peak spectrum normalised to uranium peak $^{214}$Bi 1764 keV for Yaragadee, Moyagee, Elashgin, and Waroona datasets. Irregularities in the Gaussian distribution of the uranium 1765 keV full energy peak result in the inclusion of neighbouring $^{228}$Ac 1590-1640 keV peak energies in the standard uranium radiometric processing channel.**

During multispectral processing, window widths were individually modified to accommodate the observed irregularities. However, in standard processing there is no mechanism available for changing the window widths. This leads to an undetermined, varying fraction of thorium $^{228}$Ac contamination in the standard final uranium data, in most cases within the accepted calibration error range. The contamination subsequently produces a subtle change in the spatial distribution and patterns of the uranium data, superimposing the thorium distribution patterns onto the uranium data, as evidenced by a reduction in colour range and contrast in the resulting ternary imagery. This situation is described in more detail in Chapter 6, Case Study 2.

## 4.6 Conclusion

A multispectral processing technique was developed in this study to isolate peak gamma ray energies from standard 256-channel NaI spectrometry data. This was achieved by using a hull, created from the decreasing, negative gradient of local spectrum minima as a surrogate for the Compton continuum and bremsstrahlung energy at each reading. By subtracting the hull from the original 265-channel

spectrum, the peak gamma ray anomalies present in the 256-channel data became emphasised.

The source of the anomalies can then be determined by comparing the peak energy against standard reference responses for sodium iodide crystals. Seven different gamma ray emissions were identified from the peak spectrum:

- $^{40}$K full energy peak at 1461 keV [source: potassium-40],
- $^{214}$Bi full energy peak at 1764 keV [source: uranium-238],
- $^{208}$Tl full energy peak at 2614 keV [source: thorium-232],
- combined $^{228}$Ac full energy peaks at 908 keV, 960 keV and 966 keV [source: thorium-232],
- $^{214}$Bi full energy peak at 1120 keV [source: uranium-238],
- combined $^{228}$Ac full energy peaks at 1590-1640 keV [source: thorium-232], and
- $^{214}$Bi single escape energies at 1253 keV from pair-production reaction at 1764 keV [source: uranium-238] with influences from $^{40}$K 1461 keV Compton edge.

Relationships between the identified gamma ray emissions were subsequently explored with respect to their application for mapping soil/regolith characteristics and local environmental conditions. The physical interaction of gamma rays and radionuclide behaviour in the environment were thought to provide indicators of soil characteristics or local environmental conditions in the following multispectral response:

- The ratio of uranium 1120 keV to 1764 keV has the potential to differentiate soil density and/or soil overburden.
- The ratio $^{208}$Tl full energy peak at 2614 keV to combined $^{228}$Ac full energy peaks of 908 keV, 960 keV and 966 keV has the potential to identify the separation of $^{228}$Th from $^{232}$Th, with associated changes to soil chemistry and water movement.

In addition, the combination of three uranium related channels and three thorium related channels enabled the production of new uranium and thorium ternary imagery. The additional imagery serves to highlight characteristics that were difficult to identify in standard processed imagery, as well as highlighting

changes in soil characteristics and local environmental conditions unique to their respective elements.

# Chapter 5 - Mapping methodology using multispectral processing

This chapter describes the methodology developed to interpret soil texture distribution, soil units, and soil type using radiometric data.

## 5.1 Introduction

As documented in Chapters 2 and 3, the relationship between radiometric response and soil type is not linear. Consequently, soil type is derived through interpretation of the radiometric response with respect to:

- surrounding radiometric responses,
- patterns expressed through radiometric imagery,
- geomorphology of the landscape, and
- *a priori* knowledge of soil type across survey areas, including soil formation history.

This can often amount to a considerable volume of information that cannot be readily digested by an interpreter. Automated classification systems and interpretation methodologies (eg Cook *et al.*, 1996a; Anderson-Mayes, 1999) have been developed to assist the interpretation process, predominantly by way of deriving data significance. Although currently, no singular classification or interpretation methodology is universally supported for deriving soil type for radiometric data.

The following methodology was developed and applied during this project to interpret soil type from high resolution, multispectral processed radiometric data. Full and partial interpretation results, derived using this methodology, are presented in Chapter 6, case studies 4, 5, and 6.

## 5.2 Soil classification

The classification methodology employed throughout this thesis was developed with the aim of isolating areas with similar radiometric response. Combinations of grouping/clustering techniques are used to isolate the units with similar radiometric

response. In combination with *a priori* information, the radiometric units are interpreted to determine the soil texture, soil units, and finally soil type; if sufficient information is available. A review of the contributing soil characteristics specifically applied to the production of soil texture and soil unit maps in this thesis is provided below.

### 5.2.1 Soil texture

Soil texture is a measure of the sand, clay and silt fractions in a soil layer (Leeper and Uren, 1993; Miller and Donahue, 1990). The sand, silt, and clay reflect the size of the particles, rather then the geological composition of the soil, as described in Table 5.1. These may be measured in the field through "sense of touch" techniques or through laboratory size measurements. Occasionally the percentage of organic matter will also be considered (Moore, 1998).

**Table 5.1. Definitions of textural fractions in a soil (after Leeper and Uren, 1993)**

| Fraction | Limiting Diameter | Conventional name |
|---|---|---|
| 1 | Greater than 2 mm | Gravel |
| 2 | 2 mm to 0.2 mm | Coarse sand |
| 3 | 0.2 mm to 0.02 mm | Fine sand |
| 4 | 0.02 mm to 0.002 mm | Silt |
| 5 | Less than 0.002 mm | Clay |

The soil texture is subsequently defined by the percentage of these fractions within the soil sample. The fractions as defined by Marshall (1947) and illustrated in Figure 5.1 were used within this thesis.

Soil texture has a direct influence on radiometric response through particle size and mineral radioactivity (refer to Chapters 2 and 3). Soil texture may also influence cation exchange capacity, such that adsorbed particle radioactivity can be evident in the radiometric response and assist in defining soil texture.

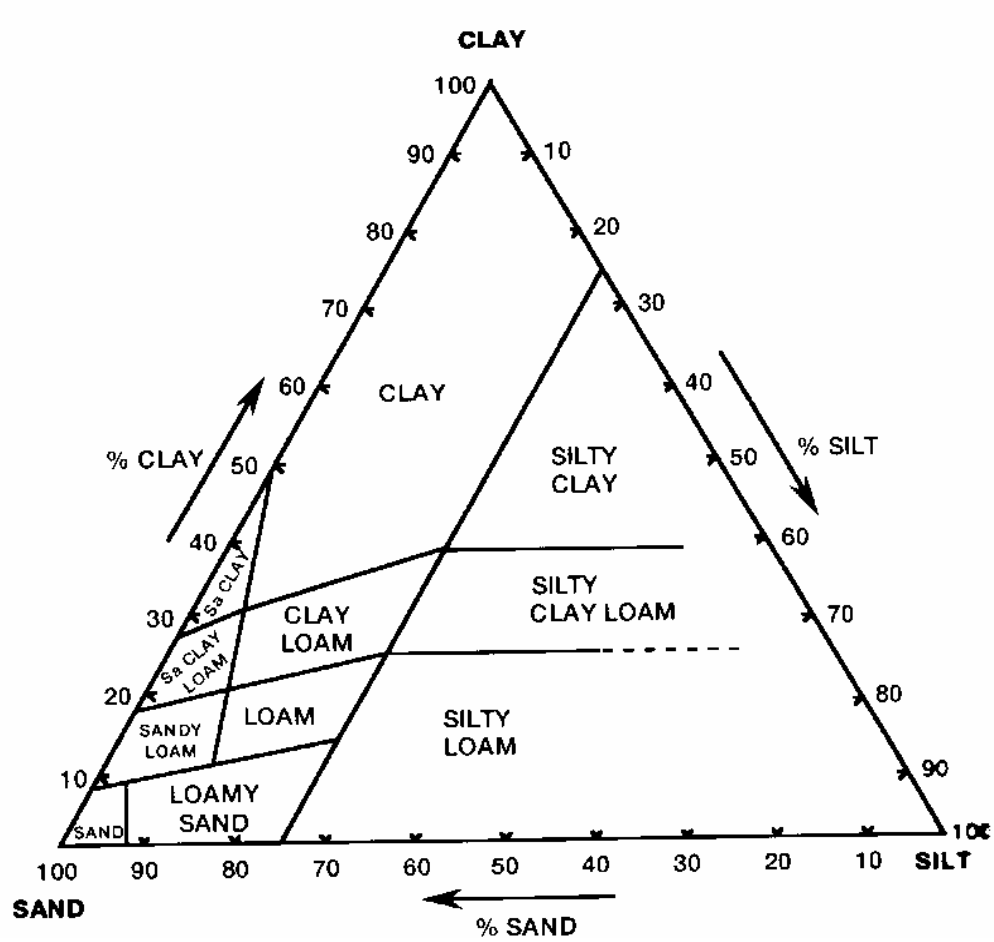


**Figure 5.1. Soil texture defined in terms of sand, silt and clay (after Marshall, 1947).**

### 5.2.2 Soil units

Radiometric response is the summation of radioactivity within the top 40 cm. However, within the top 40 cm of a soil profile, soil texture is not constant. In general, the soil profile within the top 40 cm can be divided into two or three texture layers:

- Layer A - approximately 0 cm to 10 cm that includes the bulk of the organic matter,
- Layer B - approximately 10 cm to 20 cm, and
- Layer C - approximately 20 cm to 40 cm.

Only two layers may be visible if A and B, or B and C layers are the same. Note that the layer names A, B, and C do not represent Australian standard soil horizons as described by Isbell (1997). The contribution of the radiometric response from each layer to the total radiometric response recorded at the surface is illustrated in Figure 5.2.

For soil mapping purposes when working with radiometric data, a soil unit is defined as an area with similar radiometric response and comparable soil layers. As the root zone for most plants is within the range of the radiometric response, radiometrically defined soil units are suitable in most land management situations where land use decisions are based on soil properties or soil type.

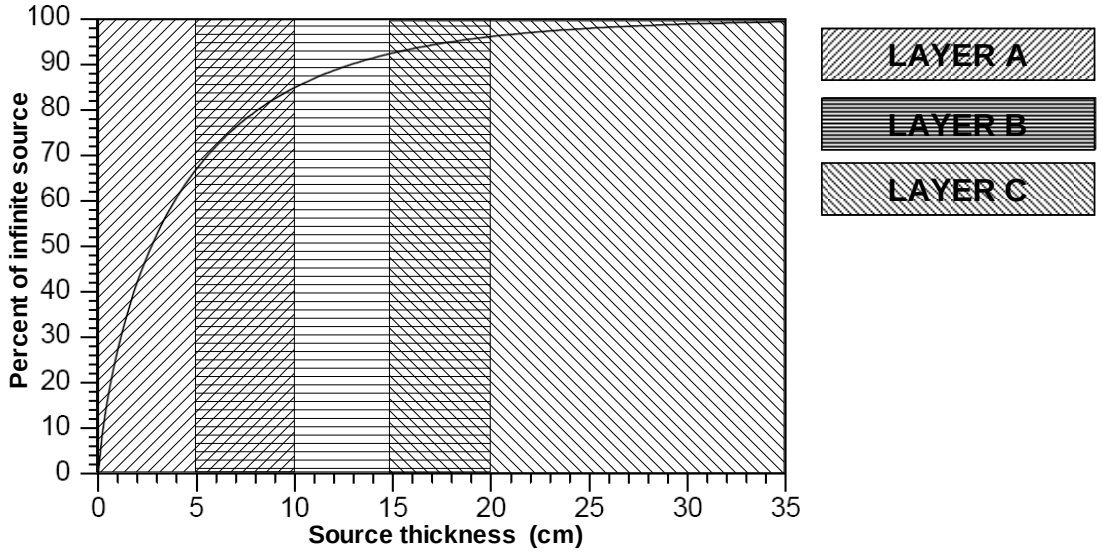


**Figure 5.2. Approximate percentage contribution from each soil layer to the total radiometric response. The soil profile, an infinite radiometric source, contributing to the total measured radiometric response was divided into three, variable layers A, B, and C. The soil layers are used to trace significant changes in soil properties with depth. The percentage provided on the y axis is an approximation only and will vary at each sample location. Illustrated percentage of infinite source curve produced from thorium gamma rays of density of 2.2 gcm$^{-3}$, from IAEA (2003).**

### 5.2.3 Soil maps

An understanding of the texture and textural differences between the layers helps to predict the behaviour of the soil under different local environmental conditions (Moore, 1998). Thus maps of soil texture derived from radiometric soil unit data can have an important role in land management where conventional soil maps at an appropriate scale are not available.

Maps of soil texture layers A, B, and C provide a simple method of examining subsurface textual trends within the data. The significance of the trends are subject to interpretation. However, the information contained in these maps may form the basis of additional GIS (Geographic Information System) interrogations and map

products such as water infiltration rates and waterlogging potential, water retention and repellence, and drainage management maps.

#### 5.2.3.1 Water infiltration rates and waterlogging potential

Water infiltration rates and waterlogging potential can be empirically determined from the relative percentages of clay, silt and sand, or textural soil type, within a soil. Water infiltration is faster when the pore spaces are large and permeability is high (Leeper and Uren, 1993). As illustrated in Figure 5.3, the larger diameter of sands and gravels result in larger pore spaces and therefore a higher porosity, while silts and clays form smaller pore spaces with lower porosity.

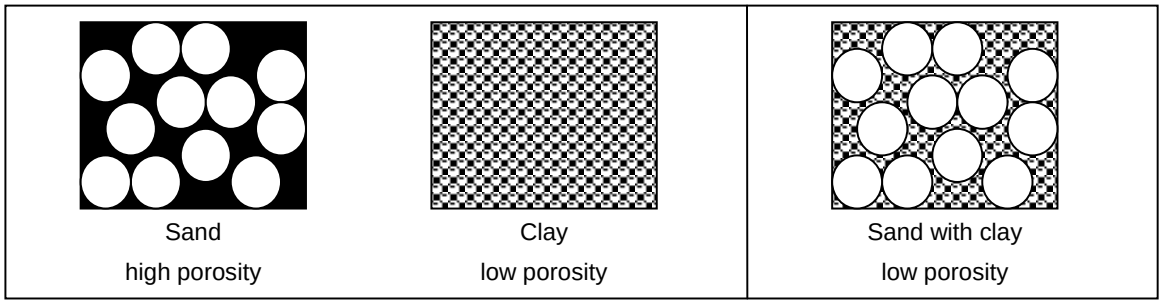


**Figure 5.3. Porosity relative to textural fraction. The white areas represent the soil particles, the black areas represent the pore space. Sandy soils generally exhibit high porosity, while clays exhibit low porosity. However, whenever clay is present the porosity is generally low.**

When both small and large fractions are present, the smaller fractions fill the large pore spaces, reducing porosity. The resulting clogged pores obstruct infiltration and reduce pore space connectivity, thereby reducing permeability.

Surface ponding and waterlogging occurs when inundation rate exceeds the infiltration rates and runoff is prevented by land morphology (Moore, 1998). An understanding of inundation or irrigation rates with respect to the textural composition of the soil provides an empirical, relative estimate of waterlogging potential. For example, high infiltration rates are found in sandy layers and low infiltration rates in clay rich layers. By extension, clay layers located in valley floors, where rainfall or irrigation rates are high, are the most likely soil units to become waterlogged.

Waterlogging within a soil profile can occur when successive soil layers possess lower infiltration and transmissivity rates. Rapid infiltration from high permeability at the surface will cause water to pool on underlying layers with lower transmissivity when there is insufficient capacity within the lower layer to accept the water. This is most likely to occur above a clay layer, which is characterised by low porosity and permeability. Alternatively, if the pore space within the lower layer is filled, water will pool or perch within the soil profile. When the saturating water is held within the soil profile for an extended period of time, the pool is referred to as a perched water table.

Perched water can provide a source of water for plant growth during periods of low inundation, but it can also reduce oxygen supplied within the soil. If the water is perched in the root zone, plant deaths will often occur. Thus the potential for a soil to become waterlogged is an import factor for land management. To assist in the land management decision process, an empirical system for comparing soils, the potential waterlogging index, was developed in this thesis. This methodology is presented to highlight the application of classified radiometric data for three dimensional, near surface modelling.

The potential waterlogging index established in this thesis was developed by intuitively assigning coefficients to different combinations of soil layer texture transitions based on field observations from Waroona, Western Australia (Table 5.2). For specific study areas, these values should be calibrated to observed, historical waterlogging and local soil types.

The potential waterlogging index represents the potential for a location to become waterlogged, should rainfall conditions produce waterlogging, as a result of a change in soil texture in the top 40 cm. Small changes in soil texture attract a lower index value and have lower potential to become waterlogged, while significant textural changes were given a higher index value, demonstrating a higher potential to become waterlogged. Within the radiometric classification process, soil waterlogging potential could be determined for the layer change A to B, and layer change B to C. The summation of these values is used to calculate the total soil waterlogging potential.

**Table 5.2. Potential waterlogging as a function of soil texture change. The potential for soil to become waterlogged is related to the capacity of the receiving body. If the pore capacity and permeability of the receiving soil is lower than the supplying soil, water will pond at the soil interface. When the pore space capacity of the receiving soil is significantly lower than the supplying soil, waterlogging will occur. As soil texture is a good representative of pore capacity within a soil type, the difference between the initial soil texture and the subsequent soil texture in the direction of water movement provides an empirical measure of waterlogging potential.**

| | | Initial soil texture | | | | | | |
|---|---|---|---|---|---|---|---|---|
| | | Sand | Loamy sand | Sandy loam | Loam | Sandy clay loam | Clay loam (friable clay) | Sandy clay |
| Subsequent soil texture | Sand | 0 | 0 | 0 | 0 | 0 | 0 | 0 |
| | Loamy sand | 0.5 | 0 | 0 | 0 | 0 | 0 | 0 |
| | Sandy loam | 0.75 | 0.5 | 0 | 0 | 0 | 0 | 0 |
| | Loam | 6 | 2 | 1 | 0 | 0 | 0 | 0 |
| | Sandy clay loam | 7 | 2.5 | 2 | 1 | 0 | 0 | 0 |
| | Clay loam (friable clay) | 8 | 6 | 5 | 3 | 2 | 0 | 0 |
| | Sandy clay | 9 | 8 | 7 | 5 | 4 | 1 | 0 |

#### 5.2.3.2 Water retention and repellence

Texture can also be linked to water retention and repellence. The clay minerals have properties that attract and hold water to their surfaces through adsorption (Donahue *et al.*, 1983). The textural fraction of clay is not equivalent to the percent of mineral clay in a soil. Clay minerals can be larger than 0.002 mm and non-clay minerals smaller than 0.002 mm. However, soils with a significant portion of clay minerals will possess a high textural clay fraction. Thus the percentage clay fraction or soil texture can be used as a surrogate for mineral clay percentage and therefore water retention. Conversely, soil textures with lower clay fractions, especially high percentages of sand, are more likely to develop water repellent soils.

#### 5.2.3.3 Drainage management

The movement of surface water across a farm or across a catchment is largely based on the infiltration and Manning's *n* roughness characteristics of the soil (Leeper and Uren, 1993). In agricultural areas where the land is largely cleared of native vegetation, these characteristics can be directly related soil texture. Soils with rough characteristics, such as gravels and sands, slow the movement of water across the surface. The high transmissivity of these soils results in rapid infiltration of the surface water, and reduces the volume of surface water runoff.

Surface water controls are considered to divert and deliver water to locations where surface water can be effectively managed, i.e. areas with low waterlogging potential. In areas where waterlogging potential is high, but surface textures are light (sandy), engineering options, such as intercept and tile drains (subsurface drains), may be required to capture and transport excess water to appropriate areas. In areas with high waterlogging potential, but dominantly clay textured soils, simple intercept and cutoff drains are the preferred option. Thus a simple drainage management map can be created from the radiometric soil unit information.

### 5.2.4 Soil type

As discussed in Chapter 3, soil type as defined by the *Australian Soil Classification* (ASC) (Isbell, 1997), is based on soil texture, structure, and chemical properties. However, often the key soil characteristics important to land management at a local scale are not well represented by ASC units and local soil type classification systems are employed instead (for example Moore, 1998; Cooper et al., 2001; GeoAg Pty Ltd, 2004). Radiometric data has a role to play in defining soil texture, and this links to soil erosion potential, water holding characteristics, and nutrient holding capability. Through detailed interpretation, radiometric data can also offer local information on landscape processes, including erosion/deposition (particle re-distribution), leaching, and wet and drying cycles. These conditions, in turn, influence soil characteristics such as redox state and sesquioxide, carbonate, and organic matter content. Consequently, in order for the radiometric classification and interpretation methodology to generate the most useful products, it is important to understand the soil type classification system relevant to the land management

activity. Once links between the radiometric soil unit products and the local soil type classification system are established, local soil type maps can be produced.

## 5.3 Radiometric classification methodology

### 5.3.1 Overview

Although there is no universally accepted methodology for the classification of radiometric data, a relatively standardised procedure demonstrated by Cook *et al.* (1996b) is often used. The generalised stages employed to classify radiometric data are:

1. classify radiometric data,
2. observe and sample soil texture within each classified unit to ensure soil properties are consistent throughout classified units, and
3. assign soil texture and through extrapolation with *a priori* knowledge soil type for each classified unit.

The generalised classification procedure relies on the radiometric classification to accurately define the soil boundaries from radiometric data without the influence of *a priori* information. As a result, the classifications are often influenced by noise in the data and can be biased against subtle radiometric changes that may have greater significance for defining a soil boundary, rather than radiometric changes resulting from changes in mineralogy rather than soil type.

The radiometric interpretation/classification methodology presented here was developed to overcome these deficiencies. The new classification methodology provides the interpreter with greater control over the significance of changes in radiometric response, while utilising the data sorting advantages of classification. The methodology is divided into four parts:

1. Preliminary investigation
2. Soil texture distribution
3. Soil unit definition
4. Soil type definition (optional)

Figure 5.4 demonstrates how the developed methodology differs from previous generic methodologies through the addition of multiple classification stages and by providing different levels of outcomes.

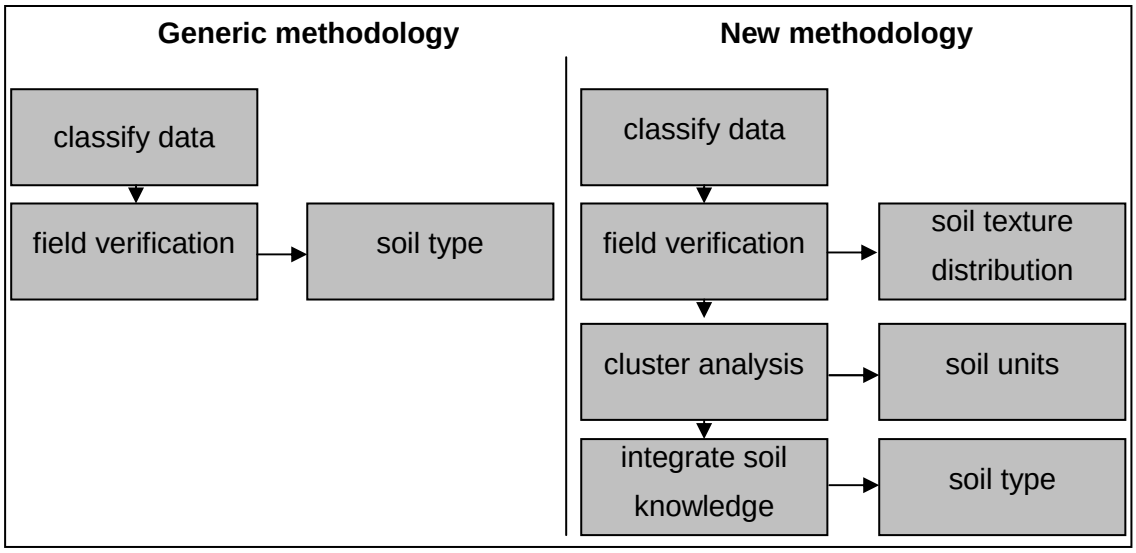


**Figure 5.4. Comparison of previous generic radiometric classification methodology and the methodology developed in this study. The methodology flow charts illustrate the stages involved in previous generic radiometric classification routines (left) compared with the new methodology developed to generate soil maps from radiometric data in this thesis (right).**

As with the previous classification process, field verification is an important element of the methodology. However, in the new methodology, specific details are required from the field data. In the previous methodologies, single bulk sample or inferred soil type information were collected from the field for verification. In the new methodology, soil samples are measured from multiple soil texture layers (A to C). This provides an opportunity for the interpreter to determine soil texture distribution without biases inferred in the field.

Secondly, the cluster analysis or reclassification stage enables the interpreter to group soil texture units with similar radiometric response and field soil textures to form larger soil units. The acceptable error tolerance associated with radiometric response variability and field sample variability within each unit is subsequently controlled by the interpreter and can be varied according to the quality of the data. This clustering stage also enables the interpreter to consider the significance of the different radiometric channels, as described in Chapters 2, 3, and 4. Thus, the soil maps generated through the cluster analysis are subject to interpretation skill and

purpose of the interpretation, with the objective of producing functional soil unit maps.

Finally, if required, the classification process is open to the integration of the derived soil information with the *Australian Soil Classification* soil types to produce a soil map to Australian soil standards.

### 5.3.2 Stage 1. Preliminary investigation

Before commissioning a radiometric survey for soil mapping, it is important to review the available soil information for the area and determine whether the required soil characteristics will be reflected in the radiometric data. This can be accomplished from *a priori* knowledge, literature review including historical soil information, both local and regional, land use, interviews with local land managers (particularly their use of fertilisers, watering rates, and any soil knowledge), and review of the results from previous surveys over similar soil types, or through field assessment.

For example, in the Waroona Case Study (refer to Chapter 6, Case Study 5) the potential for radiometrics to produce a soil map was determined through an examination of the soil composition. Locations were randomly selected from generic soil units expected to represent the range of soil types in Waroona. Soil samples from the top 40 cm of each generic soil unit were assessed by hand for texture and composition. The samples were concluded to be dominantly comprised of quartz and feldspathic sands (particles >0.05mm diameter), kaolinitic clays with variable amounts of smectitic clay (most likely montmorillonite) present in the subsoil (<0.002mm diameter), and little to no silt component (0.002mm to 0.05mm diameter). The radioactivity and cation exchange capacity of these minerals were subsequently compared (Table 5.3) to evaluate the radiometric mapping potential.

**Table 5.3. Composition, radioactivity, and cation exchange capacity of dominant soil minerals found in Waroona soils.**

| Soil | Mineral | Mineral composition | Radioactivity1 (source element) | Relative cation exchange capacity |
|---|---|---|---|---|
| Sand | Quartz | $SiO_2$ | None | None |
| Sand | Feldspar (orthoclase) | $KAlSi_3O_8$ | Low (K), GRapi = 200.97 | None |
| Clay | Kaolinite | $Al_2Si_2O_5(OH)_4$ | None | Low |
| Clay | Smectite | $(K,Na,Ca)Al_4(Si,Al)_8O_{20}(OH)_4 \cdot 2(H_2O)$ | Low (K), GRapi = 7.20 | High |

1. Source – http://www.webmineral.com, accessed January 27 2006. GRapi = Gamma Ray American Petroleum Institute Units.

The comparison showed the background levels in Waroona would be low, due to the low radioactivity of the dominant minerals quartz, feldspar, kaolinite, and smectite. However, the cation exchange capacity of the clays (refer to Chapter 3) would provide a means of discerning lighter textured (sandy) soils from heavy textured soils (clays). Thus it was concluded that a soil texture map could be interpreted from radiometric response. Additionally, due to the low radioactivity of the dominant minerals, a high resolution survey would be required to accurately measure the radiometric response.

### 5.3.3 Stage 2. Soil texture distribution

Once the data is acquired, a simple unsupervised classification algorithm is used to divide the radiometric response into discrete groups with similar radiometric response and spatial distribution. In the Waroona Case Study (refer to Chapter 6, Case Study 5), the data was classified using the unsupervised *ERMapper™ Isocluster* algorithm. Use of this algorithm required a reduction of the radiometric dynamic range of each channel to -1 to 1, such that the average was approximately 0. The data was then classified using unrealistically high number of classes, using a range of 0.1 standard deviations to constitute a class. These settings allowed the variance in the data to control the number of classes established.

Field validation is used to establish the soil textural properties of the radiometric classes and ensure that the soil characteristics and local environmental conditions within the classified units are consistent within the natural variability expected in

soil. The number of soil samples required to produce statistically a significant correlation between the classified data and the field samples can be augmented by the size and quality of the survey, mapping objective and *a priori* knowledge. Thus the number of soil samples required is at the discretion of the interpreter. In practice, it was found that approximately 10 random samples per generated class provided sufficient coverage and confidence for interpretation.

At each sample location, a 40 cm soil core is extracted. Soil characteristics including texture, mottling characteristics, presence of laterite, and general moisture and organic matter content are recorded. In the Waroona Case Study (refer to Chapter 6, Case Study 5), soil texture changes in the soil were noted to occur in three layers. These were referred to as layer A (approximately 0 cm to 10 cm), layer B (approximately 10 cm to 20 cm), or layer C (approximately 20 cm to 40 cm). Note that the layer names A, B, and C do not represent Australian standard soil horizons as defined by Isbell (1997). In the Elashgin Case Study (refer to Chapter 6, Case Study 6), only two soil layers were noted in the field samples.

Soil texture maps are subsequently created by assigning properties sampled in the field to the respective radiometric classes. The samples within each radiometric class are not expected to be identical. However, the samples should be similar, within a degree of freedom as determined by the interpreter. Thus the experience of the interpreter or interpretation team is crucial to a successful outcome. Soil texture of the top 40 cm can then be displayed in three dimensions using the spatial attributes of the combined radiometric classes and field values (Figure 5.5).

Where the samples taken within a radiometric unit are clearly different, the problem may be resolved by increasing the number of classes defined in the original classification. However, radiometric response is not unique to a singular soil type. Cluster analysis is subsequently employed to handle these non-unique conditions.

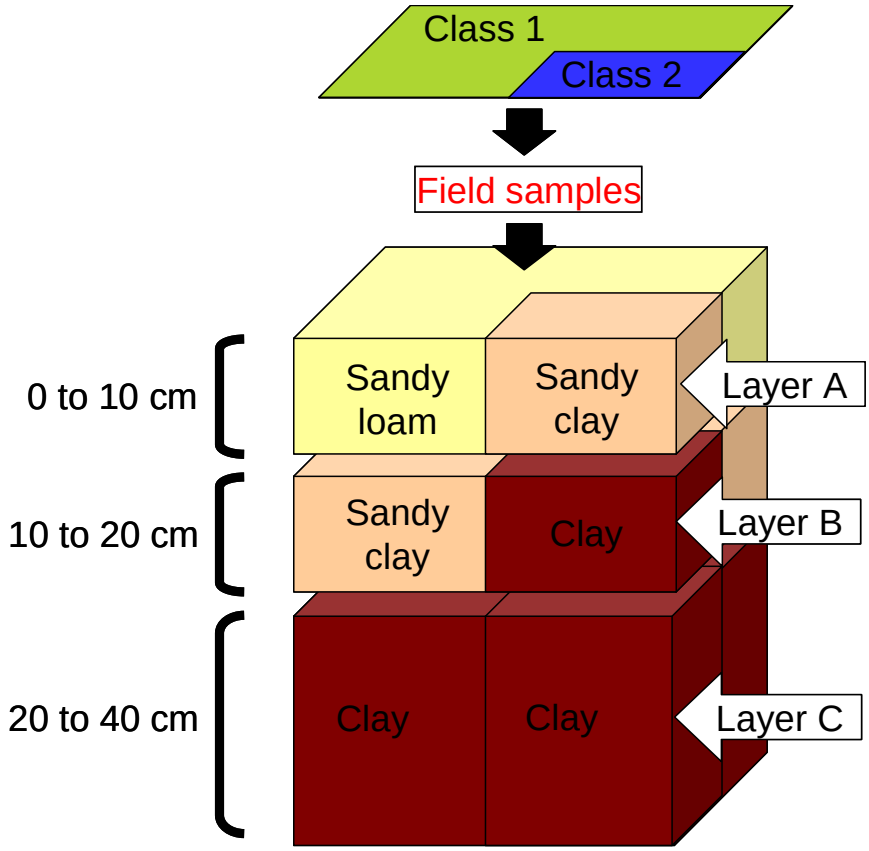


**Figure 5.5. Radiometric classification is transformed into a soil model, describing the variability of soil texture in three dimensions.**

### 5.3.4 Stage 3. Soil unit definition

Cluster analysis, which may be performed manually or using neural networks, creates soil units by grouping radiometric classes with similar physical properties and spatial distributions or spatial patterns. Cluster analysis also enables the interpreter to split radiometric classes (regions with similar radiometric response) by spatial distribution and physical properties. This creates groups of radiometric classes representing similar soil properties or soil units (Figure 5.6). The soil units are subsequently characterised based on the soil properties assigned to the radiometric classes and objective of the interpretation.

By splitting the original classified radiometric classes, cluster analysis overcomes the problem of radiometric non-uniqueness, enabling similar radiometric responses to represent different soil properties. These techniques can also be useful in areas under irrigation where the moisture in the soil creates different radiometric response for the same soil type.

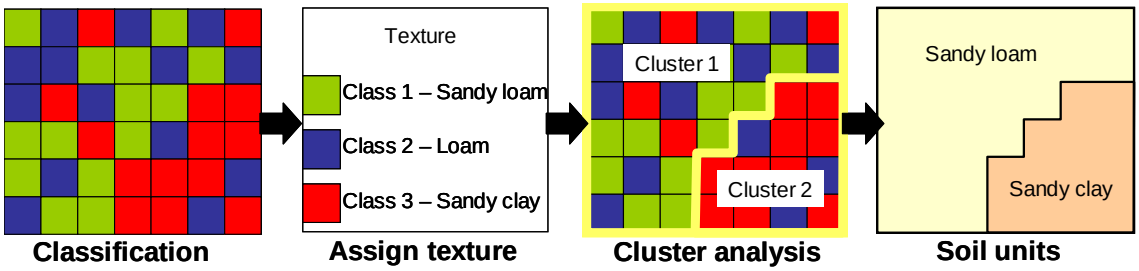


**Figure 5.6. Soil unit definition using the new radiometric classification methodology. Once the radiometric classification is performed and the field data acquired and verified, cluster analysis is performed to group radiometric classes with similar spatial patterns, spatial distribution, and assigned physical properties to create new soil units.**

### 5.3.5 Stage 4. Soil type definition

For communication purposes it may be necessary to derive ASC or local soil types from radiometric soil units. This can be achieved by acquiring and integrating ancillary data used to define the soil types, such as colour, chemical and/or structural characteristics, into the cluster analysis. However, many soil type classifications include large variability of specific soil properties such as texture, which may have been resolved in greater detail through the radiometric classification and interpretation methodology. Where these details are important for the land management the detail should be preserved and the soil type amended to reflect the increased knowledge. For example, by dividing a yellow sandy clay soil type into yellow sandy clay over clay and yellow sandy clay over sand.

Soil maps employing the ASC were not produced in this thesis due to the absence of adequate soil chemistry and structural information. However, local soil type has been adopted where applicable and supported by available ancillary data.

## 5.4 Conclusion

The new classification methodology developed in this thesis provides the interpreter with greater control over the significance of changes in radiometric response for determining soil boundaries, while utilising the data sorting advantages of classification. The classification methodology is presented in four parts and is summarised as follows:

1. Preliminary investigation
    - Establish the survey resolution required for the mapping purpose

- Collate available soil information

2. Soil texture distribution
    - Classify radiometric data
    - Collect and integrate field survey data
    - Create 3D soil texture map
3. Soil unit definition
    - Integrate soil knowledge
    - Cluster radiometric classes to form units
4. Soil type definition (optional)
    - Integrate chemical and structural soil data
    - Simplify soil textural changes

The classification methodology is flexible, and suitable for a range of mapping applications. Examples of different mapping applications described here include soil texture maps, water infiltration rates and waterlogging potential, water retention and repellence, drainage management, and soil type. Full and partial interpretation examples, derived using this methodology, are presented in Chapter 6, Case Studies 4, 5, and 6.

# Chapter 6 - Case Studies

During this project different aspects of 256-channel radiometric data analysis and interpretation were evaluated. This chapter addresses issues arising from the analysis of the 256-channel radiometric data, compares imagery produced through the multispectral processing methodology with standard processed imagery, and examines the application of the multispectral processing methodology with respect to soil and regolith mapping applications.

## 6.1 Case Study 1: Introduction to the study areas

### 6.1.1 Overview

Five example radiometric datasets from four study areas in Western Australia, illustrated in Figure 6.1, were examined during this project:

- Yaragadee in the Tuart Forrest National Park in the south-west of WA,
- Elashgin in the northern wheatbelt district, northeast of Perth,
- Moyagee in the salt lake district of central WA, south of Cue, and
- Waroona in the intensive agricultural region in south-west WA.

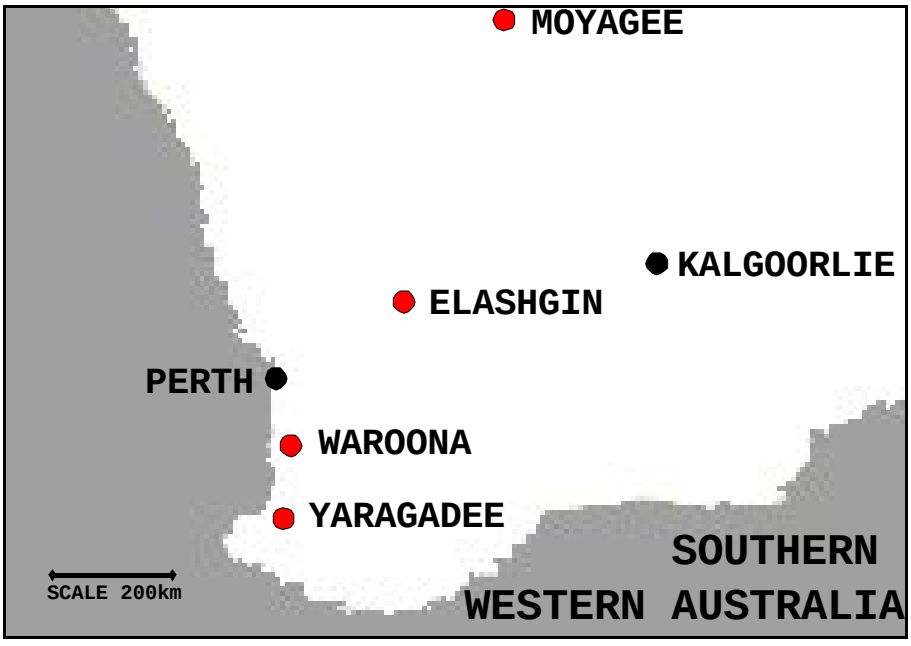


**Figure 6.1. Locations (represented by red dots) of the study areas in this thesis.**

The radiometric data sets represent the range of high-resolution acquisition parameters currently employed across Australia for radiometric surveying for soil, regolith, and mineral exploration.

During analysis of the standard and multispectral processing methods, a large volume of radiometric imagery was generated for each example dataset. This imagery is presented in Appendix C, together with available supporting information for each site. An index to the imagery is provided in Table 6.1.

A large volume of information was similarly collated when reviewing the geological and environmental settings and assessing the differences between the multispectral and standard processing results. Rather than duplicate the results at the beginning of each case study, the background information is provided here. This section also includes a general discussion on the benefits arising from the new multispectral processing and other issues arising from the comparisons with the standard radiometric processing results that may impact on the interpretation of soil or regolith types from the radiometric data.

**Table 6.1. Figure numbers corresponding to study area imagery presented in Appendix C.**

| Image | Yaragadee | Elashgin | Moyagee | Waroona Airborne | Waroona Ground |
|---|---|---|---|---|---|
| 256-channel spectra | | | | | |
| Original full spectra | 1.1.1 | | 1.3.1 | | 1.5.1 |
| Multispectral processed RAW peak only | 1.1.2 | 1.2.1 | 1.3.2 | | |
| Multispectral processed MNF peak only | | 1.2.2 | | | |
| Multispectral processed NASVD peak only | 1.1.3 | 1.2.3 | 1.3.3 | 1.4.1/2 | 1.5.2 |
| Multispectral processed Compton continuum | 1.1.4 | | 1.3.4 | | 1.5.3 |

**Table 6.1. cont'd. Appendix C imagery index for study areas.**

| Image | Yaragadee | | | Elashgin | Moyagee | Waroona Airborne | Waroona Ground |
|---|---|---|---|---|---|---|---|
| Standard processing | | | | | | | |
| Potassium | 1.1.5 | | | 1.2.4 | 1.3.5 | 1.4.3 | 1.5.4 |
| Thorium | 1.1.6 | | | 1.2.5 | 1.3.6 | 1.4.4 | 1.5.5 |
| Uranium | 1.1.7 | | | 1.2.6 | 1.3.7 | 1.4.5 | 1.5.6 |
| Total count | | | | 1.2.7 | 1.3.8 | 1.4.6 | 1.5.7 |
| Ternary | 1.1.8 | | | 1.2.8 | 1.3.9 | 1.4.7 | 1.5.8 |
| Multispectral processing | | | | | | | |
| Spectral smoothing | RAW | NASVD | spNASVD | NASVD | NASVD | NASVD | NASVD |
| Potassium 1 | 1.1.9 | 1.1.19 | 1.1.29 | 1.2.9 | 1.3.10 | 1.4.8 | 1.5.9 |
| Thorium 1 | 1.1.10 | 1.1.20 | 1.130 | 1.2.10 | 1.3.11 | 1.4.9 | 1.5.10 |
| Thorium 2 | 1.1.11 | 1.1.21 | 1.1.31 | 1.2.11 | 1.3.12 | 1.4.10 | 1.5.11 |
| Thorium 3 | 1.1.12 | 1.1.22 | 1.1.32 | 1.2.12 | 1.3.13 | 1.4.11 | 1.5.12 |
| Uranium 1 | 1.1.13 | 1.1.23 | 1.1.33 | 1.2.13 | 1.3.14 | 1.4.12 | 1.5.13 |
| Uranium 2 | 1.1.14 | 1.1.24 | 1.1.34 | 1.2.14 | 1.3.15 | 1.4.13 | 1.5.14 |
| Uranium 3 | 1.1.15 | 1.1.25 | 1.1.35 | 1.2.15 | 1.3.16 | 1.4.14 | 1.5.15 |
| Ternary | 1.1.16 | 1.1.26 | 1.136 | 1.2.16/17 | 1.3.17 | 1.4.15 | 1.5.16 |
| Uranium ternary | 1.1.17 | 1.1.27 | 1.1.37 | 1.2.18 | 1.3.18 | 1.4.16 | 1.5.17 |
| Thorium ternary | 1.1.18 | 1.1.28 | 1.1.38 | 1.2.19 | 1.3.19 | 1.4.17 | 1.5.18 |
| Uranium ratio | | | 1.1.39 | 1.2.20 | 1.3.20 | 1.4.18 | 1.5.19 |
| Ancillary data | | | | | | | |
| Aerial photo | 1.1.40 | | | 1.2.21 | | 1.4.19 | 1.5.20 |
| Geology | 1.1.41 | | | 1.2.22 | 1.3.21 | 1.4.20 | 1.5.21 |
| Soil/regolith | | | | 1.2.23 | | | |
| Salinity | | | | 1.2.24 | | | |
| Low resolution ternary | | | | 1.2.25 | | | |
| Digital terrain (elevation) | | | | 1.2.26 | | 1.4.21 | |
| Magnetics | | | | 1.2.27 | | | |

## 6.1.2 Yaragadee

### 6.1.2.1 Background

The Yaragadee study area is located to the east of Collie in the southwest of Western Australia, and is the subject of a larger study by the Water Corporation of Western Australia to define the Yaragadee groundwater aquifer. Parameters specified for the acquisition of the Yaragadee dataset and resulting acquisition geometry are listed in Table 6.2.

**Table 6.2. Acquisition specifications for the Yaragadee survey.**

| | |
|---|---|
| **Acquisition platform** | Airborne |
| **Spectrometer** | Exploranium GR280 |
| **NaI crystal pack volume** | 32 l |
| **Survey height** | 60 m |
| **Average survey speed** | 70 m/sec |
| **80% signal source radius#** | 112.5 m |
| **Equivalent ground footprint (80% signal)#** | 5.6 Ha |
| **Sample rate** | 1 Hz |
| **Station spacing** | 70 m |
| **Line spacing** | 200 m |
| **Survey configuration** | East/west traverses |

# Calculations based on Billings (1998)

The dataset was acquired in conjunction with a regional magnetic dataset, with the purpose of defining the Bunbury Basalt flows which act as subsurface obstructions to groundwater movement and, due to their hardness, are a potential drilling hazard. The area is dominantly state forest and geology maps are only available at a scale of 1:250,000.

#### 6.1.2.2 Environmental and geological setting

The Yaragadee study area is located on the Perth Basin, a feldspathic sandstone succession containing siltstones and carbonaceous shale deposits. The dominantly sandy soils are a mixture of coastal, well sorted, and rounded sand deposits and angular, subrounded grains (Leederville Formation) derived from the Yilgarn Plateau to the east.

#### 6.1.2.3 Benefits derived from the additional processing

There is a marked difference between the standard processed and the multispectral imagery. Processing of the data using the standard methods resulted in a strong correlation between the uranium and thorium channels. In the ternary imagery, this correlation is highlighted through the poor colour contrast and dominance of cyan/aqua green and red colour tones (Figure 6.2a).

Analysis of the raw 256-channel spectrum and the 256-channel spectrum following hull removal (as described in Chapter 4) highlighted the previously ignored thorium $^{228}$Ac (Th2) energy peak between the primary uranium and potassium channels. With the low uranium count in this area, the proportion of the Th2 peak within the standard uranium channel becomes a significant contributor to the total standard uranium channel count rate, producing the false uranium-thorium correlation within the final data.

Using the new multispectral methodology established in this project, the width of the uranium and thorium window was controlled to isolate individual peak energies from K1, U1 and Th2, excluding the Th2 contributions from the U1 window. The success of this method for reducing thorium:uranium correlation is demonstrated by the improved colour contrast in the resulting multispectral processed ternary imagery (Figure 6.2b).

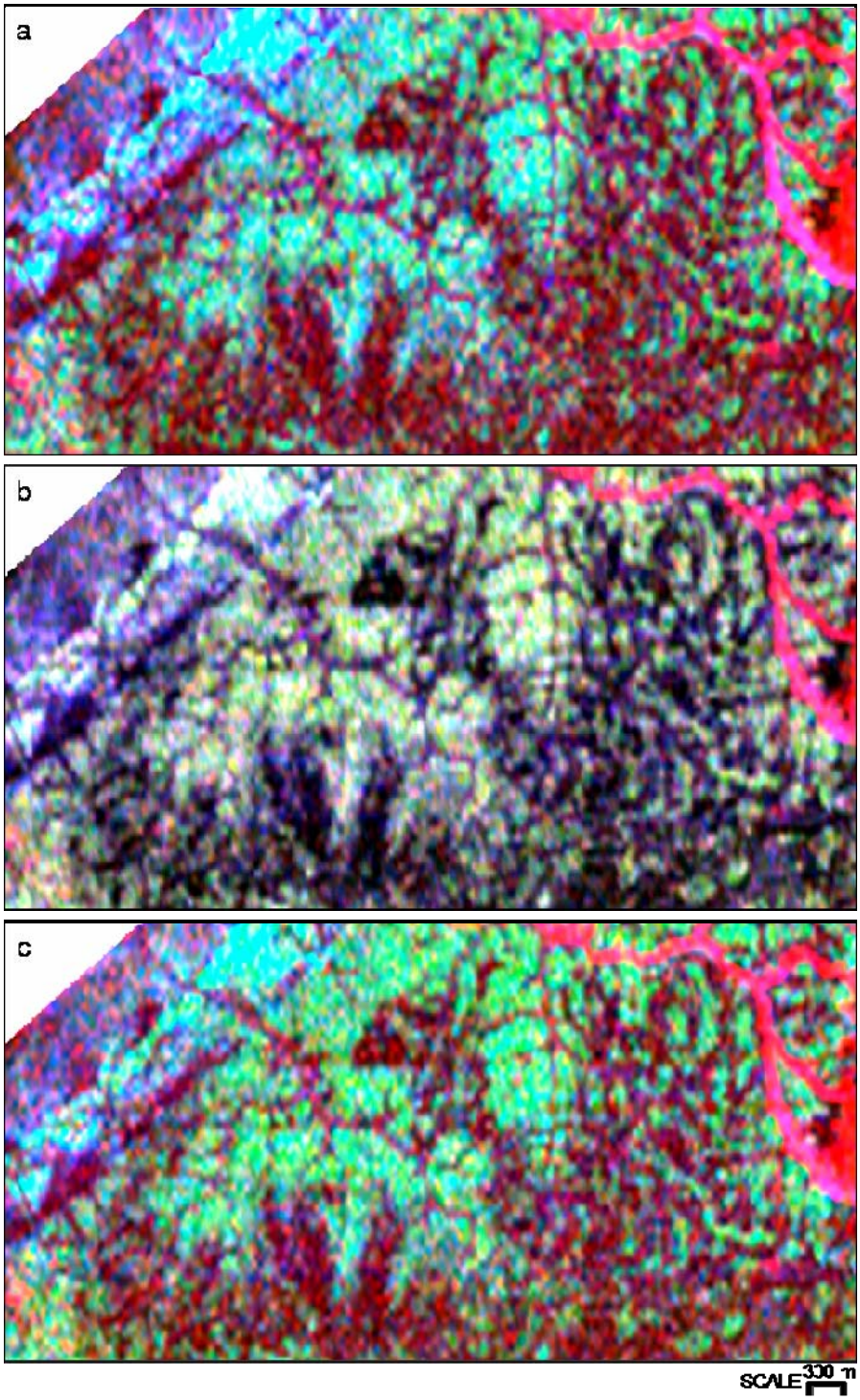


**Figure 6.2. Comparison of ternary imagery from multispectral and standard processed data, from Yaragadee, Western Australia.**

**a) High uranium and thorium correlation in the standard processed radiometric data results in poor colour contrast, and dominance of cyan/aqua green and red colour tones.**

**b) By reducing the width of the uranium channel to exclude contributions from thorium using the multispectral processing technique, colour and tone are dramatically improved.**

**c) In areas with low potassium, a significant proportion of the Compton continuum was retained within the potassium channel during multispectral processing. This alternate composite ternary image composed of the standard processed potassium data (red) with the multispectral processed uranium (blue) and thorium data (green) provides a more spatially accurate representation of the radioelement distributions in the Yaragadee area, particularly the increase in green (thorium) and yellow (thorium and uranium contributions) tones compared with the standard processed image (a).**

#### 6.1.2.4 Other processing issues

The multispectral processing methodology relies on the local minima of the data to produce a hull to act as a surrogate for the Compton continuum. However, the Compton continuum is more complex than this simple representation, and in datasets with low recorded radioactivity, poor energy resolution, or the absence of potassium, thorium, or uranium from the spectra, the shape of the Compton continuum is not represented by the hull.

In the high altitude survey for Yaragadee, the energy resolution was very poor, as is evidenced by the high noise response in the average spectra with and without spectral smoothing (Appendix C, Figures C.1.1 to C.1.4). In addition, potassium was not detected in some samples, as illustrated below in Figure 6.3. These conditions contributed to a considerable increase in the percentage of Compton continuum to signal retained using the multispectral methodology. As a result, the potassium channel, which should demonstrate low to no potassium counts across most of the area, demonstrates a strong correlation to thorium and uranium in the multispectral processed imagery.

Consequently, the benefits obtained through the application of the multispectral methodology to separate the thorium from the uranium response are not correctly represented by the multispectral ternary imagery (Figure 6.2b). As a more accurate representation of the benefit of the multispectral processed data, as a support data set for improving imagery for soil mapping, a composite image of the standard processed potassium data with the multispectral processed uranium and thorium data is supplied in Figure 6.2c.

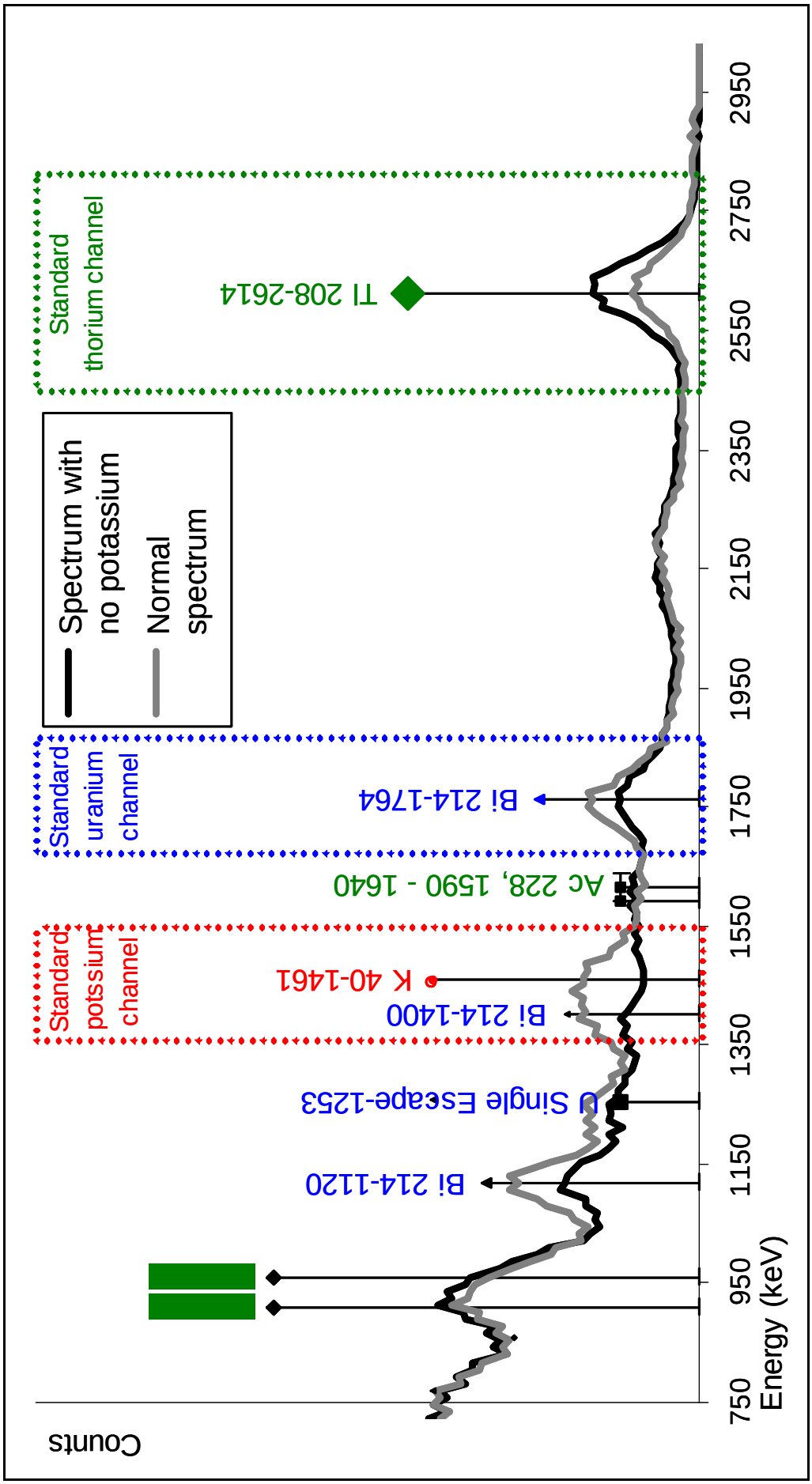


**Figure 6.3. Individual 256-channel spectra for Yaragadee following NASVD spectral smoothing.**

### 6.1.3 Elashgin

#### 6.1.3.1 Background

The Elashgin dataset is located to the south of the town of Elashgin, in the Shire of Wyalkatchem in the northern 'wheatbelt' area of Western Australia. Most of the survey area covers a valley floor. The major agricultural activities are centred on the production of sheep and growing wheat, with additional rotational crops used to boost field productivity and supply fodder for the sheep.

#### 6.1.3.2 Environmental and geological setting

The wheatbelt is an ancient landscape located on weathered granitic gneiss of the Yilgarn Craton, which receives sufficient rainfall (~300 mm per year) for broad acre agricultural use. The wheatbelt is dominated by an ancient internal drainage system that was once incised deeply into the crystalline bedrock. The internal drainage system has since been in-filled with alluvial, colluvial and fluvial sediments creating large, flat-bottomed valley floors that were once highly productive farming area in the wheatbelt. The removal of perennial species including native vegetation and its replacement with annual crops has lead to a rise in groundwater, as annual rainfall has exceeded plant water use since the time of clearing (Cooper *et al.*, 2001). Subsequently, salinisation and waterlogging, produced as a result of rising groundwater, has reduced productivity.

The ancient drainage system, referred to as palaeochannels, provide a preferential pathway for subsurface water movement, especially groundwater. Along with water, mineral accumulations, notably salts, are transported along these palaeochannels to be discharged at selected locations along the valley floor. The salts and the waterlogging contribute to reduce productivity.

Parts of the Elashgin area covered by the example dataset were originally studied by the Western Australian Department of Agriculture in the late 1990s following reports of increased salinity causing low crop yields. Soil maps were produced using standard soil mapping techniques, aided by the use of 200 m line spaced radiometric

data (Appendix C, Figure C.2.23). The soils in the area were mapped as dominantly reworked yellow sandplains on topographic highs, lateritic gravels, granitic outcrops, sandy loam to clay loam soils derived from colluvial granitic materials on the slopes of outcrops, and grey cracking and non cracking clays across the valley floor.

The high resolution radiometric dataset assessed in this project was acquired in 2001 as part of an additional study by the Department of Agriculture and Food, Western Australia to determine if additional detail could be extracted from high resolution radiometric data to produce "better soils map". The specifications for the data are shown in Table 6.3. Although the general consensus from the Department of Agriculture and Food was that the high resolution data did provide additional detail (R. George, Department of Agriculture and Food, Western Australia 2001, pers. comm., March 18), no papers or publicly available reports have been published addressing the additional information available from the high resolution data compared with the original radiometric surveys assessed in the 1990s.

**Table 6.3. Acquisition specifications for the Elashgin survey.**

| | |
|---|---|
| **Acquisition platform** | Airborne |
| **Spectrometer** | Exploranium GR280 |
| **NaI crystal pack volume** | 64 l |
| **Survey height** | 20 m |
| **Average survey speed** | 50 m/sec |
| **80% signal source radius#** | 37.5 m |
| **Equivalent ground footprint (80% signal)#** | 0.8 Ha |
| **Sample rate** | 2 Hz |
| **Station spacing** | 25 m |
| **Line spacing** | 25 m |
| **Survey configuration** | North/south traverses |

# Calculations based on Billings (1998)

#### 6.1.3.3 Benefits derived from the additional processing

Some additional soil mapping was conducted in the Elashgin region in 2000 (Cooper *et al.*, 2001) with the aid of standard processed Elashgin example dataset. In particular, changes in colour contrast were used to define boundaries between soil units, which were then classified in accordance with field observations.

With the application of the new multispectral processing imagery, colour contrast in the Elashgin example dataset was improved, and new subtle gradations and boundaries between soil types and environmental conditions were visible. As discussed further in Case Study 4, the thorium and uranium ternary images provided another means of differentiating soil units, such that the full multispectral radiometric suite of imagery, when interpreted, was suggestive of leaching, groundwater recharge/discharge, clay eluviation, and locations with decreased porosity or shallow bedrock.

The Elashgin data is discussed further in Case Studies 2, 4, and 6.

## 6.1.4 Moyagee

### 6.1.4.1 Background

The Moyagee study area is located 35 km south of Cue in central Western Australia. The dataset was originally acquired for mineral exploration. Parameters for the data acquisition are located in Table 6.4.

**Table 6.4. Acquisition specifications for the Moyagee survey.**

| | |
|---|---|
| **Acquisition platform** | Airborne |
| **Spectrometer** | Exploranium GRS280 |
| **NaI crystal pack volume** | 32 l |
| **Survey height** | 20 m |
| **Average survey speed** | 50 m/sec |
| **80% signal source radius#** | 37.5 m |
| **Equivalent ground footprint (80% signal)#** | 0.8 Ha |
| **Sample rate** | 1 Hz |
| **Station spacing** | 50 m |
| **Line spacing** | 25 m |
| **Survey configuration** | East/west traverses |

# Calculations based on Billings (1998)

### 6.1.4.2 Environmental and geological setting

The Moyagee dataset was acquired over a historical mine site. The mine was situated on a small outcrop of the Mt Magnet-Meekatharra Greenstone Belt, surrounded by colluvial and alluvial materials, and fluvial salt pans. No digital terrain information was available for the area; however it is assumed that all materials generally slope toward the salt pan area. The salt pan itself contains a series of depressions, containing high concentrations of salts. The depressions are surrounded by sand dunes, which form local topographic highs. No specific information on the soils of the area was available.

### 6.1.4.3 Benefits derived from the additional processing

There was little difference between the standard (Figure 6.4a) and multispectral processed (Figure 6.4b) ternary imageries, with both images containing a similar range of colour tones and textures. This suggests that the contribution from the Th2 channel is very small, as illustrated in the 256-channel Compton continuum removed spectrum (Appendix C, Figure C.3.2), and does not contribute to the standard uranium channel in this dataset.

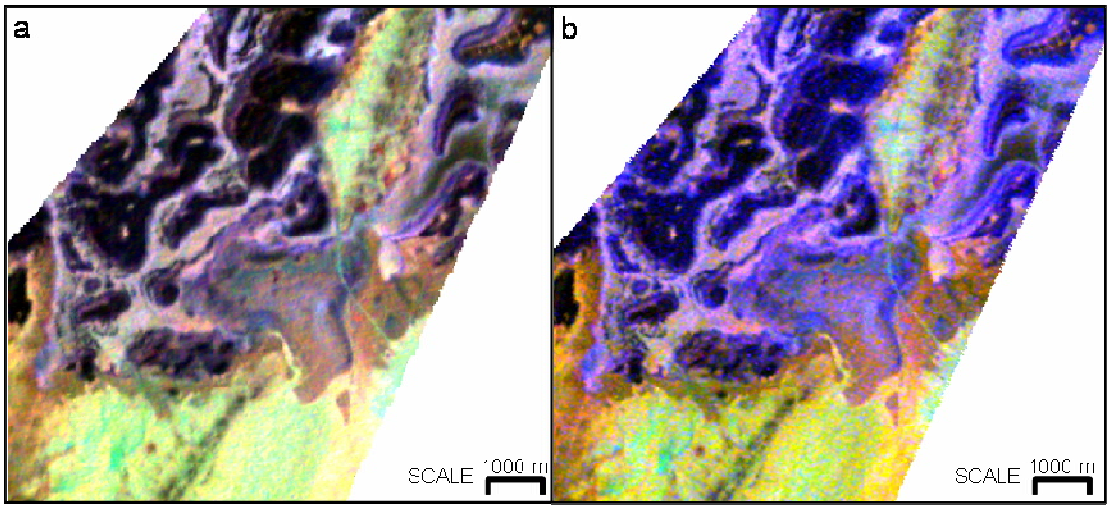


**Figure 6.4. Comparison of standard processed (a) and multispectral processed (b) ternary imagery for Moyagee, Western Australia. Both images produce similar colour contrast.**

The similarity between the standard and multispectral processed ternary imagery also serves to support the use of the Compton continuum approach employed in the multispectral processing methodology to remove the influence of Compton scattered energy from the channels.

However, the speckled response of the U1 channel in the multispectral processed data, when compared with the standard uranium channel, suggests there is still a noise component influencing the U1 channel (Figure 6.5). Although the Compton removal routine was designed only to remove the bulk of the Compton scattered energy, the U1 channel may therefore contain noise from this source. Radon background corrections have not been applied to the multispectral processed data and are the most likely source of noise in this channel. The influence of radon correction

for improving uranium response in channels U1, U2, and U3 is recommended for future research.

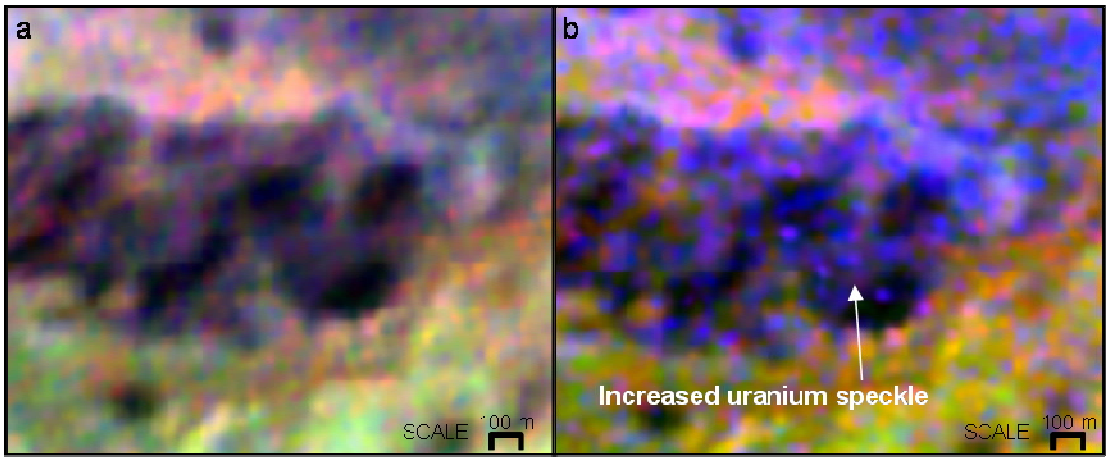


**Figure 6.5. Noise in the multispectral process U1 (uranium) channel. Increased speckled response of the U1 channel (blue) in the multispectral processed imagery (b), when compared with the standard processed imagery (a), suggests there is still a noise component influencing the U1 channel. Radon background corrections have not been applied to the multispectral processed data and are the most likely source of noise in this channel.**

## 6.1.5 Waroona

### 6.1.5.1 Background

The Waroona study area is located to the west of the townsite of Waroona, in the northern end of the Harvey Irrigation District. Set up in 1916, the Waroona agricultural area started as an irrigated citrus growing area, but by 2000 more than half the area of irrigation was used for dairy and beef pasture. Recent Government deregulation of the dairy industry has resulted in farmers seeking alternative agricultural industries.

To assist farmers with selecting appropriate agricultural options, an understanding of the variability of the dominantly Chromosol soils (soils characterised by abrupt textural changes) within farms and their spatial distribution and complexity was required. Harvey Water, who manages the irrigation area as a co-operative, commissioned the original ground survey and data interpretation in 2002 and completed by GeoAg Pty Ltd in 2003 (GeoAg Pty Ltd, 2004). The airborne data was later acquired through funding provided by CRC LEME and Harvey Water in 2003. The parameters for the acquisition of these datasets are shown in Table 6.5.

**Table 6.5. Acquisition specifications for the Waroona surveys.**

| | **Airborne** | **Ground** |
|---|---|---|
| **Acquisition platform** | Airborne | Ground |
| **Spectrometer** | Exploranium GR280 | Exploranium GRS320 |
| **NaI crystal pack volume** | 32 l | 8 l |
| **Survey height** | 30 m | 1 m |
| **Average survey speed** | 50 m/sec | 5 - 8 m/sec |
| **80% signal source radius**[#] | 55 m | 2 m |
| **Equivalent ground footprint (80% signal)**[#] | 1.5 Ha | 0.003 Ha |
| **Sample rate** | 1 Hz | 1 Hz |
| **Station spacing** | 50 m | 5 - 8 m |
| **Line spacing** | 25 m | 25 m |
| **Survey configuration** | North/south traverses | Parallel traverses adjusted to paddock shape and orientation |

# Calculations based on Billings (1998)

Harvey Water aim to use the detailed soil maps resulting from radiometric data to evaluate watering and drainage practices, and identify alternative land uses for members of the co-operative.

#### 6.1.5.2 Environmental and geological setting

Soil texture was recognised by the Harvey Water and the local community as the major control on soil water holding capacity in the Waroona area, and consequently the most important soil property to map. A shallow electromagnetic (EM) and radiometric survey was conducted in 2003 to assist in mapping soil texture in the region. EM is generally considered to be an effective method of separating soil texture, because fine clay soils retain moisture and are more conductive than the coarser sandy textured soils. However, the EM survey data was strongly influenced by the presence of salts in the area, as a result of the older swamp and lacustrine formations underlying the local geology of the region. Instead, the strong physical and chemical relationships between radionuclide concentration and soil particulate size were used to differentiate soil texture and map soils in the region.

Patterns in the radiometric data reflect a combination of local geological history and pedological processes (Figure 6.6) (GeoAg Pty Ltd, 2004). A colluvial/alluvial fan emanating from the Samson Brook dominates the area and overlies soils of the Guildford Formation. This alluvial material originates from erosion of deeply weathered granitic gneiss rocks at the Darling Scarp to the east. The alluvial fan represents a long history of braided stream deposition on the slope of the Darling escarpment. Radionuclide leaching was observed in the recent fan deposits and radionuclide accumulation with clay eluviation was observed in older deposits. Along the northern edge of the study area, more recent beach sands from the Yoganup Formation have encroached over the alluvial fan; while along the western edge deflated dunes of Bassendean Sands sit unconformably on top of Quaternary swamp and lacustrine deposits. The Bassendean Sands were differentiated from the Yoganup deposits by a lower potassium radiometric response.

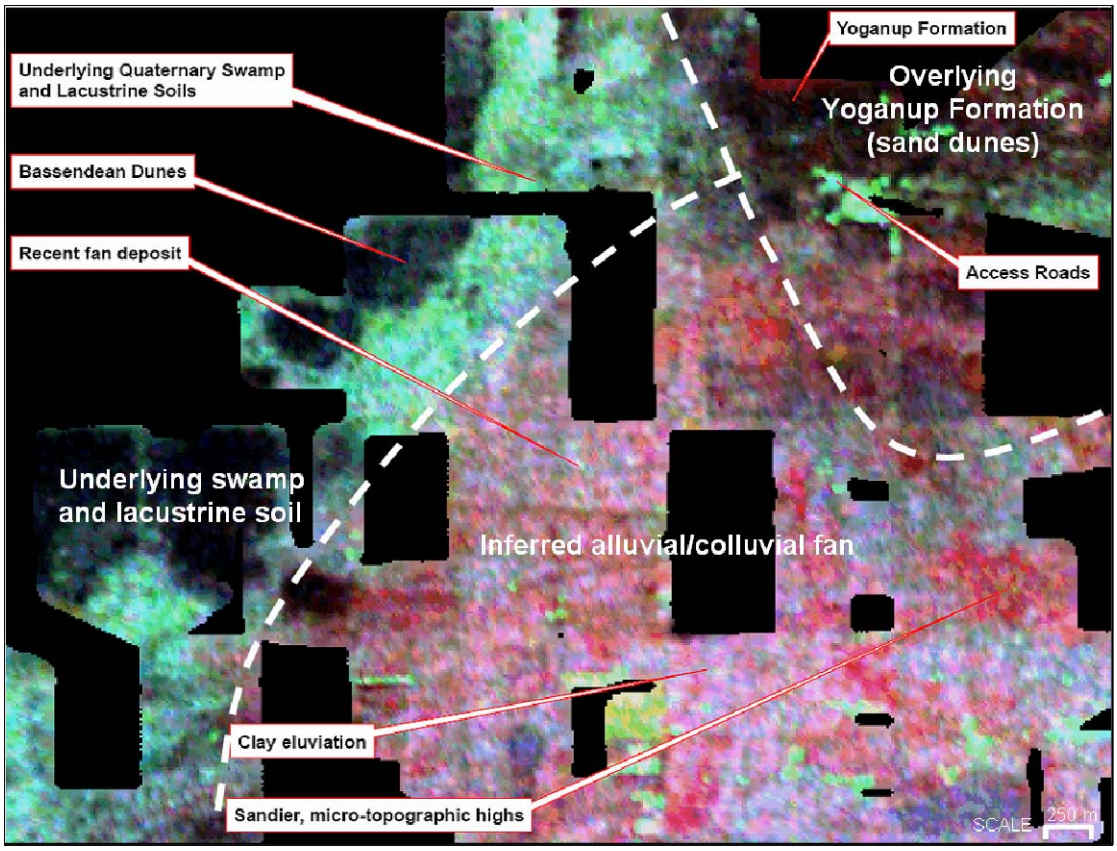


**Figure 6.6. Interpretation of geological history and pedological processes from ground high resolution radiometric ternary imagery for Waroona, Western Australia (after GeoAg Pty Ltd, 2004).**

### 6.1.5.3 Benefits derived from the additional processing

There was little difference between the standard and multispectral processed ternary imagery, largely as a result of the two dominant soil units in the area: the Quaternary swamp clays and the sands of the Guildford Formation, producing little variability in the signal response.

However, the additional radiometric channels derived from the new multispectral processing methodology, U2, U3, Th2, and Th3, provided additional information for separating radiometric classes during classification. For example, the Guildford Formation clays and the Guildford Formation sands expressed similar K1, U1, and Th1 channel response in some areas. These classes were separated by elevated Th3, U2, and U3 radiometric response in the Guildford Formation clay member (Figure 6.7).

The Waroona data is discussed further in Case Studies 3 and 5.

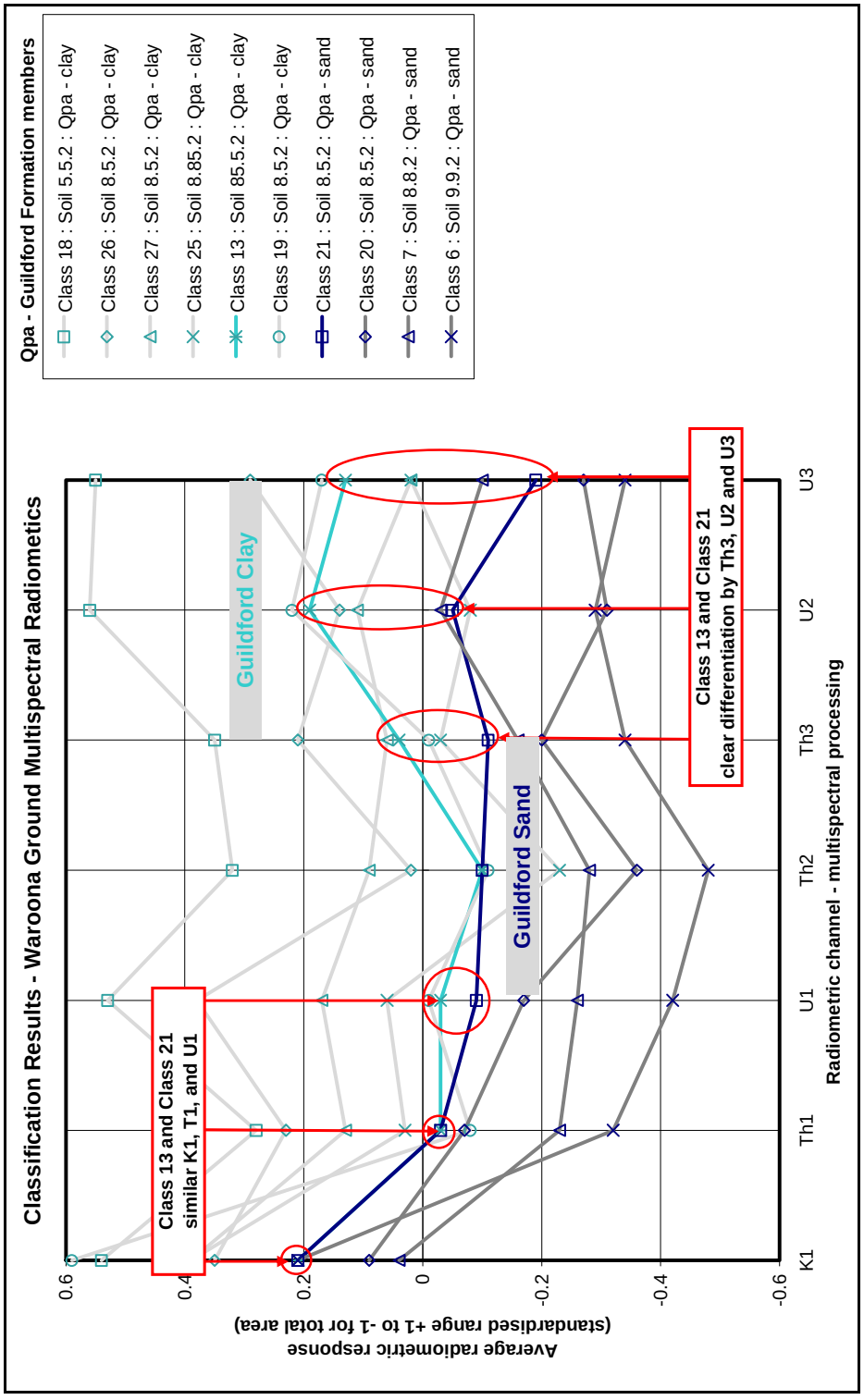


**Figure 6.7. Using additional multispectral processing derived radiometric channels to classify data in Waroona, Western Australia. Classes 13 and 21, derived from the unsupervised classification of the Waroona ground radiometric data, exhibit similar K1, Th1, and U1 average response. Field samples, location, and the spatial distribution of Class 13 suggested this unit was a member of the Guildford Formation clays, and Class 21 a member of the Guildford Formation sands. Based on standard radiometric channels, these units would have been inseparable. However, differences in the additional multispectral channels Th3, U2, and U3 enable these soils to be separated.**

### 6.1.6 Summary

In the Yaragadee standard processed imagery, the standard ternary image (potassium [red], uranium [blue], thorium [green]) demonstrated poor colour range and contrast, which had a negative impact on interpretation from radiometric data. Inspection of the 256-channel raw and spectral smoothed data with respect to the standard processing channels showed that during standard processing, energy from neighbouring thorium peak $^{228}$Ac 1590-1640 keV (also referred to as the Th2 peak in Chapter 4), was incorporated with the uranium channel counts. As the true uranium count rate was very small, the incorporation of counts from the thorium peak was responsible for the strong, artificial correlation between the uranium and thorium. Using the multispectral methodology developed in this study, the uranium channel widths were tailored to fit the observed spectrum, thereby excluding the contaminating thorium counts. The resulting ternary image produced using multispectral processing: $^{40}$K full energy peak at 1461 keV [red], $^{214}$Bi full energy peak at 1764 keV [blue], $^{208}$Tl full energy peak at 2614 keV [green], demonstrated increased colour and contrast compared to the equivalent standard processed ternary image.

The high correlation between thorium and uranium was observed in other datasets to varying degrees. However, the high uranium-thorium correlation was most notable in the Elashgin imagery, which formed the basis for the discussion of uranium-thorium correlation in Case Study 2.

The multispectral processing methodology relies on the hull removal process to remove a significant proportion of Compton continuum from the seven radiometric channels. In the Yaragadee dataset, the poor energy resolution and absence of potassium in the soil in the Yaragadee survey resulted in a higher than expected proportion of Compton energy remaining in the potassium channel compared to true response. Thus differences between the results from the Yaragadee multispectral processed and standard processed datasets were not as impressive as other datasets.

## 6.2 Case Study 2: Artificial correlation between uranium and thorium in Western Australian radiometric data

### 6.2.1 Abstract

In spite of conforming to industry standards, the Elashgin high resolution radiometric dataset exhibited a strong correlation between the uranium and thorium channels after standard processing. The strong correlation between these channels was exemplified by the dominance of red and cyan/aqua green tones in the standard ternary radiometric image presentation [red: potassium, green: thorium, blue: uranium].

Extensive investigation of the recorded 256-channel gamma ray spectral response showed that the $^{228}$Ac response at approximately 1610 keV, between the standard uranium 1764 keV and potassium 1461 keV peaks, was contributing counts to the standard uranium window. As a daughter product of the thorium-232 decay series, the $^{228}$Ac response should be removed from the uranium channel as part of the stripping algorithm during standard radiometric processing. However, the ratio of $^{228}$Ac 1610 keV to $^{208}$Tl (standard thorium) 2614 keV peaks for individual spectral samples for the Elashgin radiometric dataset demonstrated a nonlinear relationship. As a result, during standard processing, the total influence of the $^{228}$Ac 1610 keV peak was not removed from the uranium channel. This resulted in an increase in the correlation between uranium and thorium channels in the standard processed Elashgin radiometric data.

Using the multispectral processing methodology to remove excess Compton continuum and bremsstrahlung energies, it was possible to create a new uranium channel with a reduced window width of 1700 – 1860 keV. The narrower uranium window successfully eliminated a significant proportion of the thorium contamination from the uranium channel, reducing correlation between the uranium and thorium channels. The reduced correlation between the uranium and thorium channels subsequently facilitated the return of the full colour range to the standard ternary image presentation.

Consequently, modification of the standard radiometric acquisition, processing, and calibration system to use the reduced standard uranium window of 1700 – 1860 keV is recommended to prevent artificial uranium and thorium correlation.

### 6.2.2 The issue

In Australia, radioelement maps of percentage potassium (%K), equivalent ground concentration thorium in ppm (eTh), equivalent ground concentration uranium in ppm (eU), and total gamma-ray dose rate are routinely generated from airborne and ground gamma ray spectrometry (radiometric) data following acquisition and processing along international guidelines (IAEA, 2003). In spite of conforming to industry standards, users of radiometric data in Western Australia are often dismayed at the high correlation between the uranium and thorium radioelements in their final data (A Bissett 2001, pers. comm., 6 June; R George 2001, pers. comm., 10 November).

The natural correlation between uranium and thorium in Australian geology and soils is well documented (Dickson and Scott, 1997). However, in some Western Australian datasets the correlation between uranium and thorium appears to increase as a result of processing, with raw channel data demonstrating better image contrast than its processed counterpart. Figure 6.8 illustrates the difference between (a) the raw channel data and (b) the standard processed data.

In spite of the improved image clarity following processing, the loss of colour contrast causes problems as radiometric interpretation relies on contrast to resolve potential geological, regolith or soil units. The strong correlation between the thorium and uranium channels decreases the colour contrast in standard ternary radiometric image presentation [red: potassium, green: thorium, blue: uranium], resulting in a dominantly red (from potassium) and cyan/aqua green (from the uranium and thorium) image (Figure 6.8b).

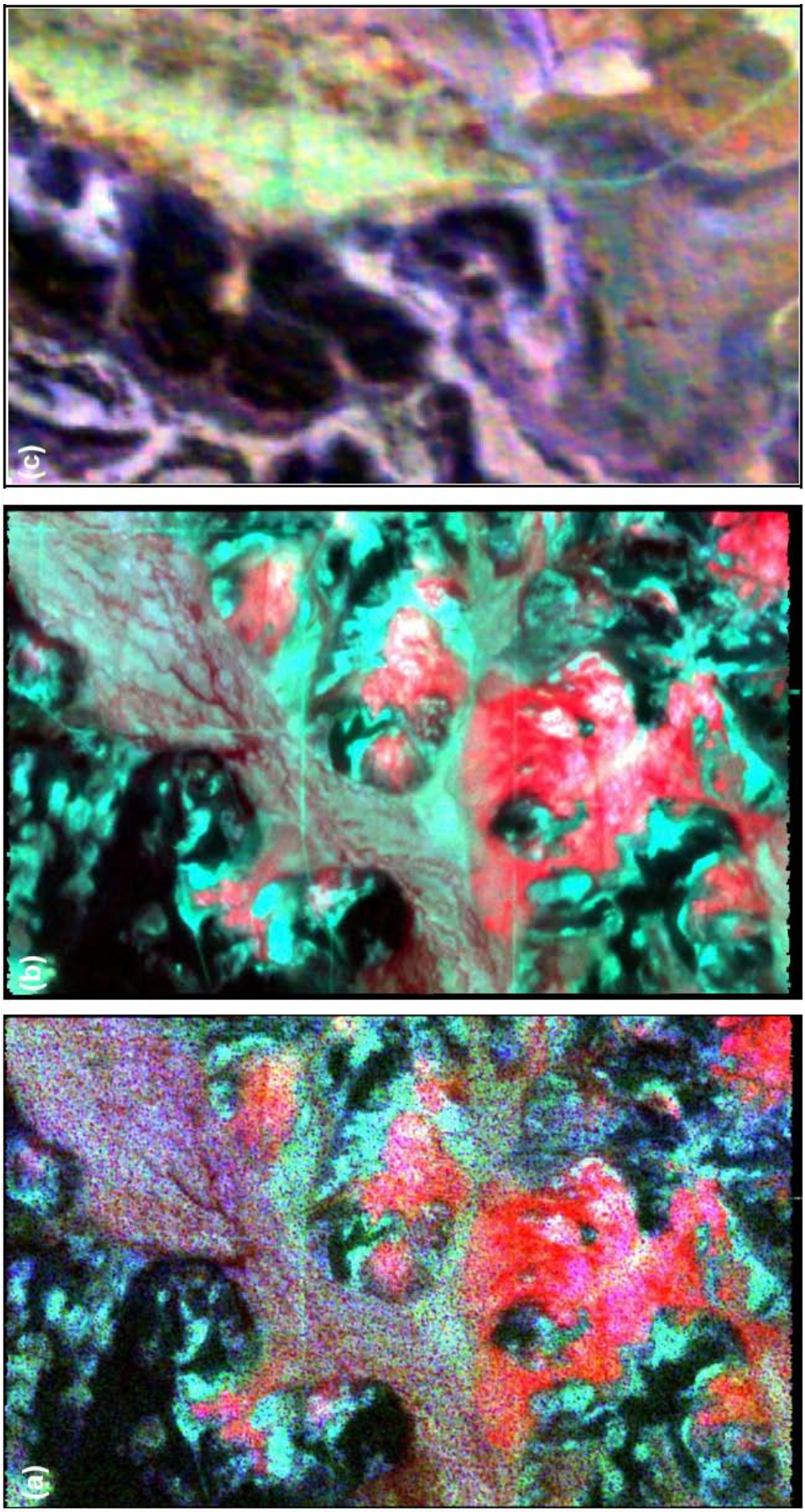


**Figure 6.8. Ternary radiometric imagery of (a) Elashgin raw radiometric data, (b) Elashgin standard processed radiometric data with high U/Th correlation, and (c) Moyagee standard processed radiometric data.**

### 6.2.3 Spectra analysis

Figure 6.9 illustrates the average survey spectra for the Moyagee and Elashgin datasets derived from a 256-channel Exploranium spectrometer following the extraction of the Compton continuum (refer to Chapter 4 for a description of this process).

For the Moyagee dataset, which demonstrated the colour range and contrast expected of a radiometric ternary image (Figure 6.8c), the gamma ray standard potassium, uranium, and thorium peaks were solely contained within the internationally recommended extents for the potassium, thorium, and uranium windows for data processing.

In the Elashgin dataset, however, the extent of the uranium anomaly appeared smaller than the Moyagee uranium anomaly, such that a proportion of the neighbouring $^{228}$Ac 1610 keV peak encroached into the uranium window. The uranium channel is defined as the sum of the counts within the uranium window. Consequently, in the Elashgin dataset, counts derived from a thorium source ($^{228}$Ac) were inadvertently incorporated in the uranium channel. This had the effect of increasing thorium and uranium correlation within the Elashgin dataset.

Consequently, the difference between the colour ranges in the raw data and the processed data resulted from the contributing fraction of the $^{228}$Ac 1610 keV peak to the uranium channel. When the data was raw, the count rate was higher as a result of the contribution from the Compton continuum, as shown in Figure 6.10. Thus the influence of the $^{228}$Ac 1610 keV peak was small, only around 4%. During processing, stripping removed a significant proportion of the Compton continuum from the uranium window as a fraction of the observed thorium $^{208}$Tl (2.41 – 2.81 MeV), lowering the counts in the uranium window, as illustrated in Figure 6.10. As the count rate for the uranium channel decreased, the proportion of the $^{228}$Ac 1610 keV peak to the uranium contribution was increased to approximately 13%, resulting in the higher uranium/thorium correlation in the processed imagery.

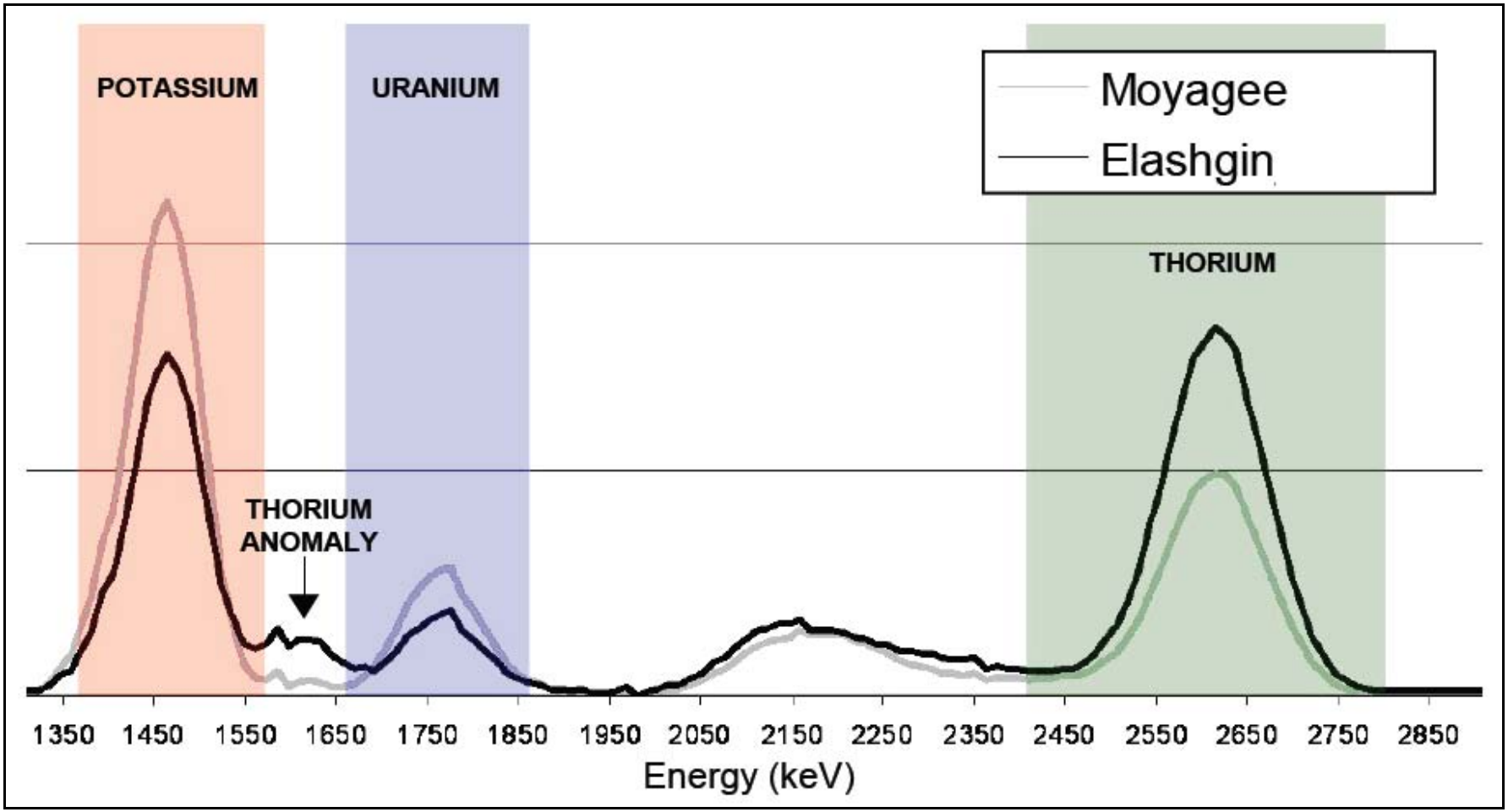


**Figure 6.9. Average survey spectra for Moyagee and Elashgin data with Compton continuum removed. The boundaries for the international standard potassium, uranium, and thorium windows are marked in red, blue, and green respectively. In the Elashgin spectrum, the uranium peak is observed to start at approximately 1700 keV, instead of the expected 1660 keV, while the $^{228}$Ac 1610 keV peak (described above as the thorium anomaly) extends through the uranium window boundary at 1660 keV to 1680 keV.**

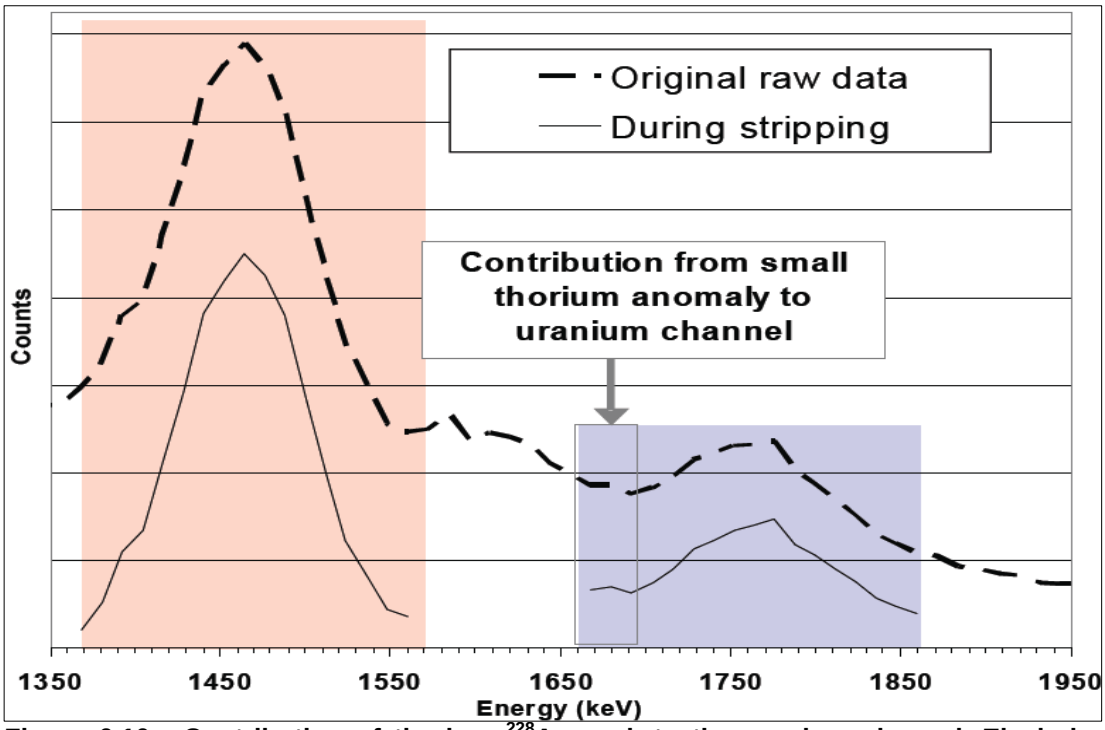


**Figure 6.10. Contribution of thorium $^{228}$Ac peak to the uranium channel, Elashgin, Western Australia. Additional energy from the $^{228}$Ac peak (described above as the small thorium anomaly) is inadvertently incorporated in to the uranium channel. Although this contribution is small, the relative proportion is increased as a result of the stripping process.**

The simplicity of this overlap problem suggested that narrowing the width of the uranium window to exclude a larger proportion of the $^{228}$Ac 1610 keV peak would reduce the thorium contamination within the uranium window and thereby reduce the false contribution from the thorium to the uranium channel before stripping. As illustrated in Figure 6.11, by reducing the width of the uranium window by 40 keV to 1700 - 1860 keV the correlation was indeed reduced with restoration of the full colour range to the Elashgin standard radiometric ternary image.

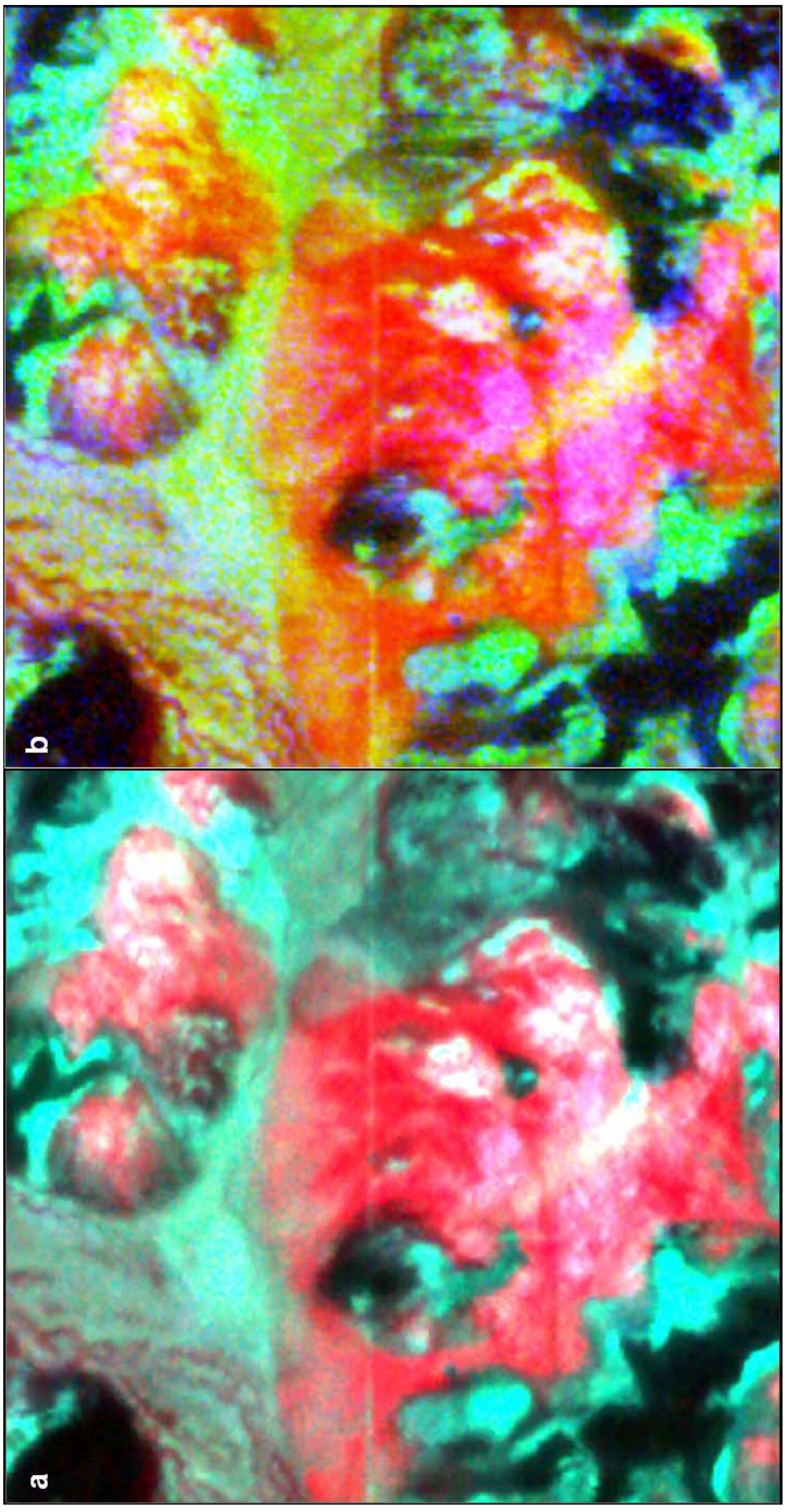


**Figure 6.11. Comparison of standard ternary imagery for Elashgin radiometric data without (a) and with (b) recommended reduced uranium window width. Reduction of the uranium window (b) reduces uranium/thorium channel correlation, significantly increasing the colour contrast and textures within the Elashgin imagery when compared with (a) equivalent imagery produced from standard processing results.**

### 6.2.4 Characteristics of the $^{228}$Ac peak

The small $^{228}$Ac 1610 keV peak neighbouring the standard uranium 1764 keV peak (Figure 6.9) is a daughter product of the thorium-232 decay sequence. The decay of thorium to $^{228}$Ac occurs around 1.9 years (half-life) before $^{208}$Tl is formed. Although the half life of $^{228}$Ac is very short at 6.13 hours, such that any disequilibrium from the movement of $^{228}$Ac is quickly restored, intermediate gaseous and other mobile nuclides between the decay of $^{228}$Ac and $^{208}$Tl, including $^{224}$Ra and $^{220}$Rn can cause disequilibrium in the decay sequence.

In a solid geology setting it would be rare for disequilibrium to occur in the thorium decay series. In the chemically dynamic environment of the plant root zone, however, up to 1 m in depth, gaseous elements are easily lost to the atmosphere as soils degas each night, or transported further down the soil profile when adsorbed to other elements or in solution. Thus decay equilibrium can not always be assumed in soil and regolith, nor can a 1:1 correlation between the $^{228}$Ac anomaly and the standard $^{208}$Tl channel be assumed (Figure 6.12). (For more information on the use of the $^{228}$Ac anomalies for soil mapping, refer to Chapter 4 and Chapter 6, Case Study 4.

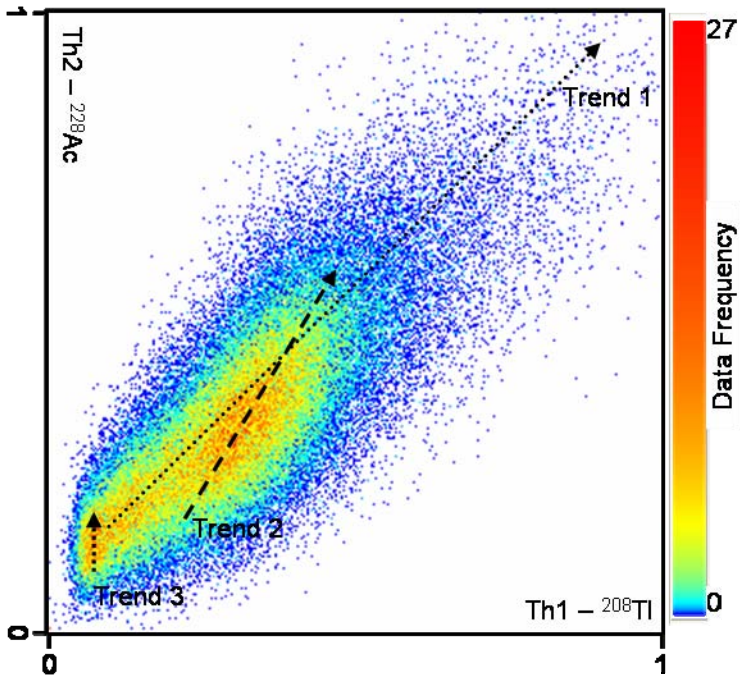

**Figure 6.12. Non linear correlation between the standard thorium $^{208}$Tl intensity (x axis) and $^{228}$Ac intensity (y axis) in the Elashgin multispectral processed dataset. Black arrows illustrate three trends visible in the data.**

### 6.2.5 Issues arising from the presence of the $^{228}$Ac peak

Detection of the $^{228}$Ac 1610 keV peak appeared to be dependent on the resolution of the system, survey elevation, and ground conditions. However, the exact conditions under which the $^{228}$Ac 1610 keV peak can be detected were beyond the scope of this thesis. Thus, at present, whether the $^{228}$Ac 1610 keV peak is likely to cause processing issues can only be resolved by examining the individual spectra response prior to processing.

The inability to predict the occurrence of a $^{228}$Ac 1610 keV peak is a potential source of problems in the application of spectral smoothing techniques. Spectral smoothing techniques are designed to preserve the spectral shape of the data. If the spectral shape used to train the data during spectral smoothing contains a $^{228}$Ac peak which is not representative of the whole area, false $^{228}$Ac response will be propagated throughout the rest of the dataset (IAEA, 2003). Whilst the fraction of thorium energy contributing to the uranium channel is, in most cases, likely to be within the accepted error range of relative ground concentration measurements, the contamination produces a subtle change in the spatial distribution and patterns of the uranium data. Thus the false $^{228}$Ac peak artificially increases uranium and thorium correlation.

### 6.2.6 Conclusion

In the Elashgin dataset, increased correlation between thorium and uranium in the standard processed radiometric data resulted from the inclusion of a proportion of the $^{228}$Ac 1610 keV peak in the uranium window. The conditions under which the $^{228}$Ac 1610 keV peak forms and can be detected remains unsolved, and an area for future research. Nevertheless, for the Elashgin dataset, artificial uranium and thorium correlation was reduced by excluding $^{228}$Ac 1610 keV peak energy from the uranium channel by contracting the uranium window width to 1700 – 1860 keV.

Although the reduced channel width provided immediate benefits of a more accurate representation of the data and increased colour range in the Elashgin image, the approach lead to processing difficulties. The standard calibration routine employed

during the acquisition of the Elashgin data and used to calculate concentration was based on the standard uranium channel width. This made it difficult to calculate the equivalent ground concentrations using a reduced uranium window. In the future, this can be resolved by modifying the standard radiometric acquisition, processing, and calibration system to use the reduced standard uranium window of 1700 – 1860 keV.

## 6.3 Case Study 3: Comparison of high-resolution NaI 256-channel radiometric airborne and ground data

### 6.3.1 Abstract

Data quality, data resolution, and cost differences between the airborne and ground high resolution data were compared for soil or regolith mapping applications. Surveys were conducted using a line spacing of 25 m, with airborne data acquired at an altitude of 30 m. For the airborne system, 64% of the equivalent footprint was included in the next sample along the flight line and up to 75% of the equivalent footprint area was repeated in samples from the neighbouring line (dependent on the total distance between the sample locations). For the ground system, only around 30% of the equivalent footprint was included in the next sample along the traverse line, and 0% was repeated in samples from the neighbouring line. The increased overlap in the airborne data served to produce more coherent, continuous images of the surface radiometric response.

Eleven line profiles, where the airborne data was recorded directly above a north-south ground traverse, were extracted and analysed with respect to along line resolution, interpreted changes in soil type, ground ternary imagery, airborne ternary imagery, and aerial photography. Comparison showed both platforms produced comparable imagery, suitable for identifying changes in radionuclide distribution for soil or regolith mapping applications. For the ground platform, the line data demonstrated an accuracy of ±7 m, with the imaged products suitable for 1:10,000 scale interpretations. For the airborne platform, the line data demonstrated an accuracy of ±50 m, with the imaged products suitable for 1:25,000 scale interpretations.

Finally, a cost comparison of the airborne and ground platforms demonstrated the ground platform was the most cost effective option for small surveys close to Perth requiring less than 500 line kilometres or 1,250 Ha at 25 m line spacing. While for most surveys great than 500 line kilometres the airborne platform was the more cost effective option. A simple cost benefit comparison established that the ground platform was the best option for areas of intensive agriculture. However, the ground

platform was only preferred for broad acre farming and non-agricultural, non residential land use areas when the survey area covered less than 1,000 line kilometres and located more than 200 km from an airport.

### 6.3.2 Introduction

In Australia two radiometric platforms are available commercially for collecting high resolution data suitable for soil mapping: a low altitude airborne platform that uses the Exploranium GR810 detector and a ground platform that uses the Exploranium GR320 detector mounted on/behind a four-wheel motorbike. Due to cost limitations, it is rare for the same area to be covered with both the airborne and ground high resolution systems. However, with funding from the Co-operative Research Centre for Landscape, Environment, and Mineral Exploration (CRC LEME), a small, high resolution airborne radiometric survey was conducted over a high resolution ground survey recently acquired by Harvey Water in Waroona, Western Australia. These surveys provided sufficient coverage for practical comparison of high-resolution NaI 256-channel radiometric airborne and ground data for soil mapping applications in a rural area.

This case study compares the data quality, data resolution, and cost differences between the airborne and ground high resolution data for mapping soil or regolith at 1:50,000 scale or less. The study also examines the survey logistics associated with the different survey styles, and reviews subsequent problems that arise, including survey timing, local community co-ordination, and noise issues.

### 6.3.3 Acquisition parameter comparison

Acquisition specifications and survey parameters employed in this study are summarised in Table 6.4. The airborne Exploranium GR810 and the ground Exploranium GR320 radiometric detectors utilised similar acquisition parameters and recording software, recording radiometric response in 256-channels at rates of 1 sample per second. The major differences between the systems were the volume of the crystal packs, the survey height, and the velocity of the survey platforms.

The airborne platform was fitted with two 16 L crystal packs while the ground system was fitted with an 8 L crystal pack. The larger volume in the airborne platform was required to enable the system to detect the smaller magnitude and volume of radiation that would reach the airborne platform as a result of the airborne systems altitude.

The altitude for the airborne survey was fixed as a function of the height of obstacles in the flight path. Trees and overhead wires in the area were estimated to have a height of around 20 – 25 m. A minimum 5 m clearance was required for safety reasons on top of the maximum obstacle height, giving a total survey height of 30m. The height of the ground survey was also fixed, as a function of the distance between the mounted system and the ground, approximately 1 m.

The height or altitude of the surveys determines the size of the area on the ground that will contribute gamma rays to the recorded sample. As the contributing area is determined by an infinite, nonlinear function, a cut off value of 80% of the contributing area was used to compare the systems (after Billings, 1998; Billings and Hovgaard, 1999). This contributing area, referred to as the equivalent ground footprint, incorporates both the perpendicular radius of the system and the distance covered during a single sample interval. The equivalent footprint for the airborne platform was calculated at 1.5 Ha and ~0.003 Ha for the ground platform.

As both surveys were conducted using a line spacing of 25m, the altitude or height of the survey was the most significant contributor to the overlap between recorded samples and neighbouring lines. Overlap serves to produce a more coherent, continuous image of the surface radiometric response, minimising interpolation between lines. For the airborne system, 64% of the equivalent footprint was included in the next sample along the flight line and up to 75% of the equivalent footprint area was repeated in samples from the neighbouring line (dependent on the total distance between the sample locations). For the ground system, only around 30% of the equivalent footprint was included in the next sample along the traverse line, and 0% was repeated in samples from the neighbouring line. The impact of the overlap

differences are discussed with respect to line data and imagery comparisons in following sections.

A minimum velocity for the airborne system of 50 m/sec was observed for the survey, while an average velocity of 5 m/sec to 8 m/sec was observed for the ground system. The speed variability in ground system resulted from acceleration and deceleration required to navigate the motorbike and ground platform around the paddocks. As both systems were acquiring data at a rate of one sample per second, the velocity of the systems controlled the distance between the samples, referred to as the sample spacing.

The speed variability encountered in the ground platform impacted on the visual quality of the imaged ground data. The changing velocity of the system altered the distance between and equivalent ground footprint of each sample, such that inconsistencies between the sample spacing made it difficult to convert the data to a uniform gridded dataset and preserve the maximum degree of detail. However, this is a minor issue, which has been addressed in other studies of ground radiometric data through the application of alternative, non-standard gridding algorithms.

The velocity of the systems also controls the total time required to complete the survey. The airborne data was acquired in 1.5 days, while the ground data was acquired sporadically over four weeks (due to staff shortage and staff availability.), the equivalent of 5 days full time to cover the same area as the airborne system. As the best quality radiometric data is recorded with consistent atmospheric conditions and soil moisture (IAEA, 2003), the longer survey time required to collect data using the ground platform increases the potential for significant change in the atmospheric or soil moisture conditions, thereby increasing the potential of reducing the overall quality of the ground survey data.

While both platforms were capable of acquiring high resolution radiometric data, different survey parameters were required as a result of the requirements of the different platforms. As a consequence, it was expected that the systems would record different radiometric responses, leading to significant differences between

radiometric imagery, and resulting in different interpretations of soil/regolith units. To quantify these differences, line data and imagery generated for the area from the two platforms were compared.

### 6.3.4 Line data comparison

Counts for the radiometric channels K1, Th1, Th2, Th3, U1, U2, and U3 derived using the multispectral processing methodology developed coincident to this study, were determined for the ground and airborne data. Eleven line profiles, where the airborne data was recorded directly above a north-south ground traverse, were then extracted and analysed with respect to along line resolution, interpreted changes in soil type, ground ternary imagery, airborne ternary imagery, and aerial photography. The compiled data is located in Appendix D and an example is presented in Figure 6.13.

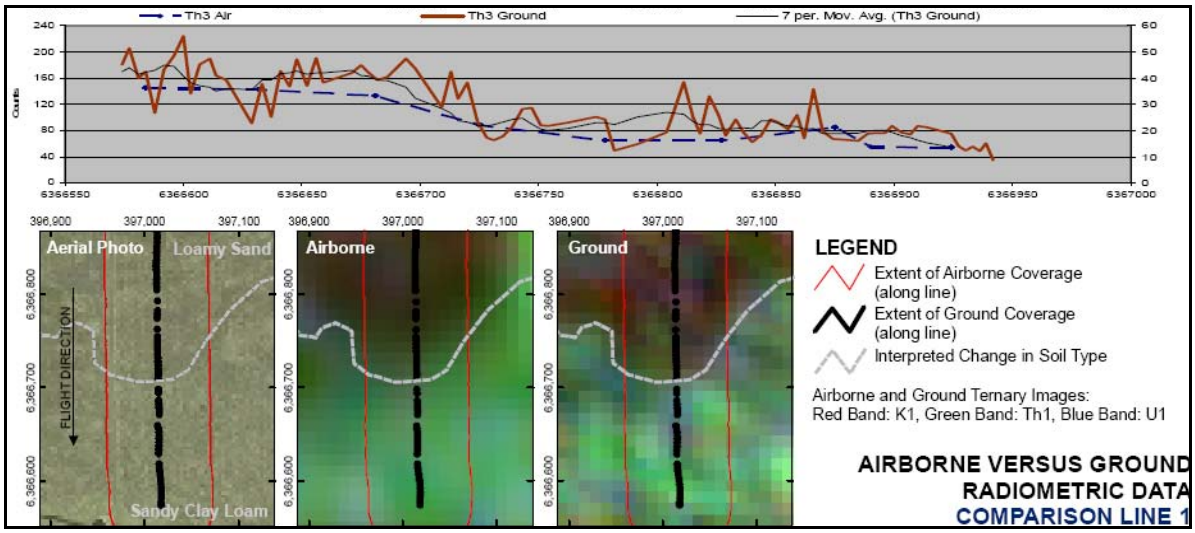


**Figure 6.13. Example comparison of airborne and ground high resolution radiometric line profile data for Th3, as presented in Appendix D. Line profiles for all seven radiometric channels derived using the multispectral processing methodology developed coincident to this study are illustrated in Appendix D.**

In the analysis of the compilations, ground and airborne data exhibited similar profiles, with the difference between the line data attributable to the different equivalent ground footprint, along line station spacing, and increased noise component in the ground data as a result of detector movement experienced while the system travelled over the uneven paddock. In spite of the increased distance from the ground, airborne count values were approximately three to four times larger than the

ground count values, comparable to the four-fold difference in acquisition crystal volume. This suggested the increased atmospheric component from 1 m to 30 m did not significantly reduce the gamma ray energy and any increase in noise at 30 m altitude was adequately resolved by using the larger crystal volume.

The change in response of ground and airborne data to interpreted soil boundaries was also examined (for example Figure 6.14). Whilst the change in response was considered with respect to interpreted soil boundaries, representing instantaneous change in radiometric response, in truth soil boundaries are most likely gradational. It was found that, in general, ground data could resolve an instantaneous change in soil response after 25 m or 4 to 6 samples, while the airborne data required at least 150 m of continuous data acquisition or 3 to 4 samples. These resolution factors are a result of the sample spacing and noise fraction within the individual radiometric systems.

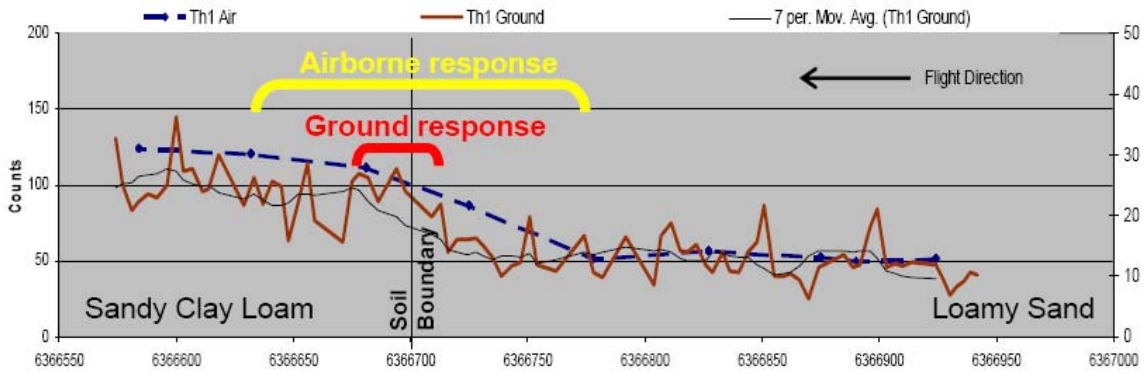


**Figure 6.14. Response distance required by ground and airborne data to register a change in soil type. Ground data resolved the change in soil response in 25 m or 4 to 6 samples, while the airborne data required at least 150 m of continuous acquisition or 3 to 4 samples. (Resolution implies an instantaneous soil boundary)**

The requirement to use 4 to 6 samples to define a soil boundary with ground data suggests that the resolving capability of the system is limited by the noise fraction in the data, and reducing the soil sample spacing would not improve the resolution. Thus the ground radiometric system is limited to resolving radiometric soil units larger than 20-25 m with a precision of ±7 m. Conversely, the requirement for at least 150 m of airborne samples in order to resolve the same soil boundary, which is the minimum requirement to resolve any change in response, suggests that it may be possible to improve the resolution of the airborne system by reducing the sample

spacing. The airborne system used in this study was capable of resolving soil units larger than 150-200 m with a precision of ±50 m.

### 6.3.5 Grid data comparison

While the accuracy of the airborne and ground line data is directly related to the survey height and survey velocity, the scale of grid data for mapping applications is a function of the accuracy of the line data, the line spacing, and the selected grid cell size. As both datasets were acquired with a line spacing of 25 m, the standard rule for imaging was to produce a grid size of 1/4 to 1/5 of the line spacing, approximately 5 m to 7 m (Street, 2004). However, the variability introduced to the ground line data as a result of the detector movement would be enhanced by such a small grid cell size. Furthermore, with a sample spacing of 50 m, gridding of the airborne data at 5-7 m would lead to a significant proportion of interpolated values in the airborne grid. To accommodate both these concerns, a grid spacing of 12.5 m was used.

For grid data to be used for mapping purposes, the width of a map line, approximately 2 mm, should represent the precision of the data. This conversion is used to define the scale at which the map products from the data should be used. For the ground data, the combined accuracy of the line data and grid cell size of 12.5 m suggested the data is suitable for use at 1:10,000 scale, where 2 mm represented 20 m. For the airborne data, the combined accuracy of the line data and grid cell size suggested the data is suitable for use at 1:25,000 scale, where 2 mm represented 50 m.

For soil and regolith mapping, simple soil maps produced at a scale of 1:25,000 were considered adequate for most land management applications (GeoAg Pty Ltd, 2004). Thus the lower resolution of the airborne provided no impediment to soil or regolith interpretation.

### 6.3.6 Imagery content comparison

The grid data was imaged for comparison, as presented in Appendix C. Figures 6.15 and 6.16 illustrate the common area covered by the airborne and ground datasets.

The ternary images also exemplify the colour range, contrast, composition, and texture expressed in the collective radiometric image suite.

The airborne and ground ternary imagery demonstrate similar colour range, composition, and contrast. In both images, sand dunes to the west and east were highlighted in black due to the dominance of quartz which has a low radioactive response. Palaeo-swamp and lacustrine regions underlying the western dunes, dominantly clay materials with comparatively higher thorium and uranium response, were highlighted in green in the radiometric ternary imagery. The remainder of the area was comprised of a complex alluvial/colluvial fan system, resulting in an intermingling of sand ridges, with low total radiometric response and sporadically elevated potassium producing black to deep red shades, and sandy clay areas, highlighted in blue due to the increased uranium response. These comparable features express similar geometry and physical extents in both airborne and ground imagery.

Locations where laterite was present are highlighted in bright green. The linear laterite trends represent transported material used to surface roads and cap heavily trafficked areas. In the airborne data, the roads are distinguished by their linear geometry. In the ground survey, data was not acquired along or across roads, thus the same linear features are not present in the ground data set.

A difference in texture was produced in the ground imagery as a result of the smaller footprint, smaller sample overlap, and subsequent increased variability between samples. However, the image textures, a term used to describe the degree of colour variability expressed over a small area, were quite similar with both images, demonstrating strong speckling over the red and blue alluvial/colluvial fan units. Accordingly, the slight increase in texture expressed by the ground image appeared to be controlled by the smaller equivalent footprint overlap, 30% along the ground compared to 64% in the air, and significantly different perpendicular overlap, 0% for the ground and up to 75% in the air. The overlap promoted a smooth transition from one sample reading to the next, producing smoother textures in the imagery. The presence of speckled texture in the airborne data suggested the ground radiometric

response varied rapidly, as captured in the ground data and accurately expressed in the ground imagery.

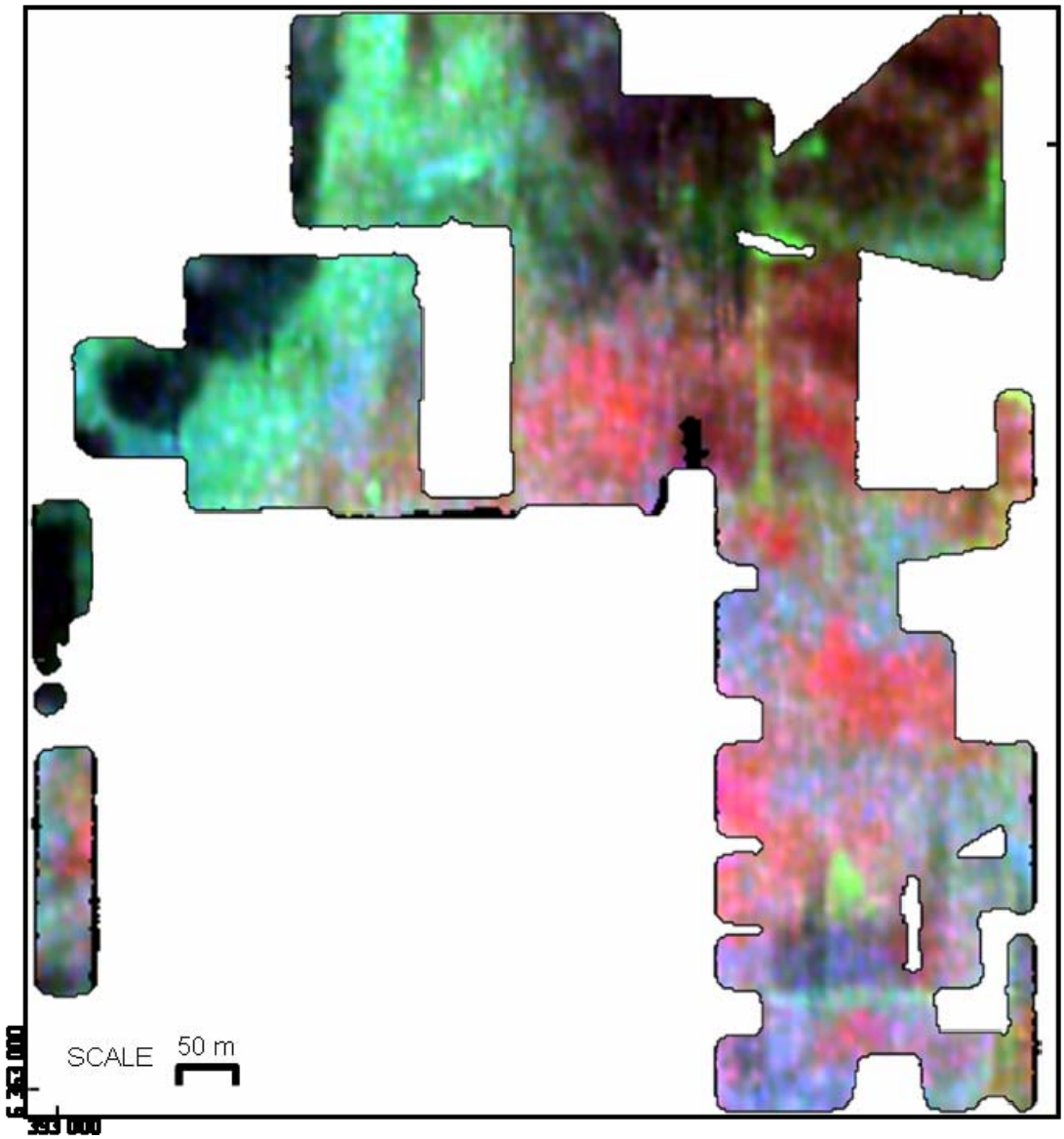


**Figure 6.15. Waroona airborne ternary image: K1 [red], U1 [blue], and Th1 [green]. The image has been clipped to the overlapping coverage between the ground and airborne datasets.**

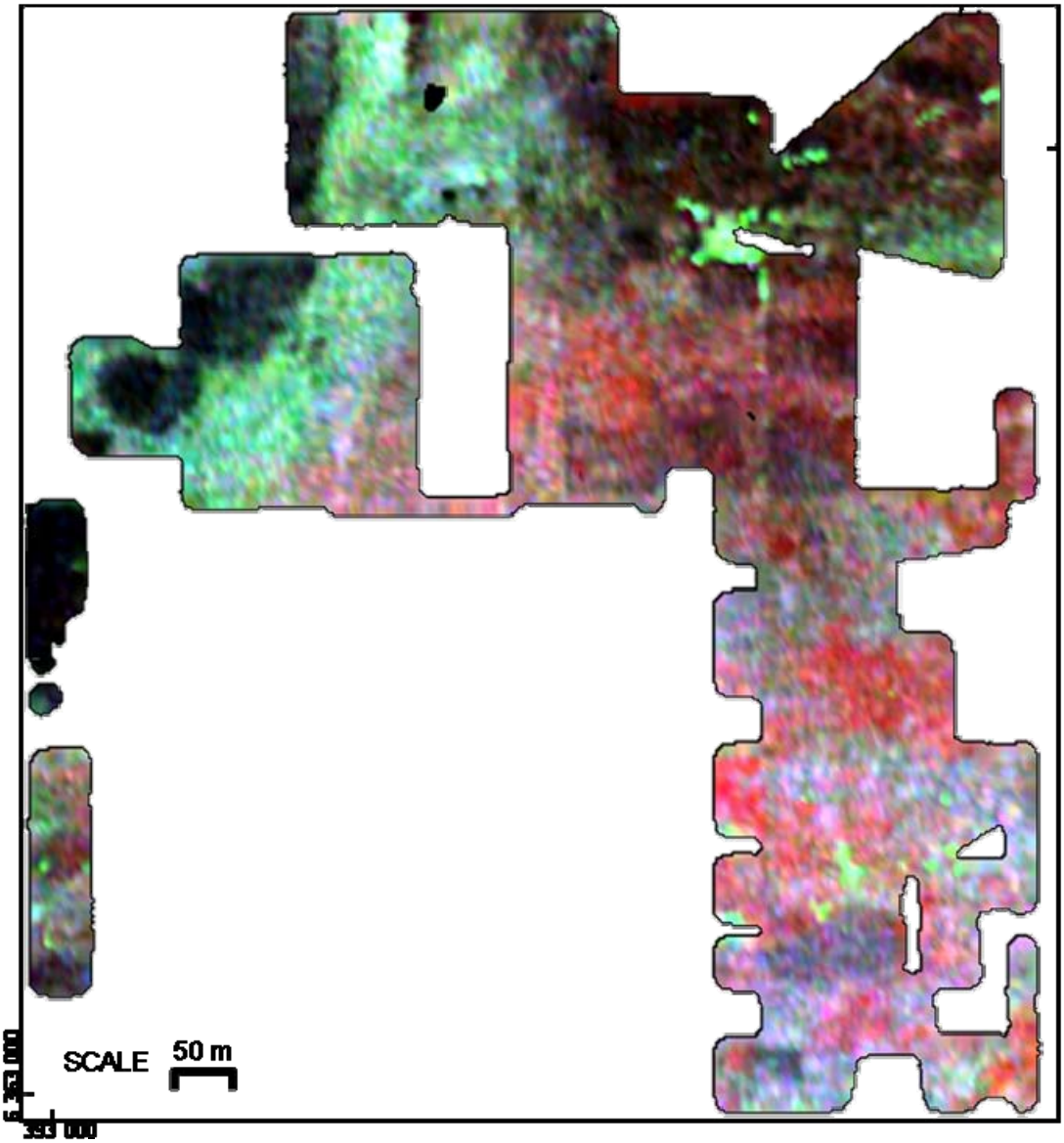


**Figure 6.16. Waroona ground ternary image: K1 [red], U1 [blue], and Th1 [green]. The image has been clipped to the overlapping coverage between the ground and airborne datasets.**

.

In an agricultural environment, fertilisers and the use of laterite or ironstone gravels introduce strong, unnatural sources of gamma rays over small areas. The strength of these sources can mask natural radiometric response making it difficult to resolve soil characteristics. As demonstrated in Figure 6.17, the strong gamma ray response from the lateritic road base used to build the road between the north and south paddocks was visible in the airborne imagery up to ~120m away from the road. While the range of the equivalent footprint and the sample spacing were used to establish the accuracy of the data, anomalous increases of ground radiometric response, particularly from anthropogenic sources, demonstrated larger zones of influence than the measured accuracy of the data. Consequently, in the airborne imagery anomalous high radiometric responses impeded the ability to identify soil units by spectral response and map continuous soil boundaries. Conversely, as a result of the ground data's smaller equivalent footprint, the anomalous high radiometric responses had little influence on the ground imagery, enabling soil units and boundaries to be mapped with defined accuracy to the paddock boundary.

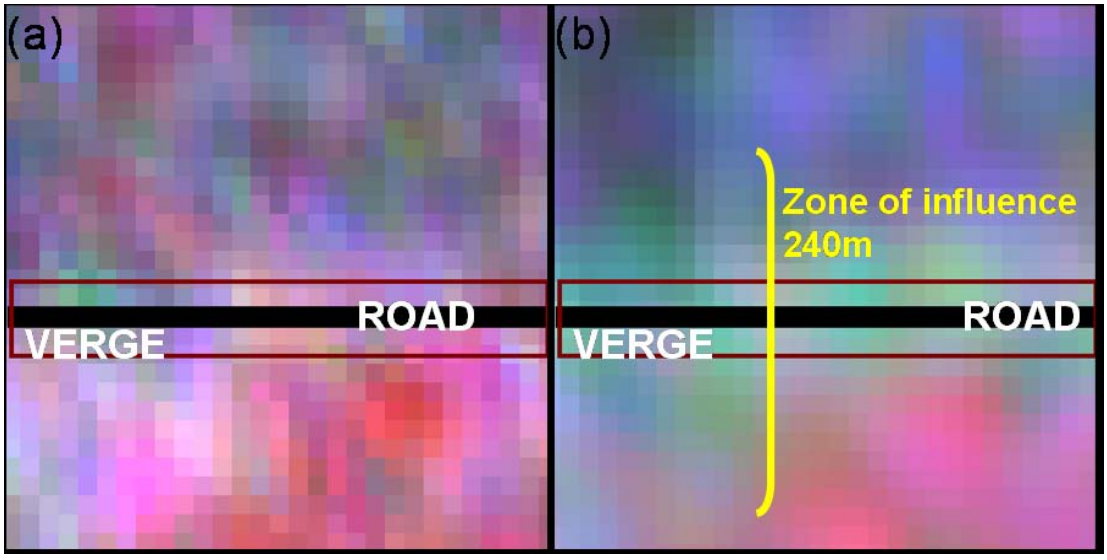


**Figure 6.17. Ground (a) and (b) airborne imagery of two paddocks separated by verge and road. Ground data was not acquired in the verge or road area. Consequently true soil patterns can be traced to the verge, while the areas within the verge are interpolated. In the airborne data, laterite from the road base produces an artificial thorium increase, influencing radiometric response within approximately 120 m either side of the road.**

Like the ground data, the airborne data was also affected by changes in sensor height. When the height of obstacles, such as powerlines and trees, were within 10 m of the

survey height, the pilot increased the height of the survey by 5 m to ensure adequate clearance, and then returned to the designated survey 30 m height. The increased altitude resulted in a comparative decrease in the recorded radiometric response. While standard processing, through calibration and height corrections was used to restore the equivalent 30 m radiometric response, the locations of the restored radiometric response could still be identified in the airborne imagery. The height difference was attributed to the increase in equivalent footprint as a result of the height increase. Although the height corrections could restore the relative magnitude of the radiometric response, the contribution from the increased footprint could not be removed. For example, in Figure 6.18 the increased altitude to 35 m increased the equivalent footprint radius to 65 m. As a result, the low radiometric response proportion was increased, producing the lower than expected response after height correction.

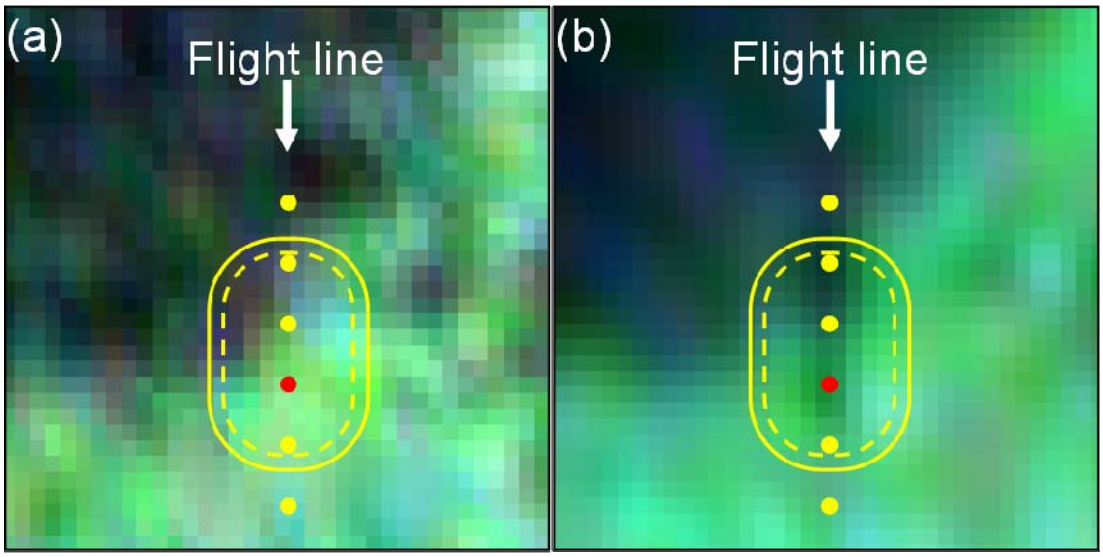


**Figure 6.18. Artificial radiometric response due to increased survey height. Ground (a) and (b) airborne radiometric imagery. The dashed yellow line marks the perimeter for the 30 m standard survey altitude, while the solid yellow line marks the perimeter of the equivalent footprint at elevated 35 m altitude, for the sample location marked in red. The increased altitude from 30 m to 35 m increases the proportion of low radiometric response in the sample. The low response cannot be restored using height correction, resulting in linear black lines within the airborne ternary imagery (b).**

Thus, where the gamma ray responses recorded in the larger equivalent footprint were not representative of the equivalent response in the standard footprint, the height corrected data was still in error. As a result, resolution of soil boundaries

required the interpreter to assume continuity through the erroneous data, creating a source of potential error in the interpretation.

### 6.3.7 The influence of irregular soil moisture content

As a consequence of irrigation, soil moisture content across the survey area was not consistent, with recently irrigated paddocks marked by confined rectangles of lower radiometric response than the neighbouring paddocks due to increased moisture. Additionally, as the airborne and ground surveys were not conducted at the same time, a comparison of the ground and air radiometric response over different soil moisture contents could not be conducted. However, there were notably more areas of low radiometric response as a result of higher soil moisture content encountered in the ground survey than the airborne survey.

The variability in the soil moisture content was to be expected, due to variable land use and subsequent differing irrigation rates and times. This variability removed the advantage of the airborne system to acquire data quickly with the hope of minimising changes in atmospheric and soil moisture conditions.

To compare local patterns in the radiometric imagery through the darker coloured regions of increased moisture content, simple image enhancements, such as the histogram enhancement illustrated in Figure 6.19, were used to alter the colour range and tones in the radiometric imagery. These enhancements improve the contrast between data channels, highlighting potential soil units. Thus, comparison of the resolution capability of the data and subsequent interpretation of the imagery required constant image interaction and enhancement to draw the maximum information from the data.

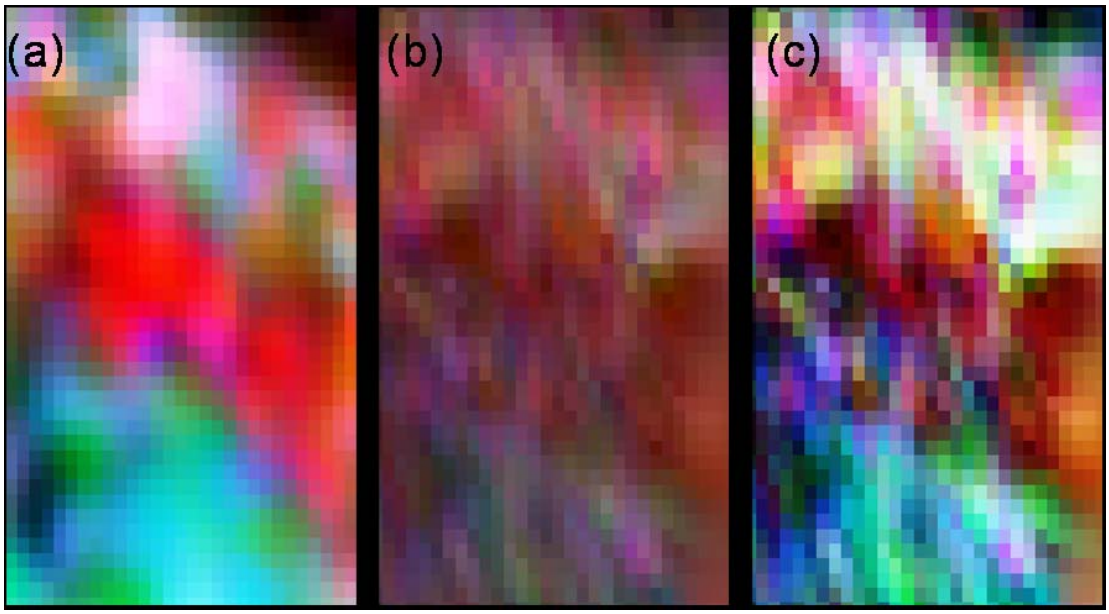


**Figure 6.19. Simple image enhancement to resolve areas of suppressed radiometric response. Airborne (a), (b) ground, and (c) histogram equalised ground ternary imagery. Airborne data (a) acquired before irrigation, has a low soil moisture level resulting good image contrast. The equivalent ground data (b) had higher soil moisture content, suppressing the radiometric response. Histogram equalisation (c) was used to improve the colour contrast in the ground imagery in the region with high soil moisture content.**

### 6.3.8 Societal and logistical issues

Survey logistics include survey planning and data acquisition issues, such as the transport of the survey platform to the location, accessibility to the survey area, and the ability to co-ordinate the survey with land owners and local residents.

For the ground survey, co-ordination with local residents and land owners, and access to the survey area, was conducted simultaneously through Harvey Water representatives. Physical access to the survey area was facilitated via sealed roads, unsealed roads, and access ways. Overall, there were few logistical problems with the acquisition of the ground data, with the survey conducted part-time over a period of 4 weeks. (The equivalent of 5 full time days to cover the same area as the airborne survey.)

For the airborne platform, permission to fly over the survey area was sought from all land owners and residents with written consent via Harvey Water representatives. The approximate timing for the survey was advertised in the local paper, and

residents were warned of the height and noise of the plane to minimise resident's surprise and potential discomfort during the survey.

Unfortunately, the limited availability of the survey platform proved to be a significant obstacle. For the acquisition of airborne data to be profitable, the airborne platform rotates continually from one job to the next all year round. As a consequence, delays on a previous job caused the initial schedule for the survey to be delayed by 2 weeks. The date of the rescheduled survey was subsequently rejected by some local residents who would not be in the area at the time and wished to be present for the survey in case stock became spooked by the aeroplane flyovers. However, with the tight scheduling and commercial demands the plane proceeded to its next appointment. Further negotiations with local residents and the survey company finally resolved, with the airborne survey completed approximately 3 months after the initial start date.

In addition, the basic access issues and platform availability that were also required for the ground survey, additional co-ordination was required to ensure all recommended Civil Aviation Safety Authority (CASA) safety and best industry practice requirements were met prior to commencing the survey.

Before the survey commenced, potential hazards to flying in the survey area were identified and recorded. Identified hazards included: trees, powerlines, aerials, buildings, potential road traffic, and railway. In accordance with CASA recommendations, the location of residential dwellings was noted and the survey was altered to avoid flying over residential dwellings. Contingencies for emergency landing were also developed, and the flight schedule was recorded with the local flight authorities.

Locations outside the survey area, where the noise or presence of the plane could cause adverse reactions in residents or livestock, were also identified and excised from the survey. In addition to the survey area, these locations needed to be avoided on the transit to and from the survey site. Included in this appraisal were: residences with infants, horses, feedlots, and stock routinely mustered with aeroplanes.

Unfortunately, muster areas and feed lots that were kept empty around the time of the initial survey start time contained stock at the rescheduled start time. As a consequence, these areas had to be excised from the proposed survey area just prior to its commencement, considerably reducing the planned survey area.

The logistical requirements of the ground survey proved to be considerably less than those required for the airborne survey. Although the delay of the airborne survey was unfortunate, the problems experienced with this survey were not unique. The most significant problems, such as the inability to survey over active feed lots and stock yards, resulted from the complexity of scheduling between the survey plane and the multiple farming activities performed in this intensive agricultural area.

However, where the airborne system required all activities to be compatible with the acquisition of airborne data on the day of the survey, the ground system was more versatile. As the four wheel motorbike was considerably quieter than the plane, it was possible for ground data to be acquired in paddocks adjacent to active stock yards and feed lots where airborne data could not be acquired. Moreover, as the ground data required a longer time frame to collect than the airborne data, it would be possible to modify the ground survey acquisition sequence, providing more opportunities to accommodate stock movement and other scheduling issues.

### 6.3.9 Cost comparison

#### 6.3.9.1 Acquisition costs

The cost of acquiring airborne and ground data, based on 2004 prices, was compared to support a basic cost-benefit analysis of the two systems.

The airborne platform acquired ~600 line kilometres a day, based on a velocity of 50 m/sec. Costs for acquiring airborne data ranged from $4,200* per day (*Western Australian Government negotiated price for over 500,000 line kilometres of data, (D Howard 2004, pers. comm., 11 January)) to $15,000^ per day (^starting price per survey for any airborne survey in Australia, provided by UTS Geophysics (D Abbott 2004, pers. comm., 15 February)), which equated to $0.35 to $1 per sample. The cost

for 475 line kilometres of airborne radiometric data acquired for this survey was AU$11,000 excluding mobilisation costs.

In contrast, the ground platform acquired ~100 line kilometres per day, at a velocity of 5 m/sec to 8 m/sec. The cost of acquiring ground data was estimated at between $3,000 and $4,000 per day (J Anning 2004, pers. comm., 18 March), which equated to $0.24 to $0.32 per sample. For this study, the cost for 475 line kilometres of ground radiometric data was AUS$15,000 excluding mobilisation costs.

Using the available airborne and ground cost estimates, a summary of the costs per line kilometre and per sample is provided in Figure 6.20. Additional costs for mobilising the ground and airborne platforms to the area have not been included in the cost estimate as they were not provided for the surveys in this study. However, in general, mobilisation costs increase with distance from Perth for ground surveys and distance from the major airports for airborne surveys.

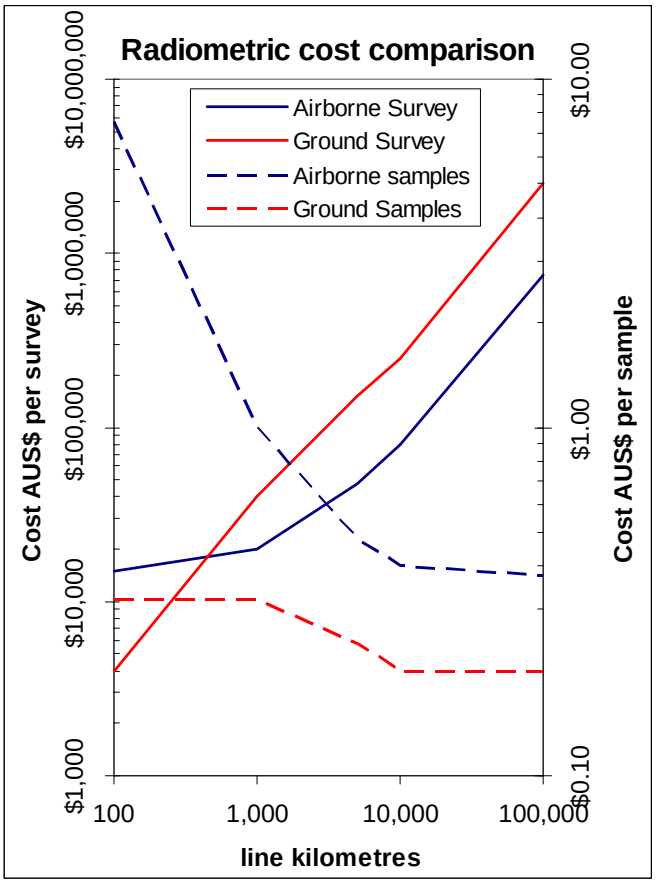


**Figure 6.20. Cost comparisons for airborne and ground radiometric surveys.**

The cost estimates showed that for small surveys close to Perth, requiring less than 500 line kilometres, equivalent to 1,250 Ha at 25 m line spacing, acquisition using the ground platform was the most cost effective option. For surveys between 500 and 1,000 line kilometres, equivalent to 1,250 to 2,500 Ha at 25 m line spacing, located more than 200 km from Perth or a regional airport where additional mobilisation costs would be incurred, the ground platform remained the more cost effective option. Ground and airborne surveys around 1,000 line kilometres showed similar costs. For large surveys, greater than 1,000 line kilometres, airborne surveys offered considerable cost savings over ground surveys.

#### 6.3.9.2 Cost benefit comparison

For the Waroona area, the airborne and ground surveys delivered data of similar quality, suitable for mapping soil changes at a scale of 1:25,000. Without limitation to survey coverage, cost and therefore the total number of line kilometres is the most significant factor to the selection of an appropriate acquisition platform.

However, significant limitations were observed in the intensive agricultural area of Waroona. These limitations revolved around the farming activities in the area, including the inability to acquire data across active stock yards and feedlots. As a result, the acquisition of ground data, which provides more opportunities to incorporate farming schedules, is a more prudent choice for area of intensive agriculture.

A summary of the most appropriate survey platform according to land use is provided in Table 6.6.

**Table 6.6. The most appropriate survey platform for different land uses.**

| | Line kilometres (Area) of coverage | | | |
|---|---|---|---|---|
| **Land use** | **<500 km (<1,250 Ha)** | **500-1,000 km (<2,500 Ha) >200km airport** | **500-1,000 km (<2,500 Ha) <200km airport** | **>1,000 km (>2,500 Ha)** |
| **Intensive agriculture** | Ground | Ground | Ground | Ground |
| **Broad-acre farming** | Ground | Ground | Airborne | Airborne |
| **Non-agricultural, non-residential** | Ground | Ground | Airborne | Airborne |

### 6.3.10 Conclusions

Line data and imagery generated from airborne and ground radiometric acquisition platforms were compared to identify differences and similarities between data quality, data resolution, logistical issues, and cost differences from the perspective of their application to soil mapping.

In comparing the data quality of the two platforms it was found that:

- Line data from the ground platform exhibited small, local fluctuations. The fluctuations were attributed to sensor movement and the general variability in the ground response.
- Line data from the airborne platform exhibited a smooth response with few fluctuations and gentle transitions from one soil type to the next.
- Both datasets produced similar images with comparable colour range, contrast, and composition.

From the comparison, the following conclusions were drawn with respect to the application of high resolution, 25 m line spaced airborne and ground radiometric data for soil or regolith mapping:

- Both platforms produced comparable imagery, suitable for identifying changes in radionuclide distribution for soil or regolith mapping applications.
- For the ground platform, the line data demonstrated an accuracy of ±7 m, with the imaged products suitable for 1:10,000 scale interpretations.

- For the airborne platform, the line data demonstrated an accuracy of ±50 m, with the imaged products suitable for 1:25,000 scale interpretations.

Cost comparison of the airborne and ground platforms demonstrated:

- For small surveys close to Perth requiring less than 500 line kilometres or 1,250 Ha at 25 m line spacing, the ground platform was the most cost effective option.
- For surveys between 500 and 1,000 line kilometres or between 1,250 to 2,500 Ha at 25 m line spacing located less than 200km from Perth or a regional airport, the airborne platform was the more cost effective option.
- For surveys >1,000 line kilometres or >2,500 Ha at 25 m line spacing there were significant cost savings by employing the airborne platform.

A simple cost benefit comparison performed to establish the most suitable survey platform for different land uses established that:

- In areas of intensive agriculture the ground platform was the best option.
- In areas of broad acre farming and non-agricultural, non residential land use, the ground platform was the best option when the survey was less than 1,000 line kilometres and located more than 200 km from an airport

.

## 6.4 Case Study 4: Improving image resolution and radiometric interpretation using multispectral processing

### 6.4.1 Abstract

In this study, seven localised soil maps were produced for selected 25 Ha (250 000 $m^2$) areas in Elashgin, Western Australia. The maps were produced using a standard interpretation approach, integrating information from available soil maps, aerial photography, and radiometric imagery. The radiometric data was presented as low resolution (200 m line spaced, 20 m flying height) and high resolution (25 m line spaced, 20 m flying height) ternary imagery (red: potassium, blue: uranium, and green: thorium), as well as high resolution thorium ternary imagery, uranium ternary imagery, and uranium ratio imagery produced using the multispectral processing methodology developed during the study.

Comparison of the low and high resolution radiometric imagery showed that where the contrast between the soil unit radiometric responses was weak, high resolution radiometric data was able to resolve boundaries between soil units. The same boundaries could only be inferred from the lower resolution data. Additionally, the comparison showed that where the radiometric response was strong, the high resolution data served to refine the boundary location. These results imply that when interpreting soil boundaries from radiometric data, high resolution radiometric data is required to resolve soil boundaries when the contrast between the radiometric responses of soil units is low, or where the overall radiometric intensity of the soil is low.

Comparison of radiometric imagery with aerial photography and available soil maps confirmed that high resolution airborne radiometric data could resolve features approximately 50 m wide, providing the extent of the characteristic radiometric response was in excess of 100 m. Features smaller than these dimensions were occasionally resolved; when the acquisition path was directly over the top of the feature and there was a high radiometric response contrast between the feature and the background. Subsequently, although the prescribed scale for the high resolution data was believed to be 1:25,000, in locations where there were strong contrasts

between the radiometric responses of the soil units, the data was considered to be suitable for mapping at scales of 1:2,500 or “paddock-scale”.

In addition, comparison of the standard radiometric and multispectral processed images in this case study showed that additional spatial patterns, beyond those exhibited by the standard ternary radiometric image, were resolved in the alternative multispectral processed radiometric imagery:

- Thorium ternary (red: $^{208}$Tl, green: $^{228}$Ac (900 keV), blue: $^{228}$Ac(1600 keV)) imagery,
- Uranium ternary [red: $^{214}$Bi (1764 keV), green: $^{214}$Bi (1120 keV), blue: $^{214}$Bi (1253 keV)] imagery, and
- Uranium ratio [214Bi 1120 keV / 214Bi 1764 keV] pseudo colour imagery.

Through interpretation, the additional patterns were used to resolve additional soil unit boundaries and to provide additional soil characteristics and local environmental conditions information in each mapping study.

### 6.4.2 Introduction

Since the mid 1990s, radiometric data has been regularly investigated as a means of improving regolith and soil maps (eg Wilford, 1992; Cook *et al.*, 1996b; Bierwirth, 1996; Wilford *et al.*, 1997). These studies, and those which followed, focused on the distribution of radioelements derived from radiometric data to map soil distribution patterns and interpreted potential soil or regolith type, acknowledging that changes in local environmental conditions hampered their interpretation. The concept of using these relationships to assist in the resolution and interpretation of soil properties, the same relationships that result in problems during using standard processing, had not been investigated.

With the development of the multispectral processing methodology, developed as part of this study (refer to Chapter 4), it was recognised that the physical as well as the chemical relationships between the seven resolved radiometric channels could be used to interpret soil type and local environmental conditions. In this case study, soil maps are produced from interpreted multispectral processed radiometric imagery, as developed in this thesis.

For comparison of the interpreted radiometric soil maps with a comparable, "real" soil map, the soil map from the Cooper *et al.* (2001) *Elashgin focus catchment report* was employed in the study. A subset of this map is reporduced in Appendix C, Figure C.2.23 for the Elasgin study area. The wider Elashgin study area was extensively studied by Cooper *et al.* (2001) for the Department of Agriculture and Food, Western Australia. The studies integrated standard soil mapping techniques and interpretation of regional radiometric data to produce a series of 1:25,000 maps: soil, salinity and waterlogging, recharge, predicted groundwater rise, and strategic revegetation locations. Although their maps are presented at 1:25,000 scales, Cooper *et al.* (2001) reports that the maps were produced at "catchment-scale" and require caution when interpreting them at the paddock and farm scales, as they are not highly accurate at these smaller scales and provide only general information for implementing local soil management practices. However, the Cooper *et al.* (2001) soil maps represent current best practice for mapping soil properties at local scales and are one of only a handful of soil maps available in Western Australia at a comparable local scale.

### 6.4.3 Interpretation of soil properties from multispectral processed radiometric imagery

#### 6.4.3.1 Elashgin Case Study Map Series

The following map series are local study sites from the Elashgin region in Western Australia. In Figure 6.21 the individual study areas used in the map series are highlighted as small ternary radiometric images overlying the available aerial photography. The map series includes data commonly used for making land management decisions, including:

- soil maps from the Cooper *et al.*, (2001) study,
- digital elevation model imagery,
- aerial photography, and
- radiometric imagery.

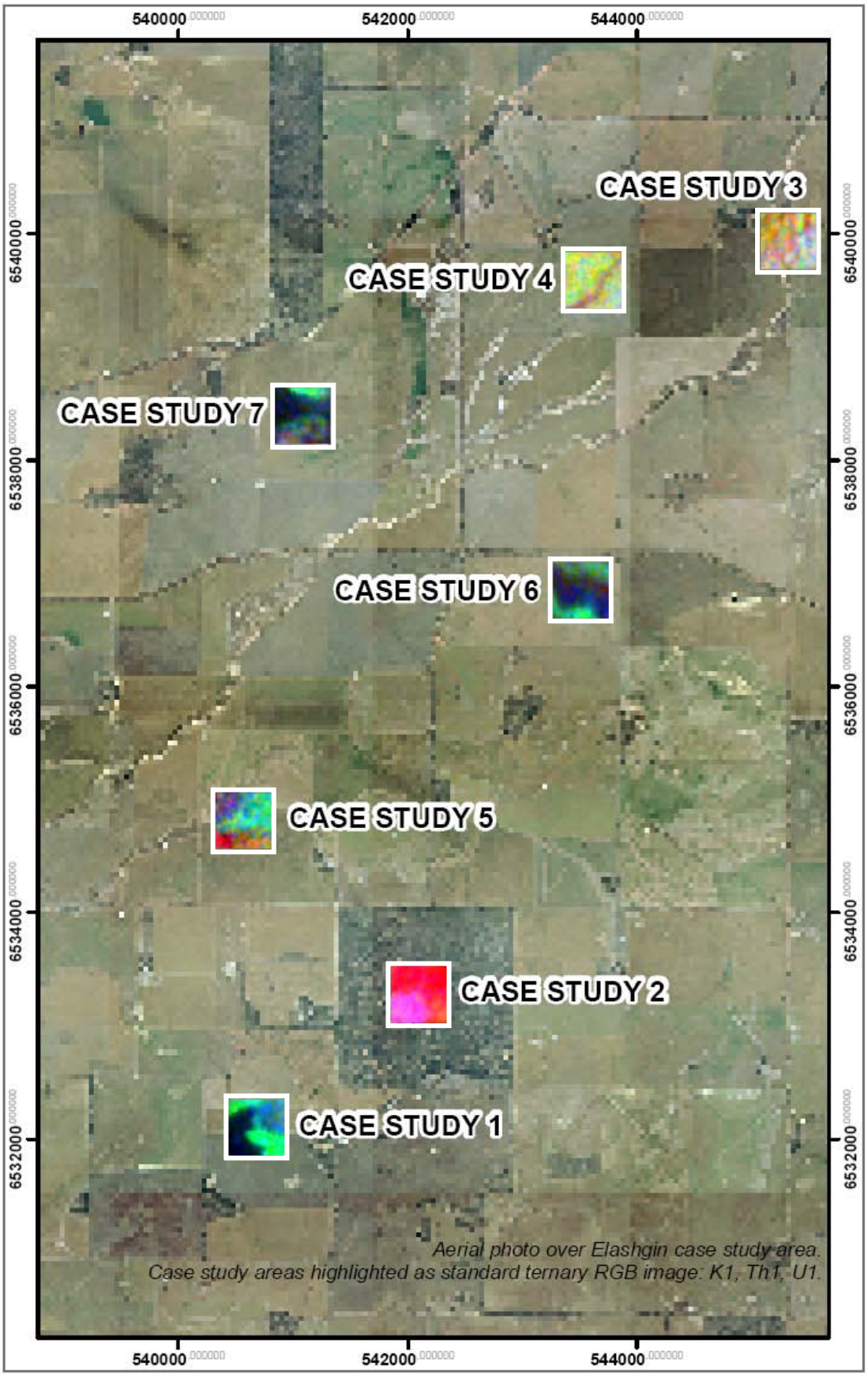


**Figure 6.21. Location of the local case study map sheets in the Elashgin area. Map series areas are highlighted as standard ternary [red: potassium, green: thorium, blue: uranium] images on an aerial photo of the wider Elashgin study area.**

The radiometric imagery presented on each map sheet is derived using the multispectral processing methodology described in Chapter 4. Colour changes within the radiometric imagery are generally attributed to changes in soil composition, but may be related to the physical interaction of gamma rays and radionuclide behaviour in the environment. This information can be interpreted and integrated with other data to define soil and local environmental conditions. The radiometric imagery employed in the map series includes:

1. High resolution ternary [red: $^{40}$K, green: $^{208}$Tl, blue: $^{214}$Bi] imagery. This is a standard radiometric image presentation that can be produced using standard processed data, using 25 m line spaced data radiometric survey data. Colour changes are generally associated with changes in soil composition.
2. Low resolution ternary [red: $^{40}$K, green: $^{208}$Tl, blue: $^{214}$Bi] imagery. This is a standard radiometric image presentation that can be produced using standard processed data, using 200 m line spaced radiometric survey data. Colour changes are generally associated with changes in soil composition.
3. Thorium ternary [red: $^{208}$Tl (1764 keV), green: $^{228}$Ac (900 keV), blue: $^{228}$Ac (1600 keV)] imagery. The radiometric data in this imagery is derived exclusively using the innovative multispectral processing technique described in Chapter 4 with 25 m line spaced data. $^{208}$Tl and $^{228}$Ac are daughter products produced during the decay of $^{232}$Th. Gamma ray emissions from $^{228}$Ac decay are produced at least 1.9 years (half-life) before the emission of $^{208}$Tl gamma rays. The separation in the concentration of $^{228}$Ac (green and blue tones) and $^{232}$Th (red tones) energies may be linked to local variations in soil chemistry, soil movement and water movement.
4. Uranium ternary [red: $^{214}$Bi (1764 keV), green: $^{214}$Bi (1120 keV), blue: $^{214}$Bi (1253 keV)] imagery. The radiometric data in this imagery is derived exclusively using the innovative multispectral processing technique described in Chapter 4 with 25 m line spaced data. As the uranium response in all three channels is derived from the same $^{214}$Bi decay reaction, ratio variation in the detected energy may result from preferential attenuation of the lower energies due to increased obstructions, such as increased density or decreased porosity. Thus changes in image tone and texture may indicate changing soil density and/or soil overburden. However, potassium energies can contaminate the $^{214}$Bi 1253 keV (blue) channel.

While this does not detract from the use of the imagery for identifying changes in soil characteristics and local environmental conditions, caution should be applied when using the imagery to directly attribute cause.

5. Uranium ratio [$^{214}$Bi 1120 keV / $^{214}$Bi 1764 keV] pseudo colour imagery. The radiometric data in this imagery is derived exclusively using the innovative multispectral processing technique described in Chapter 4 with 25 m line spaced data. As described above, both 1120 keV and 1764 keV energy gamma rays are emitted at the same time. Thus, the uranium ratio can be used to identify preferential attenuation of the lower 1120 keV energy that may indicate a decrease in soil porosity or increase in soil density.

For each data source in the map series, a short description of the information interpreted from the data is provided. This information is subsequently combined to create a new "paddock-scale" soil map and interpretation of landscape processes at each study site. The interpretation includes recommendations for land management arising from the interpreted landscape, based on "best practice" described in (Cooper *et al.*, 2001).

#### 6.4.3.2 Supplementary notes for the Elashgin Case Study Map Series

In the following Elashgin Case Study Map Series, the image source and scale bars are not provided within the map due to space limitation. This information is provided below.

##### Geological Setting

These images were clipped from the 1:250,000 Geological Survey of Western Australia Kellerberrin Geology map sheet SH5015 (Chin, 1986). Information relevant to the interpretation from this image is either labelled on the image or described in the information window.

##### Dept Agriculture 1:25,000 soil map

As described previously, these images were extracted from the Cooper *et al.* (2001) *Elashgin Focus Catchment Report* map series. The *Elashgin Foucs Catchment* map

series was developed using a mixture of farmer soils maps, ground truthing, and aerial photography. The soil units illustrated represent soil types with similar land management issues and production potential that would be best managed in the same way. Soil types that were very closely associated in the field, and thus impossible to manage separately, were not mapped separately. Information relevant to the interpretation from this image is either labelled on the image or described in the information window.

### Aerial Photography and Agricultural Use

Colour, high resolution aerial photographs were only available over the map series areas investigated. Low resolution, continuous colour photography, as shown in Figure 6.21, was used when a regional perspective was required for the interpretation. Information relevant to the interpretation from this image is either labelled on the image or described in the information window.

### Digital terrain

The digital terrain imagery presented in the map series was generated from the airborne altimeter data acquired during the radiometric survey. A linear stretch was applied to each image to show the lowest points in the study areas in dark blue through green and brown to show the highest points in white, as shown below:

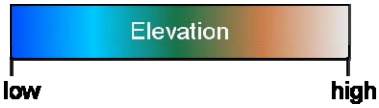


Therefore different vertical and colour scales apply to each study. Scale was not provided on these images, as the morphological characteristics of the digital terrain data were not investigated as part of this work and the imagery was used only as an indicator of landscape position. Instead, generic scale bar is provided above, and a description of the elevation change and position in the landscape is provided in the map series.

### Ternary Images

Ternary images combine three separate datasets into one image by assigning each dataset to a unique colour: red, blue, or green. All of the ternary images use the same

colour key, shown below, with the change in brightness related directly to the intensity of the value.

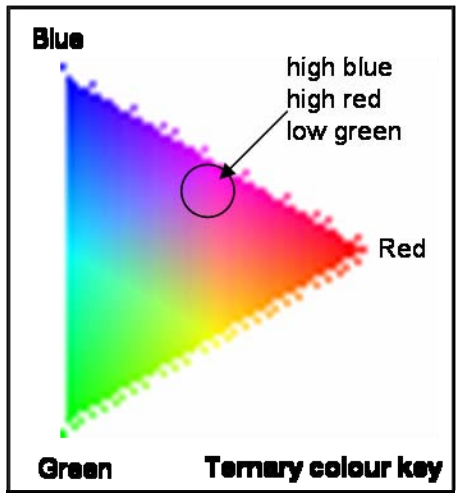


The same colour stretch was applied to all of the radiometric images across the map series. Thus the radiometric response for each image type can be directly compared across map sheets.

## Elashgin Case Study

**Map 1**

scale

250 m

KEY

- Deep yellow sand
- Sand over buried ironstone gravel
- Shallow sand over ironstone gravel
- Loam (red/brown)

**Summary:**
Four soil types were isolated within this 25Ha area. The deep yellow sands of the productive sandplain are easily identified in the radiometric data as a consistent low response. Within the unproductive sandplain area, three subdivisions were identified. The gravel subdivisions, sand over ironstone gravel and shallow sand over ironstone gravel, have similar soil characteristics with low to moderate water holding capacity, and therefore similar land management requirements. Although, the shallow sand over ironstone gravel unit will be less able to accommodate crop growth as it limits root penetration depth. The loam unit should have increased water holding capacity and better soil profile development than the gravel units do, and therefore should be a productive soil. Because of the small size of the unit and position at the edge of a paddock, the loam may simply have been incorporated in to the nearest soil unit, unproductive soils, during mapping. This unit, visible in the aerial photograph, would make an ideal location for tree planting due to the high water holding capacity and higher root penetration capacity, with the aim of reducing local recharge and lowering local groundwater levels.

**Geological setting**

Colluvium and minor alluvium – silt, sand and gravel derived from underlying and adjacent laterite and bedrock.
Granite outcrop to the north and east outside the area of seriate adamellite; medium and coarse grained, variably textured, locally porphyritic.

**Digital Terrain**

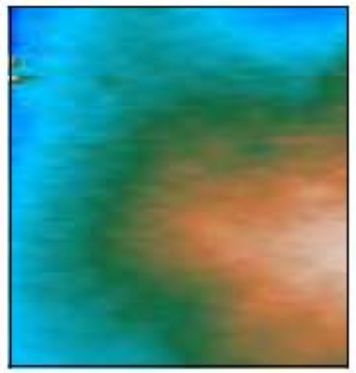

Western edge of a local topographic high. The terrain increases 7m from dark blue to white over 500m. Alluvial/colluvial plains lie to the west, south and north of the area.

**Thorium Ternary $^{208}Tl^{228}Ac(900keV)^{228}Ac(1600keV)$ RGB Image**

Four distinct units are visible: the northern light blue, western black (known productive sandplain), south east white and north east green. The light blue, white and green were mapped as the unproductive sandplain. The consistent high of all three datasets to form the white unit is indicative of the presence of ironstone gravel, confirmed by a soil sample identifying the unit as loamy gravel. The light blue signifies a slightly lower response from all datasets, probably lower gravel content resulting from buried gravel or a more dispersed distribution within the unit. The green signifies a medium response from all three datasets, indicative of an increased slightly thorium content over the productive sandplain, possible with increased absorption with increased clay content over the sandplain, or deeply buried lateritic gravel.

**Dept Agriculture 1:25,000 soil map**

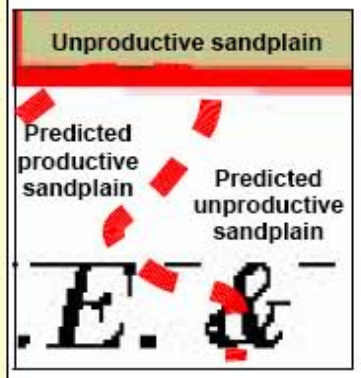


This area is located just outside the established soil map. From analysis of the mapped region to the west and north, a predicted extension (marked in dashed red line) of soil units unproductive pale sandplain (poor sands and acid wodjil) and productive sandplain are presented.

**High resolution ternary $^{40}K^{208}Tl^{214}Bi$ RGB Image**

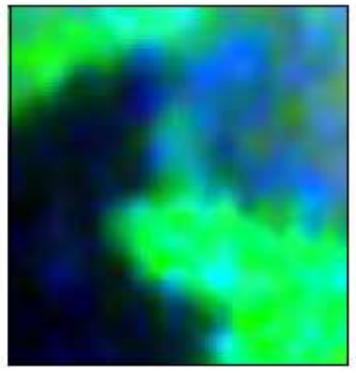

Three units are visible: western dark blue (known productive sandplain), northeast blue, and cyan/green. $^{40}K$ is relatively low throughout this area, $^{214}Bi$ is low on the western third of the area, thus the majority of the variability and differentiation is related to $^{208}Tl$. The edge of the productive sandplain (dark blue) is clearly defined by low $^{208}Tl$. The cyan/green and blue units are mapped as unproductive sandplain. The slight texture change visible in the aerial photo is differentiated (blue area) by medium $^{208}Tl$ levels and relatively higher $^{40}K$, indicating an increase in clay or granitic fragments from the neighbouring outcrop.

**Uranium Ternary $^{214}Bi(1764keV)(1120keV)(1253keV)$ RGB Image**

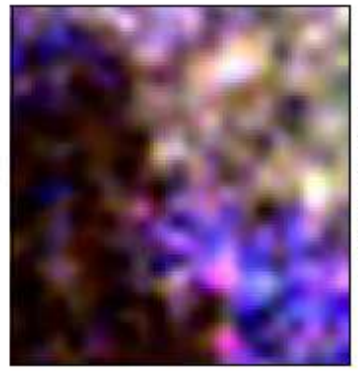

Three units are visible: western brown (known productive sandplain), northeast yellow and purple/blue. $^{214}Bi$ energies 1764 keV and 1120 keV produce nearly identical response in this area, with the western third, the productive sandplain, producing a lower response, compared to the eastern two thirds. Energy from the 1253keV emission, however, is higher over the purple/blue areas, with a relative medium response over the yellow unit.

**Aerial Photography and Agricultural Use**

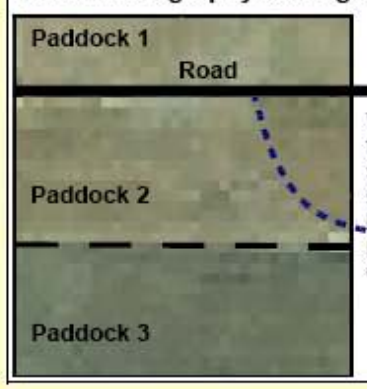


Wheat- sheep rotation area. Three fenced areas are identified. A road separates paddocks 1 and 2. A slight change in texture (marked in blue) in the aerial photo is noted in paddock 2, otherwise paddocks dominated by agricultural use.

**Low resolution ternary $^{40}K^{208}Tl^{214}Bi$ RGB Image**

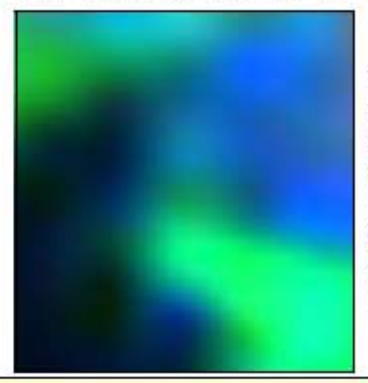

The same basic patterns seen in the high resolution image can be resolved in the low resolution data. However, small, insignificant textural components (dark green) seen in the sandplain (dark blue) high resolution data have become more prominent in the low resolution data, which may cause some problems for interpretation of low resolution data.

**Uranium Ratio $^{214}Bi$ 1120kev/1764keV**

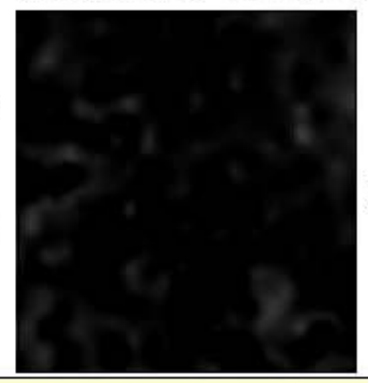

This area presents a consistently low ratio, indicating a regular soil density or permeability.

# Elashgin Case Study

## Map 2

scale

250 m

**KEY**

- Granite Outcrop
- Shallow rocky sandy soil over granite
- Jam/York Gum rocky red brown loam

**Summary:**
Three soil types were isolated within this 25Ha area, expanding on the two soil types identified in the original soil survey. The granite outcrop is more clearly defined with the radiometric data, as are the shallow rocky, sandy soil flanks that surround the fractured granite outcrop. Deep lenses of Jam/York Gum, rocky red brown loam are identified in the northern portion of the area with the aid of the thorium data. This area is currently employed as a vegetation reserve and, as a local high with fractured granite, is a probable local recharge location. Dense vegetation of this area will benefit down slope farming practices by reducing surface water runoff and groundwater recharge to intermittently waterlogged areas to the north.

**Geological setting**

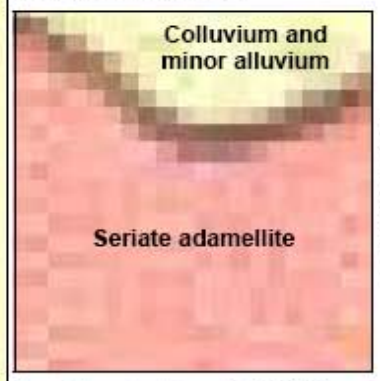


Colluvium and minor alluvium – silt, sand and gravel derived from underlying and adjacent laterite and bedrock in the north.
Seriate adamellite; medium and coarse grained, variably textured, locally porphyritic to the south.

**Digital Terrain**

Located on the northern slope of a local topographic high.

**Thorium Ternary $^{208}Tl^{228}Ac(900keV)^{228}Ac(1600keV)$ RGB Image**

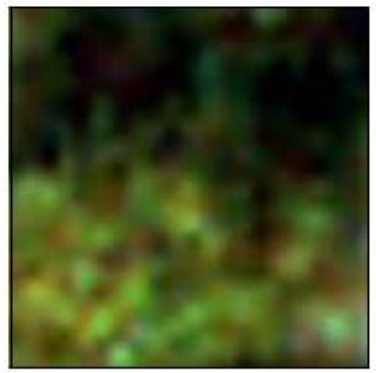

All three datasets are highly correlated, with relatively higher concentration in the southern two-thirds, and low concentration in the northern third. However, the difference in concentration between the north and south units are slightly more pronounced for the $^{228}Ac$ 900 keV dataset, thus the dominance of the green colour in the image. The difference in concentration suggests an increase in depth to source for the thorium, associated with the increasing depth to bedrock.

**Dept Agriculture 1:25,000 soil map**

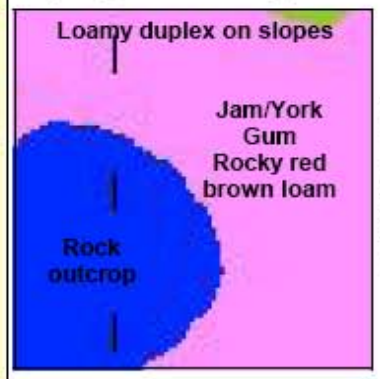


Soil is dominated by outcropping, fractured granitic bedrock, surrounded by Jam/York Gum, a resilient rocky red brown loam, not prone to degradation, associated with granitic outcrops in the area, with a soil depth to 1.5m before reaching bedrock.

**High resolution ternary $^{40}K^{208}Tl^{214}Bi$ RGB Image**

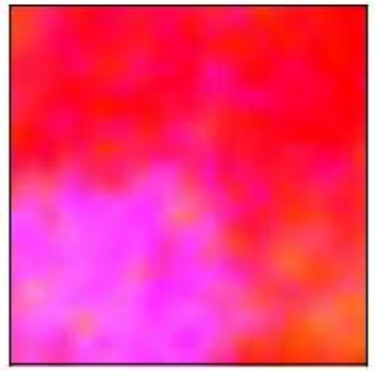

$^{40}K$ is uniformly distributed across this area, although locally high with respect to the survey area. $^{208}Tl$ distribution is dominated by an east-west trend, with the northern half of the area containing lower concentration than the southern half. $^{214}Bi$ concentration is the controlling dataset in the image, with high concentration producing the light pink unit (known outcrop) in the south west corner of the area, and low $^{214}Bi$ concentration producing the dark pink unit (known red brown loam) to the north and east.

**Uranium Ternary $^{214}Bi(1764keV)(1120keV)(1253keV)$ RGB Image**

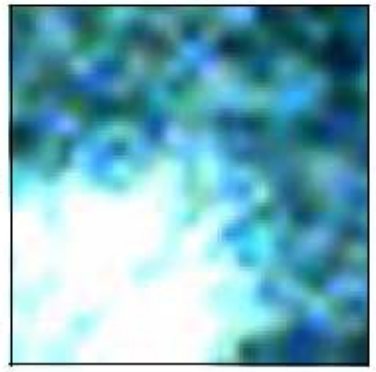

All three datasets are highly correlated, with high concentration of $^{214}Bi$ in the southwest corner highlight the location outcropping bedrock. Slightly relatively lower concentration of $^{214}Bi$ 1764 keV in the remaining area produces the light blue colour in the image.

**Aerial Photography and Agricultural Use**

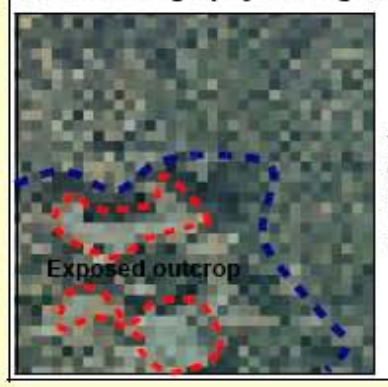


Vegetation reserve with shallow soil over bedrock. Outcropping bedrock can be identified in aerial photo (blue line) with isolated peaks identified in red.

**Low resolution ternary $^{40}K^{208}Tl^{214}Bi$ RGB Image**

The same basic patterns seen in the high resolution image can be resolved in the low resolution data. However, the shape of the outcrop has an east-west bias as a result of the wider line spacing.

**Uranium Ratio $^{214}Bi$ 1120kev/1764keV**

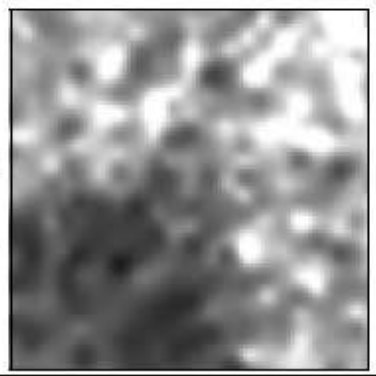

The lower ratio over the known outcrop correlates with the higher density of the fractured granite outcrop, compared with the high ratio produced from fractured rock fragments and greater permeability in the soil surrounding the outcrop.

## Elashgin Case Study

**Map 3**

scale

250 m

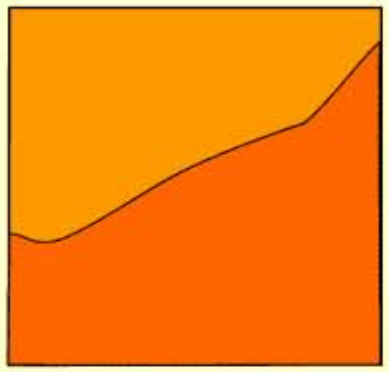

**KEY**

- Deep sand over clay
- Shallow sandy loam over clay

**Summary:**
Two duplex soils were isolated within this 25Ha area, deep sand over clay and shallow sandy loam over clay. Although originally classified as a single unit, the soil properties and management options for these units are very different. The deep sand over clay is capable of supporting a perched aquifer of relatively fresh water, accessible to crops at the end of the growing season. Thus, as long as recharge to these areas is kept to a minimum, cropping is possible even though water holding capacity and nutrient levels are low. Conversely, perched aquifers in the shallow loam over clay cause waterlogging, increase salinity at the surface, and restrict plant growth. These areas require a high level of management. The high sodicity of the clay in this area causes clay dispersion and clogging of available pore space, in turn increasing waterlogging. Effective drainage and low recharge is imperative to the management of these soils. Revegetation is a highly recommended option for shallow loam over clay soils when small pockets of the soil are identified.

**Geological setting**

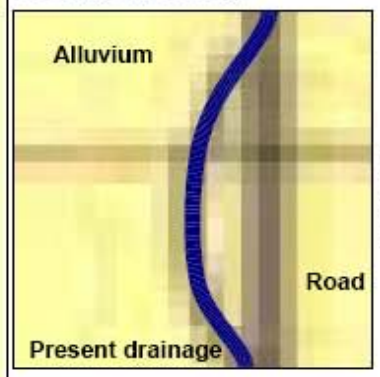


Alluvium – silt and sand in broad valley flats, extensively reworked by present drainage. Current drainage marked (from geology map) in blue.

**Digital Terrain**

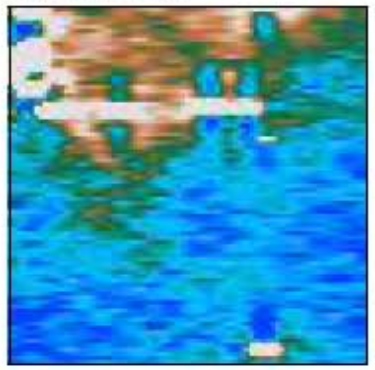

The digital terrain is very subtle, increasing 2.5 over 500 m. The low in the south looks to be part of a subtle channel running northeast- southwest through the area, and across the north-south road.

**Thorium Ternary $^{208}Tl^{228}Ac(900keV)^{228}Ac(1600keV)$ RGB Image**

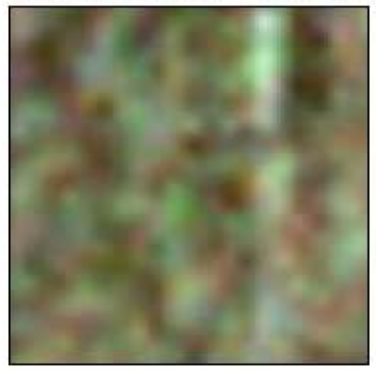

The datasets are highly correlated, with a strong response over the road, fluctuating count rates across the bulk of the area and an even texture in the southeast corner.

**Dept Agriculture 1:25,000 soil map**

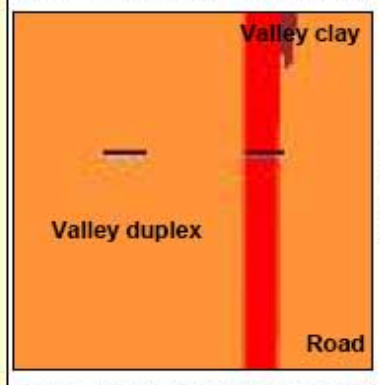


Soil is dominantly valley duplex, a sand over clay soil including deep sandy duplexes and shallow sandy duplexes.

**High resolution ternary $^{40}K^{208}Tl^{214}Bi$ RGB Image**

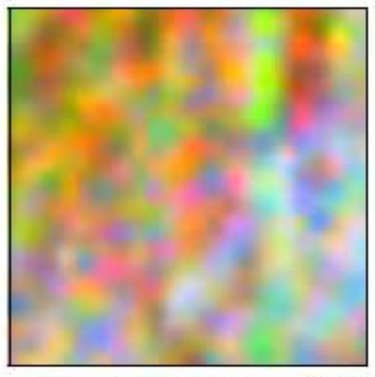

Two units are visible in the area, the northwest orange unit and a southeast pale blue/pink unit. $^{40}K$ is evenly distributed across the area. $^{208}Tl$ is relatively evenly distributed across the area, with a high response over the north-south road, and a more even texture in the southeast corner. $^{214}Bi$ provides the majority of the colour contrast in the image, with low response across the orange northwest unit, and high response across the blue/pink southeast unit.

**Uranium Ternary $^{214}Bi(1764keV)(1120keV)(1253keV)$ RGB Image**

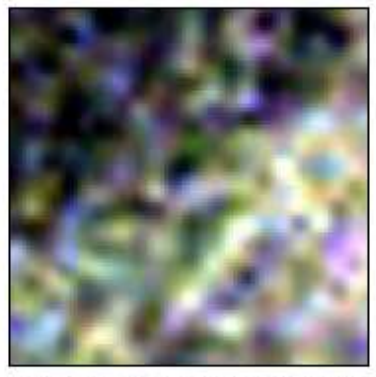

The datasets are highly correlated, highlighting two units in the area, a dark northwest unit with low response and a bright southeast unit with high response. The low response is an indicator of increasing depth to source (clay), in this case deeper sand over clay. The high response is likely indicator of increased clay content in the southeast unit.

**Aerial Photography and Agricultural Use**

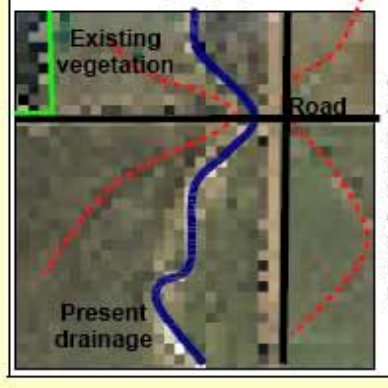


Wheat- sheep rotation area. Four fenced areas are identified, separated by roads (indicated by solid black lines), with a patch of vegetation in the northwest corner. The present drainage runs north-south, west of road (marked in blue). Subtle textural changes in the photo are marked in red.

**Low resolution ternary $^{40}K^{208}Tl^{214}Bi$ RGB Image**

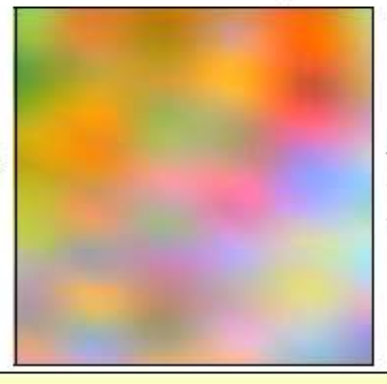

The same patterns seen in the high resolution image can be resolved in the low resolution data.

**Uranium Ratio $^{214}Bi$ 1120kev/1764keV**

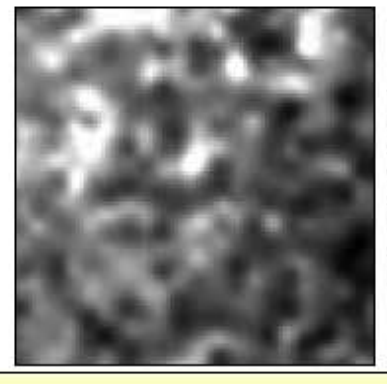

The higher ratio in the northern unit indicates a relatively lower density, possibly correlating to an increase in pore space, compared to the southern unit. This is consistent with the evidence in the uranium ternary image, which suggests a higher volume of sand over the clay in the northwest unit than the southeast unit. Similarly, this situation is also indicative of dispersed clay, clogging pore space and lowering porosity in the southeast unit.

## Elashgin Case Study

### Map 4

scale

250 m

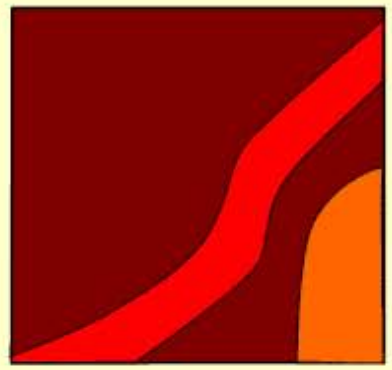

KEY

- Red valley loam
- Shallow sandy loam over clay
- Sand seam

**Summary:**
Three soils were isolated within this 25Ha area, red valley loam, shallow sandy loam over clay and a sand seam. Both the shallow sandy loam over clay and the red valley loam are susceptible to water logging. The low porosity of both units is illustrated in the uranium ratio image, which shows both units as having low ratios. Interestingly, the sand seam does not demonstrate an increase in the uranium ratio. Usually, the high porosity of the sand seam produces a high uranium ratio. The low response over this sand seam suggests the pore space has been reduced, possibly due to compaction. This condition will limit root penetration over the sand seam, restricting vegetation growth, and will facilitate the vertical movement of saline water from depth, increasing salinity at the surface along the length of the sand seam.

**Geological setting**

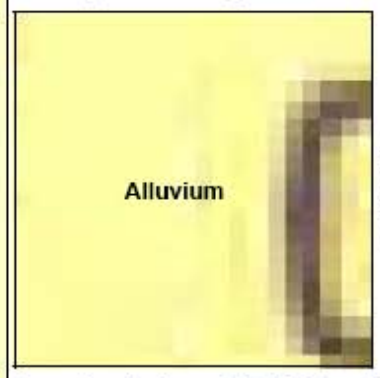


Alluvium – silt and sand in broad valley flats, extensively reworked by present drainage. Current drainage marked (from geology map) in blue.

**Digital Terrain**

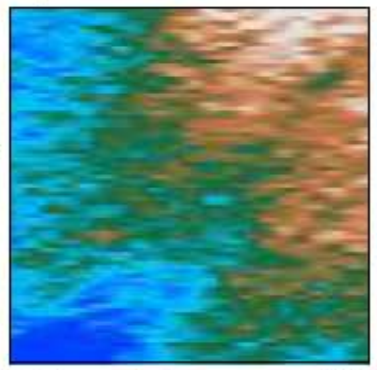

The digital terrain is very subtle, increasing 3m over 500 m. A subtle channel runs northeast- southwest through the area.

**Thorium Ternary $^{208}Tl^{228}Ac(900keV)^{228}Ac(1600keV)$ RGB Image**

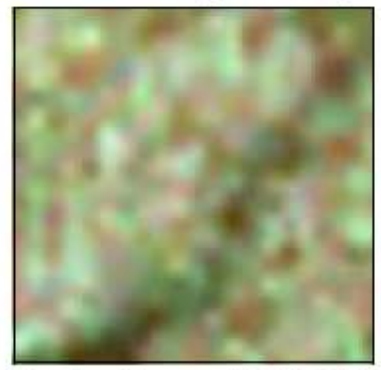

The datasets are highly correlated, with a low linear response running northeast-southwest, indicative of a sand seam.

**Dept Agriculture 1:25,000 soil map**

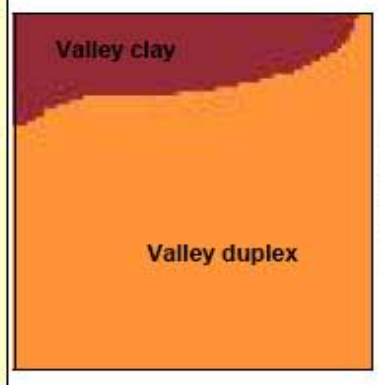


Soil contains valley duplex, a sand over clay soil including deep sandy duplexes and shallow sandy duplexes, and valley clay (red valley loam), soils with sandy loam texture or heavier located in the flat valley positions.

**High resolution ternary $^{40}K^{208}Tl^{214}Bi$ RGB Image**

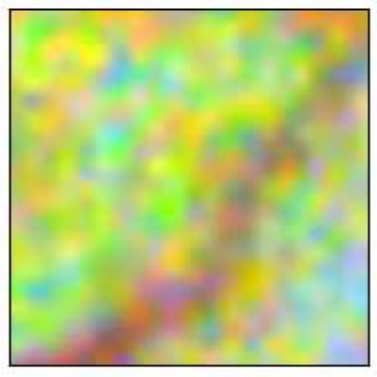

Three units can be seen in the area, the speckled yellow/green unit over the majority of the area, red linear unit running northeast-southwest and pale blue/pink unit in the southeast corner. $^{208}Tl$ is relatively high over both the yellow/green and pale blue/pink units and low over the red unit. $^{214}Bi$ is relatively higher over the pale blue/pink unit, and relatively uniformly lower distributed over the red and yellow/green units. $^{40}K$ is relatively evenly distributed across the area. Because $^{208}Tl$ and $^{214}Bi$ decrease over the red unit, the relative levels of $^{40}K$ appear to increase, producing the linear red colour indicative of a sand seam.

**Uranium Ternary $^{214}Bi(1764keV)(1120keV)(1253keV)$ RGB Image**

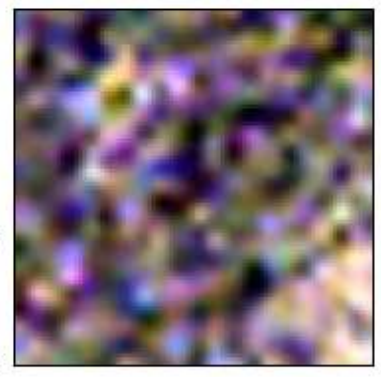

The datasets are highly correlated. The average response across the majority of the area produces a speckled purple response, while a high response in the southwest corner produces a white/yellow response. The higher response is a likely indicator of higher clay content in the surface soil. A subtle green unit running northeast-southwest is distinguished over the sand seam unit identified in the thorium ternary image, however, it would be impossible to identify without supporting evidence from the thorium data.

**Aerial Photography and Agricultural Use**

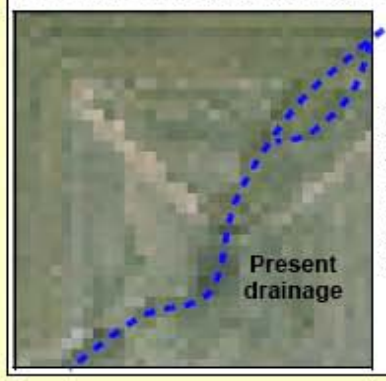


Wheat- sheep rotation area. Located within a single paddock. Subtle textural changes identifying the present drainage in the photo are marked in blue. Other textural changes in the photo are related to agricultural, cropping, practice.

**Low resolution ternary $^{40}K^{208}Tl^{214}Bi$ RGB Image**

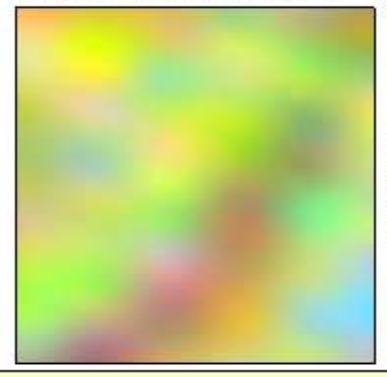

The same patterns seen in the high resolution image can be resolved in the low resolution data. However, resolving the extents of the red unit (sand steam) is challenging.

**Uranium Ratio $^{214}Bi$ 1120kev/1764keV**

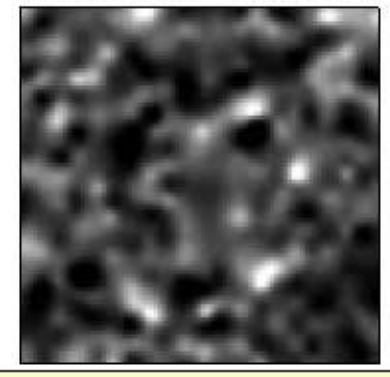

The ratio response across the area is relatively even, with a slight decrease and more even response in the southeast corner. The even response suggests density, soil porosity, is similar across the area.

## Elashgin Case Study

**Map 5**

scale

250 m

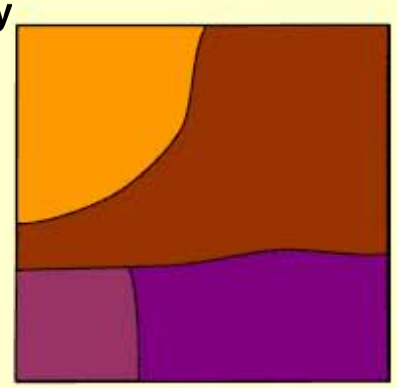

**KEY**

- Red valley clay loam
- Sandy loam over clay
- Loamy sand over clay
- Shallow loamy sand over clay

**Summary:**
Four soils were isolated within this 25Ha area, red valley clay loam, sandy loam over clay, loamy sand over clay, and shallow loamy sand over clay. The uranium ratio over the red valley clay loam is low, indicating low porosity. Combined with low landscape position, this unit will be highly susceptible to waterlogging. Similarly, the shallow loamy sand over clay, although containing higher porosity, has the potential to become waterlogged as water is shed from southern, local uplands and the local, eastern drainage system. The loamy sand over clay may also suffer water logging during periods of heavy induration, due to its location at the base of the local southern uplands, good porosity enabling water to move freely, and bounding clay loam to the north prohibiting further water movement. However, this unit should drain faster than the shallow loamy sand over clay and clay loam unit. The sandy loam over clay also has relatively good porosity, and due to its landscape position, probably acts as the main drainage source for the area. This juncture of clay loam and sandy loam is a critical point for drainage in the surveyed area. Waterlogged areas may rapidly become saline as a result of evaporation, with sand units continually supplying water to less permeable clay zones.

**Geological setting**

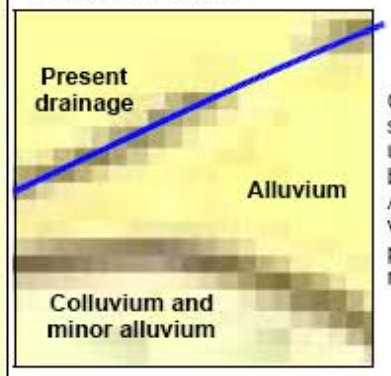


Colluvium with minor alluvium – silt, sand and gravel derived from underlying and adjacent laterite and bedrock
Alluvium – silt and sand in broad valley flats, extensively reworked by present drainage. Current drainage marked (from geology map) in blue.

**Digital Terrain**

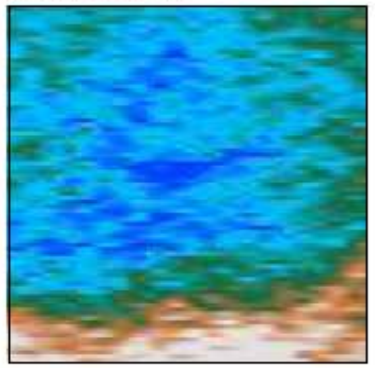

The digital terrain is very subtle, increasing 2.5m over 500 m, and varying only l m over the northern three-quarters of the area. This area is located towards the centre of the regional drainage system, in the valley floor, at the intersection of two local drainage systems.

**Thorium Ternary $^{208}Tl^{228}Ac(900keV)^{228}Ac(1600keV)$ RGB Image**

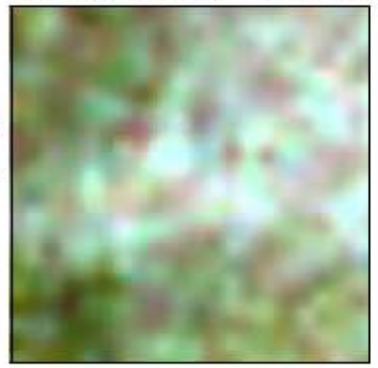

The datasets are relatively correlated, with subtle differences in intensity resolving four units. All three datasets display high response over the northeast unit, and low response over the southwest unit. The high response is indicative of a thorium bearing clay, while the low response in the southwest indicates considerably lower clay content. In the northwest, $^{208}Tl$ and $^{228}Ac$ 900 keV presents a lower response than the southeast unit does. In the $^{228}Ac$ 1600 keV dataset, the difference between the northwest unit and southeast unit is less pronounced. The average medium response of the northwest and southeast units suggests the presence of clay in the profile, although not dominant.

**Dept Agriculture 1:25,000 soil map**

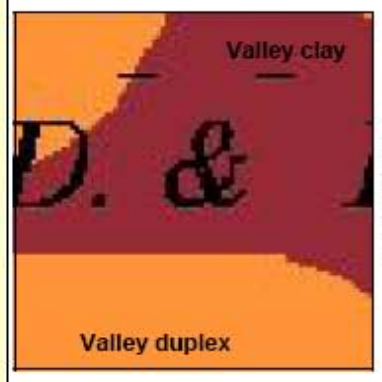


Soil contains valley duplex, a sand over clay soil including deep sandy duplexes and shallow sandy duplexes, and valley clay (red valley loam), soils with sandy loam texture or heavier located in the flat valley positions.

**High resolution ternary $^{40}K^{208}Tl^{214}Bi$ RGB Image**

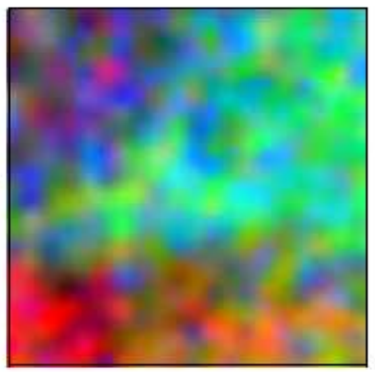

Four units are visible in this area, a cyan unit in the southeast, a purple/blue unit in the northwest, red unit in the southwest and orange in the southeast. $^{40}K$ is relatively low over the cyan and purple/blue units, slightly higher over the orange unit, and high over the red unit. $^{208}Tl$ is low over the purple/blue unit and red unit, slightly higher over the orange unit, and high over the cyan unit. $^{214}Bi$ is low over the red and orange units and high over the cyan and purple/blue units.

**Uranium Ternary $^{214}Bi(1764keV)(1120keV)(1253keV)$ RGB Image**

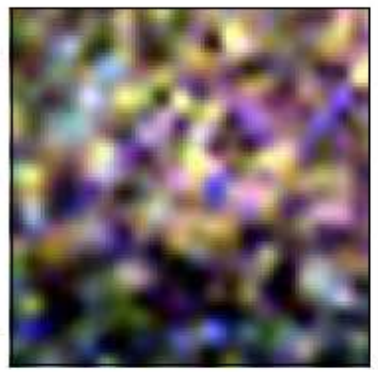

The datasets are relatively correlated, with subtle differences in the dataset intensities resolving three units. The average response across the majority of the area is a speckled purple, produced by high response from all three datasets. This response is similar to that seen in the red valley loam, case study 8U. To the south, a blue/green unit is identified by a low response from all three datasets. The contrast between the blue/green and purple units suggests different pedological processes are active. This is supported by the digital terrain data, which shows the start of a slope along the same boarder. In the northwest, a subtle green speckle is introduced. This suggests a lower clay content, or increase in reworked (low radiometric response) sand content than the neighbouring purple unit..

**Aerial Photography and Agricultural Use**

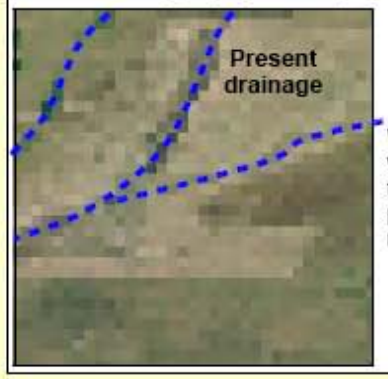


Wheat- sheep rotation area. Located within a single paddock. Subtle textural changes identifying the present drainage in the photo are marked in blue.

**Low resolution ternary $^{40}K^{208}Tl^{214}Bi$ RGB Image**

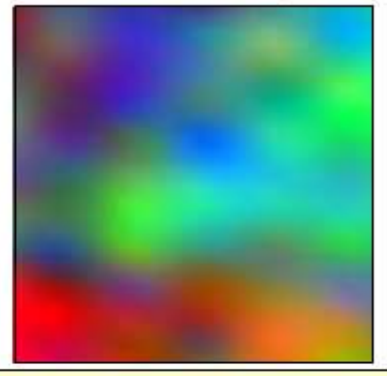

The same patterns seen in the high resolution image can be resolved in the low resolution data. However, resolving the boundary between the purple/blue unit and the cyan units is difficult.

**Uranium Ratio $^{214}Bi$ 1120kev/1764keV**

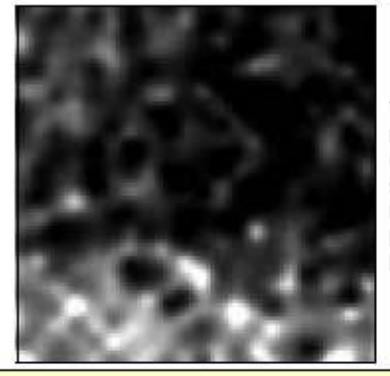

Three units can be identified by changes in the uranium ratio. A low ration over the unit in the northeast implies a comparatively low porosity. The high ratio in the south, suggests this unit has a high porosity. The medium response in the northwest suggests the soil has higher porosity than the unit to the east, but considerably lower porosity than the unit in the south.

# Elashgin Case Study

## Map 6

scale

250 m

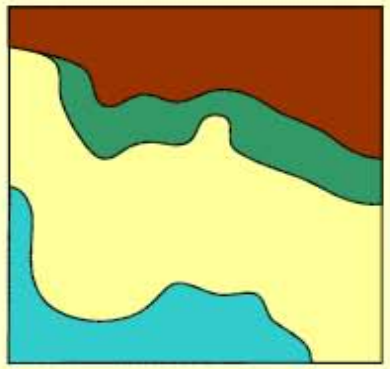

KEY

- Sand grading to clay
- Clay loam on slope
- Shallow sand over ironstone gravel
- Sandy loam duplex

**Summary:**
Four soils were isolated within this 25Ha area, shallow sand over ironstone gravel, sand grading to clay, sandy loam duplex and clay loam. The shallow sand over ironstone gravel and clay loam have very similar signatures in the standard ternary imagery, but are easily separable in the thorium ternary image. The shallow sand over gravel units have a low potential for water logging, but will act as recharge areas and shed water into the sand grading to clay unit and sandy loam duplex. The high uranium ratio of the sandy loam duplex, compared to the neighbouring units, suggests the unit has higher porosity, improved soil structure, and better root penetration than surrounding units which may become hard setting.

**Geological setting**


Alluvium – silt and sand in broad valley flats, extensively reworked by present drainage.
Colluvium with minor alluvium – silt, sand and gravel derived from underlying and adjacent laterite and bedrock

**Digital Terrain**

Located on the northern slopes of a local upland, the digital terrain increases 7.5 m over 500m.

**Thorium Ternary $^{208}Tl^{228}Ac(900keV)^{228}Ac(1600keV)$ RGB Image**

The datasets are correlated, identifying three units, the northern cyan, central dark blue and southern white units. The $^{208}Tl$ response is high over the cyan and white unit, subtly lower over the northern cyan unit, and low over the central dark blue unit. $^{228}Ac$ 900 keV is equally strong over the cyan and white units, and low over the dark blue unit. $^{228}Ac$ 1600 keV also has a strong response over the white and cyan units, and lower response over the dark green unit. The consistently strong thorium response of the white unit is indicative of a lateritic gravel. In the cyan unit, the stronger $^{228}Ac$ than $^{208}Tl$ suggests the thorium in the unit is possibly a younger source derived from adsorption to clay particles rather than geological composition.

**Dept Agriculture 1:25,000 soil map**

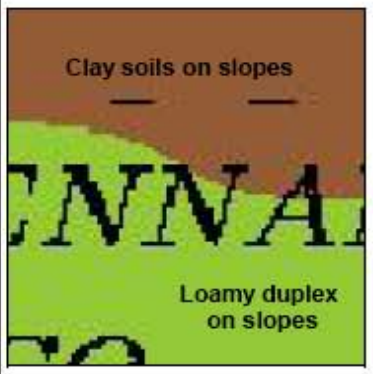


Soil consists of clay soils on slopes, found below breakaways and near subdued gravely ridges, and loamy duplex soils on slopes, loamy surface soils with an abrupt change to clay subsoil, both units include hardsetting soil.

**High resolution ternary $^{40}K^{208}Tl^{214}Bi$ RGB Image**

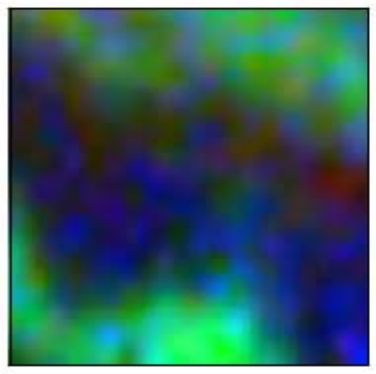

Four soil units can be identified in the area, the cyan unit to the south of the area, the speckled cyan unit in the north, the central blue unit, and adjacent to the blue unit, on the northern side, a dark green unit. $^{40}K$ is low across the southern cyan and blue units, and relatively higher over the dark green and speckled cyan units in the north. $^{214}Bi$ is low over the dark green unit, but relatively even over the other units. $^{208}Tl$ denominates the colour distribution, with high response over the south cyan and north speckled cyan units, and relatively lower response over the dark green unit, and lower again over the blue unit.

**Uranium Ternary $^{214}Bi(1764keV)(1120keV)(1253keV)$ RGB Image**

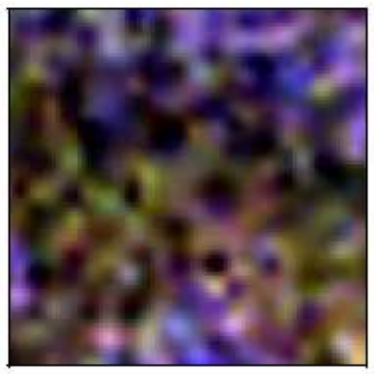

Three units are distinguished in these datasets, the northern and southern purple unit, central southern khaki unit, and adjacent north of the khaki unit, a dark blue unit. $^{214}Bi$ 1764 keV and 1120 keV are highly correlated, with a low response over the dark blue unit and relatively higher response over the remaining units. $^{214}Bi$ 1253 keV demonstrates a low response over the dark blue and khaki units, and high response over the purple units.

**Aerial Photography and Agricultural Use**

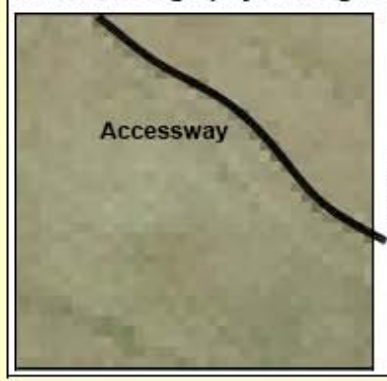


Wheat- sheep rotation area, covering two paddocks, separated by a private access way.

**Low resolution ternary $^{40}K^{208}Tl^{214}Bi$ RGB Image**

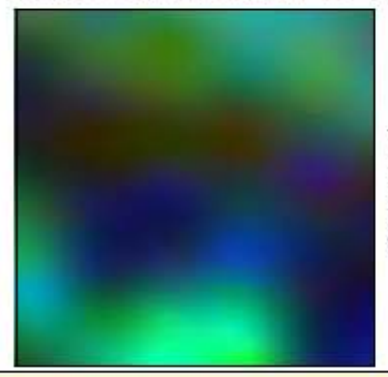

The similar patterns seen in the high resolution image can be resolved in the low resolution data, however, the identifying the division between the dark green and blue units is difficult

**Uranium Ratio $^{214}Bi$ 1120kev/1764keV**

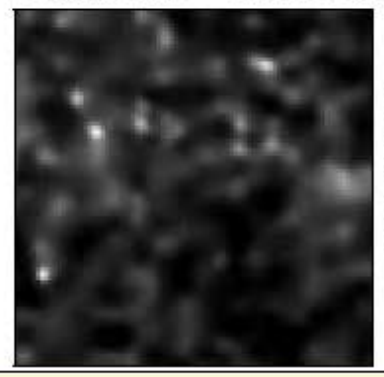

The response of the uranium ration is generally low, indicating high density, and low porosity. However, the thin central unit, identified as the dark green unit in the standard ternary image, demonstrates a high uranium ratio, indicating an increase in porosity. Combined with the topography, this would suggest this unit is a significant water delivery mechanism.

# Elashgin Case Study

## Map 7

scale

250 m

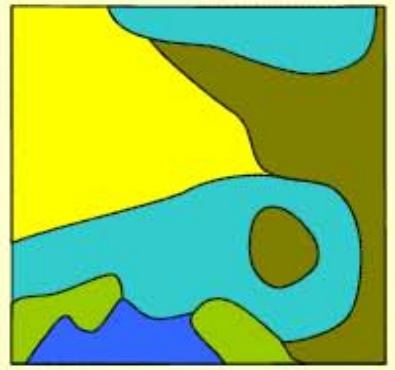

**KEY**

- Deep yellow sand
- Sand over ironstone gravel
- Shallow sand over ironstone gravel
- Shallow rocky sandy soil over granite
- Loam (red/brown)

**Summary:**
Five soils were isolated within this 25Ha area, deep yellow sand, sand over ironstone gravel, shallow sand over ironstone gravel, shallow rocky, sandy soil over granite and loam. Sand and gravel units dominate this area, making this an area of potential high groundwater recharge. However, the relatively steep slope of the area will encourage water to shed to the southeast, in subsurface flows. Clay associated with ironstone gravels and deeply weathered profiles may help improve water retention of these sandy, gravelly units. In the south, a small subcrop of granite can be identified in the radiometric data. The thin overburden of this subcrop may force subsurface water, shed from the sand and gravel units to the northeast, to the surface. However, as this water will be fresh water, there is little risk of salinisation.

**Geological setting**


Colluvium with minor alluvium – silt, sand and gravel derived from underlying and adjacent laterite and bedrock.
Laterite – limonite cemented, nodular and massive duricrust overlying deeply weathered bedrock.

**Digital Terrain**

Located on the steep southeast slopes of a local upland, the digital terrain increases 22 m over 500m.

**Thorium Ternary $^{208}Tl^{228}Ac(900keV)^{228}Ac(1600keV)$ RGB Image**

Five units are identifiable in the area, a white unit in the north, an east-west band of dark green directly below the white unit and within a speckled red central unit, and a khaki unit in the south with two dark khaki units flanking the khaki unit. The high response in all datasets in the white unit is indicative of shallow sand over ironstone gravel. A correlated, but lower response produces the red unit, indicating a thicker sand cover over ironstone gravel. The low response in all datasets in the dark green unit is indicative of sand cover. The khaki and dark khaki units are also correlated, with lower response over the dark khaki units. Compared to the ironstone units, the $^{228}Ac$ 1600 keV dataset is slightly higher relative to the $^{208}Tl$ dataset in the area.

**Dept Agriculture 1:25,000 soil map**

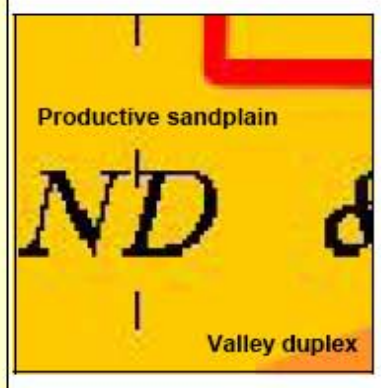


Soil consists of productive sandplain, including deep sands and sandy earths.

**High resolution ternary $^{40}K^{208}Tl^{214}Bi$ RGB Image**

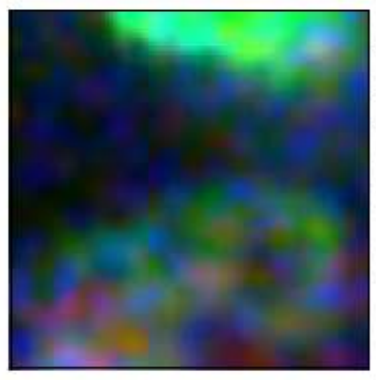

Six soil units can be identified in this area, a light green coloured unit in the north of the area, dark blue unit in the northwest, a blue/pink unit neighbouring the dark blue unit to the east and within a central green unit, a pink/orange unit in the central south, and two dark pink units flanking the pink/orange unit. $^{40}K$ is low over the dark blue and blue/pink units, slightly higher over the light green and green units, and relatively high over the pink/ orange and dark pink units. $^{208}Tl$ is low over the dark blue, blue/ pink and dark pink units, higher over the green unit, and very high over the light green unit. $^{214}Bi$ is very low over the dark blue unit, slightly higher over the blue/pink, dark pink and green unit, and relatively high over the light green unit and pink/orange unit.

**Uranium Ternary $^{214}Bi(1764keV)(1120keV)(1253keV)$ RGB Image**

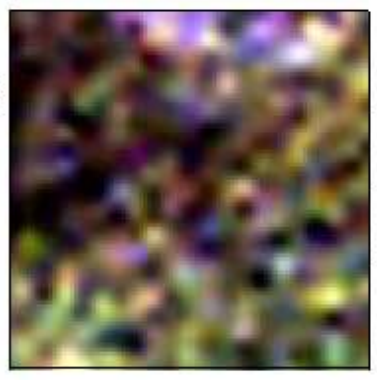

Four units are distinguished in these datasets, the northern and central south purple units, northwest dark red unit, eastern yellow unit and southern green unit. The datasets are highly correlated, with the lowest response in all three channels producing the dark red unit, a slightly higher response in all channels producing the green units, followed by the yellow unit, then purple units as the response continues to increase. These signatures help to divide the six units in the standard ternary image into related soil units, deep yellow sands (shown in this imagery as a red unit), sand over gravel (yellow and purple units), and granite related units (green units).

**Aerial Photography and Agricultural Use**


Wheat- sheep rotation area, covering two paddocks, separated by a road.

**Low resolution ternary $^{40}K^{208}Tl^{214}Bi$ RGB Image**

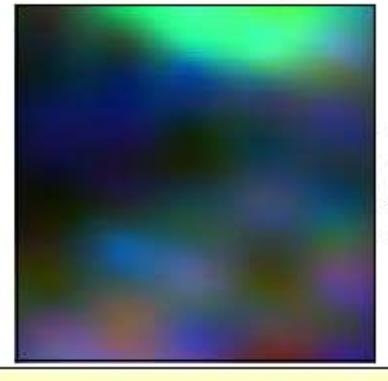

Similar patterns seen in the high resolution image can be resolved in the low resolution data, however, identifying the boundaries between the central and southern units is very difficult.

**Uranium Ratio $^{214}Bi$ 1120kev/1764keV**

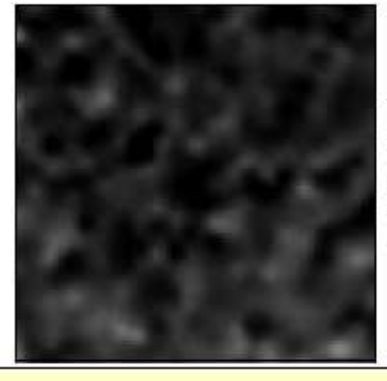

The response of the uranium ration is generally low, indicating high density. However, the southern units, identified as pink/orange and dark pink units in the standard ternary image, demonstrates a slight increase in the uranium ratio, indicating a slight increase in porosity, related to the fractured granite.

### 6.4.5 Discussion and conclusions

At all of the study sites, more information was interpreted from the radiometric data than was described in the 1:25,000 scale soil map by Cooper *et al.* (2001). Comparison of the radiometric ternary image data resolution across the map series showed that where the contrast between the soil unit radiometric response was weak, high resolution (25 m line spaced) radiometric data was able to resolve boundaries between soil units that could only be inferred from lower resolution (200 m line spaced) data (Figure 6.22 a). Where the radiometric response was strong, the high resolution data (Figure 6.22 b) served only to refine the boundary location. These results imply that high resolution radiometric data is required to resolve soil boundaries using radiometric data where the contrast between the radiometric responses of soil units is low, or where the overall radiometric intensity of the soil is low.

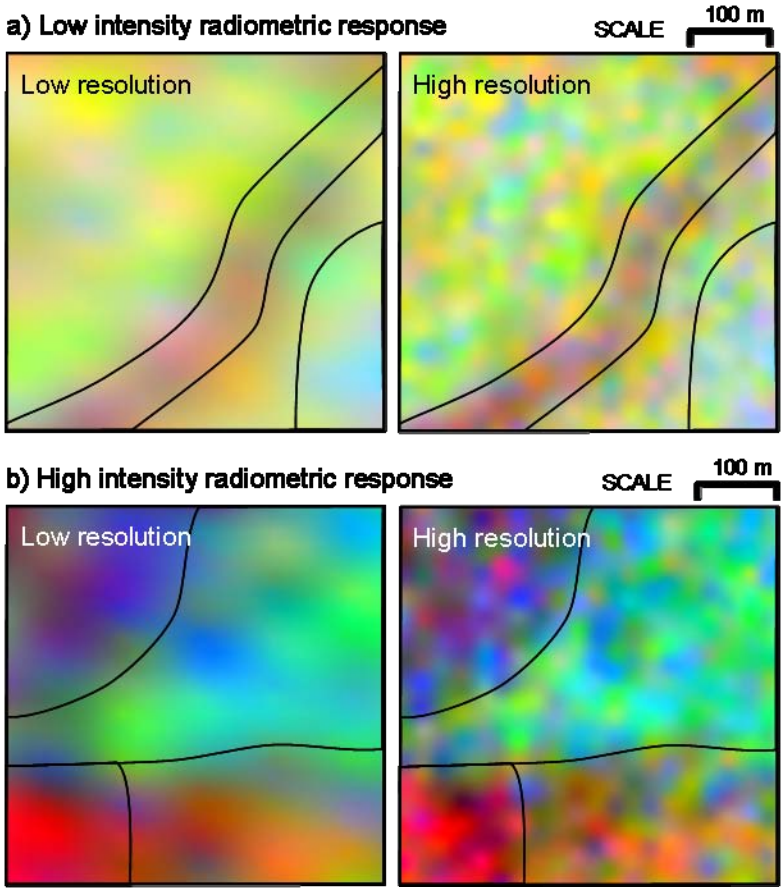


**Figure 6.22. Comparison of soil boundaries produced for high and low intensity radiometric ternary imagery. In (a), an area of low intensity radiometric soil response, definition of the soil unit boundaries (shown in black) can only be inferred in the low resolution (200 m line spaced) ternary image. However, these boundaries are resolved in the high resolution (25 m line spaced) ternary image. In (b) where soils have high intensity radiometric response, soil boundaries could be resolved in both low resolution and high resolution. Images from Elashgin case study maps 4 and 5.**

The high resolution radiometric imagery also contributed to discrimination of discreet and gradational boundaries between soil units (Figure 6.23), which reflect local pedology and influenced the interpretation of local landscape processes and subsequent land use planning.

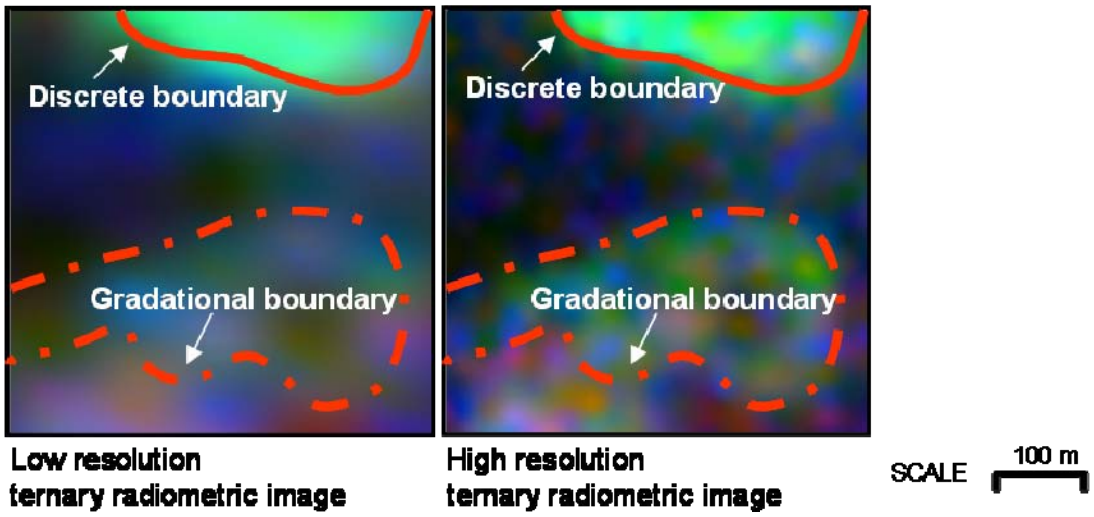


**Figure 6.23. Using high resolution radiometric data to differentiate between discrete and gradational soil boundaries. Discrete boundaries are identified by distinctive radiometric response extending away from the soil boundary. Gradational boundaries are defined by a variable response leading away from the inferred boundary, which grades into two distinct radiometric responses either side of the boundary. Discrete boundaries are visible in the same location for both high and low resolution data. The inferred location of a gradational boundary may change with the resolution of the data. Images from Elashgin Case Study Map 7.**

Within the map series, the minimum resolvable feature from the high resolution radiometric data was approximately 50 m wide (Figure 6.24a). However, that feature had to have an extent in excess of 100 m, for the changed response to be identified as a feature or boundary rather than background flux. Nevertheless, features with widths smaller than 50 m were identified within the data (Figure 6.24b). Such features, dominantly roads, were identified where there was significant radiometric response contrast between the feature and the background, and where the flight direction was directly over the feature. If the flight was not directly over features less than 50 m wide then the features were usually not resolved. This is due to the elongated (in acquisition direction) equivalent footprint that forms during acquisition.

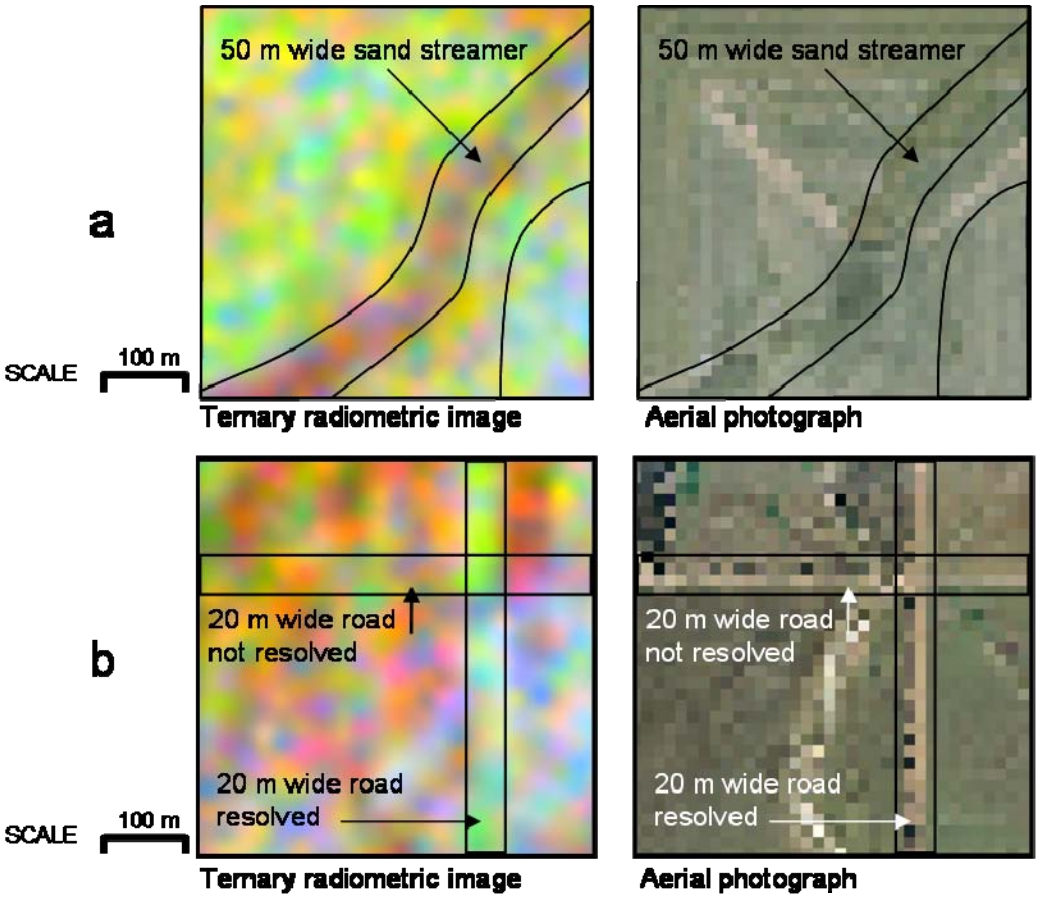


**Figure 6.24. Minimum resolvable features from high resolution radiometric data. The minimum width of a feature that could be resolved was 50 m. However, that feature must have an extent greater than 50 m, as shown in (a). Features less than 50 m wide may be resolved if the acquisition flight line occurs directly over the feature. In (b) data was acquired directly over the north-south road. The laterite road base provides a subtle contrast to the background sand over clay duplex soil response. The east-west road, with similar construction and background, was not directly overflown the feature cannot be distinguished. Images from Elashgin case study maps 4 and 3.**

As demonstrated in the map series and highlighted in Figures 6.22 and 6.24, the high resolution radiometric data was capable of consistently resolving features greater than 50 m wide. The equivalent map scale for high resolution radiometric data with a line spacing of 25 m was calculated to be 1:25,000 (refer to Chapter 6, Case Study 3). In practice, as demonstrated within the map series, with supporting data, high resolution radiometric ternary imagery could successfully map features at scales down to 1:2,500 or "paddock-scale" when the radiometric contrast between soil units was high (refer Elashgin map series case studies 1, 5, and 7).

The addition of thorium and uranium radiometric imagery served to improve boundary resolution in Elashgin Case Study Map 2 (Figure 6.25) and Elashgin Case

Study Map 3 when the contrast between standard radiometric channels: potassium, thorium, and uranium, used to produce standard radiometric ternary imagery, were low.

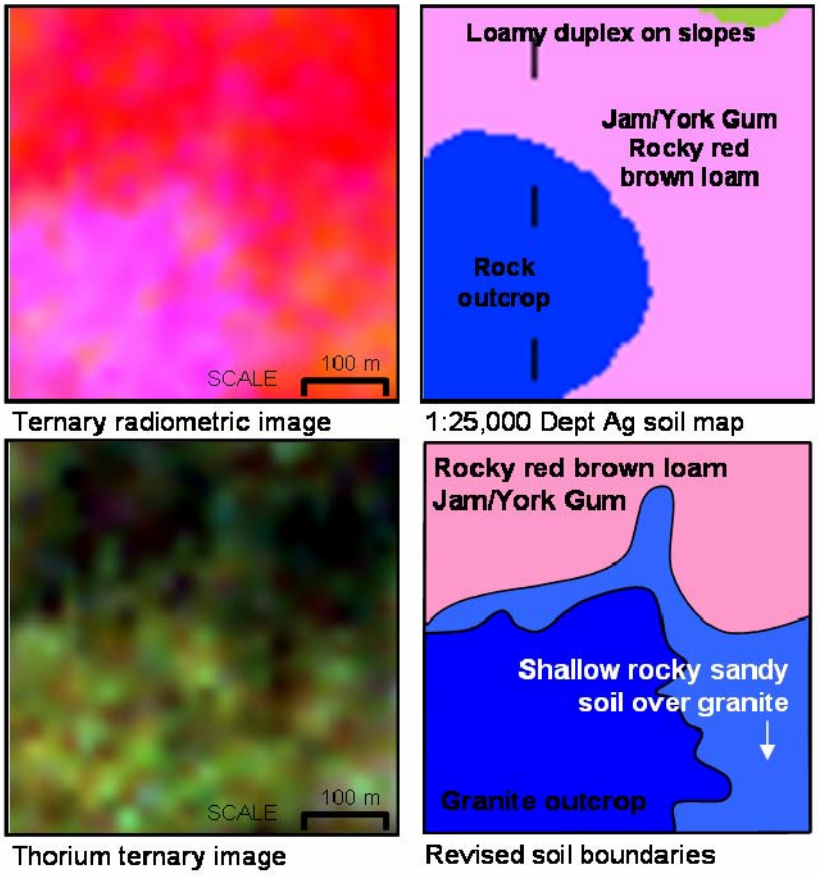


**Figure 6.25. Improved boundary resolution using additional thorium ternary imagery. The standard radiometric image presentation, ternary radiometric image, resolved the rock outcrop and the Jam/York Gum soil units, as mapped in the 1:25,000 scale (Cooper *et al.*, 2001) soil map. However, the thorium ternary image shows an additional horizontal boundary, identified by the change from black to dark green tones, which was used to differentiate the granite outcrop and subcrop from the Jam/York Gum soil. Images from Elashgin Case Study Map 2.**

The additional thorium and uranium radiometric imagery, produced only as a result of the multispectral processing methodology developed as part of this thesis (refer to Chapter 4), also facilitated the resolution of:

- Elashgin Case Study Map 1: Subtle changes in gravel depths using the thorium ternary imagery.
- Elashgin Case Study Map 2: The boundary between the outcrop and the colluvial plain, where bedrock is in excess of 40 cm, using the thorium ternary imagery.

- Elashgin Case Study Map 2: Density changes, highlighting the change from solid outcrop to weather/fragmented subcrop, using the uranium ratio imagery.
- Elashgin Case Study Map 3: Increased depth of the overlying sand unit in the valley duplex (sand over clay) soil map the using the uranium ternary imagery (Figure 6.26).
- Elashgin Case Study Map 5: Decreased porosity in the valley clay soil unit compared to valley duplex (predicted, but confirmed as per Figure 6.27) using the uranium ratio imagery.

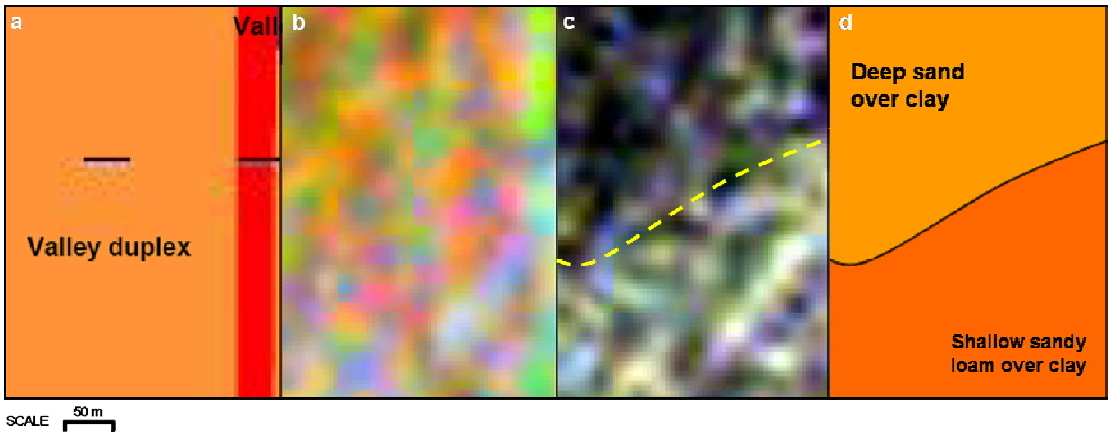


**Figure 6.26. Soil changes inferred from the physical interaction of gamma rays with the environment. Uranium ternary imagery was used to infer changes in the soil and environment not previously identified in soil maps or the multispectral ternary imagery. The uranium ternary image (c) highlights segregation, shown in yellow, where decreasing uranium response is interpreted to indicate increasing depth to the clay source. The inferred soil boundary was not identified in (a) the original soil map and is difficult to identify in (b) the multispectral ternary image. From Elashgin Case Study Map 3.**

**(a) Soil map created at 1:25,000 scale (Cooper et al., 2001).**

**(b) Multispectral ternary image: 40K full energy peak at 1461 keV [red], 214Bi full energy peak at 1764 keV [blue], 208Tl full energy peak at 2614 keV [green].**

**(c) Uranium ternary image: 214Bi full energy peak at 1764 keV [red], 214Bi single escape energies at 1253 keV [blue], 214Bi full energy peak at 1120 keV [green].**

**(d) Resulting interpretation of soil units from multispectral processed, high-resolution radiometric data.**

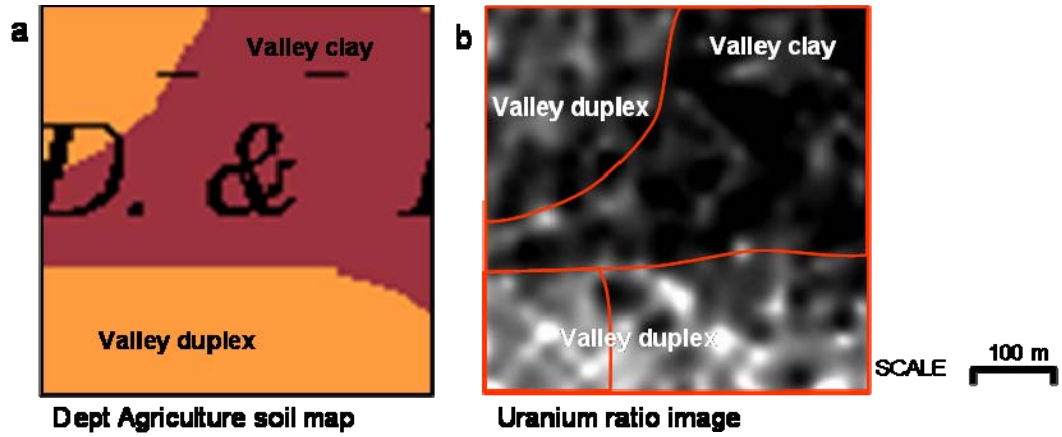


**Figure 6.27. Mapping porosity changes using the uranium ratio. The boundary between the valley clay and valley duplex (sand over clay) soil is very distinct, and was accurately captured in (a) the original soil map (Cooper *et al.*, 2001). Pore space in the valley clay within the top 40 cm is significantly lower than in the equivalent depth valley duplex soil unit. (b) The increased uranium ratio response (light grey) over the valley duplex soil compared with the valley clay (black) highlights the different porosities, illustrating the potential of this alternative radiometric imagery for mapping changes in soil density and porosity. Images from Elashgin Case Study Map 5.**

To conclude, theoretical physical and chemical soil properties and relationships resolved from the multispectral processed Elashgin radiometric data, as described in Chapter 4, were successfully correlated with soil properties as mapped by Cooper *et al.* (2001). Patterns believed to reflect local changes in soil properties and local environmental conditions were also resolved from the multispectral processed imagery that were not evident in the Cooper *et al.* (2001) soil maps. As suggested by Cooper *et al.* (2001), identification of local soil changes is beneficial to the implementation of local soil management practices. Thus areas in Western Australia currently without 1:25,000 scale or less soil maps could benefit from the acquisition, multispectral processing, and interpretation of radiometric data, to improve local soil and land management practices.

## 6.5 Case Study 5: Mapping soil textural changes in Waroona, Western Australia

### 6.5.1 Abstract

In the Waroona irrigation area soils change abruptly, in less than a metre, from sandy well drained materials that rarely become waterlogged to heavy clay soils with good water holding characteristics that become waterlogged in high rainfall. This rapid variation in soil texture results in variably waterlogged and dehydrated soils. By isolating soil textures, it is possible for farmers to alter their paddock layouts and irrigation patterns to better suit the individual soils, and thereby improve the efficiency of water and nutrient applications, crop production, and pasture growth.

In this study, ground radiometric survey data from Waroona is used to define three-dimensional variations in soil texture, down to ~40 cm. The data is subjected to a series of classification, cluster, and verification analysis procedures, incorporating field observations, to define soil texture of:

- layer A (approximately 0 cm to 10 cm),
- layer B (approximately 10cm to 20 cm), and
- layer C (approximately 20 cm to 40 cm).

Note that the layer names A, B, and C do not represent Australian standard soil horizons (Isbell, 1997). The analysis is designed to ensure soils with non-unique radiometric signatures are correctly grouped with spatially and texturally related classes.

From the soil texture information generated, a map of potential soil waterlogging was created. As a stand-alone map product and without calibration, the potential waterlogging map provides a general guide to where waterlogging could be expected to occur as a result of vertical water movement constraints. With additional information to calibrate the index system to the Waroona soil and rainfall conditions, the waterlogging potential map provides a valuable land management decision making tool when integrated with other landscape information.

### 6.5.2 Introduction

In 2002, farmers in the Shire of Waroona predicted forthcoming changes to the commercial dairy industry would make dairy farming in their region unprofitable and sought to find profitable farming alternatives. However, as with many farming communities outside the metropolitan area, the absence of local soil maps and only a vague understanding of the distribution of soil properties in the area hampered the farmers' ability to identify viable alternatives. Through this desire to understand the soil distribution across the district, the local community and the local water authority, Harvey Water, commissioned the acquisition and interpretation of high resolution ground radiometric data to develop a local soil map highlighting the distribution of sand and clay materials in the region.

This case study describes the radiometric classification methodology that was developed to assist in the production of the local soil maps for the Waroona community.

### 6.5.3 Soils in Waroona

Waroona is located to the west of the Darling Scarp, on the Bassendean Sands of the Swan Coastal Plain. Alluvial materials eroded from the granitic gneiss of the Darling Scarp are transported to the coastal plain and combine with local colluvial materials and the Bassendean Sands in a complex alluvial fan system. Underlying the area is a Quaternary lacustrine system, whose dominantly clay composition prevents local water from entering the groundwater system. This aquitard creates conditions suitable for irrigation and intensive agricultural practices of the Waroona community.

Microlevelling of the landscape to control surface water movement for irrigation has altered the already complex distribution of the alluvial, colluvial and sand materials. This redistribution of local materials to create regular surfaces that drain towards, and away, from engineered drainage channels resulted in unpredictable changes in soil conditions. As a consequence, in over less than a metre, soils in the Waroona irrigation areas change rapidly from sandy well drained materials that rarely become waterlogged to heavy clay soils with good water holding characteristics that become

waterlogged in high rainfall. It is this rapid variation in soil texture, resulting in variably waterlogged and dehydrated soils, which is of interest to the farming community. Once the soil textures are isolated, it is possible for farmers to alter their paddock layouts and irrigation patterns to better suit the individual soils, thereby improving the efficiency of water and nutrient applications and improving crop production or pasture growth.

### 6.5.4 The source of gamma rays in Waroona soils

Preliminary site investigation in Waroona revealed the top 40 cm of soil to be predominantly comprised of quartz and feldspathic sands (particles >0.05 mm diameter), kaolinitic clays with variable amounts of smectitic clay (most likely montmorillonite) present in the subsoil (<0.002 mm diameter), and little to no silt component (0.002 mm to 0.05 mm diameter). Table 6.7 describes the mineral composition of these minerals and their relative radioactive and cation exchange capacities.

**Table 6.7. Composition, radioactivity, and cation exchange capacity of dominant minerals found in Waroona soils.**

| Soil | Mineral | Mineral composition | Radioactivity[1] (source element) | Relative cation exchange capacity |
|---|---|---|---|---|
| Sand | Quartz | $SiO_2$ | None | None |
| Sand | Feldspar (orthoclase) | $KAlSi_3O_8$ | Low (K), GRapi = 200.97[1] | None |
| Clay | Kaolinite | $Al_2Si_2O_5(OH)_4$ | None | Low |
| Clay | Smectite | $(K,Na,Ca)Al_4(Si,Al)_8O_{20}(OH)_4 \cdot 2(H_2O)$ | Low (K), GRapi = 7.20[1] | High |

1. Source – http://www.webmineral.com, accessed January 27 2006. GRapi = Gamma Ray American Petroleum Institute Units.

From Table 6.7 it can be seen that the background radioactivity of soils in the Waroona area is potentially low to negligible, with no discernible difference between sand fraction and clay fraction. The cation exchange capacity of the clays, however, is relatively higher than the sand materials. The cation exchange capacity of a soil is a measure of the volume of cations that can be adsorbed to the surface of the mineral. Thus radioactive cations of potassium, thorium, and uranium, derived from

anthropogenic sources such as fertilisers or from naturally weathered local geology, are adsorbed to and concentrated with the clays. As a result, the radioactivity of the clay increases, enabling the spatial distribution of soil texture to be differentiated using high resolution radiometric techniques.

Furthermore, with radioactive cations incorporated into the general soil matrix of the region, their differential radiometric response, spatial patterns, and concentrations, which are a function of the different physical and chemical properties of potassium, thorium, and uranium cations in reaction to pedological processes, can be used to discriminate soil processes. Thus, through the interpretation of the radiometric distribution in the Waroona radiometric data it was possible to isolate differences in the sand and clay ratio of the soil and relate the changes to pedological or geological controls.

### 6.5.5 Methodology for mapping soil in Waroona

The methodology used to map soils in Waroona followed the relatively standardised process for interpreting soils with radiometric data, demonstrated by Cook *et al.* (1996) and others, as outlined below:

- classify radiometric data
- observe and sample soil texture within each classified unit to ensure soil properties are consistent throughout classified units, and
- assign soil texture and through extrapolation with *a priori* knowledge soil type for each classified unit.

Studies that have utilised radiometric data for mapping purposes generally classify the data using unsupervised (eg Anderson-Mayes, 1999) or supervised (eg Cook *et al.*, 1996a) classification techniques, dividing the radiometric signatures into clusters that are believed to be representative of different soils or regolith units in the area. The spatial boundaries derived from the clustered data were subsequently used the mark the boundaries between soil different units. This approach relies heavily upon the appropriateness of the classification algorithm to be able to separate key signatures. As a result, in locations such as Waroona, where the key soil texture changes may not be related to the strongest radiometric changes, the results generated

by either unsupervised or supervised classification alone do not produce a reliable soil map. In order to inject additional versatility into the radiometric soil mapping process and enable the interpreter to integrate *a priori* knowledge into the final soil mapping results, while still utilising the benefit of speed in identifying similar radiometric response achieved through the classification system, a modified approach to soil mapping was developed for Waroona. This modified methodology is outlined in Figure 6.28.

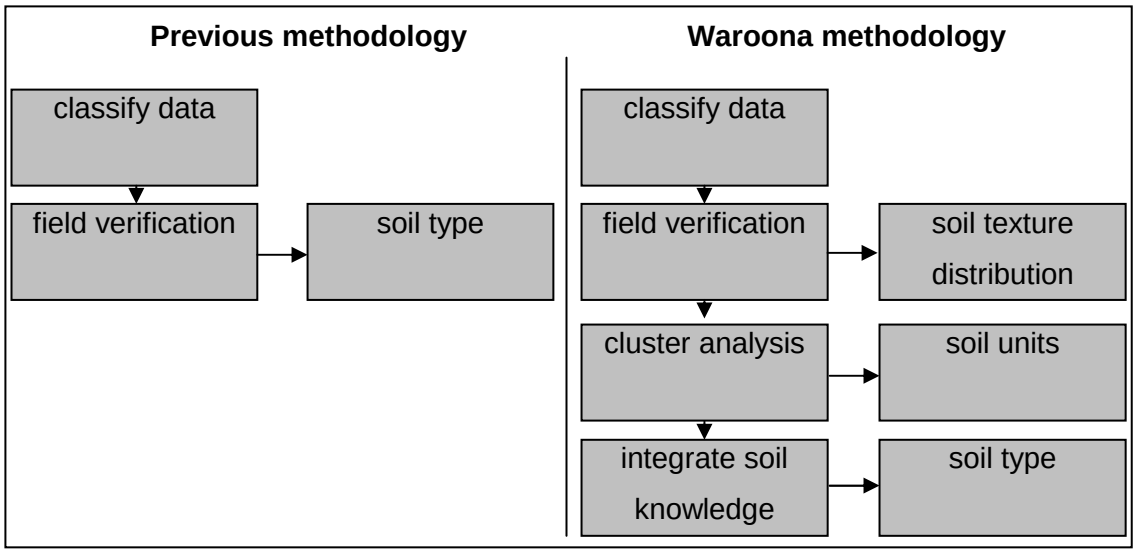


**Figure 6.28. Flow chart illustrating modified methodology employed to generate soil maps from radiometric data at Waroona, Western Australia.**

The key to the application of the classification system in this methodology was to use an unsupervised classification and over classify the data beyond the expected number of soil classes in the area. This requires the operator of the classification to have some knowledge of soils in the area and knowledge of key soil boundaries. This information was easily gathered during a preliminary assessment of the area, from pre-existing soil or geology maps, and through conversing with local farmers.

Once the classification was complete, the spatial distributions of the resulting classes were examined. No soil unit was represented by a singular classification class as a result of the classification process. Instead, soil units were identified by a group of classes. By assigning each class with a unique colour helped the interpreter to identify clusters of similar colours, repeated throughout the area that represents singular soil units. Using a local reclassification routine, these colour clusters were

recombined to form individual soil units, and the individual classes within the soil units used to highlight local pedological processes (when appropriate).

In approaching the classification in this way, non-unique radiometric signatures were free to form components of different colour clusters, i.e. different soil units. Soil boundaries were subsequently interpreted based on the desired the level of soil mapping detail. For example, soil type changes were identified at the boundary of interpreted colour clusters, while smaller internal class sub-units were used to assess local pedological changes, such as leaching or clay eluviation. Spatial filters commonly found in geographic information systems (GIS) can be utilised to assist in identifying local colour 'soil type' clusters.

### 6.5.6 Application of soil mapping methodology in Waroona

Figure 6.29 illustrates the original radiometric ternary data used for the unsupervised classification. For the purposes of land management, Harvey Water representatives believed the area contained 4 or 5 soil types. In preparing the data for the classification, the dynamic range of the potassium, thorium, uranium, and total count data sets were established to -1 to 1 with an average of approximately 0. This technique, as employed by Anderson-Mayes (1999), ensured equal weighting of the input channels in the classification algorithm. The data was then classified using the unsupervised *ERMapper Isocluster* algorithm. The number of classes was set to an unrealistically high value, while the range of values which were used to constitute a class was set to 0.1 standard deviations. This allowed the variance in the data to control the number of classes established. A total of 27 classes were derived from the Waroona data, as illustrated in Figure 6.30.

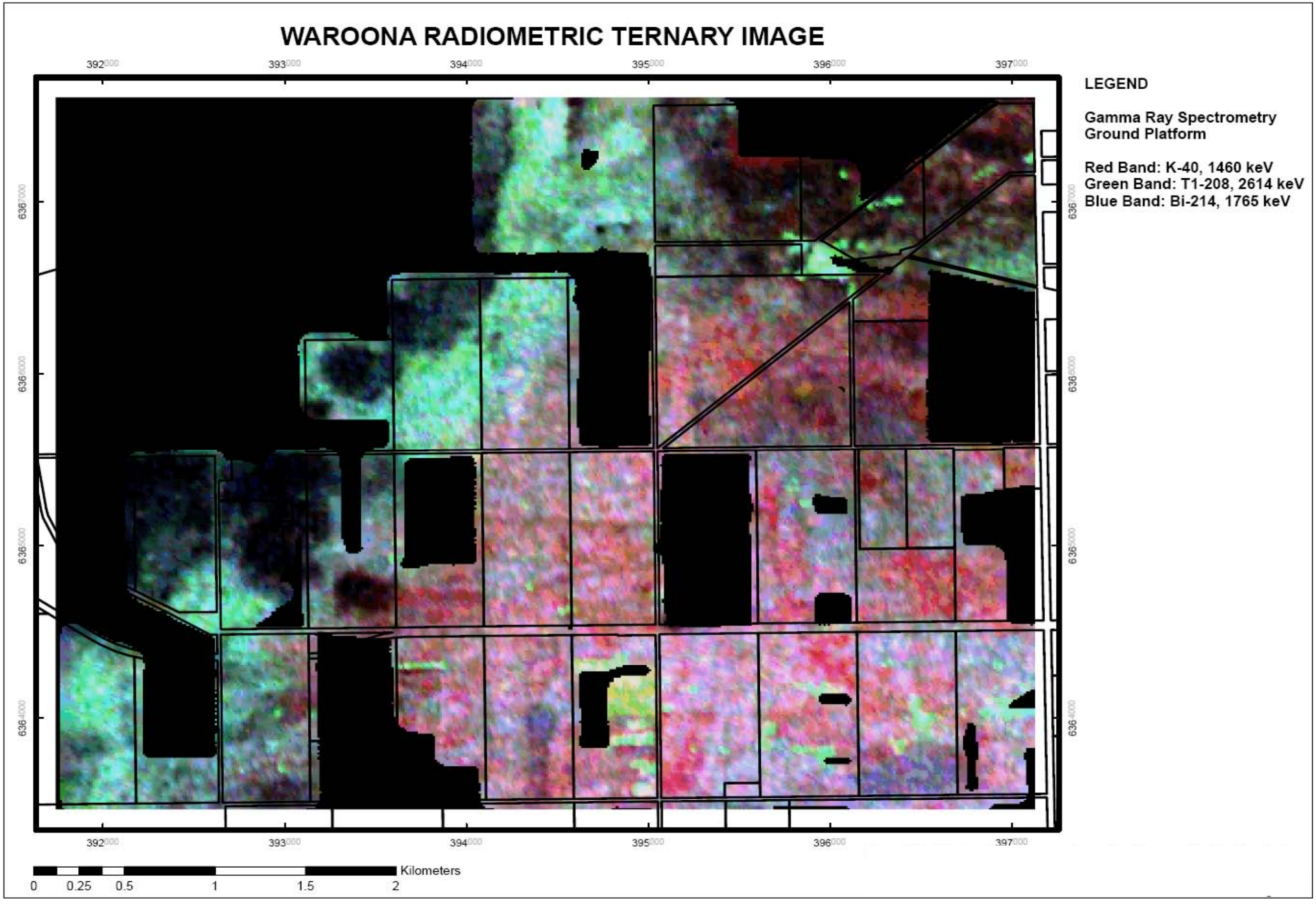


**Figure 6.29. Original radiometric ternary image from Waroona. The black lines indicate significant, permanent (barbed and electric) fencing in the area. Each of these larger areas was usually subdivided into six or more paddocks for livestock or crop management.**

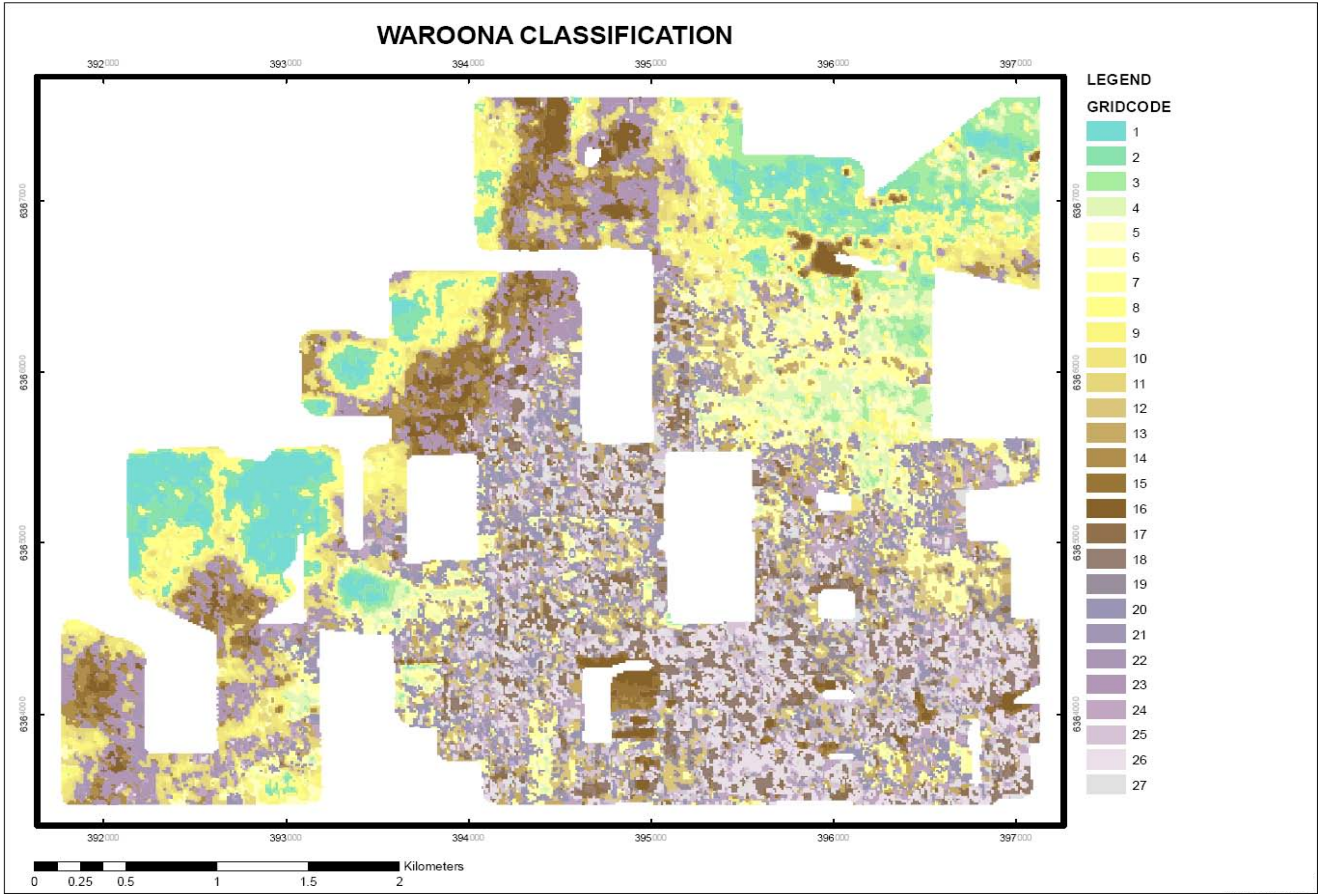


**Figure 6.30. Classification of seven channel (multispectral processed) Waroona radiometric data.**

Field validation was subsequently performed to establish the soil textural properties of the radiometric classes and ensure that the soil characteristics and local environmental conditions within the classified units were consistent within the natural variability expected in soil. Ten locations within each classified unit were selected at random to be sampled in the field. At each field sample location a 40 cm core was extracted from the ground and the texture of the three dominant soil layers (A to C), mottling characteristics, presence of laterite, and general moisture and organic matter content recorded.

The distribution of the field sample locations is illustrated in Figure 6.31 while field records for the sample sites are located in Appendix E. In practice, not all of the planned sample locations could be accessed. For some locations, the owners could not be contacted to gain permission to take samples from their land. In other locations, farmers simply did not want soil samples being taken, primarily due to a fear that livestock may be spooked or may injure themselves as a result of our presence. At other sites, livestock, especially large horned bulls, 'hot' electric fences, and recently irrigated paddocks limited sample acquisition. As a result some classes contained few or no samples (for example Class 3 and Class 26). However, this was not a significant impediment to the interpretation procedure as the sample information was not intended to validate the classification results. The under-sampled classes were subsequently assumed to have the same field characteristics as spatially adjacent classes with similar radiometric response.

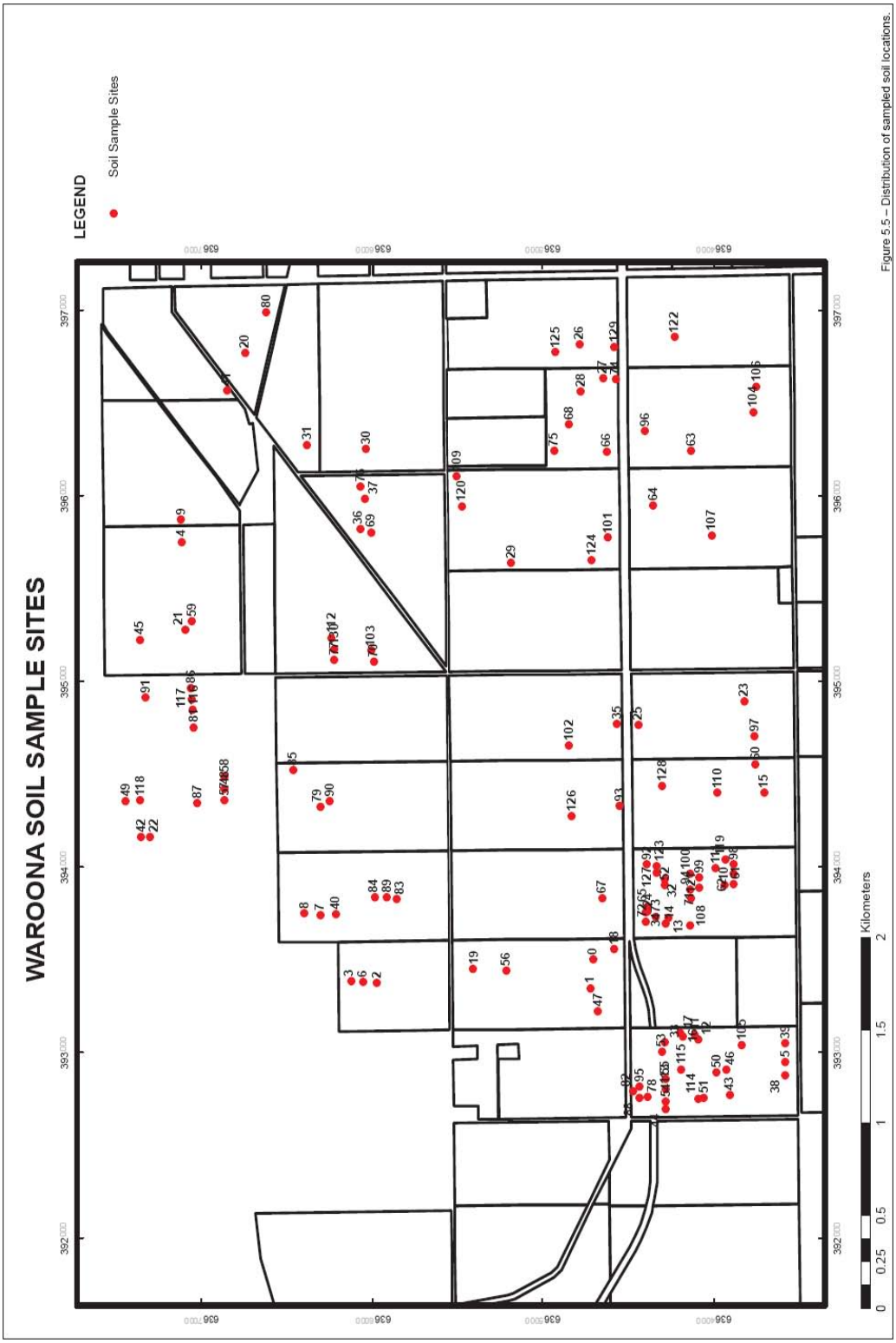


**Figure 6.31. Distribution of sampled soil locations.**

Previous studies used the field validation process to establish soil type for the sample location and validate the results of the radiometric classification as a regression function of soil type within each class. In this study, the texture results from sample sites were not immediately used to identify soil type. Instead, the results for each sample location were preserved as a three-dimensional textural response. As described previously, from the 40 cm core samples, texture was established (following Schoknecht, 2001) at the dominant three textural layers. The texture was subsequently classified as being derived from layer A (approximately 0 cm to 10 cm), layer B (approximately 10cm to 20 cm), or layer C (approximately 20 cm to 40 cm). Note that the layer names A, B, and C do not represent Australian standard (Isbell, 1997) soil horizons. The contribution of the radiometric response from each layer to the total radiometric response recorded at the surface is illustrated in Figure 6.32.

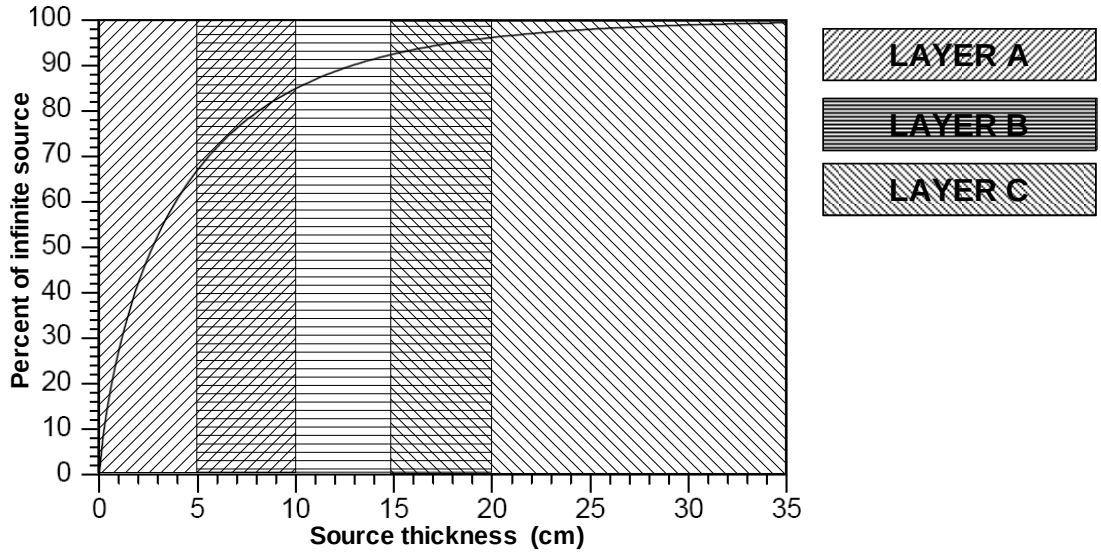


**Figure 6.32. Percentage of infinite source radiation detected from broad sources of varying thickness for thorium gamma rays at a density of 2.2 gcm$^{-3}$ (from IAEA, 2003), an approximate representation of the distribution of contributors to the total radiometric response, overlain by the range of depths used to classify layers A, B, and C.**

The original data, classification, and soil layer field results were imported into a geographic information system (GIS) to complete the soil texture mapping process. Within each radiometric class the sample descriptions for the three depth layers were evaluated using a simple comparative approach. Where the results were believed to be relatively consistent across the class, the class was assigned a three dimensional

description of the soil texture, rather than a soil type as used in previous studies. The distribution of soil samples taken for the area is illustrated in Figure 6.31.

The problem with assigning the radiometric class a soil type is that soil type encompasses more soil properties than truly expressed by the radiometric response, such as soil structure and pH. Soil texture on the other hand is a measure of the size fraction of the constituent components, for which, as described previously, different radiometric responses can be assigned. By limiting the classification description to texture, *a priori* information regarding established soil type or other soil properties could be integrated at a later stage to produce a more robust soil map.

An explanation was sought when spurious sample results were encountered during the evaluation. In some cases, spurious samples were located close to class boundaries. For example: A hand held GPS system was used to measure sample location. The accuracy of such systems varies with the position of satellites in the sky, resulting in a horizontal accuracy of around 10 m. The accuracy of the radiometric grid cell was estimated to be ±7 m (refer to Case Study 3). This produced a combined error margin of approximately 17 m. When the sample was believed to be more representative of the neighbouring class the sample was subsequently reassigned to the appropriate class.

In most cases, discrepancies resulted from changes in the layer A soil texture as a result of changing vegetation/organic matter content in the top 10 cm and not necessarily soil variation. As paddock use varied over relatively localised distances of less than 500 m, variable watering rates, fertiliser applications, livestock type and density, crop type and paddock use rotation all contributed to changes of the surface soil chemistry, structure, and texture. However, soil type is a function of the overall soil condition. Thus, these local anomalies must be considered with respect to the local condition. Consequently, when discrepancies were encountered, the following elements were considered in order to decide whether the sample was representative of the local area:

- location relative to other similar radiometric response classes,
- location relative to other similar texture response,

- field observations,
- photographs of the core and surrounds,
- designated class spatial size and distribution, and
- layer B and C compared to other class members.

When no explanation for the uniqueness of the sample description could be determined, possibly as a result of anomalous local soil conditions or error in the original texture sampling, the field sample was rejected. Six field samples were rejected following examination. These samples were close to residential homes or access roads where it was suspected that the local soils had been modified. If the sample was determined to be representative of the area, but not related to other samples within the same class, the radiometric response of the class was subsequently identified as a non-unique response; where different soils with similar or the same radiometric response form one class. These non-unique classes were later dissolved into appropriate soil units based on spatial distribution. The result of the evaluation process was the allocation of A, B, and C texture layers to each radiometric class and the identification of non-unique radiometric classes.

The classes were then dissolved, broken into groups based on their spatial separation, and the spatial distribution of the classified data manually inspected to identify clusters of radiometric classes that were likely to form soil units. In identifying the clusters, the characteristics of the classes, including spatial distribution, similarity of radiometric response and textural response, were considered. Care was taken with non-unique classes to ensure that the dissolved classes they were clustered with appropriate local classes.

During the radiometric clustering process for Waroona, clusters were identified that were spatially continuous to neighbouring clusters, i.e. they had similar spatial distribution patterns, but contained suppressed radiometric response and geometrically straight cluster boundaries (Figure 6.33). The geometry of the cluster instantly suggests an anthropogenic influence on the group, most likely a paddock boundary, with the suppression of the radiometric signature likely to be a response to increased water content through irrigation during the acquisition period.

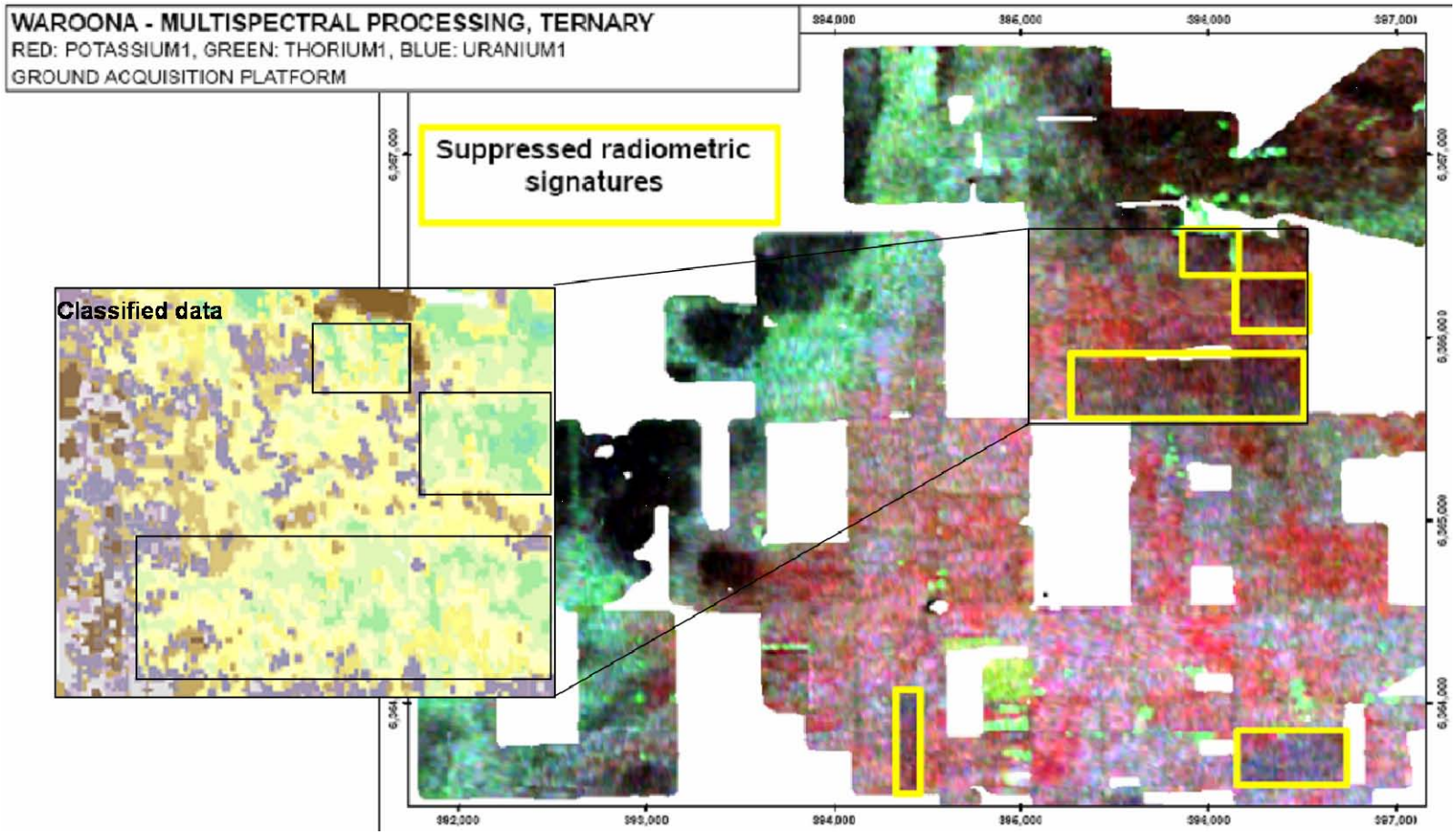


**Figure 6.33. Visual identification of anthropogenic influences. Anthropogenic influences on radiometric response usually exhibit geometric patterns, i.e. linear roads, rectangular paddocks. For example, increased water content due to irrigation practices create rectangular areas of suppressed radiometric response (highlighted in yellow) in ternary radiometric imagery. These false signatures are captured in the classified data (see insert) as clusters, i.e. the green to yellow classes, terminating with straight edges coincident with the paddock boundaries. The irregular clusters are then manually reallocated to the most likely equivalent neighbouring cluster class, ensuring continuity of radiometric spatial patterns.**

To negate the influence of the irrigated area, the texture and relative radiometric characteristics of the individual classes within the suppressed cluster were compared with the texture and radiometric characteristics of the spatially continuous neighbouring cluster classes in order to reallocate them to the most likely equivalent neighbouring cluster class. The reclassification process ensures continuity of the radiometric spatial patterns within the data to produce an accurate representation of the soil texture distribution.

As a result of this classification process, a range of soil maps could be produced for the Waroona area depending on the purpose required. The bulk classification of soil type for 4-5 soil types required for planning purposes by Harvey Irrigation (Figure 6.34) were produced by grouping radiometric units related to the four dominant soil types in the area: Guildford Formation, Bassendean Sands, Yoganup Formation, and Swamp and Lacustrine Formations, using a priori knowledge from regional geology maps. The bulk classification effectively communicated the subtle changes in local soil boundaries revealed through the radiometric data. Later, other maps such as the bulk textural distribution for A, B, or C soil layers (Figures 6.35 to 6.37) were introduced, providing additional soil information while employing local soil terminology and references. This provided an easy transfer of knowledge from the radiometric interpreter to the land user.

### 6.5.7 Interpretation

To gain the most information from the radiometric classification and available data, an interpretation of the classification results was required. Interpretation of the radiometric data requires the interpreter to have both an understanding of radiometric soil response and soil processes, and to integrate this with knowledge of soil types and other local soil studies. A full discussion of the Waroona interpretation results will not be presented here as the results are sensitive to land holders' interests. However, Figure 6.38 is presented as a brief introduction to the interpretation process.

Figure 6.38 highlights the key soil formations as a function of the ternary radiometric data. Highlighted are the locations where radiometric response is indicative of

radionuclide leaching in the recent fan deposits and radionuclide accumulation, with clay eluviation in older fan deposits. Along the central northern edge of Figure 6.38, 'recent' beach sands from the Yoganup formation form local topographic highs which have advanced over the older alluvial fan system. Along the western flank, deflated dunes from the Bassendean Sand System, differentiated from Yoganup deposits by lower potassium concentration, sit on top of a Quaternary swamp and lacustrine deposit. These lacustrine/swamp deposits were once located in the back dunes of an ancient shoreline, and are consequently likely to contain significant quantities of salts. Combined with the deposit's dominantly heavy soils, the unit provides poor soil for most farming activities. Conversely, loamy soils of the older alluvial fan plain, which have experienced clay eluviation, were identified as better soils for most intensive agriculture activities.

With this degree of additional information, the soil textural layer information can be used to subdivide the broad radiometric units into small sub-types. Figure 6.39 demonstrates how all of the available information can be integrated to sub-divide the soil types in the area. Figures 6.40 to 6.42 represent the separate layers A, B, and C. This information, presented in Figures 6.39 to 6.42, is impractical to use as a single map due to the difficulties involved in identifying individual soil units relevant to land management; note the long list of soil descriptors associated with Figure 6.39. However, it is valuable in a GIS format as a management tool for spatial interrogation and planning, as discussed in the following section.

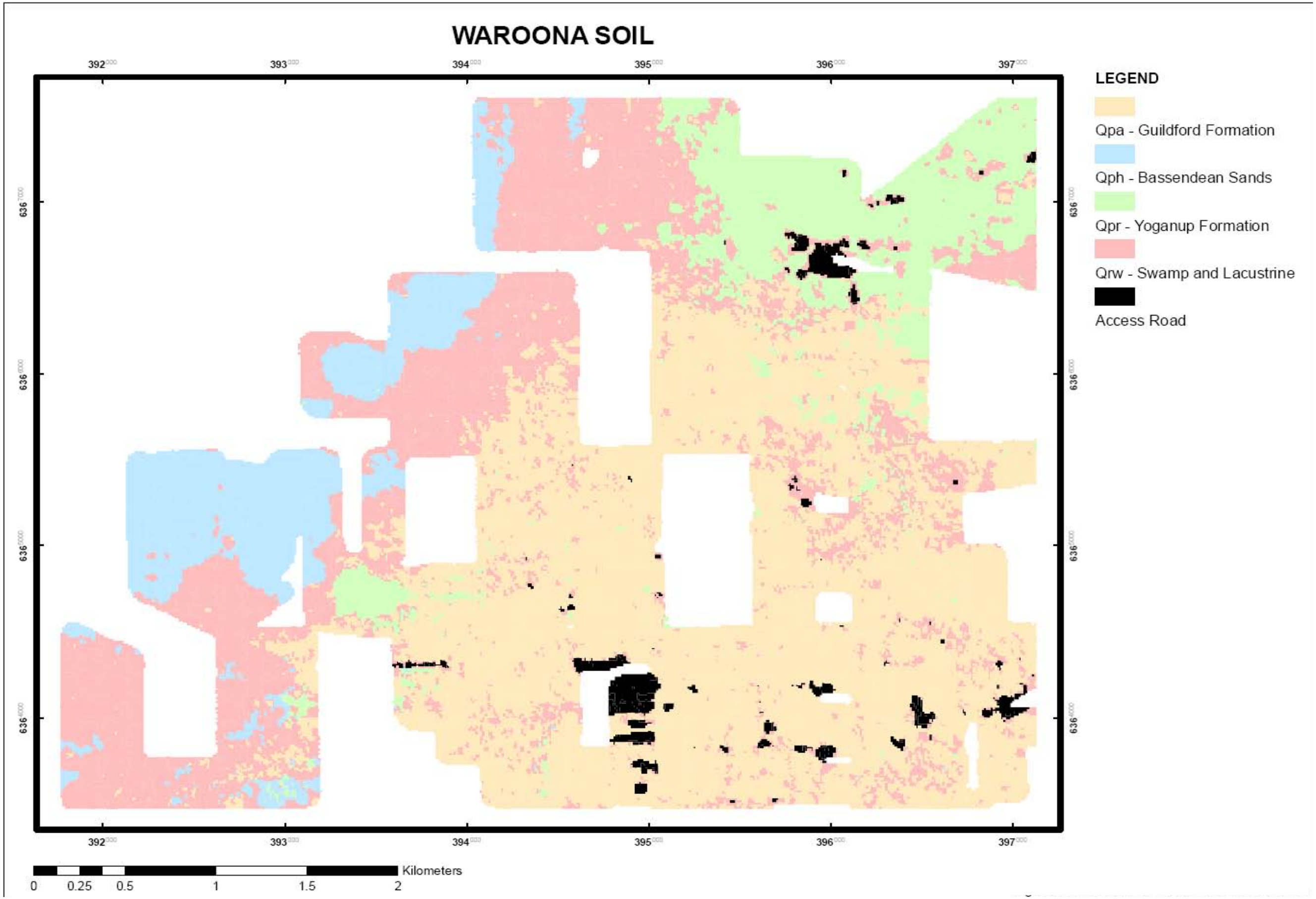


**Figure 6.34. General soil classification for Waroona.**

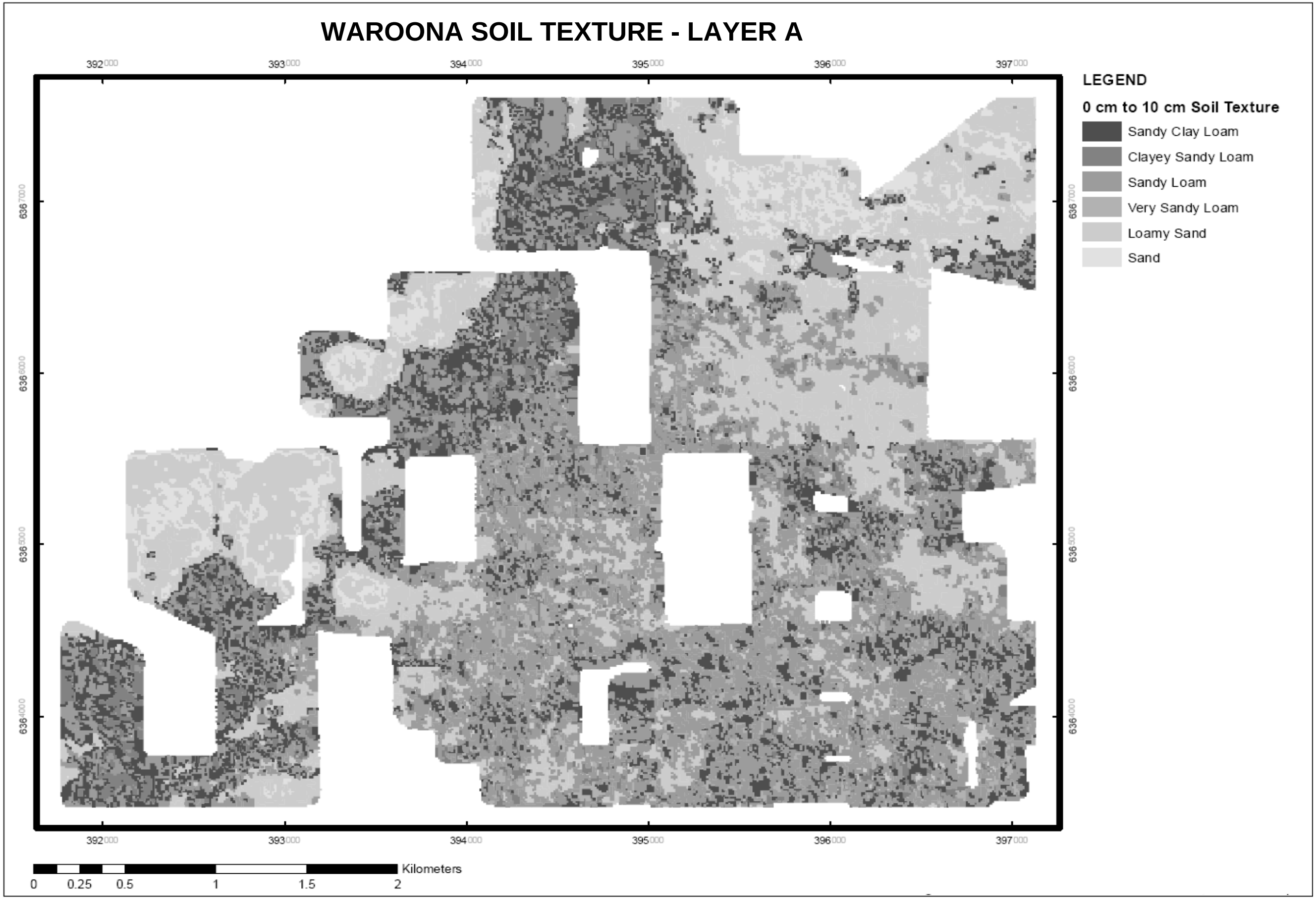


**Figure 6.35 Distribution of soil texture in layer A, 0 cm to 10 cm depth.**

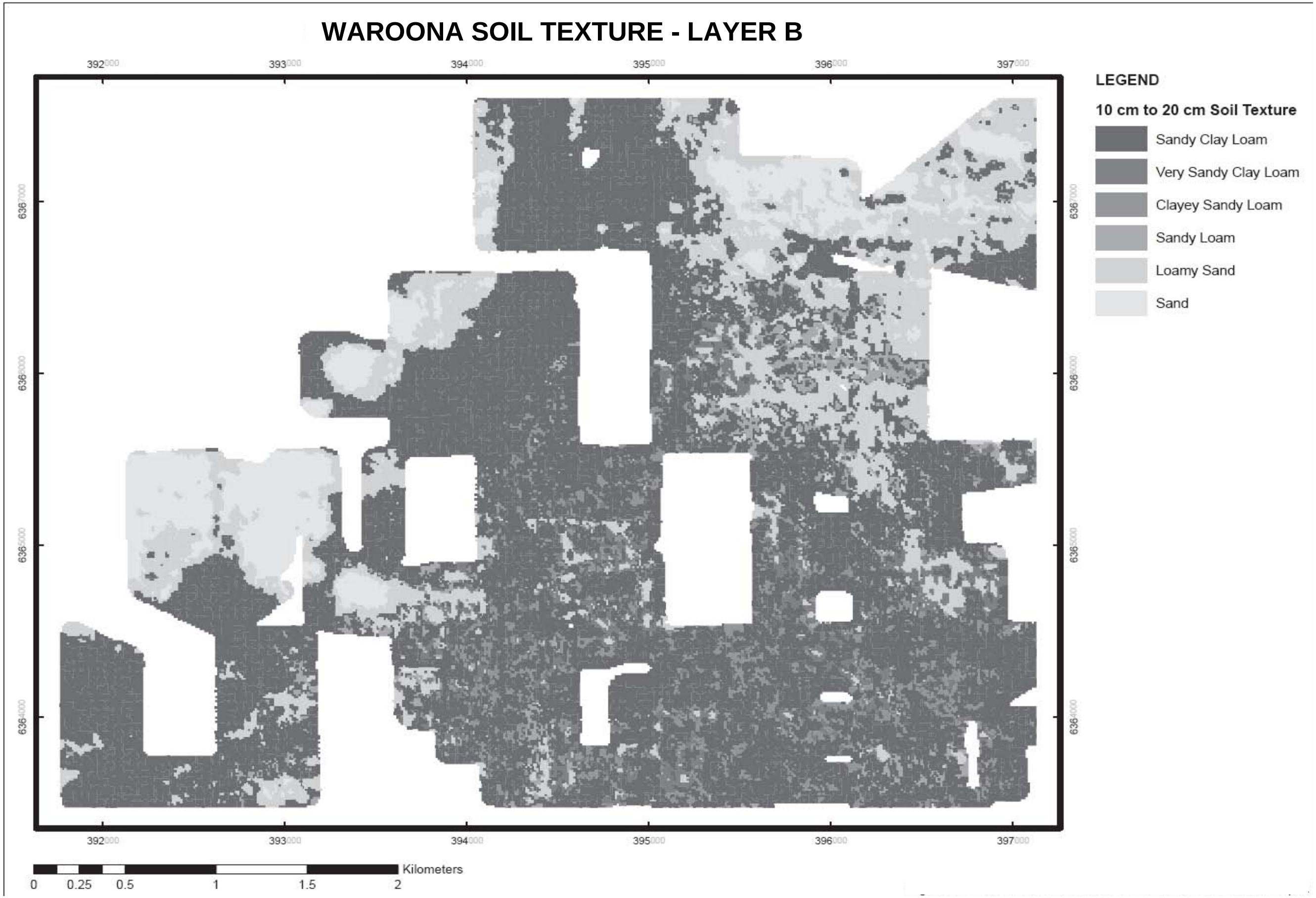


**Figure 6.36. Distribution of soil texture in layer B, 10 cm to 20 cm depth.**

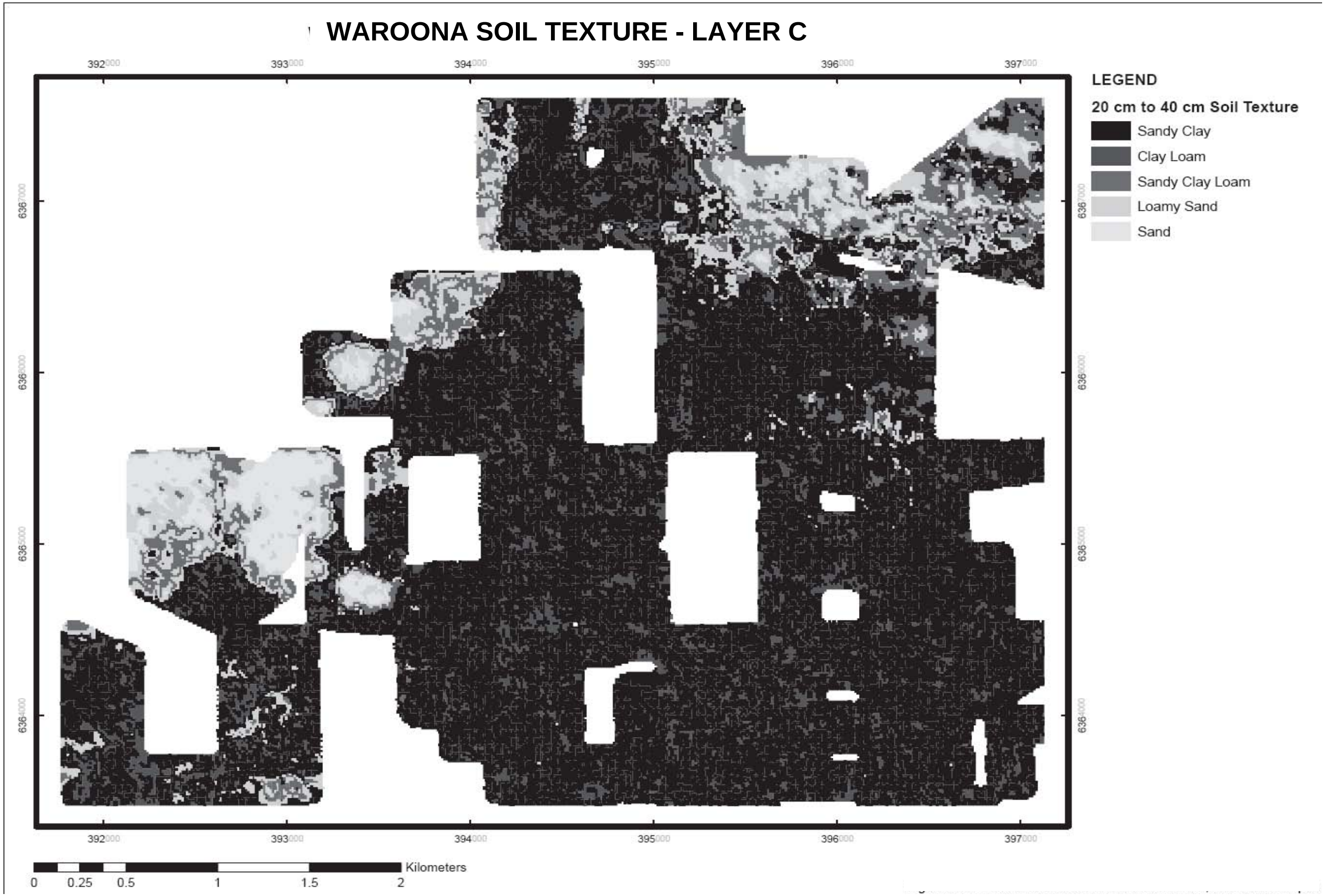


**Figure 6.37. Distribution of soil texture in layer C, 20 cm to 40 cm depth.**

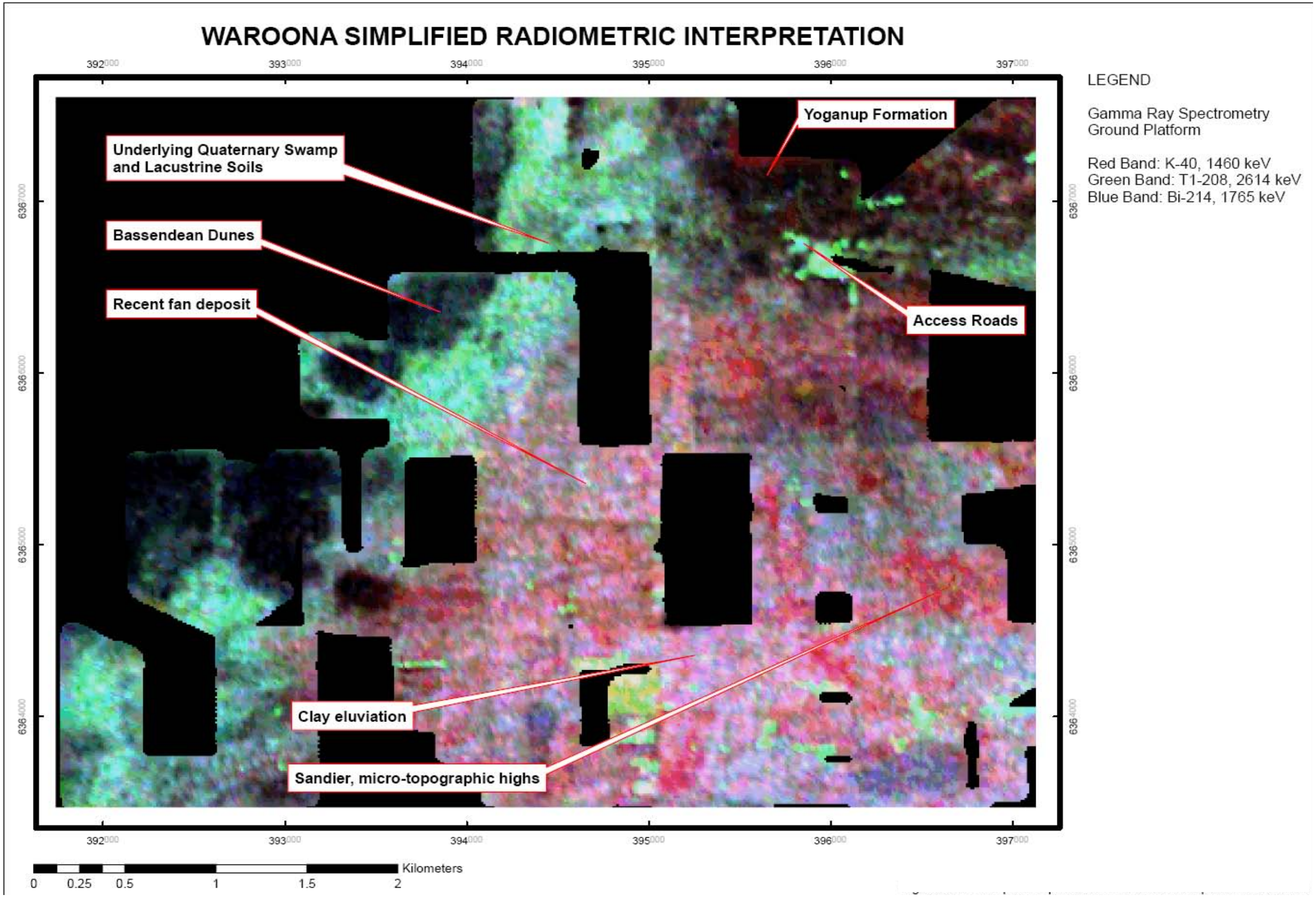


**Figure 6.38. Simple interpretation of Waroona radiometric ternary image.**

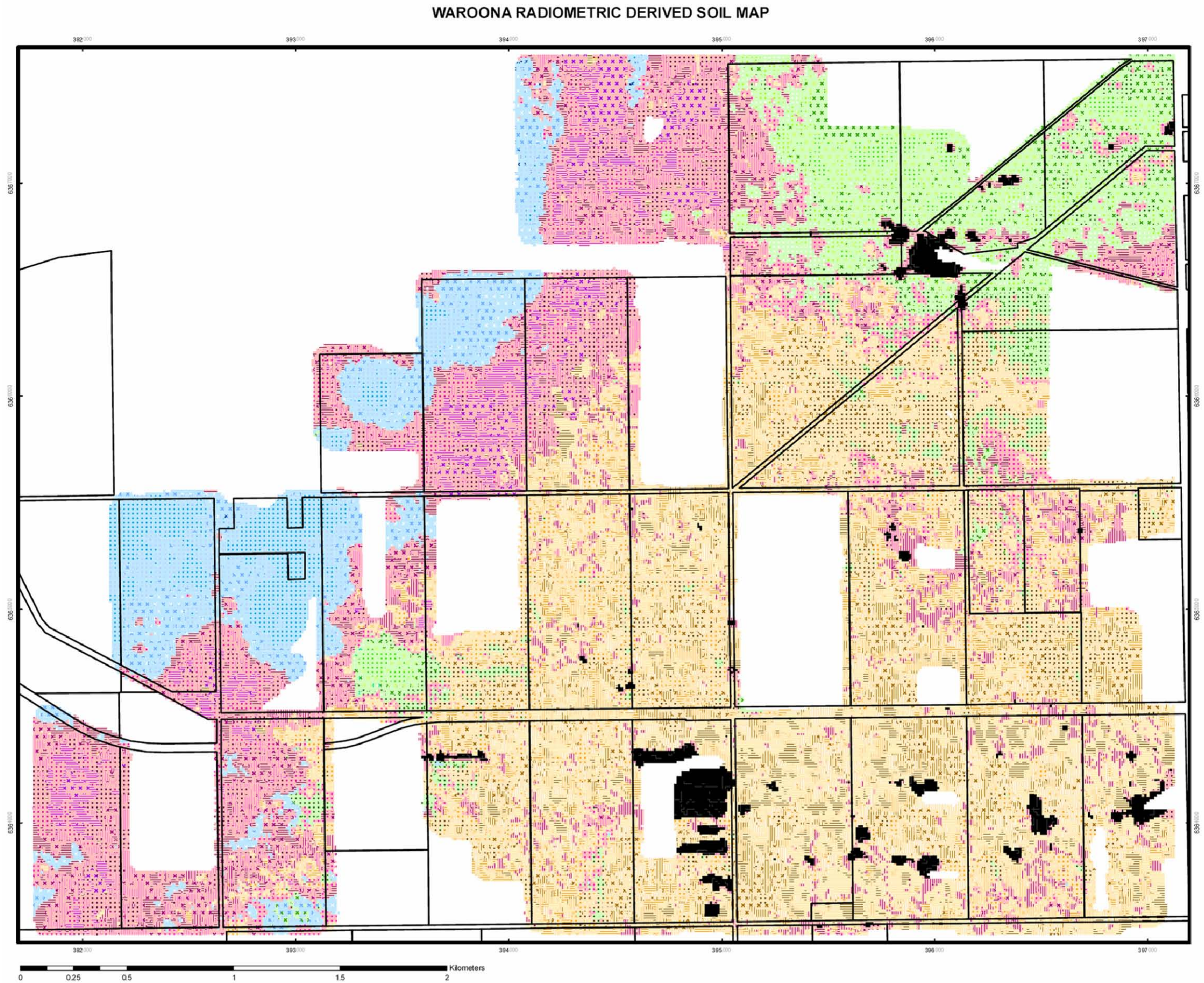


**Figure 6.39. Complete subdivision of soil type and soil texture for the Waroona survey area. (Legend on next page)**

**LEGEND**

**Soil Description**

Qpa: Guildford Formation, Clay - Brown sandy clay loam grading to orange sandy clay. Water logging evidenced by orange/red mottles at base of profile.

Qpa: Guildford Formation, Clay - Dark brown fine sandy loam grading to light brown/light orange sandy clay. Water logging evidenced by orange mottles at base of profile.

Qpa: Guildford Formation, Clay - Hard setting dark brown sandy loam grading to light brown/light orange sandy clay. Water logging evidenced by orange mottles at base of profile.

Qpa: Guildford Formation, Clay - Hard setting dark brown sandy loam grading to orange/brown sandy clay loam to orange friable fine sandy clay. Minor water logging evidenced by orange colour of soil at base of profile.

Qpa: Guildford Formation, Clay - Hard setting dark brown sandy loam grading to orange/brown sandy clay.

Qpa: Guildford Formation, Clay - Light brown sandy loam grading to light orange sandy clay.

Qpa: Guildford Formation, Sand - Dark brown fine loamy sand grading to light brown loamy sand on light brown/yellow sandy clay. Water logging evidenced by orange mottles at base of profile.

Qpa: Guildford Formation, Sand - Dark brown loamy sand grading to brown sandy clay loam on light brown/light orange sandy clay. Water logging evidenced by orange mottles at base of profile.

Qpa: Guildford Formation, Sand - Dark brown sandy loam grading to brown sandy clay loam on light brown/orange sandy clay. Water logging evidenced by orange mottles at base of profile.

Qpa: Guildford Formation, Sand - Dark brown sandy loam grading to brown sandy clay loam on orange sandy clay loam. Minor water logging evidenced by orange colour of soil at base of profile.

Qpa: Guildford Formation, Sand - Dark brown sandy loam on brown/orange sandy clay. Water logging evidenced by orange mottles at base of profile.

Qph: Bassendean Sands - Grey loamy sand grading to light brown sandy clay loam. Water logging evidenced by orange mottles at base of profile.

Qph: Bassendean Sands - Grey loamy sand on light grey sandy clay loam.

Qph: Bassendean Sands - Grey loamy sand grading to light grey sand. Loamy sand at surface resulting from sustained presence of organic matter.

Qph: Bassendean Sands - Grey loamy sand grading to light grey/light orange sandy clay loam. Minor water logging evidenced by orange colouring at base of profile

Qph: Bassendean Sands - Grey sand grading to light grey to white loamy sand

Qph: Bassendean Sands - Grey/brown loamy sand grading to light grey/light brown/orange loamy sand. Water logging evidenced by orange mottles at base of profile.

Qpr: Yoganup Formation - Grey loamy sand grading to light brown sandy clay loam. Water logging evidenced by orange mottles at base of profile.

Qpr: Yoganup Formation - Grey loamy sand on light grey sandy clay loam.

Qpr: Yoganup Formation - Grey loamy sand grading to light grey sand. Loamy sand at surface resulting from sustained presence of organic matter.

Qpr: Yoganup Formation - Grey loamy sand grading to light grey/light orange sandy clay loam. Minor water logging evidenced by orange colouring at base of profile

Qpr: Yoganup Formation - Grey loamy sand grading to light grey/light orange sandy clay loam. Minor water logging evidenced by orange colouring at base of profile.

Qpr: Yoganup Formation - Grey sand grading to light grey to white loamy sand

Qpr: Yoganup Formation - Grey/brown loamy sand grading to light grey/light brown/orange loamy sand. Water logging evidenced by orange mottles at base of profile.

Qrw: Swamp and lactustrine - Hard setting dark brown sandy clay loam grading to brown sandy clay. Water logging evidenced by orange mottles at base of profile.

Qrw: Swamp and lacustrine - Hard setting brown sandy clay loam grading to orange fine sandy clay. Significant water logging evidenced by strong orange colour of soil and red mottles at base of profile.

Qrw: Swamp and lacustrine - Hard setting dark brown sandy clay loam grading to dark brown sandy clay. Significant water logging evidenced by orange mottles in central and lower profile horizons.

Qrw: Swamp and lacustrine - Hard setting dark brown sandy clay loam grading to orange friable sandy clay. Significant water logging evidenced by strong orange colour of soil at base of profile.

Qrw: Swamp and lacustrine - Hard setting dark brown sandy loam grading to brown/orange friable sandy clay. Significant water logging evidenced by strong orange colour of soil and orange mottles at base of profile. Occasional laterite present.

Qrw: Swamp and lactustrine - Hard setting dark brown sandy loam grading to brown/orange sandy clay. Water logging evidenced by orange mottles at base of profile.

Qrw: Swamp and lacustrine - Hard setting dark brown sandy loam grading to dark brown sandy clay. Significant water logging evidenced by orange mottles in central and lower profile horizons.

Qrw: Swamp and lacustrine - Hard setting brown sandy loam grading to dark brown sandy clay.

Qrw: Swamp and lactustrine - Brown loamy sand grading to brown/orange sandy clay. Water logging evidenced by orange mottles at base of profile.

Road, accessway

**Figure 6.39 cont'd. Legend for complete subdivision of soil type and soil texture for the Waroona survey area.**

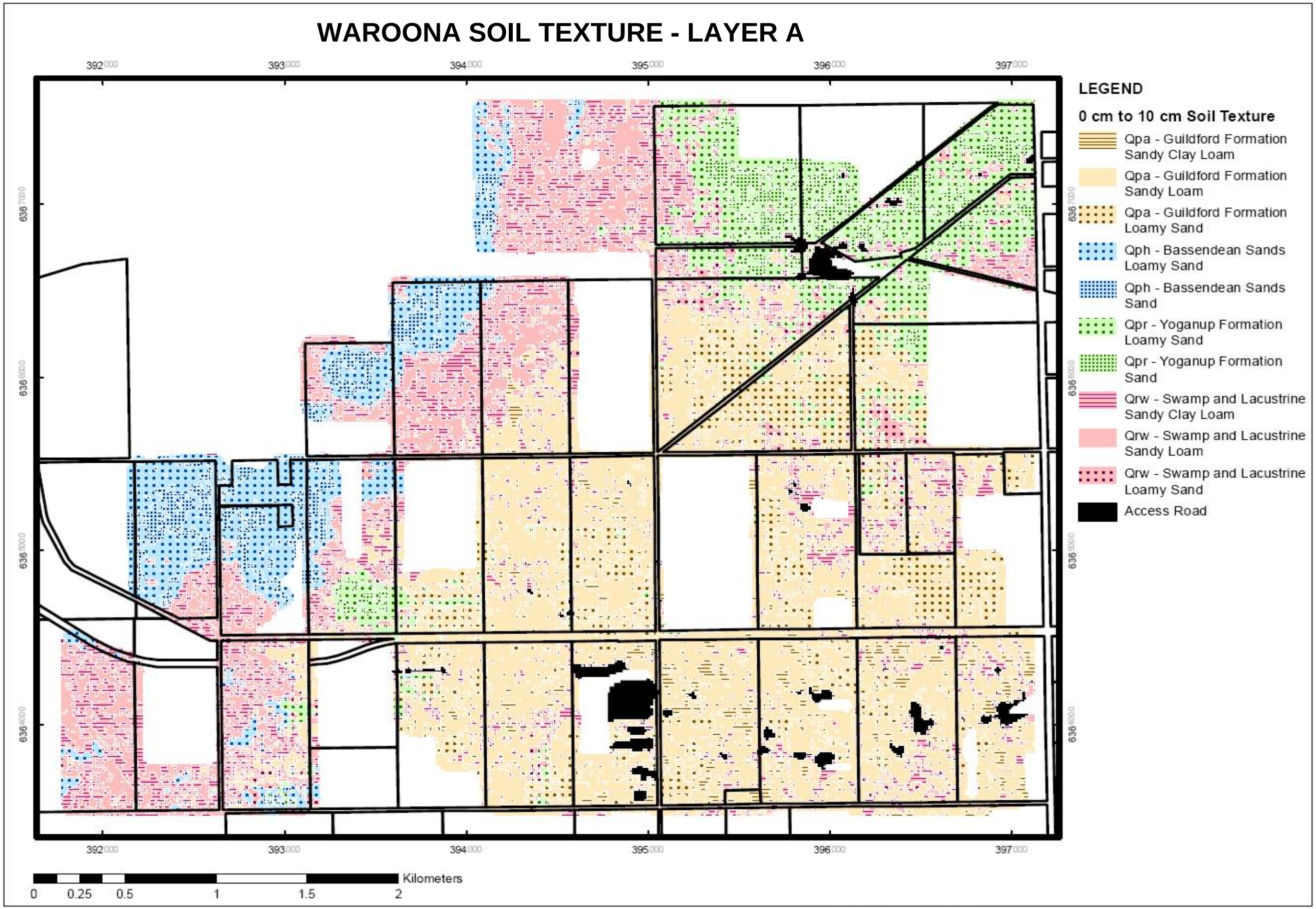


**Figure 6.40. Layer A (0 cm to 10 cm) subdivision of soil type and soil texture for the Waroona survey area.**

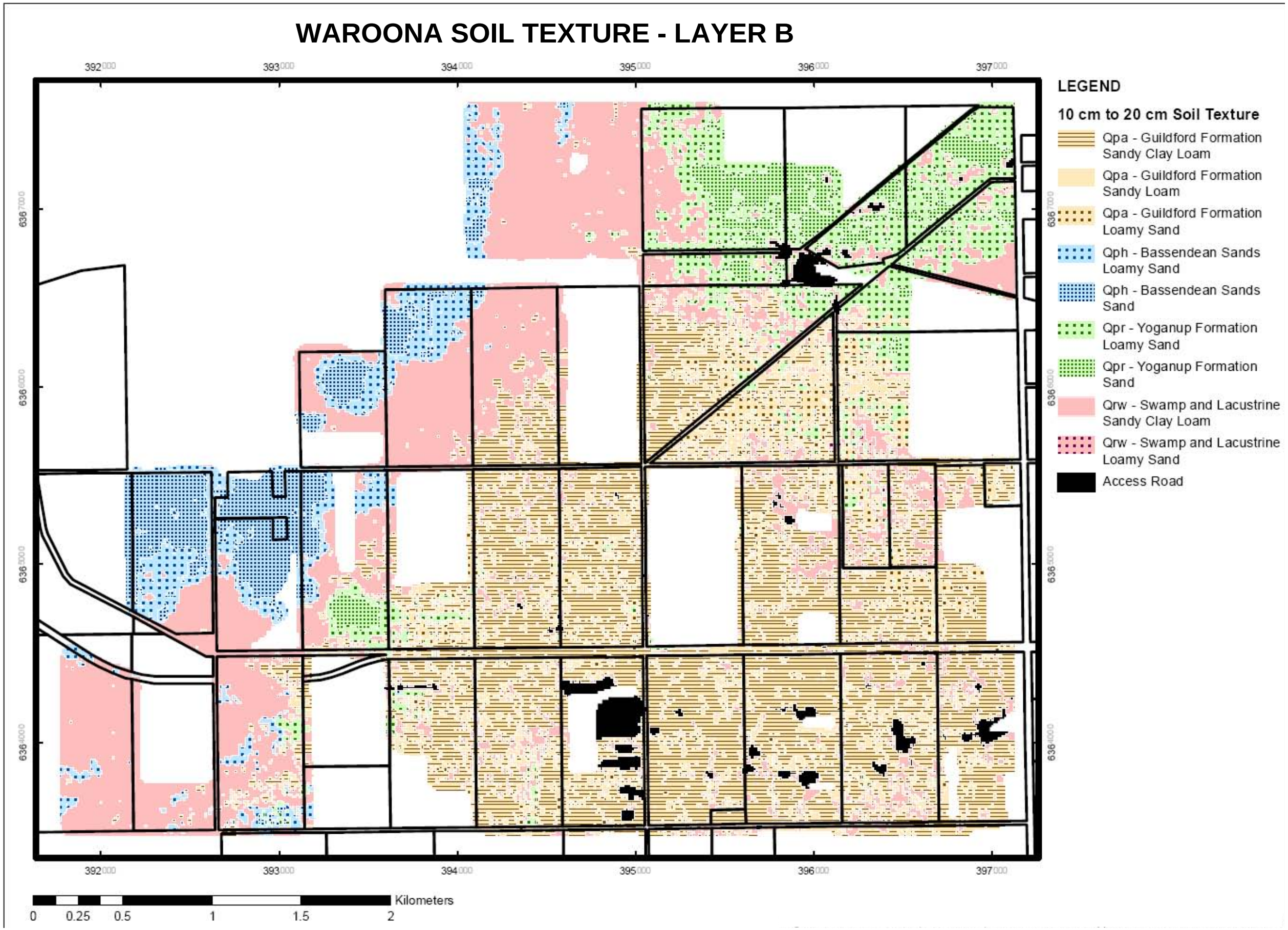


**Figure 6.41. Layer B (10 cm to 20 cm) subdivision of soil type and soil texture for the Waroona survey area.**

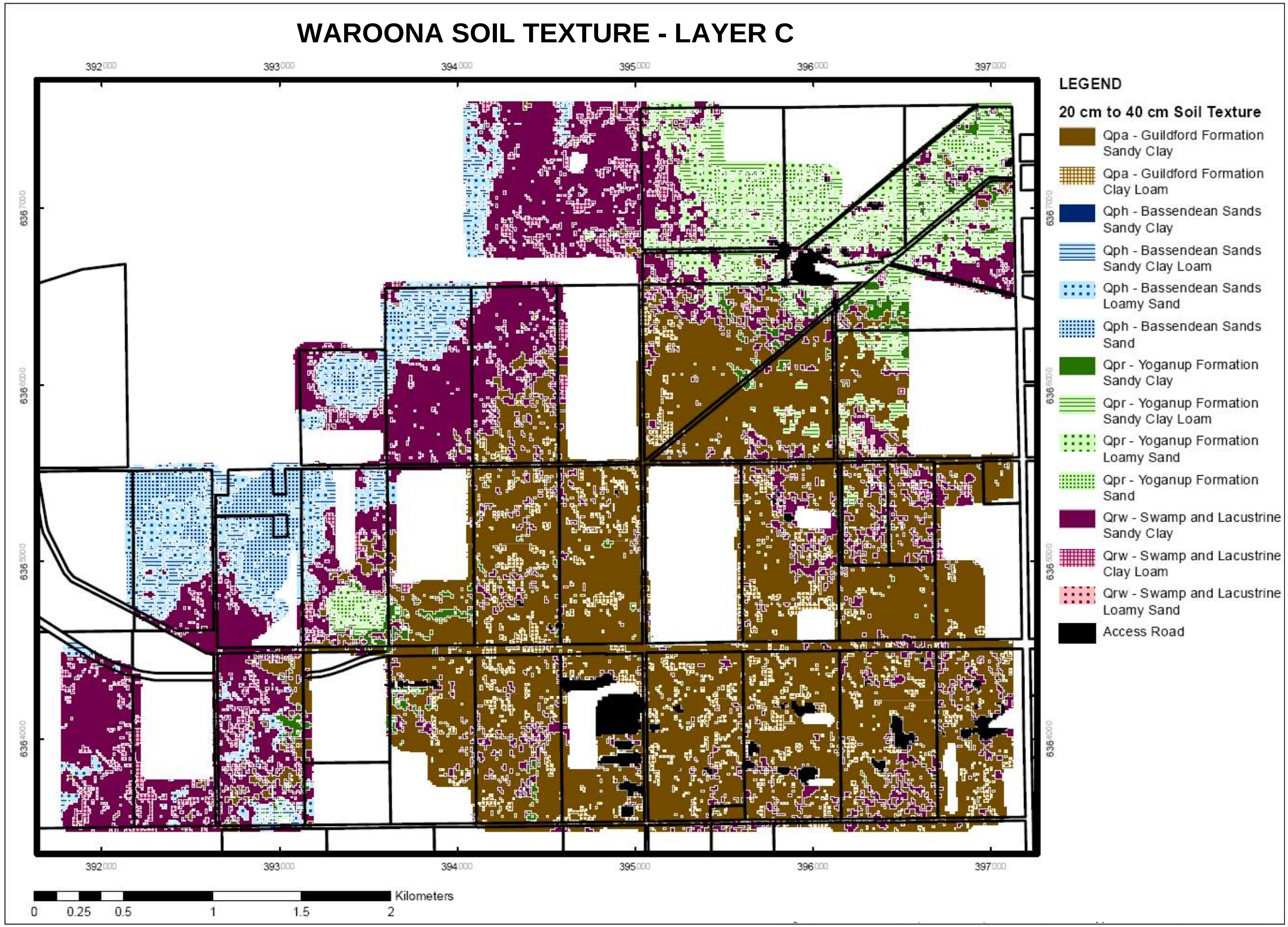


**Figure 6.42. Layer C (20 cm to 40 cm) subdivision of soil type and soil texture for the Waroona survey area.**

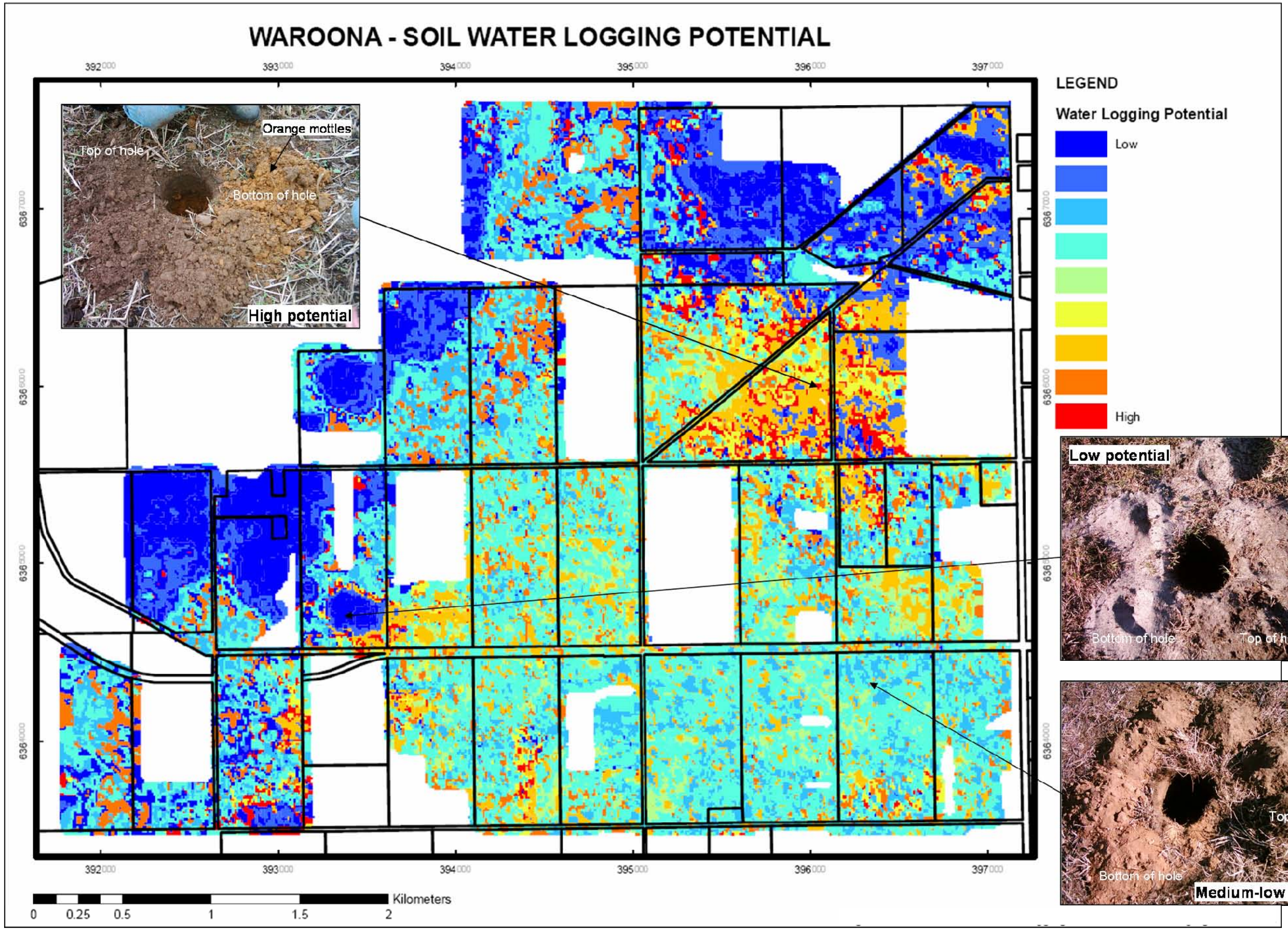


**Figure 6.43. Potential for waterlogging as a result of vertical changes in soil texture.**

### 6.5.8 Soil waterlogging potential

Radiometric data is not limited to the creation of soil maps. Soil waterlogging potential is a function of changing soil condition. Once three-dimensional soil conditions are established, it is possible to evaluate the potential of a soil type to become waterlogged.

The potential for soil to become waterlogged is a function of changing soil texture, porosity, and permeability. These are characteristics that can be inferred from radiometric data. As water infiltrates through the soil profile, soil will become waterlogged where the lower soil layer does not have adequate permeability to accept the incoming water at the same rate as the previous soil layer or adequate pore space to store the volume of water.

In Waroona, locations where the vertical soil profile changed rapidly from light textured sandy soils to heavier textured clay soils, were observed to have a high potential for waterlogging. In order to capture and map these observations, a potential waterlogging index was created for the Waroona area. The potential waterlogging index intuitively assigned non linear coefficients to different soil layer texture transition combinations based on field observation (Table 6.8). Small changes in soil texture attracted a lower value, while significant textural changes were given a higher value. Potential waterlogging values were assigned to changes in soil layers A to B and B to C according to the classified radiometric soil types. The total vertical soil waterlogging potential was subsequently calculated by summing these values.

Without calibration data, the total vertical soil waterlogging potential is only a relative value for the Waroona area. Thus the total vertical soil waterlogging potential was represented in Figure 6.43 as low to high. For reference, the minimum score was 0 and the maximum score was 16, with an average value for potential waterlogging of 6.5.

**Table 6.8. Potential waterlogging index. A value, representing the potential for a soil type transition to cause waterlogging, is assigned according to the transition from one soil type to another. A higher value represents a higher potential for waterlogging.**

| Subsequent soil texture \ Initial soil texture | Sand | Loamy sand | Sandy loam | Loam | Sandy clay loam | Clay loam (friable clay) | Sandy clay |
|---|---|---|---|---|---|---|---|
| Sand | 0 | 0 | 0 | 0 | 0 | 0 | 0 |
| Loamy sand | 0.5 | 0 | 0 | 0 | 0 | 0 | 0 |
| Sandy loam | 0.75 | 0.5 | 0 | 0 | 0 | 0 | 0 |
| Loam | 6 | 2 | 1 | 0 | 0 | 0 | 0 |
| Sandy clay loam | 7 | 2.5 | 2 | 1 | 0 | 0 | 0 |
| Clay loam (friable clay) | 8 | 6 | 5 | 3 | 2 | 0 | 0 |
| Sandy clay | 9 | 8 | 7 | 5 | 4 | 1 | 0 |

Classes identified with medium to high waterlogging potential scores showed mottling in field soil samples layer C, consistent with observed waterlogged areas (Figure 6.43).

Nevertheless, it is recognised that the vertical distribution of soil texture is not the sole contributor to actual waterlogging. The location in the landscape, slope of the surrounding area, subsurface horizontal water movement, and groundwater discharge are also major contributors to waterlogging. However, as a stand-alone map product and without calibration, the potential vertical waterlogging map in Figure 6.43 provides a general guide to where waterlogging could be expected to occur as a result of vertical water movement constraints. With additional information to calibrate the index system to the Waroona soil and rainfall conditions, the waterlogging potential map provides a valuable land management decision making tool when integrated with other landscape information.

For example, a drainage management option map was created using the potential waterlogging map and layer A soil textures (Figure 6.44). For this map, surface

water controls were considered appropriate where the surface soil texture consisted of sandy clay loam or heavier. Engineering options, such as tile drains, were considered appropriate where waterlogging potential was medium or higher and the layer A contained light soil textures. As a result, it is possible to isolate paddocks that would benefit from the use of tile drains, e.g. paddocks dominated by no preference (green) and engineering options (blue), rather than surface water controls in Figure 6.44.

### 6.5.9 Conclusion

Radiometric data was acquired across an area in the Shire of Waroona for the purpose of mapping 4 or 5 significant soil types. A unique methodology was established to map the Waroona soils by modifying the traditional classification and field verification approach to soil mapping with radiometric survey data. In this new methodology, the classification algorithm was used exclusively to group radiometric responses to isolate spatial regions with similar radiometric response. Soil units were subsequently identified as a function of the spatial distribution of the classes and field derived soil textures for the classes, thereby ensuring non-unique radiometric signatures were correctly grouped with spatially and texturally related classes.

As a result of the clustering and reclassification processes, a large volume of data describing the spatial soil texture variability of Waroona was generated. The data handling capabilities of the GIS were utilised to integrate *a priori* knowledge and other data sets and produce a range of map products to assist land managers:

- broad soil type (refer to Figure 6.34),
- simple texture boundaries (refer to Figures 6.35 to 6.37),
- sub-soil changes (refer to Figures 6.39 to 6.42) ,
- soil waterlogging potential (refer to Figure 6.43), and
- drainage management (refer to Figure 6.44).

While the soil classification maps may be used in isolation, the soil database created within the GIS as a result of the new classification process, lends itself to other land management situations that require knowledge of local textural spatial variations,

including erosion management, crop selection and local surface-ground water management models.

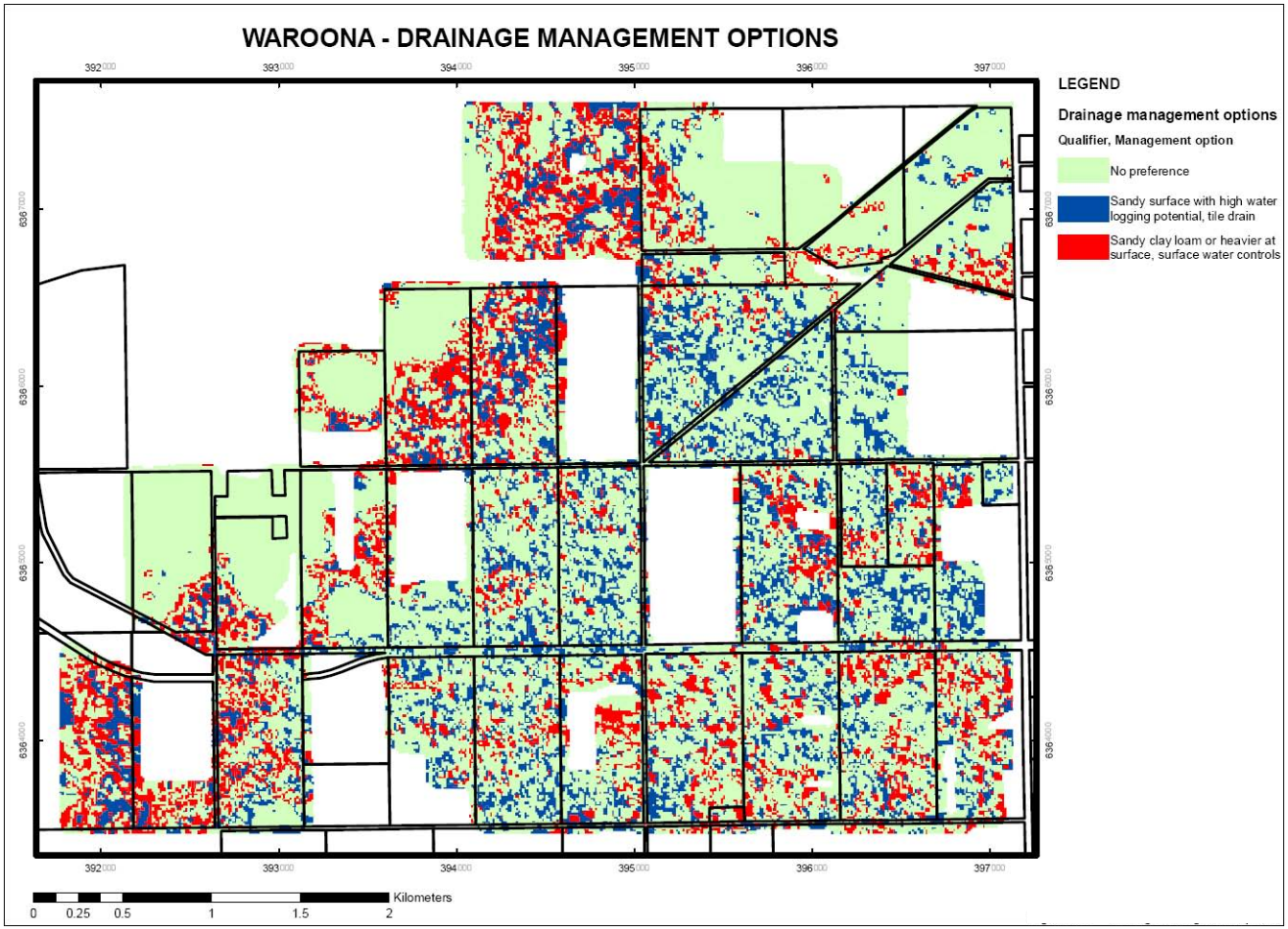


**Figure 6.44. Drainage management options. Surface water controls (red) were considered appropriate where the surface soil texture consisted of sandy clay loam or heavier. Engineering options, such as tile drains, were considered appropriate where waterlogging potential was medium or higher and the layer A contained light soil textures.**

Chapter 6 – Case Studies

## 6.6 Case Study 6: Mapping local recharge and discharge locations from soil textural changes

### 6.6.1 Abstract

Total waterlogging potential as a result of incident rainfall was calculated from a three-dimensional soil model, using the methodology developed in this thesis, and a digital terrain model. From the total waterlogging potential map, areas relating to surface water recharge, discharge, and waterlogging were identified, independent of groundwater movement. These results enabled complex groundwater and surface water relationships to be separated from observed waterlogging.

While the results of the waterlogging modelling were unsubstantiated, due to an absence of field data, the methodology suggests a potential application in identifying local recharge and discharge zones. Identification of these recharge and discharge zones is expected to assist in the selection of appropriate land management or surface water management controls in areas prone to waterlogging.

### 6.6.2 Introduction

In the previous case study for Waroona, Western Australia (Case Study 5), ground radiometric survey data from Waroona was used to define three-dimensional variations in soil texture, down to approximately 40 cm. From the soil texture information, a map of potential soil waterlogging was created using the vertical relationship between soil texture and inferred porosity. However, infiltration is not limited to vertical movement. During storms, shallow flows in saturated soil macropores will move approximately parallel to the topography, given suitable rainfall and soil saturation conditions. If the lateral receiving body can not contain the volume of water delivered through the macropores, waterlogging will occur at the interface between the soil units.

The methodology developed for the Waroona case study for identifying water logging through the potential waterlogging index provided an interesting premise for identifying locations prone to waterlogging as a result of their soil texture profile. To

expand this concept further and integrate the lateral relationships between soil units and water as a result of topography, radiometric data from the Elashgin, Western Australia study area was modelled in conjunction with available soil sample and digital terrain information (provided by Department of Agriculture and Food). The lateral and vertical waterlogging potentials for the area were subsequently combined to define the total waterlogging potential. The total waterlogging potential information was subsequently interpreted to identify areas of recharge and discharge.

### 6.6.3 Vertical waterlogging potential

The methodology employed to highlight areas with a potential to become waterlogged was described in Chapter 5, Section 5.2.3.1 and employed for the Waroona study area in Case Study 5, Section 6.5.8. In summary, the potential for soil to become waterlogged is a function of changing soil texture, porosity, and permeability. As water infiltrates through the soil profile, soil will become waterlogged where the available pore space and permeability of the receiving soil unit is insufficient to accept the incoming water volume at the delivery rate.

As shown in Case Studies 3 to 5, three-dimensional soil characteristics, down to approximately 40 cm, relating to waterlogging, such as soil texture, porosity, and permeability, can be inferred from radiometric data. In Case Study 5, vertical changes in soil characteristics were assessed against the potential waterlogging index (refer to Table 6.8). A summation of the scores from the change in soil texture at the soil horizon interfaces was used to identify areas with high (high score) and low (low score) waterlogging potential.

Using the same interpretation methodology established in Chapter 5, Section 5.2.3.1 and employed in Case Study 5, Section 6.5.8, a soil map was produced from the Elashgin radiometric data (Figure 6.45). The vertical soil waterlogging potential was subsequently calculated (Figure 6.46). Note, only two soil horizons were interpreted for the top 40 cm in the Elashgin soil samples, thus the three-dimensional soil model contains only layers A and B.

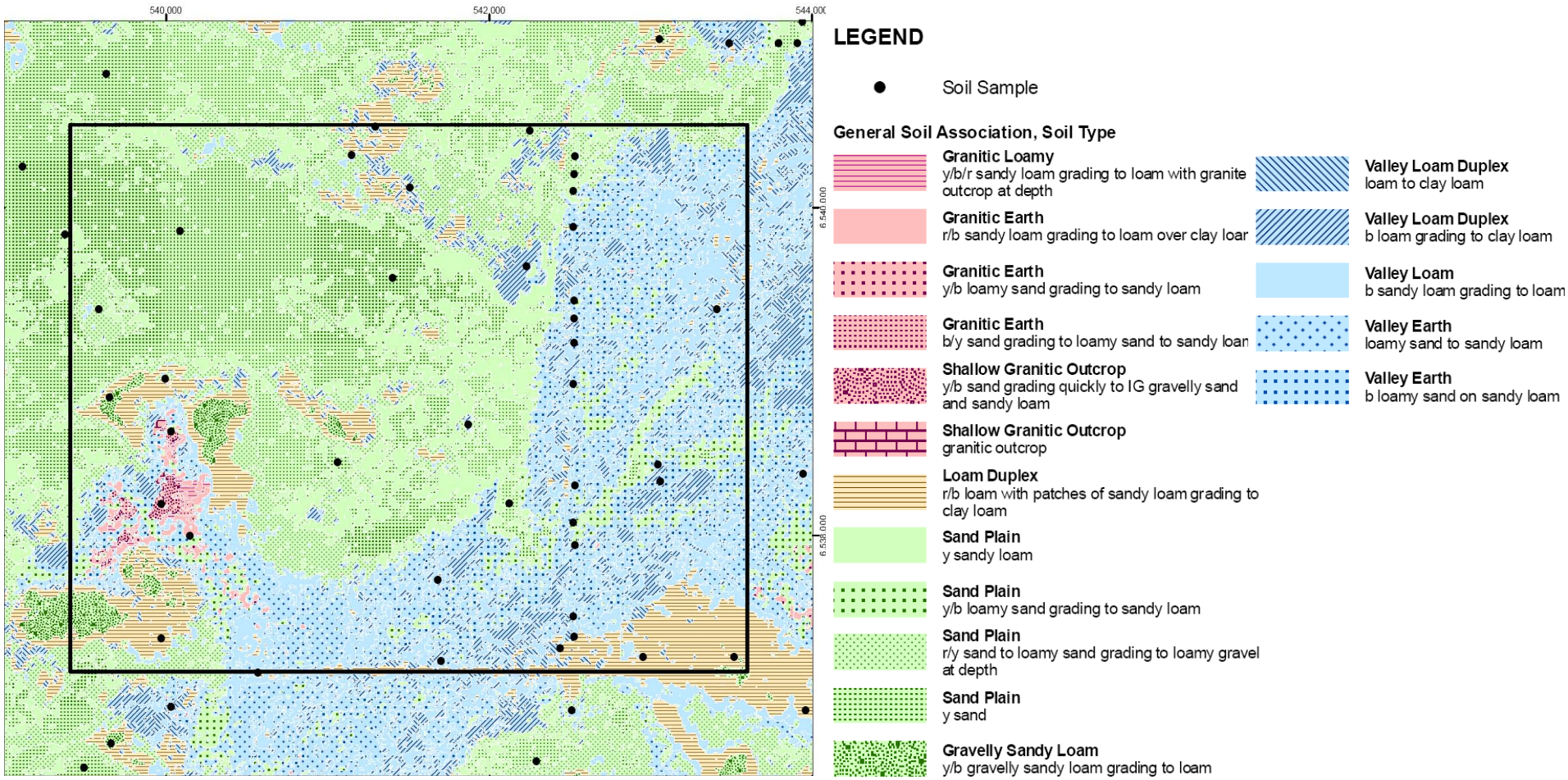


**Figure 6.45. Interpreted soil map for Elashgin, Western Australia. The black square is the focus area for this case study. The soil map was produced using the radiometric interpretation methodology established in this thesis. The preliminary investigation and data acquisition was conducted by the Department of Agriculture and Food, Western Australia in 2001, prior to the commencement of this thesis. Soil texture distribution was established by classifying the radiometric data, clustering, and integrating the results with available field information (shown as black dots) to create a two layer, three-dimensional soil map.**

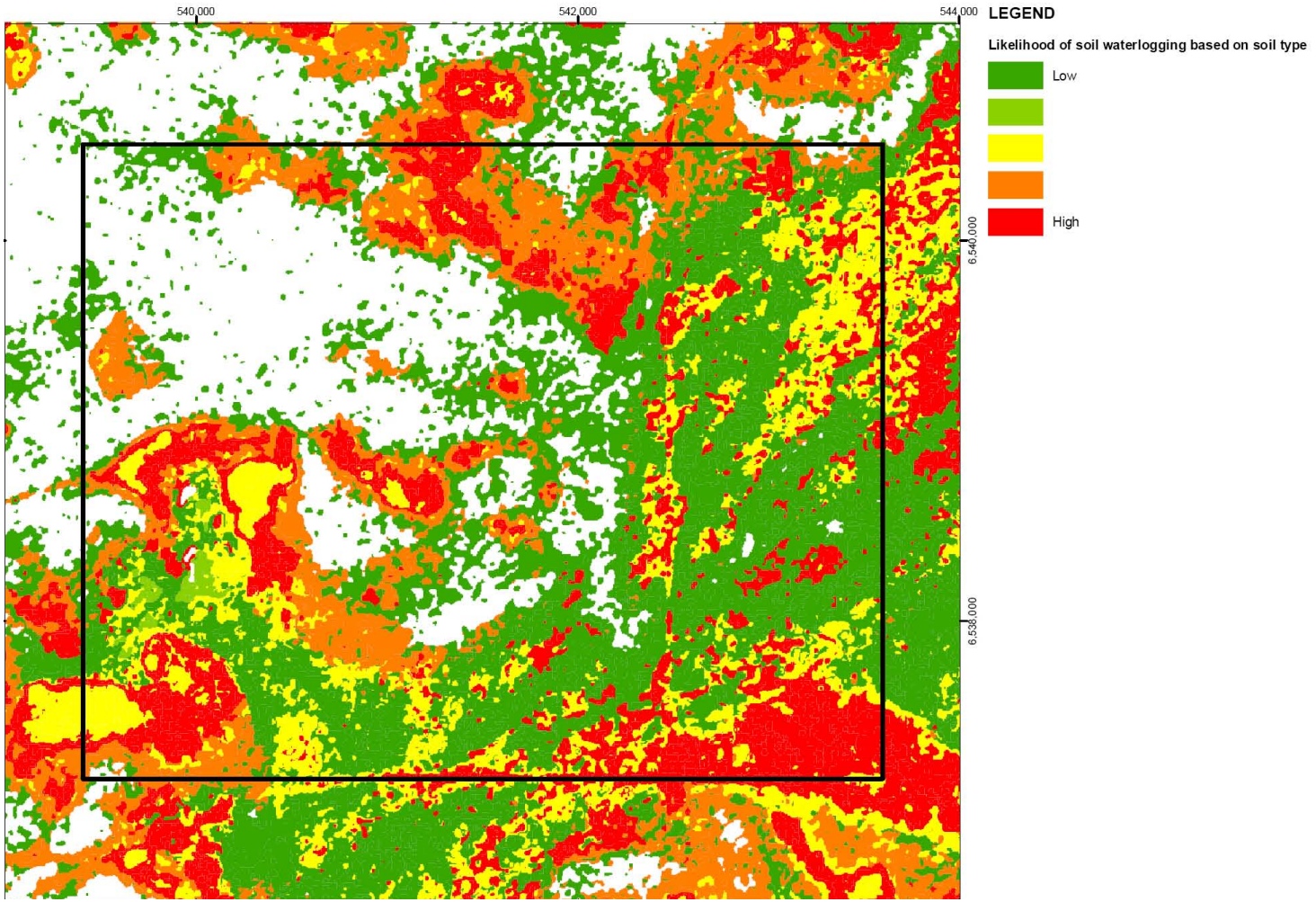


**Figure 6.46. Vertical waterlogging potential. This map was produced using the vertical waterlogging potential methodology developed during this thesis. Vertical changes in soil characteristics were assessed against the potential waterlogging index (Table 6.8). A summation of the scores from the change in soil texture at the soil horizon interfaces were used to identify areas with high (high score) and low (low score) waterlogging potential.**

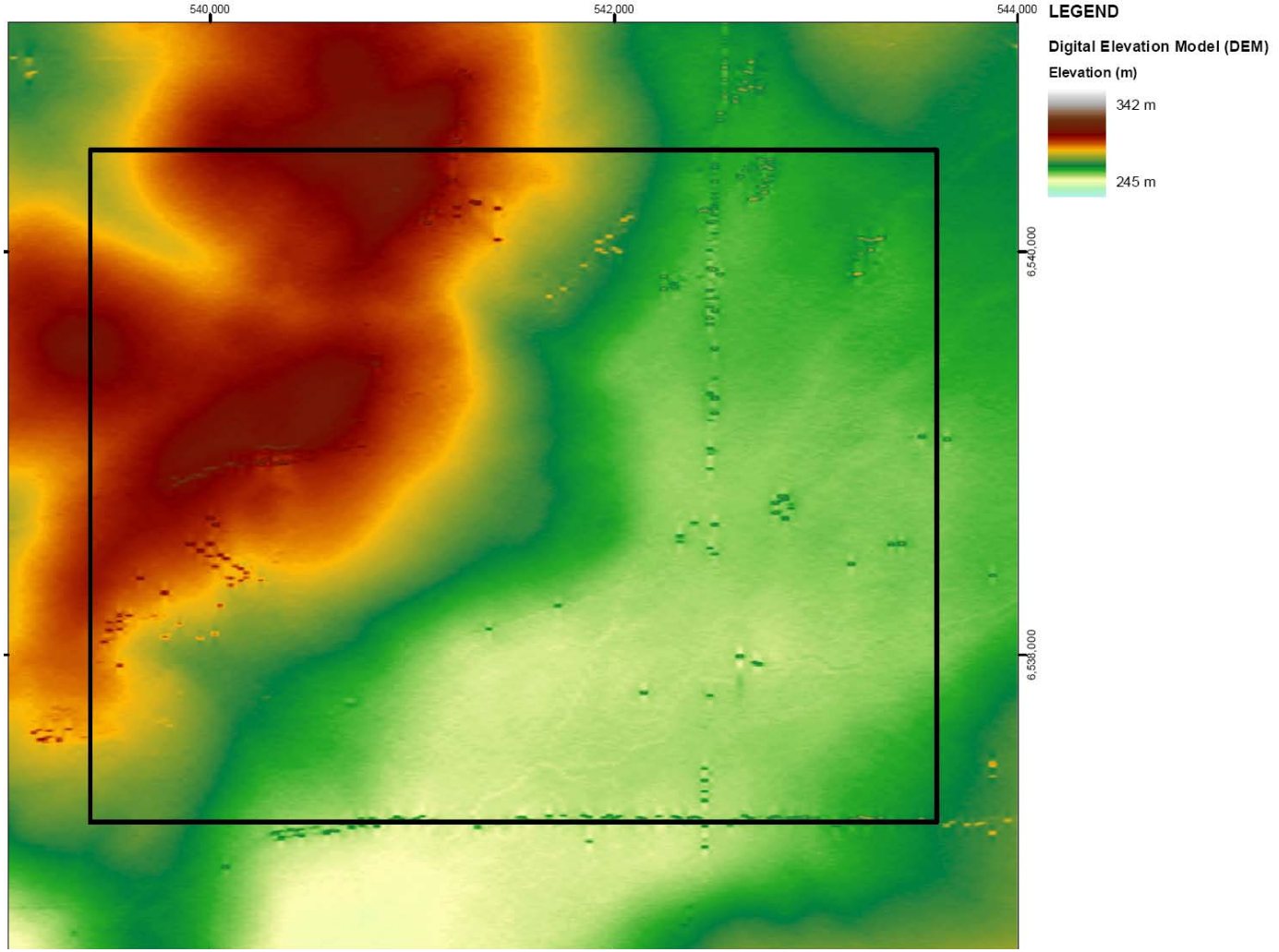


**Figure 6.47. Digital terrain model for the Elashgin Case Study area. Pseudo colour image. This data was acquired during the airborne radiometric survey. The small anomalies in the data are the result of the radar altimeter, used to acquire the data, reflecting off the top of fence posts (linear trends) and trees.**

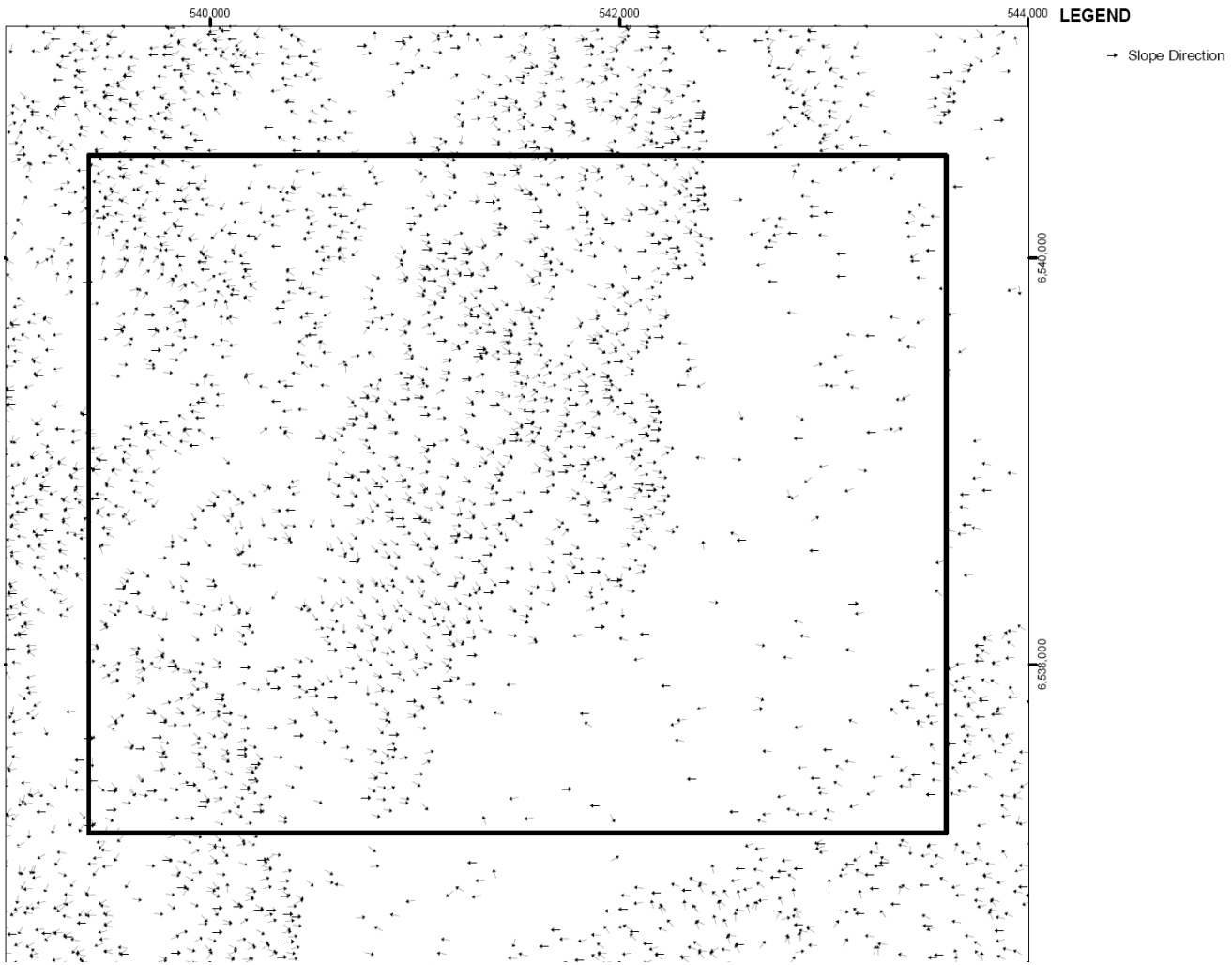


**Figure 6.48. Slope direction. Slope direction (illustrated by the arrow direction) is described as the direction from each cell to the neighbouring cell with the lowest elevation. Where the change in elevation is greater than 1 m the slope direction is represented by an arrow.**

### 6.6.4 Lateral waterlogging potential

In order to define the lateral potential for waterlogging, slope direction and overland flow accumulation were derived from available digital terrain data for the Elashgin study area (Figure 6.47). Slope direction (Figure 6.48) is described as the direction from each cell to the neighbouring cell with the lowest elevation. This direction is represented in Figure 6.48 as an arrow. Note, where the change in elevation between the cells was less than 1 m, i.e. below the accuracy of the data, the area was classified as flat, and no direction arrow was shown on Figure 6.48.

Overland flow accumulation was defined as the summation of the number of drops of water that would accumulate in each cell if a drop of water was placed in every cell as a function of topography. Flow accumulation plots (Figure 6.49) illustrate accumulation paths, for example of soil or water, as a function of topography. Higher accumulation values described preferential flow paths. Low accumulation values are used to identify hills and local topographical crests.

In this study, the flow accumulation plots illustrate lateral water movement direction, and low to high accumulation of shallow saturated water flows following infiltration. Water movement is expected to change where the accumulation values ends, the highest accumulation value along the accumulation strings, as overland flow movement changes to dominantly vertical infiltration. The overland flow accumulation results for the Elashgin Case Study are illustrated in Figure 6.50.

Once the slope direction and flow accumulation models were generated, the lateral potential for waterlogging score was established by the change in soil type in the slope direction, using the values from Table 6.8, for soil layer A, then soil layer B. These scores were subsequently added to the vertical potential for waterlogging score, to create a total waterlogging potential map (Figure 6.51).

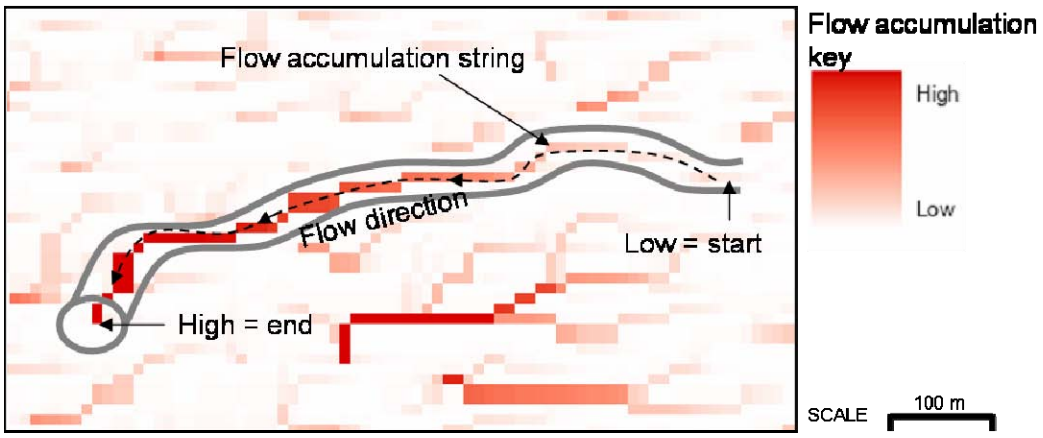


**Figure 6.49. Flow accumulation plot. Flow accumulation values are derived from the sum of the contributing upslope cells. Flow accumulation strings highlight preferential flow paths as a result of surface morphology. In this case study, the strings illustrate the lateral water movement. The end of the strings, marked by the highest accumulation values visible along the string, show where lateral movement stops and vertical infiltration dominates.**

### 6.6.5 Identifying recharge and discharge

Recharge, discharge, and associated waterlogging areas are important management locations in land management. For example, in Elashgin, where the groundwater is saline, land management focuses on minimising discharge and draining areas prone to waterlogging (Cooper *et al.*, 2001). By combining the total waterlogging potential map with the flow accumulation plot (Figure 6.51), it is possible to identify areas of:

- Recharge
    - where slope is low, such that vertical infiltration dominates, and there is a low potential for waterlogging, or
    - at the base of slope (the end of the flow accumulation strings) where vertical infiltration dominates and there is a low potential for waterlogging.
- Discharge
    - where there is lateral water movement (along flow accumulation strings) across medium to high waterlogging potential areas.
- Waterlogging
    - where there is low slope and medium to high waterlogging potential such that water is likely to pool on the surface.

The interpreted recharge, discharge, and waterlogging areas provided in Figure 6.52 are not biased by observed or reported waterlogging conditions and are solely based on topography and interpreted soil in the top 40 cm. Thus the interpretation is independent of groundwater movement and describes how the landscape is likely to react to rainfall.

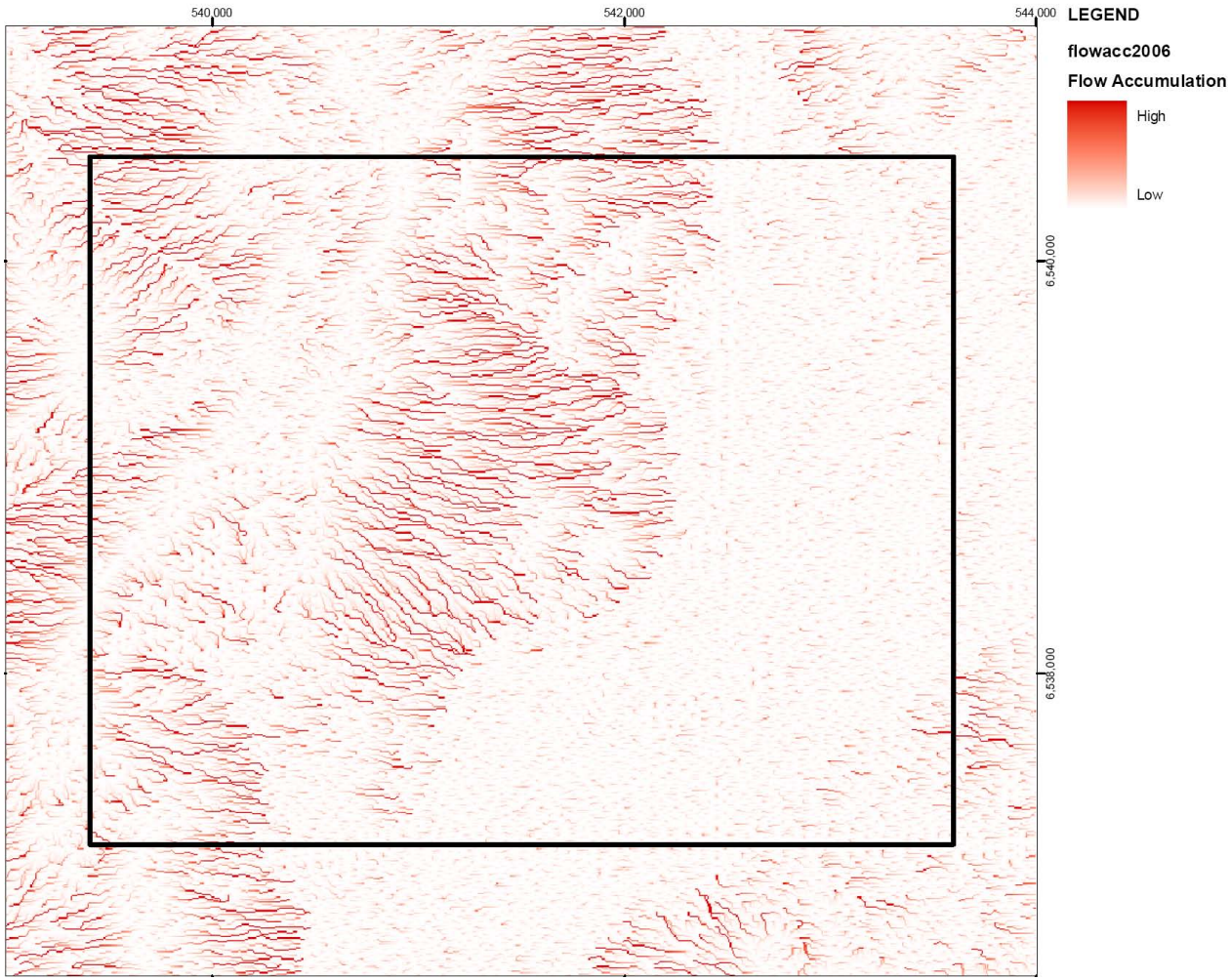


**Figure 6.50. Overland flow accumulation. Overland flow accumulation represents the summation of the number of drops of water that would accumulate in each cell if a drop of water was placed in every cell. The flow strings illustrate the preferential lateral movement, from low to high, of soil water as a function of topography.**

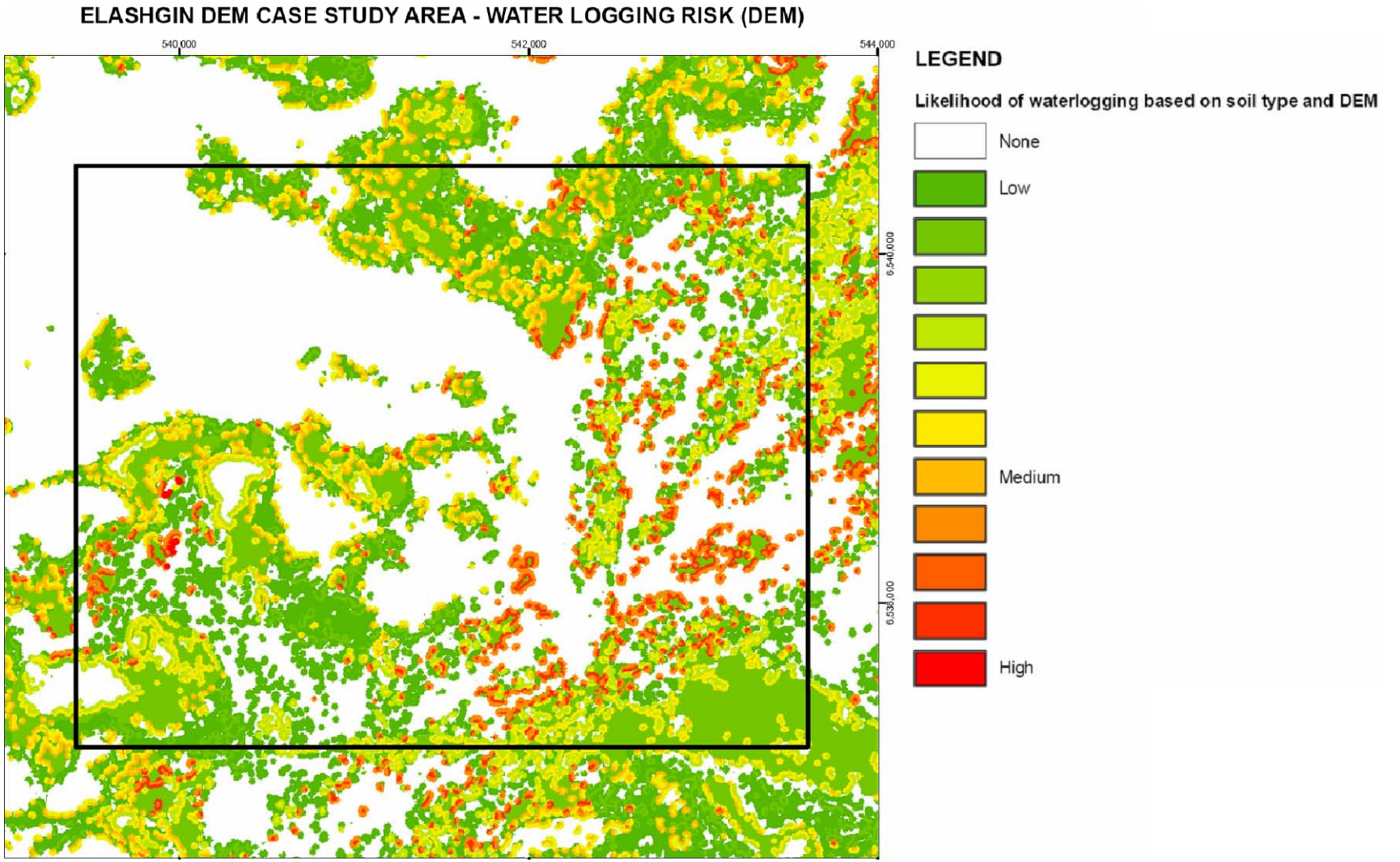


**Figure 6.51. Total waterlogging potential for Elashgin, Western Australia Case Study. The total waterlogging potential is an empirical measure of potential for a soil to become waterlogged, derived from the summation of the vertical and lateral waterlogging scores.**

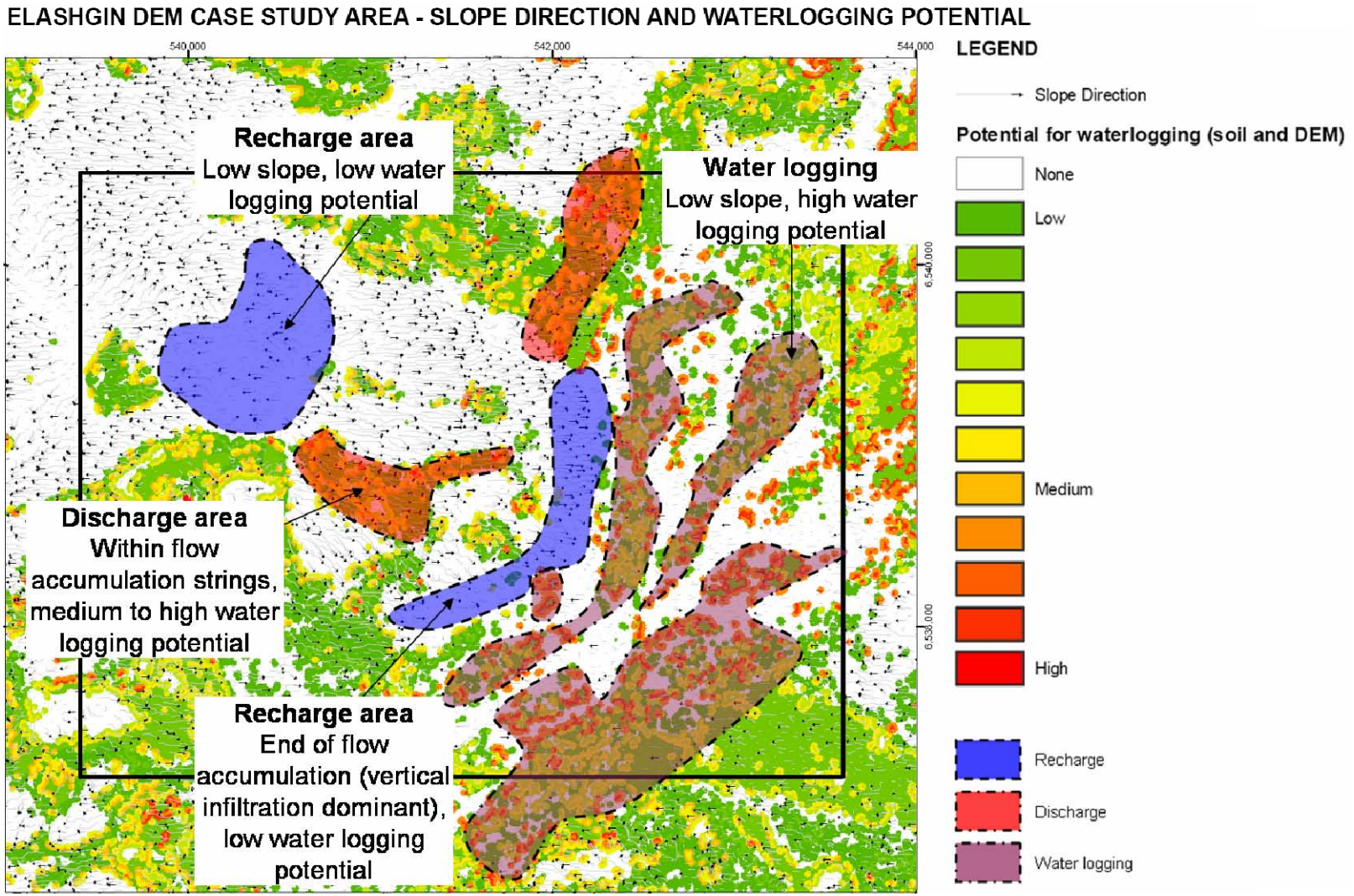


**Figure 6.52. Interpreted recharge, discharge, and waterlogging potential. Areas of recharge (blue), discharge (red), and waterlogging (purple) potential are interpreted based on slope and waterlogging potential.**

### 6.6.6 Discussion

The addition of topography (digital terrain) information to the previously established waterlogging potential methodology enabled lateral waterlogging potential to be resolved. When combined with the vertical waterlogging potential, the resulting total waterlogging potential can be used to describe how the landscape is likely to react to rainfall, independent of groundwater systems.

This methodology has not been calibrated with observed landscape waterlogging. However, a comparison of interpreted recharge, discharge, and waterlogging from the total waterlogging potential maps against observed salinity and waterlogging from the *Elashgin focus catchment report* (Cooper *et al.*, 2001) (Figure 6.53) highlights similar trends. At location 1 in Figure 6.53 the sandy soil, low waterlogging potential, and low slope characteristics were used to map an area with high recharge potential. Although this area falls just outside of the mapped recharge area in Cooper *et al.* (2001), similar conditions mapped elsewhere in the catchment by Cooper *et al.* were identified as high recharge potential.

At location 2 in Figure 6.53 mid-slope discharge was mapped. At this location the soil changes from an upper subcatchment sandy soil to clay dominated soil. The lower permeability and porosity of the clay unit is expected to force lateral, subsurface (interstitial) water flows to the surface, producing localised discharge. As this analysis is independent of the local groundwater system, the potential to discharge is linked to rainfall events.

At location 3 in Figure 6.53 a base of slope recharge area was identified. At this location, surface water runoff from the upper subcatchment is likely to pond and infiltrate into the sandy soil. The interpretation of this area as recharge contradicts the Cooper *et al.* (2001) interpretation, which describes the area as saline and waterlogged. The salinity is the result of saline groundwater discharging. Capillary action draws the salty water to the surface throughout the year, resulting in surface salt scalds and poor crop performance (Cooper *et al.*, 2001). Thus this location may be linked to both groundwater discharge and surface water recharge. The combined

discharge and recharge conditions are likely to result in an area that is continually waterlogged, as reported by Cooper *et al.* (2001) and illustrated in Figure 6.53.

At location 4 in Figure 6.53 valley floor waterlogging was identified. At this location, the soil has a medium to high potential for waterlogging and low slope. These conditions prevent the surface water from leaving the area, resulting in surface water ponding and eventual waterlogging. As the valley floor area is also subjected to rising saline groundwater (Cooper *et al.*, 2001), waterlogging and ponding may continue long after rainfall events.

### 6.6.7 Conclusion

As an extension to the radiometric soil classification, the potential waterlogging results can be generated in less than a day. Results from the potential waterlogging map demonstrated reasonable correlation with observed and mapped waterlogging conditions in the Elashgin Case Study area. Although the results could be improved through calibration of the potential waterlogging index, without calibration the technique provides a simple analysis of landscape reaction to rainfall.

Additionally, as the waterlogging results are independent of groundwater conditions, the results can also be used to guide land management and surface water management decision processes. By identifying and differentiating surface water related discharge and waterlogging areas from groundwater discharge and waterlogging areas, the cause of observed waterlogging is easier to resolve. This facilitates the correct selection of land management or surface water management controls, such as diverting surface water runoff away from groundwater discharge areas to minimise waterlogging.

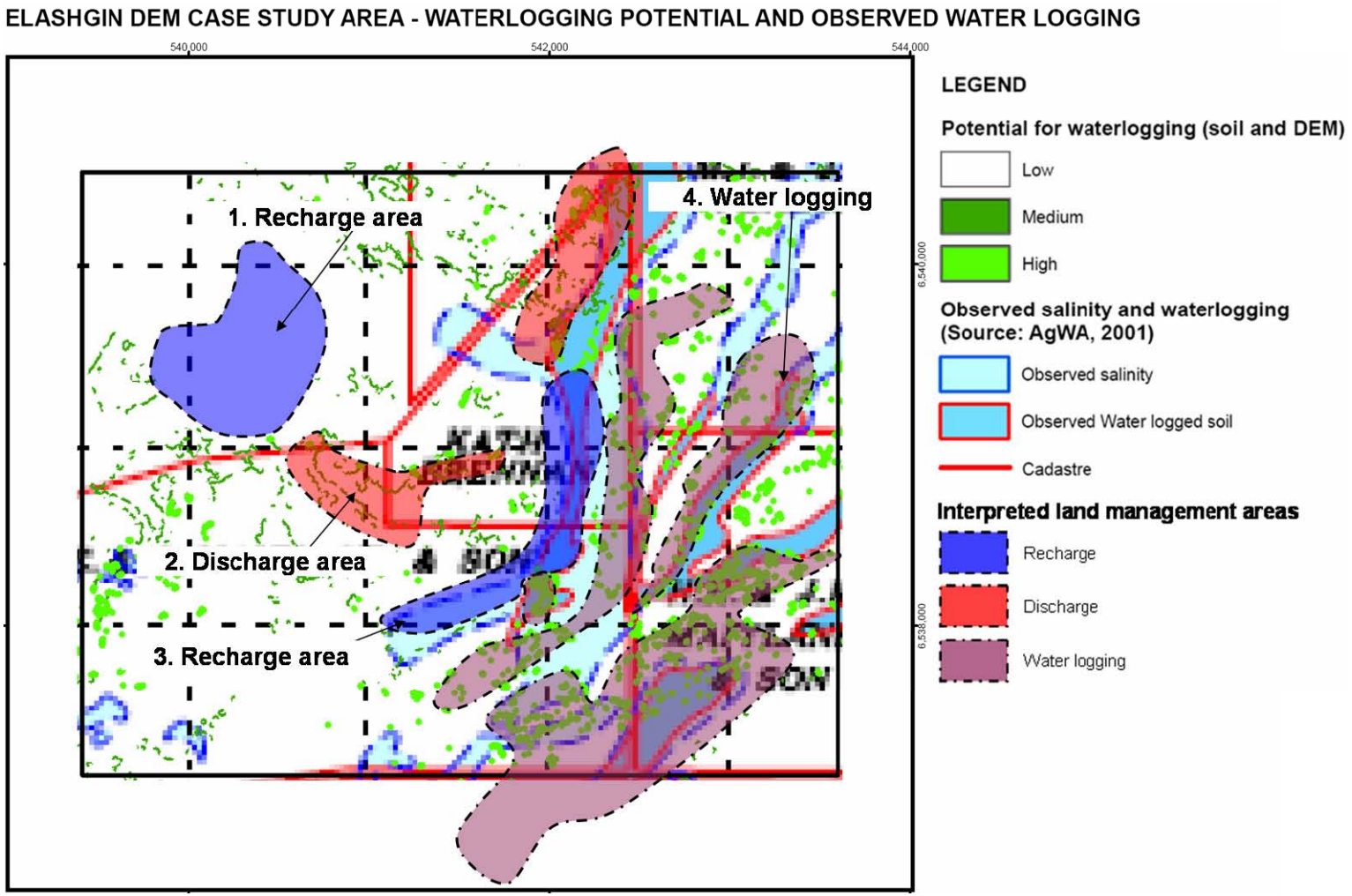


**Figure 6.53. Waterlogging comparison, Elashgin. High and medium waterlogging potential results produced from the classified 3D radiometric soil model are compared against observed waterlogging and salinity (Cooper *et al.*, 2001) and interpreted surface water recharge, discharge, and waterlogging potential.**

# Chapter 7 - Conclusions and recommendations

The aim of this thesis was to improve radiometric processing methods and study the soil mapping potential of radiometric data. This was achieved through the development of an alternative radiometric data analysis and interpretation methodology. This chapter summarises how these aims were achieved and provides recommendations for future studies.

## 7.1 Development of a new multispectral processing methodology

A multispectral processing technique was developed to isolate peak gamma ray energies from standard 256-channel NaI spectrometry data. This was achieved by using a hull, created from the decreasing, negative gradient of local spectrum minima as a surrogate for the Compton continuum and bremsstrahlung energy at each reading. By subtracting the hull from the original 265-channel spectrum, the peak gamma ray anomalies present in the 256-channel data became emphasised.

Seven distinct gamma ray energy peaks were identified in the 256-channel radiometric data following the removal of spectral noise:

- $^{40}$K full energy peak at 1461 keV [potassium],
- $^{214}$Bi full energy peak at 1764 keV [uranium],
- $^{208}$Tl full energy peak at 2614 keV [thorium],
- combined $^{228}$Ac full energy peaks at 908 keV, 960 keV and 966 keV [thorium],
- $^{214}$Bi full energy peak at 1120 keV [uranium],
- combined $^{228}$Ac full energy peaks at 1590-1640 keV [thorium], and
- $^{214}$Bi single escape energies at 1253 keV from pair-production reaction at 1764 keV [uranium] with influences from $^{40}$K 1461 keV Compton edge.

The channels facilitated the production of new radiometric uranium and thorium ternary imagery, which highlighted characteristics in the radiometric imagery that were difficult to identify in the standard imagery.

The new imagery also highlighted unique changes in soil characteristics and local environmental conditions. These unique changes were attributed to the physical

interaction of gamma rays and radionuclide behaviour in the environment, providing direct indicators of soil characteristics and local environmental condition:

- The ratio of uranium 1120 keV to 1764 keV demonstrated the potential to differentiate soil density and/or soil overburden.
- The ratio $^{208}$Tl full energy peak at 2614 keV to combined $^{228}$Ac full energy peaks of 908 keV, 960 keV and 966 keV demonstrated the potential to identify the separation of $^{228}$Th from $^{232}$Th, and associated changes to soil chemistry and water movement.

## 7.2 Classification assisted interpretation

A radiometric classification and interpretation approach was developed to accommodate the variable confidence levels associated with the seven multispectral processed radiometric channels. Specifically, the classification and interpretation methodology provides greater control over the significance of changes in radiometric response for defining soil boundaries than standard classification approaches.

The classification and interpretation methodology was presented in four parts:

1. Preliminary investigation: Establish the survey resolution required for the mapping purpose and assemble available soil information.
2. Soil texture distribution: Classify the radiometric data, collect and integrate field survey data, and create a three-dimensional soil texture map.
3. Soil unit definition: Integrate soil knowledge and cluster radiometric classes to form units.
4. Soil type definition (optional): Integrate chemical and structural soil data and simplify soil textural changes.

The classification and interpretation approach was applied throughout the Case Studies examined in this thesis. The approach was flexible and suitable for a range of mapping applications, demonstrated through the production of a range of map products, including: soil texture maps, water infiltration rates and waterlogging potential, water retention and repellence, drainage management, and soil type.

## 7.3 Case Studies

Case Studies were used to explore issues, problems, solutions, and new approaches to the interpretation of radiometric data for soil/regolith mapping applications. Case Study 1 provided a background to the imagery, geological, and environmental settings for the four study areas: Yaragadee, Elashgin, Moyagee, and Waroona. It defined uncommon and new terminology used in the thesis, and conveyed observations made from careful inspection of the 256-channel data.

In Case Study 2, attention was drawn to the increased correlation of uranium and thorium as a result of standard processing in the Elashgin radiometric data. Inclusion of neighbouring thorium response in the uranium channel count was determined to be the cause of the increased correlation. This drawback in standard processing was subsequently alleviated by reducing the standard uranium channel window width to 1700 - 1860 keV. However, calibrated ground concentrations could not be derived from the data using the reduced width uranium window without first incorporating the reduced window width into the standard processing calibration routine.

During the multispectral processing, radiometric channels were tailored to the distribution of the energy peak. Consequently the narrower channel widths prevented the thorium counts from significantly contaminating the uranium count, ensuring the maximum preservation of colour range and contrast within the equivalent standard ternary image: $^{40}$K full energy peak at 1461 keV [red], $^{214}$Bi full energy peak at 1764 keV [blue], $^{208}$Tl full energy peak at 2614 keV [green].

In Case Study 3, data and imagery generated from airborne data collected at an altitude of 30 metres was compared with ground data collected at the same 25 metres line spacing to assess the resolution capability of the data with respect to soil and regolith mapping applications. The study showed that for ground data, image products were suitable for mapping applications at 1:10,000 scale, while for the airborne data the image products were suitable for mapping applications at 1:25,000 scale. A simple cost-benefit comparison of the same data showed that in areas of intensive agriculture the ground platform radiometric system provided the best survey option due to the logistical constraints associated with conducting airborne surveys in areas of intensive agriculture; although, the airborne platform was the more cost effective option for surveys with more than 1,000 line kilometres.

Case Study 4 demonstrated how 1:25,000 scale high resolution radiometric data could be used to refine soil boundaries produced by standard soil mapping techniques at 1:25,000 scale. Comparison of the low and high resolution radiometric imagery showed that where the contrast between the soil unit radiometric responses was weak, high resolution radiometric data was able to resolve boundaries between soil units. The same boundaries could only be inferred from the lower resolution data. Additionally, the comparison showed that where the radiometric response was strong, the high resolution data served to refine the boundary location. These results imply that when interpreting soil boundaries from radiometric data, high resolution radiometric data is required to resolve soil boundaries when the contrast between the radiometric responses of soil units is low, or where the overall radiometric intensity of the soil is low.

Case Study 4 also showed that features smaller than 50 m and 100 m long could be resolved when the acquisition path was directly over the top of the feature and there was a high radiometric response contrast between the feature and the background. Subsequently, although the prescribed scale for the high resolution data in Case Study 4 was believed to be 1:25,000, in locations where there were strong contrasts between the radiometric responses of the soil units the data was considered to be suitable for mapping at scales of 1:2,500 or “paddock-scale”.

In addition, Case Study 4 demonstrated how the multispectral thorium ternary, uranium ternary, and uranium ratio images highlight changes in soil characteristics and local environmental condition that were not identified in the previous soil maps or standard ternary imagery, to improve soil mapping.

Case Study 5 presented the interpretation methodology developed as part of this thesis for soil and regolith mapping applications with multispectral processed data. Additional GIS interpretation products including soil waterlogging potential and preferred locations for engineering drainage options were developed as a function of the interpretation methodology.

The concept of mapping soil waterlogging potential with radiometric data was extended in Case Study 6, with the integration of digital terrain information to

calculate three dimensional water movements in the survey area. While the results presented were only speculative, the methodology demonstrated the potential to quickly identify local soil variability, potential waterlogging hazards, local recharge and discharge zones, and differentiate waterlogging resulting from poor surface water management from waterlogging due to rising groundwater.

## 7.4 Recommendations for future studies

1. The hull removal method developed here and used in the multispectral processing methodology as a surrogate for the Compton continuum and bremsstrahlung energies has limited application. As demonstrated in the Yaragadee data, when using the multispectral processing methodology a significant proportion of the Compton continuum remains in the data if the continuum does not continually decrease.

   While the use of the hull removal facilitated the identification of additional gamma ray peaks from 256-channel sodium-iodide (NaI) data for the purposes of this study, it is not a replacement for standard radiometric processing as the technique does not resolve equivalent ground concentrations. To further studies of the additional peaks and their relationship to each other as well as soil characteristics and local environmental condition, it is recommended that a new processing methodology be developed to isolate only the seven gamma ray peaks discussed in this study. By isolating only these peaks of interest, alternate approaches to modelling Compton continuum and bremsstrahlung energies can be employed to ensure noise levels within the data are minimal.

2. The artificial increase in uranium and thorium correlation as a result of standard processing presents a significant problem for the general application of radiometric data. Multispectral processing offered a means of identifying potential correlation problems and provided alternate radiometric imagery. However, it could not replicate calibrated, equivalent ground concentrations of potassium, thorium, and uranium required from radiometric surveys.

   Modification of the standard radiometric acquisition, processing, and calibration system to use the reduced standard uranium window of 1700 – 1860 keV is

recommended to prevent artificial uranium and thorium correlation. However, the conditions under which the $^{228}$Ac 1590 – 1640 keV peak forms remains unresolved. Additional study into the formation of the $^{228}$Ac 1590 – 1640 keV peak is recommended to improve the predictability of the disruptive energies and reduce artificial uranium and thorium correlation within standard processed radiometric data.

3. Radon corrections were omitted from the multispectral processing. This was done to ensure the radon correction routines did not unduly influence the correlation between the derived uranium peaks. It is recommended that a radon removal routine is introduced to the multispectral processing to reduce the noise fraction within the uranium channels.

4. The relationships established between radiometric response, soil and environment in this thesis are exclusively for characterisation of soils in the study areas. To confidently apply these relationships outside the study areas and facilitate the production of standard soil and regolith maps at 1:50,000 scales or higher resolution, robust examination and cataloguing of the multispectral radiometric response of Australian soil and regolith types is required.

   It is recommended that these additional studies be conducted under controlled conditions, with known soil compositions, moisture profiles, and porosities. Additional sensors should be used to monitor these conditions during experimentation. During these additional studies, it is also recommended that higher energy resolution spectrometers be used in conjunction with the standard NaI survey spectrometers, to verify the positioning of and relationships between the multispectral peaks.

5. Although there was substantial reference literature available on the behaviour of radionuclides under different soil conditions, literature on spatial variability relative to radionuclide behaviour was scarce. To further the application of high resolution radiometric data for soil mapping applications, it is recommended that controlled spatial experiments be performed to catalogue the radiometric response of changing surface and subsurface water content, acidity, texture, and soil boundary mixing.

# Appendix A: Overview of standard radiometric processing

## A.1 Introduction

The fundamentals of radiometric acquisition and processing were recently reviewed by the International Atomic Energy Agency (2003) in its publication *Guidelines for radioelement mapping using gamma ray spectrometry*. This publication is part of a series of publications on uranium mining, and addresses the basics of radiometric survey acquisition, acquisition systems, standard processing, and map production. Rather than duplicate the content of this comprehensive publication, this chapter summarises the components of standard radiometric processing that are referenced in this thesis.

*Note: Unless explicitly stated, information in this chapter is referenced from IAEA (2003).*

## A.2 Principles of radioactivity

There are selections of naturally occurring elements, sometimes referred to as radioelements, whose atomic nuclei contain a surplus of energy. The surplus energy causes the nuclei to be unstable and in order to gain stability the nuclei decays by releasing particles (i.e. alpha or beta particles), energy as gamma radiation, or a combination of the two. The release usually leaves the nuclei in an excited state, and the remaining surplus energy is radiated as gamma rays. The energy of the released gamma ray is characteristic of the decaying nuclei. Gamma ray spectrometers are designed to measure the intensity and energy of the gamma ray, enabling the source of the gamma ray to be diagnosed.

Gamma rays form part of the electromagnetic spectrum of energy. They travel at the speed of light, and have a discreet energy, frequency, and wavelength. This allows the energy to travel vast distances very quickly. As a result, orbiting satellites can be used to detect gamma ray emissions from different galaxies, and airborne gamma ray spectrometers can be used detect gamma ray emission from the Earth.

However, the diagnostic identification of radioelements is limited by interaction of the high frequency gamma ray with atoms. In space, there are few interactions due

to the sparsity of atoms. However, gamma rays emitted from the Earth encounter atoms in rocks, soil, flora, and fauna and in the atmosphere. The gamma ray loses a fraction of its energy with each interaction. As a consequence, naturally emitted gamma rays generally loose all energy after travelling through approximately 50 cm of rock, soil etc., or around 700 m of air.

There are three basic ways through which gamma rays interact with atoms: the photoelectric effect, Compton scattering and pair-production. The interaction is largely dependent on the energy of the gamma ray, as illustrated in Figure A.1. Gamma ray surveys usually use spectrometers designed to detect energies between 40 keV and 2.6 MeV. Thus the Compton scattering is the dominant method of interaction of the target energies.

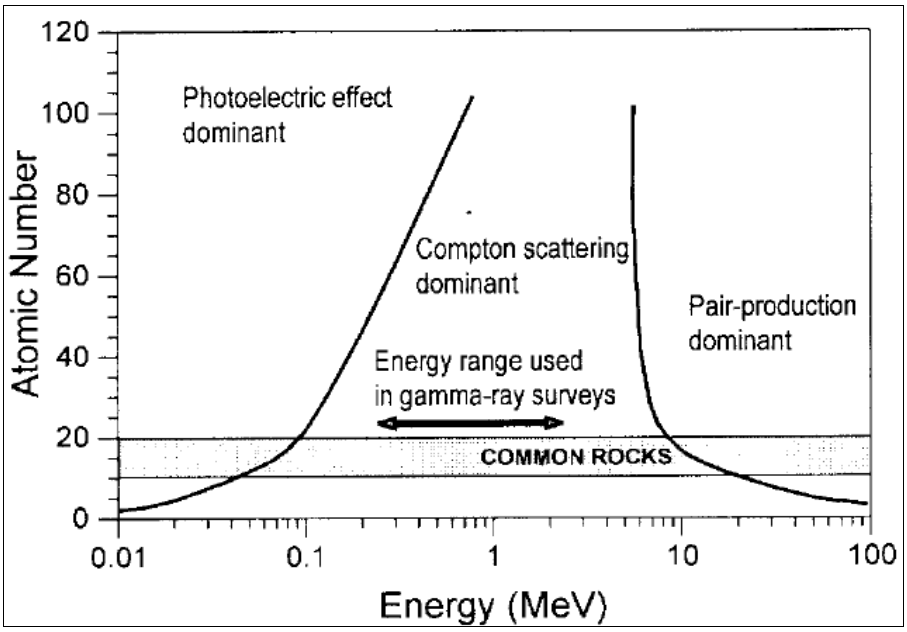


**Figure A.1. Interaction of gamma rays with matter (from IAEA, 2003).**

With Compton scattering, gamma rays lose a proportion of their energy after every collision with an atom's electron. The gamma ray is scattered at an angle relative to the incident angle of the collision, losing energy with each subsequent interaction. The result of the numerous interactions and scattering is the formation of the Compton continuum. As illustrated in Figure A.2, the Compton continuum from a single mono-energetic gamma ray source resembles a decay curve, representing the statistically higher fraction of lower energies undergoing numerous interactions

compared with the lower fraction of higher energies that have undergone fewer interactions.

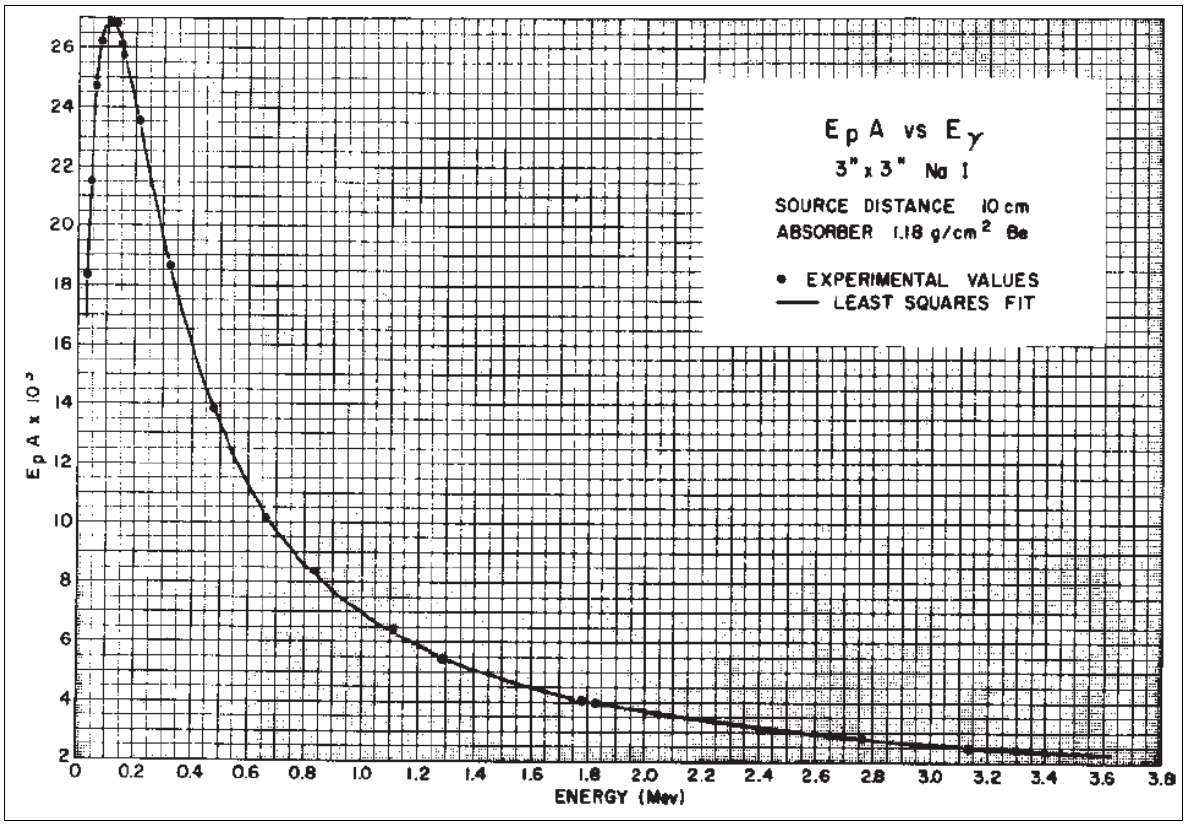


**Figure A.2. The energy distribution resulting from a mono-energetic gamma ray source. The peak at 100 keV is due to iodine x-ray escape from the surface of the detector (from Heath, 1964).**

It is also common for gamma ray spectrometers measuring energies at the lower end of the spectrum to detect bremsstrahlung radiation. Bremsstrahlung is produced when an electrically charged particle is slowed down by the electric field of an atomic nucleus. As illustrated in Figure A.3, these energies can form a steep peak at the beginning of the spectrum. The combination of Compton continuum and bremsstrahlung reduces the resolving capability of the average 256-channel NaI gamma ray spectrometer, especially for energies lower than 600 keV.

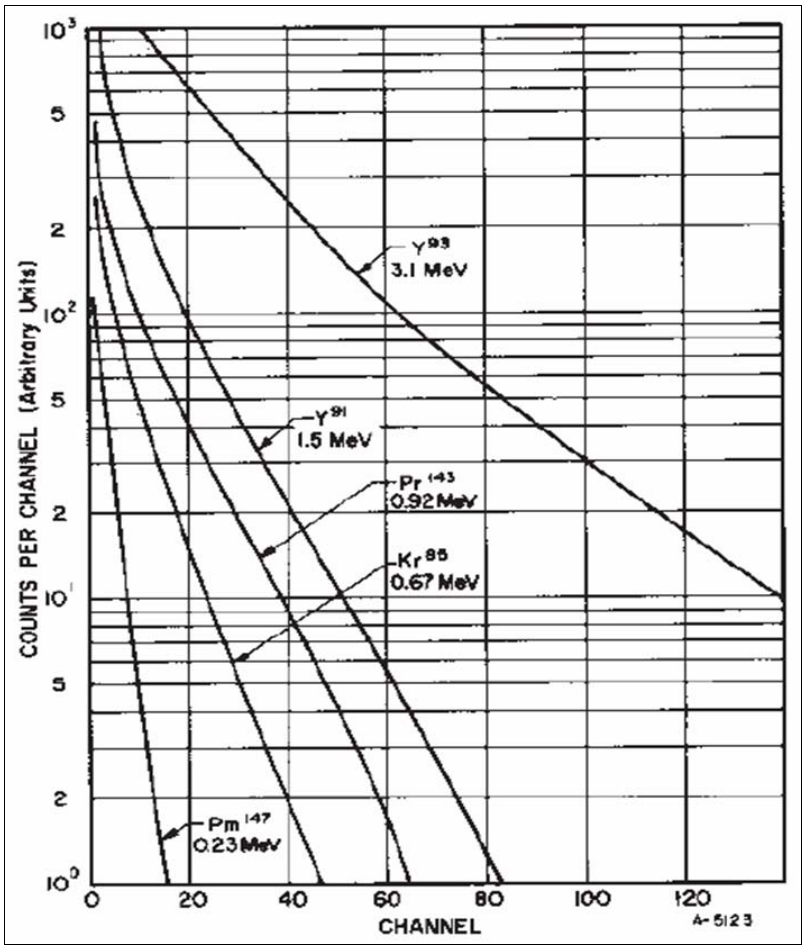


**Figure A.3. Typical bremsstrahlung spectra on a 3"x3" NaI detector. All spectra are normalised in intensity to $10^7$ disintegrations (from Heath, 1964).**

## A.3 Natural radioelements

There are many naturally occurring radioelements. However, only thorium, uranium, potassium, and their daughter products emit gamma radiation with sufficient energy to be detected using a sodium-iodide (NaI) spectrometer. Fortunately, these elements are in relative abundance within the Earth's crust, facilitating interpretation through variations in their relative combinations and concentrations.

However, chemical interactions, leaching and degassing during the decay process can disrupt the relative abundance of daughter products. These disruptions are known as decay series disequilibrium. Uranium is particularly susceptible, with several of the uranium daughter products prone to selective leaching. As the standard processing methodology is based on the premise of decay equilibrium, any disruption to the decay series will result in erroneous processing results.

## A.4 Standard processing of 256-channel NaI spectrometry

In Australia, natural radioelement maps of potassium (K), thorium (Th) and uranium (U) are routinely generated from gamma ray spectrometry data and delivered as gridded radioelement maps of %K, eTh in ppm, eU in ppm, and total count (total gamma-ray dose rate). Whether the data are obtained from airborne or ground systems, the procedure for converting the gamma ray spectra to radioelement concentrations involves the following steps:

1. pre-processing,
2. spectral smoothing (optional),
3. live time correction,
4. energy calibration,
5. background correction,
6. radon correction (optional),
7. stripping correction,
8. height correction (optional),
9. reduction to elemental count rates, and
10. levelling.

The development and shortcomings of standard processing has been documented by various researchers including, Clark *et al.* (1972), Gunn (1978), Grasty and Minty (1995), Minty (1997), Allyson and Sanderson (1998), Minty *et al.* (1998), Dickson and Taylor (2000), and Billings *et al.* (2003), with the outcomes summarised in IAEA (2003).

### A.4.1 Preprocessing

Preprocessing is generally carried out in the field and includes procedures such as validating the recorded data and checking for missing or spurious data. At this stage smoothing filters may be applied to radar altimeter data and the cosmic channel.

### A.4.2 Spectral smoothing

This is an optional process which may be applied to the data to reduce noise in the data. There are currently two different standards employed: noise adjusted singular

value decomposition (NASVD) and maximum noise fraction (MNF). Both techniques statistically manipulate the data to separate random noise features from the data on the basis of similarity in spectral shape. Although the advantages of these techniques are a two fold improvement in noise reduction, the disadvantages include the removal of real anomalies if the spectral shape is not well represented in the data and the introduction of false anomalies when the dominant trend in absent.

### A.4.3 Live time correction

The base measurement of radioactivity is counts/second. In order to correctly calculate the number of counts per second, the "dead time" or the time during which the one pulse is being processed and all other incoming pulses are being rejected must be accounted for. The result is the live time correction.

### A.4.4 Energy calibration

The energy calibration procedure corrects for any spectral drift that may occur in the spectrometer during surveying. It is designed to ensure that the prominent energy peaks are continuously recorded in the same channel.

### A.4.5 Background correction

Extraneous gamma rays from the survey platform, whether aircraft, car, or motorcycle, and cosmic rays will be included in the recorded response and must be removed from the data. In general the survey platform is a constant gamma ray source, whose response can be determined in a calibration environment and subtracted from the survey response. Cosmic rays produce a variable gamma ray response. Consequently, the cosmic energy must be recorded in a separate channel, and removed using linear regression.

### A.4.6 Radon correction

Radon is a gaseous product of uranium decay that can be degassed from soil, transported in the atmosphere, and concentrated in shallow topographic depression during calm, inverted atmospheric conditions. Radon correction is an optional processing correction that is applied when the survey is believed to have encountered atmospheric radon. There are three standard methods: spectral-ratio, full spectrum,

and upward looking detector, with the spectral-ratio method being the most commonly employed technique.

### A.4.7 Stripping correction

Stripping ratios are used to remove gamma rays from radioelements other than the target element windows of K, U, or Th. In particular, gamma rays from thorium in the K and U windows and uranium in the K window. The correction is applied as a series of fractions:

$n_{Th(corrected)} = (n_{Th}\text{-}a.n_U)/(1\text{-}a.\alpha)$,

$n_{U(corrected)} = (n_U\text{-}\alpha.n_{Th})/(1\text{-}a.\alpha)$, and

$n_{K(corrected)} = n_K\text{-}\beta n_{Th(corrected)}\text{-}\gamma n_{U(corrected)}$,

where n are the relative gamma ray counts, and $\alpha$, $\beta$, and $\gamma$ are the stripping ratios.

$\alpha$ are the counts in the U window per unit count in the Th window for a pure Th source.

$\beta$ are the counts in the K window per unit in the Th window for a pure Th source.

$\gamma$ are the counts in the K window per unit in the U window for a pure U source.

a are the counts in the Th window per unit count in the U window for a pure U source.

The stripping ratios are determined through a series of calibration experiments, usually performed using specially designed calibration pads with known radioactive content.

### A.4.8 Height correction

Gamma rays attenuated in the air column between the source and the receiver can be restored using a height attenuation coefficient. The coefficient uses a simple formula (shown below), derived with respect to height, barometric pressure, and temperature, to enable the equivalent counts on the ground to be calculated.

$h_{STP} = (273.15 \times P \times h_{obs})/((T+273.15)x(101.325)$

where $h_{STP}$ is the equivalent height at standard pressure and temperature.

$h_{obs}$ is the observed height above ground level.

T is air temperature in °C.

P is barometric pressure in kPa.

### A.4.9 Reduction to elemental concentrations

As the measured count rates are dependent on the ground radioelement concentration, survey platform/system and survey height, count rates are usually reduced to an equivalent ground radioelement concentration to facilitate comparison between different surveys. A sensitivity coefficient derived experimentally is usually used to convert the count rate to equivalent ground concentrations.

### A.4.10 Levelling

Errors in background corrections and environmental conditions such as soil moisture can produce long wavelength "level shift" variations in the data. Levelling is frequently used to remove these effects and produce a smoother looking dataset. One or more methods of smoothing may be used on a data set. These methods include:

- conventional levelling using cross-over ties,
- use of between channel correlation information, and
- micro-levelling using directional grid filtering techniques

## A.5 Summary

Standard radiometric processing is designed to calculate the natural radioelement equivalent ground concentration of potassium-40, thorium-232, and uranium-238 from NaI gamma ray spectrometry data. The methodology is relatively robust when applied to solid geology under equilibrium conditions.

# Appendix B:  Multispectral processing Matlab code

```
% MAIN ML_ALL

% This program is designed to link those sub programs which identify
remove
% the compton continuum from the original radiometric data and
correlate the
% anomalies. Then applies

%%%%%%%%%% Known Variable used in this program %%%%%%%%%%%%%%
%%%%    ch256 is a data set containing the original 256 (or ch 21 to
256).
%%%%
%%%%%%%%%%%%%%%%%%%%%%%%%%%%%%%%%%%%%%%%%%%%%%%%%%%%%%%%%%%%%%%%%%%
initialchan = input('Please enter initial channel number ');


disp('Checking for maximum starting values');
max_check; %run max_check program;
            %imports ch256;
            %exports channels
            %saves channels.mat
disp('Running anomalies - remove_compton.m');
remove_compton;  % Run remove_compton.m
            %imports channels;
            %exports anomalies
            %saves compton.mat, anomalies.mat
disp('Identifying peaks');
peaks_channels; % Run peaks_channels.m
            %imports anomalies
            %exports extents
            %saves extents.mat
disp('Calculating channel frequencies');
chfreq;  % Run chfreq.m
            %imports extents
            %exports freq
            %saves freq.mat, chfreq.csv


%%%%%%%%%%%%%%%%%%%%%%%%%%%%%%%%%%%%%%%%%%%%%%%%%%%%%%%%%%%%%%%%%%%%%%%
%%%
%%%
%%%
%%%%%%%%%%%%%%%%%%%%%%%%%%%%%%%%%%%%%%%%%%%%%%%%%%%%%%%%%%%%%%%%%%%%%%%
```

```
% max_check.m
%
% This program is designed to check that the starting value of the
data
% point is the largest value. If the value is notthe largest it will
be
% replaced with the largest value in the data set.
%

%%%%%%%%%%% Known Variable used in this program %%%%%%%%%%%%%%%
%%%%    ch256 is a data set containing the original 256 (or ch 21 to
256).
%%%%
%%%%%%%%%%%%%%%%%%%%%%%%%%%%%%%%%%%%%%%%%%%%%%%%%%%%%%%%%%%%%%%%%%%

%%%%%%%%%%%% Final dataset %%%%%%%%%%%%%%%%%%%%%%%%%%%%%%%%%%%%
%%% This program produces
%%%                       channels.mat
%%%%%%%%%%%%%%%%%%%%%%%%%%%%%%%%%%%%%%%%%%%%%%%%%%%%%%%%%%%%%%%%%%%%

[pts,ch] = size(ch256);

%preallocate arrays
channels = zeros(pts,ch);

for i = 1:pts
    m = max(ch256(i,:));
    j=1;
    stop = 0;
    while j <= ch & stop == 0
        if ch256(i,j)== m
            stop = 1;
        else
            j=j+1;
        end
    end

    channels(i,1:j)=m;
    channels(i,j+1:ch) = ch256(i,j+1:ch);
end

clear i j m stop pts ch ch256;

save channels.mat;
```

```
% remove_compton.m
% Compton removal program for 256-channels radiometrics



%%%%%%%%%%%% VERSION 1.22
%%%%%%%%%%%%%%%%%%%%%%%%%%%%%%%%%%%%%%%%%%%%%%%%%%%
%
% This programs uses the following data sets:
% channels -  a data set starting and finishing with any number of
channels
%
%%%%%%%%%%%%%%%%%%%
```

```
        if i == P(j);
            comp(i)= chan(i);
            j=j+1;
        elseif j==1;
            comp(i)= chan(1)-(Q(1)*((i-1)));
        else %if i < P(j);
            comp(i)=(chan(P(j-1)))-(Q(j)*((i - P(j-1))));
        end
        anom(i) = chan(i)-comp(i);
    end

    % Assign to end matrix
    compton(m,:)= comp;
    anomalies(m,:)= anom;

    clear P Q comp anom % recycled indexes
end

clear i j k index high d diff m pts chan %variable clean up

save compton.mat compton;
save anomalies.mat anomalies;
clear compton
```

```
% peaks_channels
% This revised algorithm merges Peaks, toughs and channels program

%%%%%%%%%% Known Variable used in this program %%%%%%%%%%%%%%
%%%%    anomalies is a data set containing the 256 (or ch 21 to 256)
%%%%                 channel data with the compton continuum removed.
%%%%%%%%%%%%%%%%%%%%%%%%%%%%%%%%%%%%%%%%%%%%%%%%%%%%%%%%%%%%%%%%%%%%%%%

%%%%%%%%%Outputs from this program %%%%%%%%%%%%%%%%%%%%%%%%%%
% extents - peak of channel, start of channel and end of channel for
each
%           data point
%%%%%%%%%%%%%%%%%%%%%%%%%%%%%%%%%%%%%%%%%%%%%%%%%%%%%%%%%%%%%%%%%%%%%%%

%%%%%%%%%% V3.0\1 changes %%%%%%%%%%%%%%%
% COMPLETE OVERHAUL
% Using external party local minima and maxima IDs
% Noise is no longer used
% Addition of extents preallocation
%%%%%%%%%%%%%%%%%%%%%%%%%%%%%%%%%%%%%%%%%%%%%%%%%%%%%%%%%%%%%%%%%%%%%%%

%TTHIS INITIAL VALUE IS READ FROM THE MASTER_PROCESS FILE
%initialchan = 21 ; % This is the initial channel value for the data
set

[pts,ch] = size(anomalies);

% Preallocate array
extents = zeros(pts,65,3);


nt = 0;
np = 0;
for i = 1:pts
    zct = 0;
    bv1 = 1;
    bv2 = 1;

    TA = anomalies(i,:);
    if TA == 0, continue, end; % Test for dud values

    %LOCATE PEAKS
    [TAPval,TAP] = lmax(TA,1);
    [junk,a] = size(TAP);

    if a > np;
        np = a; %np is the maximum number of peaks in any data set
    end;

    %LOCATE MINIMA
    [TAMval,TAM]=lmin(TA,1);
    [junk,b] = size(TAM);

    if b > nt;
        nt = b;
    end;

    %LOCATE ZEROS
    for j = 1:ch;
        if TA(j) == 0;
            zct = zct +1;
```

```
            TAZ(zct) = j;
        end;
    end;
    [junk,c] = size(TAZ);

    %LOCATE CHANNELS AND SIGNIFICANT PEAKS
    % We use the location of the peaks to trace back to the closest
trough
    % to the left (start) and right (end) of the peak. The number of
peaks between trough
    % points is irrelevant.


    for j = 1:a

        % LOCATE START
        for s = b:-1:1;
            if TAM(s) < TAP(j);
                bv1 = TAM(s);
                break;
            end;
        end;
        for s = c:-1:1;
            if TAZ(s) < TAP(j);
                bv2 = TAZ(s);
                break;
            end;
        end;
        if bv1 > bv2;
            TAS(j) = bv1;
        else TAS(j) = bv2;
        end;

        % LOCATE END
        for s = 1:b;
            if TAM(s) > TAP(j);
                bv1 = TAM(s);
                break;
            end;
        end;
        for s = 1:c;
            if TAZ(s) > TAP(j);
                bv2 = TAZ(s);
                break;
            end;
        end;
        if bv1 < bv2;
            TAE(j) = bv1;
        else TAE(j) = bv2;
        end;
    end



    extents(i,1:a,1) = TAP(:);
    extents(i,1:a,2) = TAS(:);
    extents(i,1:a,3) = TAE(:);

    clear TA TAP TAS TAT TAM TAE TAZ TAMval TAPval zct a b c bv1 bv2
j s junk;
end
```

```
disp('saving extents');
save extents_new.mat extents;

clear      i j  k   np nt ;
```

```
% ch_freq
% This program is designed to work with the output from the channels
% programs to identify common start and end points within the data
set.

% This will be accomplished by looking at the frequency at which
start and
% and peak locations occur within the data set.

%%%%%%%%%%%%% V1.03 Known variables used in this program
%%%%%%%%%%%%%%%%%%%%
%%% extents is the data output from the channels.m program
%%% anomalies is the ch256 with compton continuum removed.
%%%
%%%
%%%%%%%%%%%%%%%%%%%
```

```
% sum_channels
% This program is designed to sum new channels based on input from
an
% external anlysis of the channels extents and the extents.mat data
set
% generated from channels.m

%%%%%%%%%%%% Known variables used in this program
%%%%%%%%%%%%%%%%%%%%
%%% ch256 is a data set containing the original 256 (or 21 to 256).
%%%
%%% extents is a data set generated from channels.m containing the
peak
%%%         locations, start and end point of "channels" in the
ch256
%%%         dataset;
%%% EN is the location data set for ch256
%%%%%%%%%%%%%%%%%%%%%%%%%%%%%%%%%%%%%%%%%%%%%%%%%%%%%%%%%%%%%%%%%%%%%%%
%

%%%%%%%%%Outputs from this program %%%%%%%%%%%%%%%%%%%%%%%%%%
% newchannels.csv is a database in the format X Y Z1 Z2 etc
%             where channels are in the order
%newchannels.txt is the header file explaing the significance of the
columns
%%%%%%%%%%%%%%%%%%%%%%%%%%%%%%%%%%%%%%%%%%%%%%%%%%%%%%%%%%%%%%%%%%%%%%%

%%%%%%%%%%V1.03%%%%%%%%%%%%
%%% Addition of channels Th4 & U4
%%% Fix for Y location trunction
%%% num added for total number of channels
%%% arbitary channel names
%%%%%%%%%%%%%%%%%%%%%%%%%%%%

% Channel extents
% These extents have been selected through an analysis of the
correlation
% of the 256-channel data with compton removed.

% First Channels Value
cv = 22; % This is the first channel used in thc ch256 data set
% cv is used to reduce the data back to a start value of 1
c=cv-1;

Z1 = [76-c];
Z2 = [80-c];
Z3 = [76-c:81-c];
Z4 = [92-c:96-c];
Z5 = [103-c:104-c];
Z6 = [122-c:124-c];
Z7 = [134-c:136-c];
Z8 = [144-c:150-c];
Z9 = [216-c:220-c];
Z10 = [108-c];
Z11 = [108-c];

% Write header file to recall channel information at later stage
fid = fopen('newchannels.txt','w');
fprintf(fid,'X, Y, Z1..., \n');
fprintf(fid,'This data was generated using the original 256-channel
data.\n');
```

```
fclose(fid);

% Number of channels isolated plus 2 channels for EN
num = 13;

% Establish the extents for the known data sets
[pts,ch]=size(ch256);
[x,y,z] =size(extents);
% note x should equal pts

%Preallocate final array
newchannels = zeros(x,num);

i=0;
% START PROGRAM
for it = 1:pts
    if ch256(it,:)== 0;
        continue;
    else;
        i = 1+i;
        %create temporary data sets for each point
        orig = ch256(it,:);
        peaks = extents(i,:,1);
        strt = extents(i,:,2);
        ennd = extents(i,:,3);

        %set check markers (so that each channel is only sum is
made)
        checkZ1 = 0;
        checkZ2 = 0;
        checkZ3 = 0;
        checkZ4 = 0;
        checkZ5 = 0;
        checkZ6 = 0;
        checkZ7 = 0;
        checkZ8 = 0;
        checkZ9 = 0;
        checkZ10 = 0;
        checkZ11 = 0;


        %sum channels
        for j = 1 : y
            if (peaks(j) ~= Z1(:)); else;
                % peak value is the Z range & allows double peaks in
the
                % channel to be summed if the peak is in the Z
range.
                if (checkZ1 < peaks(j));
                    newchannels(i,3) = newchannels(i,3) +
sum(orig(strt(j):ennd(j)));
                    checkZ1 = ennd(j);
                end
            end
            if (peaks(j) ~= Z2(:)); else;
                if (checkZ2 < peaks(j));
                    newchannels(i,4) = newchannels(i,4) +
sum(orig(strt(j):ennd(j)));
                    checkZ2 = ennd(j);
                end
            end
```

```
            if (peaks(j) ~= Z3(:)); else;
                if (checkZ3 < peaks(j));
                    newchannels(i,5) = newchannels(i,5) +
sum(orig(strt(j):ennd(j)));
                    checkZ3 = ennd(j);
                end
            end
            if (peaks(j) ~= Z4(:)); else;
                if (checkZ4 < peaks(j));
                    newchannels(i,6) = newchannels(i,6) +
sum(orig(strt(j):ennd(j)));
                    checkZ4 = ennd(j);
                end
            end
            if (peaks(j) ~= Z5(:)); else;
                if (checkZ5 < peaks(j));
                    newchannels(i,7) = newchannels(i,7) +
sum(orig(strt(j):ennd(j)));
                    checkZ5 = ennd(j);
                end
            end
            if (peaks(j) ~= Z6(:)); else;
                if (checkZ6 < peaks(j));
                    newchannels(i,8) = newchannels(i,8) +
sum(orig(strt(j):ennd(j)));
                    checkZ6 = ennd(j);
                end
            end
            if (peaks(j) ~= Z7(:)); else;
                if (checkZ7 < peaks(j));
                    newchannels(i,9) = newchannels(i,9) +
sum(orig(strt(j):ennd(j)));
                    checkZ7 = ennd(j);
                end
            end
            if (peaks(j) ~= Z8(:)); else;
                if (checkZ8 < peaks(j));
                    newchannels(i,10) = newchannels(i,10) +
sum(orig(strt(j):ennd(j)));
                    checkZ8 = ennd(j);
                end
            end
            if (peaks(j) ~= Z9(:)); else;
                if (checkZ9 < peaks(j))
                    newchannels(i,11) = newchannels(i,11) +
sum(orig(strt(j):ennd(j)));
                    checkZ9 = ennd(j);
                end
            end
            if (peaks(j) ~= Z10(:)); else;
                if (checkZ10 < peaks(j))
                    newchannels(i,12) = newchannels(i,12) +
sum(orig(strt(j):ennd(j)));
                    checkZ10 = ennd(j);
                end
            end
            if (peaks(j) ~= Z11(:)); else;
                if (checkZ11 < peaks(j))
                    newchannels(i,13) = newchannels(i,13) +
sum(orig(strt(j):ennd(j)));
                    checkZ11 = ennd(j);
```

```
                end
            end

        end
    end
end

% Add EN components to beginning of newchannels

newchannels(:,1:2) = EN(:,1:2);

clear ch  y z i j orig peaks strt ennd checkZ1 checkZ2 checkZ3
checkZ4 checkZ5 checkZ6 checkZ7 checkZ8 checkZ9 checkZ10 checkZ11 ;
clear cv c  it Z1 Z2 Z3 Z4 Z5 Z6 Z7 Z8 Z9 Z10 Z11

save newchannels.mat newchannels;


%%%%%%% PRINT RESULTS TO EXPORT FILE

% fid = fopen('newchannels.csv','w');
% fprintf(fid,'X, Y, REPLACE2, Th3, U3b, U3a, U2, K, Th2, U1, Th1,
Ca, \n');
% for i = 1 : x
%     for j = 1:num
%         fprintf(fid,'%8.2f, ',newchannels(i,j));
%     end
%     fprintf(fid,'\n');
% end
% fclose(fid);

csvwrite('newchannels.csv',newchannels);


clear pts num
```

# Appendix C: Case Study 1 - Standard and multispectral processed imagery

Colour bars illustrating the value range are not provided with the imagery in this appendix. This is because the count values generated by the different processing techniques are not comparable. Rather, the images should be examined with respect to the spatial patterns resolved by comparable radiometric channels, as the spatial patterns revealed in the data are used to map soil and regolith and not the individual gamma ray intensities. Linear colour stretches have been applied to the images, unless otherwise specified.

**Table C.1. Index to study area imagery.**

| Image | Yaragadee | Elashgin | Moyagee | Waroona Airborne | Waroona Ground |
|---|---|---|---|---|---|
| 256-channel spectra | | | | | |
| Original full spectra | 1.1.1 | | 1.3.1 | | 1.5.1 |
| Multispectral processed RAW peak only | 1.1.2 | 1.2.1 | 1.3.2 | | |
| Multispectral processed MNF peak only | | 1.2.2 | | | |
| Multispectral processed NASVD peak only | 1.1.3 | 1.2.3 | 1.3.3 | 1.4.1/2 | 1.5.2 |
| Multispectral processed Compton continuum | 1.1.4 | | 1.3.4 | | 1.5.3 |
| Standard processing | | | | | |
| Potassium | 1.1.5 | 1.2.4 | 1.3.5 | 1.4.3 | 1.5.4 |
| Thorium | 1.1.6 | 1.2.5 | 1.3.6 | 1.4.4 | 1.5.5 |
| Uranium | 1.1.7 | 1.2.6 | 1.3.7 | 1.4.5 | 1.5.6 |
| Total count | | 1.2.7 | 1.3.8 | 1.4.6 | 1.5.7 |
| Ternary | 1.1.8 | 1.2.8 | 1.3.9 | 1.4.7 | 1.5.8 |

**Table C.1. cont'd. Figures numbers corresponding to study area imagery presented.**

| Image | Yaragadee | | | Elashgin | Moyagee | Waroona Airborne | Waroona Ground |
|---|---|---|---|---|---|---|---|
| Multispectral processing | | | | | | | |
| Spectral smoothing | RAW | NASVD | spNASVD | NASVD | NASVD | NASVD | NASVD |
| Potassium 1 | 1.1.9 | 1.1.19 | 1.1.29 | 1.2.9 | 1.3.10 | 1.4.8 | 1.5.9 |
| Thorium 1 | 1.1.10 | 1.1.20 | 1.130 | 1.2.10 | 1.3.11 | 1.4.9 | 1.5.10 |
| Thorium 2 | 1.1.11 | 1.1.21 | 1.1.31 | 1.2.11 | 1.3.12 | 1.4.10 | 1.5.11 |
| Thorium 3 | 1.1.12 | 1.1.22 | 1.1.32 | 1.2.12 | 1.3.13 | 1.4.11 | 1.5.12 |
| Uranium 1 | 1.1.13 | 1.1.23 | 1.1.33 | 1.2.13 | 1.3.14 | 1.4.12 | 1.5.13 |
| Uranium 2 | 1.1.14 | 1.1.24 | 1.1.34 | 1.2.14 | 1.3.15 | 1.4.13 | 1.5.14 |
| Uranium 3 | 1.1.15 | 1.1.25 | 1.1.35 | 1.2.15 | 1.3.16 | 1.4.14 | 1.5.15 |
| Ternary | 1.1.16 | 1.1.26 | 1.136 | 1.2.16/17 | 1.3.17 | 1.4.15 | 1.5.16 |
| Uranium ternary | 1.1.17 | 1.1.27 | 1.1.37 | 1.2.18 | 1.3.18 | 1.4.16 | 1.5.17 |
| Thorium ternary | 1.1.18 | 1.1.28 | 1.1.38 | 1.2.19 | 1.3.19 | 1.4.17 | 1.5.18 |
| Uranium ratio | | | 1.1.39 | 1.2.20 | 1.3.20 | 1.4.18 | 1.5.19 |
| Ancillary data | | | | | | | |
| Aerial photo | 1.1.40 | | | 1.2.21 | | 1.4.19 | 1.5.20 |
| Geology | 1.1.41 | | | 1.2.22 | 1.3.21 | 1.4.20 | 1.5.21 |
| Soil/regolith | | | | 1.2.23 | | | |
| Salinity | | | | 1.2.24 | | | |
| Low resolution ternary | | | | 1.2.25 | | | |
| Digital terrain (elevation) | | | | 1.2.26 | | 1.4.21 | |
| Magnetics | | | | 1.2.27 | | | |

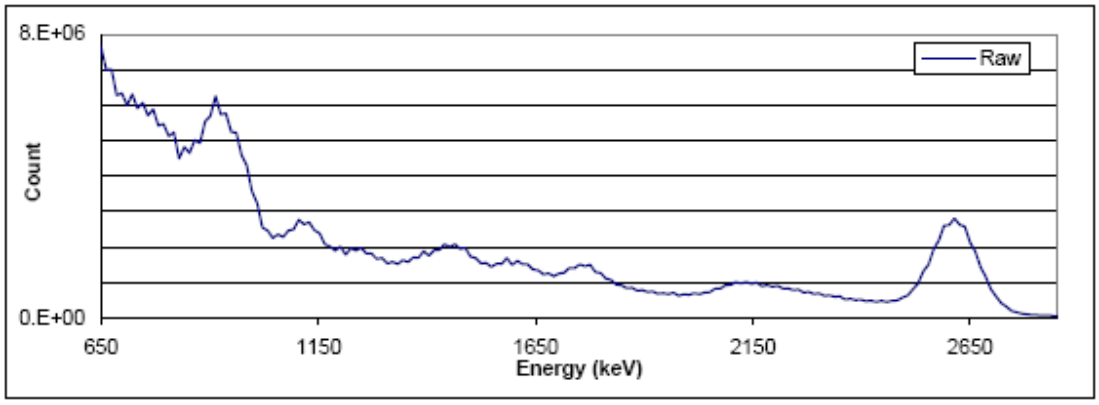


**Figure C.1.1. Average raw spectrum derived from 256-channel data, Yaragadee.**

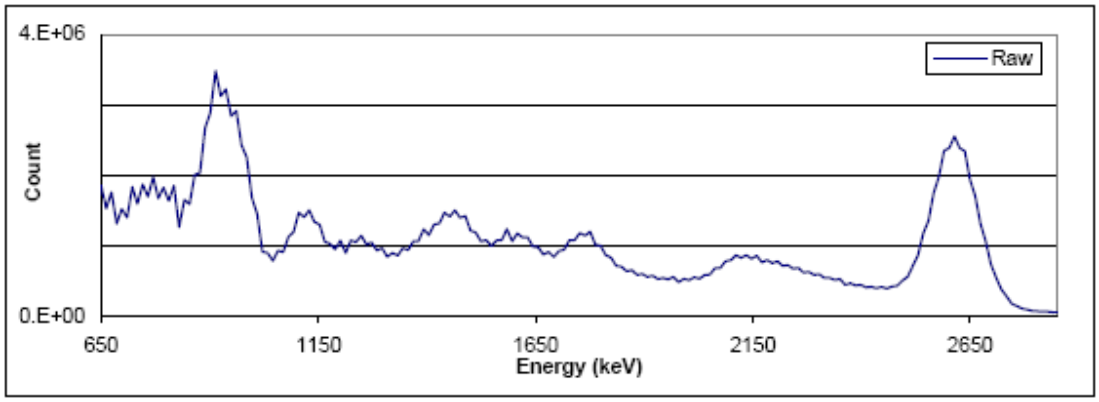


**Figure C.1.2. Average raw spectrum following Compton continuum removal, Yaragadee.**

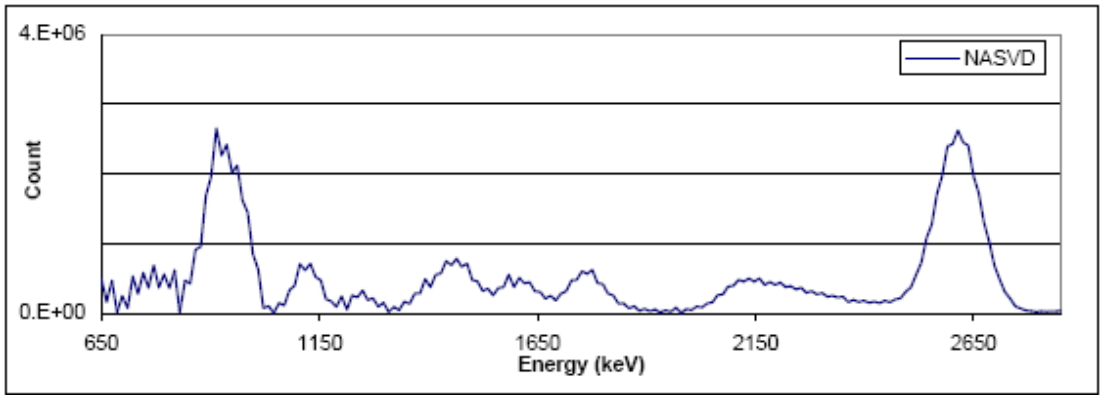


**Figure C.1.3. Average NASVD smoothed spectrum following Compton continuum removal, Yaragadee.**

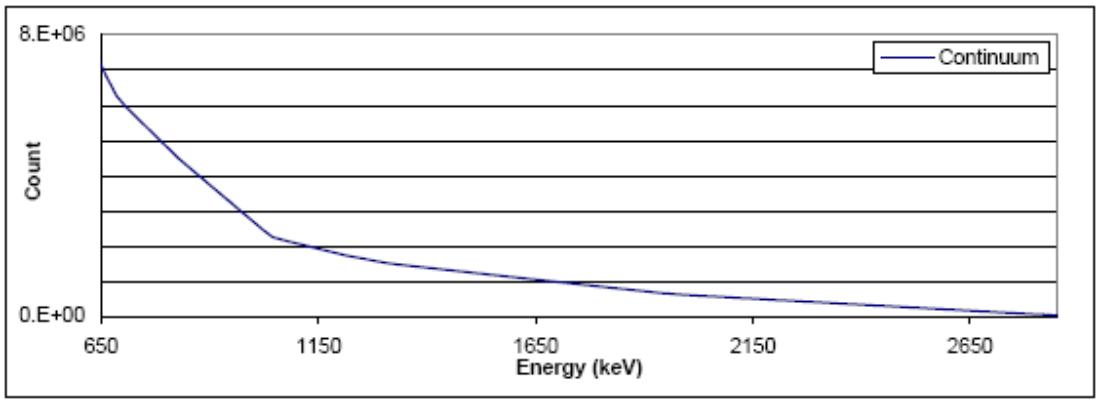


**Figure C.1.4. Average continuum removed from the raw spectrum, Yaragadee.**

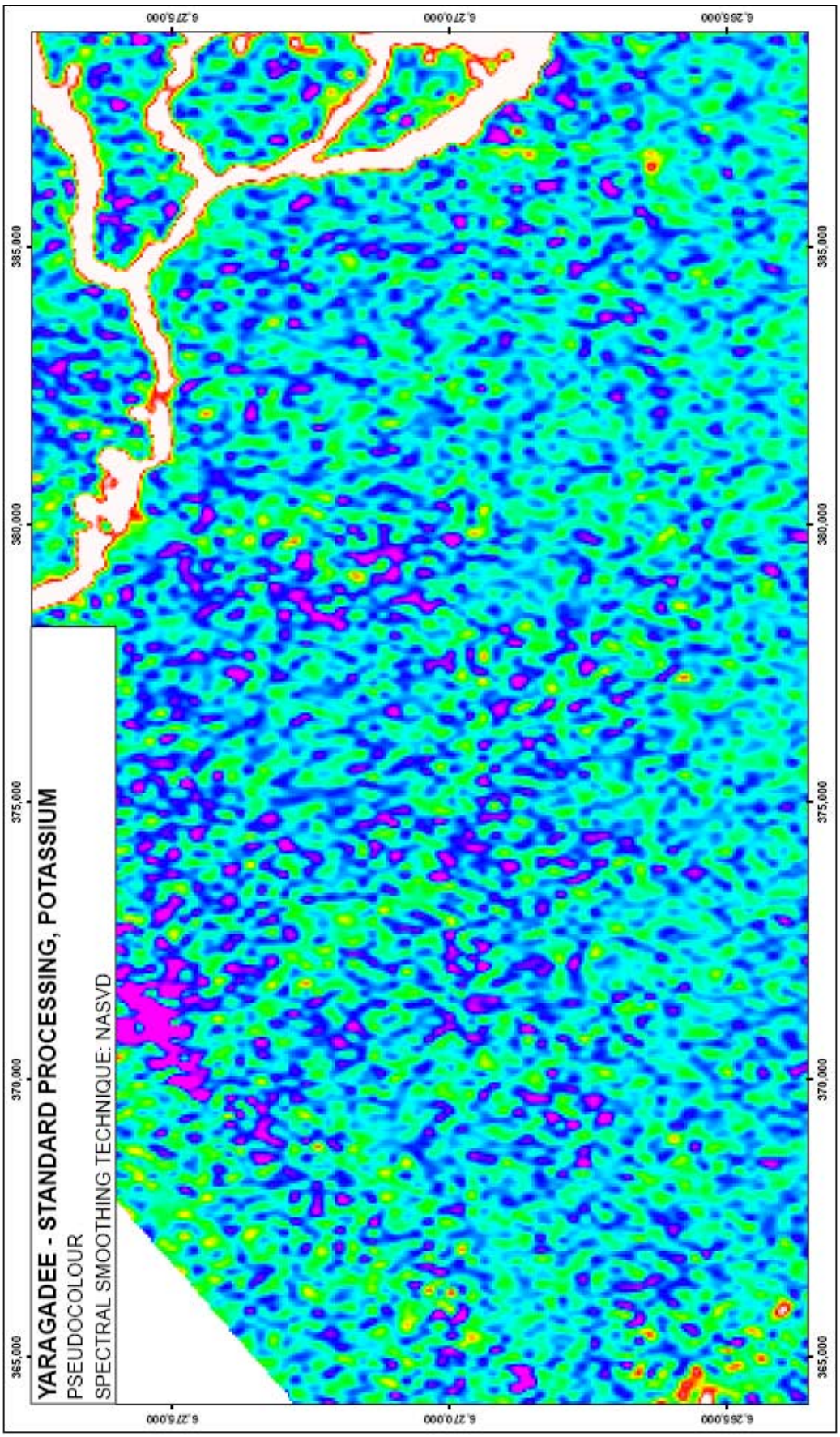


**Figure C.1.5. Potassium standard processed pseudocolour image, Yaragadee.**

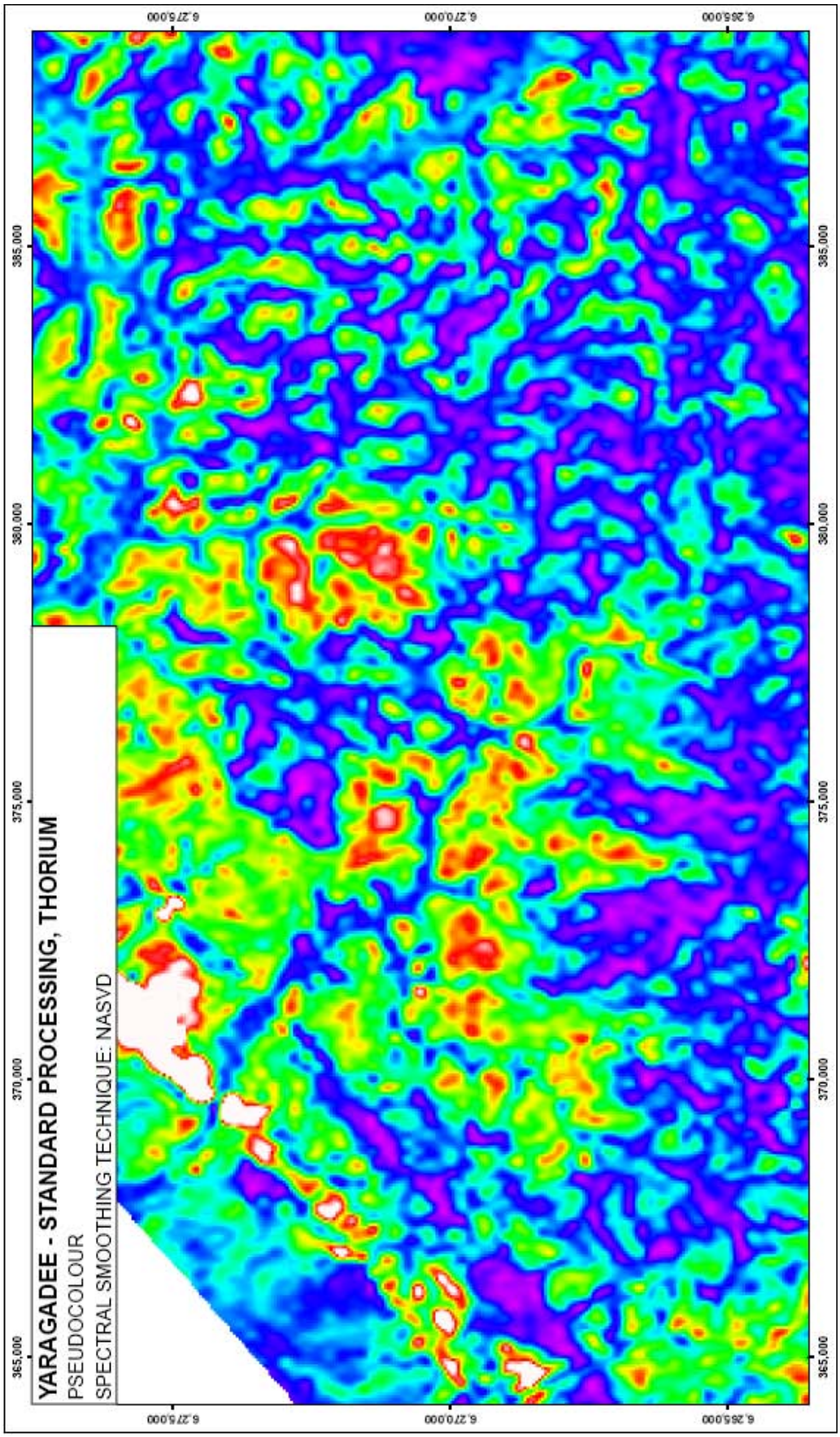


**Figure C.1.6. Thorium standard processed pseudocolour image, Yaragadee.**

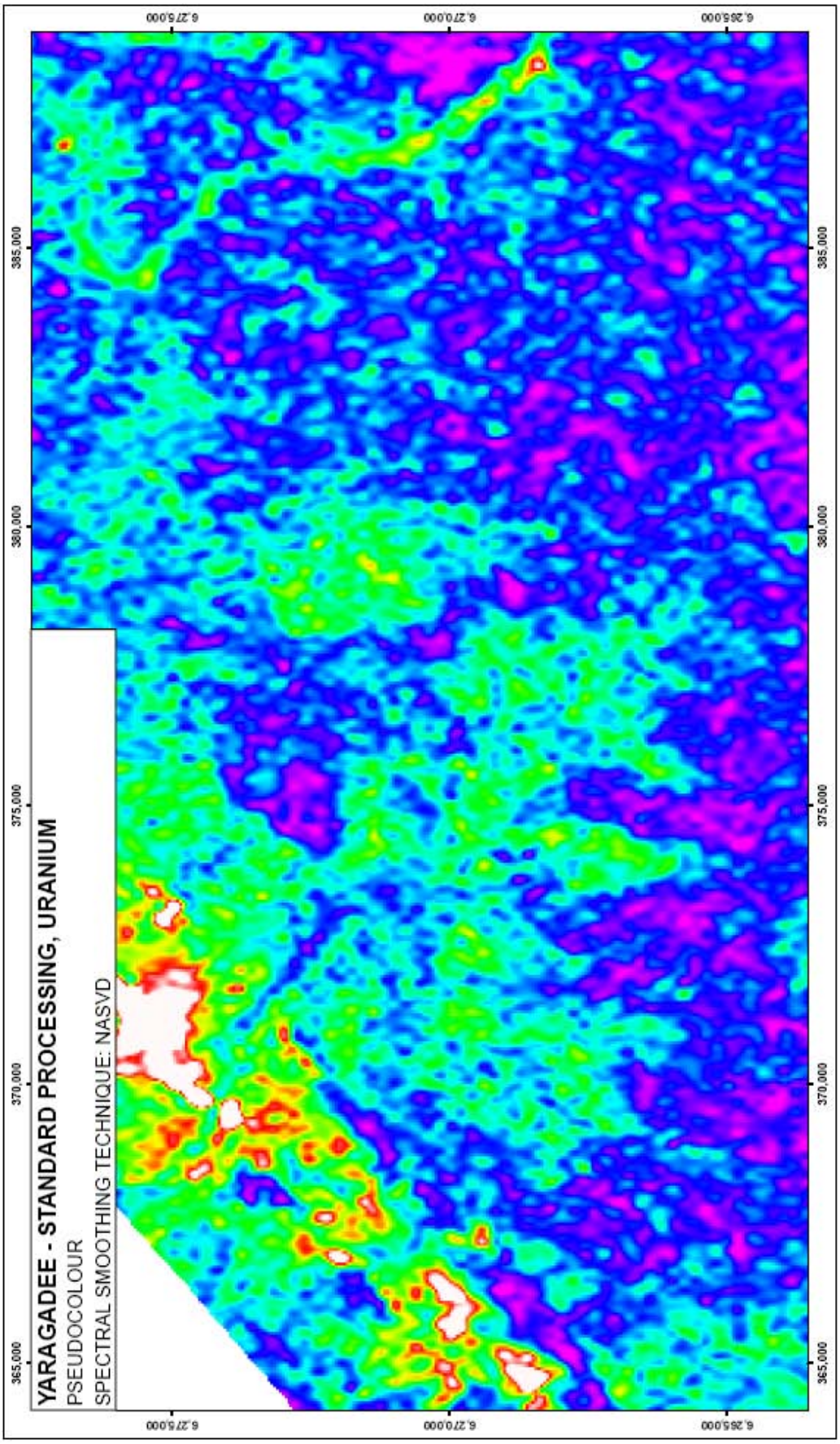


**Figure C.1.7. Uranium standard processed pseudocolour image, Yaragadee.**

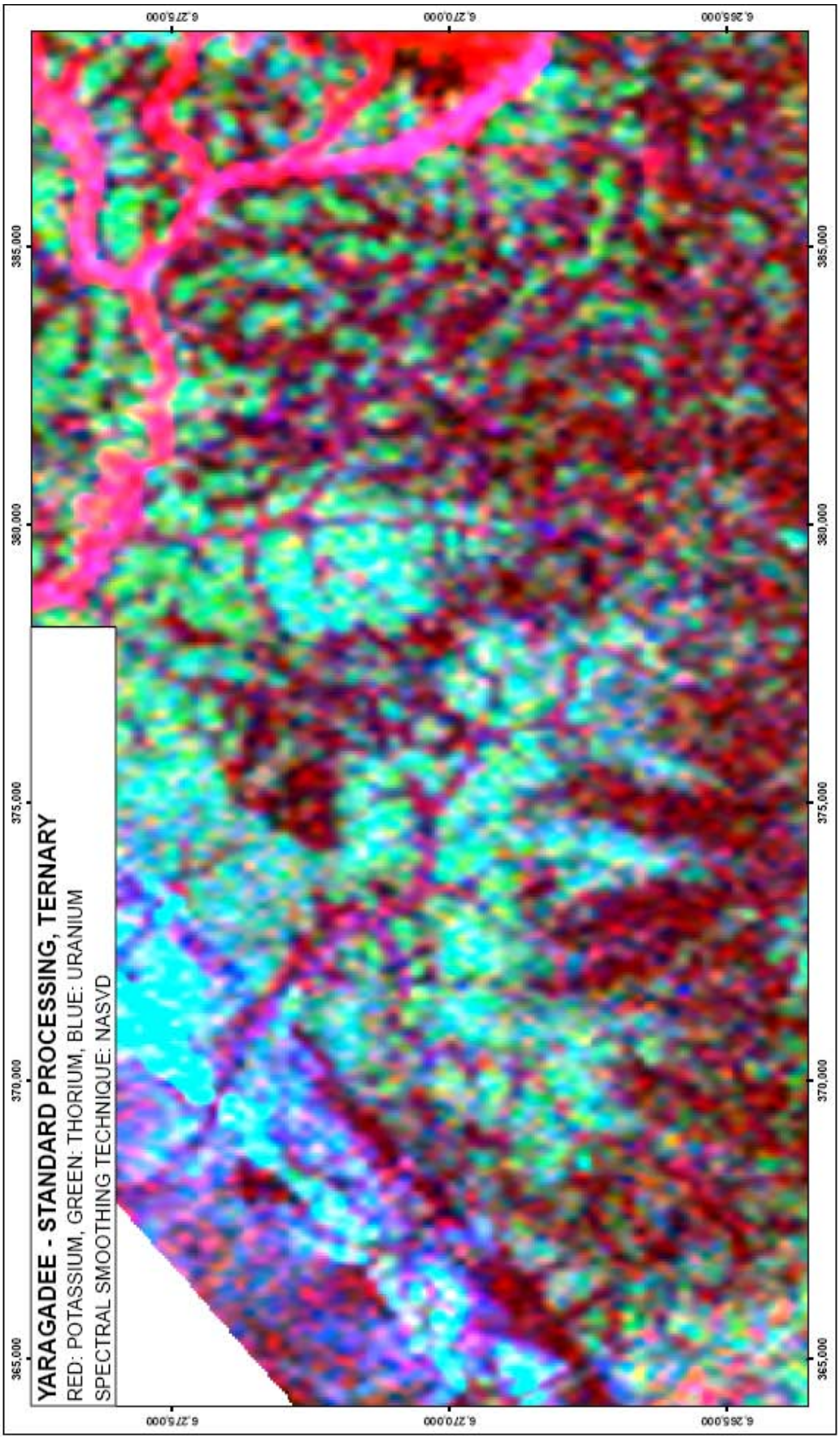


**Figure C.1.8. Ternary standard processed pseudocolour image, Yaragadee.**

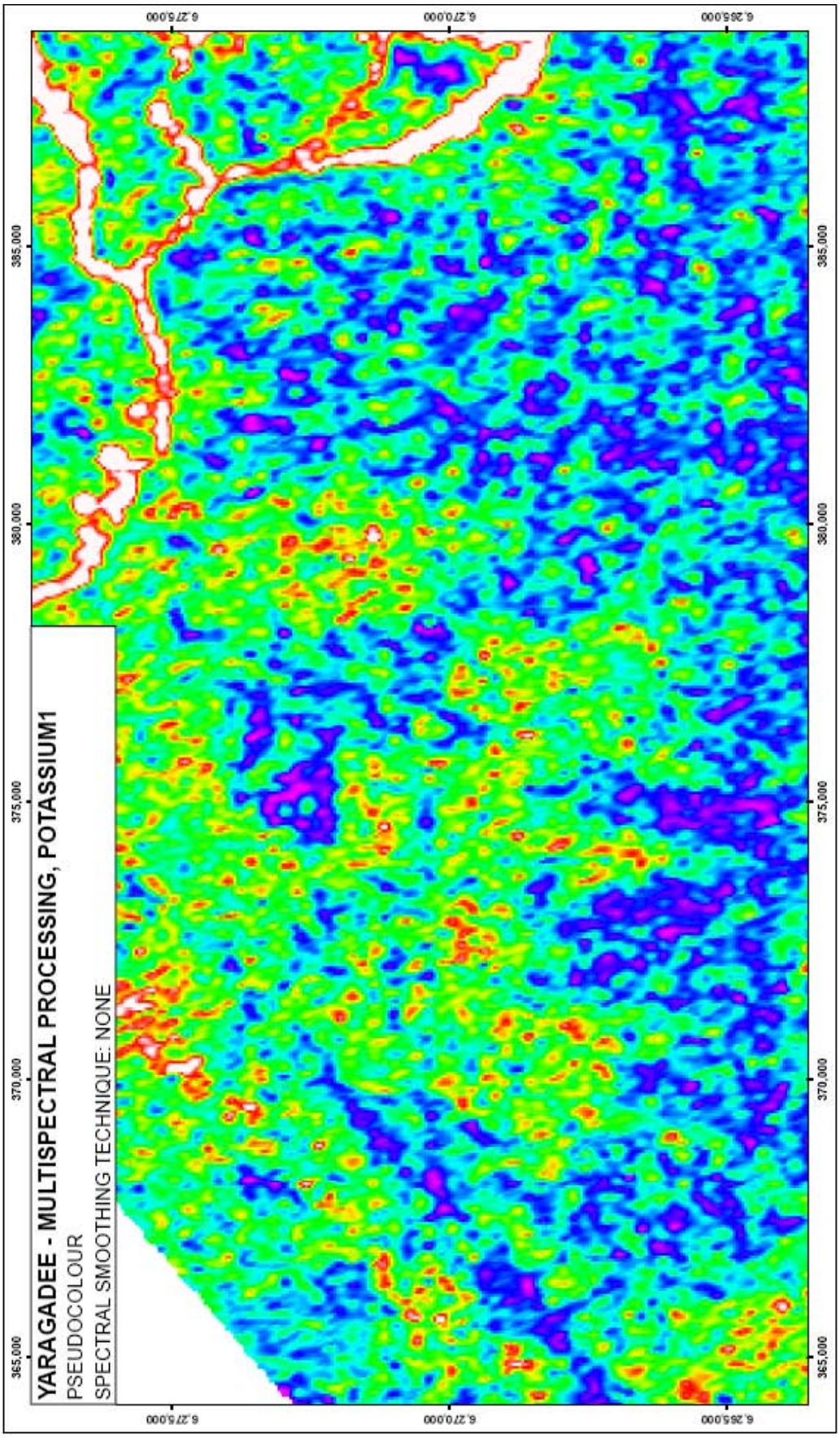


**Figure C.1.9. Potassium 1 multispectral processed, no spectral smoothing, pseudocolour image, Yaragadee.**

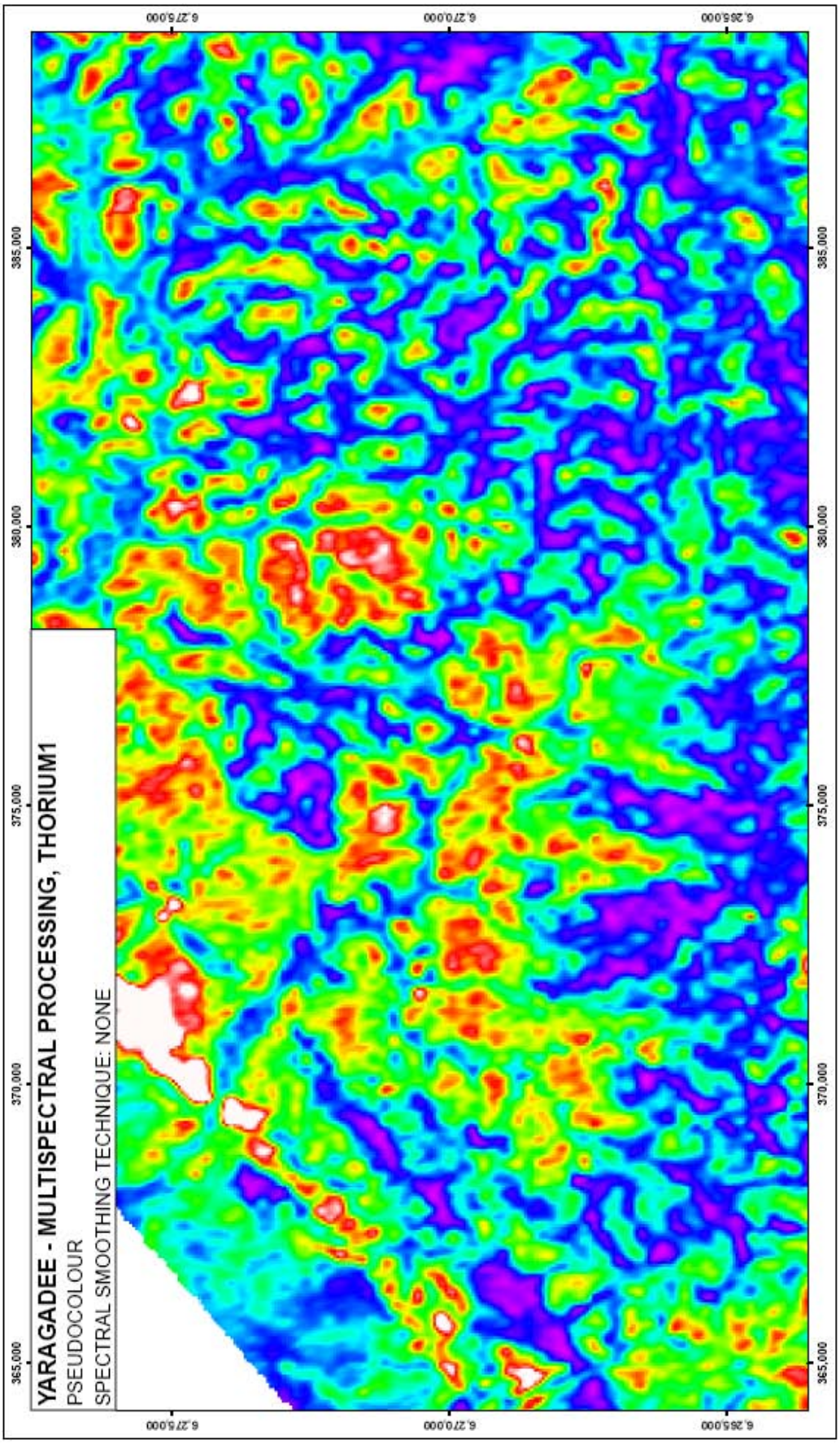


**Figure C.1.10. Thorium 1 multispectral processed, no spectral smoothing, pseudocolour image, Yaragadee.**

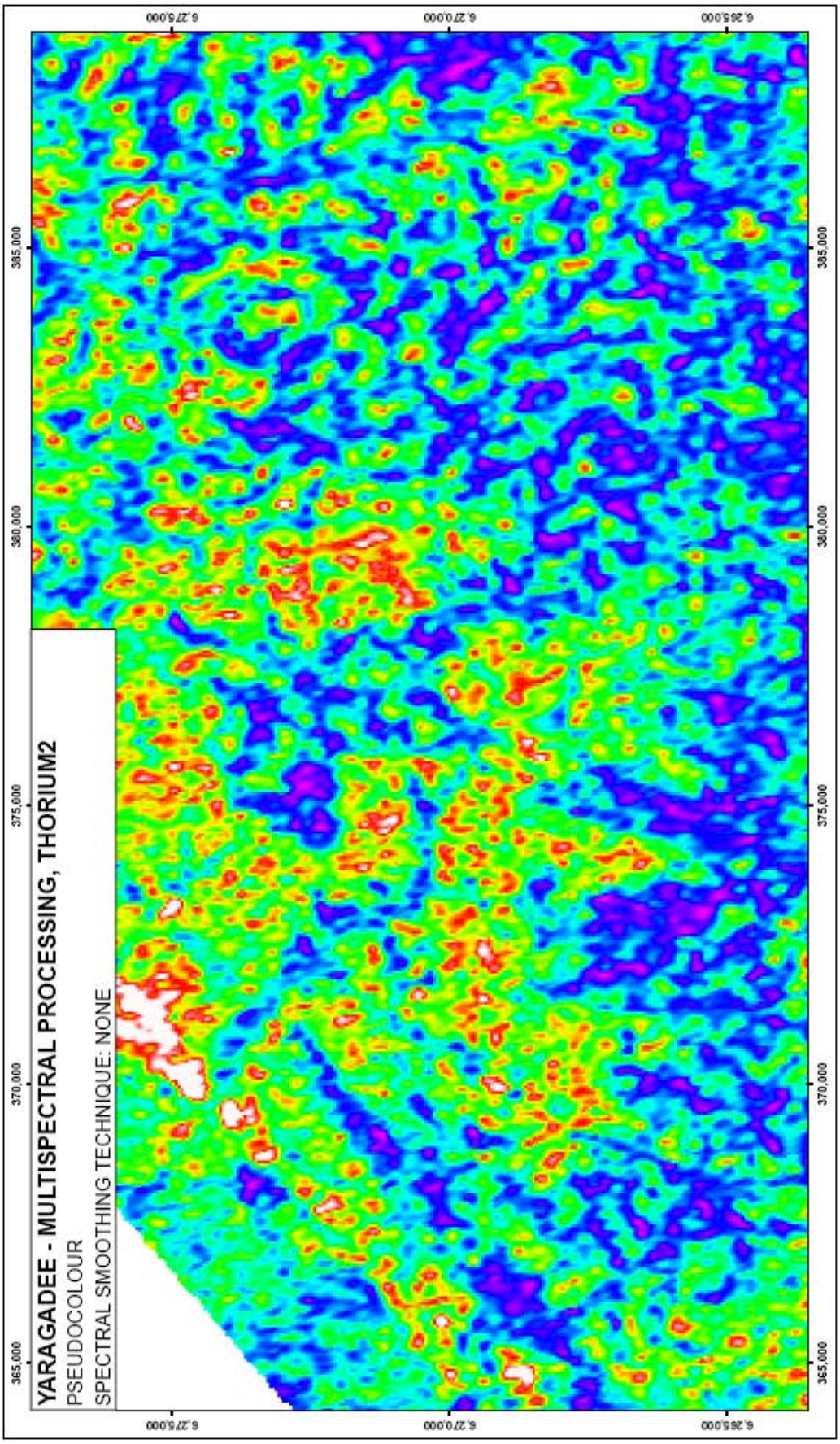


**Figure C.1.11. Thorium 2 multispectral processed, no spectral smoothing, pseudocolour image, Yaragadee.**

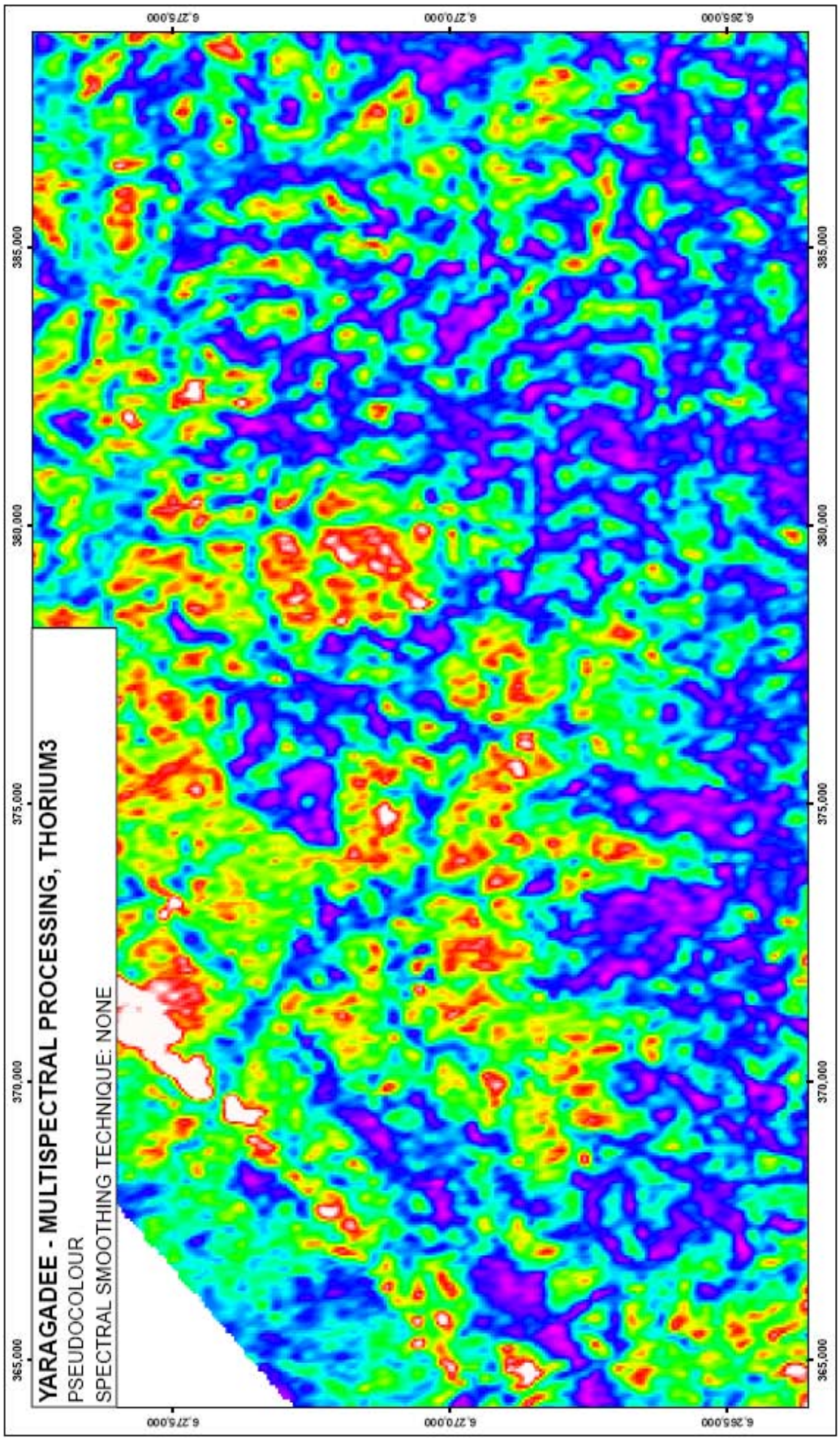


**Figure C.1.12. Thorium 3 multispectral processed, no spectral smoothing, pseudocolour image, Yaragadee.**

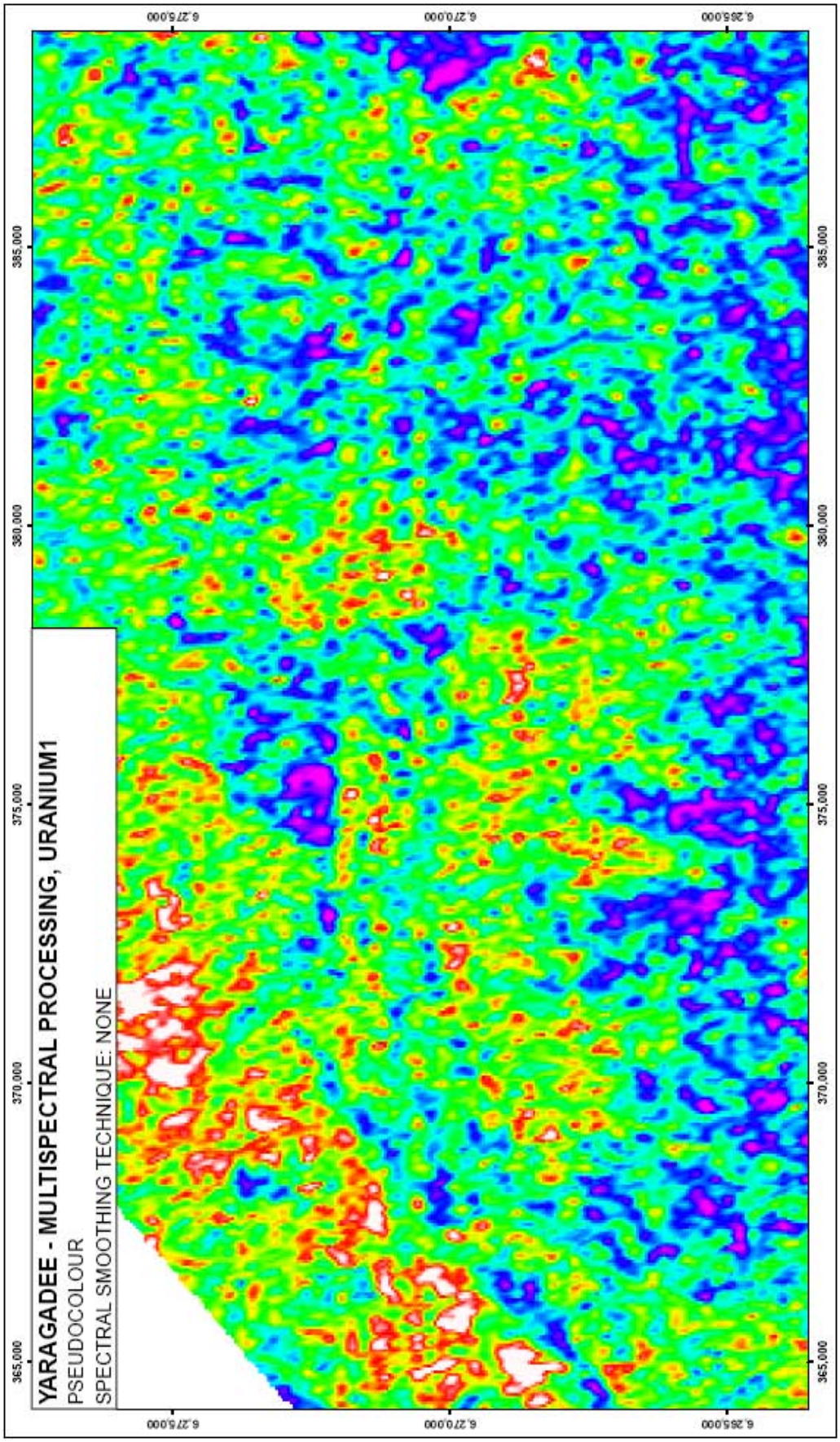


**Figure C.1.13. Uranium 1 multispectral processed, no spectral smoothing, pseudocolour image, Yaragadee.**

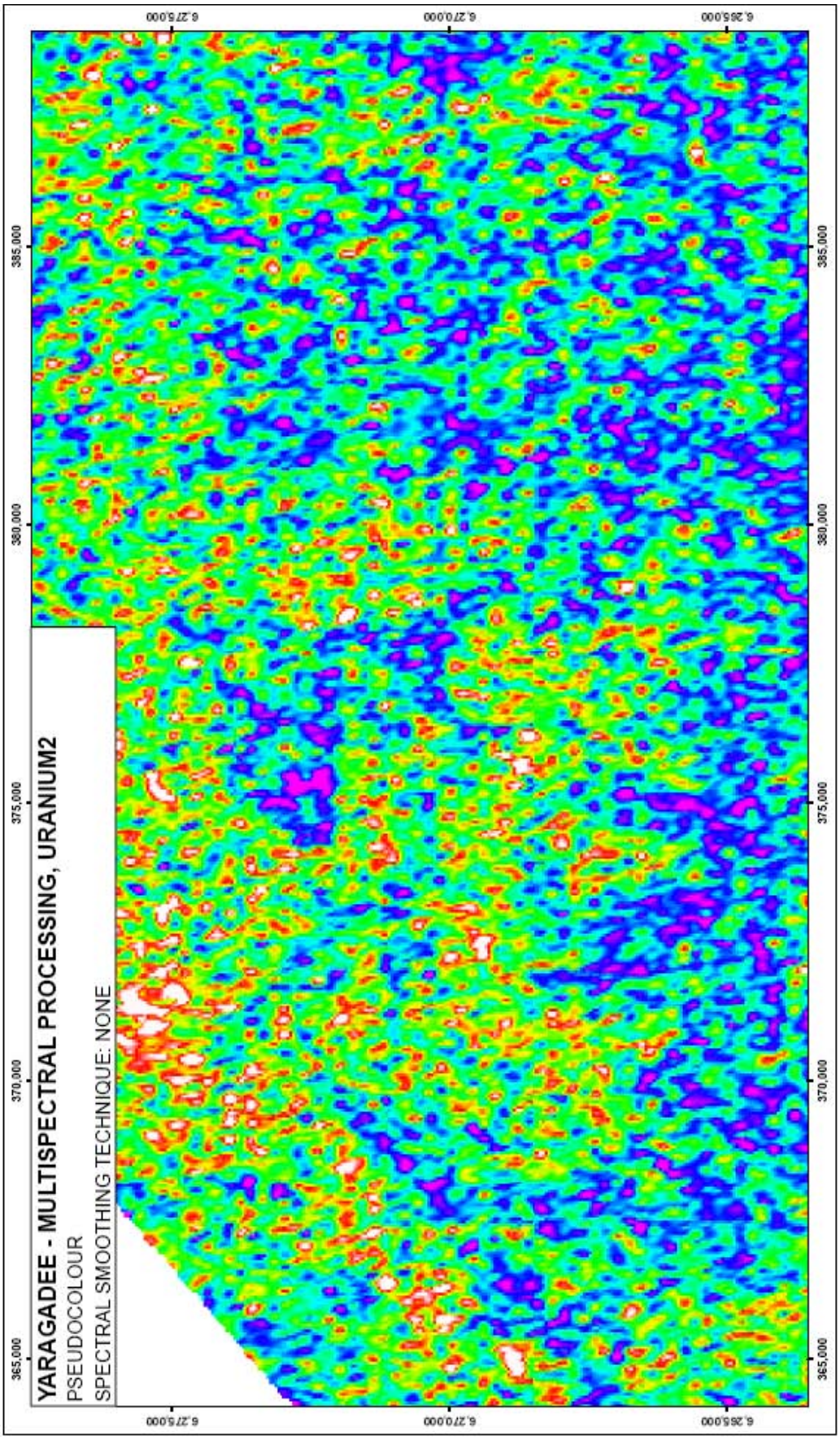


**Figure C.1.14. Uranium 2 multispectral processed, no spectral smoothing, pseudocolour image, Yaragadee.**

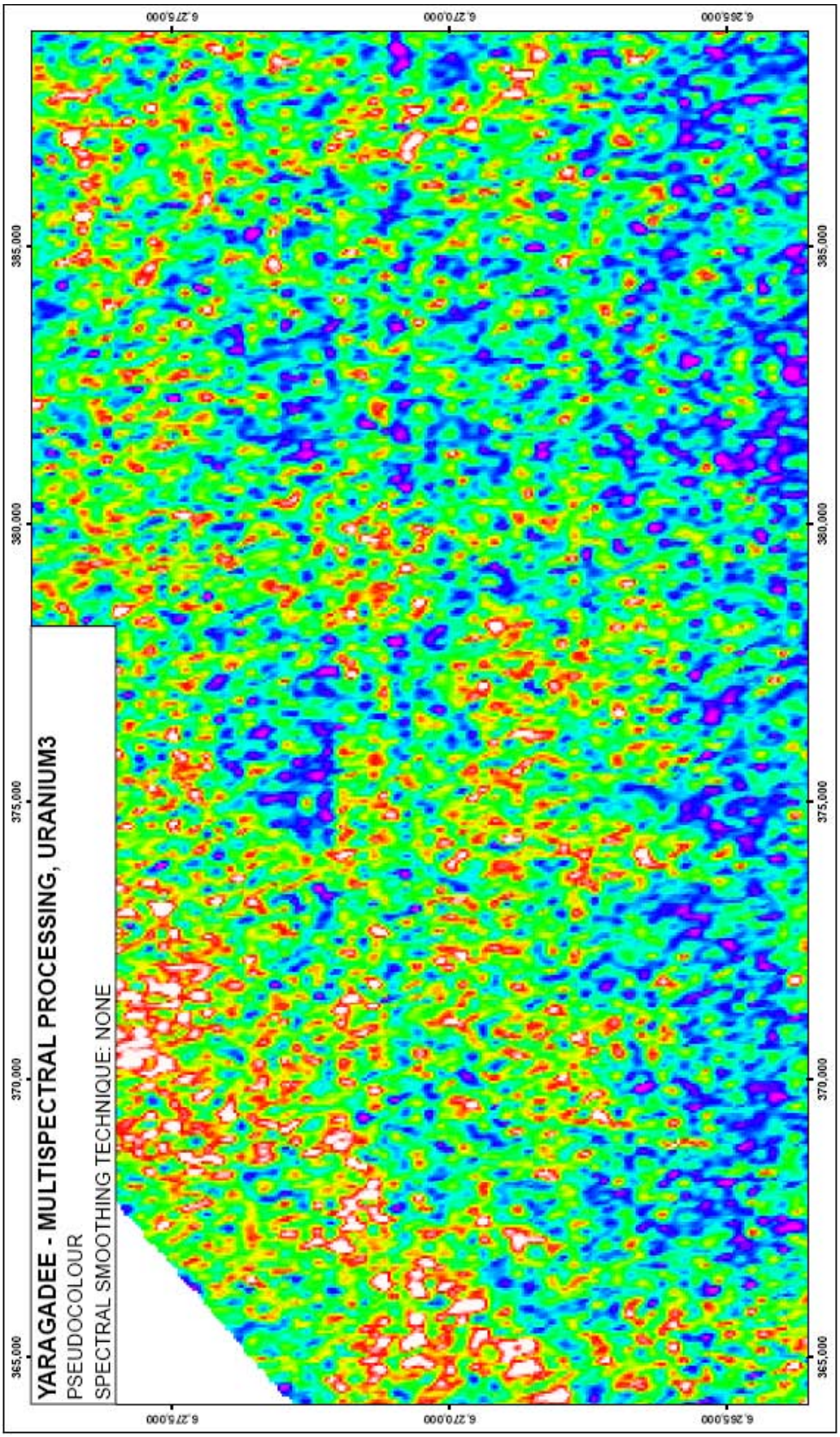


**Figure C.1.15. Uranium 3 multispectral processed, no spectral smoothing, pseudocolour image, Yaragadee.**

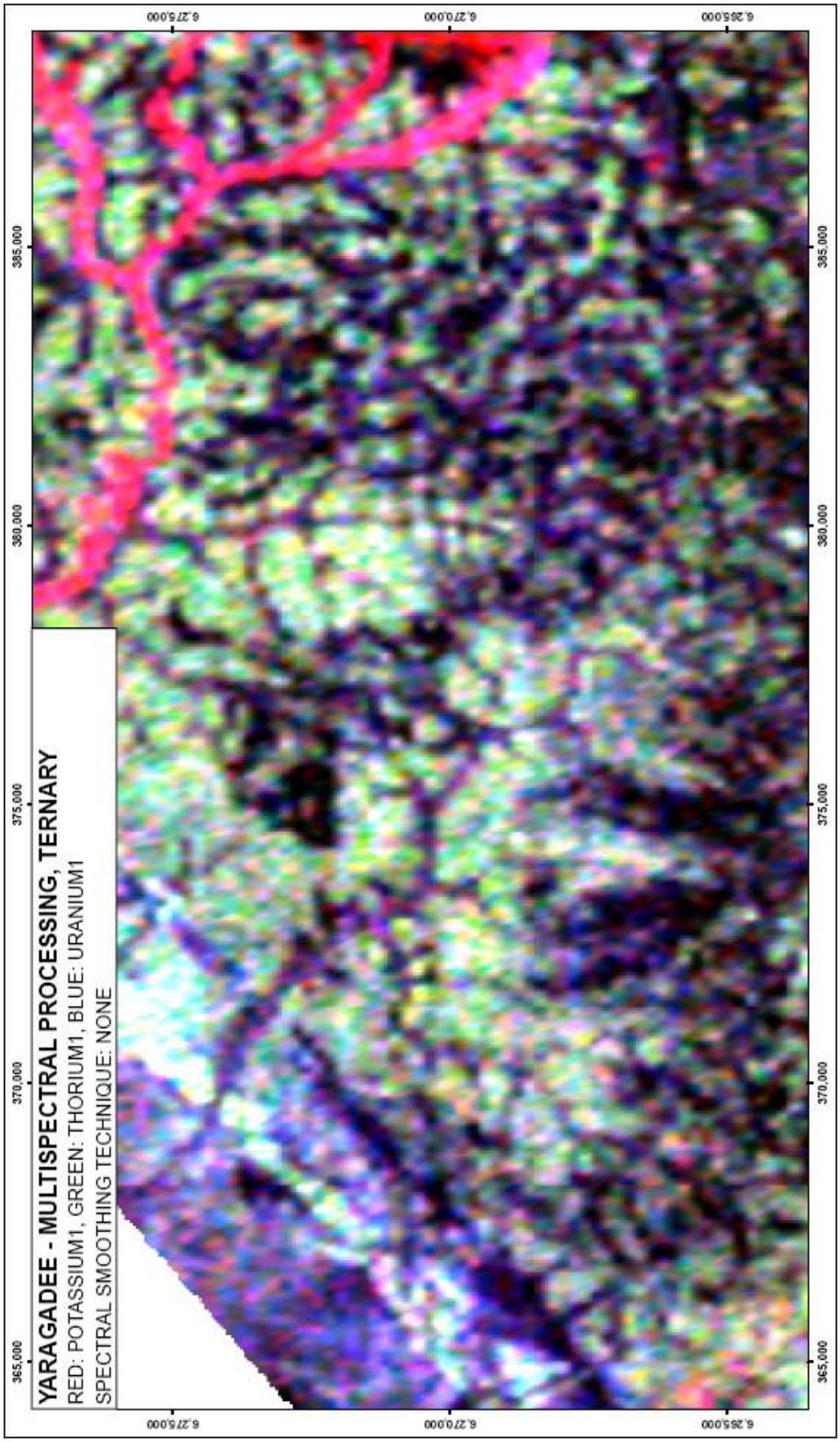


**Figure C.1.16. Ternary multispectral processed, no spectral smoothing, ternary image, Yaragadee.**

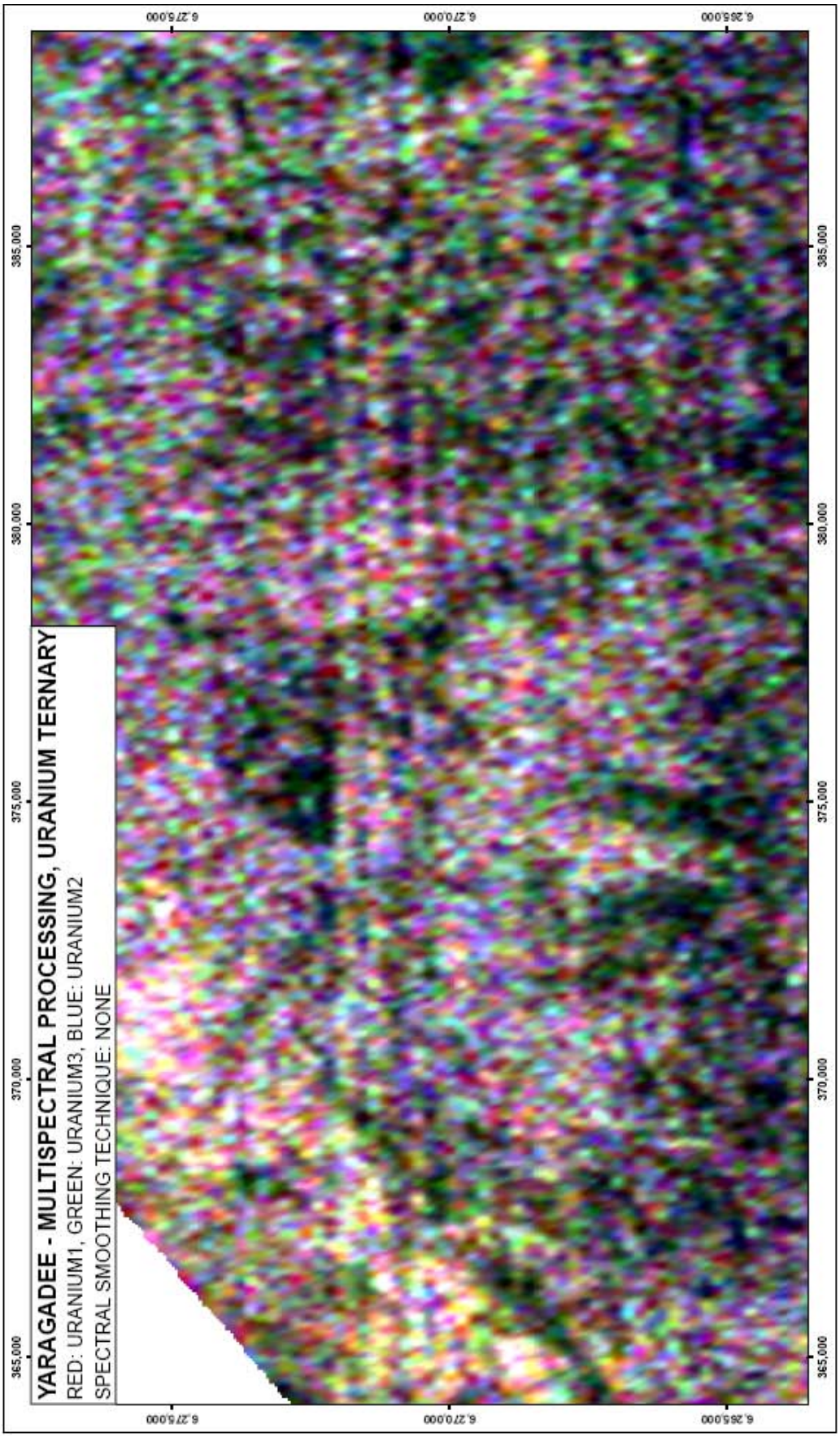


**Figure C.1.17. Uranium ternary multispectral processed, no spectral smoothing, ternary image, Yaragadee.**

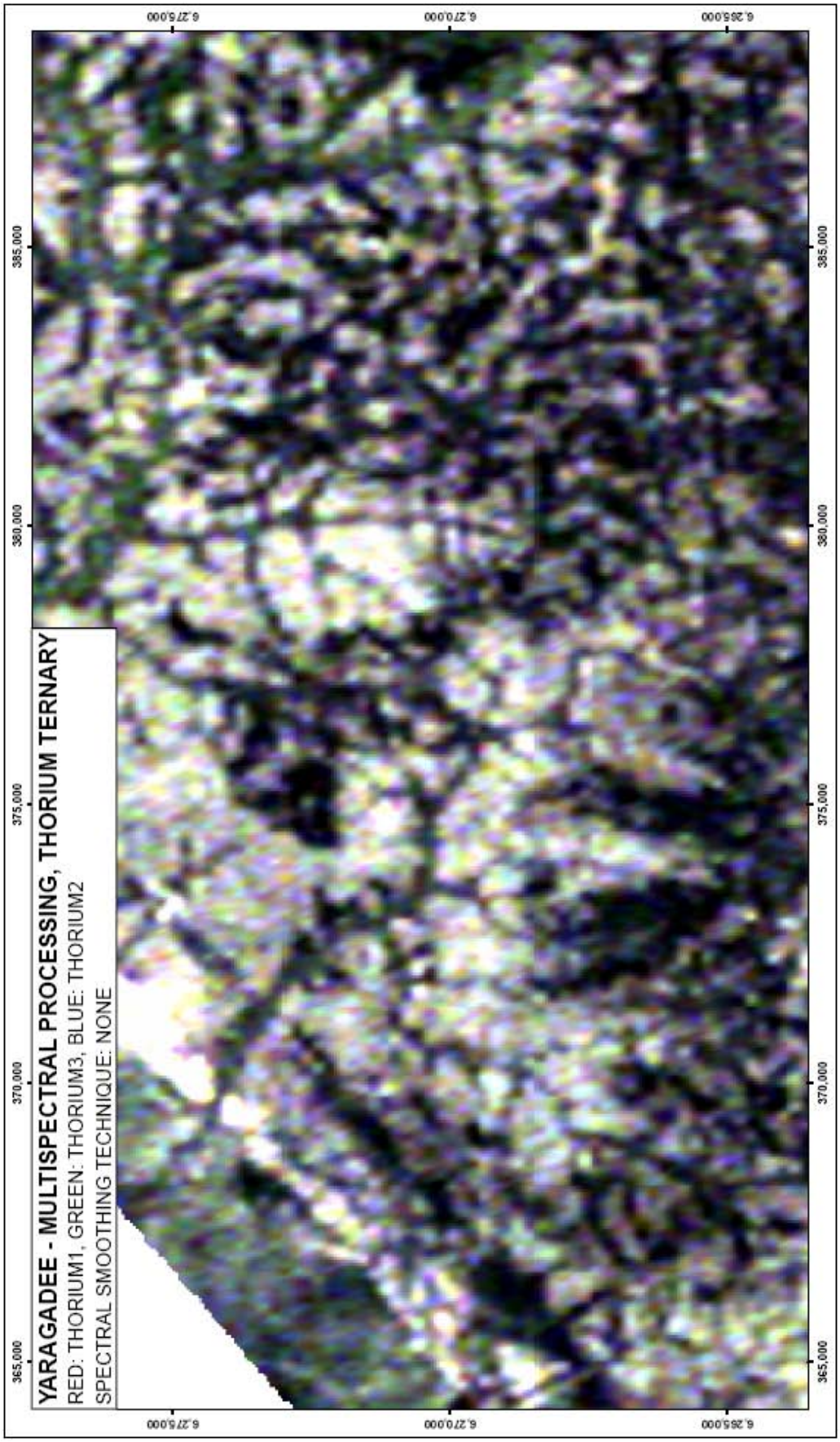


**Figure C.1.18. Thorium ternary multispectral processed, no spectral smoothing, ternary image, Yaragadee.**

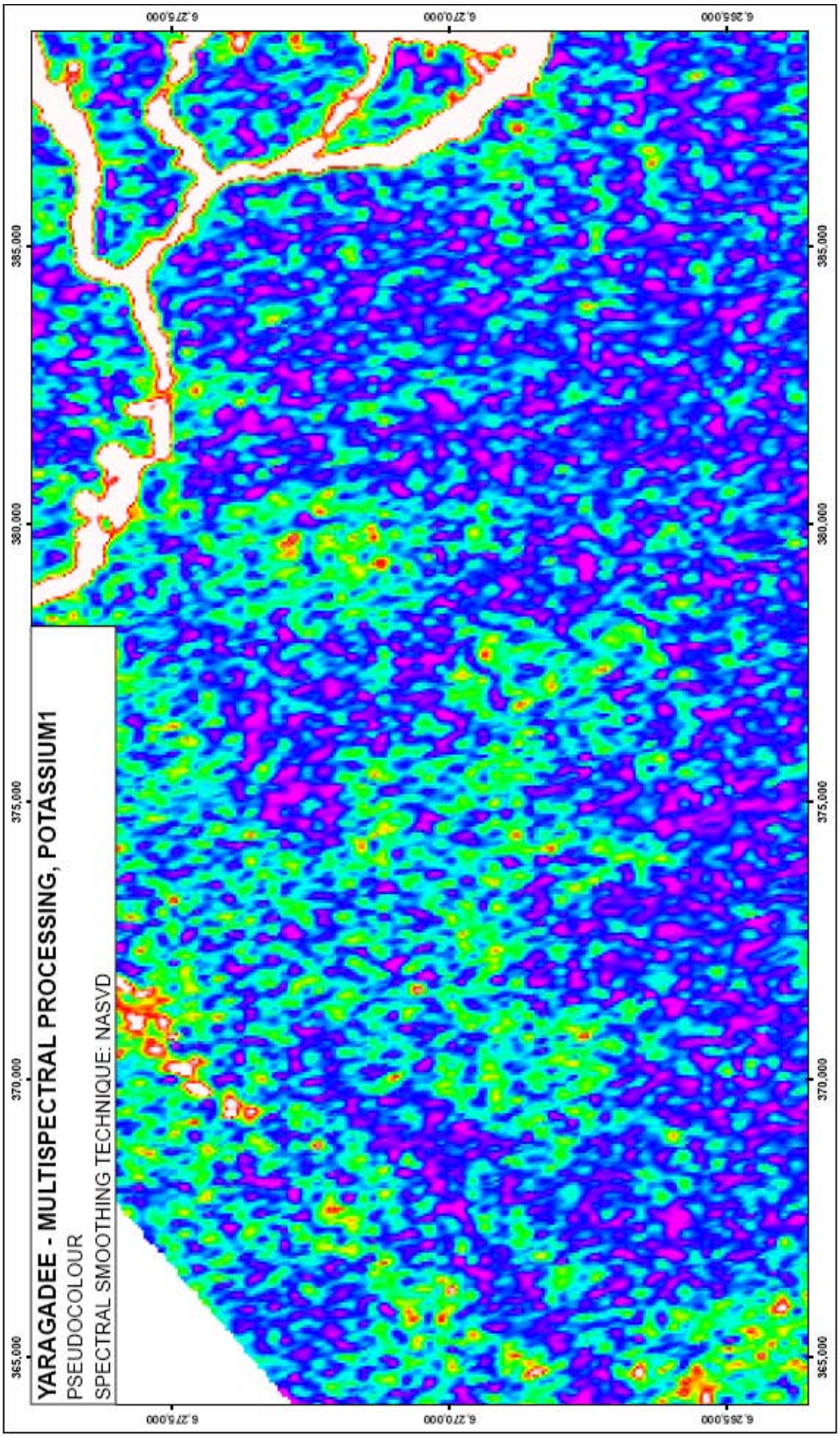


**Figure C.1.19. Potassium 1 multispectral processed, NASVD spectral smoothing, pseudocolour image, Yaragadee.**

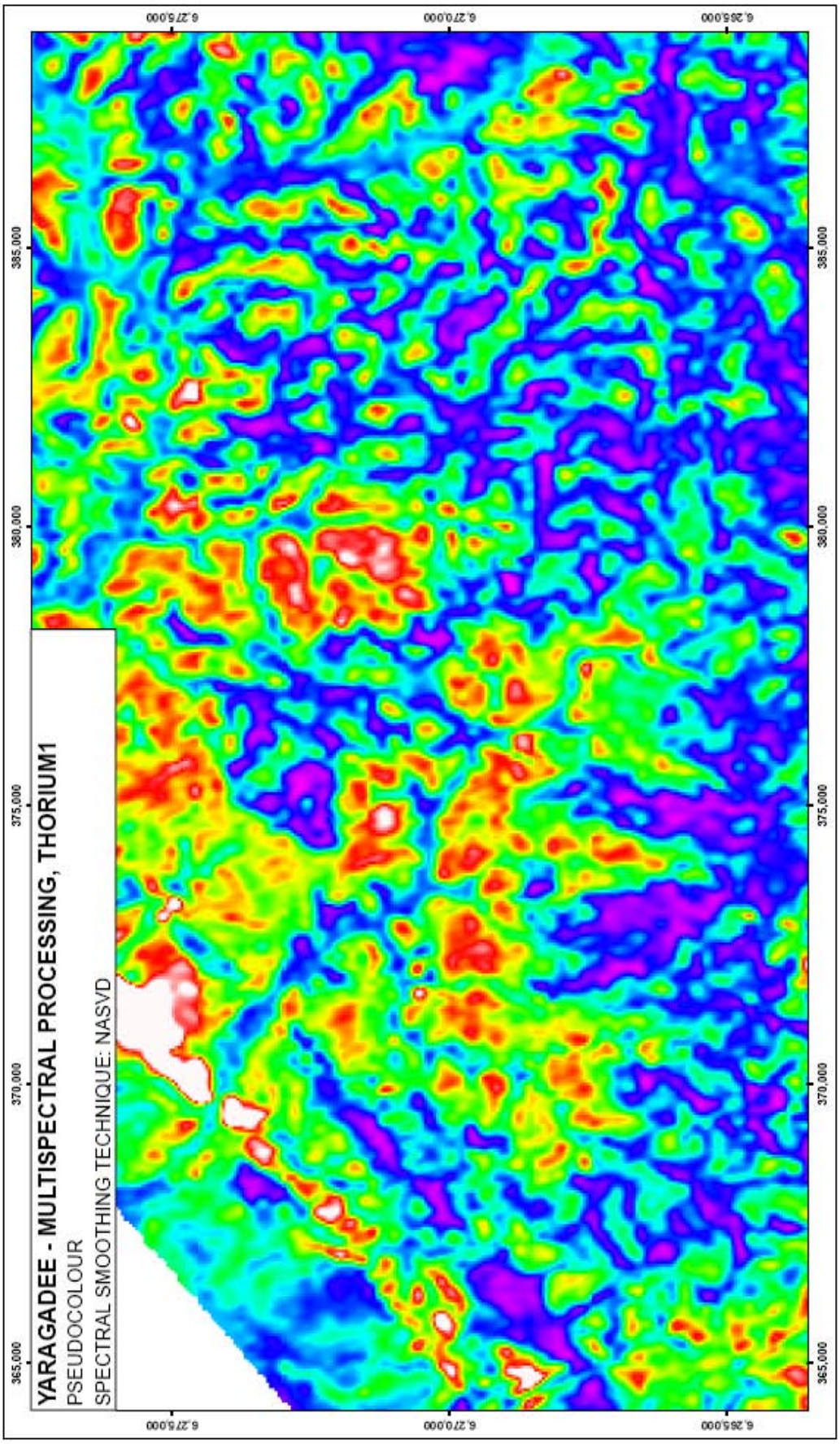


**Figure C.1.20. Thorium 1 multispectral processed, NASVD spectral smoothing, pseudocolour image, Yaragadee.**

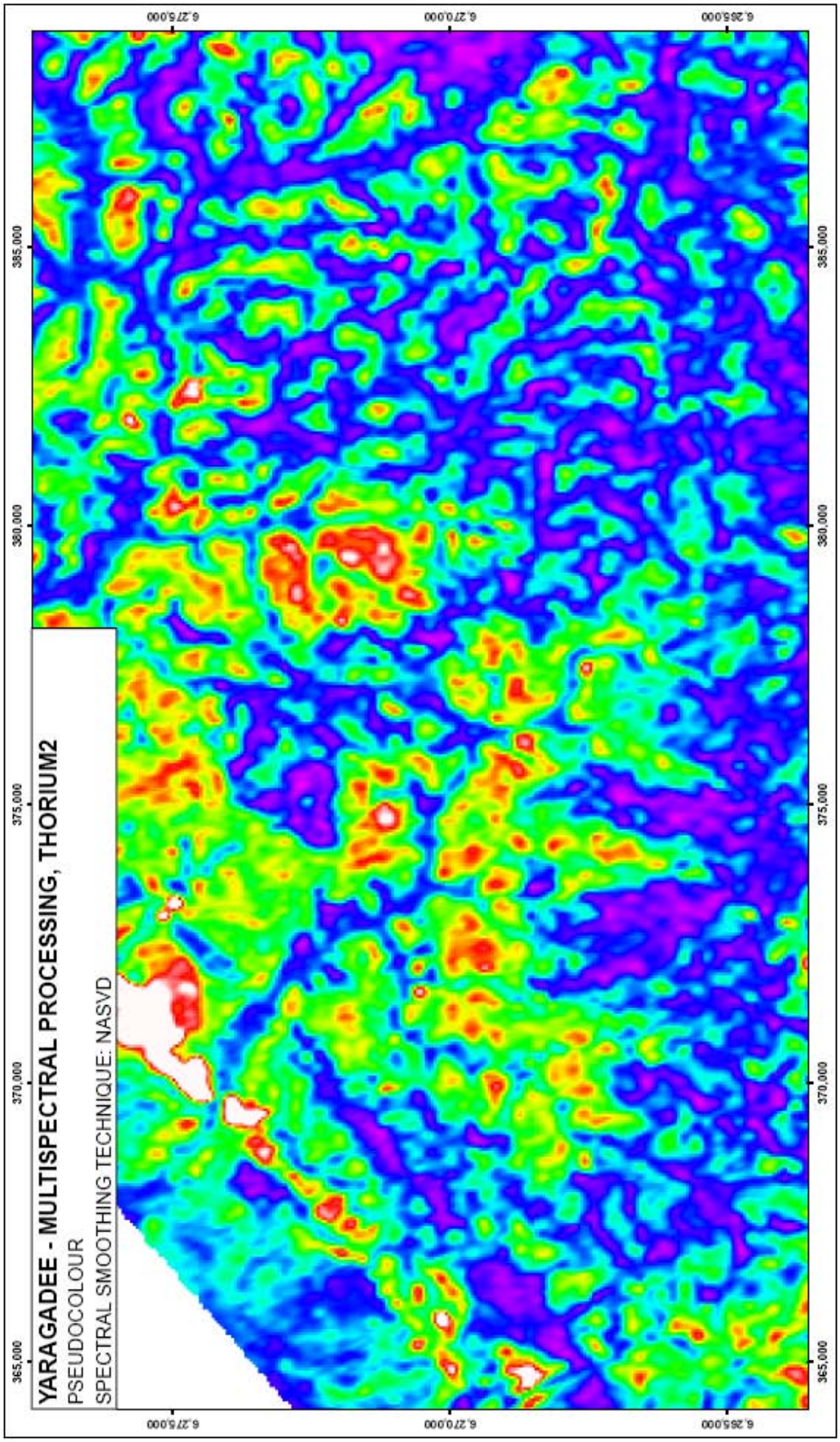


**Figure C.1.21. Thorium 2 multispectral processed, NASVD spectral smoothing, pseudocolour image, Yaragadee.**

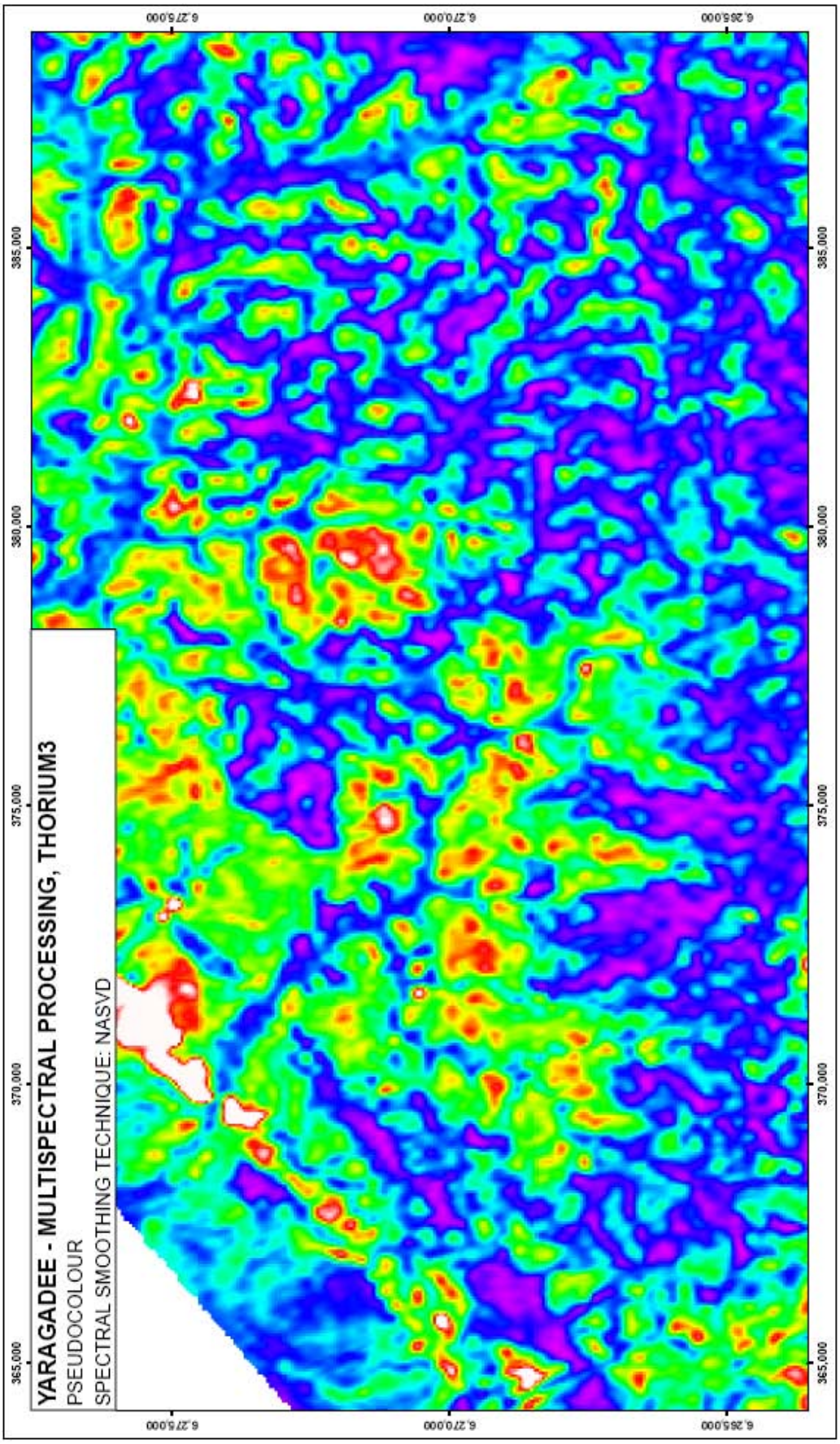


**Figure C.1.22. Thorium 3 multispectral processed, NASVD spectral smoothing, pseudocolour image, Yaragadee.**

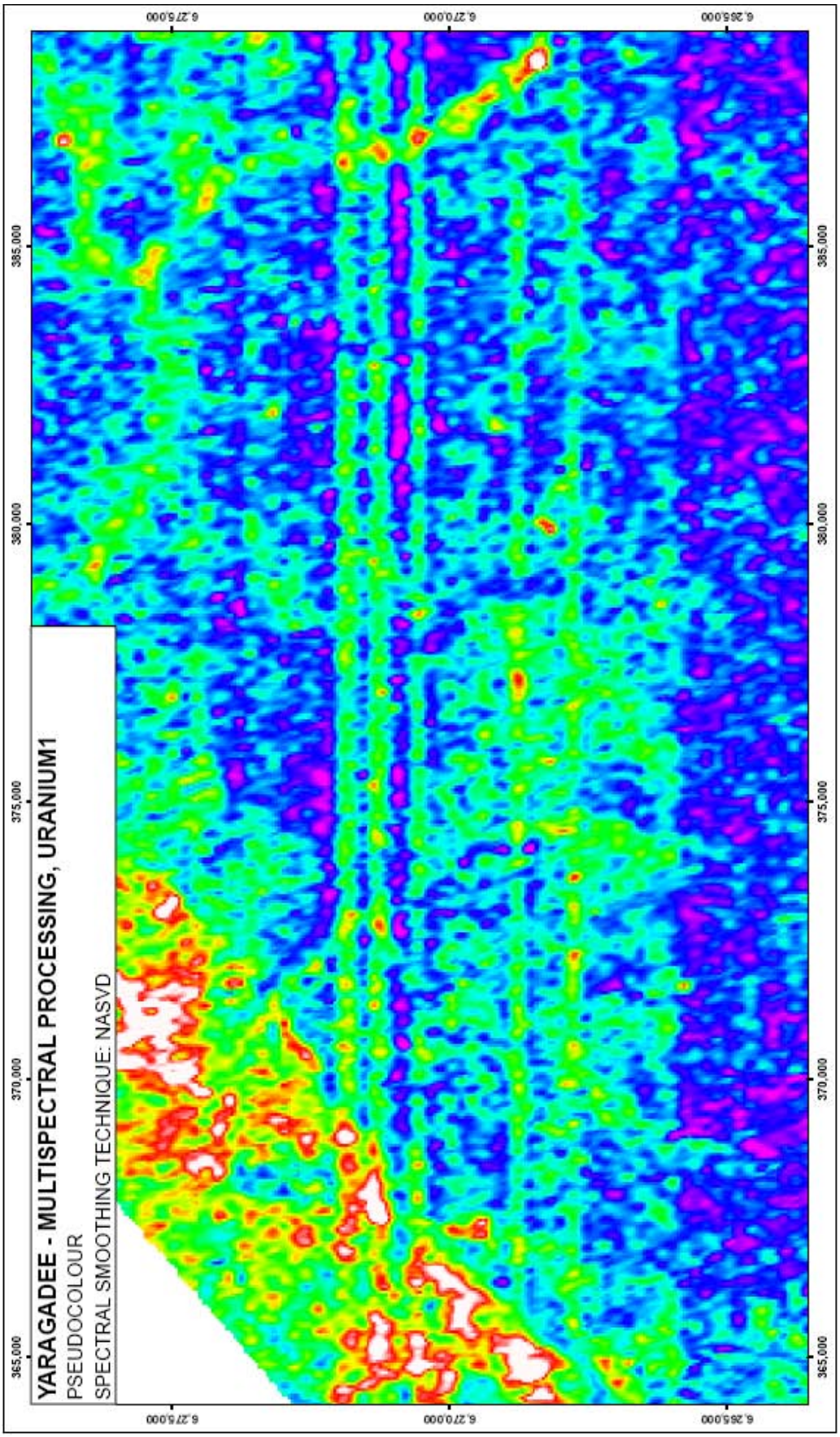


**Figure C.1.23. Uranium 1 multispectral processed, NASVD spectral smoothing, pseudocolour image, Yaragadee.**

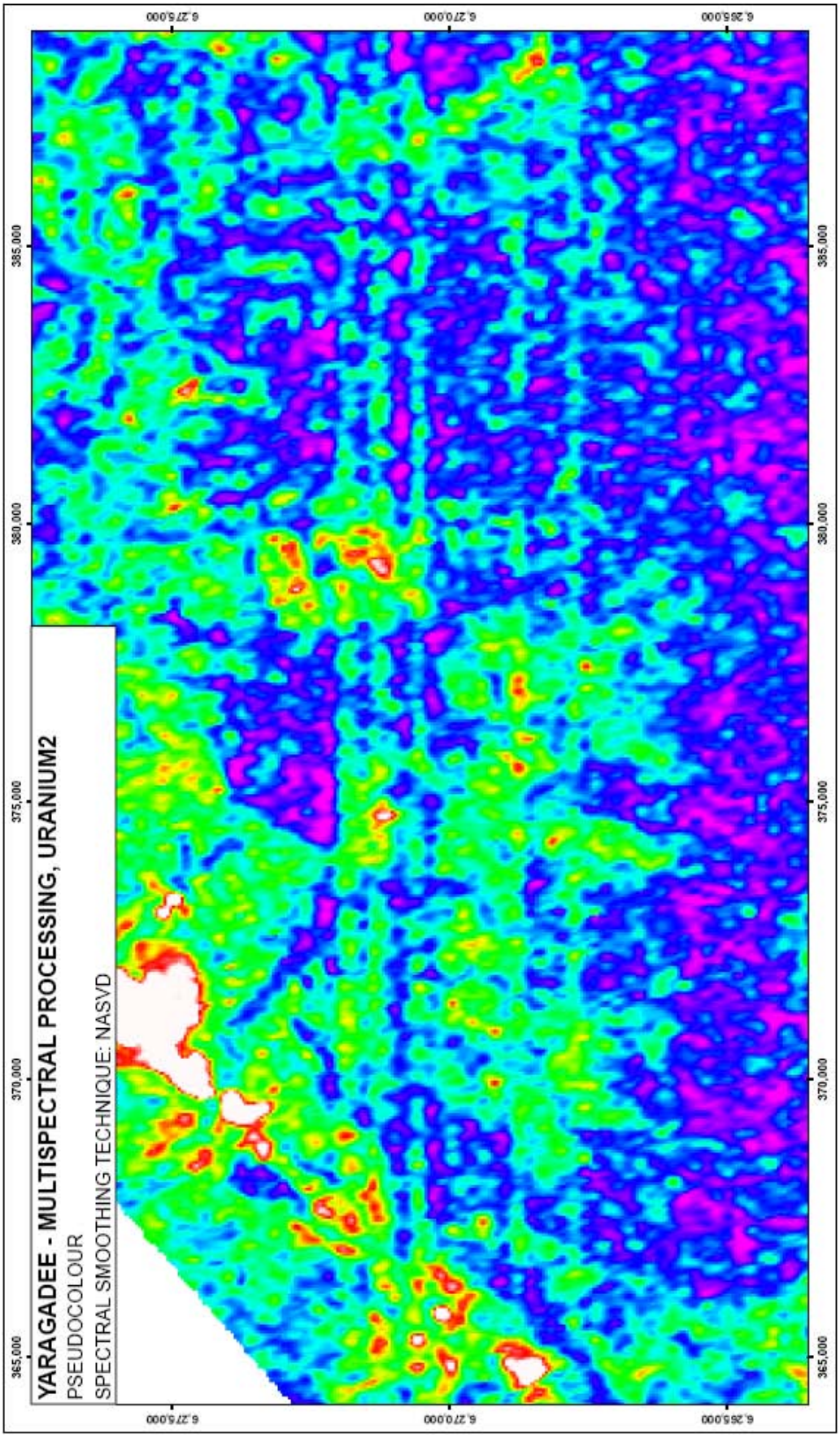


**Figure C.1.24. Uranium 2 multispectral processed, NASVD spectral smoothing, pseudocolour image, Yaragadee.**

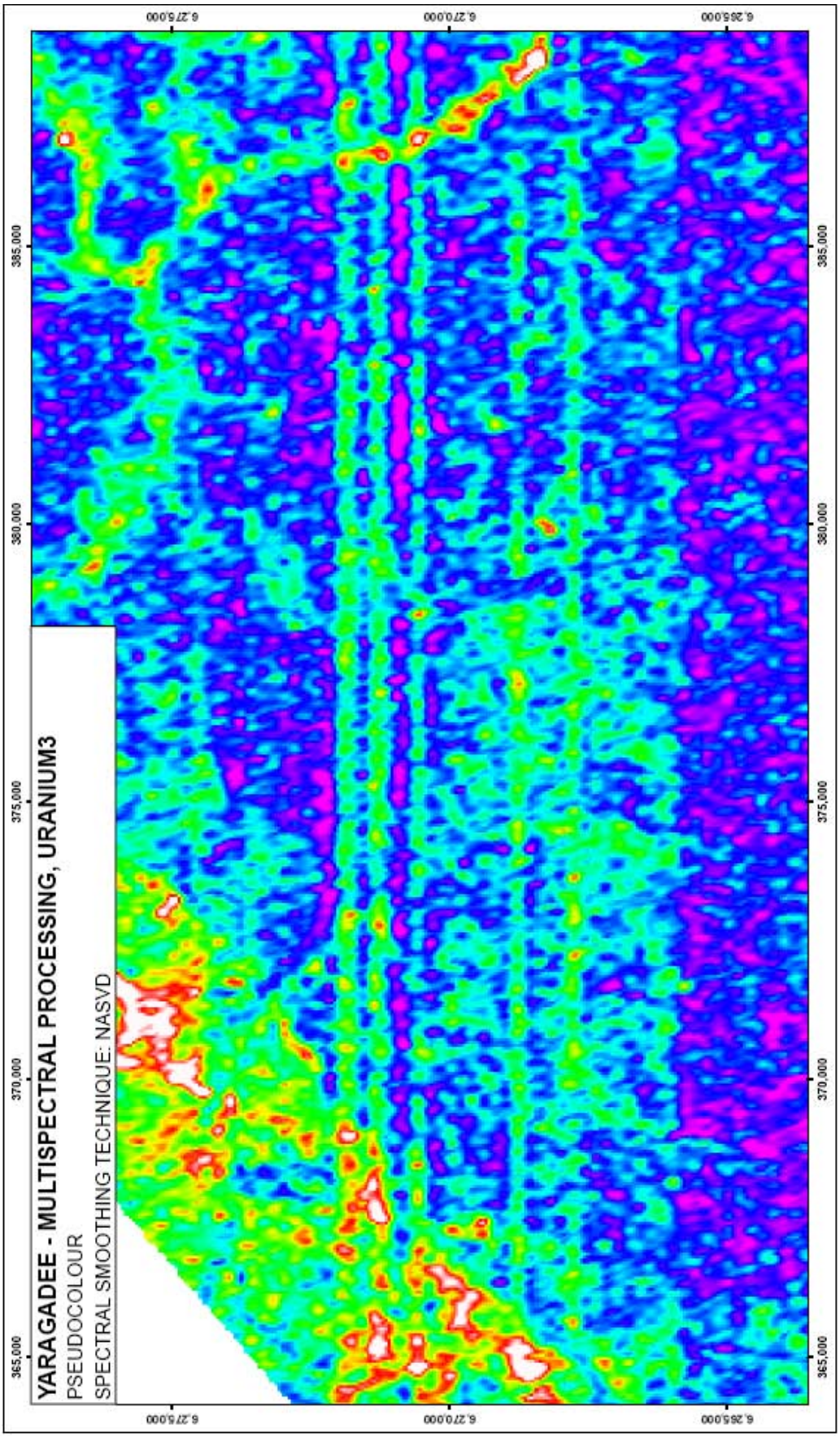


**Figure C.1.25. Uranium 3 multispectral processed, NASVD spectral smoothing, pseudocolour image, Yaragadee.**

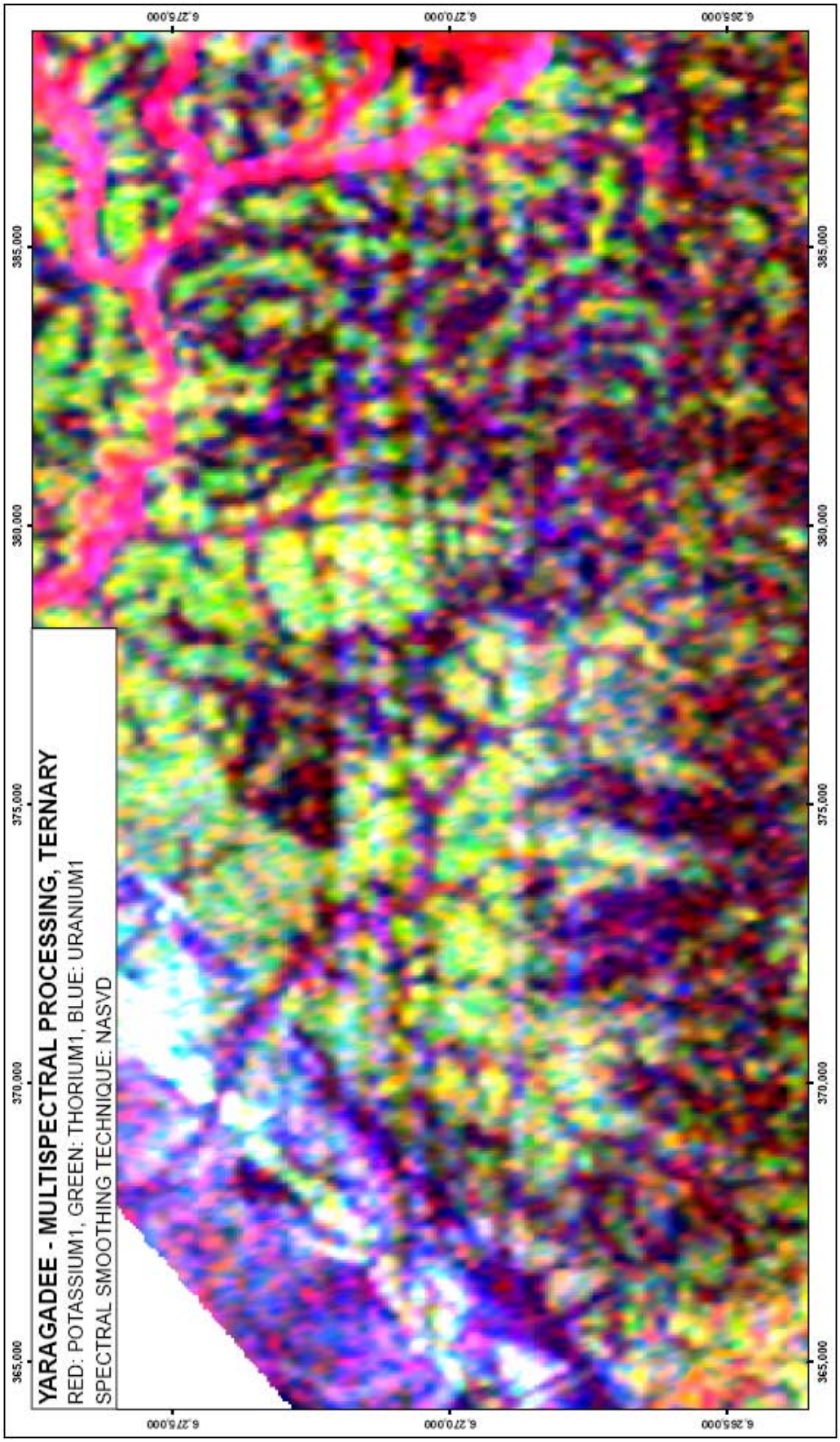


**Figure C.1.26. Ternary multispectral processed, NASVD spectral smoothing, ternary image, Yaragadee.**

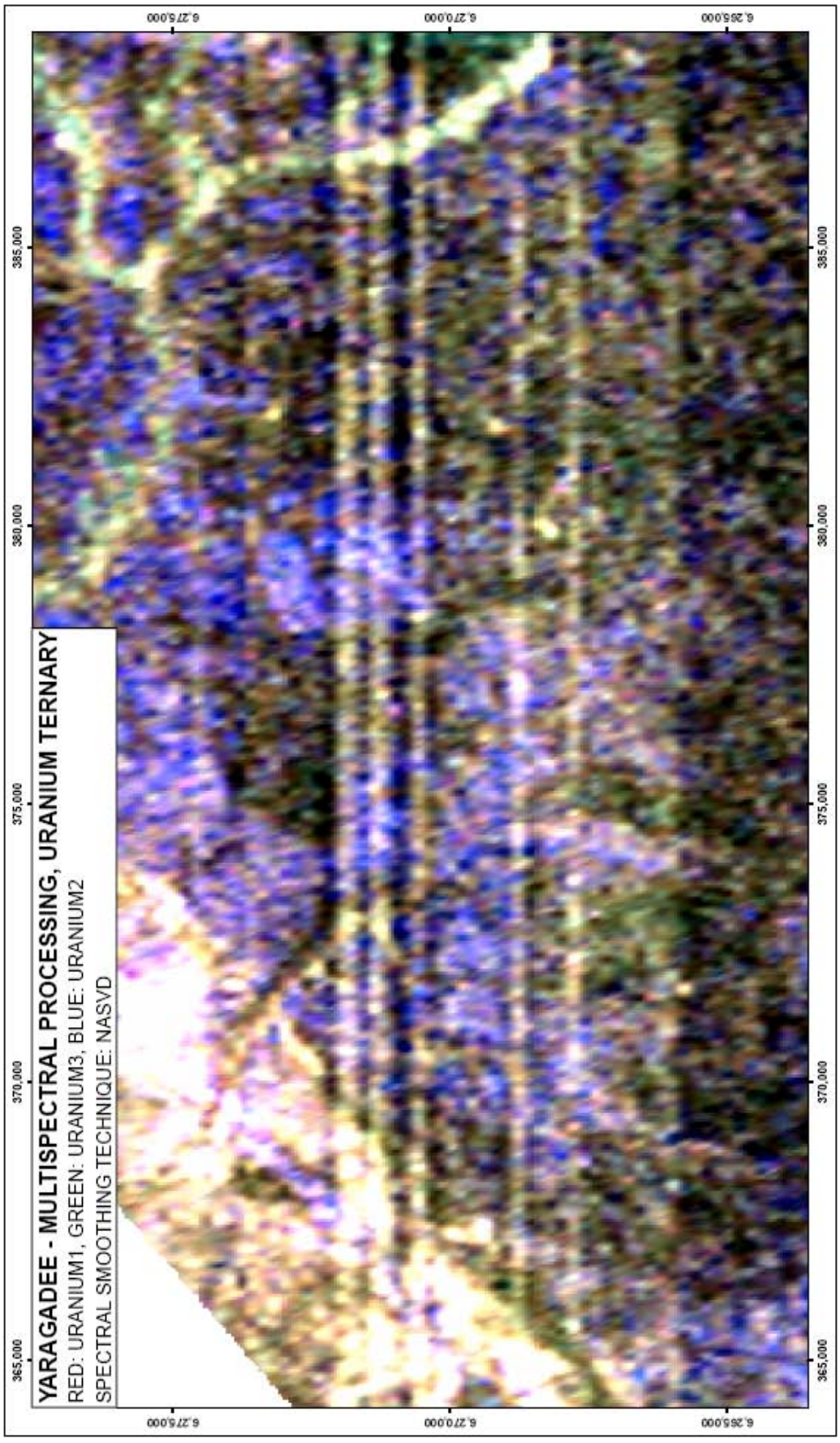


**Figure C.1.27. Uranium ternary multispectral processed, NASVD spectral smoothing, ternary image, Yaragadee.**


**Figure C.1.28. Thorium ternary multispectral processed, NASVD spectral smoothing, ternary image, Yaragadee.**

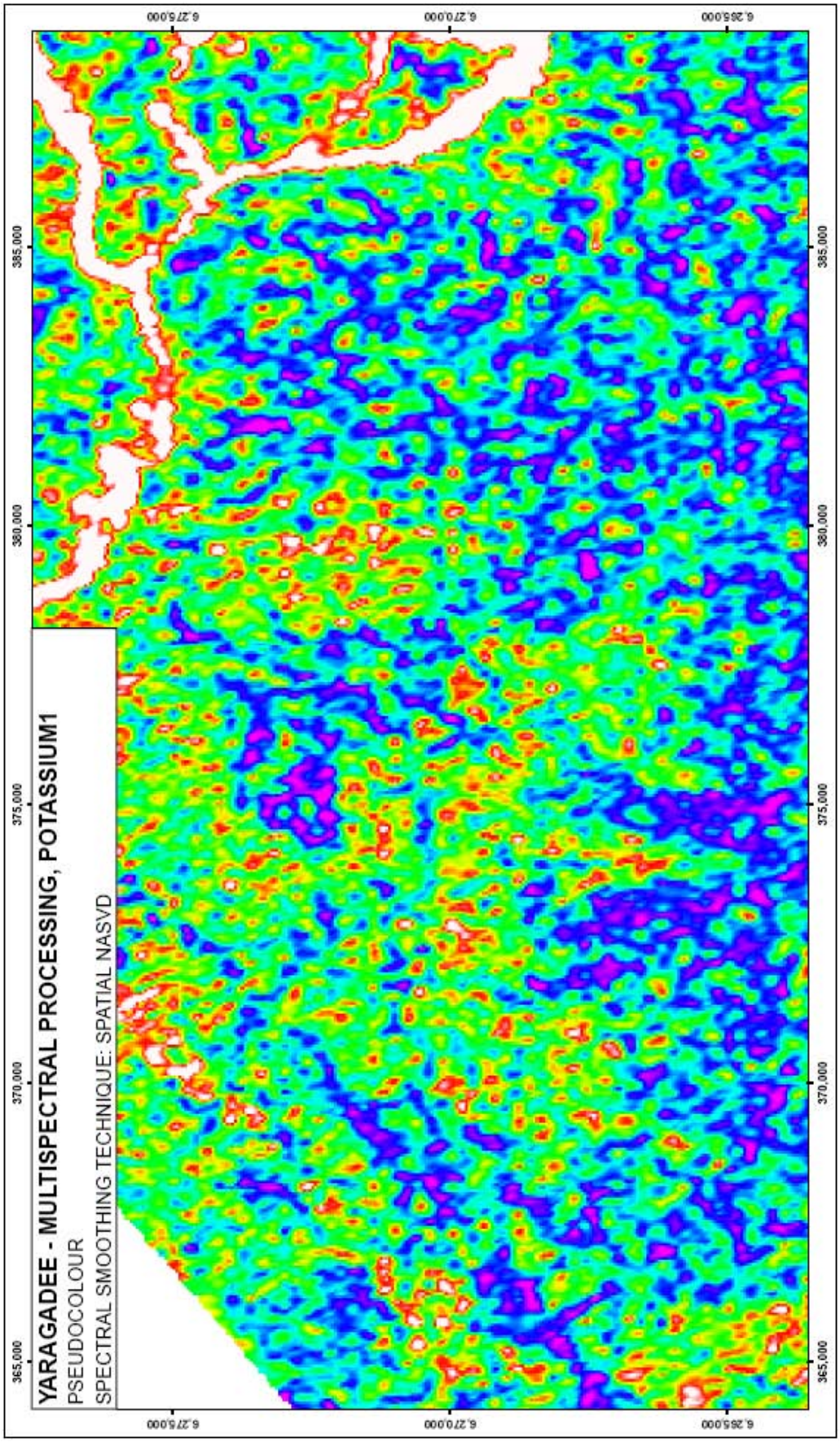


**Figure C.1.29. Potassium 1 multispectral processed, NASVD spectral smoothing, pseudocolour image, Yaragadee.**

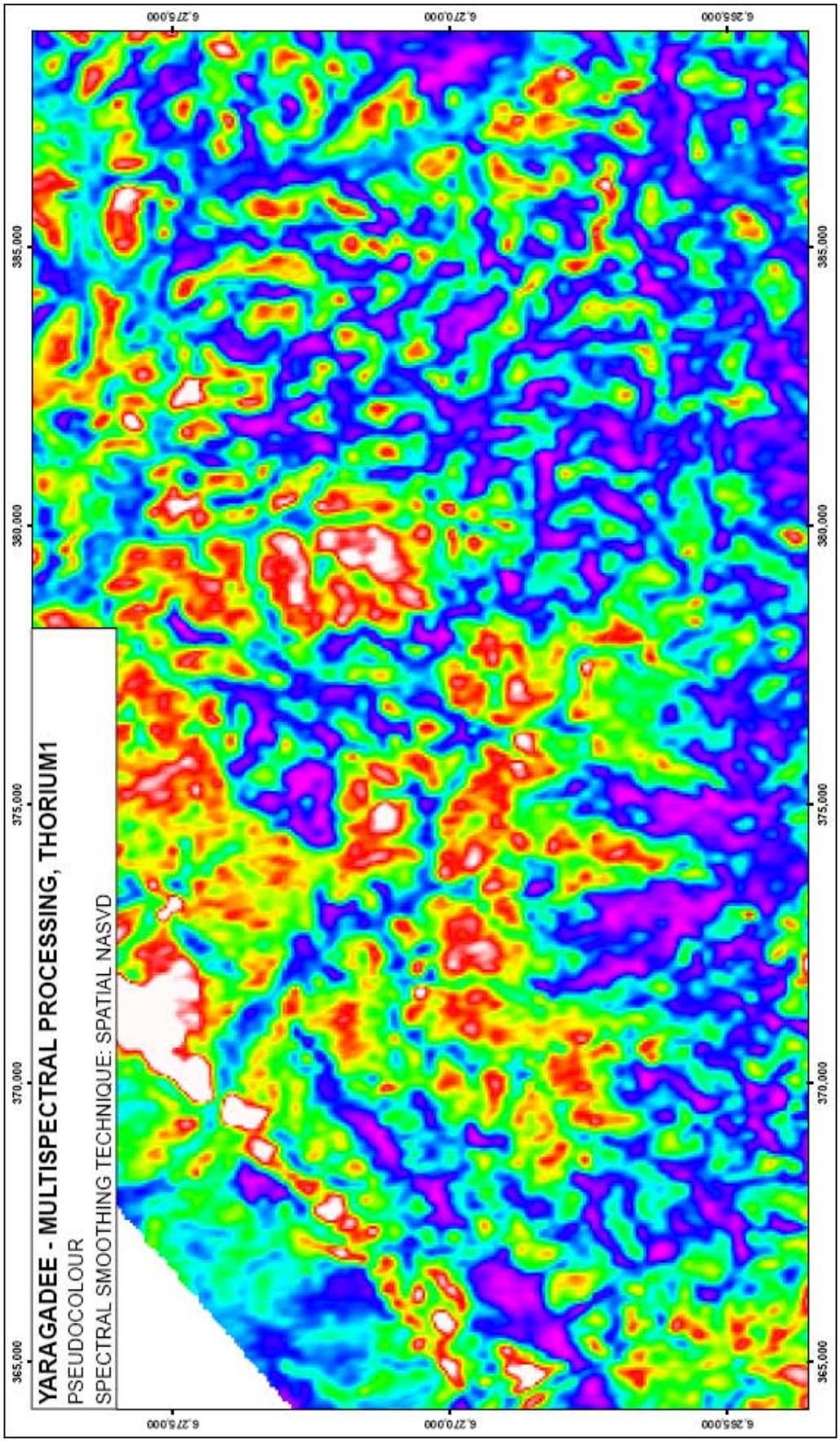


**Figure C.1.30. Thorium 1 multispectral processed, spatial NASVD spectral smoothing, pseudocolour image, Yaragadee.**

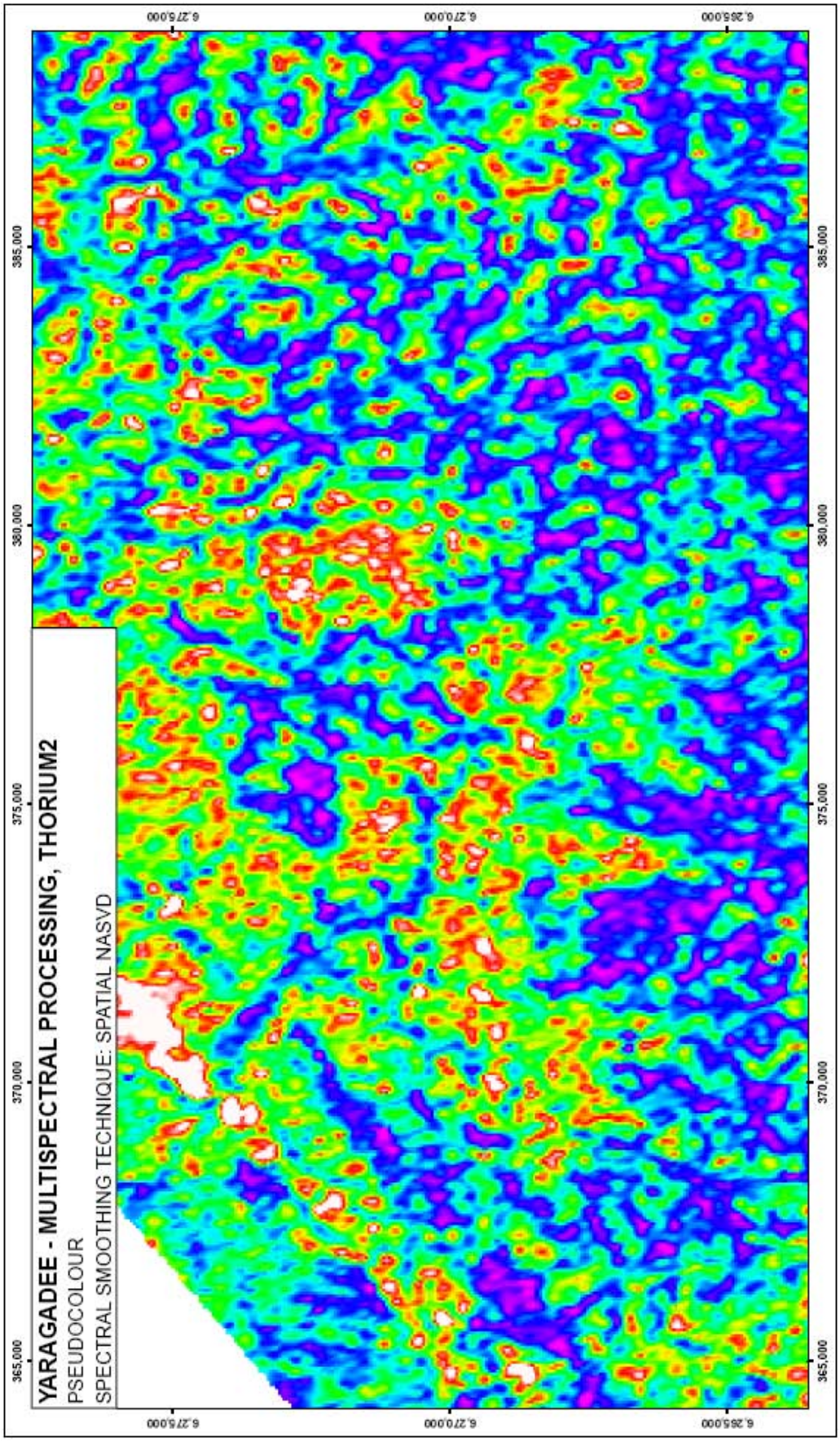


**Figure C.1.31. Thorium 2 multispectral processed, spatial NASVD spectral smoothing, pseudocolour image, Yaragadee.**

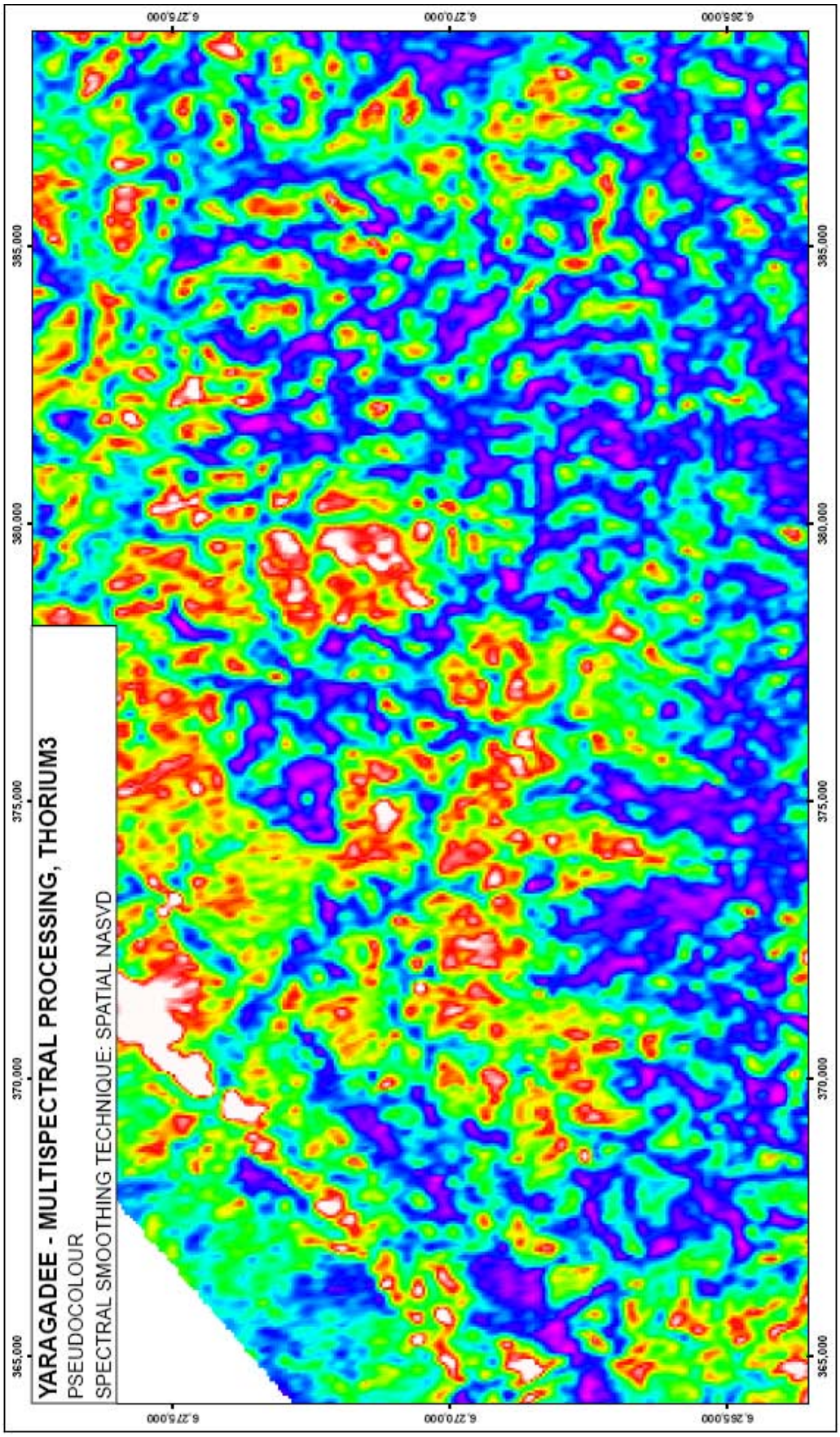


**Figure C.1.32. Thorium 3 multispectral processed, spatial NASVD spectral smoothing, pseudocolour image, Yaragadee.**

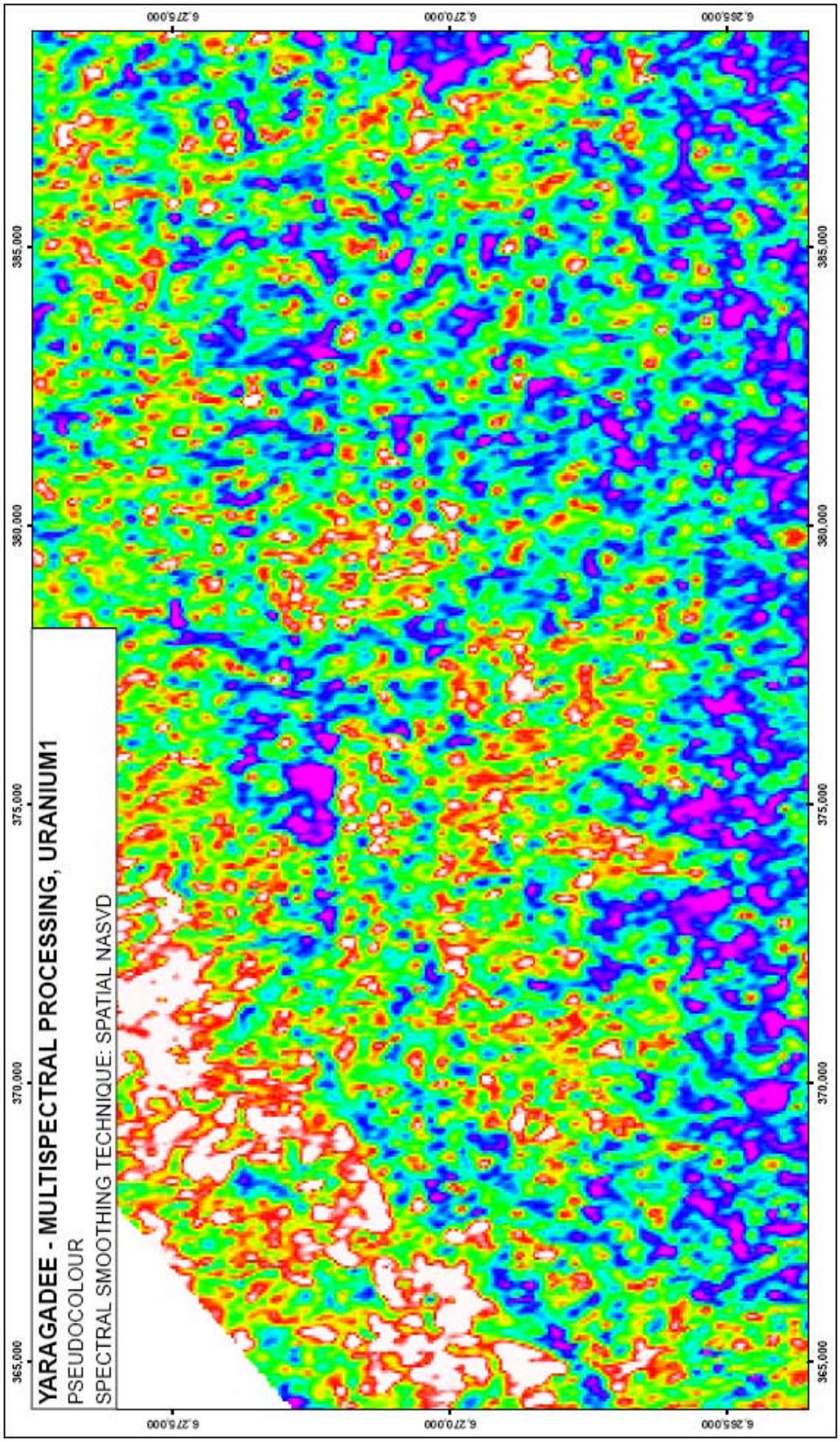


**Figure C.1.33. Uranium 1 multispectral processed, spatial NASVD spectral smoothing, pseudocolour image, Yaragadee.**

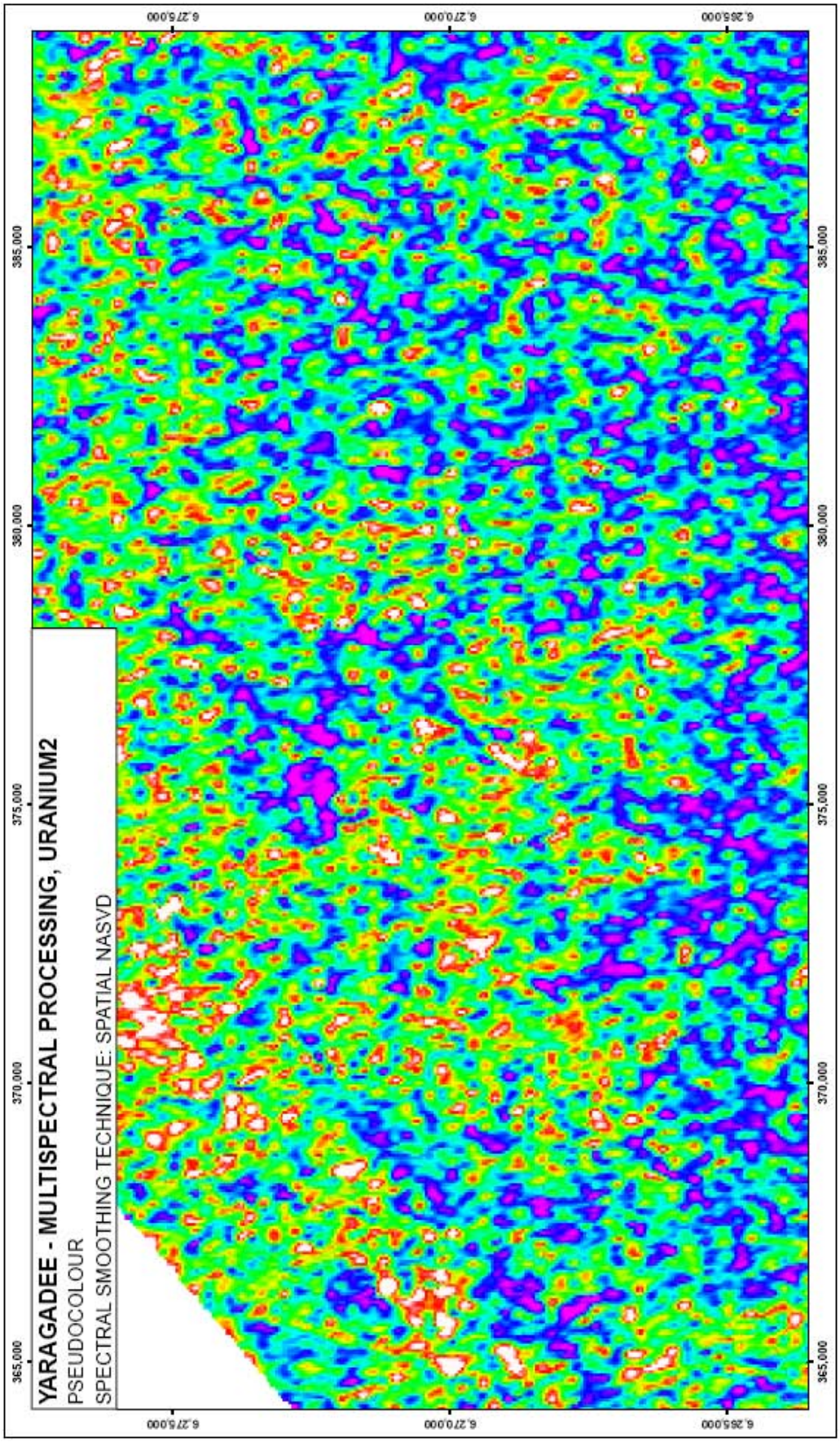


**Figure C.1.34. Uranium 2 multispectral processed, spatial NASVD spectral smoothing, pseudocolour image, Yaragadee.**

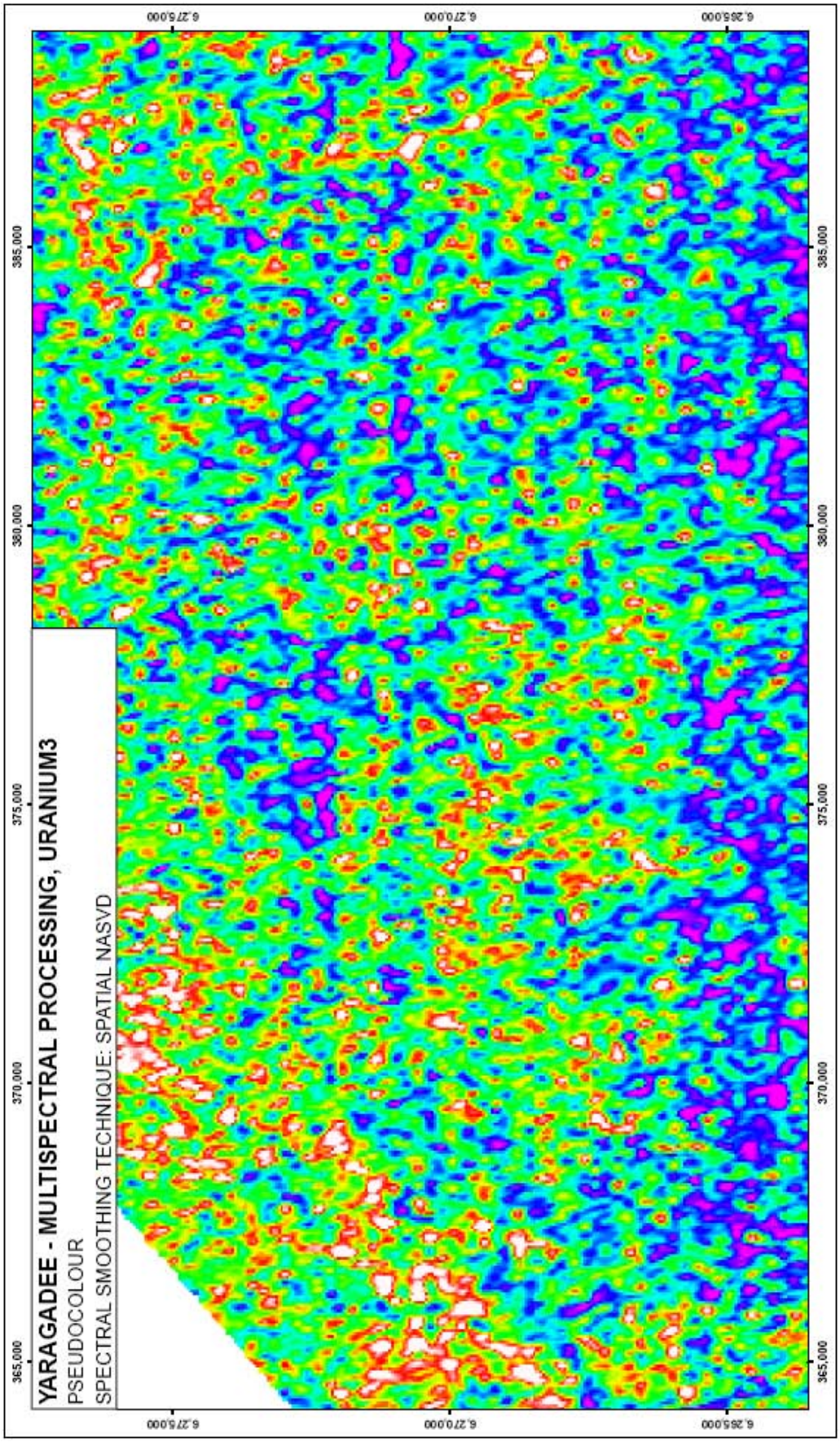


**Figure C.1.35. Uranium 3 multispectral processed, spatial NASVD spectral smoothing, pseudocolour image, Yaragadee.**

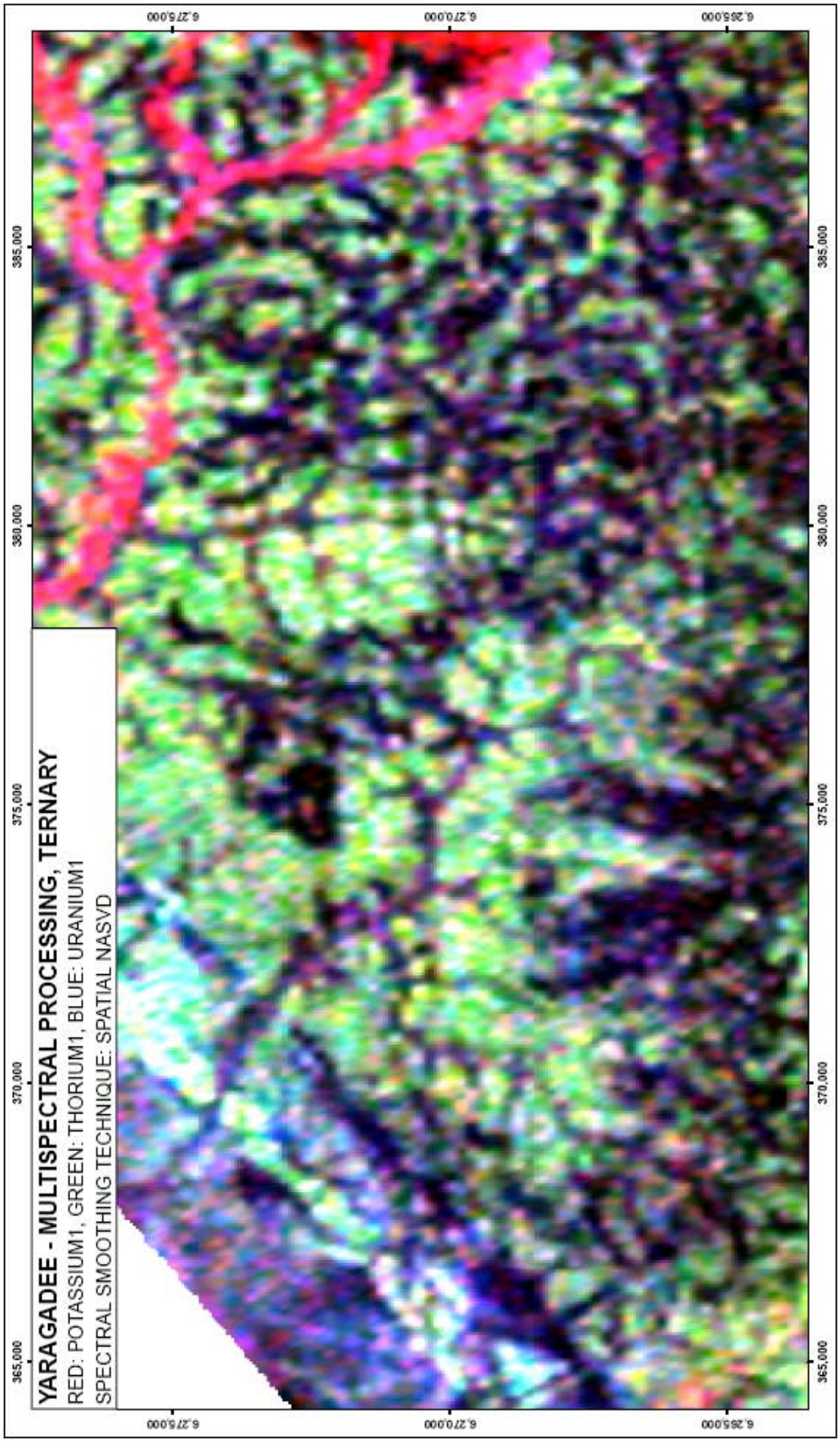


**Figure C.1.36. Ternary multispectral processed, spatial NASVD spectral smoothing, ternary image, Yaragadee.**

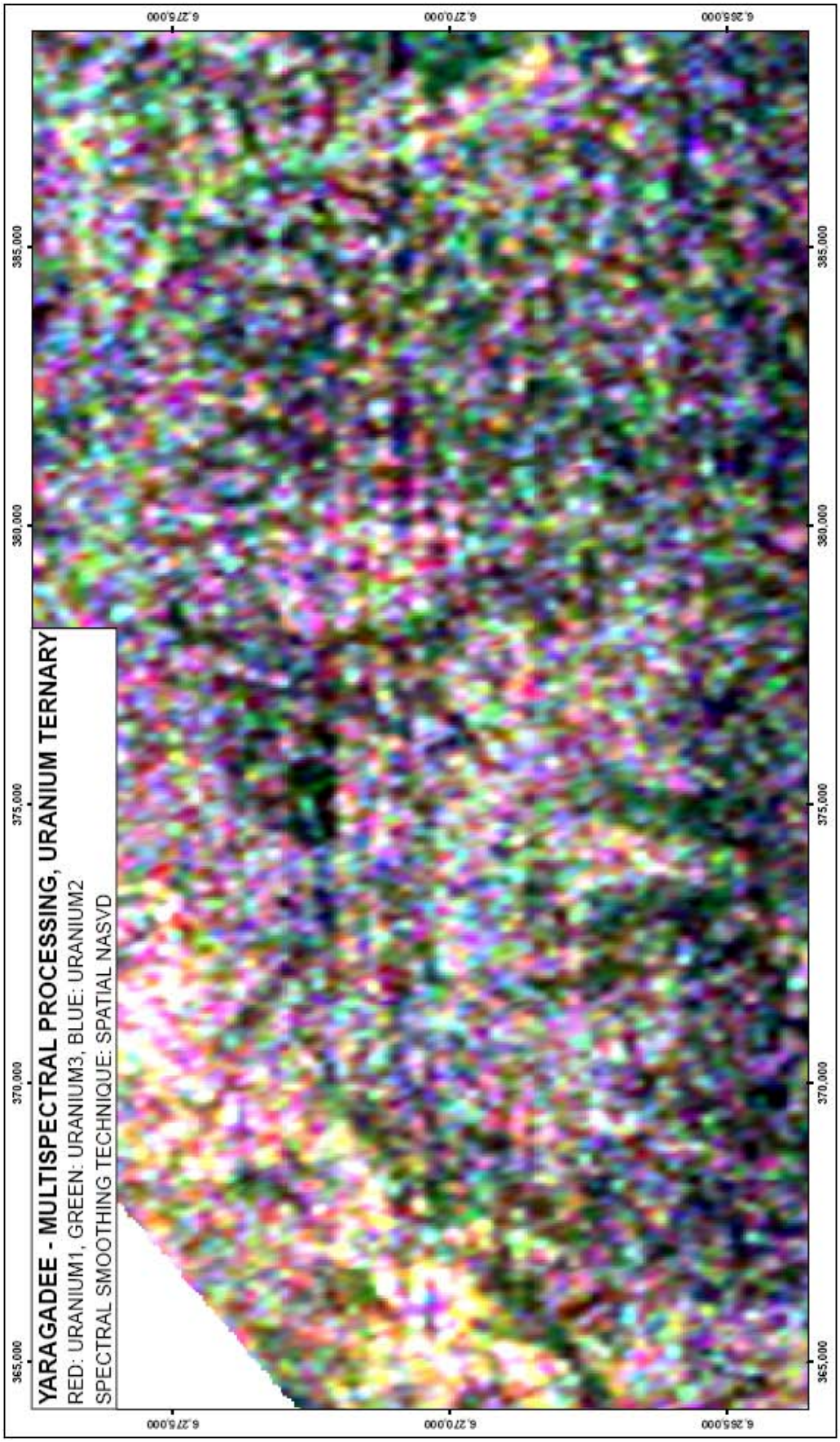


**Figure C.1.37. Uranium ternary multispectral processed, spatial NASVD spectral smoothing, ternary image, Yaragadee.**


**Figure C.1.38. Thorium ternary multispectral processed, spatial NASVD spectral smoothing, ternary image, Yaragadee.**

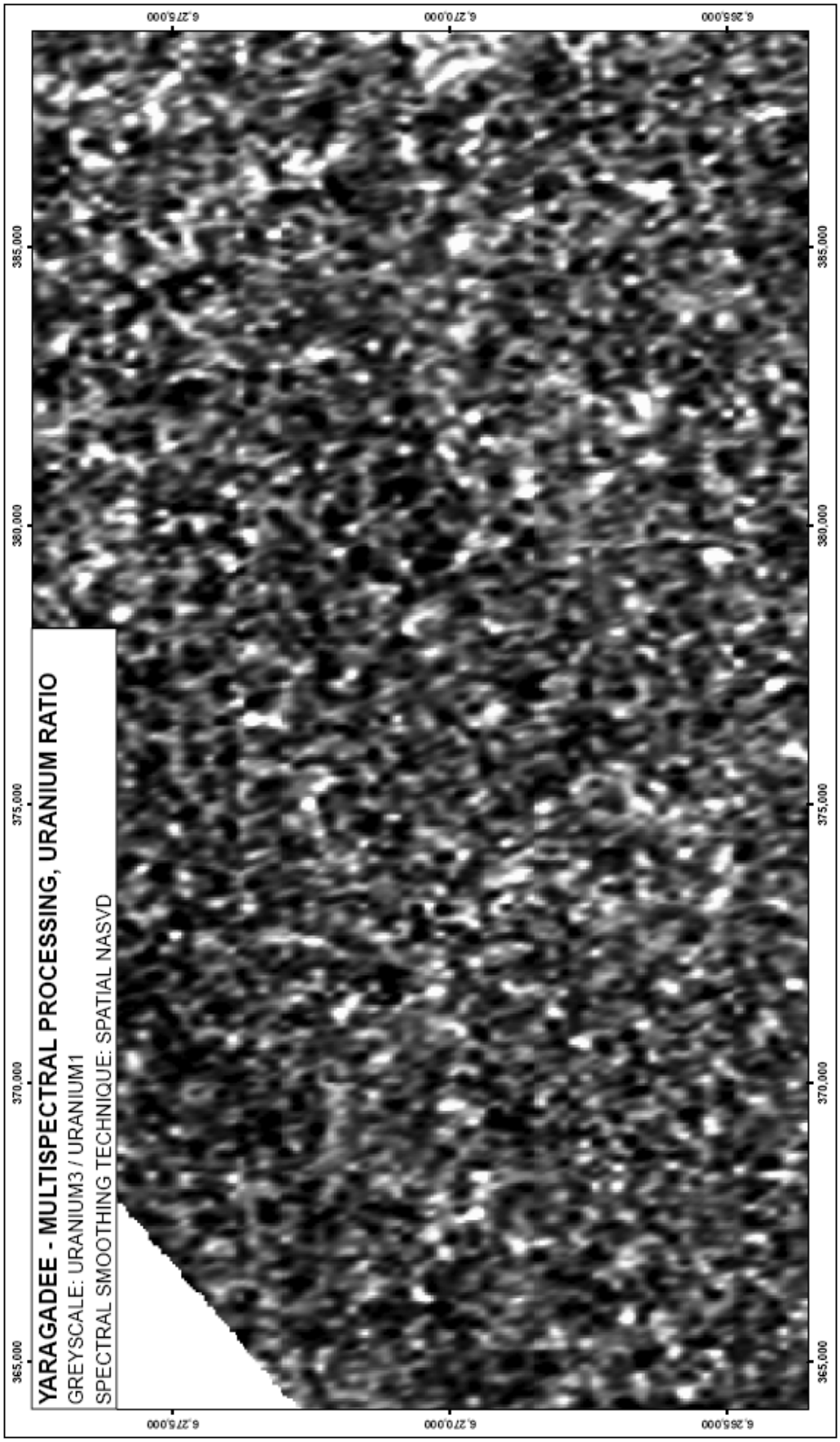


**Figure C.1.39. Uranium ratio multispectral processed, spatial NASVD spectral smoothing, greyscale image, Yaragadee.**

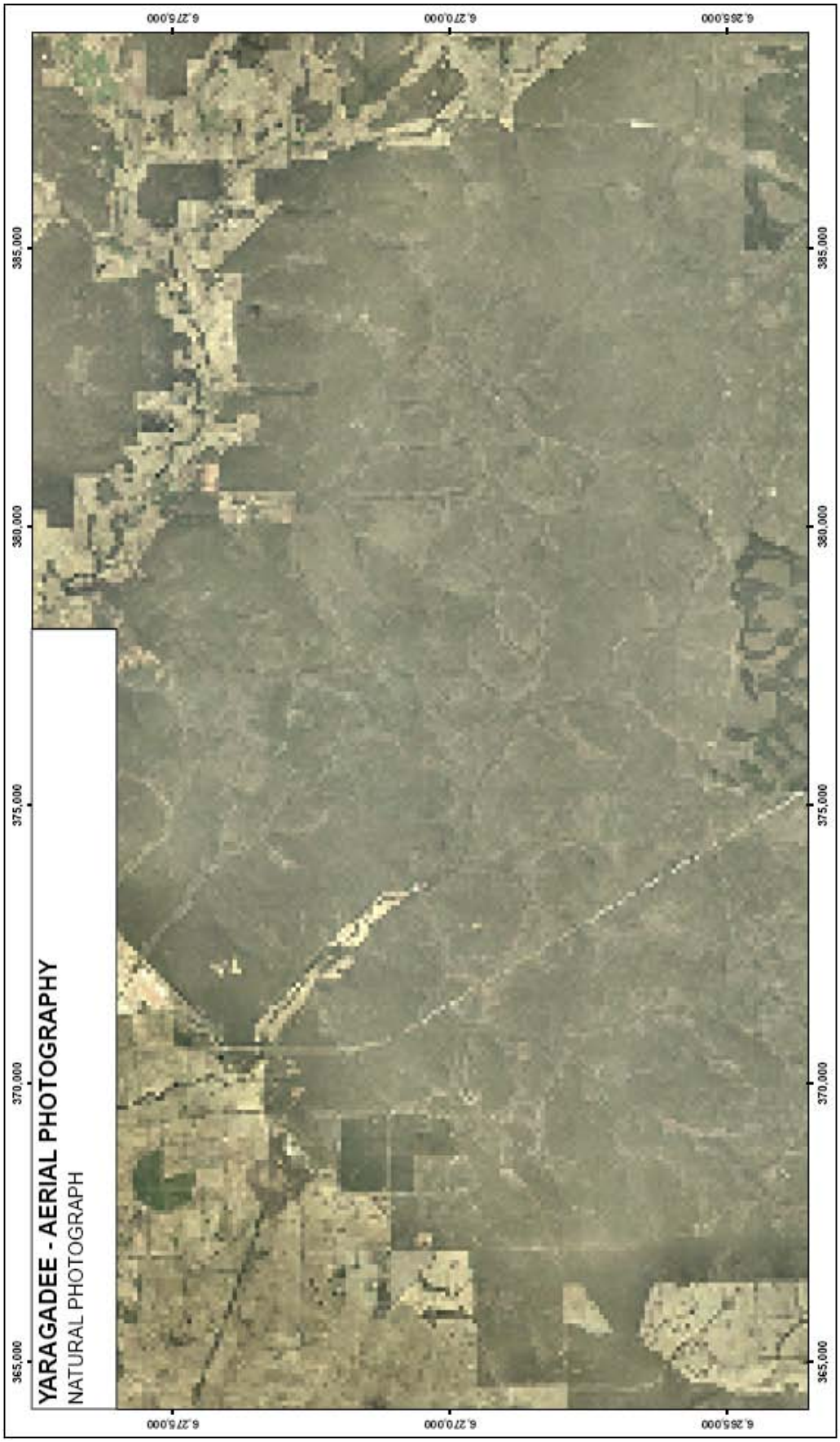


**Figure C.1.40. Natural colour aerial photo, Yaragadee.**

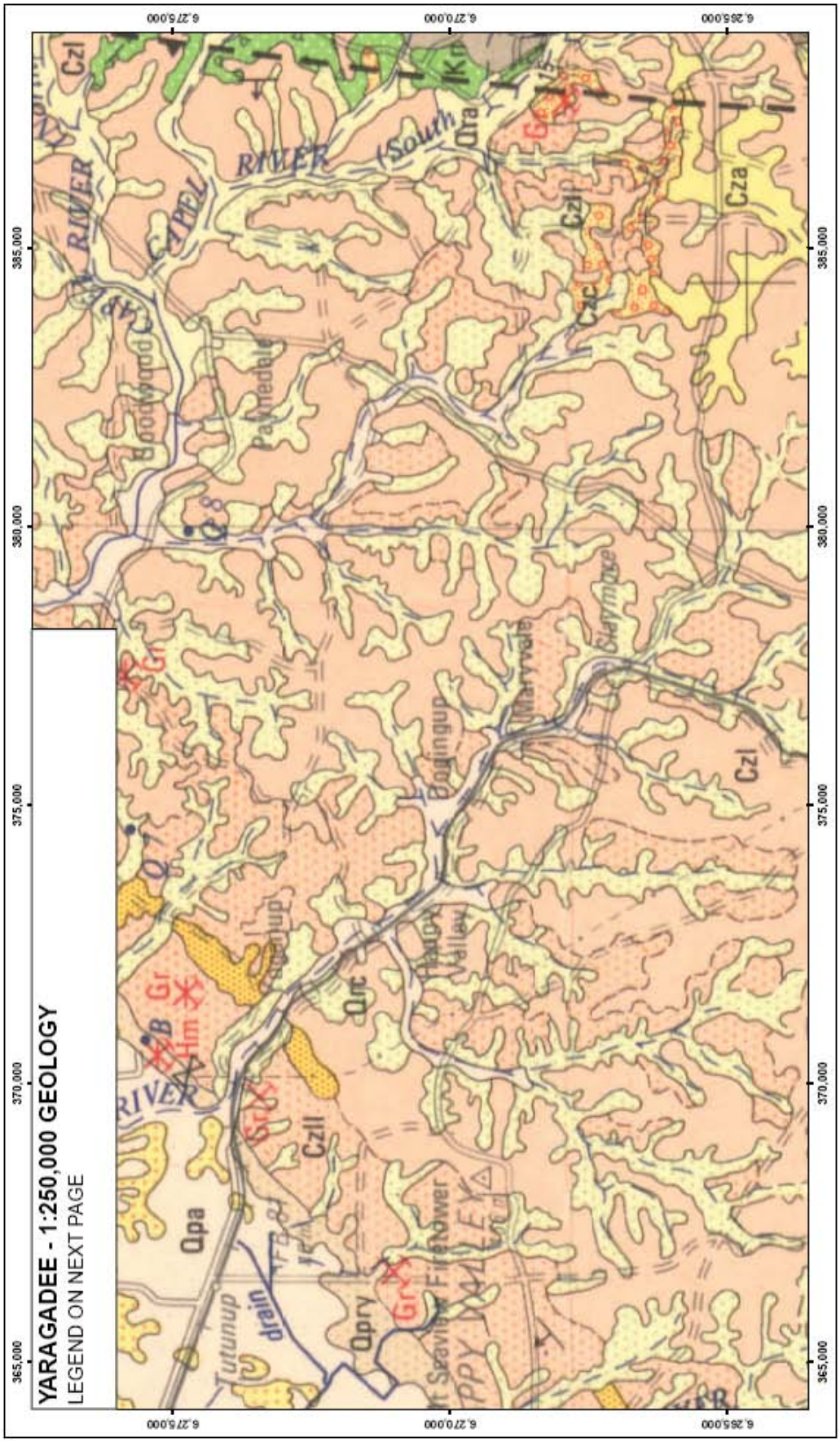


**Figure C.1.41. 1:250,000 geology of Yaragadee (from Baxter and Lipple, 1985).**

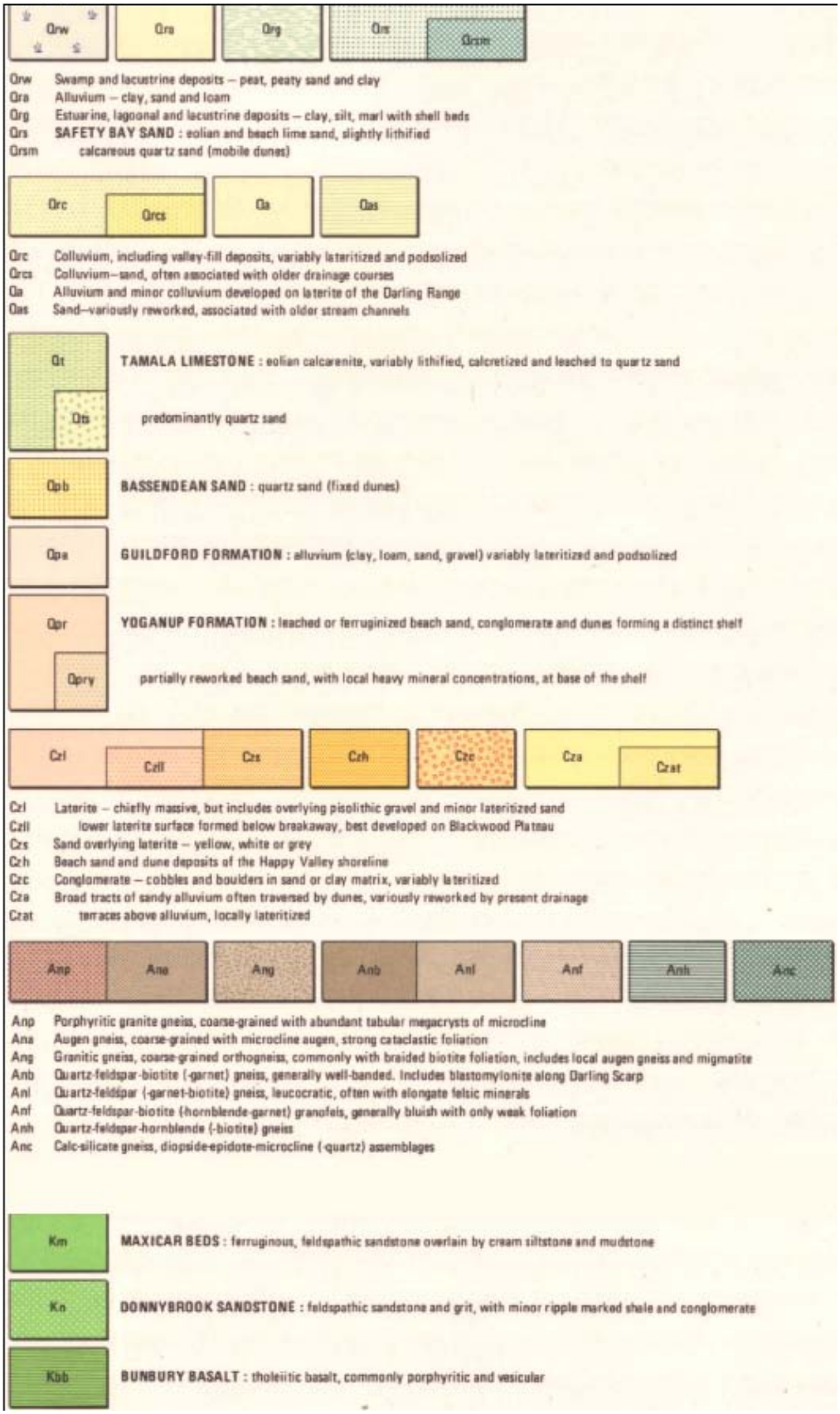


**Figure C.1.41 cont'd. 1:250,000 geology legend for Yaragadee (from Baxter and Lipple, 1985).**

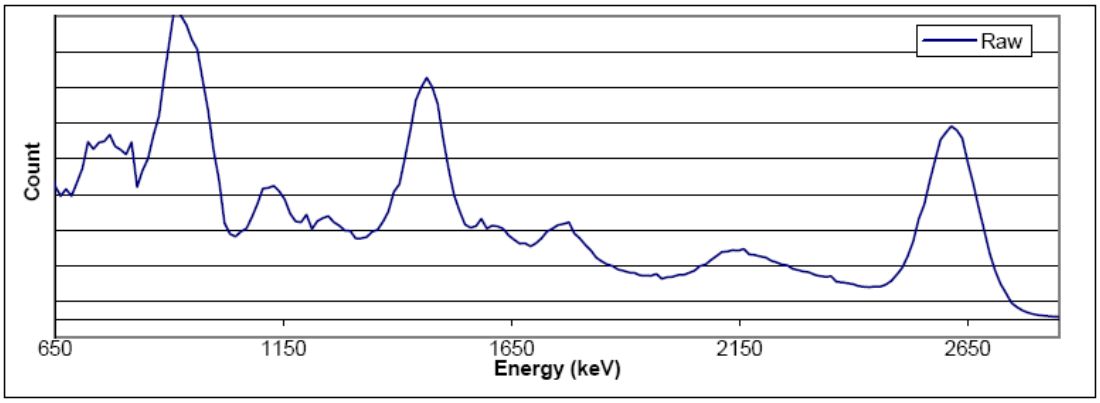


**Figure C.2.1. Average raw spectrum following Compton continuum removal, Elashgin.**

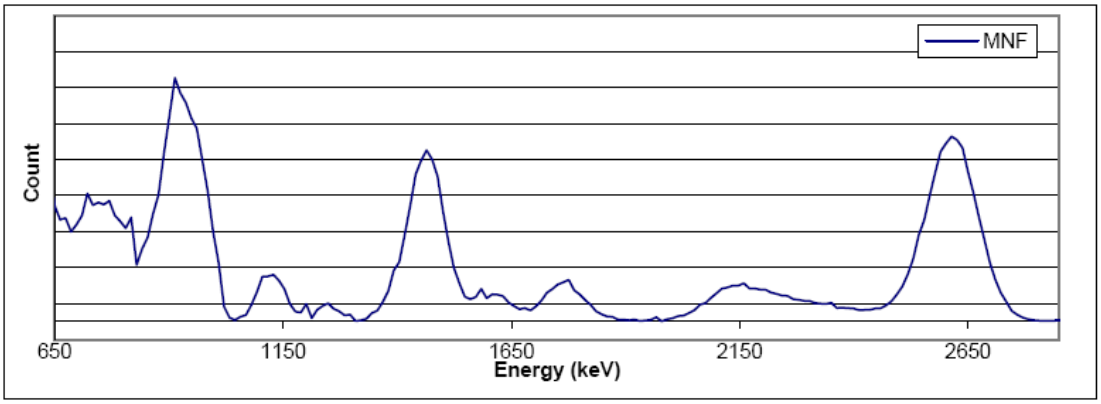


**Figure C.2.2. Average MNF smoothed spectrum following Compton continuum removal, Elashgin.**

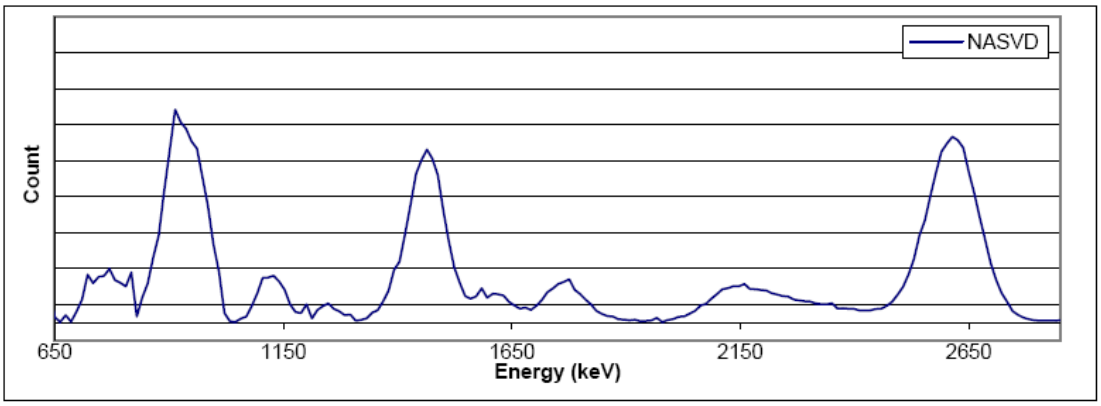


**Figure C.2.3. Average NASVD smoothed spectrum following Compton continuum removal, Elashgin.**

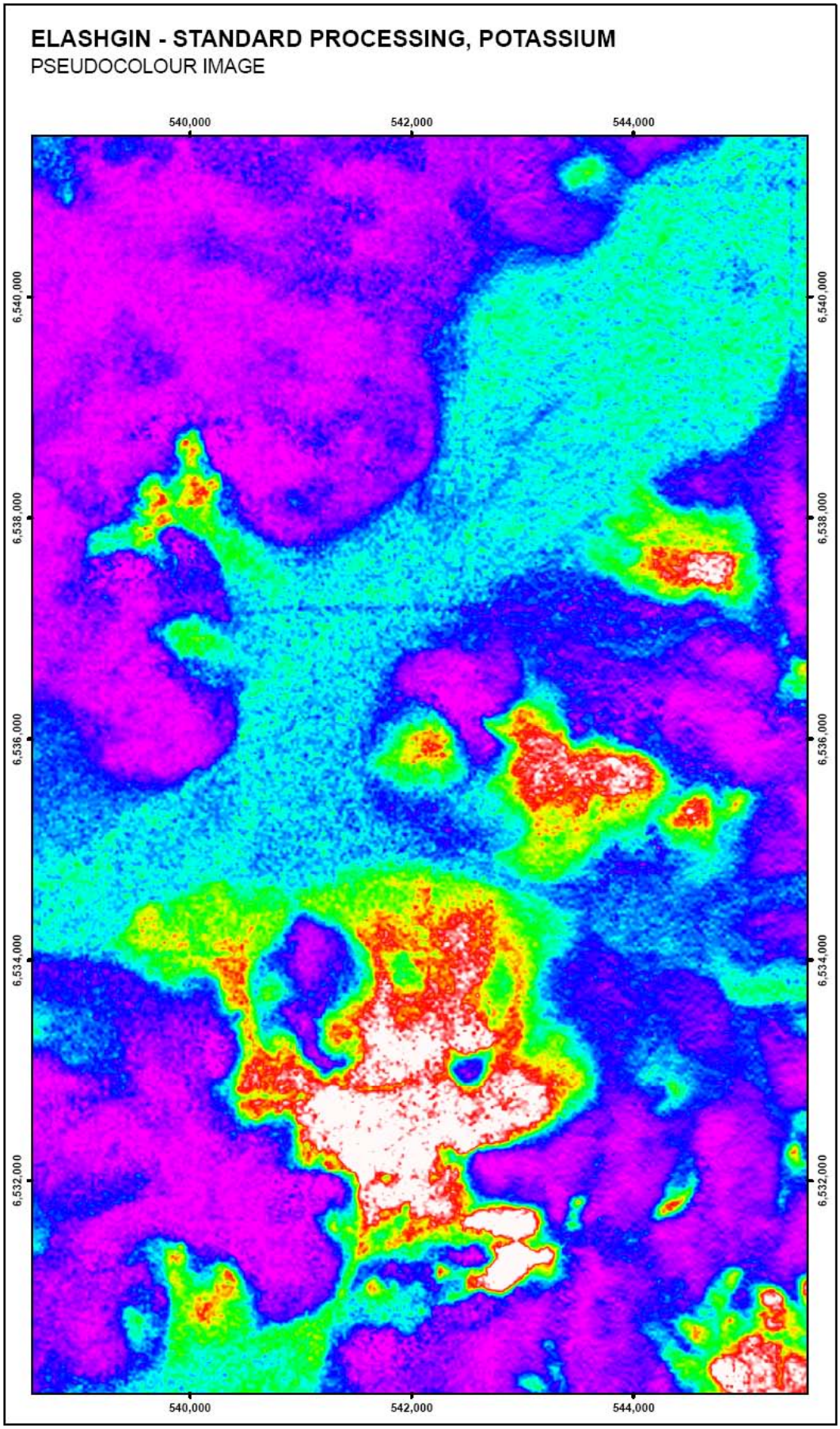


**Figure C.2.4. Potassium standard processed pseudocolour image, Elashgin.**

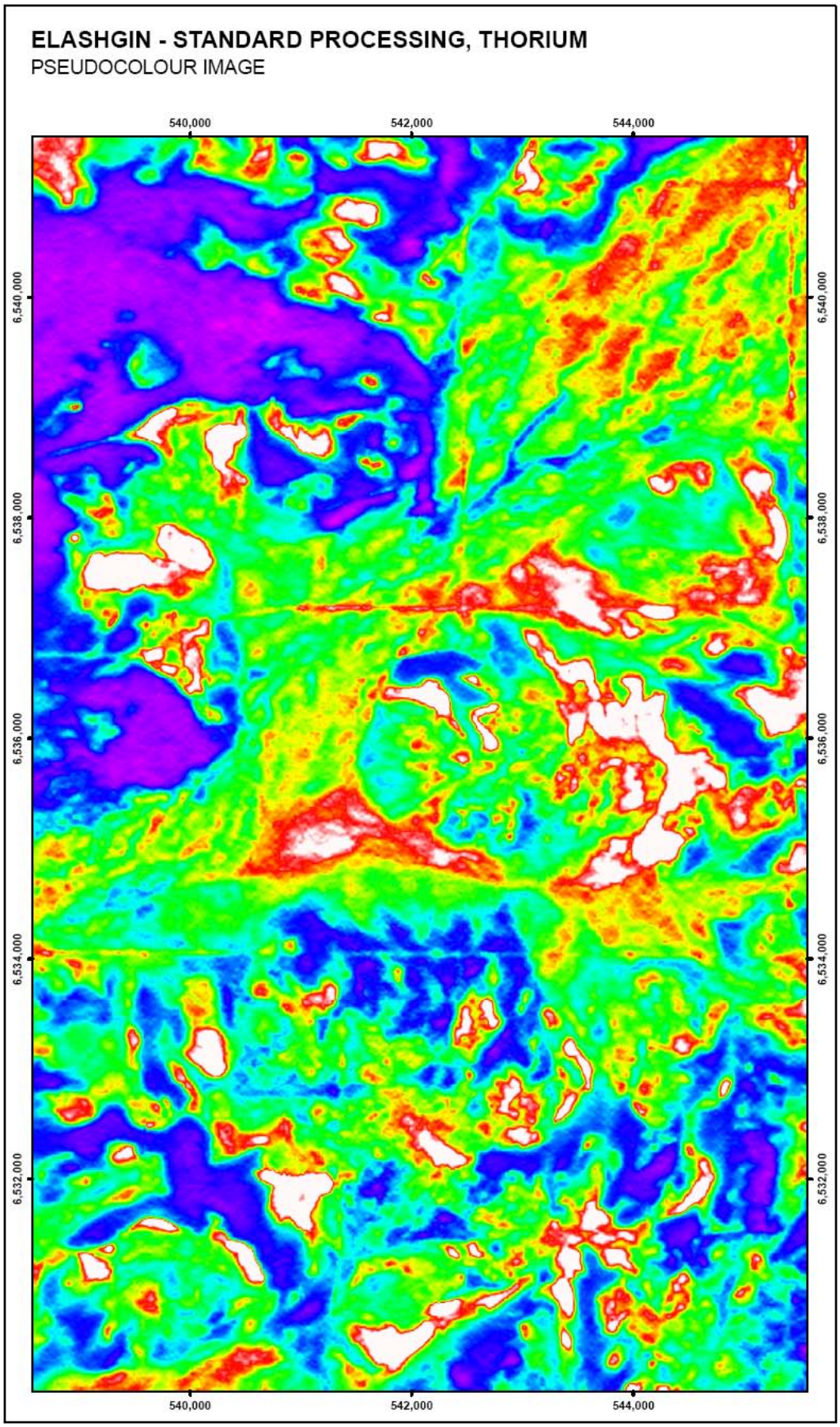


**Figure C.2.5. Thorium standard processed pseudocolour image, Elashgin.**

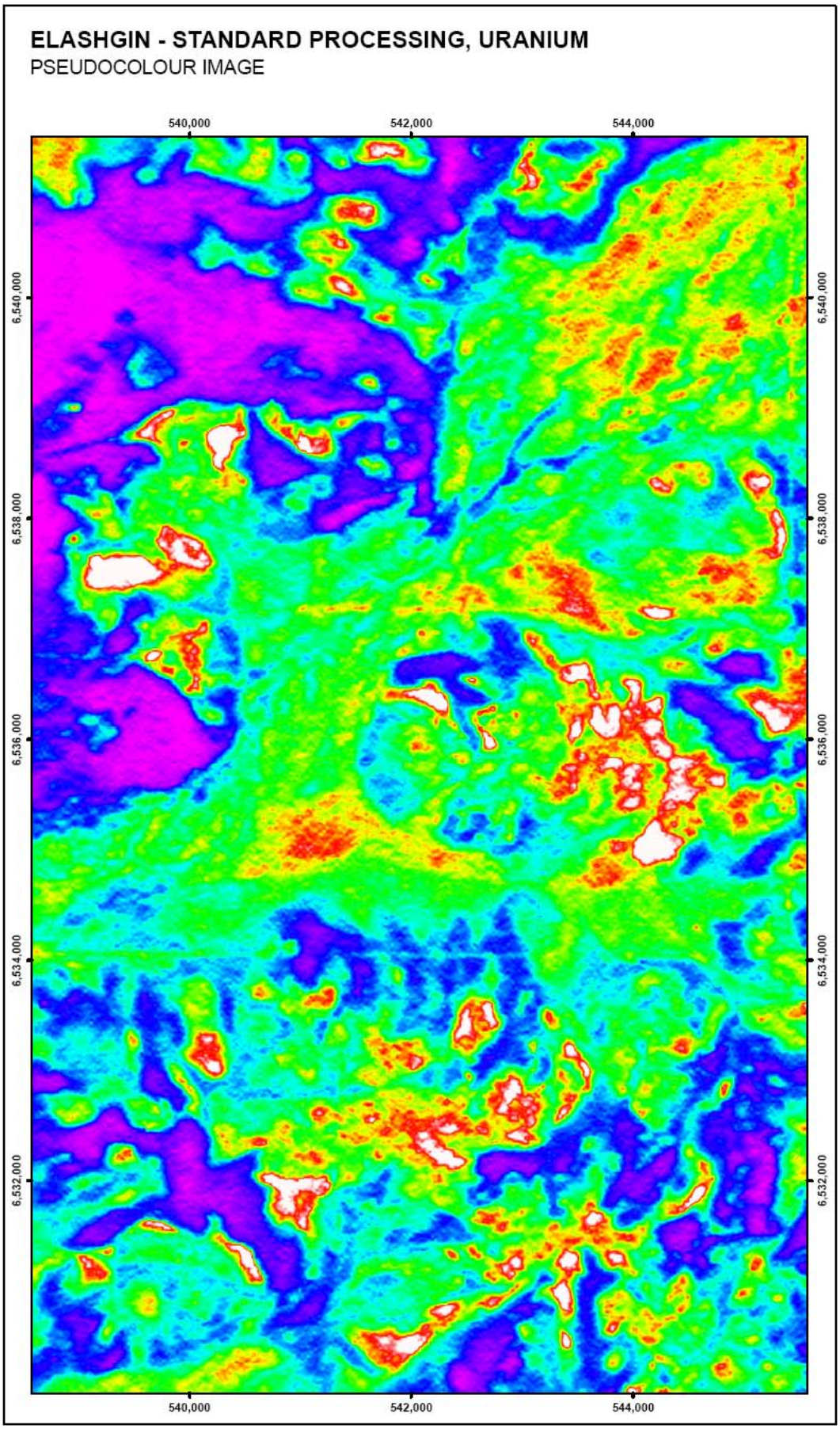


**Figure C.2.6. Uranium standard processed pseudocolour image, Elashgin.**

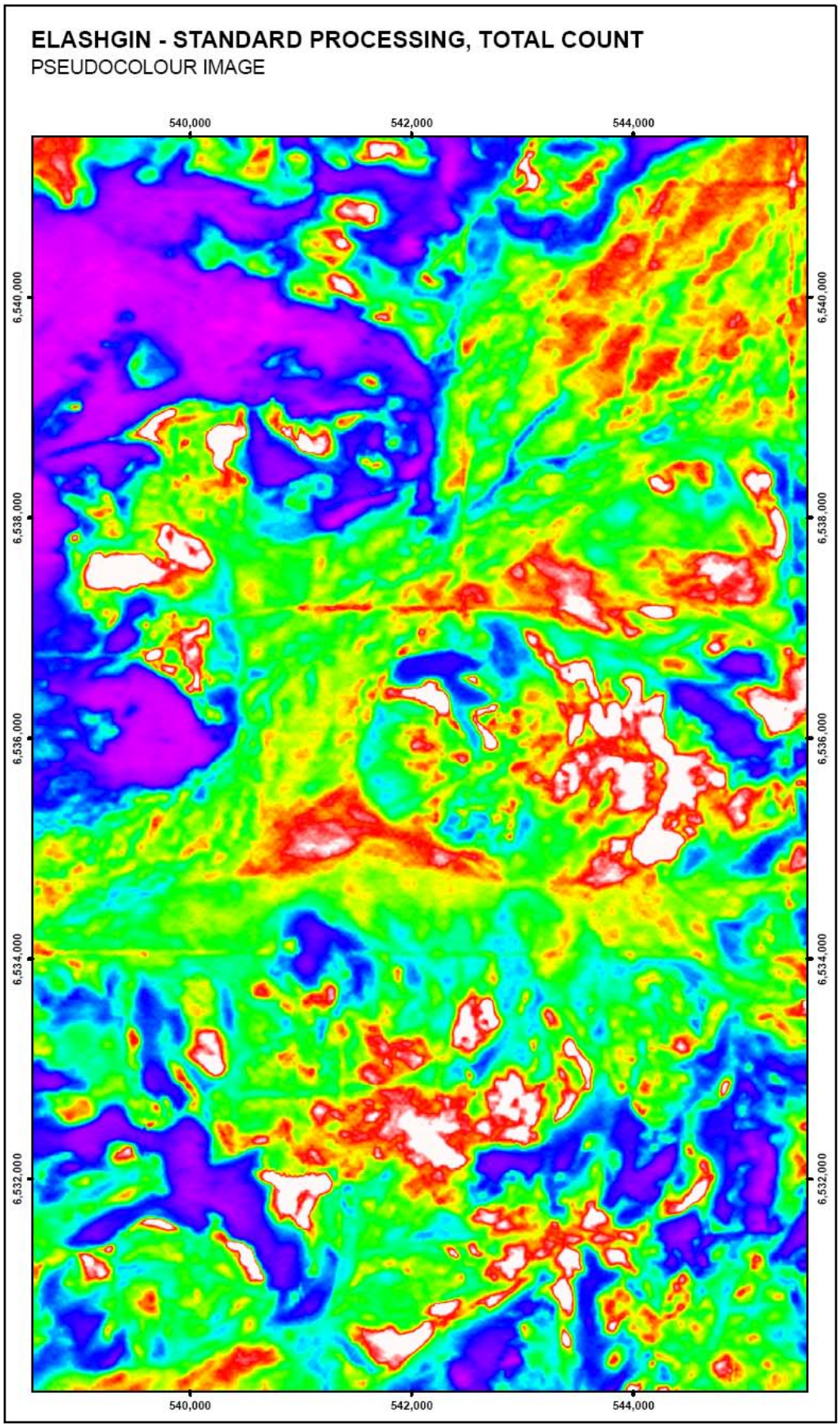


**Figure C.2.7. Total count standard processed pseudocolour image, Elashgin.**

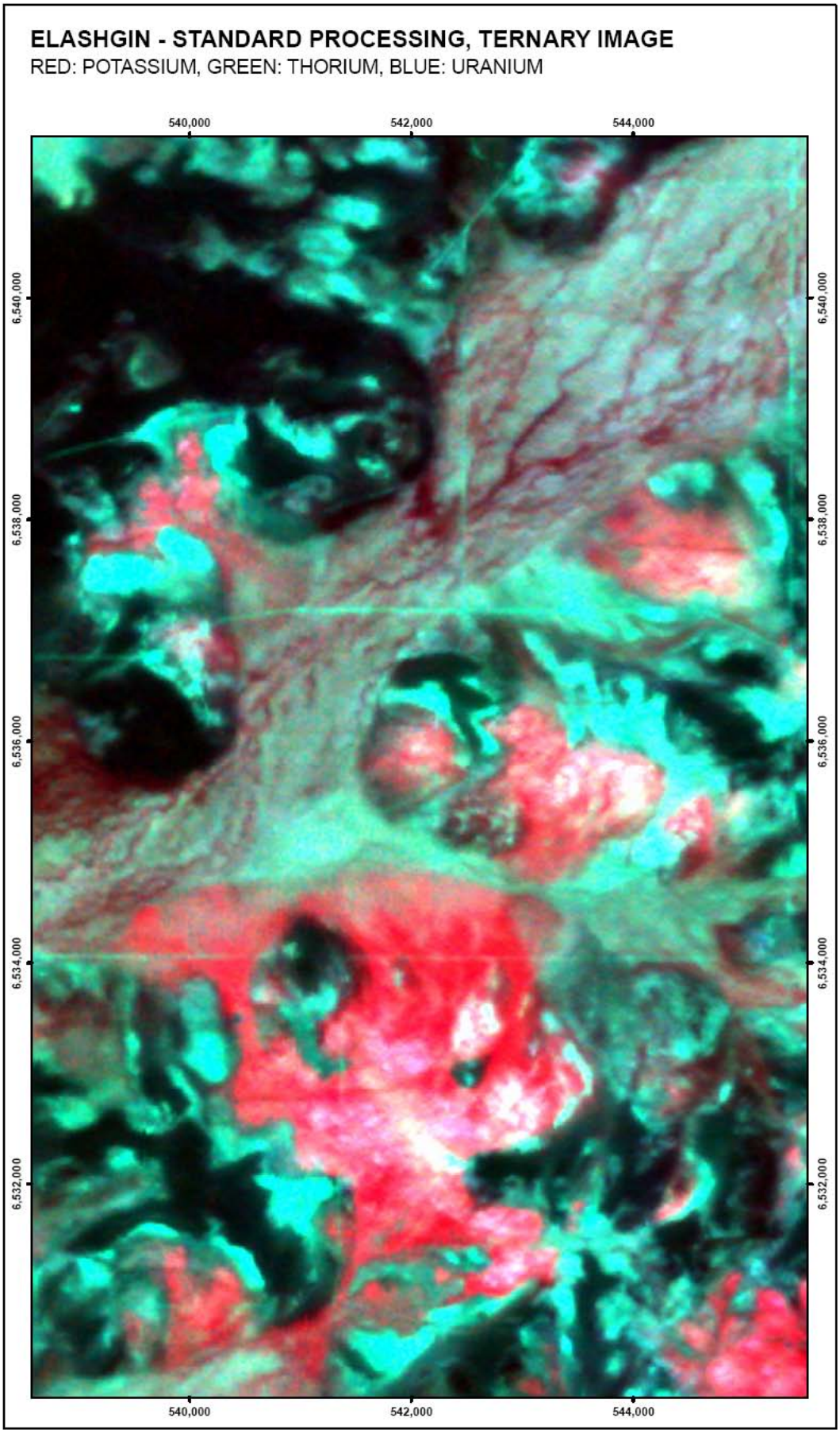


**Figure C.2.8. Ternary standard processed pseudocolour image, Elashgin.**

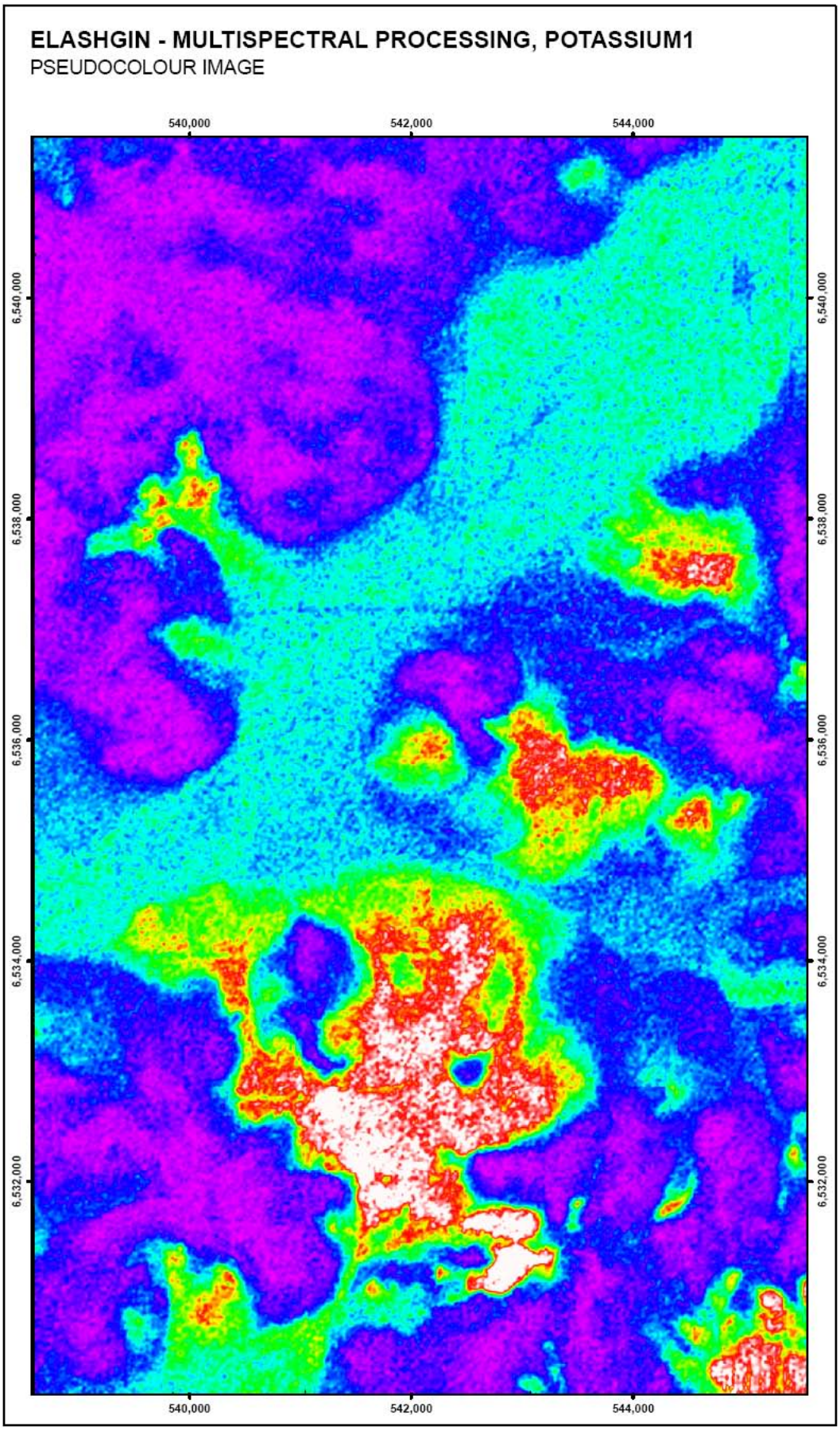


**Figure C.2.9. Potassium 1 multispectral processed, NASVD spectral smoothing, pseudocolour image, Elashgin.**

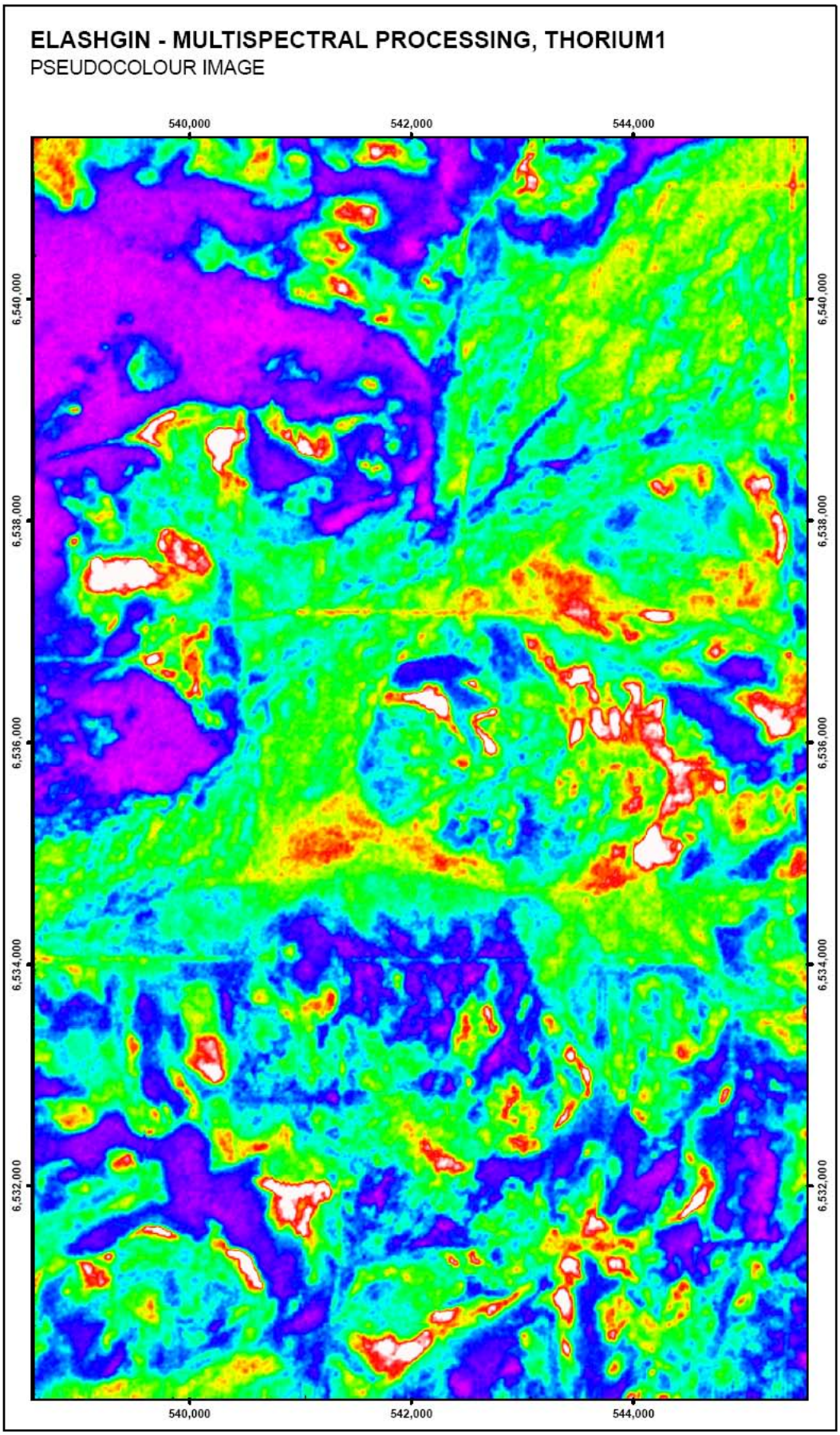


**Figure C.2.10. Thorium 1 multispectral processed, NASVD spectral smoothing, pseudocolour image, Elashgin.**

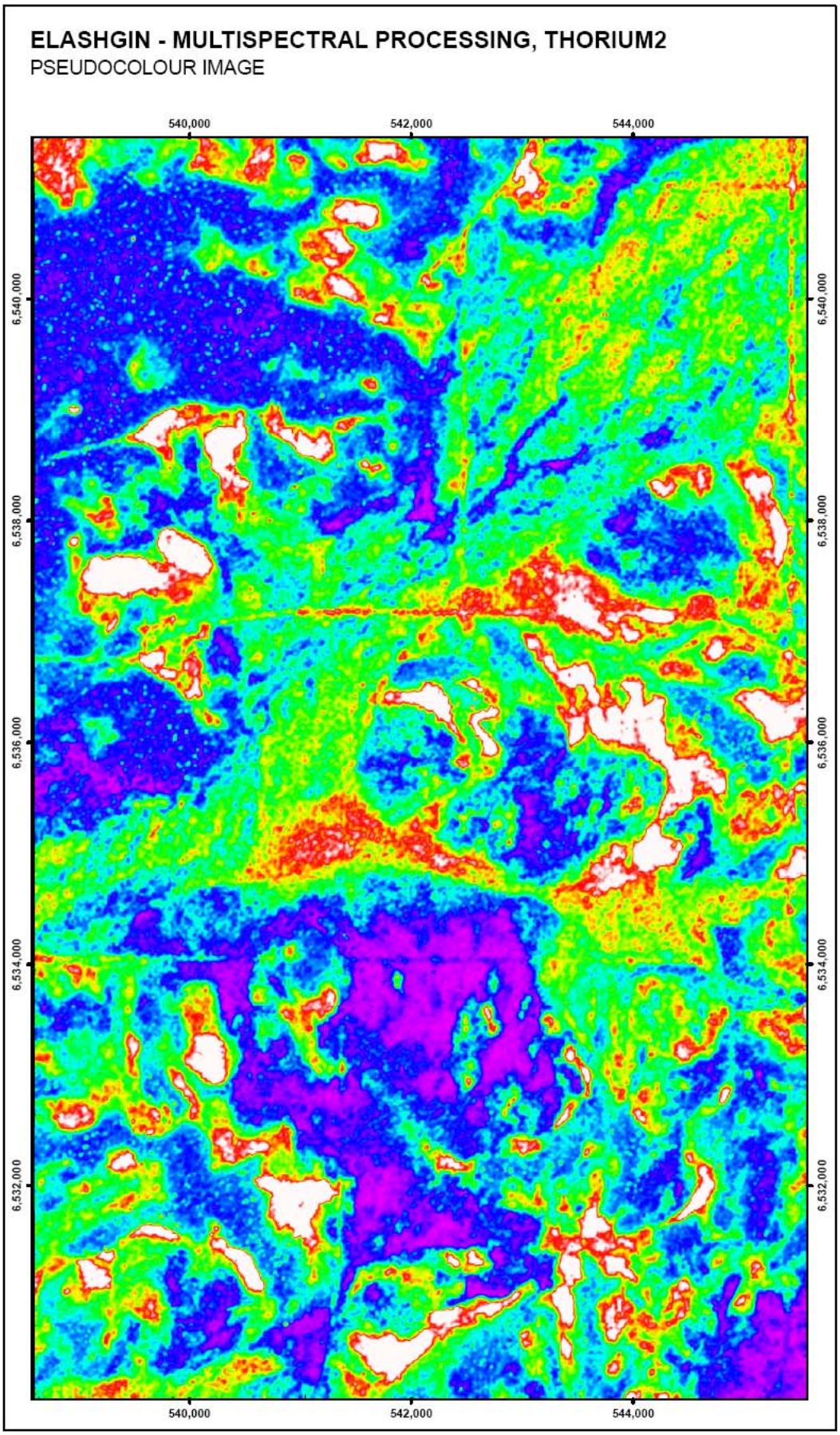


**Figure C.2.11. Thorium 2 multispectral processed, NASVD spectral smoothing, pseudocolour image, Elashgin.**

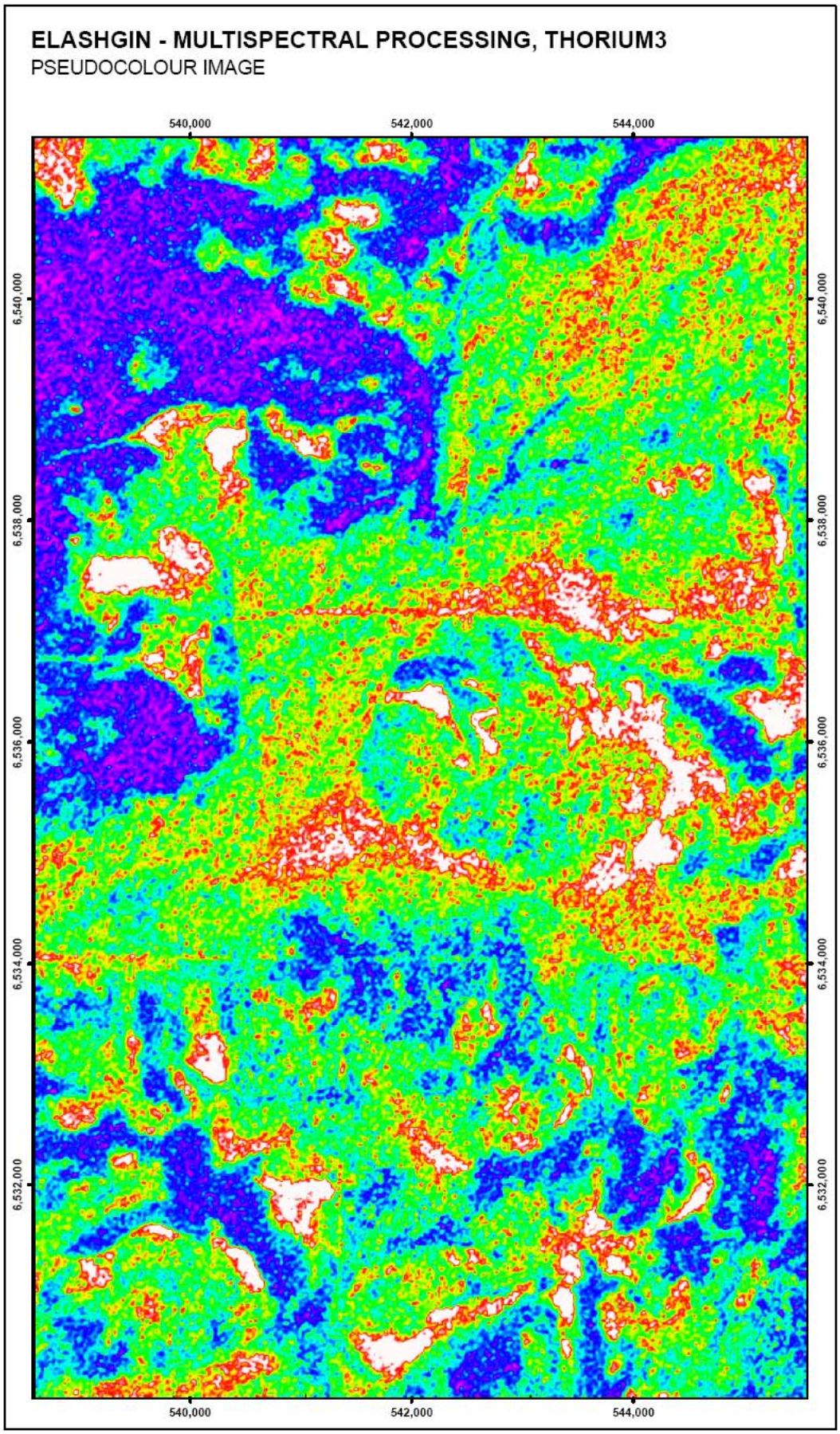


**Figure C.2.12. Thorium 3 multispectral processed, NASVD spectral smoothing, pseudocolour image, Elashgin.**

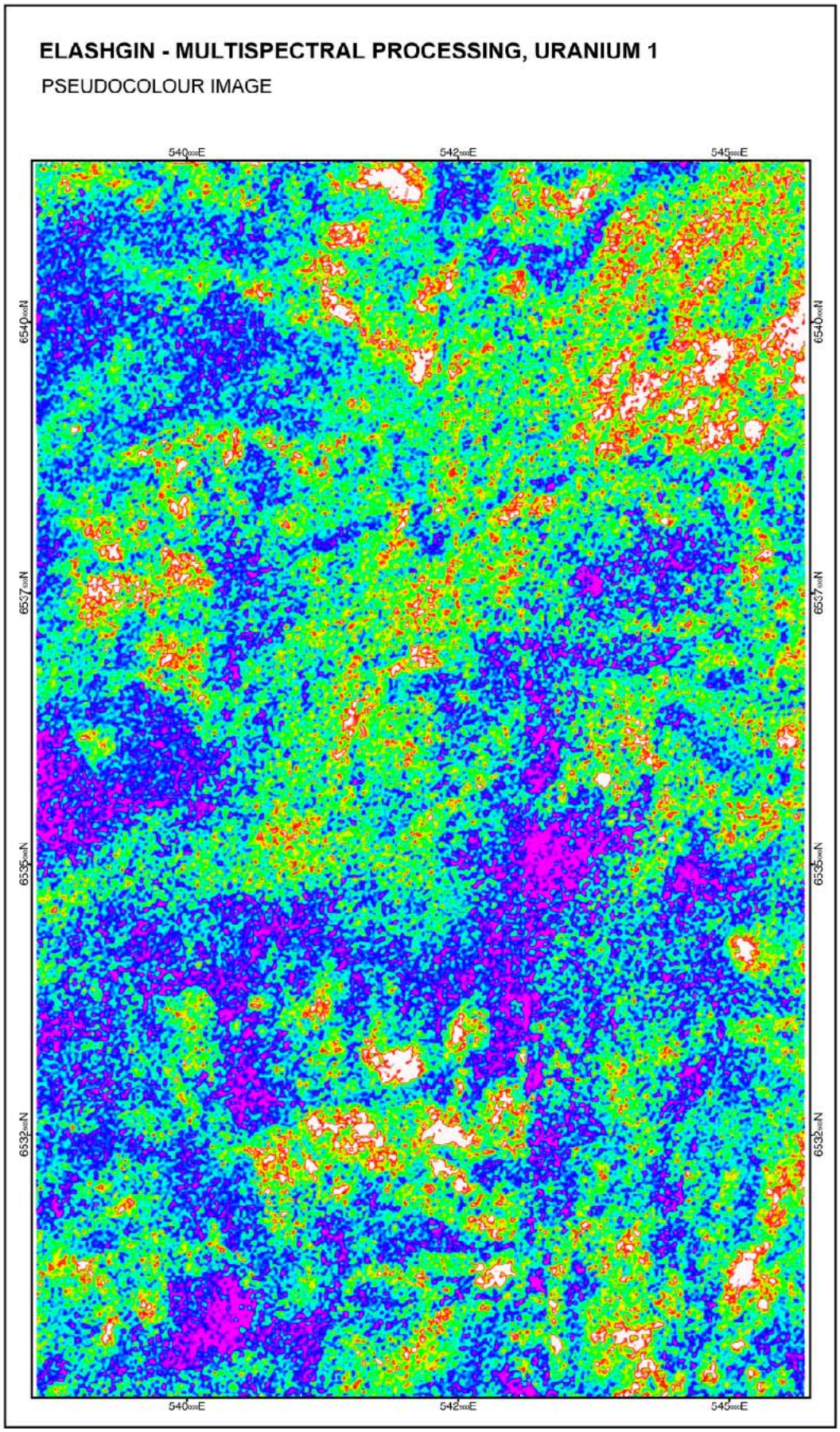


**Figure C.2.13. Uranium 1 multispectral processed, NASVD spectral smoothing, pseudocolour image, Elashgin.**

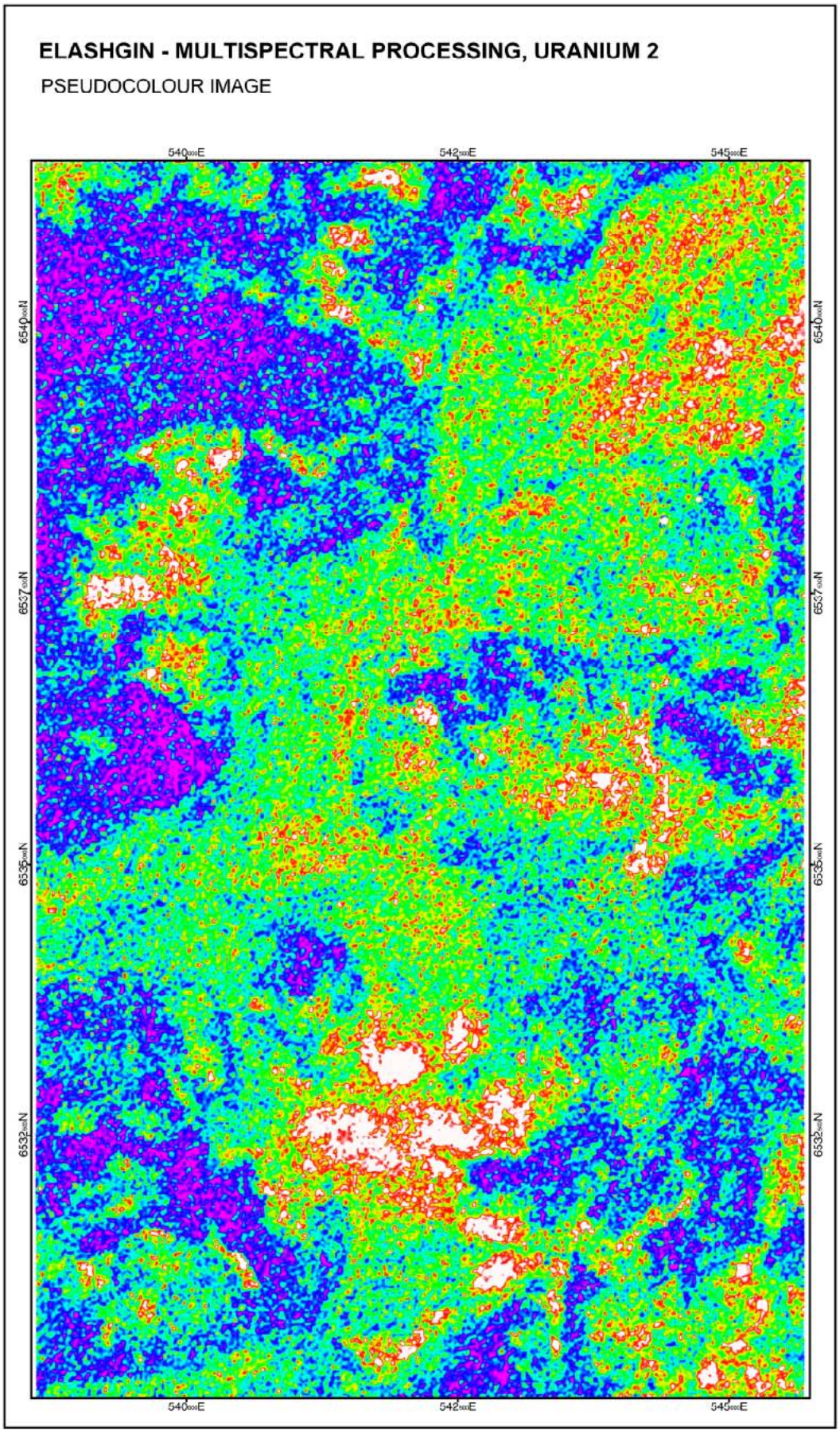


**Figure C.2.14. Uranium 2 multispectral processed, NASVD spectral smoothing, pseudocolour image, Elashgin.**

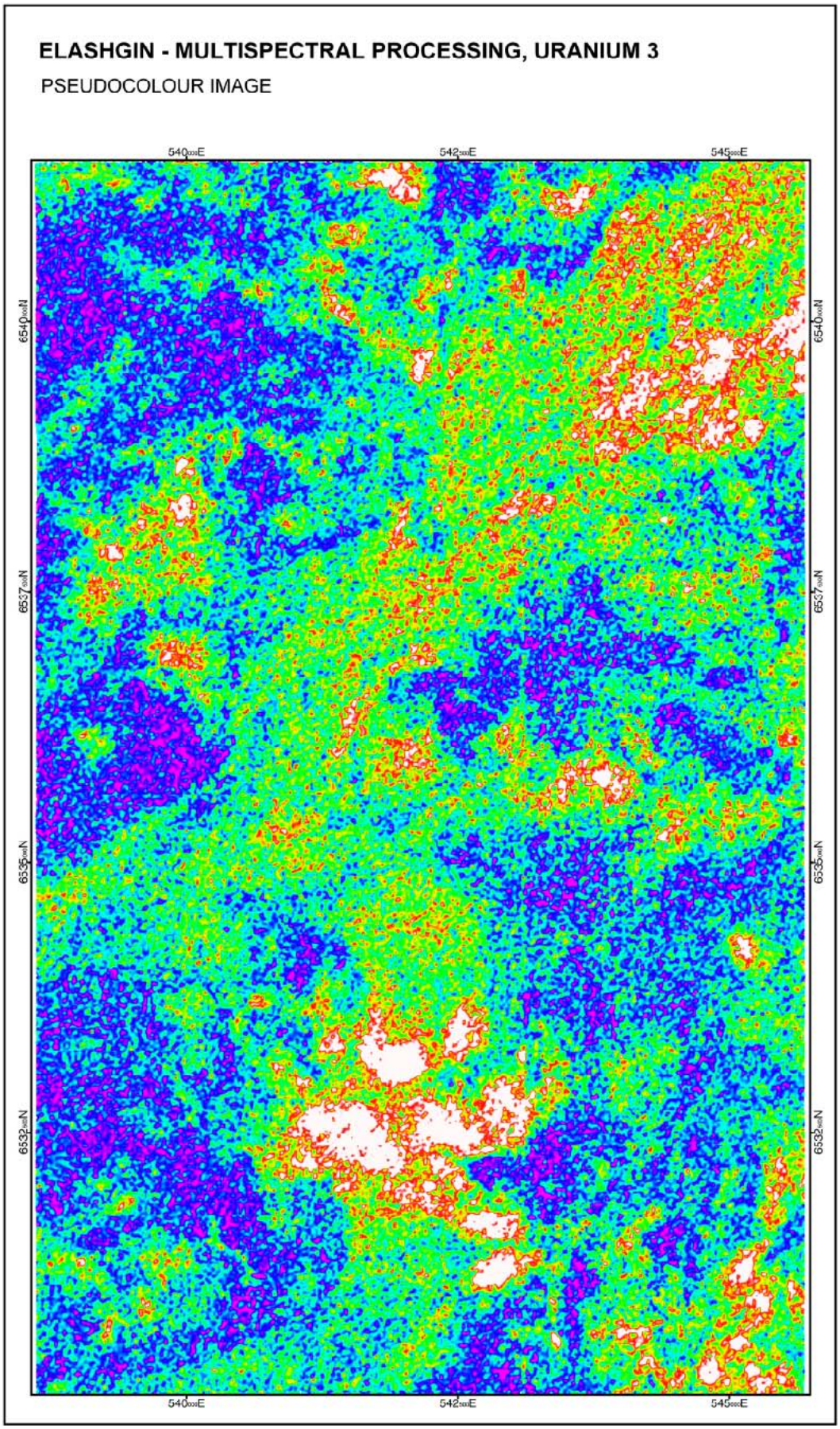


**Figure C.2.15. Uranium 3 multispectral processed, NASVD spectral smoothing, pseudocolour image, Elashgin.**

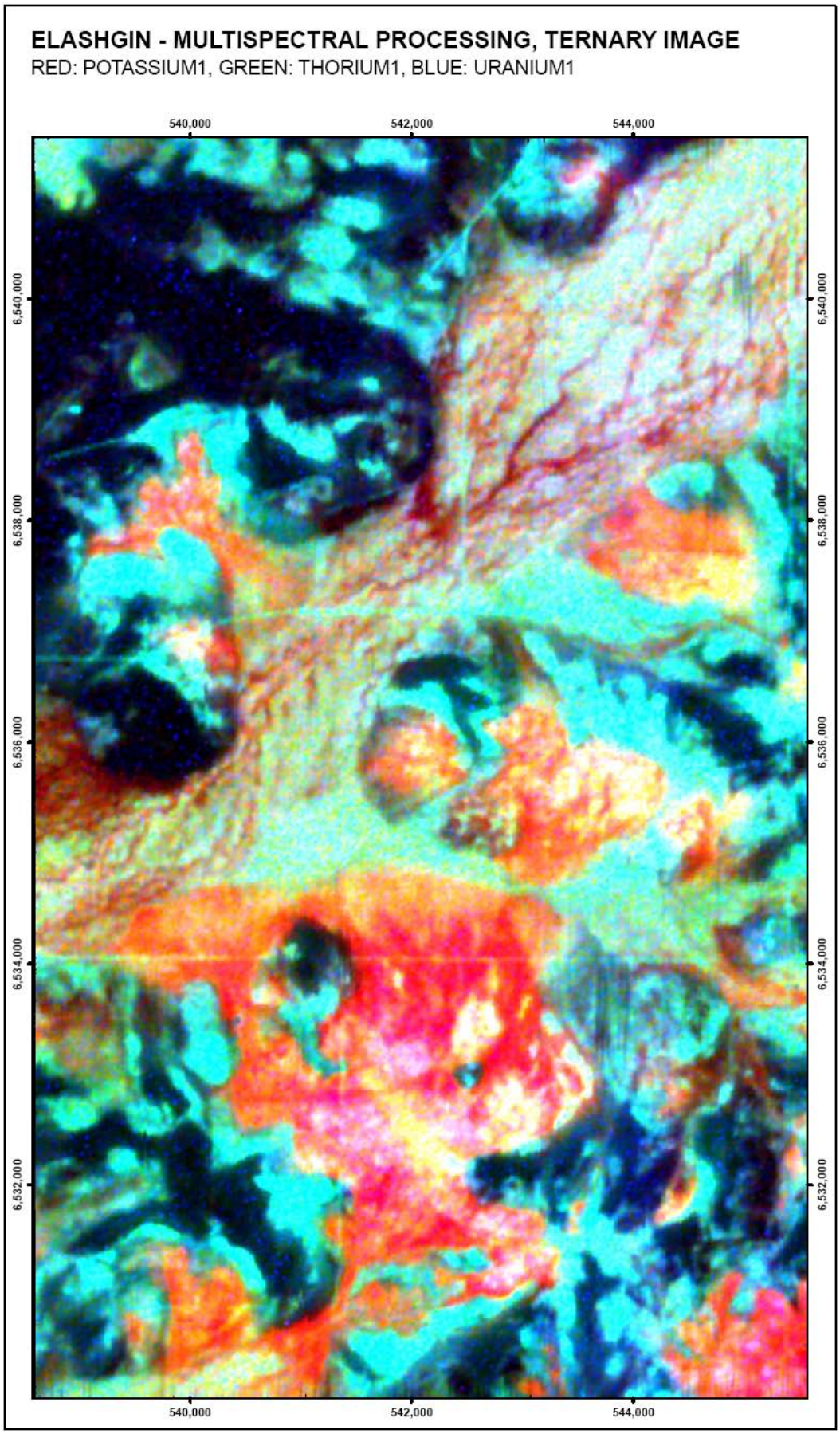


**Figure C.2.16. Ternary (linear stretch) multispectral processed, NASVD spectral smoothing, ternary image, Elashgin.**


**Figure C.2.17. Ternary (histogram stretch) multispectral processed, NASVD spectral smoothing, ternary image, Elashgin.**

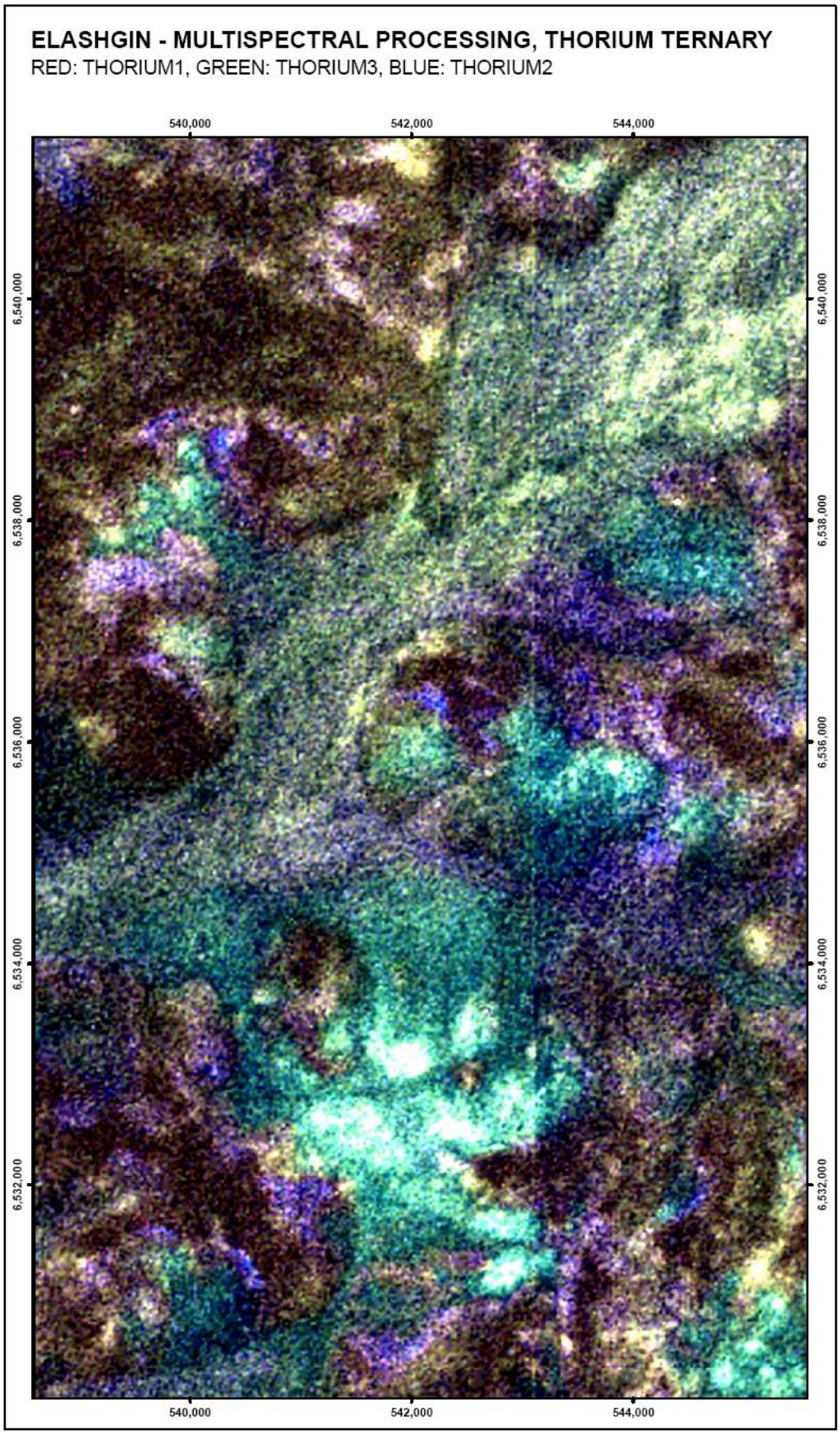


**Figure C.2.18. Uranium ternary multispectral processed, NASVD spectral smoothing, ternary image, Elashgin.**


**Figure C.2.19. Thorium ternary multispectral processed, NASVD spectral smoothing, ternary image, Elashgin.**

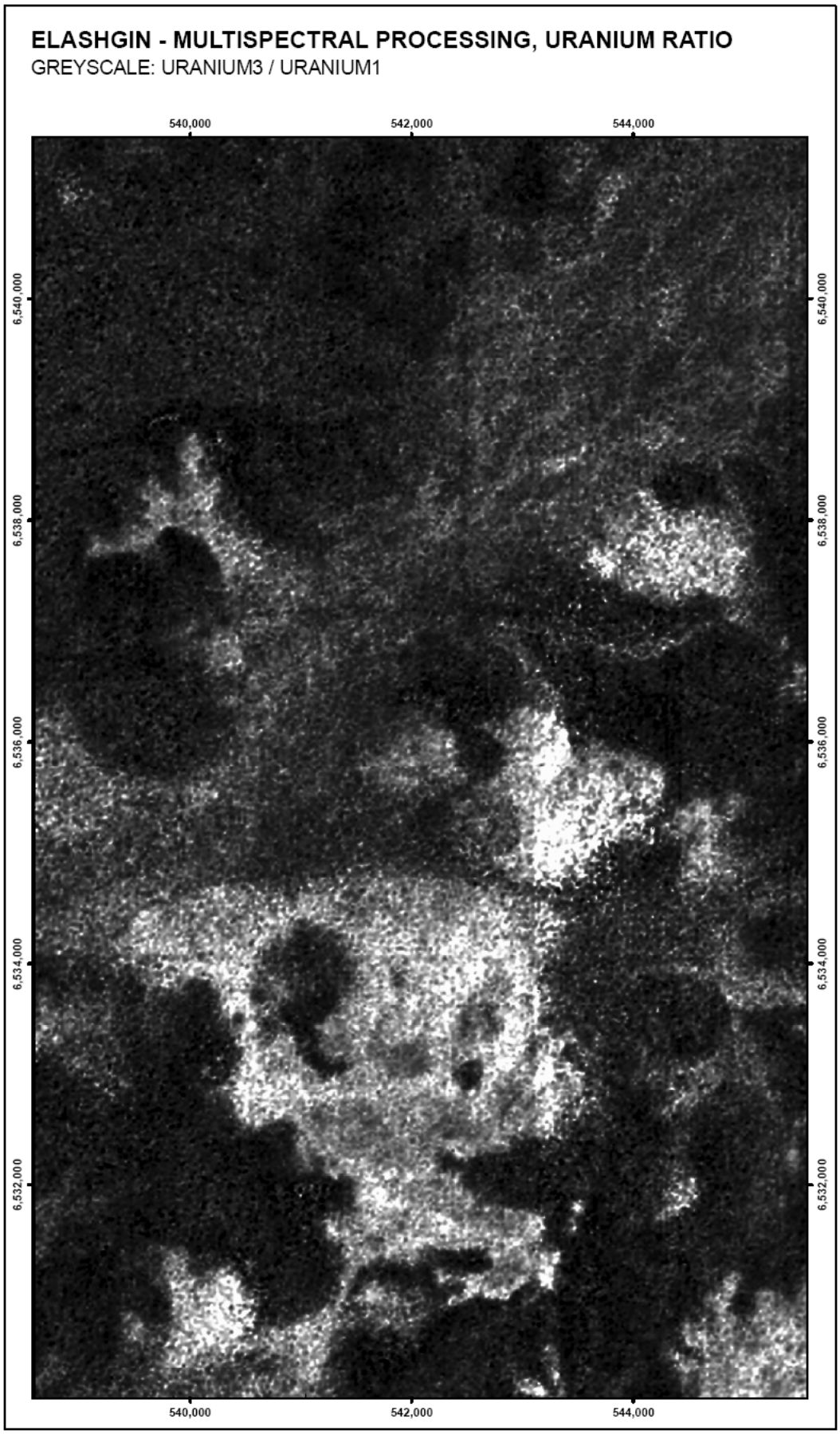


**Figure C.2.20. Uranium ratio multispectral processed, NASVD spectral smoothing, greyscale image, Elashgin.**

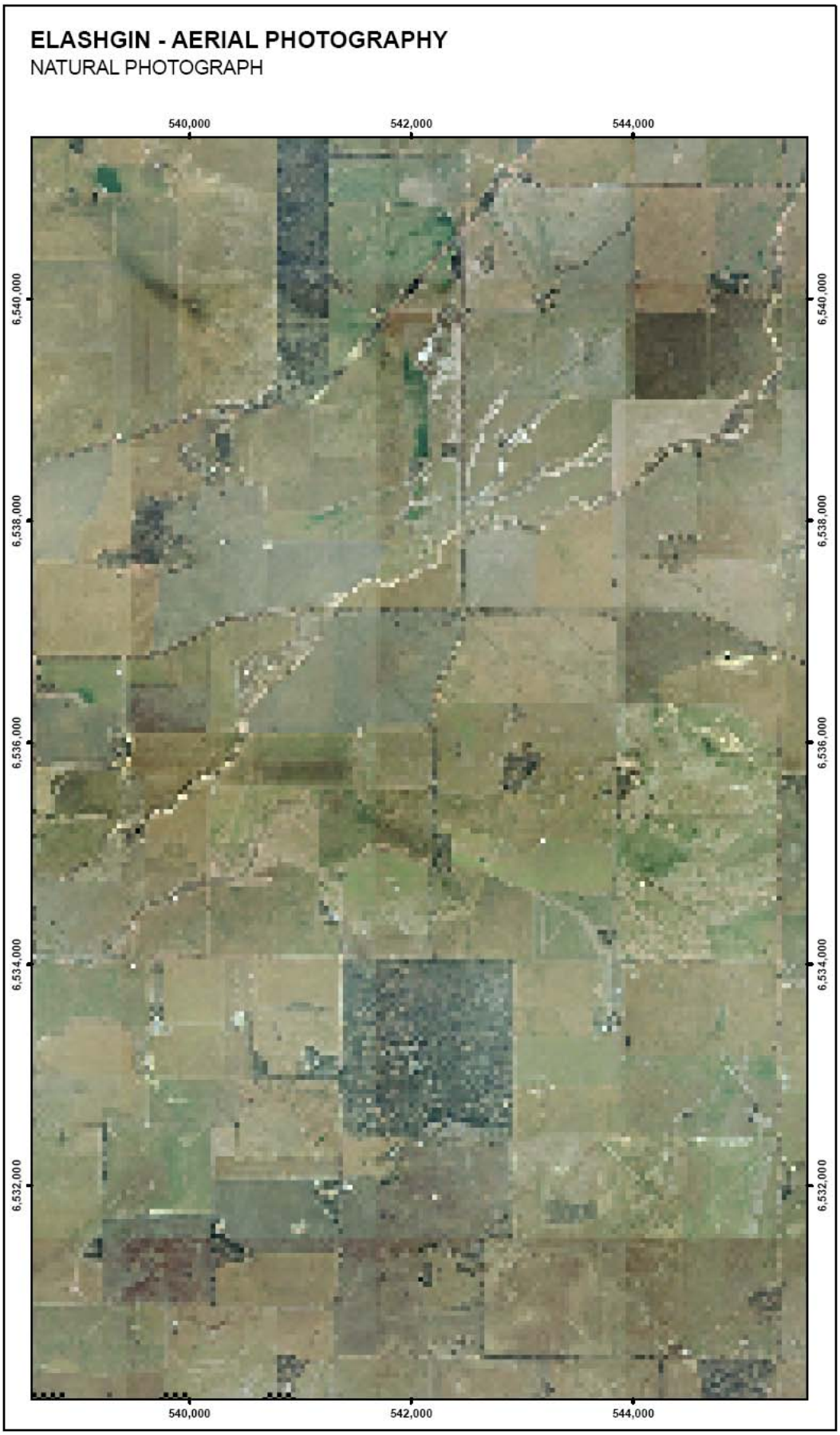


**Figure C.2.21. Natural aerial photo, Elashgin.**

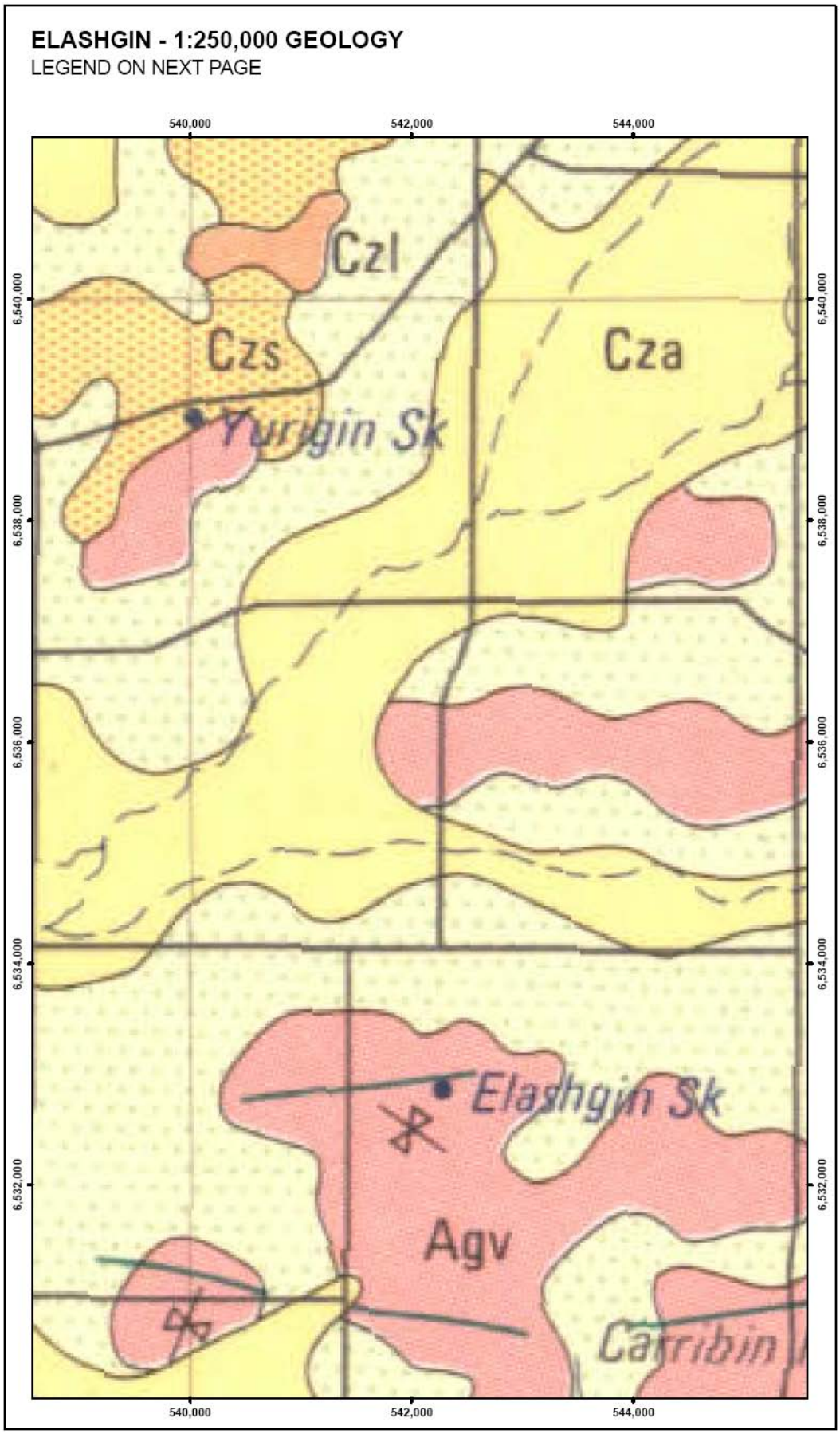


**Figure C.2.22. 1:250,000 geology of Elashgin (from Chin, 1986).**

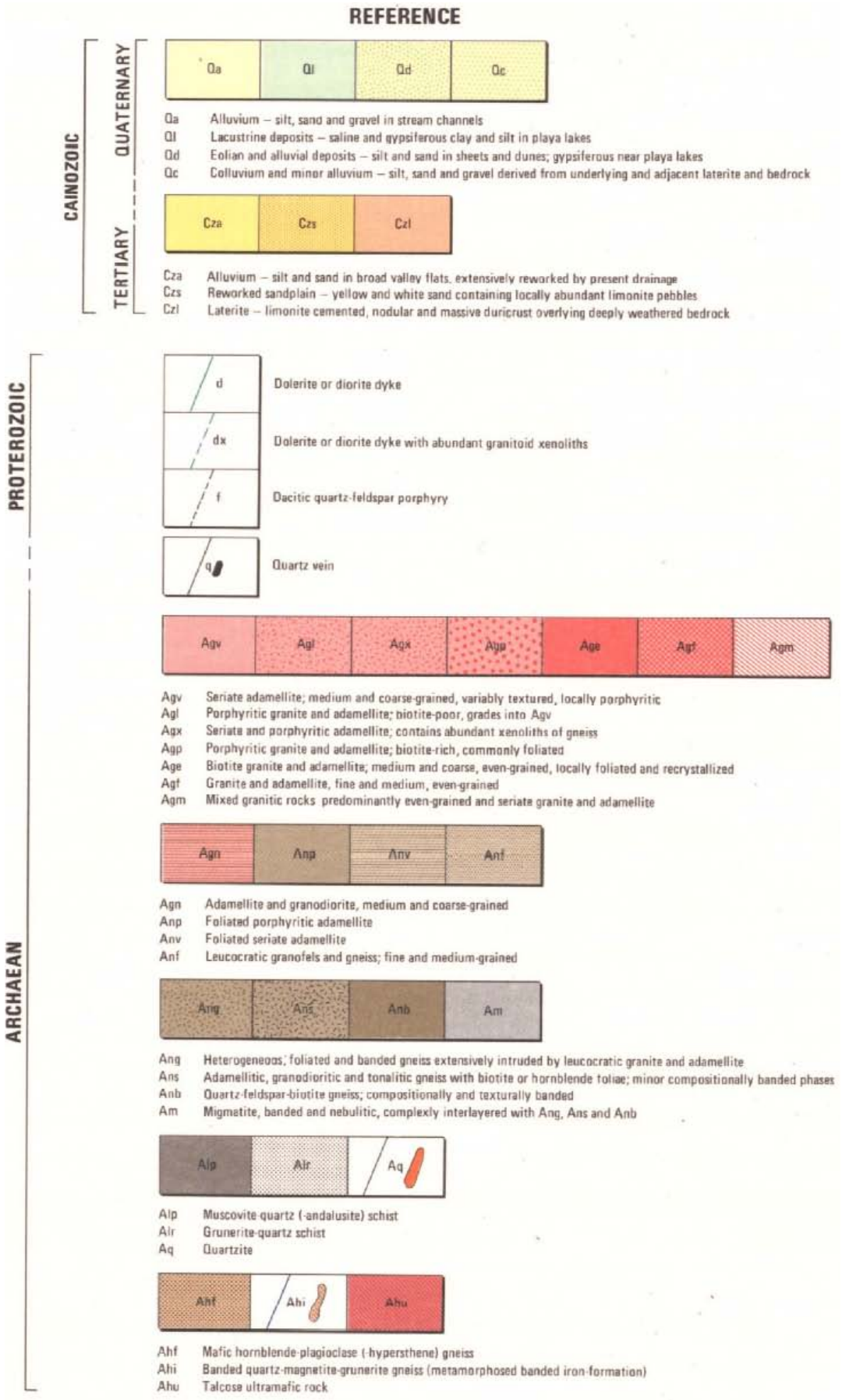


**Figure C.2.22 cont'd. 1:250,000 geology legend for Elashgin (from Chin, 1986).**

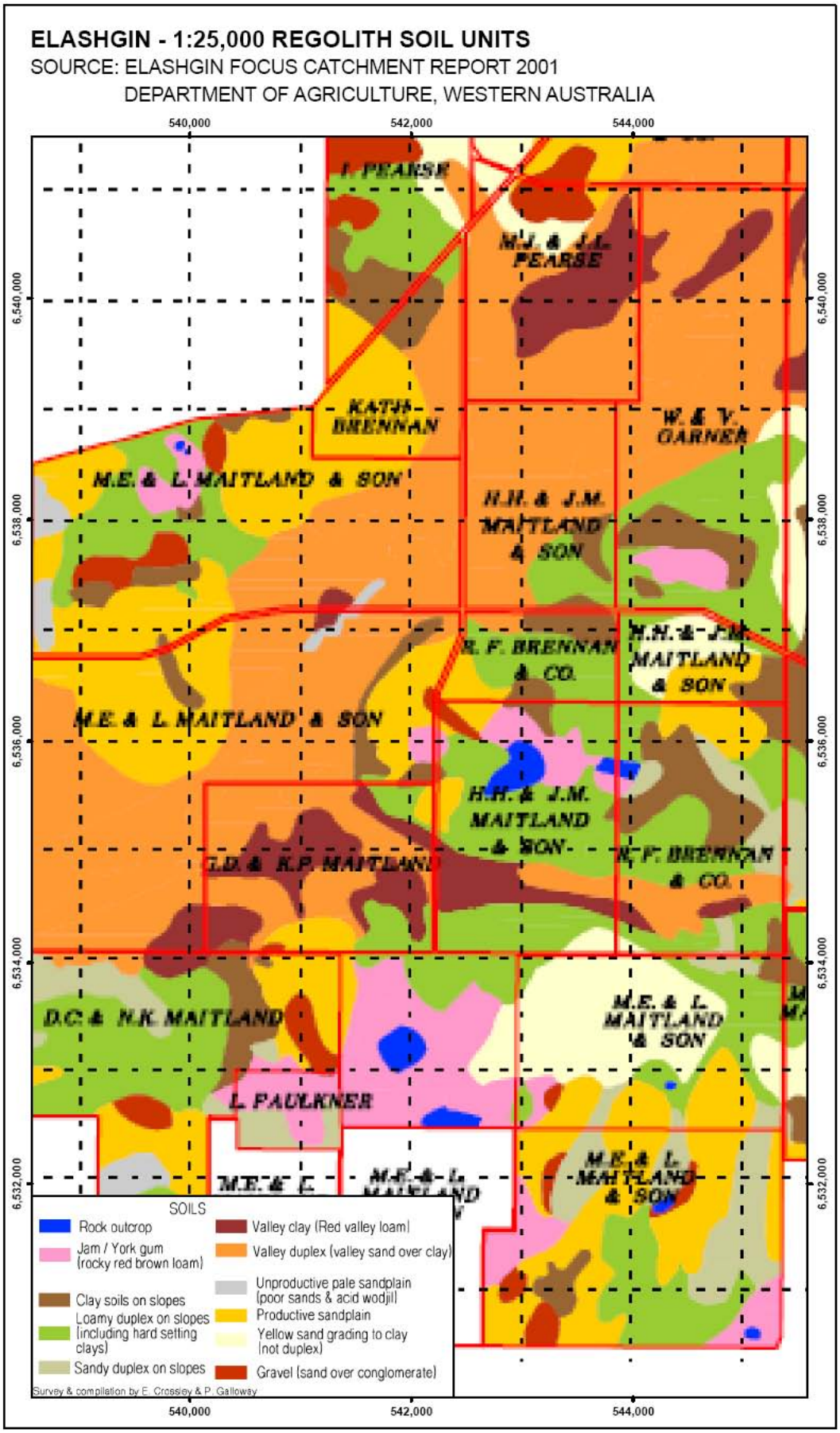


**Figure C.2.23. Existing soil/regolith map, Elashgin (from Cooper *et al.*, 2001).**

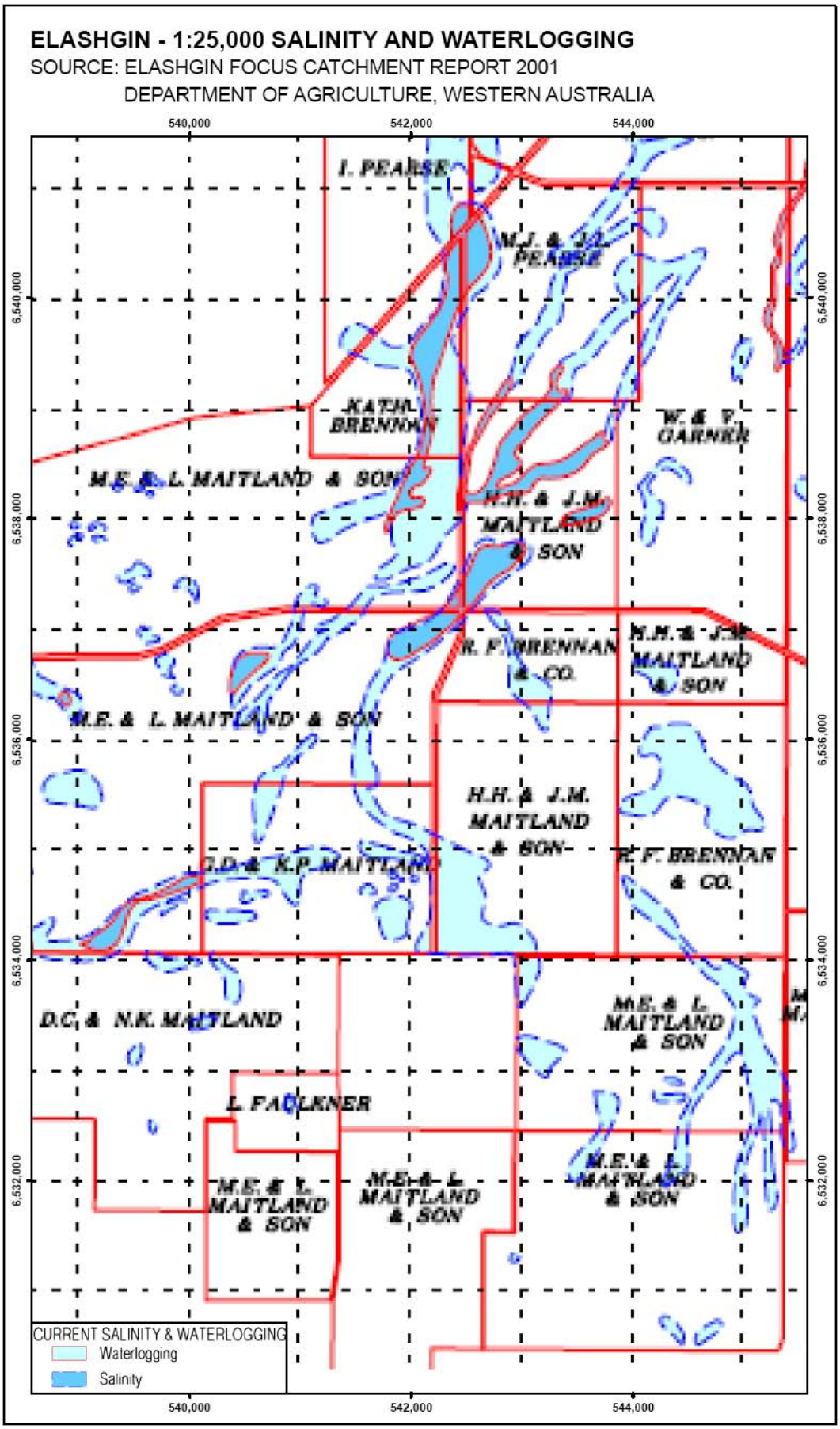


**Figure C.2.24. Existing salinity map, Elashgin (from Cooper *et al.*, 2001).**

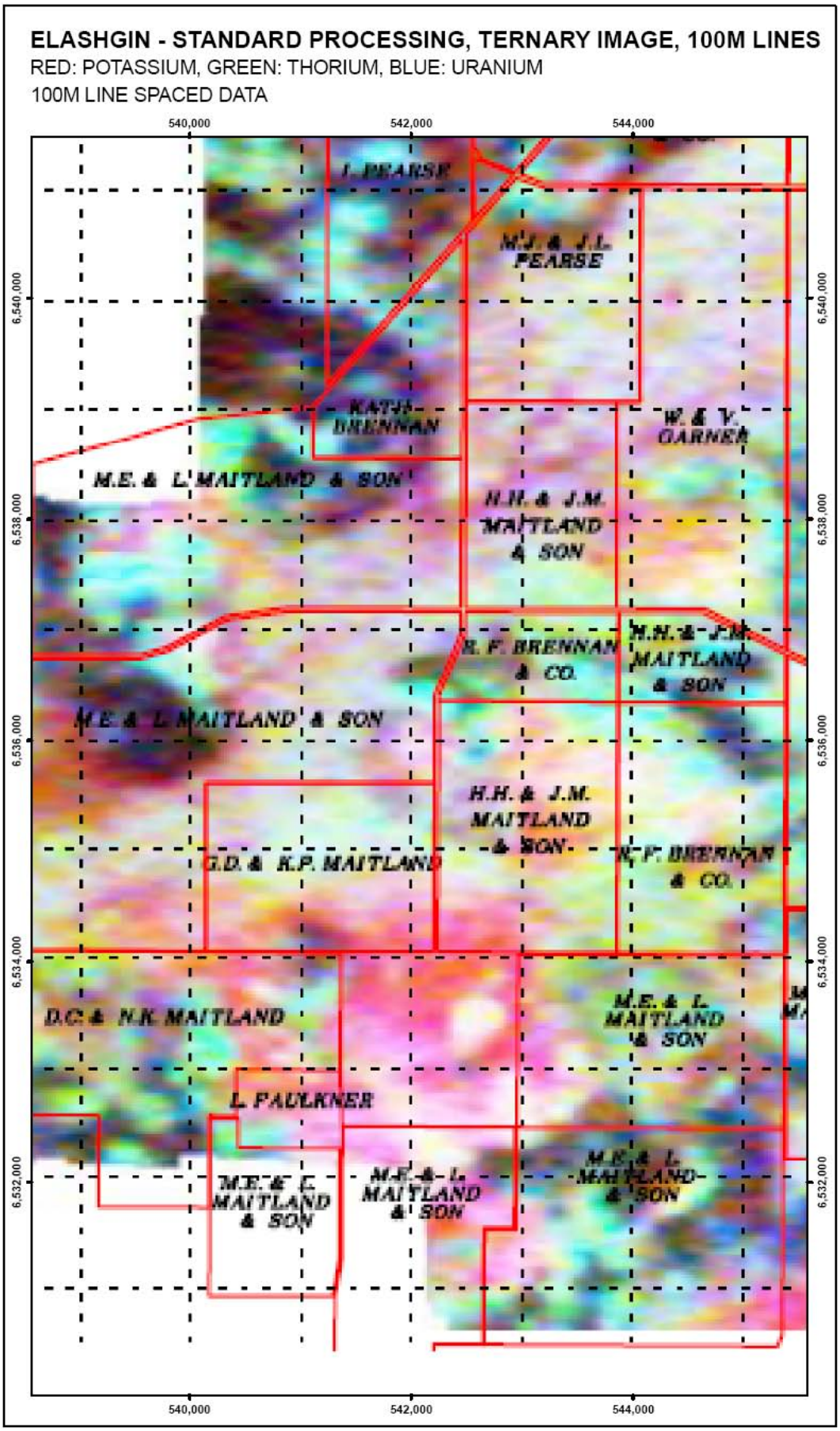


**Figure C.2.25. Lower resolution, 200 m line spaced, ternary radiometric image, Elashgin (from Cooper *et al.*, 2001).**

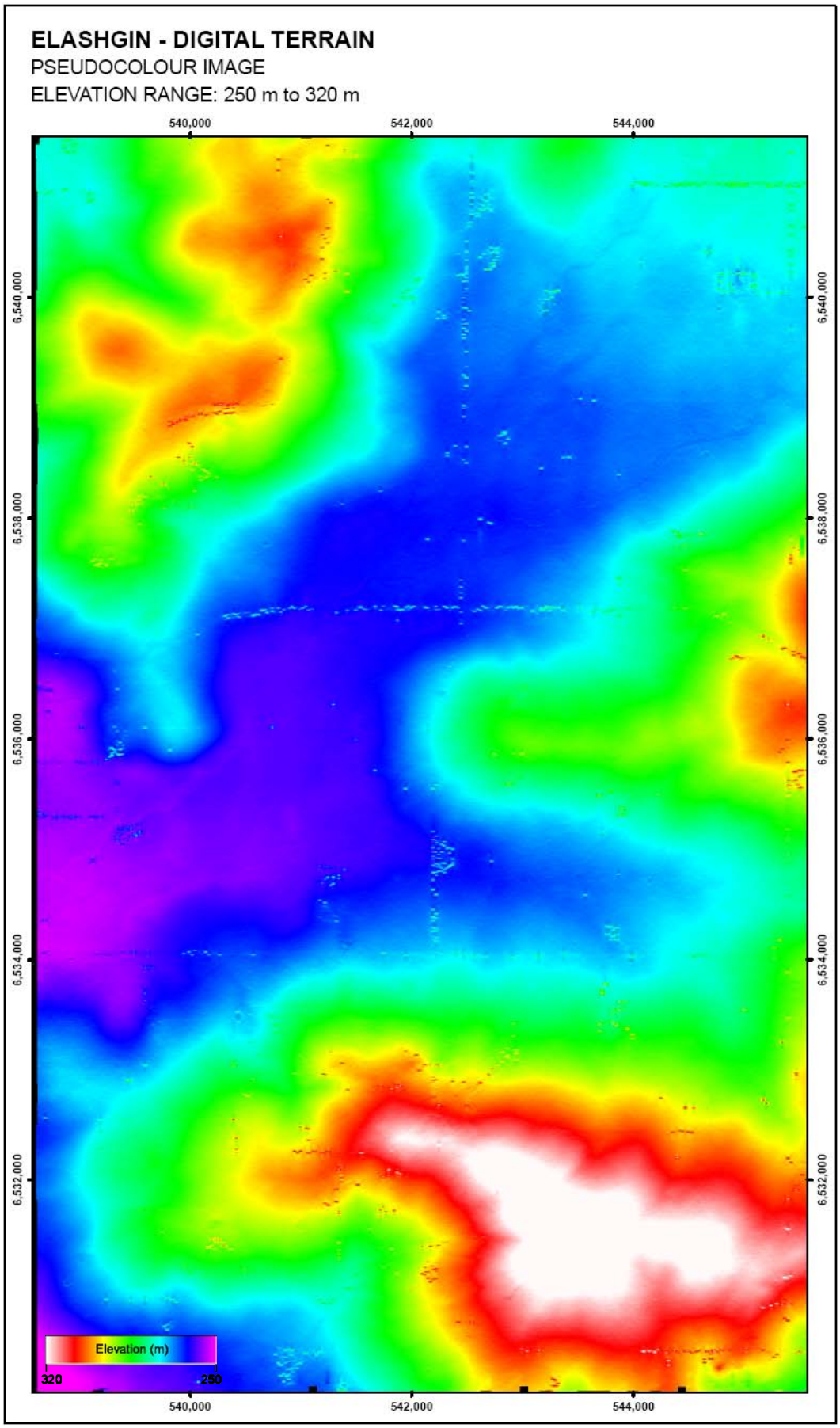


**Figure C.2.26. Digital terrain (elevation) image, Elashgin.**

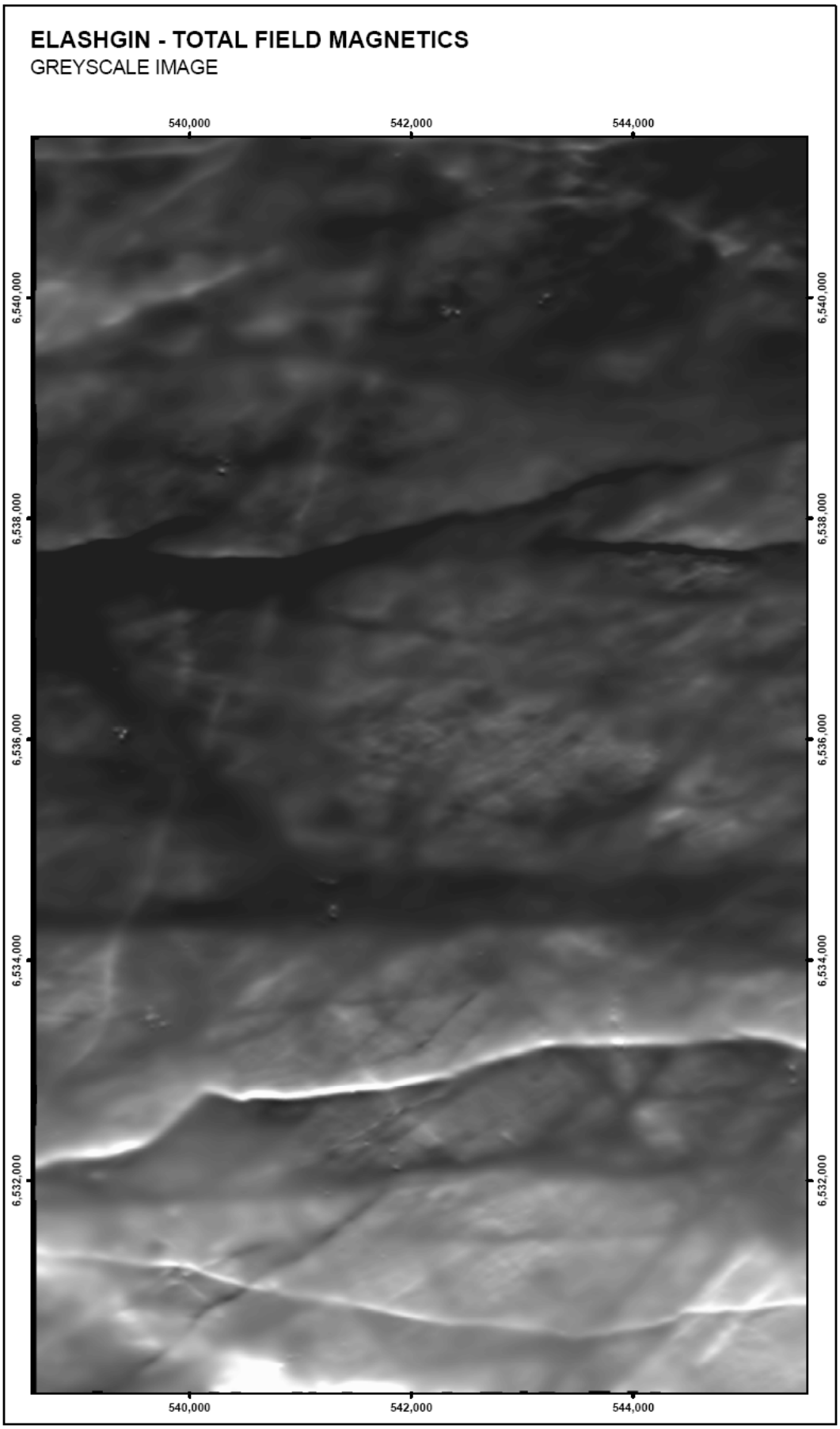


**Figure C.2.27. Airborne magnetic greyscale image, Elashgin.**

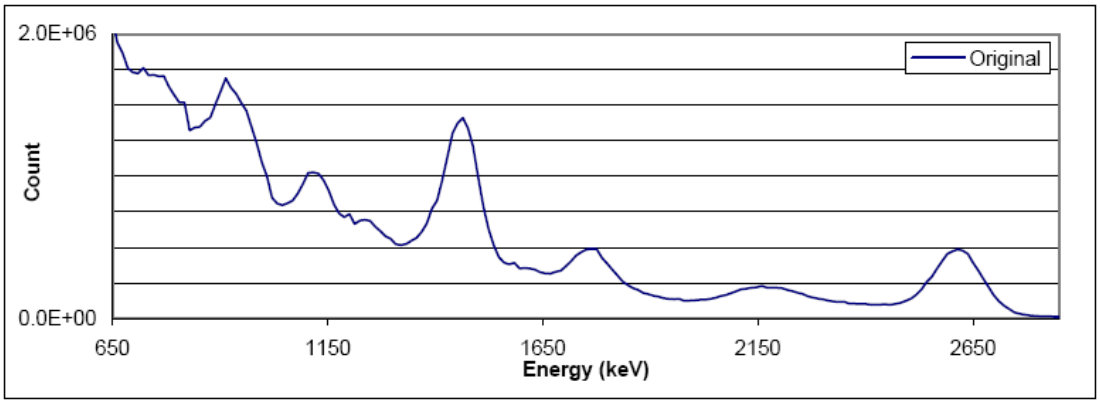


**Figure C.3.1. Average raw spectrum derived from 256-channel data, Moyagee.**

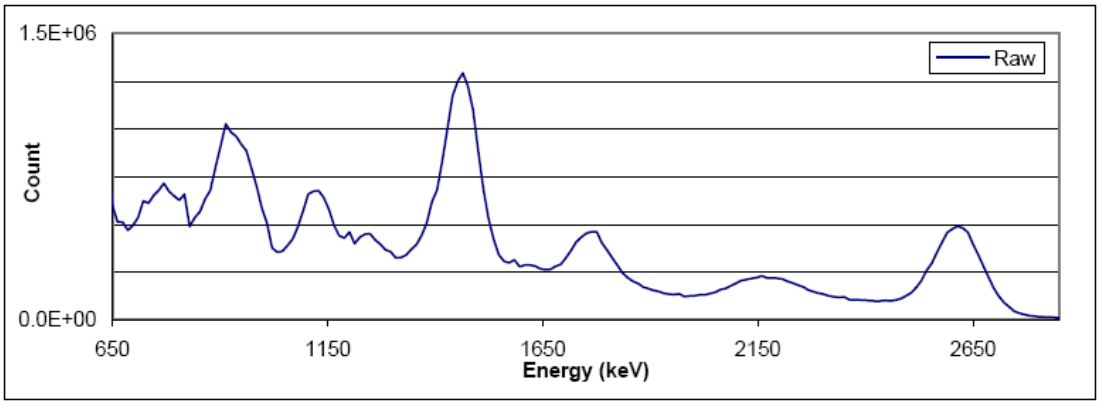


**Figure C.3.2. Average raw spectrum following Compton continuum removal, Moyagee.**

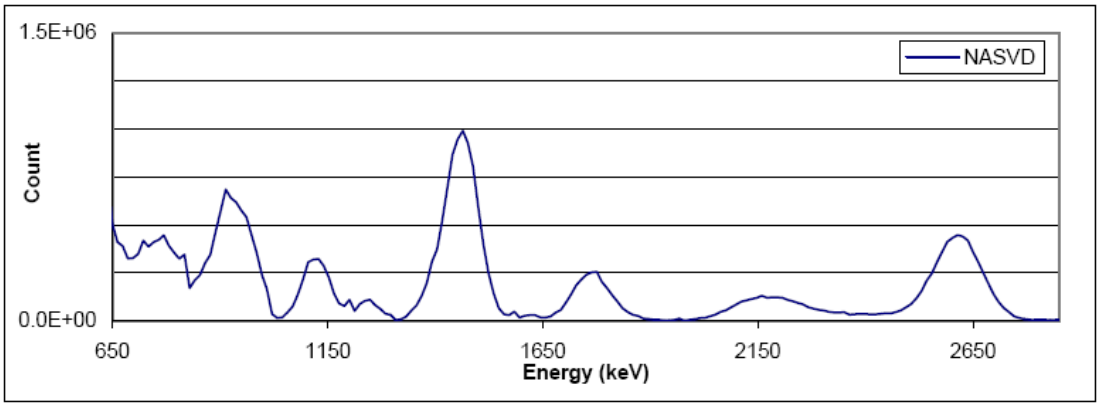


**Figure C.3.3. Average NASVD smoothed spectrum following Compton continuum removal, Moyagee.**

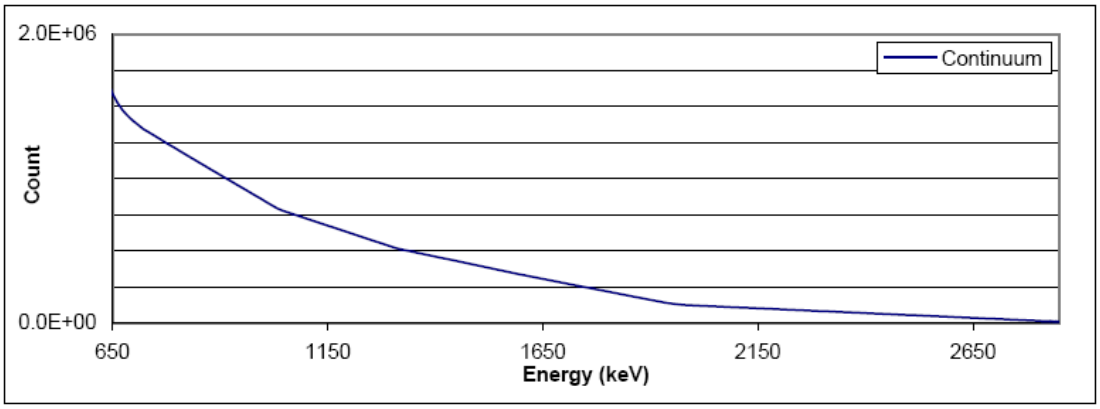


**Figure C.3.4. Average continuum removed from the raw spectrum, Moyagee.**

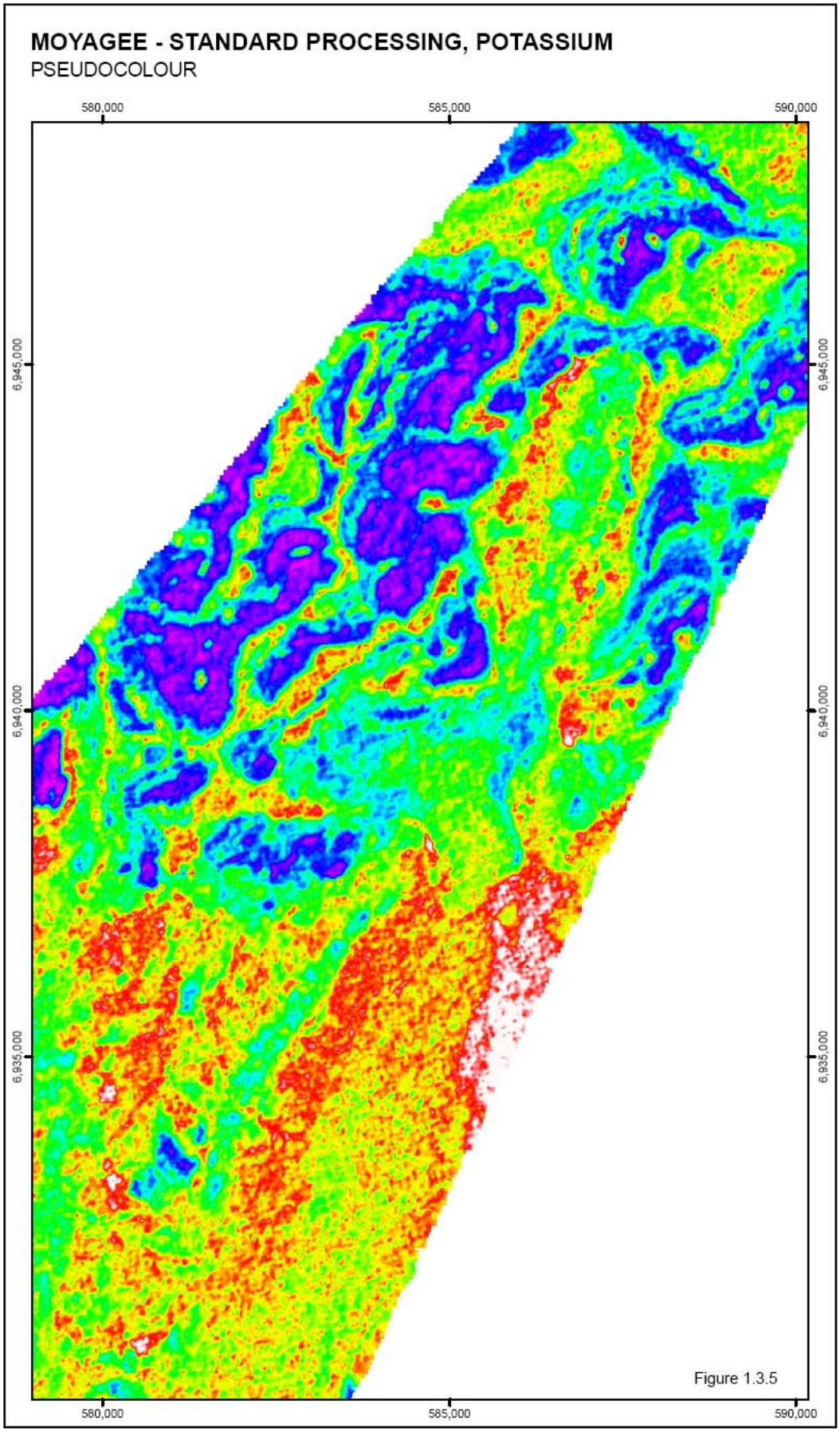


**Figure C.3.5. Potassium standard processed pseudocolour image, Moyagee.**

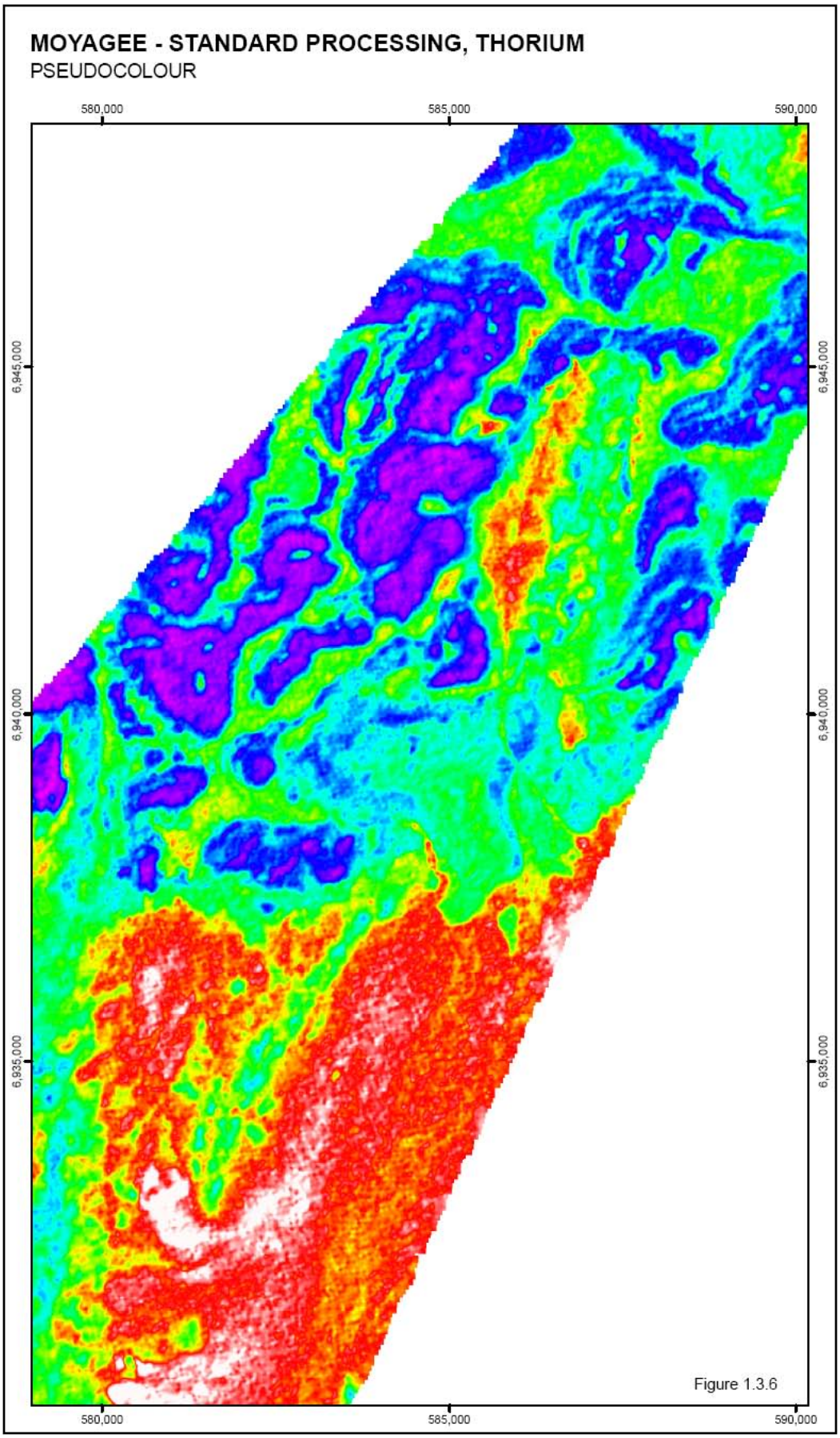


**Figure C.3.6. Thorium standard processed pseudocolour image, Moyagee.**

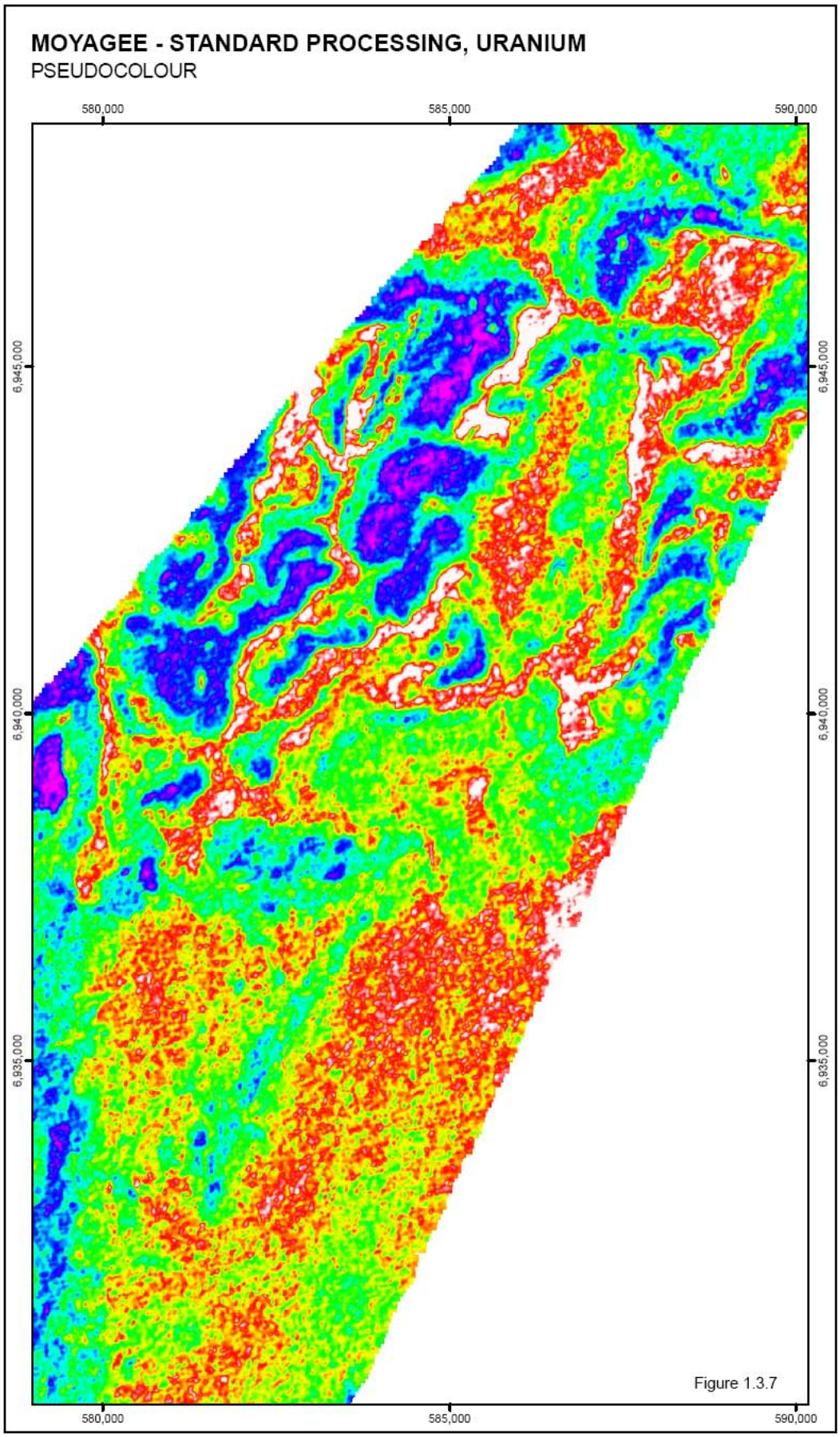


**Figure C.3.7. Uranium standard processed pseudocolour image, Moyagee.**

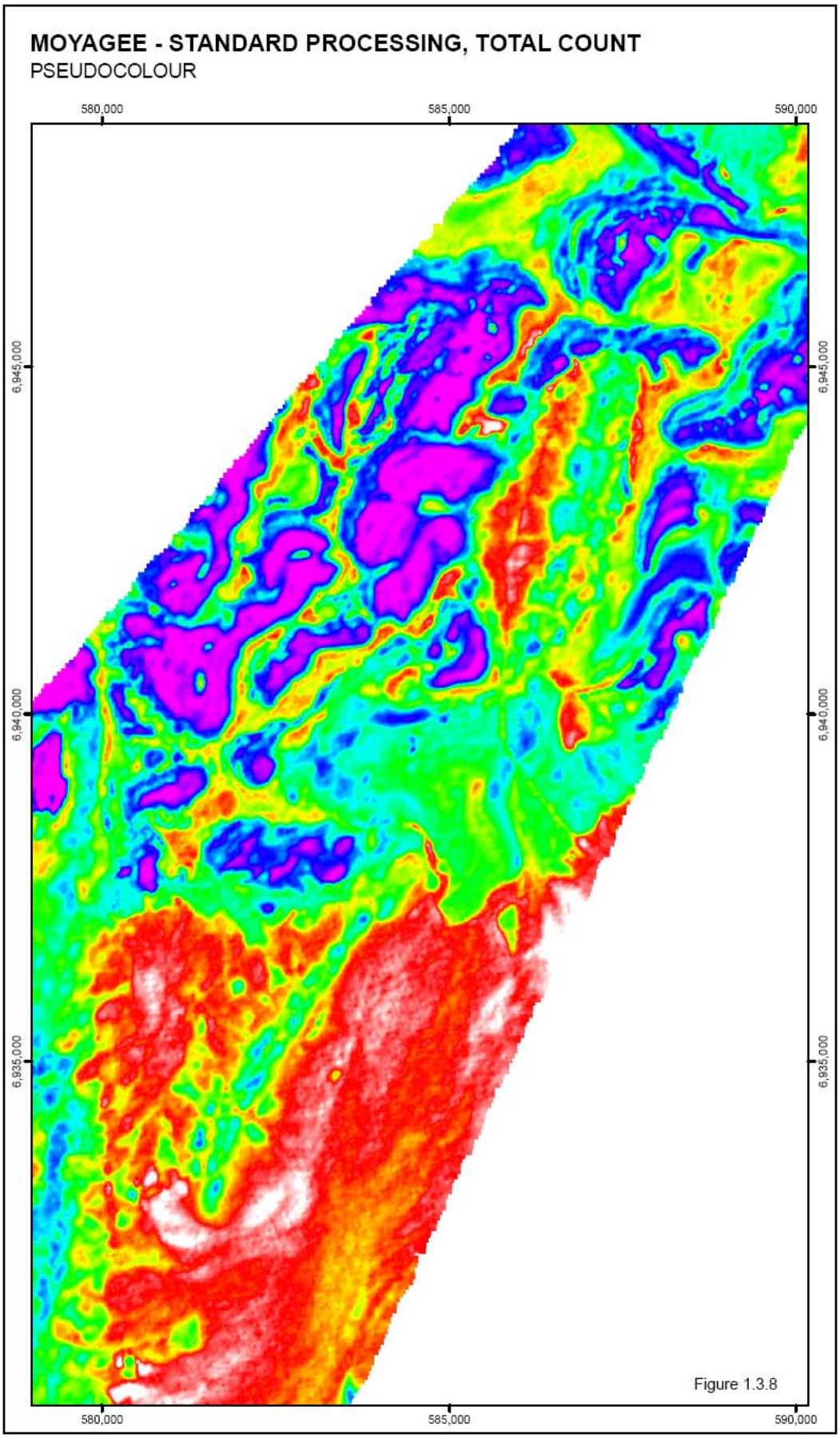


**Figure C.3.8. Total count standard processed pseudocolour image, Moyagee.**

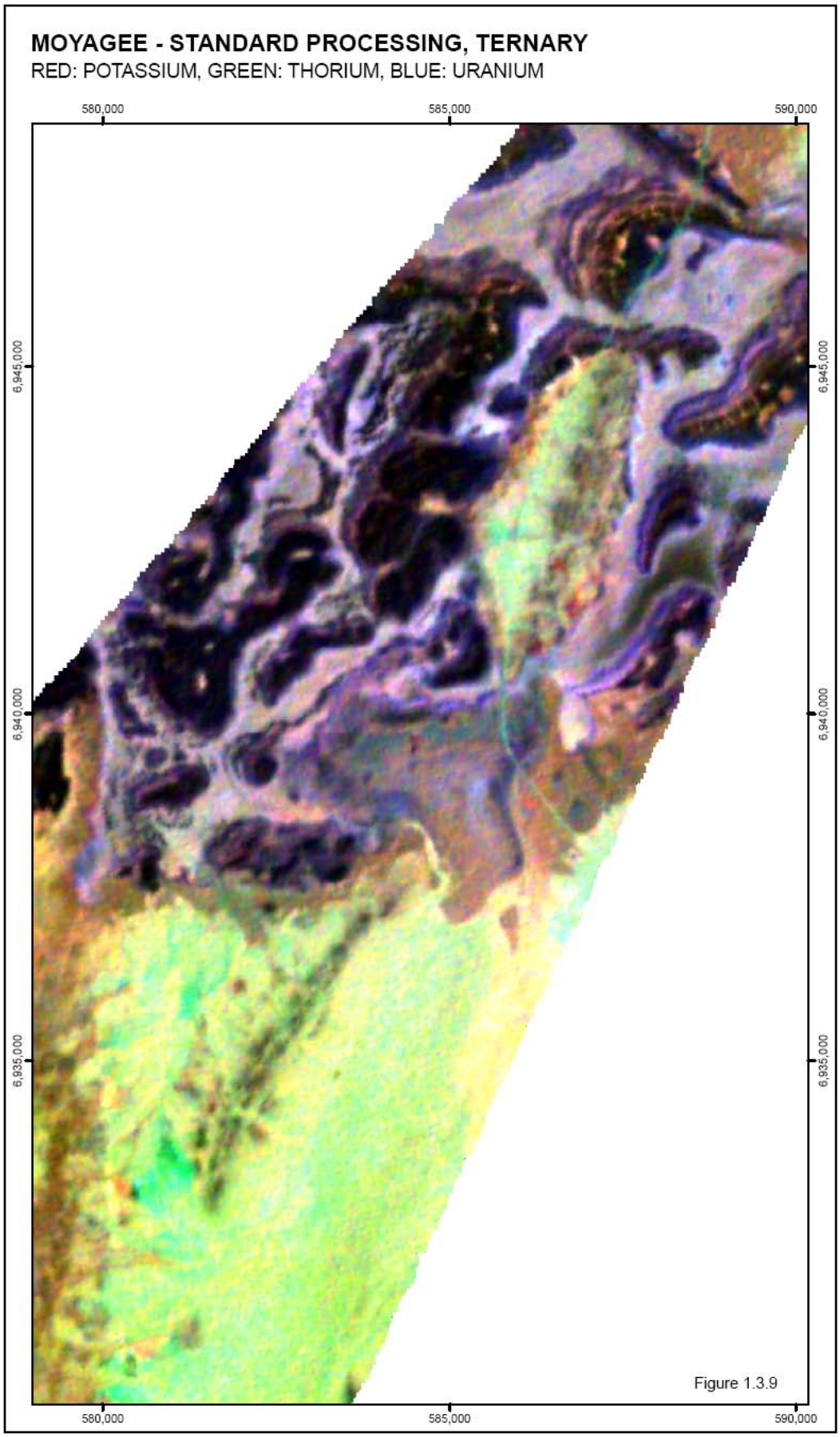


**Figure C.3.9. Ternary standard processed pseudocolour image, Moyagee.**

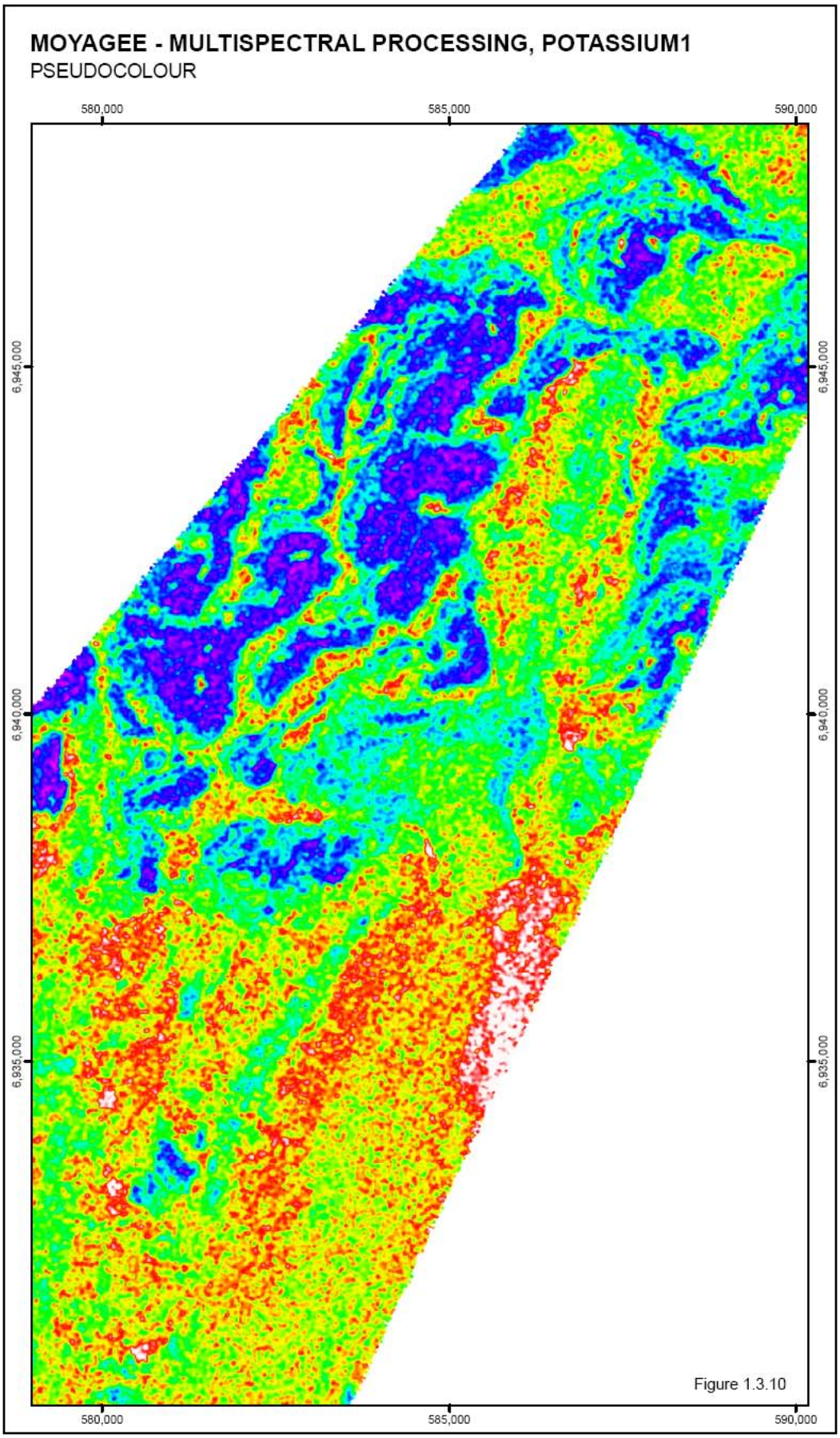


**Figure C.3.10. Potassium 1 multispectral processed, NASVD spectral smoothing, pseudocolour image, Moyagee.**

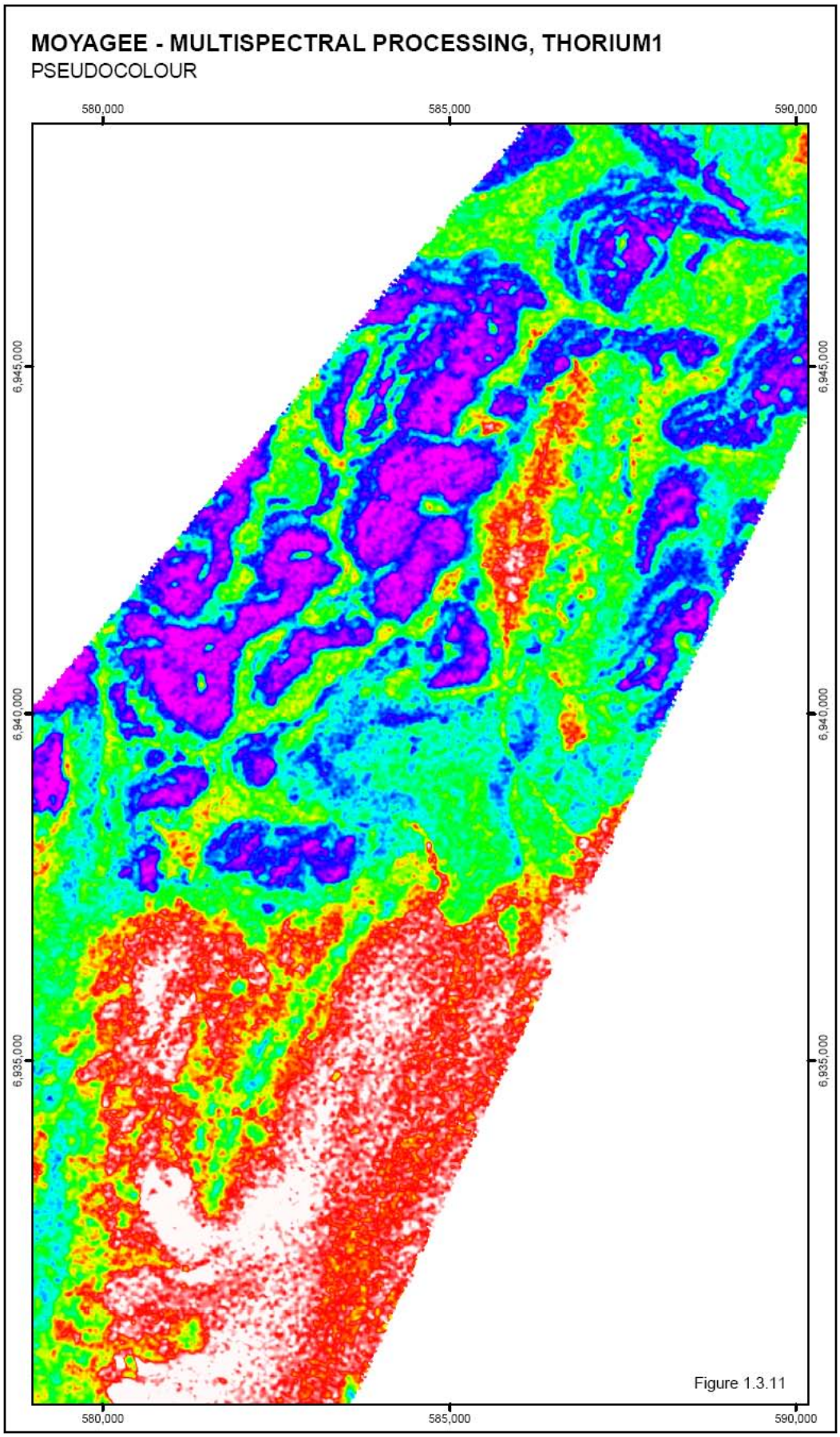


**Figure C.3.11. Thorium 1 multispectral processed, NASVD spectral smoothing, pseudocolour image, Moyagee.**

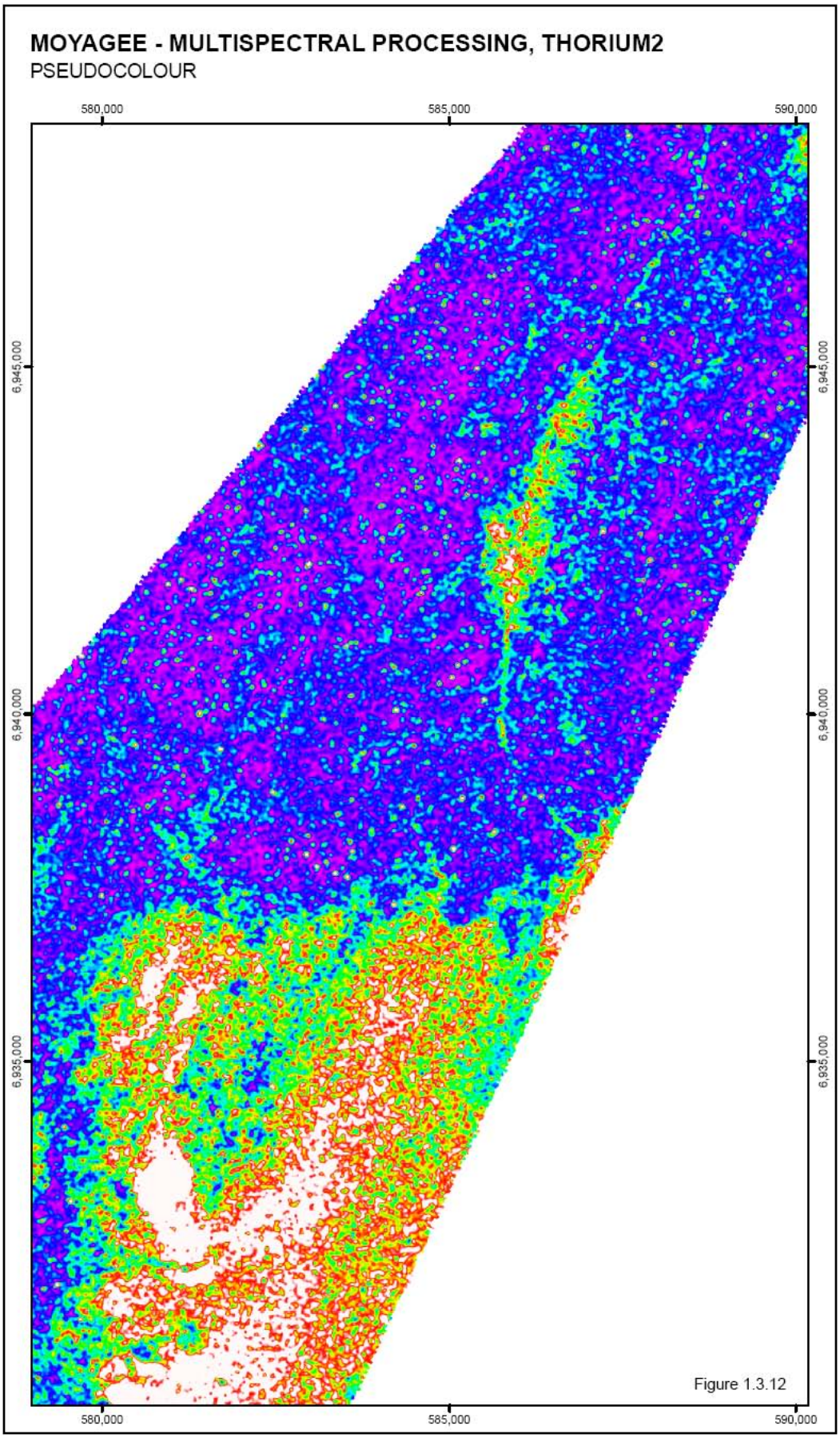


**Figure C.3.12. Thorium 2 multispectral processed, NASVD spectral smoothing, pseudocolour image, Moyagee.**

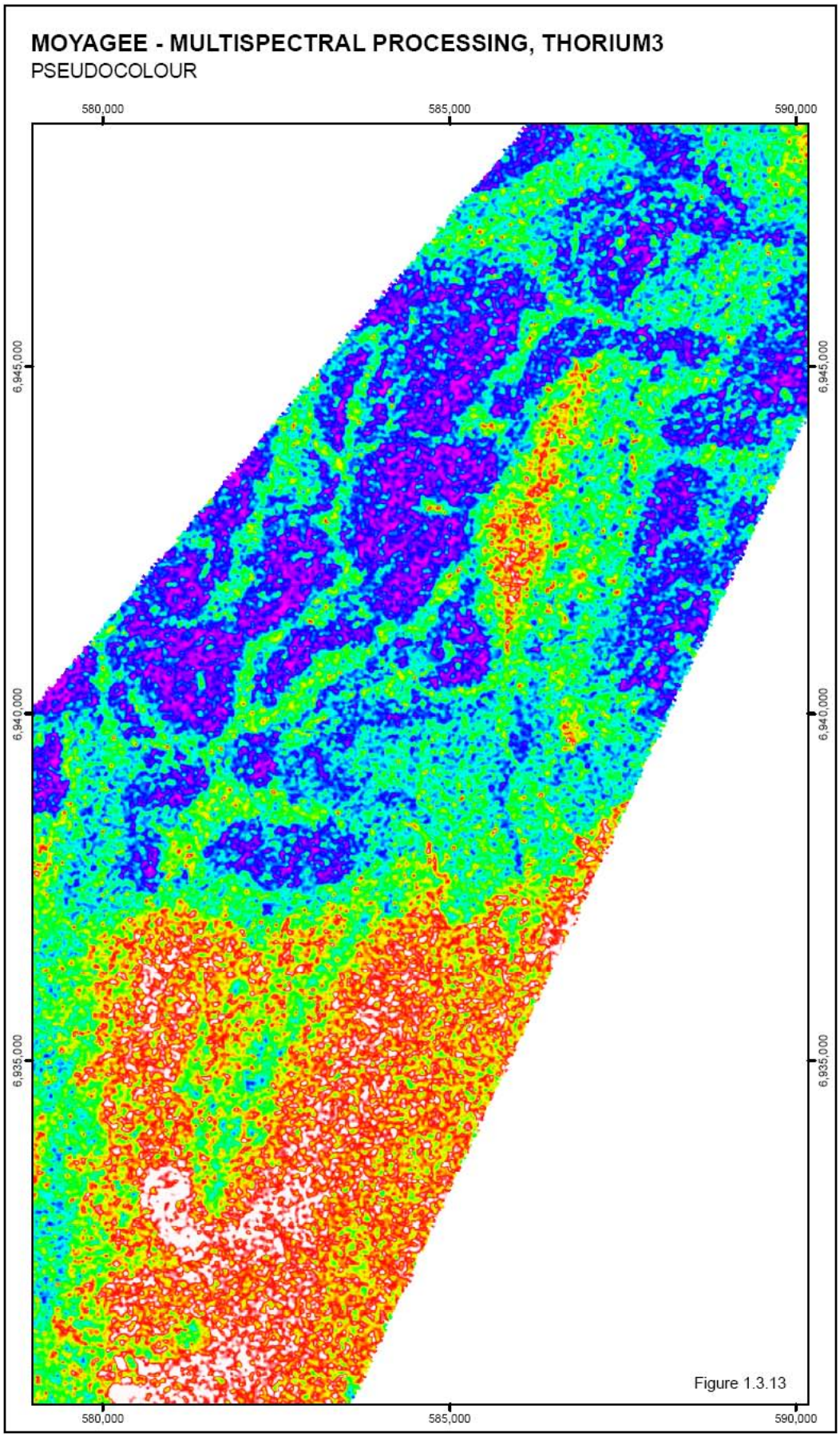


**Figure C.3.13. Thorium 3 multispectral processed, NASVD spectral smoothing, pseudocolour image, Moyagee.**

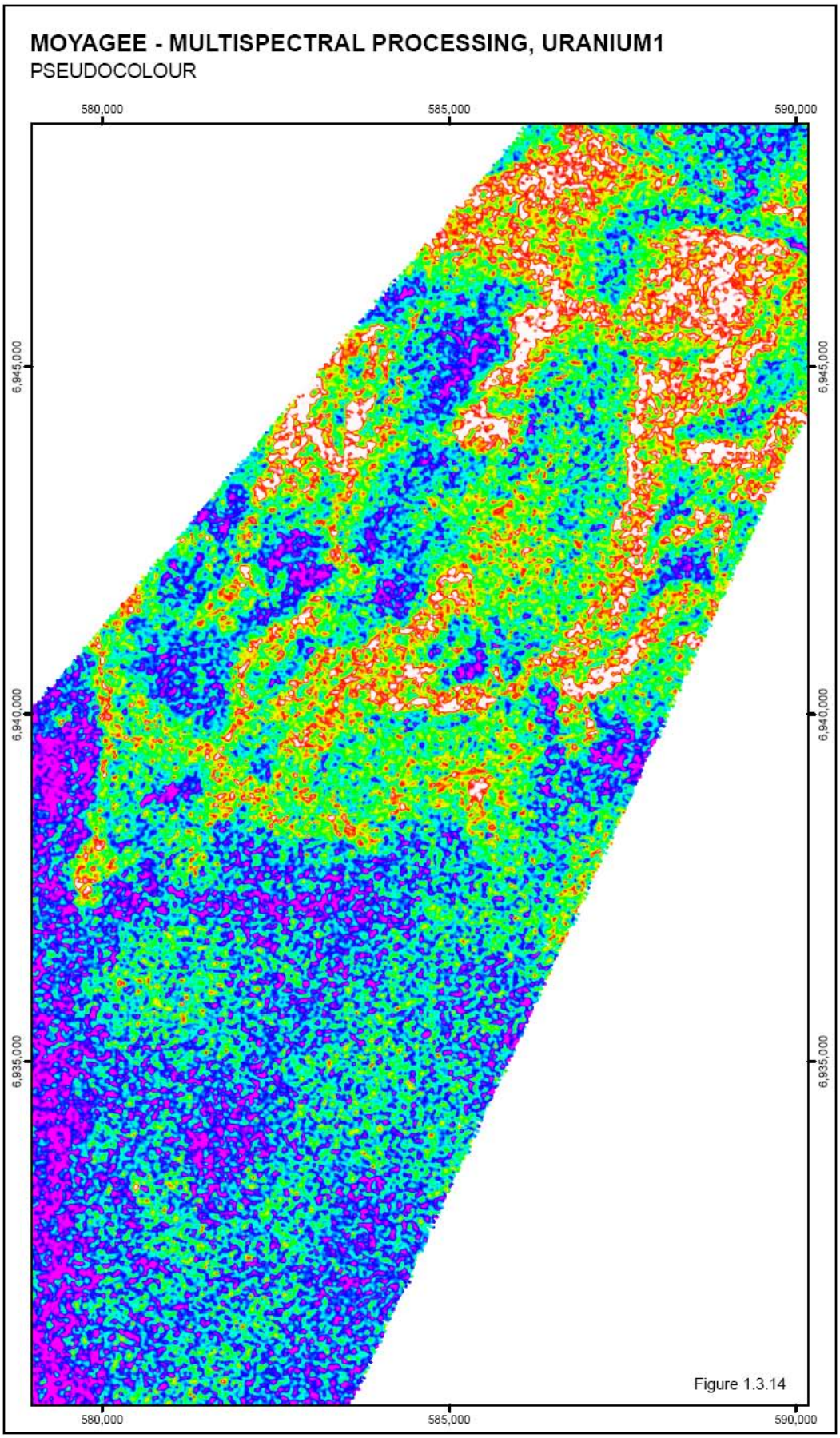


**Figure C.3.14. Uranium 1 multispectral processed, NASVD spectral smoothing, pseudocolour image, Moyagee.**

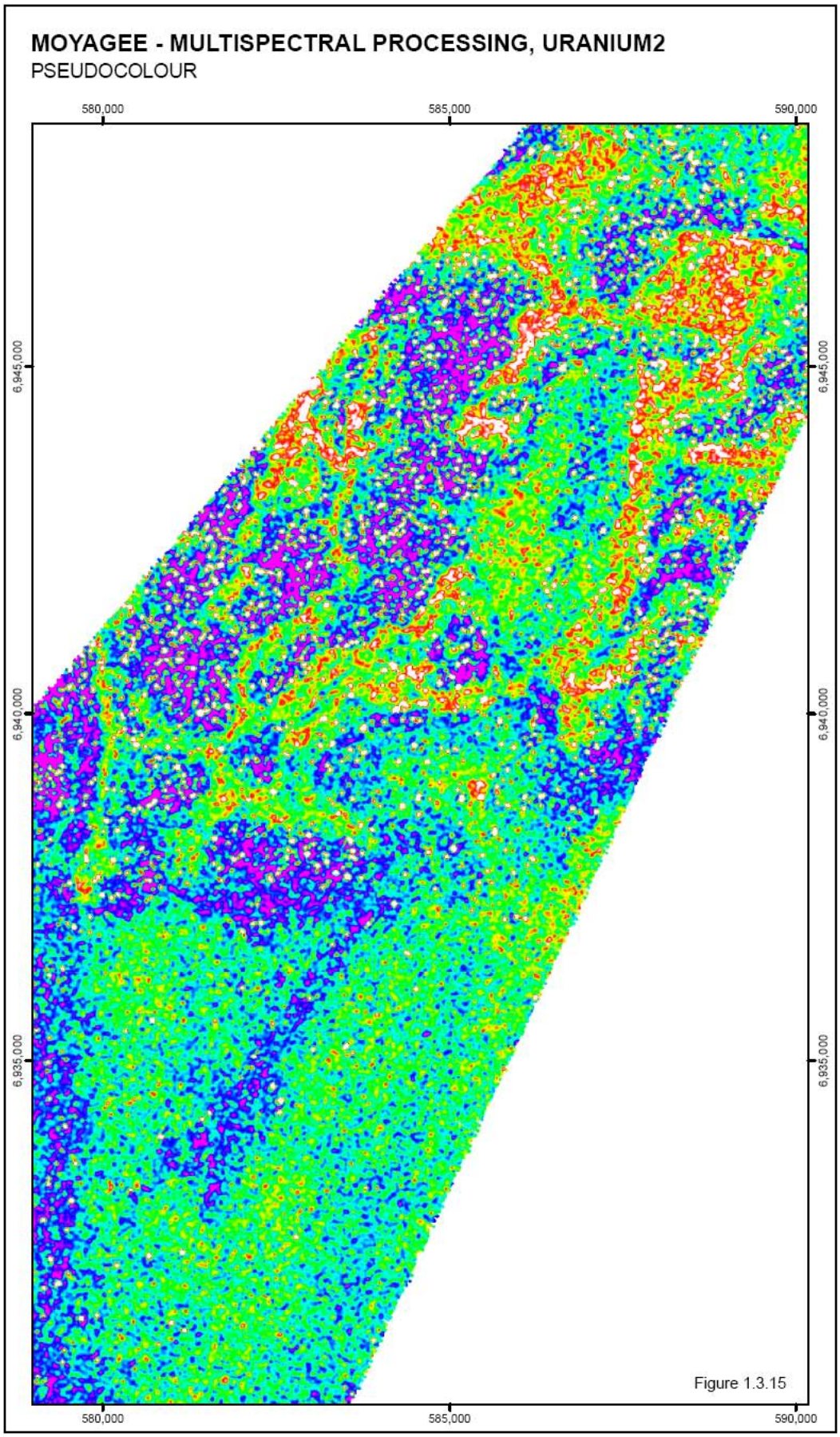


**Figure C.3.15. Uranium 2 multispectral processed, NASVD spectral smoothing, pseudocolour image, Moyagee.**

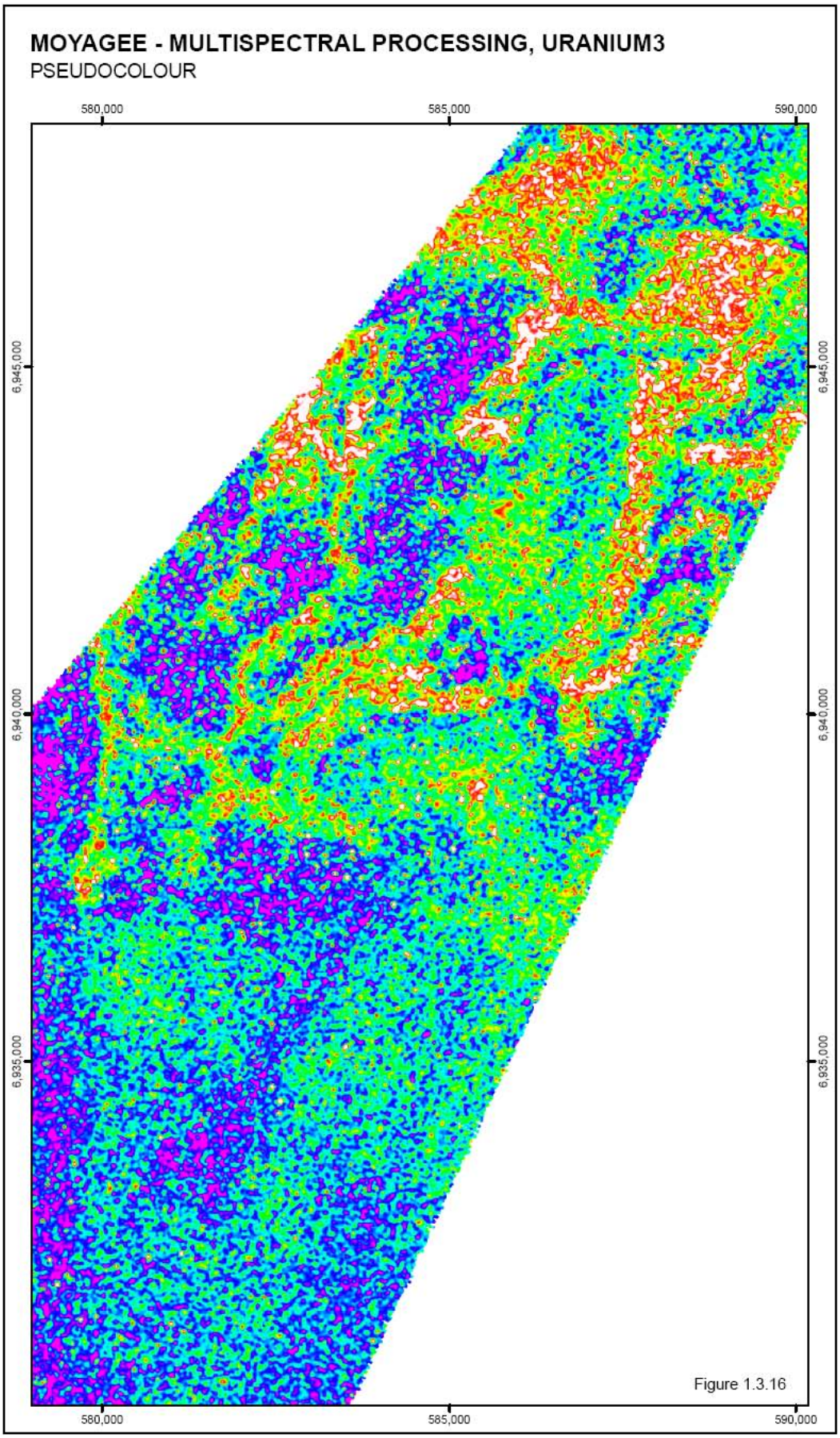


**Figure C.3.16. Uranium 3 multispectral processed, NASVD spectral smoothing, pseudocolour image, Moyagee.**

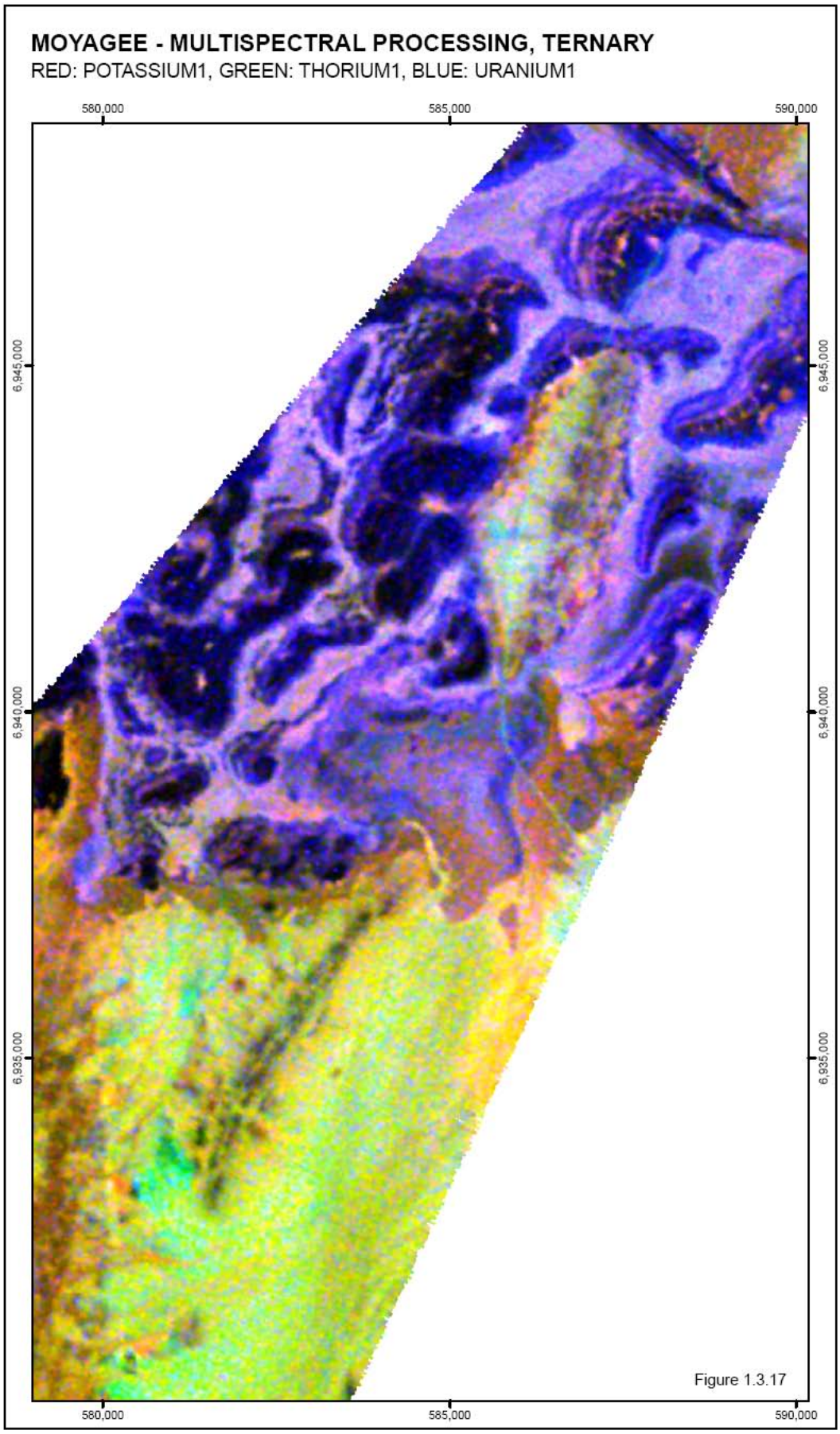


**Figure C.3.17. Ternary multispectral processed, NASVD spectral smoothing, ternary image, Moyagee.**

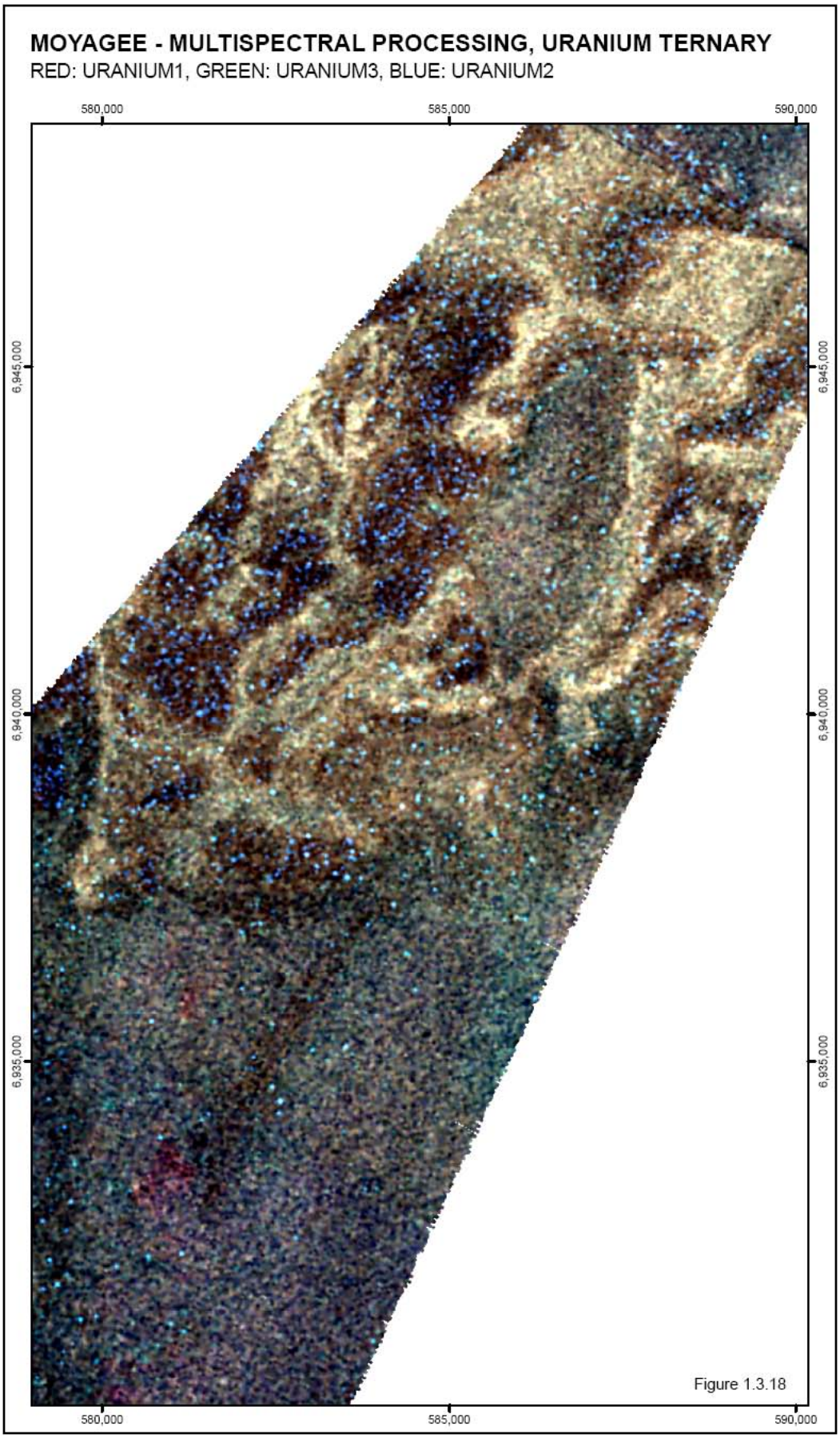


**Figure C.3.18. Uranium ternary multispectral processed, NASVD spectral smoothing, ternary image, Moyagee.**

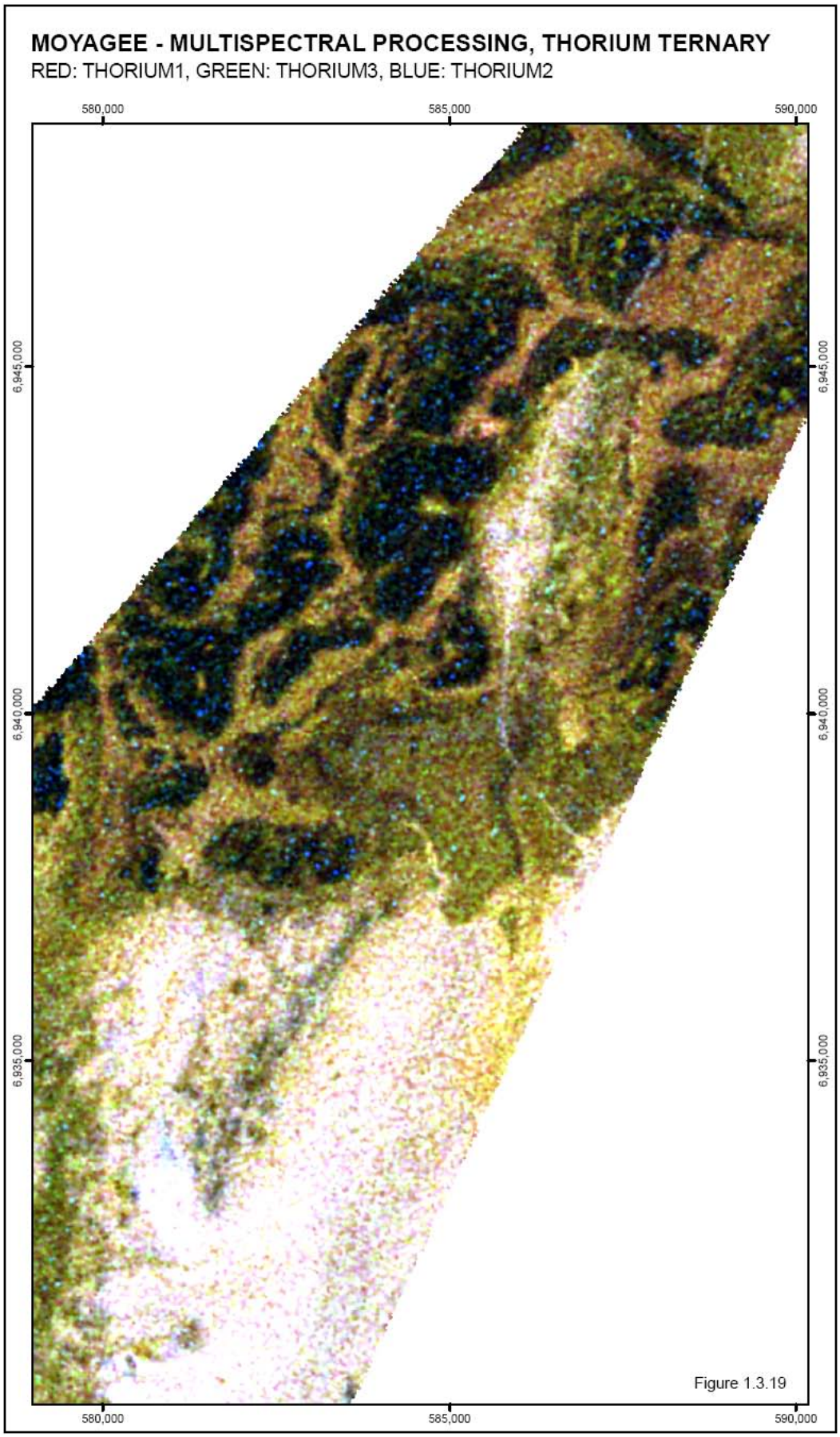


**Figure C.3.19. Thorium ternary multispectral processed, NASVD spectral smoothing, ternary image, Moyagee.**

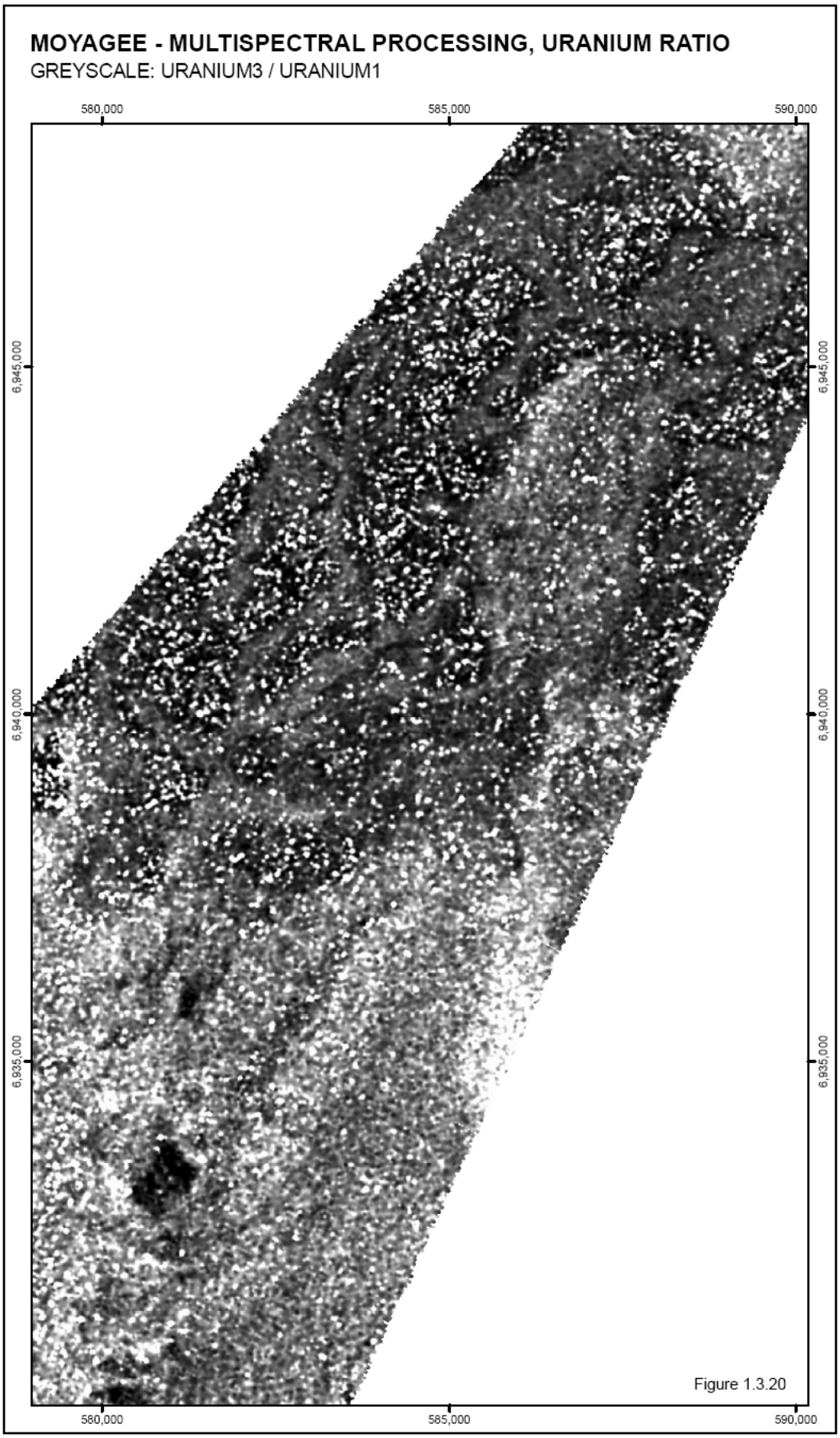


**Figure C.3.20. Uranium ratio multispectral processed, NASVD spectral smoothing, greyscale image, Moyagee.**

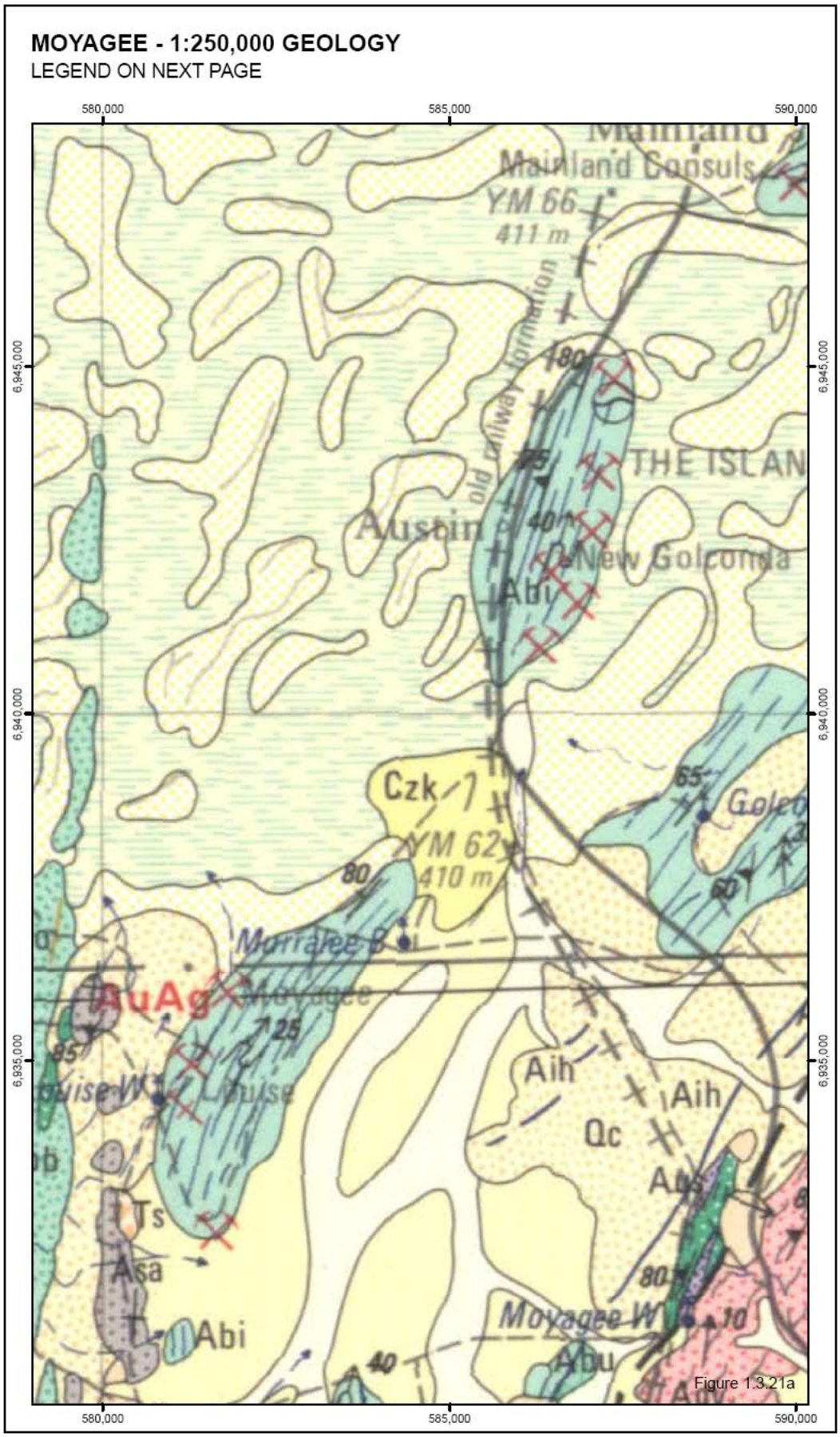


**Figure C.3.21. 1:250,000 geology for Moyagee (from Watkins *et al.*, 1986).**

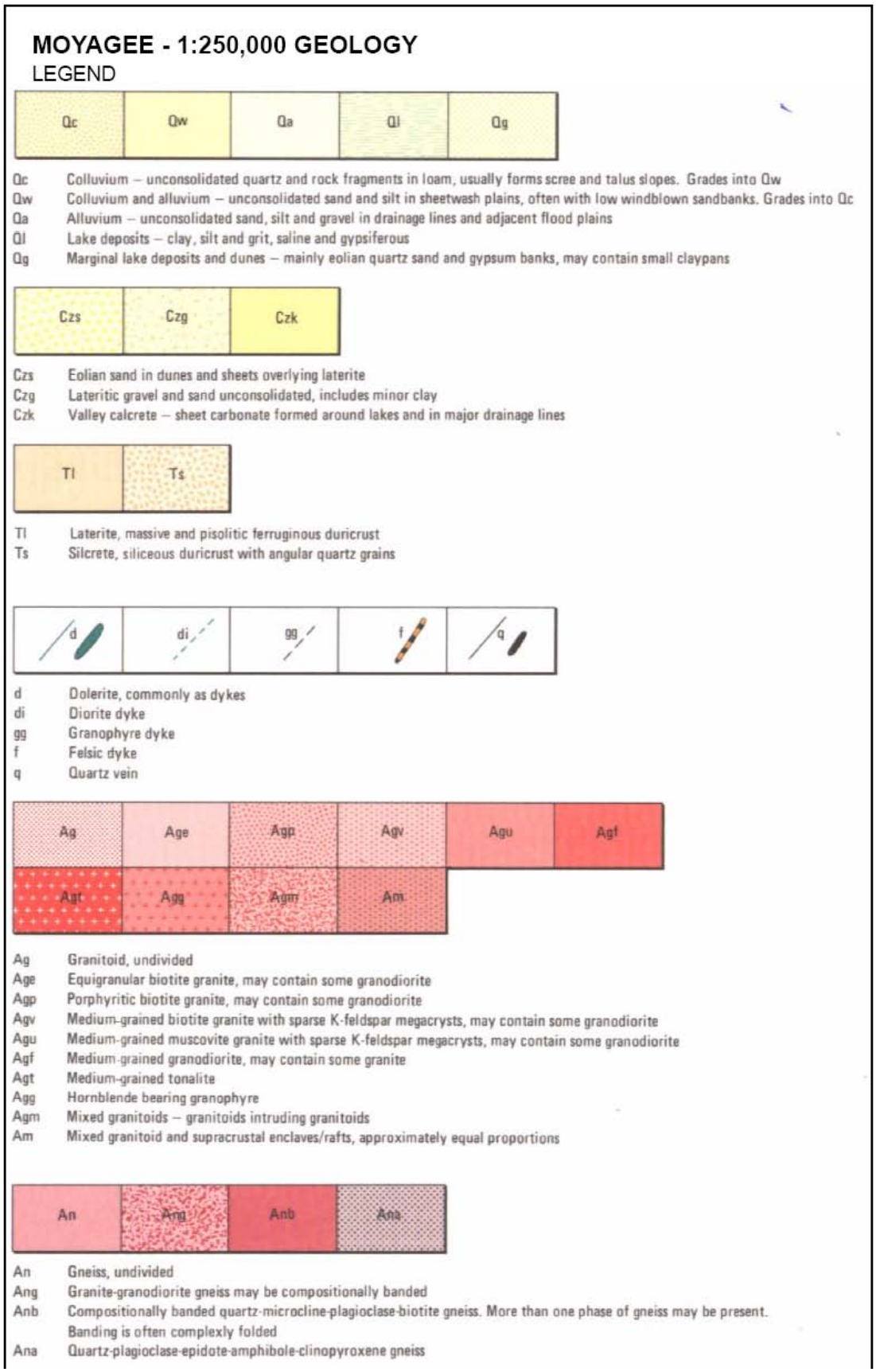


**Figure C.3.21 cont'd. 1:250,000 geology legend for Moyagee (from Watkins *et al.*, 1986).**

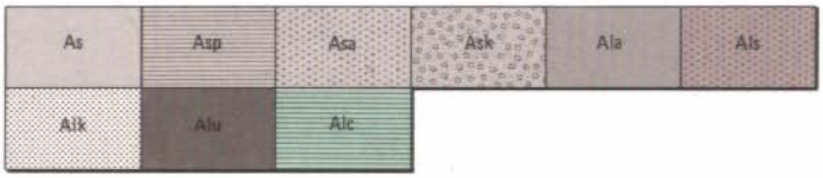


As Sedimentary rocks, undivided
Asp Shale, may contain some siltstone and sandstone
Asa Sandstone, may contain some shale, siltstone and conglomerate
Ask Arkosic sandstone, locally conglomeratic, derived from felsic igneous rocks
Ala Andalusite ± cordierite ± garnet ± staurolite bearing pelitic schist
Als Sillimanite bearing pelitic schist
Alk Kyanite bearing quartzite
Alu Corundum bearing chlorite-sericite schist
Alc Calc-silicate rock interbanded with amphibolite


Ai Banded iron-formation and chert, undivided
Aij Jaspilitic banded iron-formation, red, black and white bands (about 50% iron oxide)
Aih Quartz-hematite banded iron-formation may contain magnetite
Aic Grey-white banded chert, may contain some red bands
Aif Ferruginous chert ( < 50% iron oxide)
Aia Quartz-hematite-magnetite-amphibole banded iron-formation


Af Felsic to intermediate volcanic and volcanogenic rocks (undivided)
Afv Felsic lava, rhyolite to dacite, may contain some felsic tuff
Aft Felsic tuff, rhyolite to dacite, including crystal, lithic and crystal-lithic tuffs, may contain some felsic lava
Afs Felsic volcanogenic sediments, may contain some felsic lava and tuff
Afo Felsic porphyry, quartz and feldspar phenocrysts


Ab Mafic volcanic rocks, undivided
Abb Tholeiitic basalt, fine-grained, may be variolitic or porphyritic, usually intruded by minor dolerite and gabbro sills. May contain minor Abu units
Abu High-Mg basalt, pyroxene needle spinifex texture, generally pseudomorphed by amphibole, may be variolitic, usually intruded by minor dolerite, gabbro and ultramafic sills. May contain minor Abb units
Abm Mafic volcanics consisting of Abb and Abu units, usually intruded by minor dolerite, gabbro and ultramafic sills
Abi Mafic rocks and minor ultramafic rocks interlayered with banded iron-formation
Abf Chlorite ± amphibole ± carbonate schist
Aba Amphibolite, fine to medium-grained
Abe Amphibolite, coarse-grained
Abg Gabbro, medium to coarse-grained
Abo Leucogabbro, <30% mafic minerals, usually contains quartz
Abd Dolerite, fine to medium-grained, ophitic texture

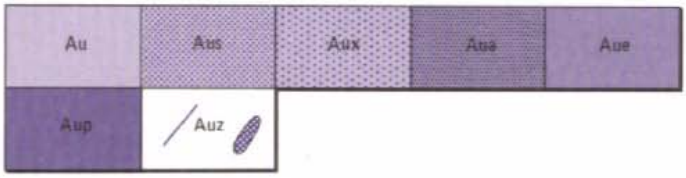


Au Ultramafic rocks, undivided
Aus Serpentinite, cumulate texture may be preserved
Aux Pyroxenite
Aua Mg-amphibole ± chlorite ± talc schist

Figure 1.3.21c

**Figure C.3.21 cont'd. 1:250,000 geology legend for Moyagee (from Watkins *et al.*, 1986).**

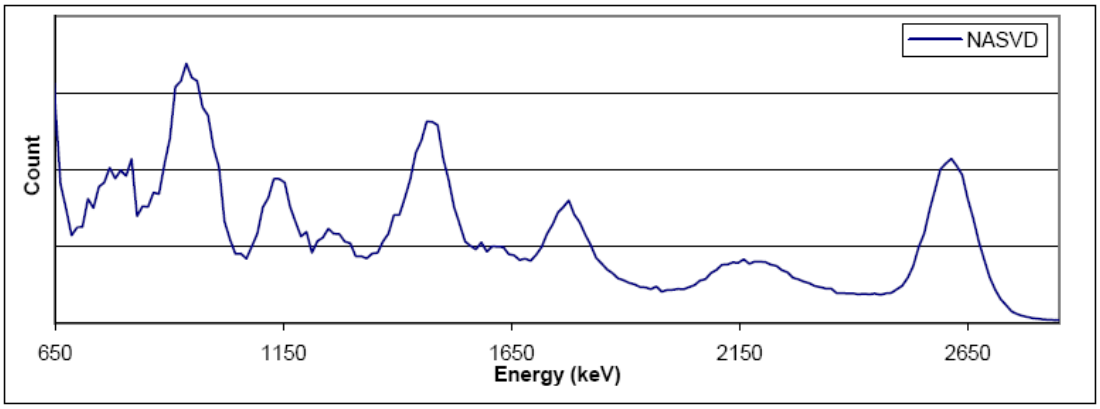


**Figure C.4.1. Average NASVD smoothed spectrum following Compton continuum removal, Waroona, airborne platform.**

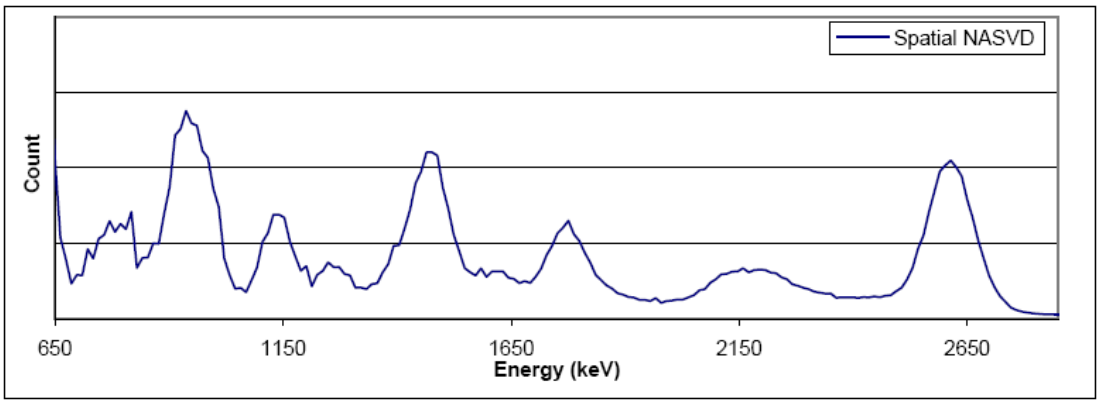


**Figure C.4.2. Average spatial NASVD smoothed spectrum following Compton continuum removal, Waroona, airborne platform.**

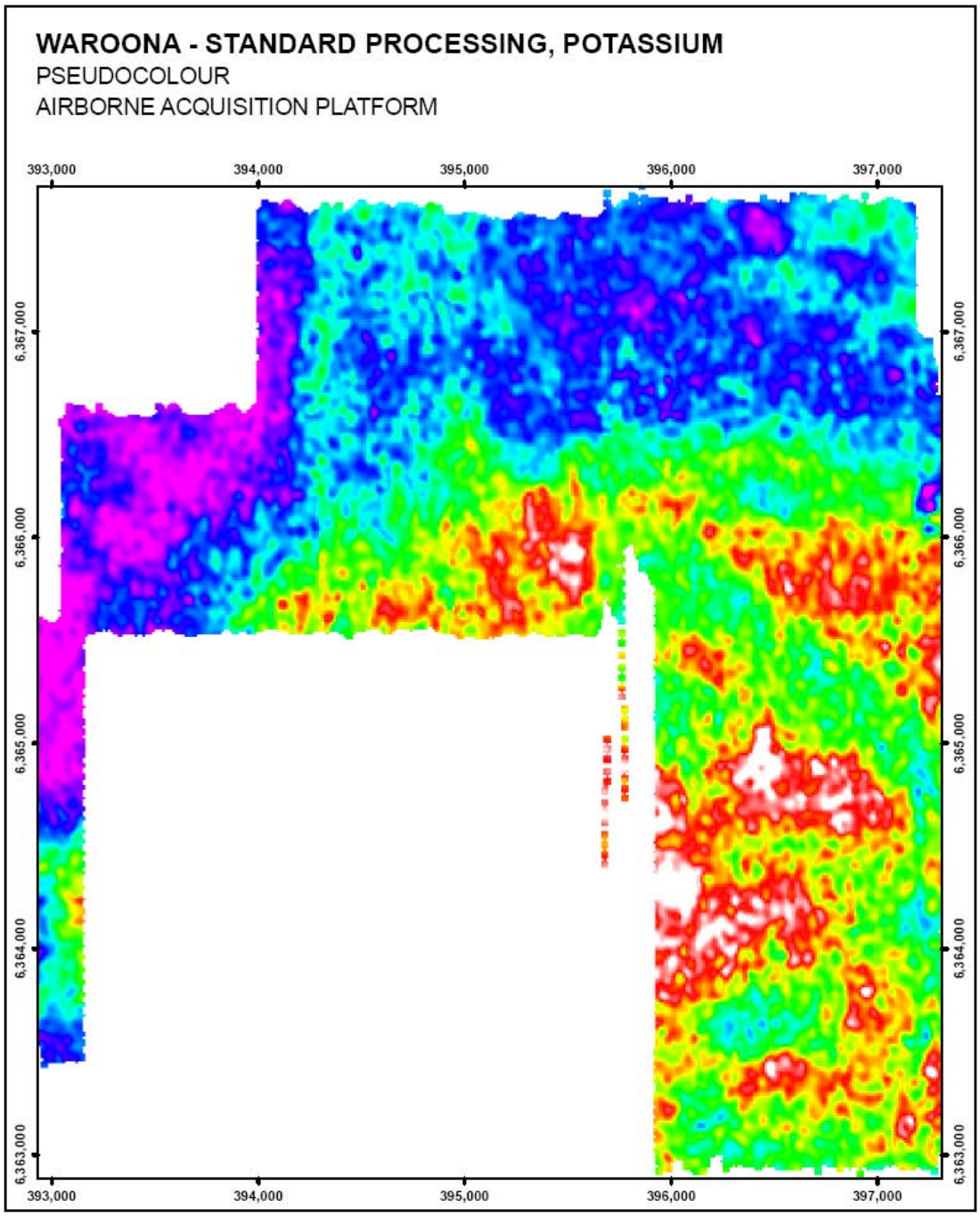


**Figure C.4.3. Potassium standard processed pseudocolour image, Waroona, airborne platform.**

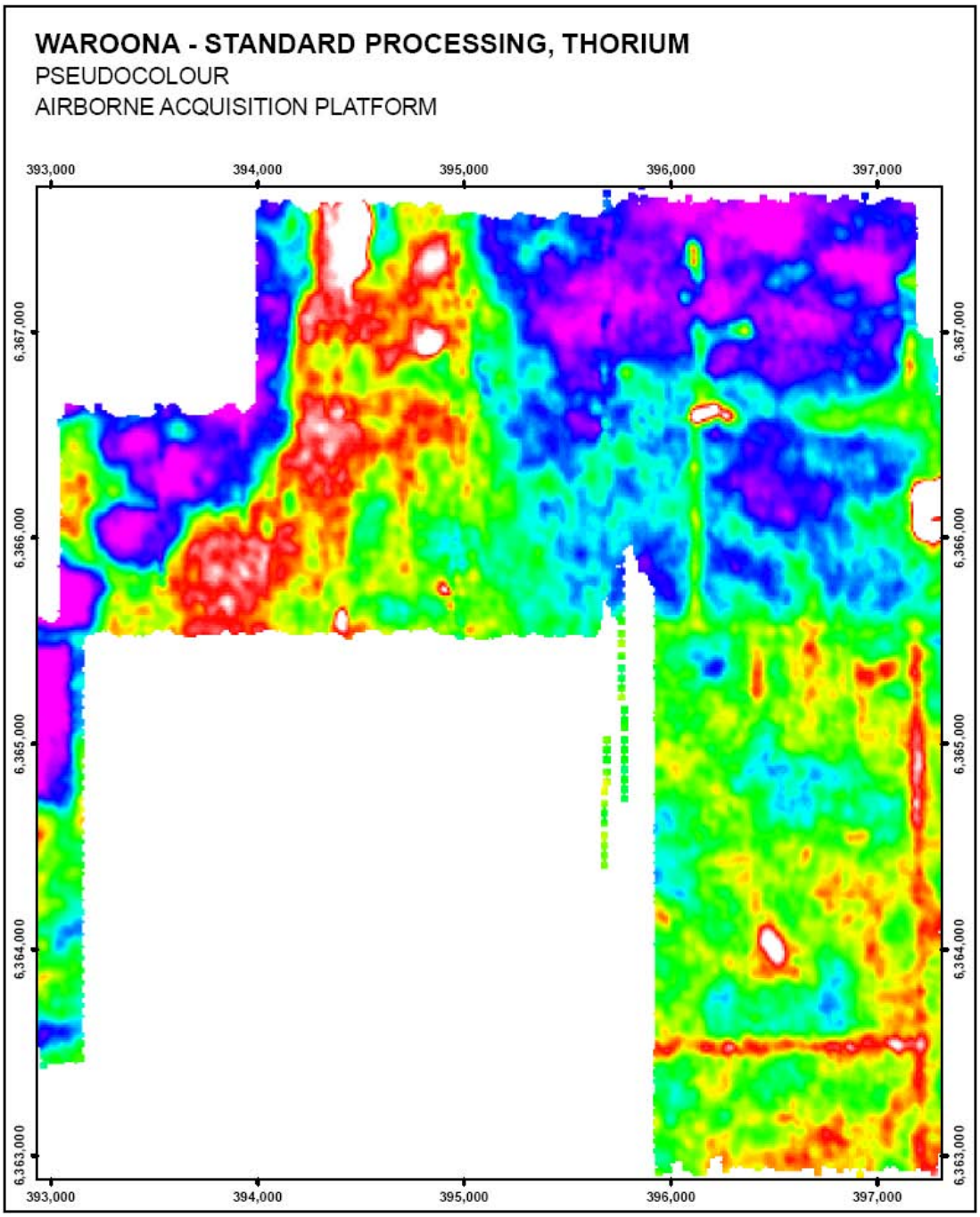


**Figure C.4.4. Thorium standard processed pseudocolour image, Waroona, airborne platform.**

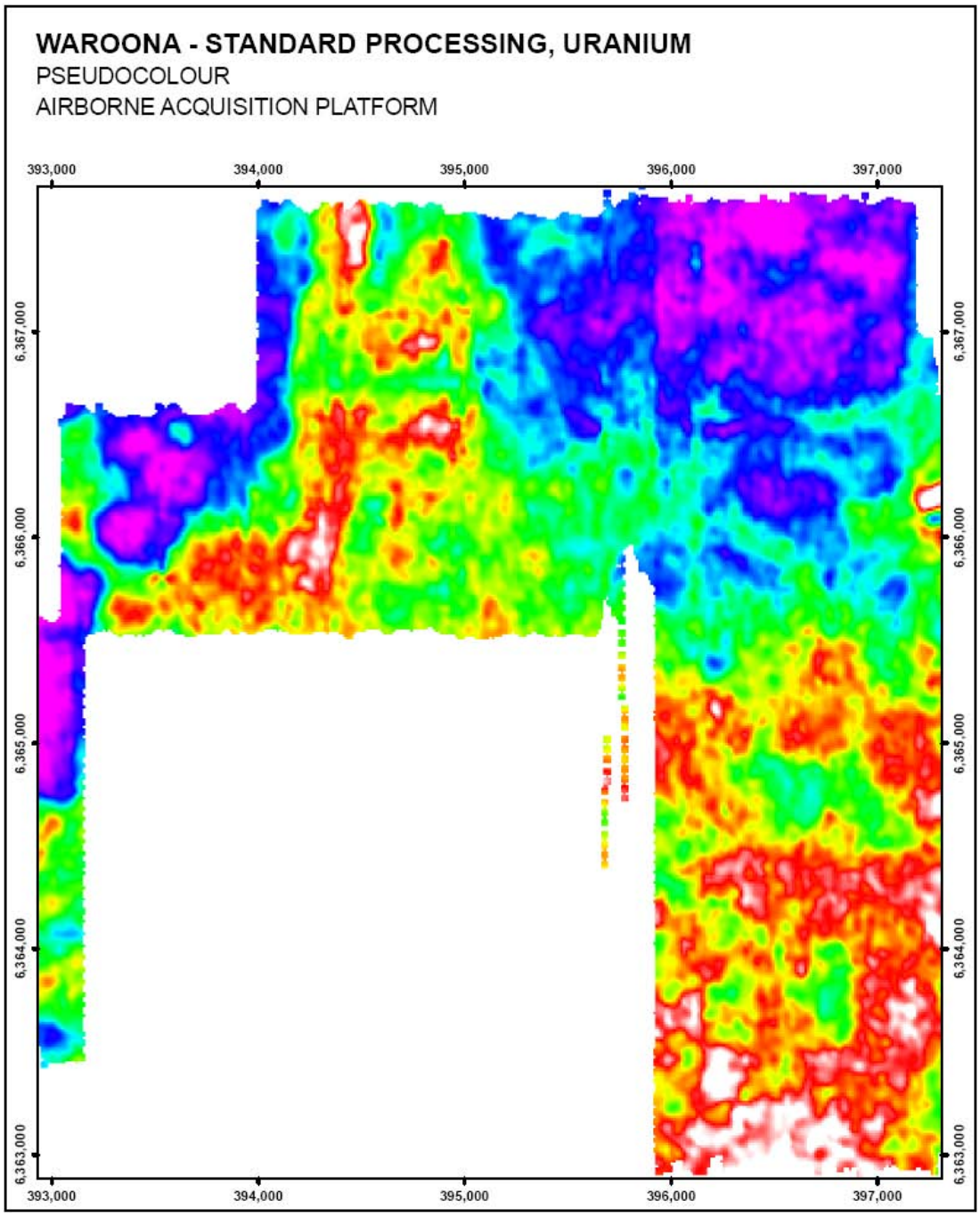


**Figure C.4.5. Uranium standard processed pseudocolour image, Waroona, airborne platform.**

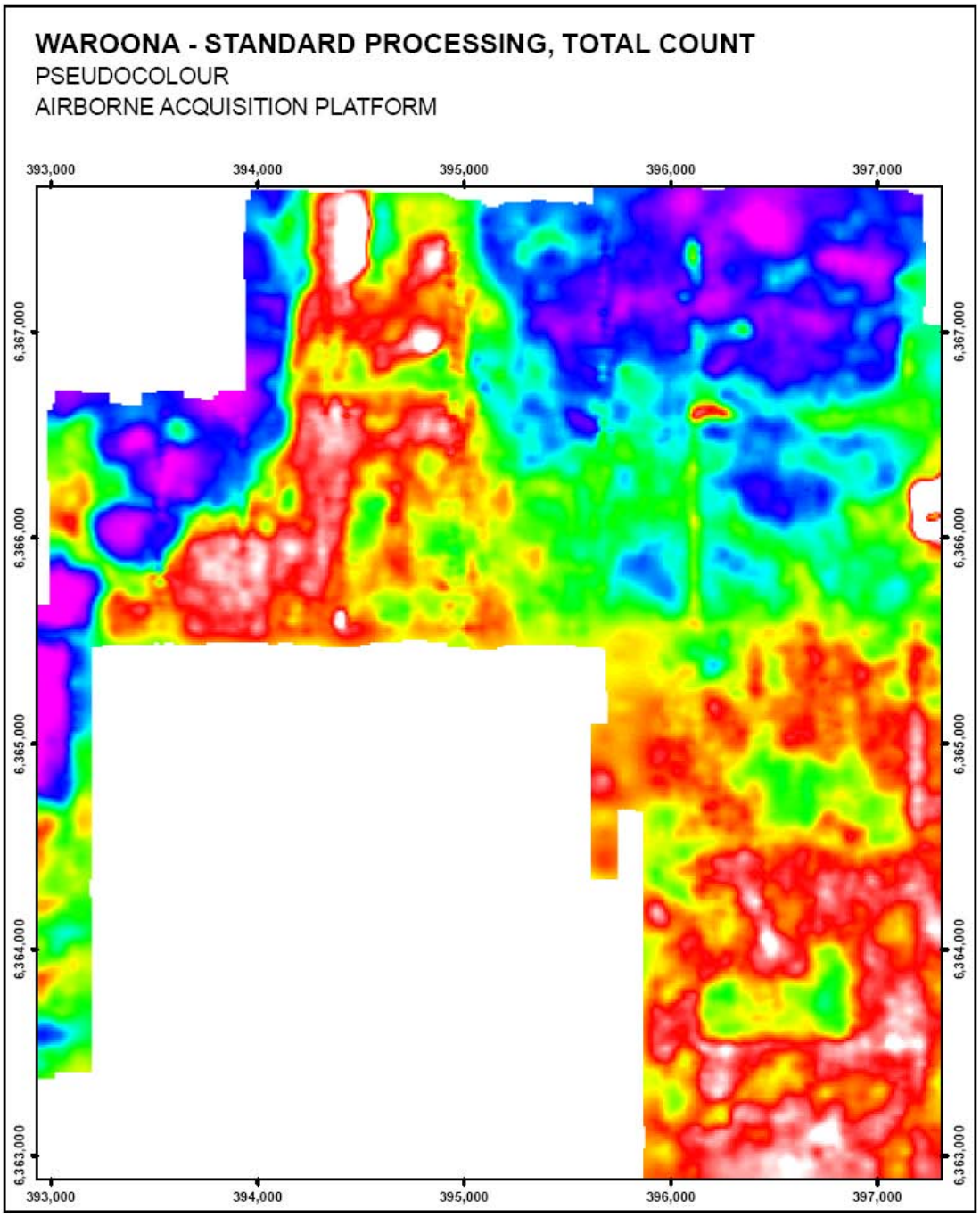


**Figure C.4.6. Total count standard processed pseudocolour image, Waroona, airborne platform.**

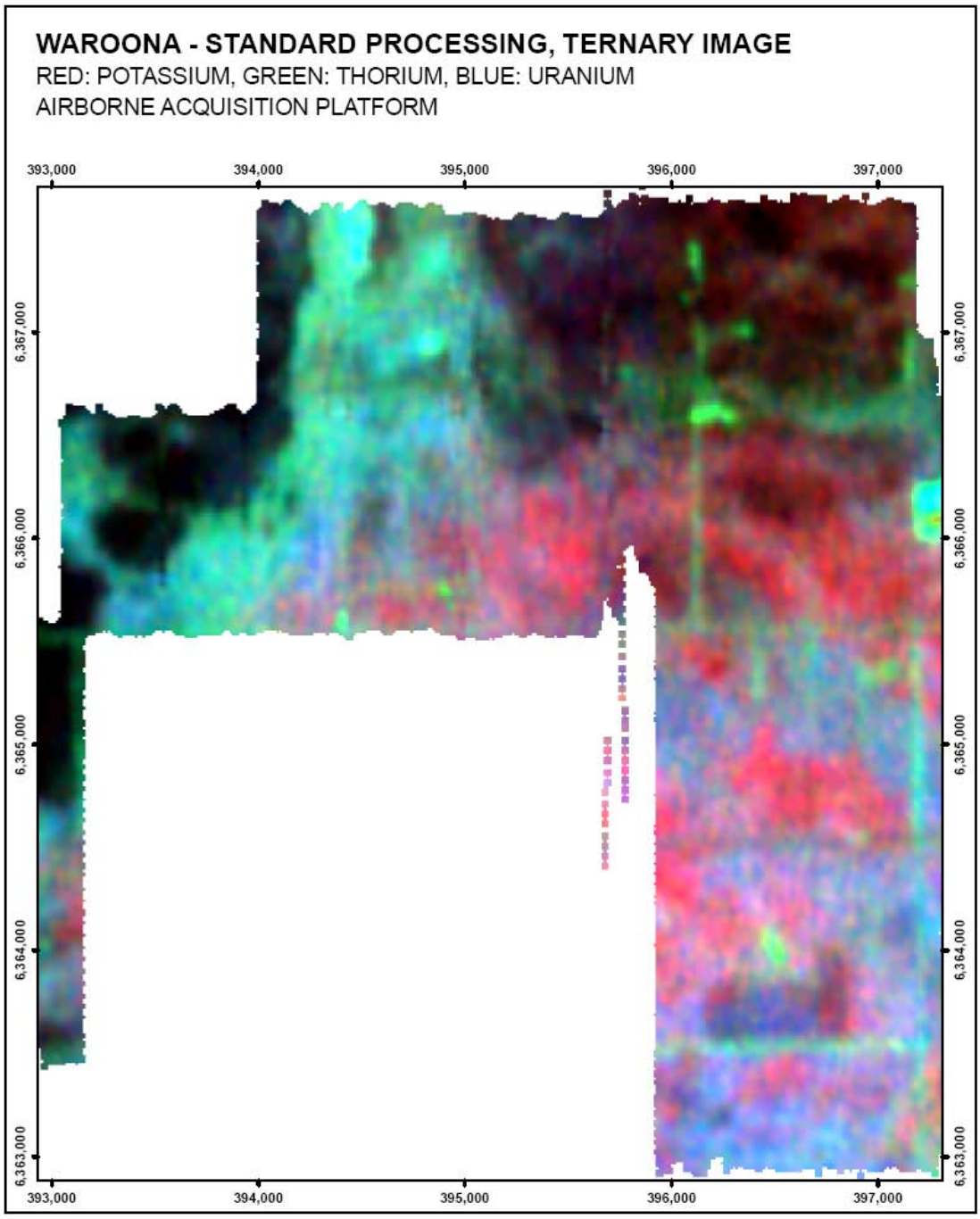


**Figure C.4.7. Ternary standard processed pseudocolour image, Waroona, airborne platform.**

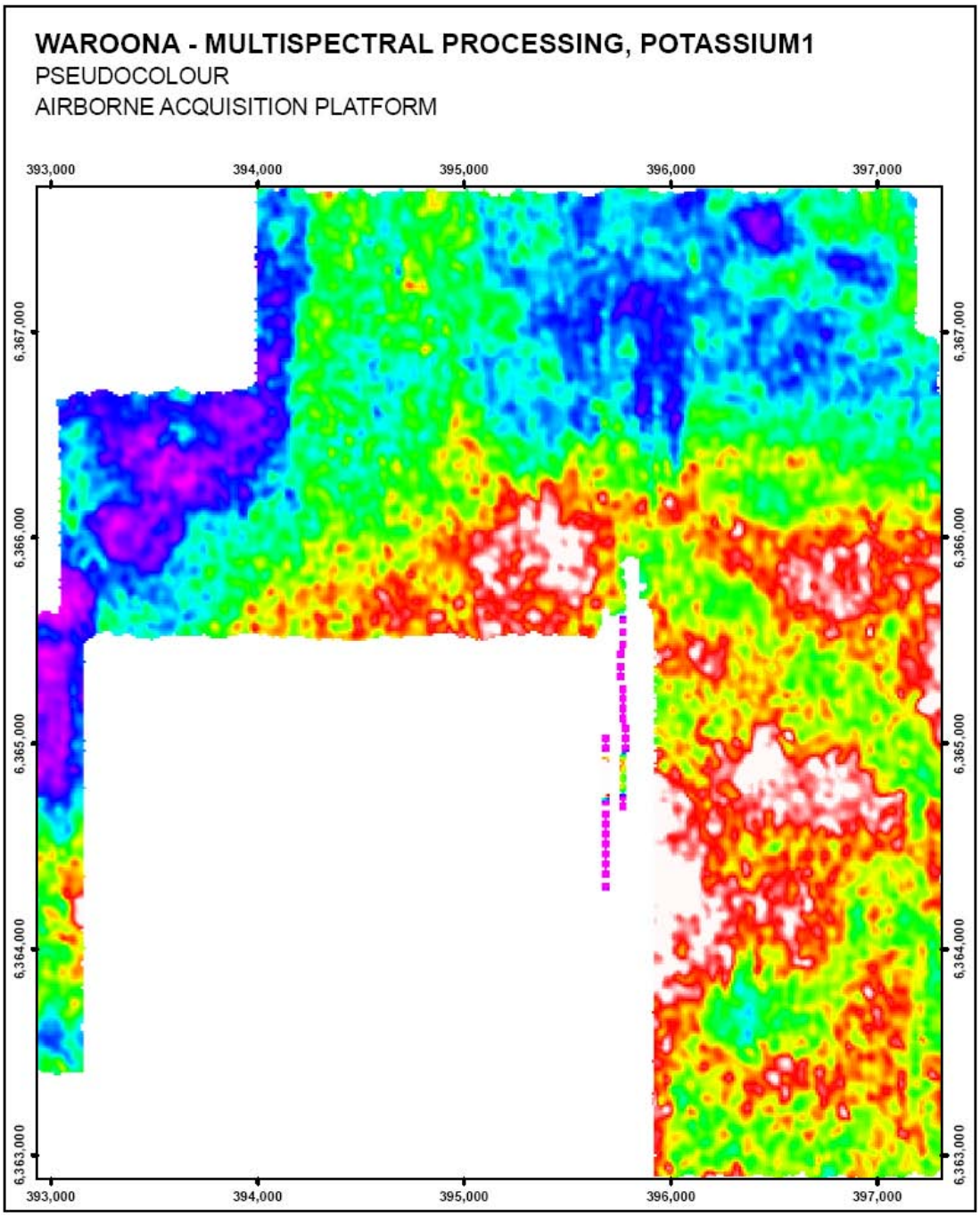


**Figure C.4.8. Potassium 1 multispectral processed, NASVD spectral smoothing, pseudocolour image, Waroona, airborne platform.**

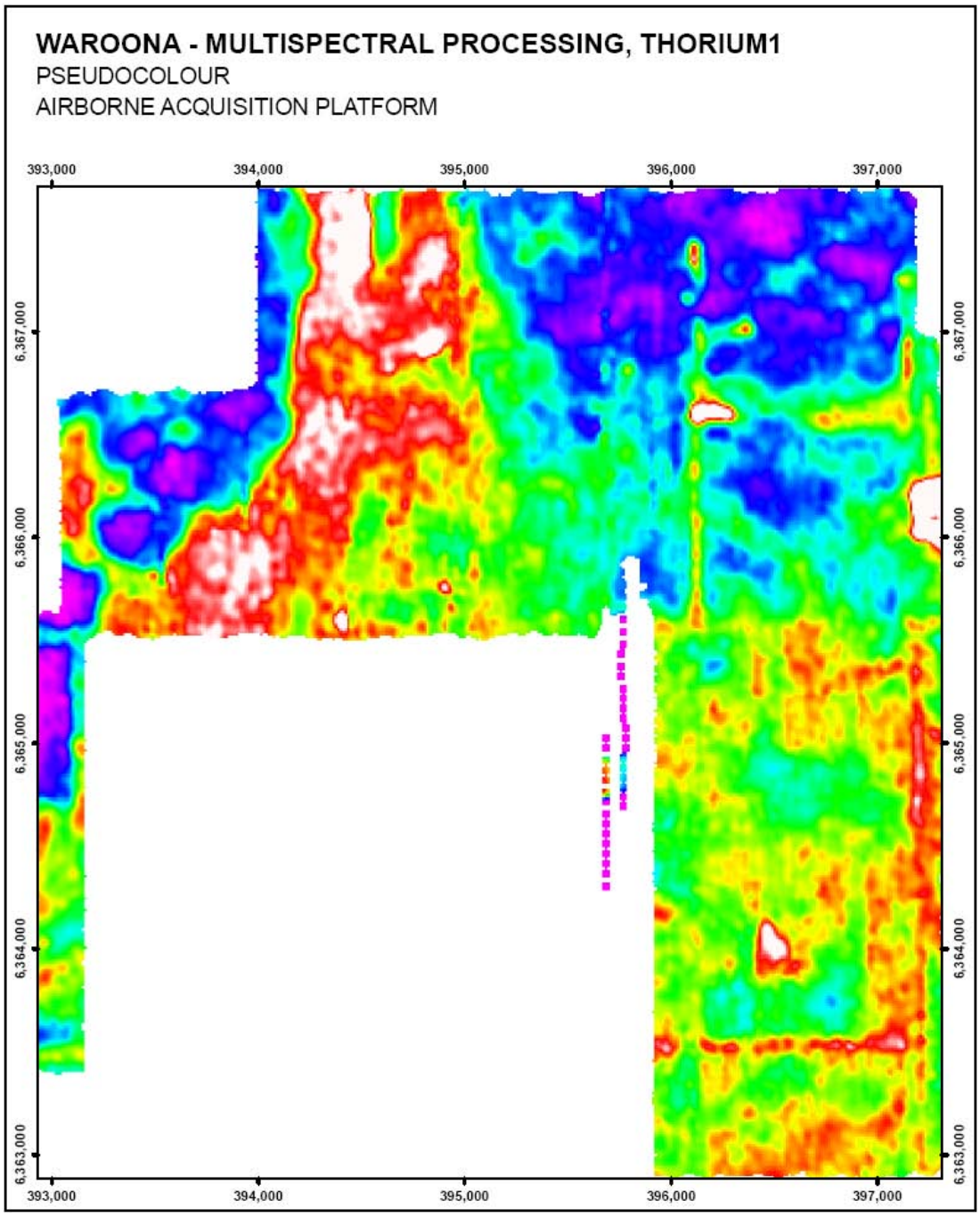


**Figure C.4.9. Thorium 1 multispectral processed, NASVD spectral smoothing, pseudocolour image, Waroona, airborne platform.**

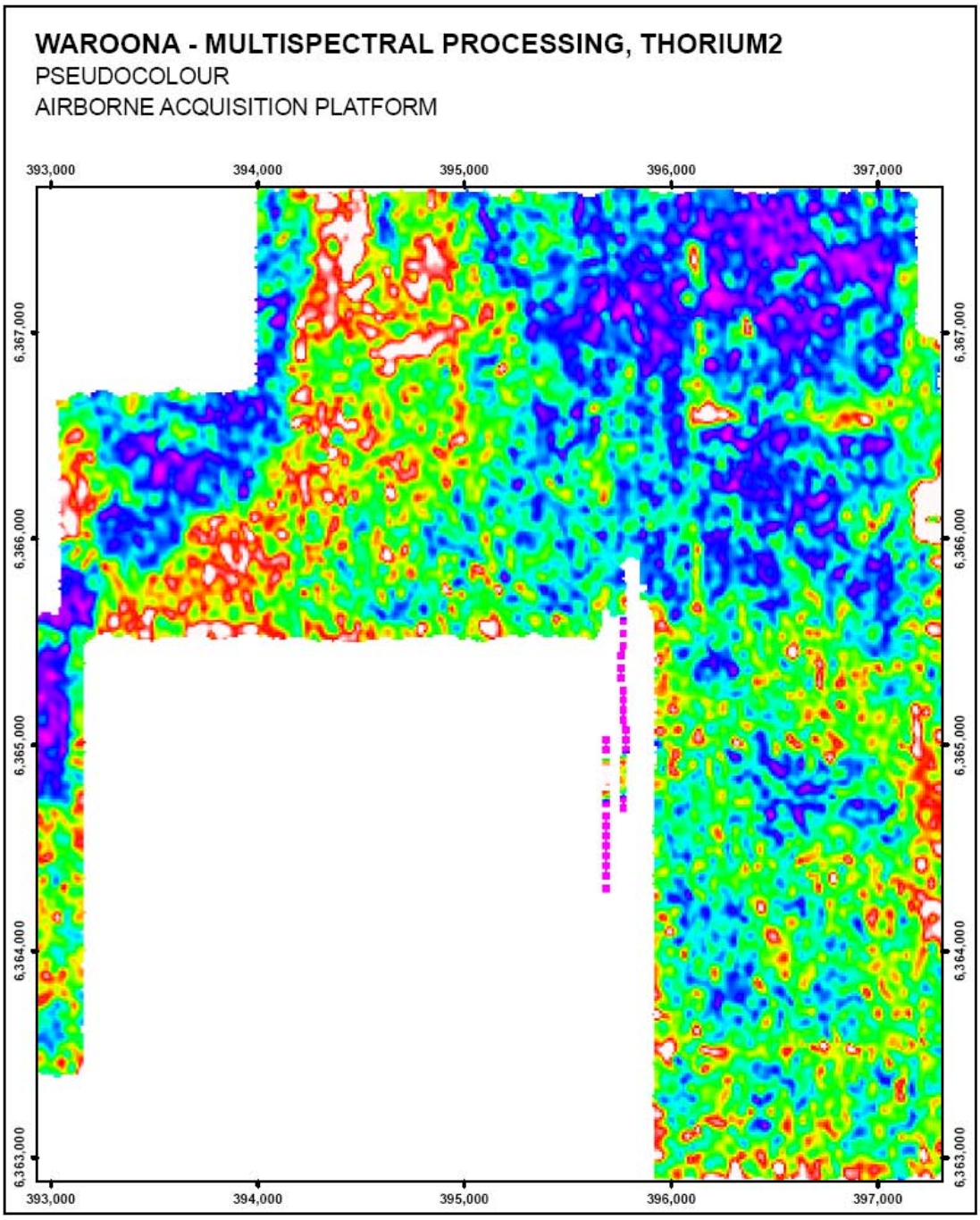


**Figure C.4.10. Thorium 2 multispectral processed, NASVD spectral smoothing, pseudocolour image, Waroona, airborne platform.**

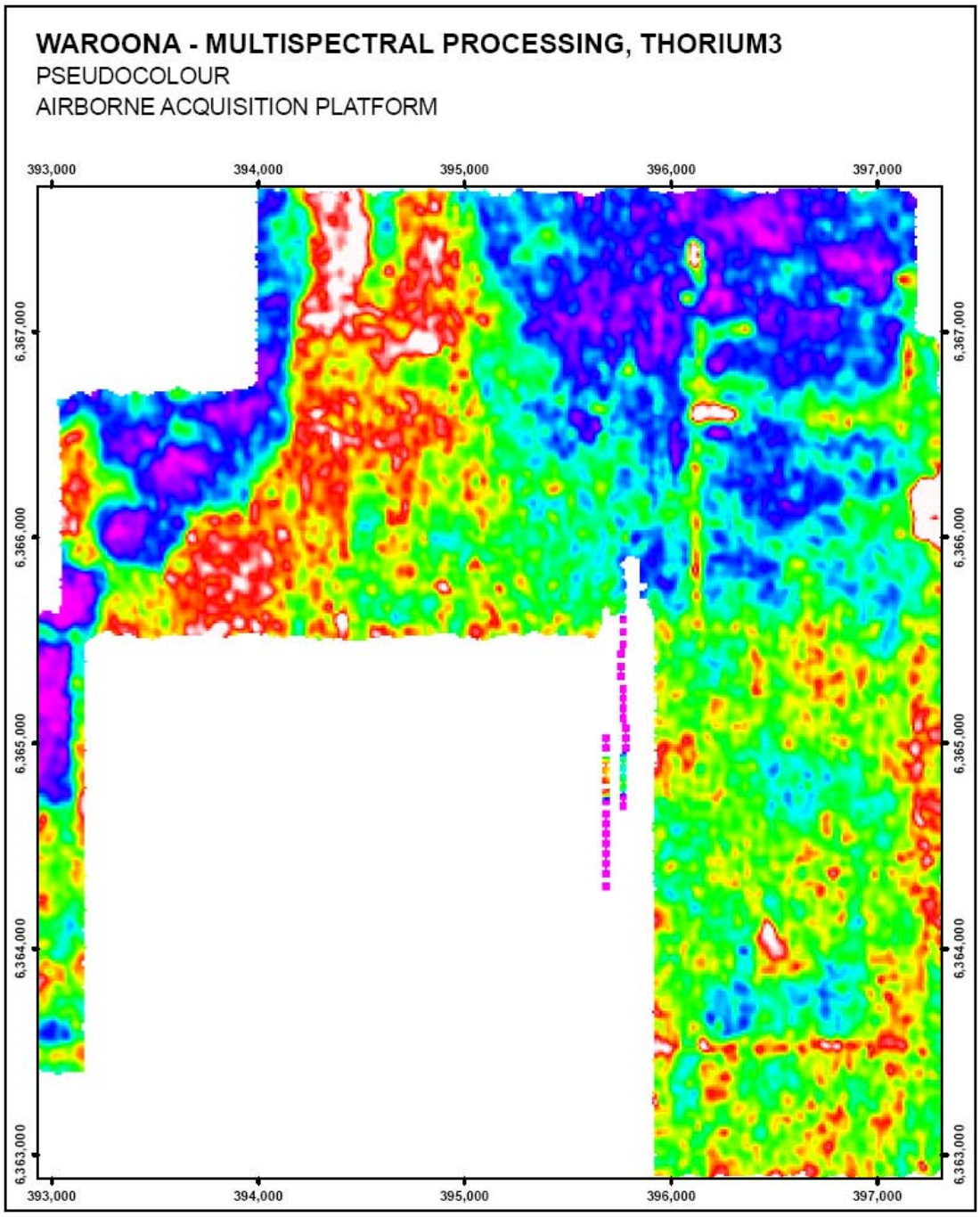


**Figure C.4.11. Thorium 3 multispectral processed, NASVD spectral smoothing, pseudocolour image, Waroona, airborne platform.**

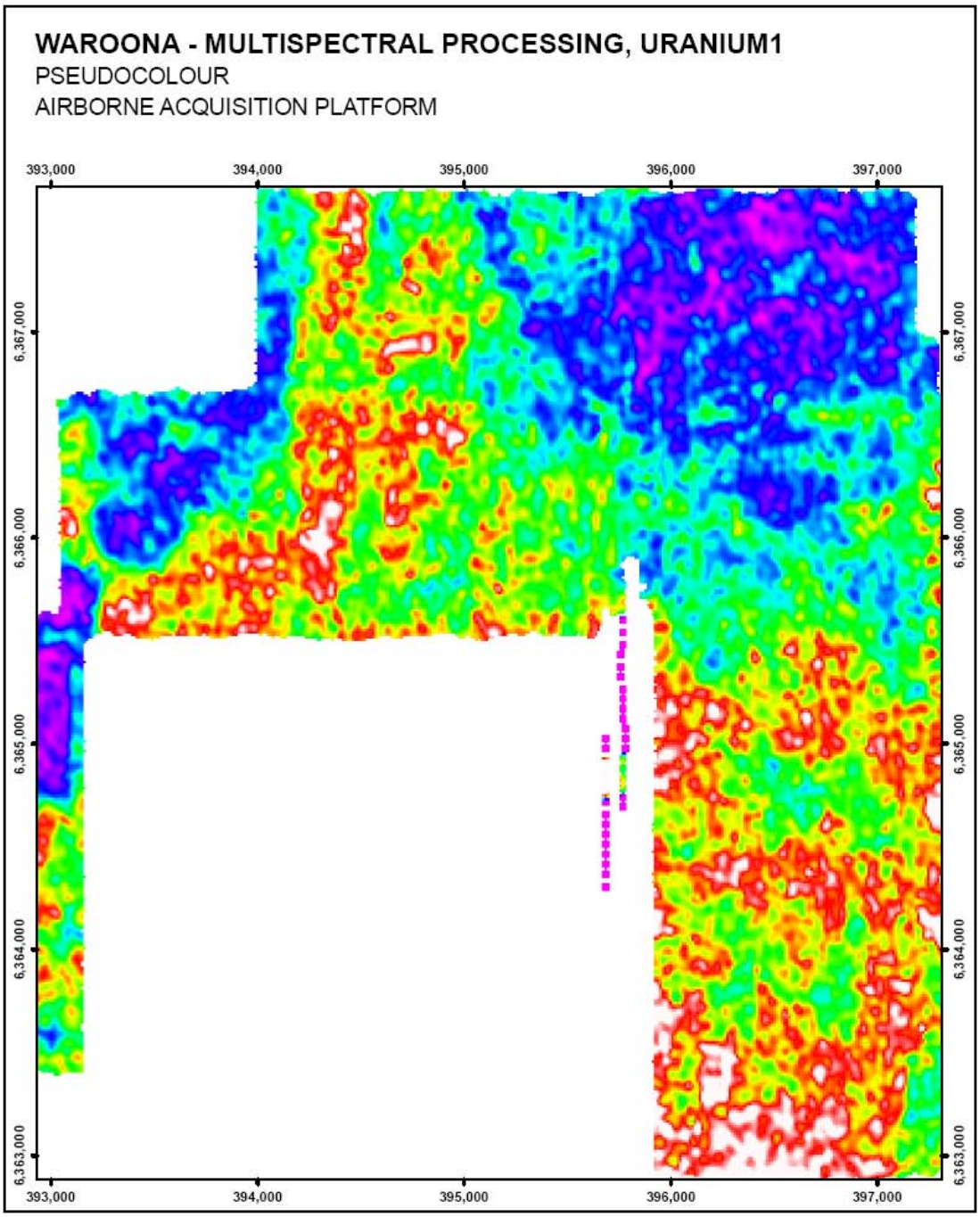


**Figure C.4.12. Uranium 1 multispectral processed, NASVD spectral smoothing, pseudocolour image, Waroona, airborne platform.**

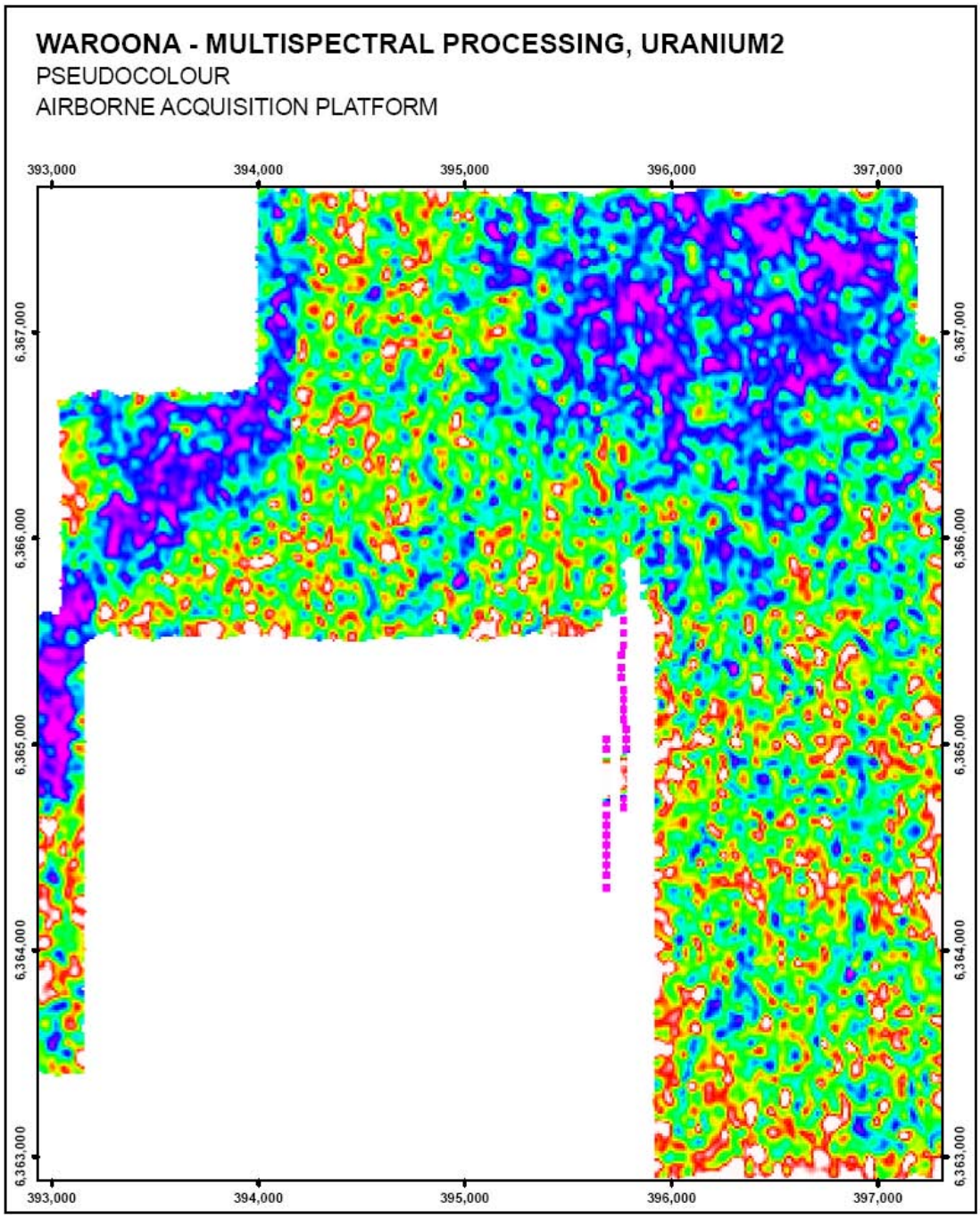


**Figure C.4.13. Uranium 2 multispectral processed, NASVD spectral smoothing, pseudocolour image, Waroona, airborne platform.**

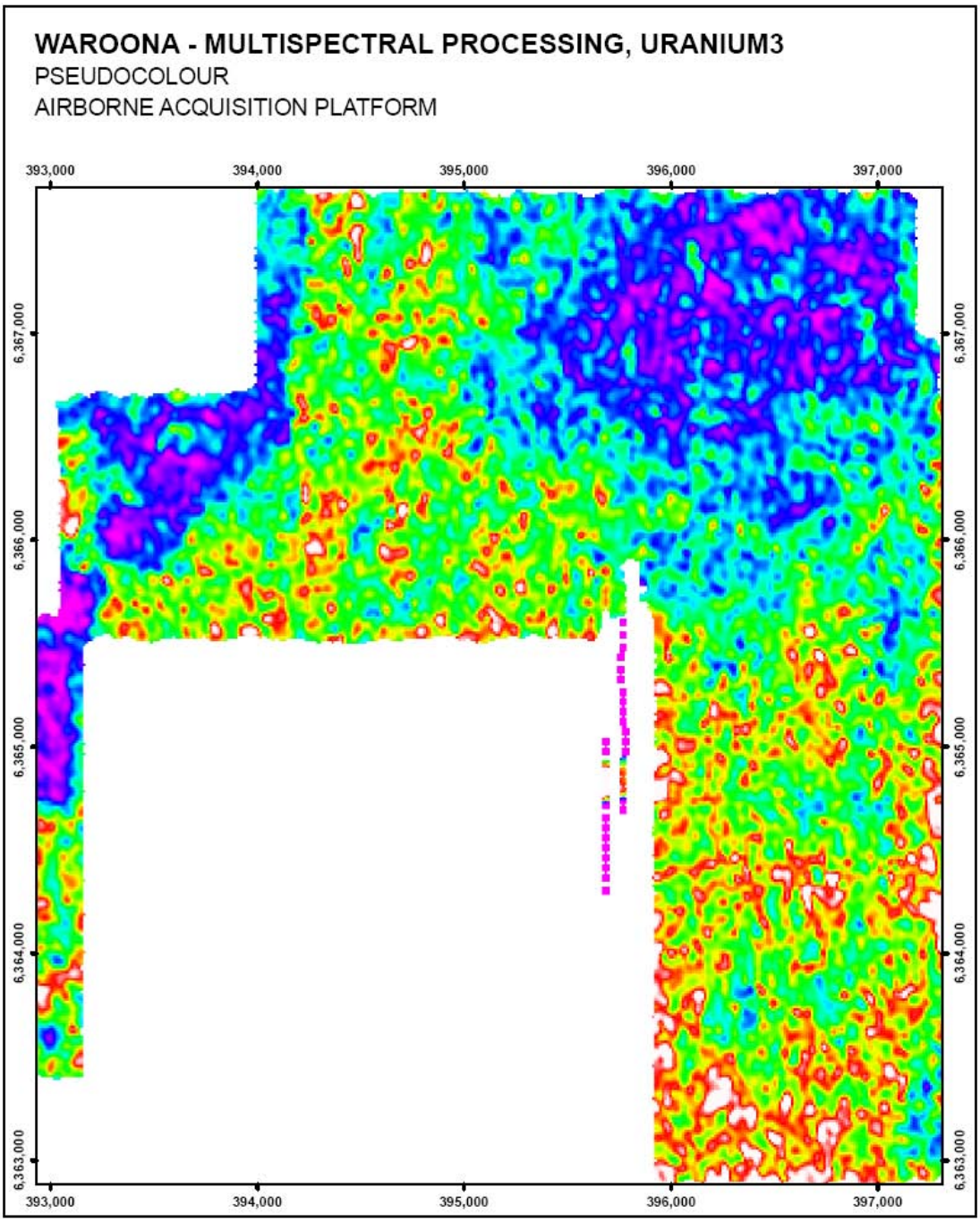


**Figure C.4.14. Uranium 3 multispectral processed, NASVD spectral smoothing, pseudocolour image, Waroona, airborne platform.**

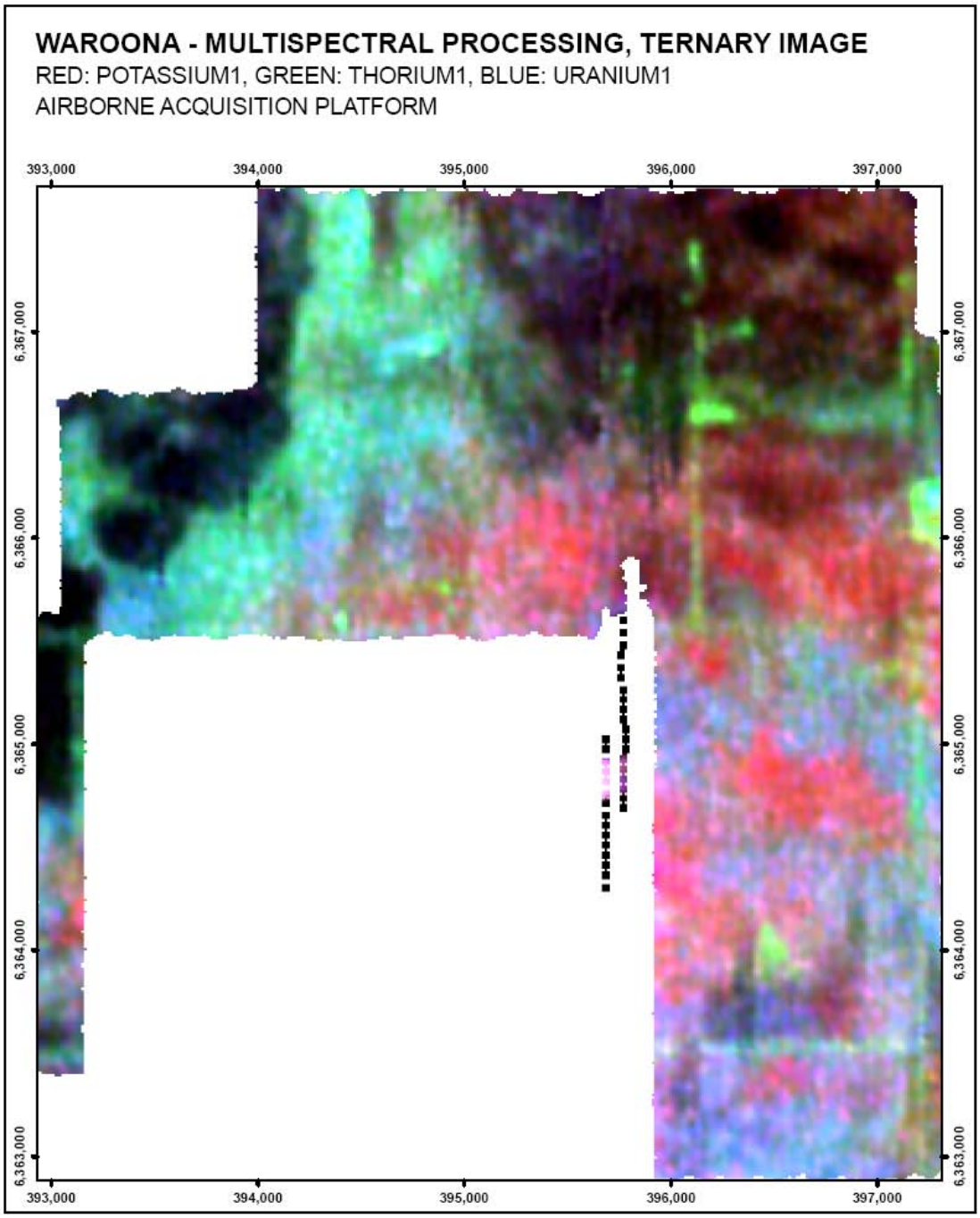


**Figure C.4.15. Ternary multispectral processed, NASVD spectral smoothing, ternary image, Waroona, airborne platform.**

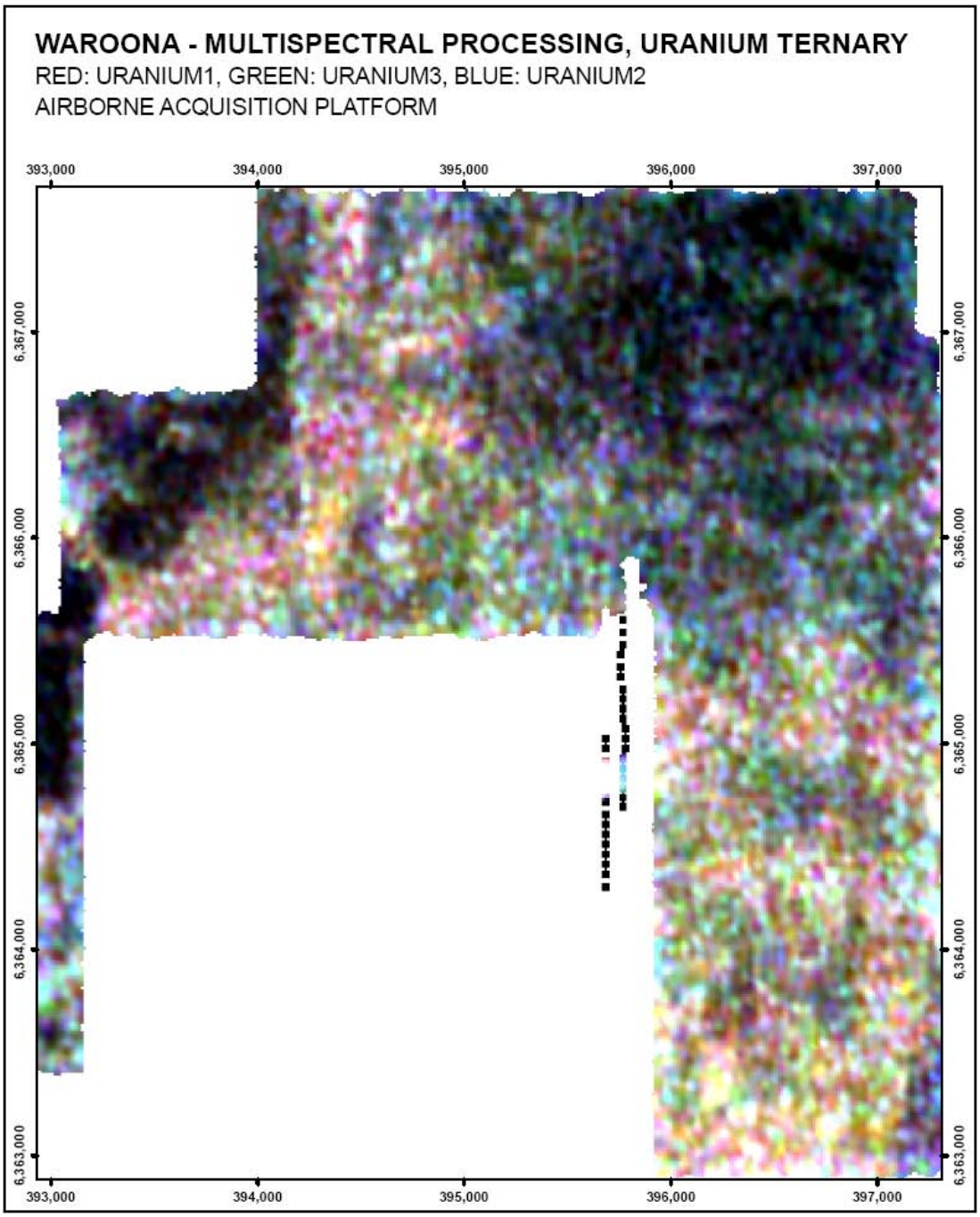


**Figure C.4.16. Uranium ternary multispectral processed, NASVD spectral smoothing, ternary image, Waroona, airborne platform.**

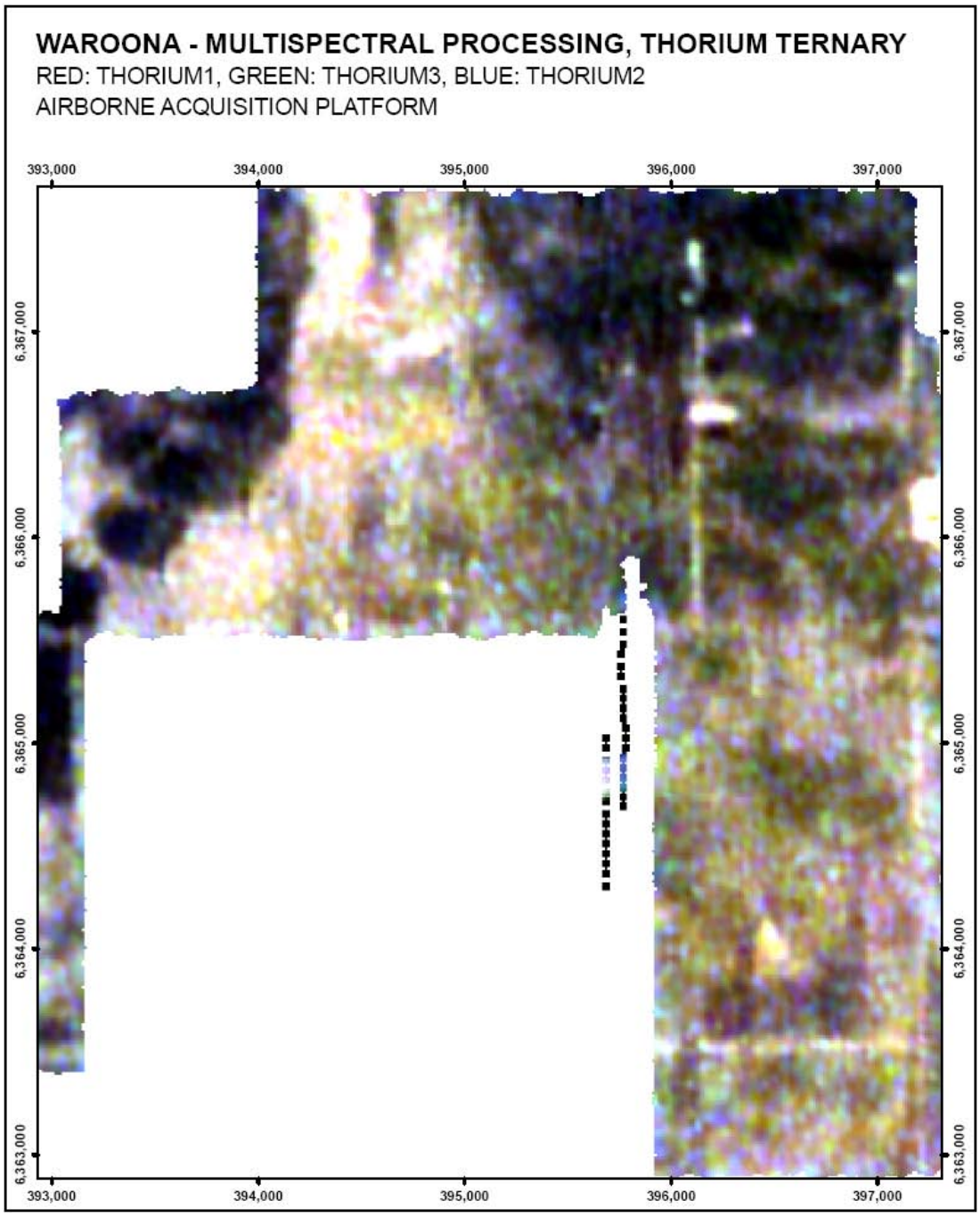


**Figure C.4.17. Thorium ternary multispectral processed, NASVD spectral smoothing, ternary image, Waroona, airborne platform.**

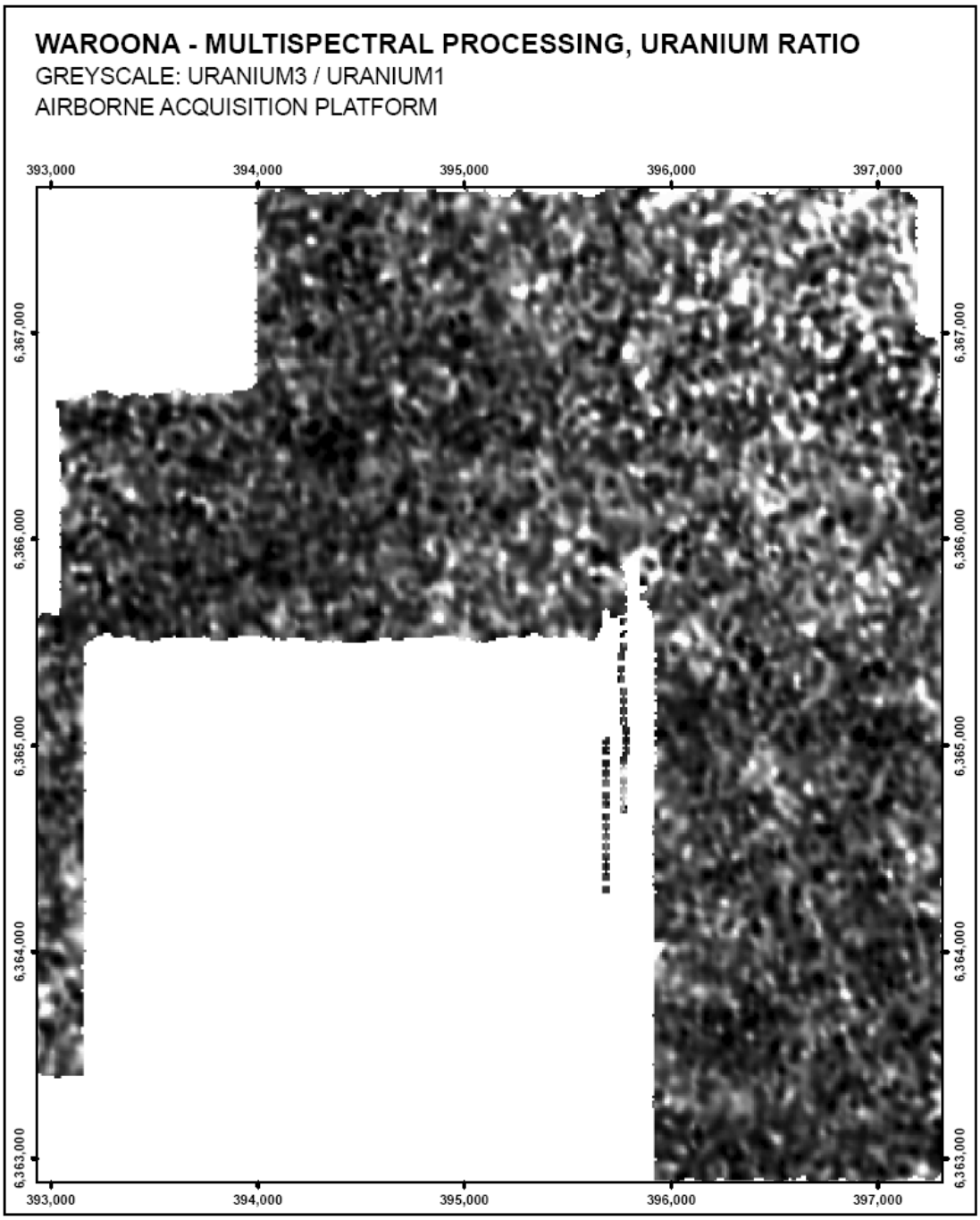


**Figure C.4.18. Uranium ratio multispectral processed, NASVD spectral smoothing, greyscale image, Waroona, airborne platform.**

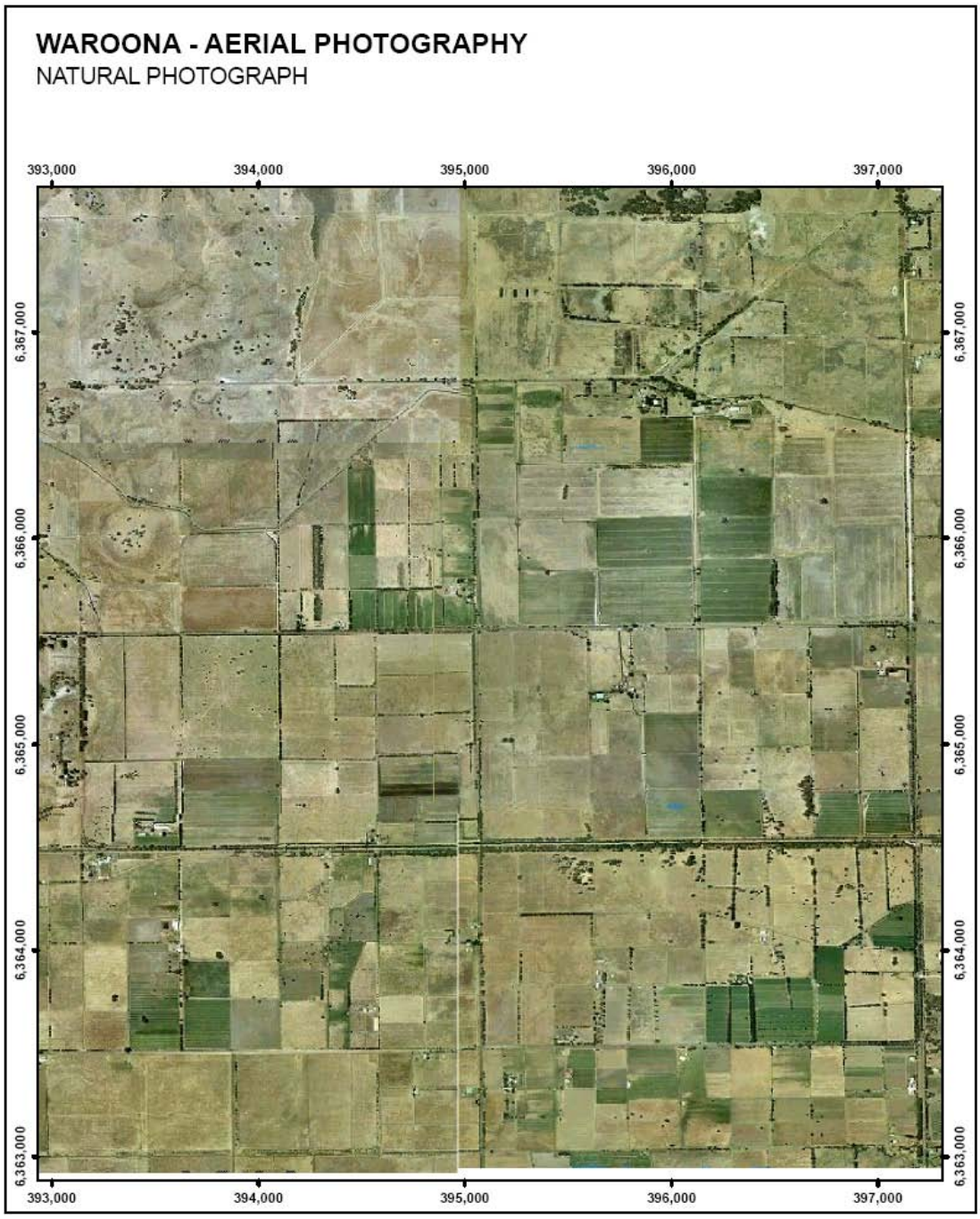


**Figure C.4.19. Natural colour aerial photo, Waroona, airborne survey area.**

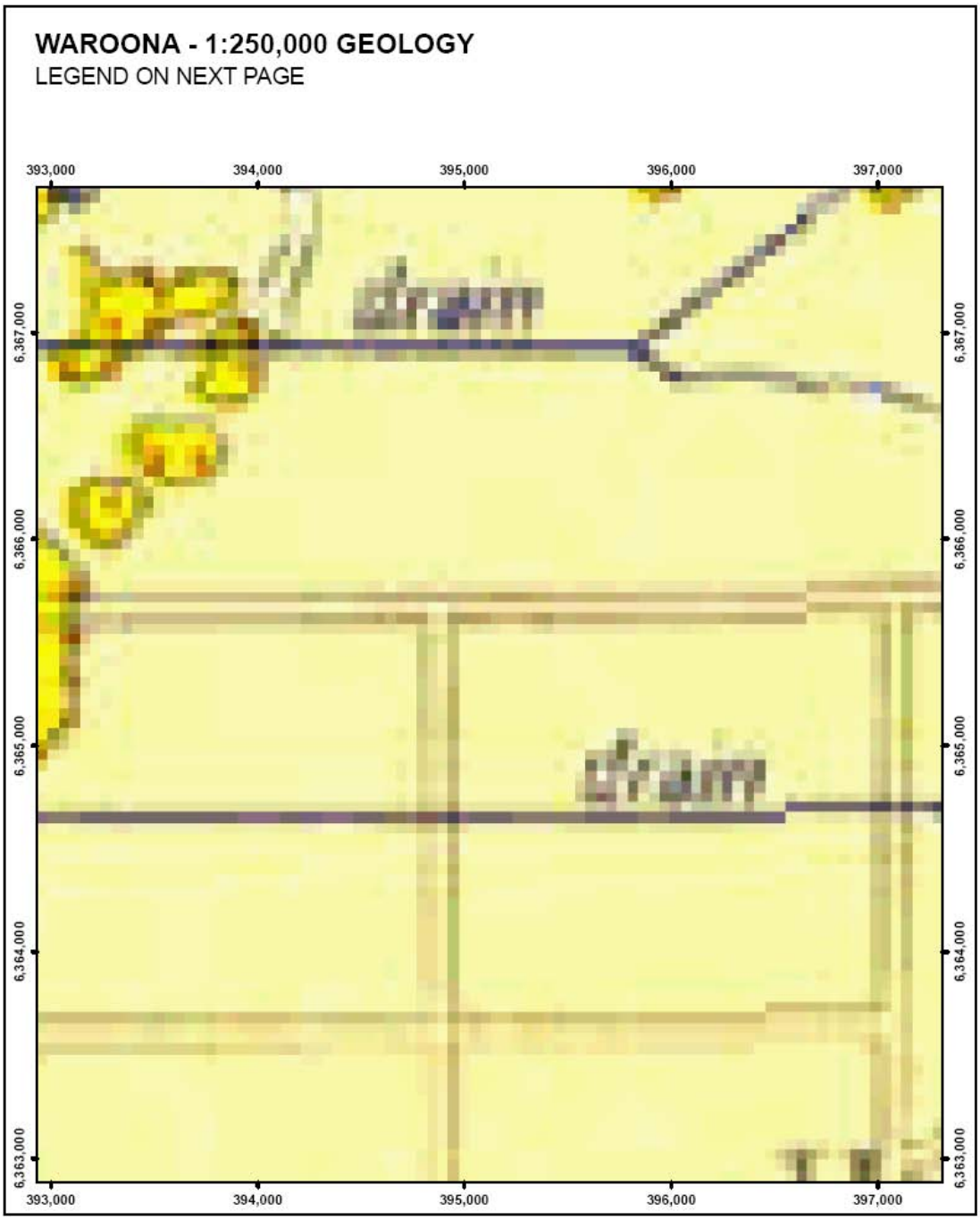


**Figure C.4.20. 1:250,000 geology for Waroona airborne survey area (from Low *et al.*, 1980).**

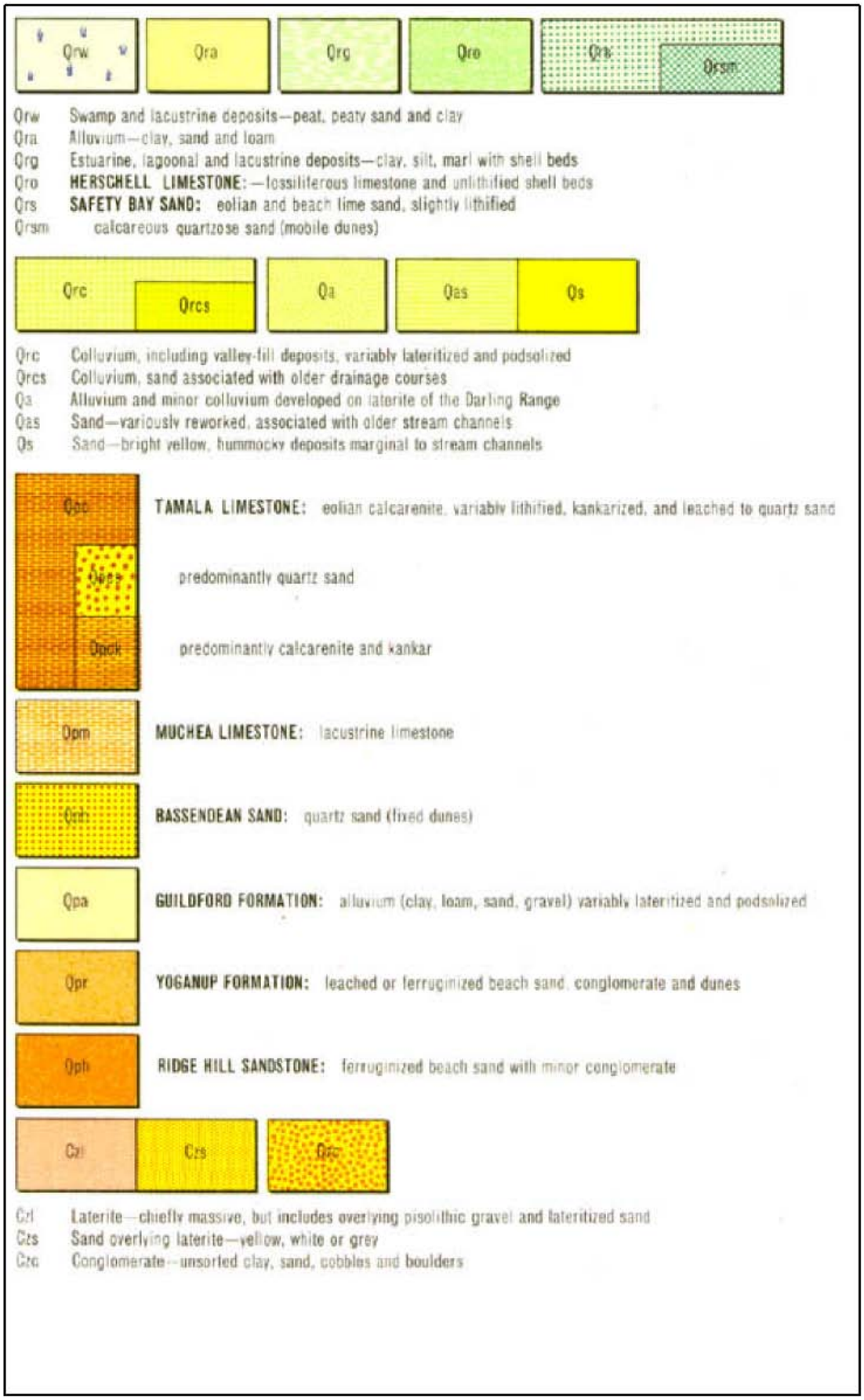


**Figure C.4.20 cont'd. 1:250,000 geology legend for Waroona airborne survey area (from Low *et al.*, 1980).**

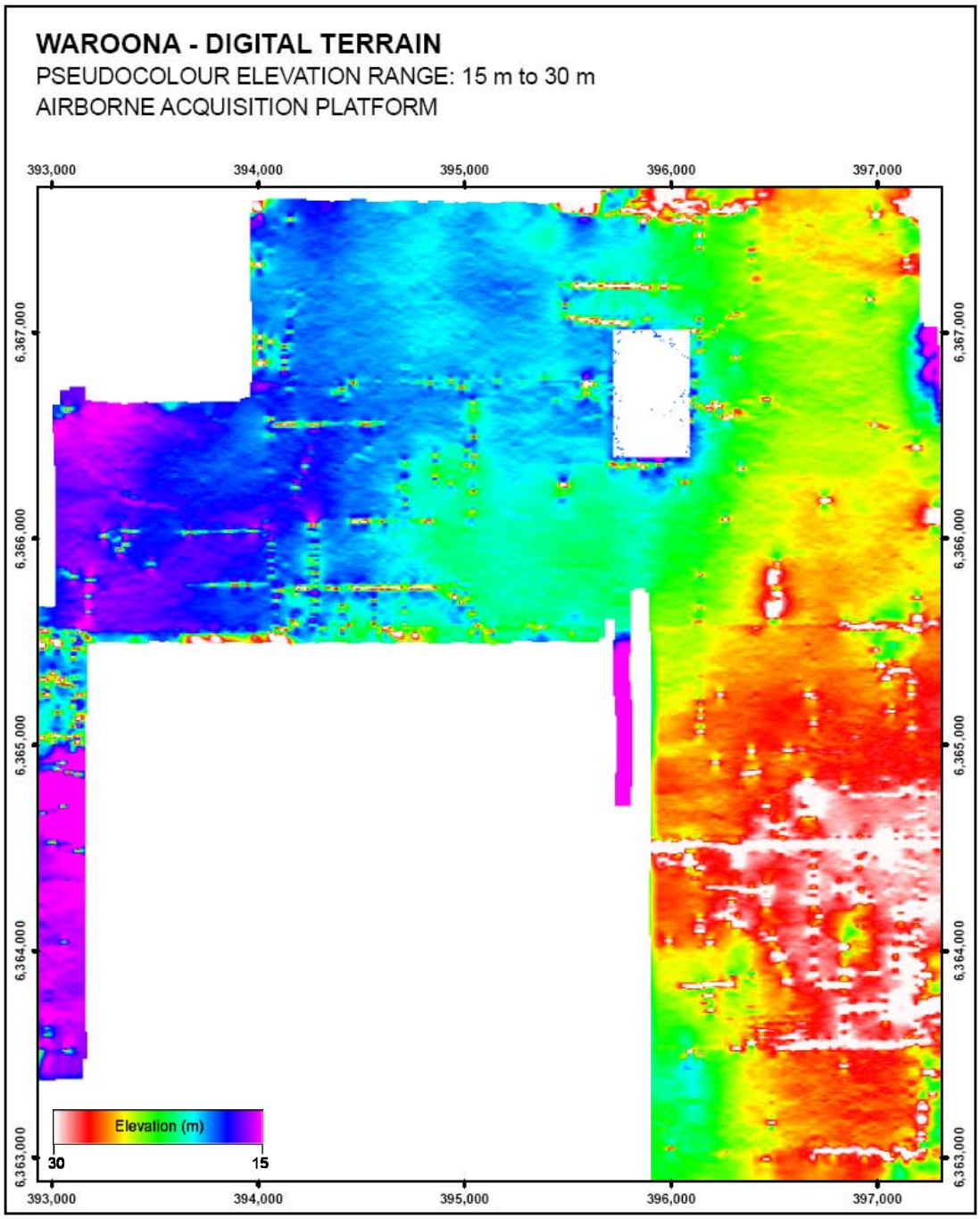


**Figure C.4.21. Digital terrain (elevation) image, Waroona airborne survey area.**

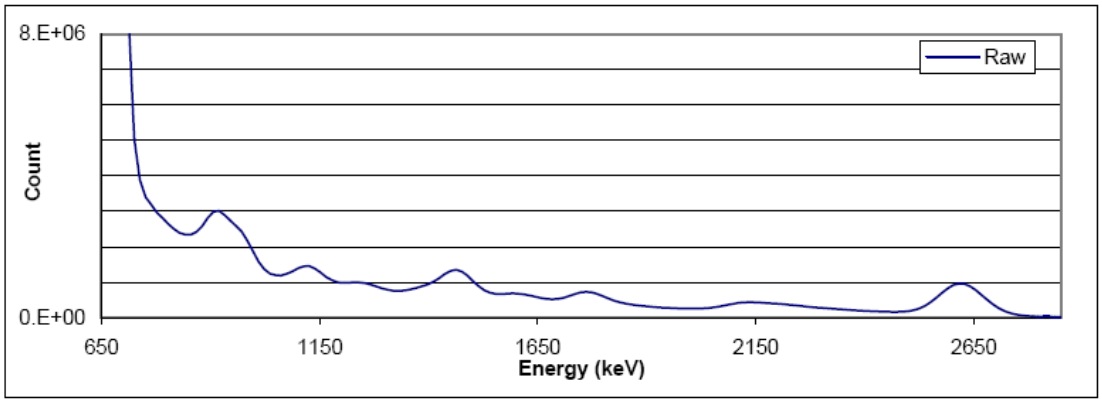


**Figure C.5.1. Average raw spectrum derived from 256-channel data, Waroona, ground platform.**

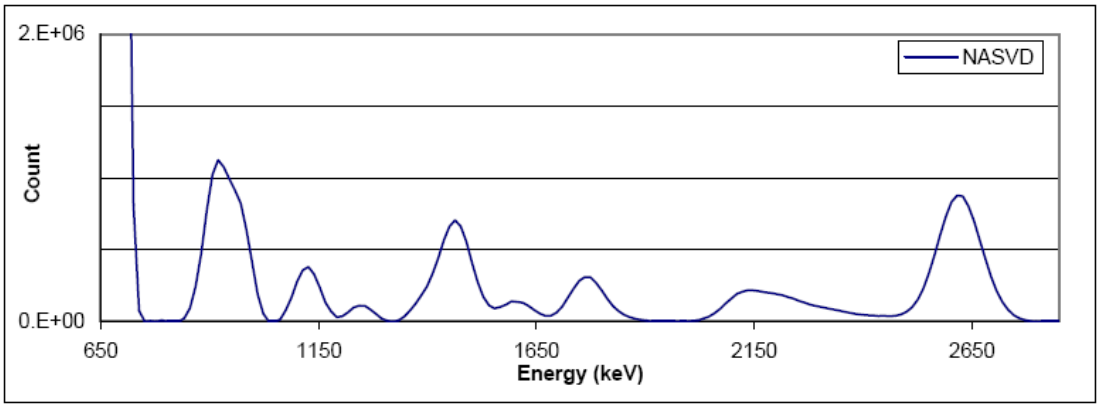


**Figure C.5.2. Average NASVD smoothed spectrum following Compton continuum removal, Waroona, ground platform.**

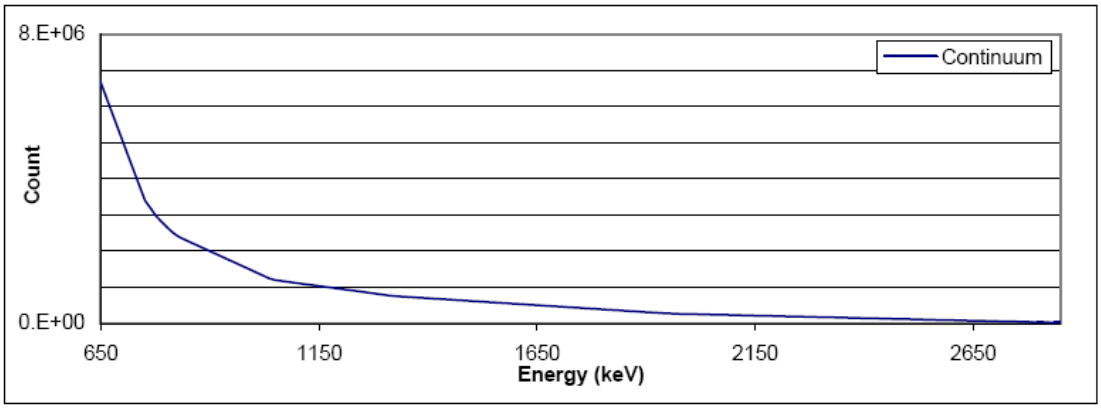


**Figure C.5.3. Average continuum removed from the raw spectrum, Waroona, ground platform.**

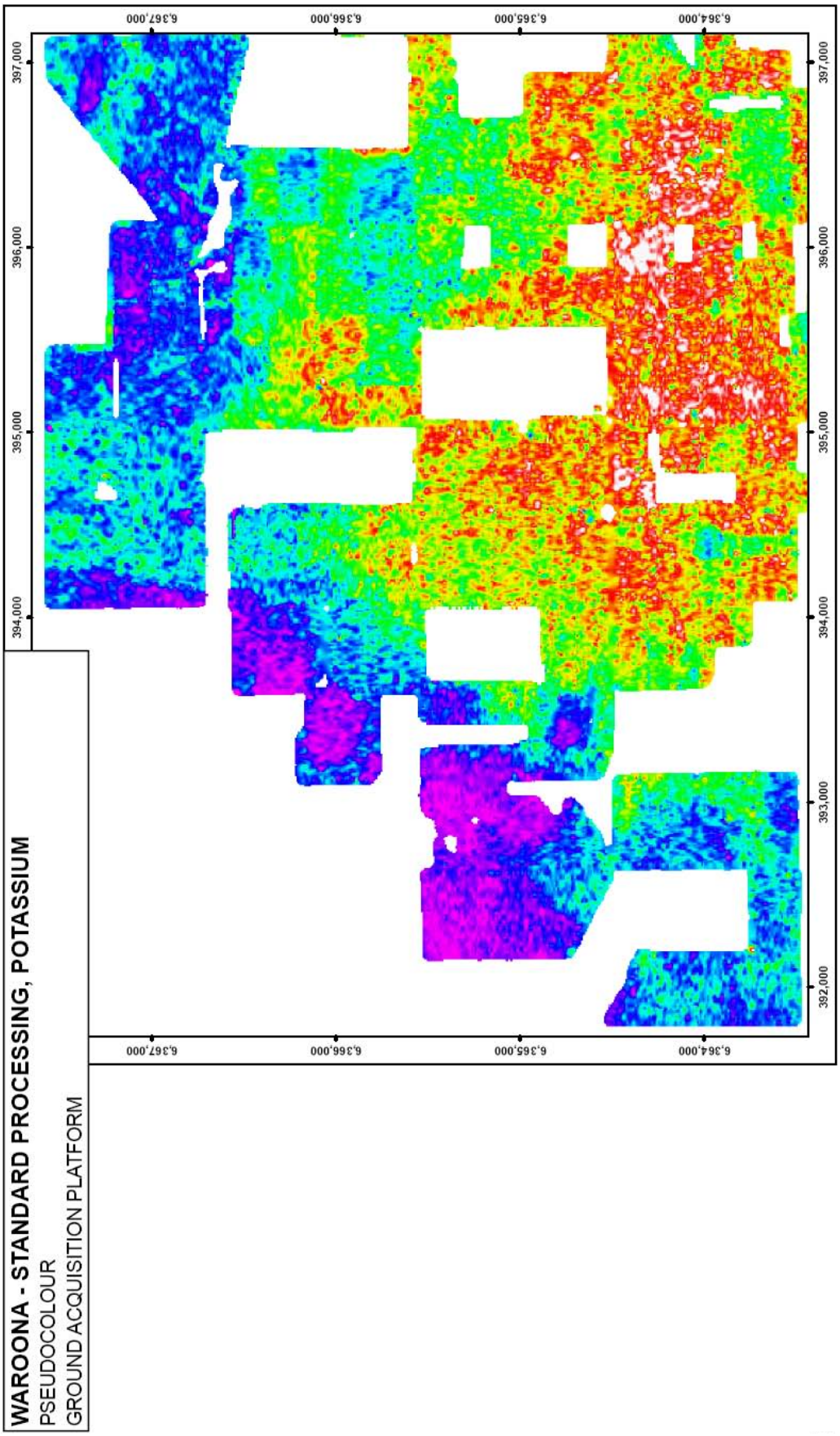


**Figure C.5.4. Potassium standard processed pseudocolour image, Waroona, ground platform.**

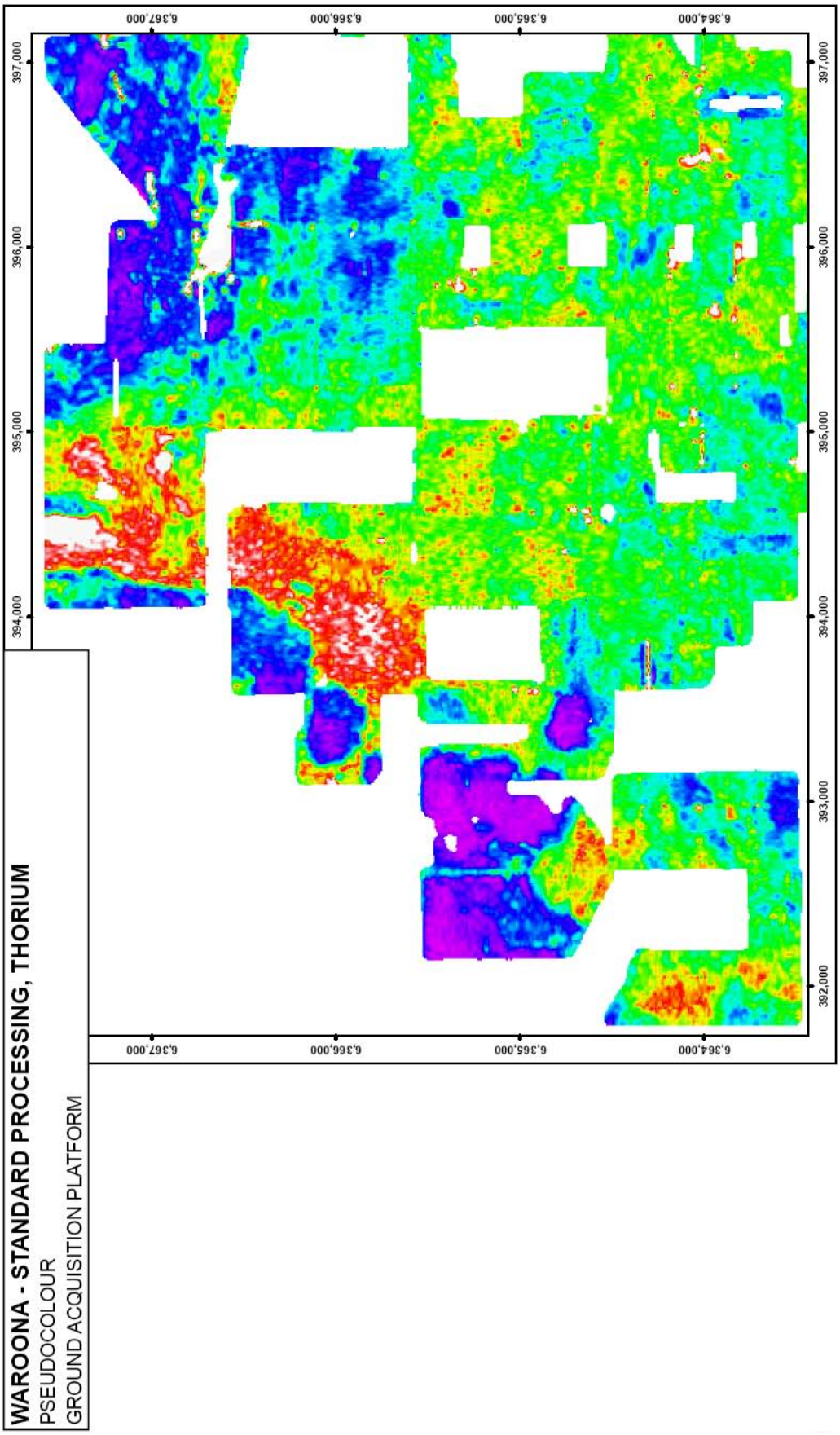


**Figure C.5.5. Thorium standard processed pseudocolour image, Waroona, ground platform.**

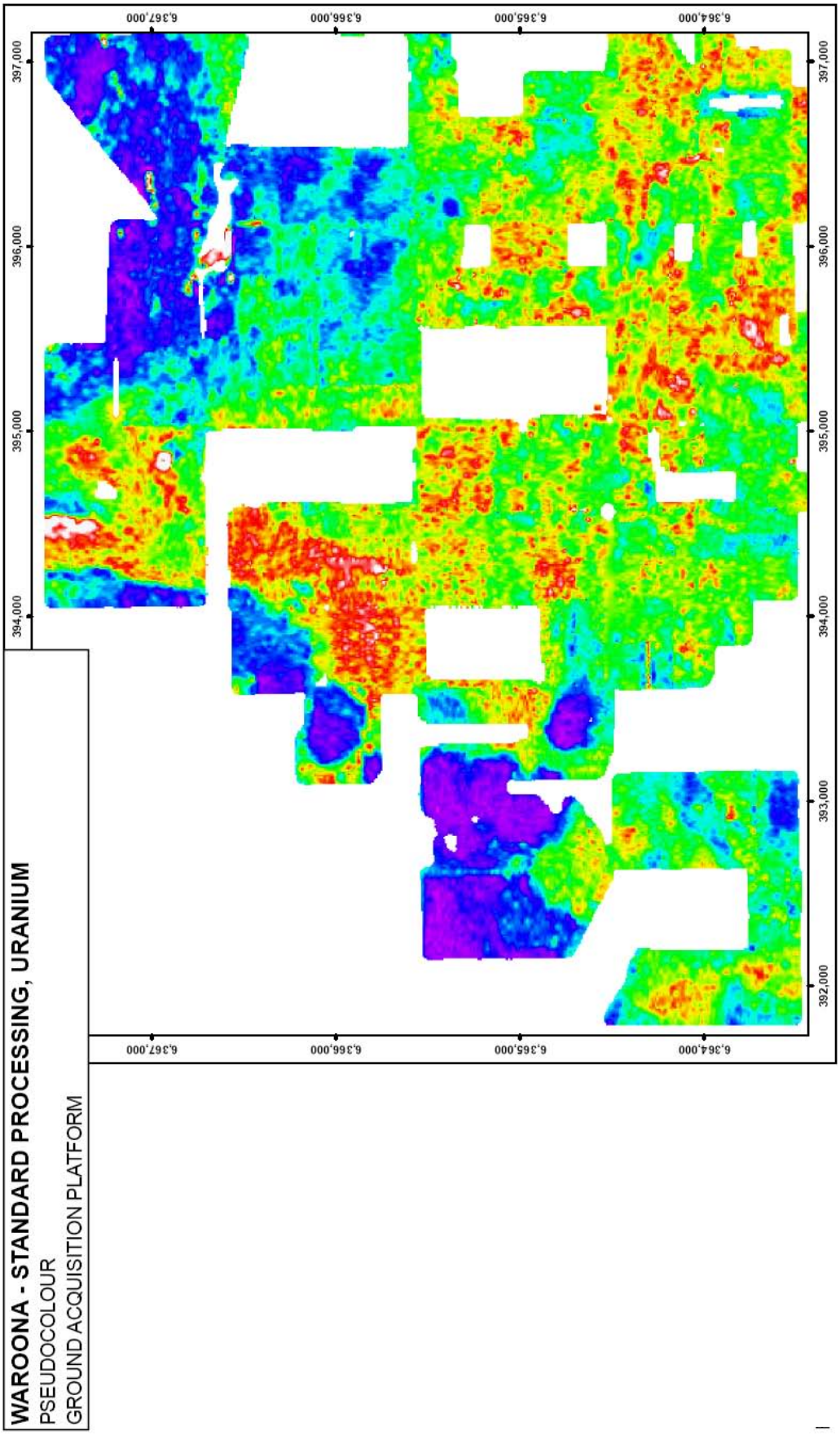


**Figure C.5.6. Uranium standard processed pseudocolour image, Waroona, ground platform.**

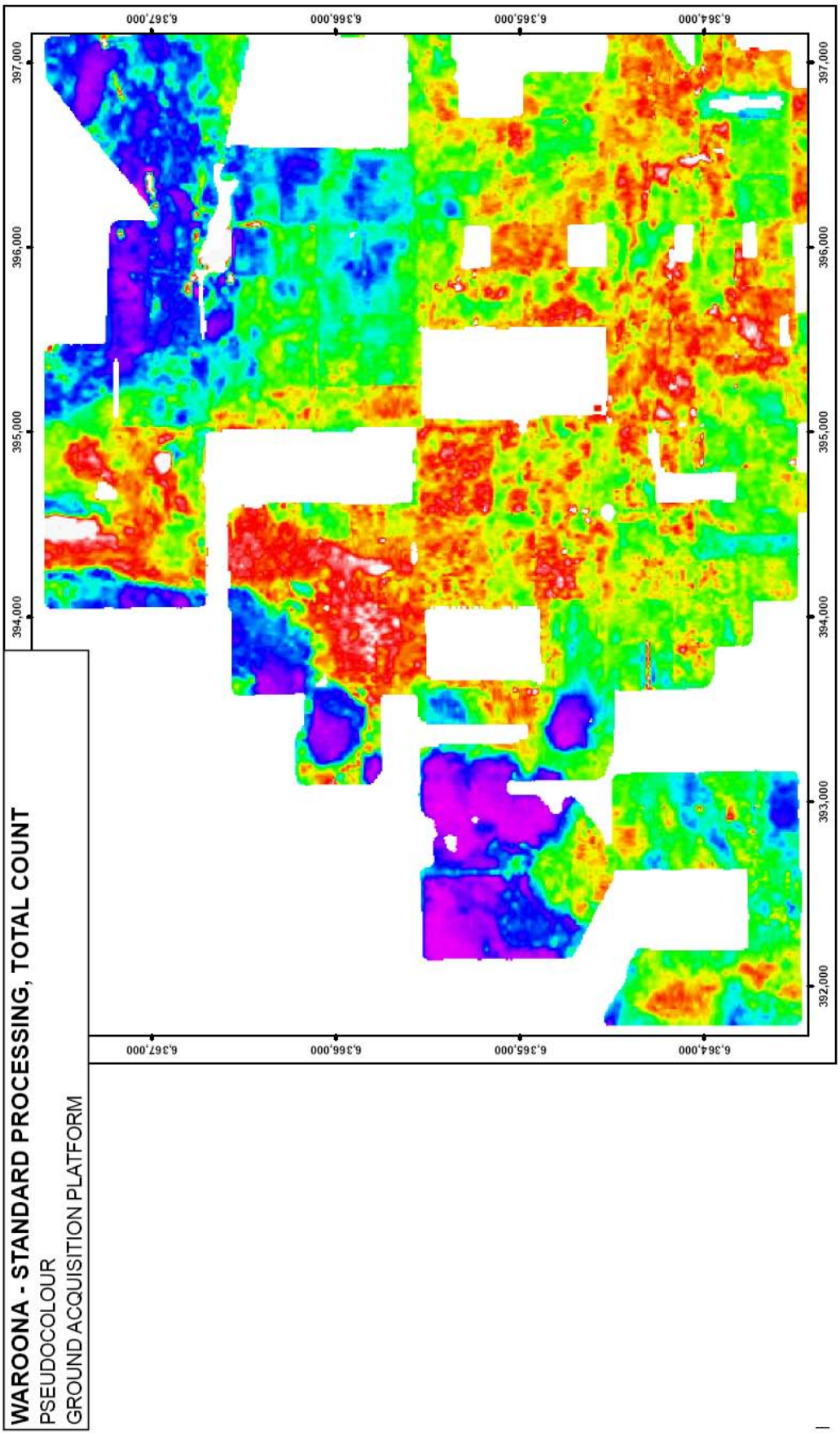


**Figure C.5.7. Total count standard processed pseudocolour image, Waroona, ground platform.**

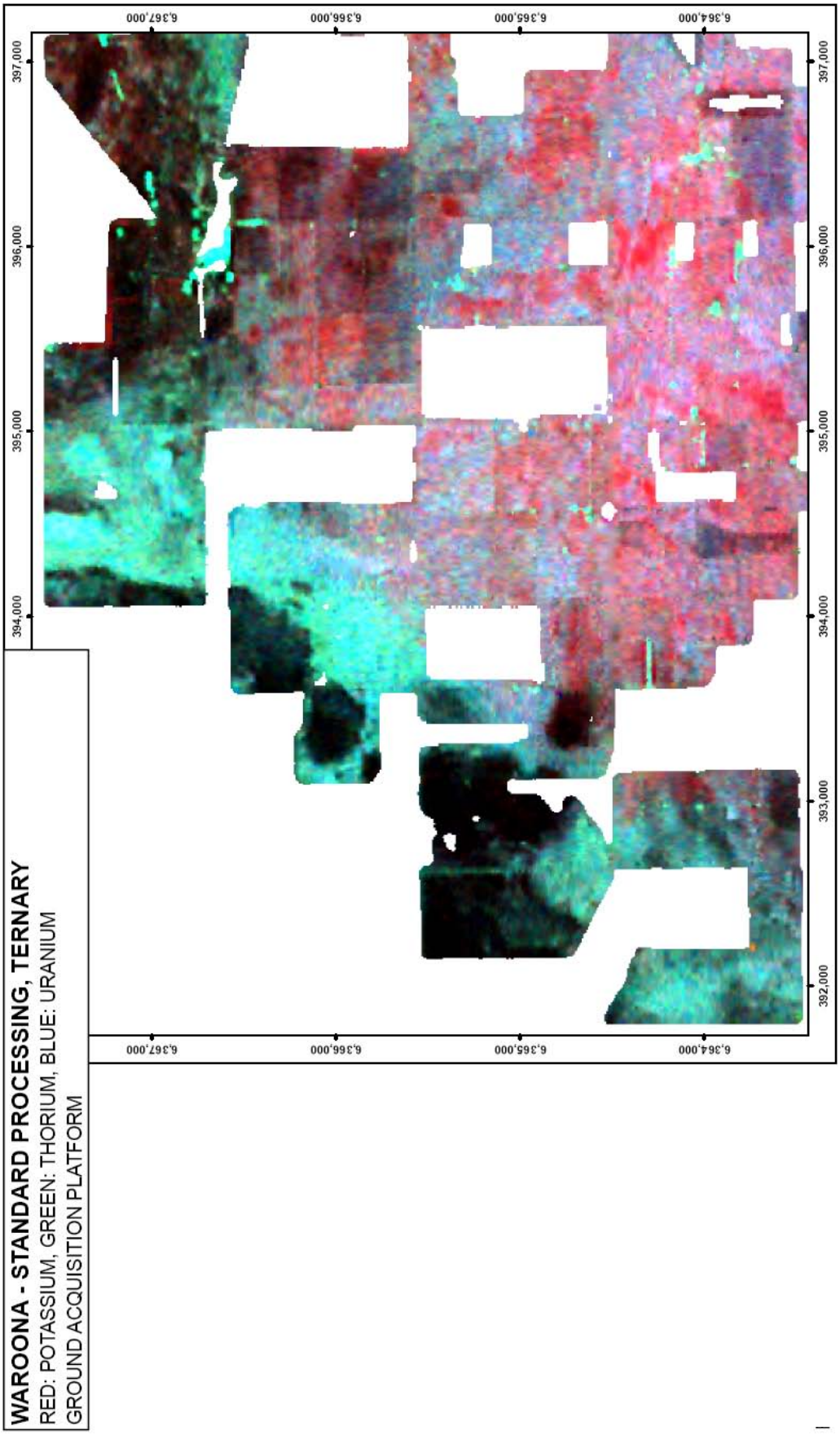


**Figure C.5.8. Ternary standard processed pseudocolour image, Waroona, ground platform.**

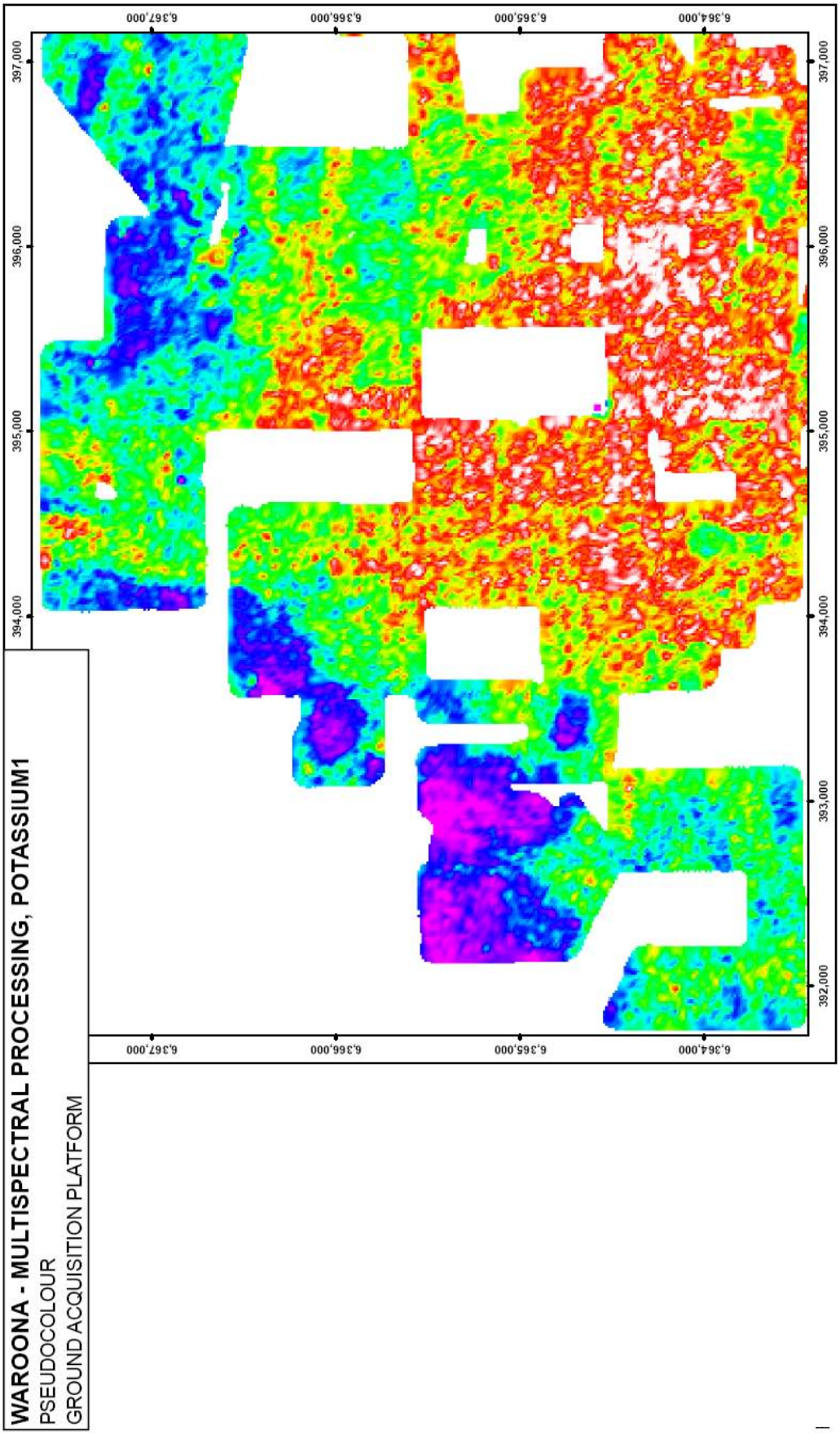


**Figure C.5.9. Potassium 1 multispectral processed, NASVD spectral smoothing, pseudocolour image, Waroona, ground platform.**

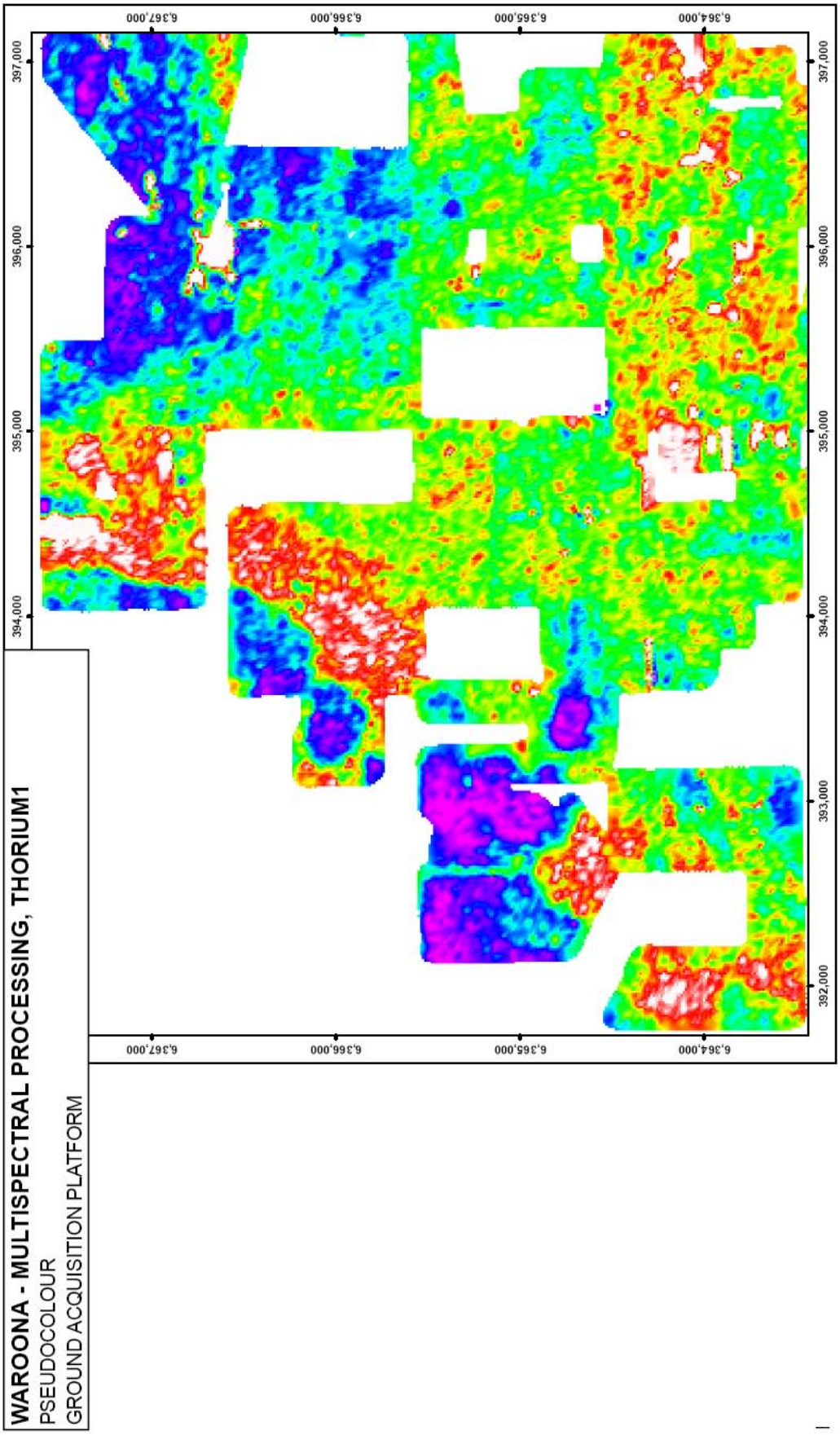


**Figure C.5.10. Thorium 1 multispectral processed, NASVD spectral smoothing, pseudocolour image, Waroona, ground platform.**

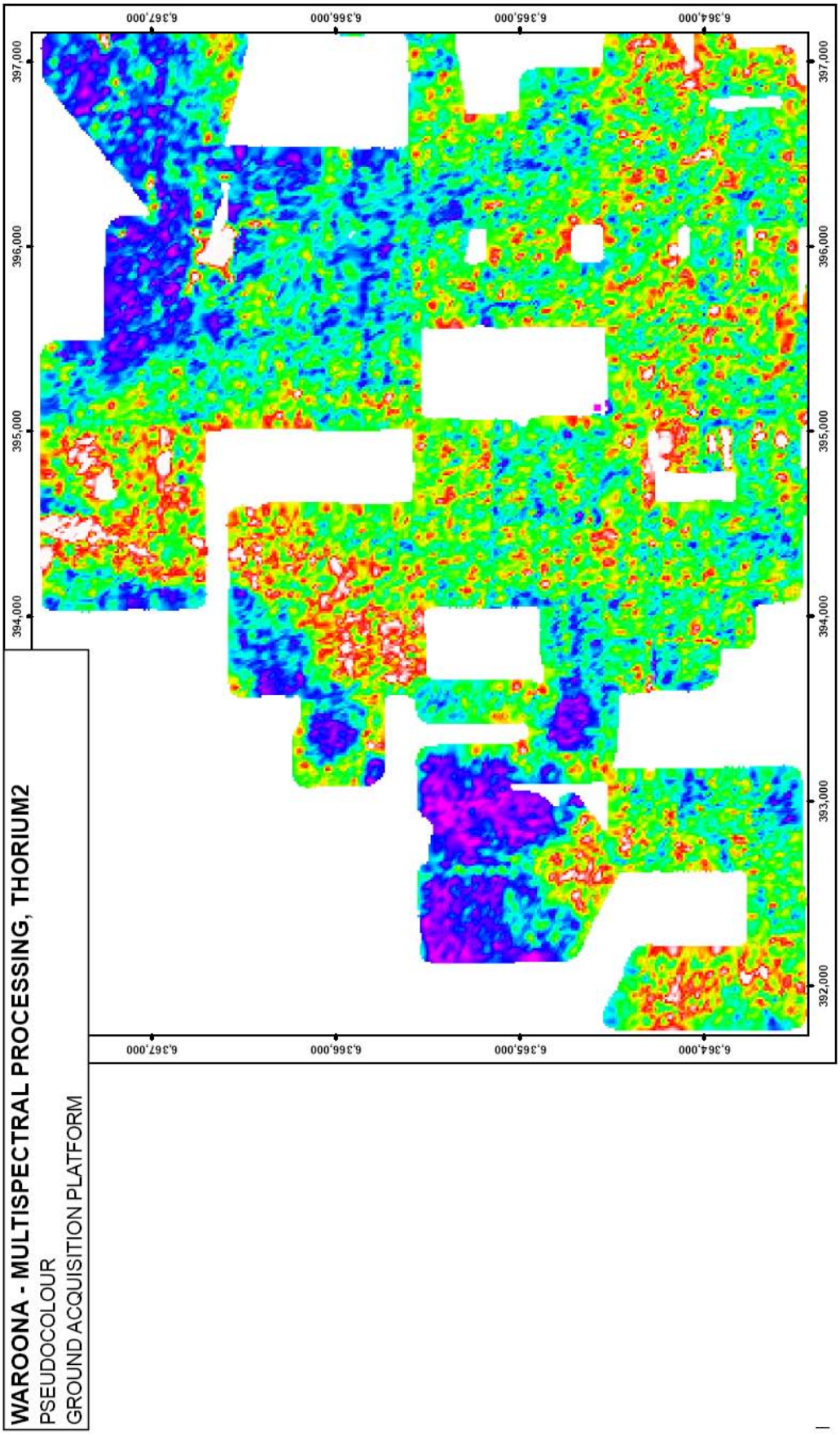


**Figure C.5.11. Thorium 2 multispectral processed, NASVD spectral smoothing, pseudocolour image, Waroona, ground platform.**

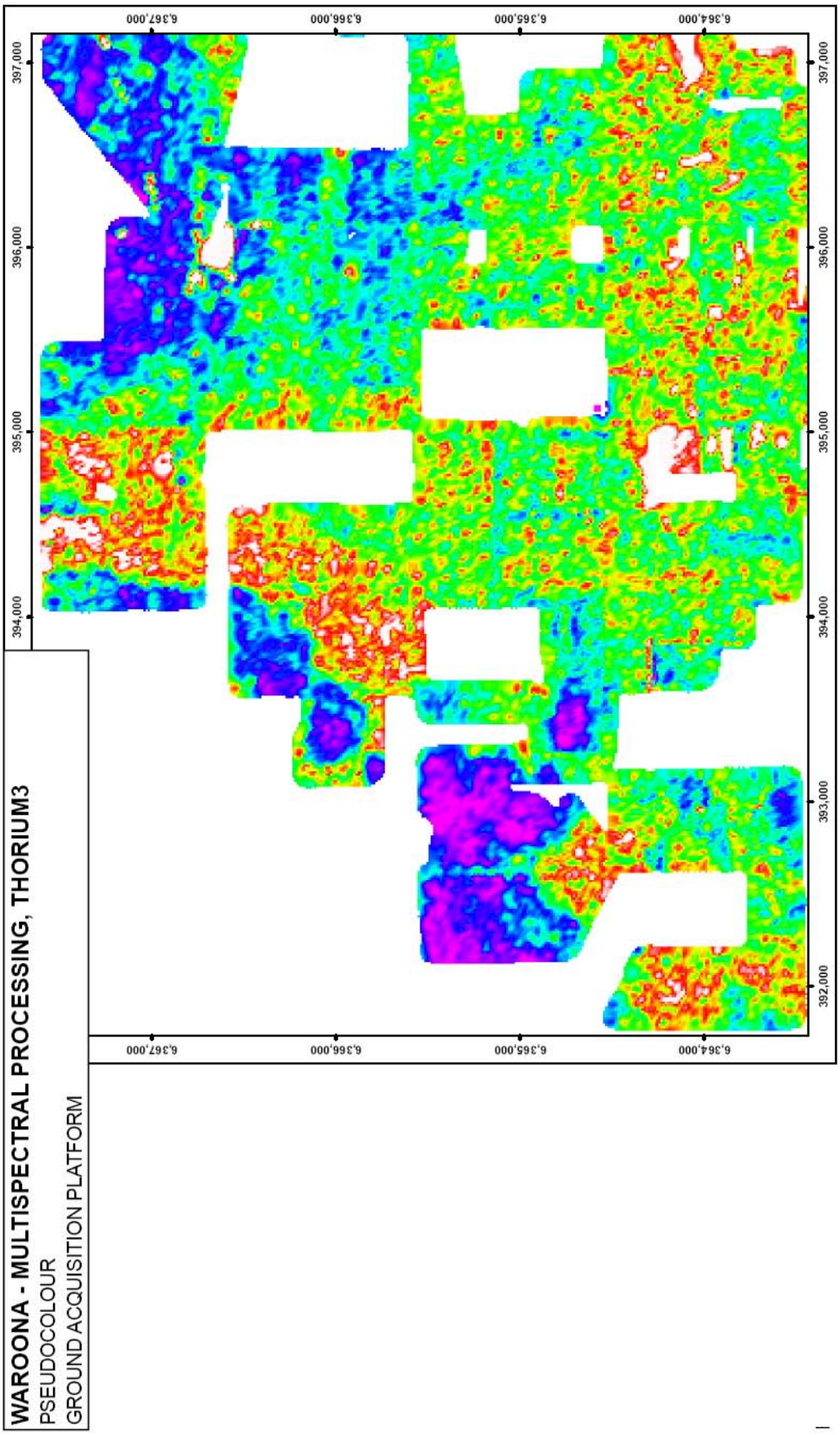


**Figure C.5.12. Thorium 3 multispectral processed, NASVD spectral smoothing, pseudocolour image, Waroona, ground platform.**

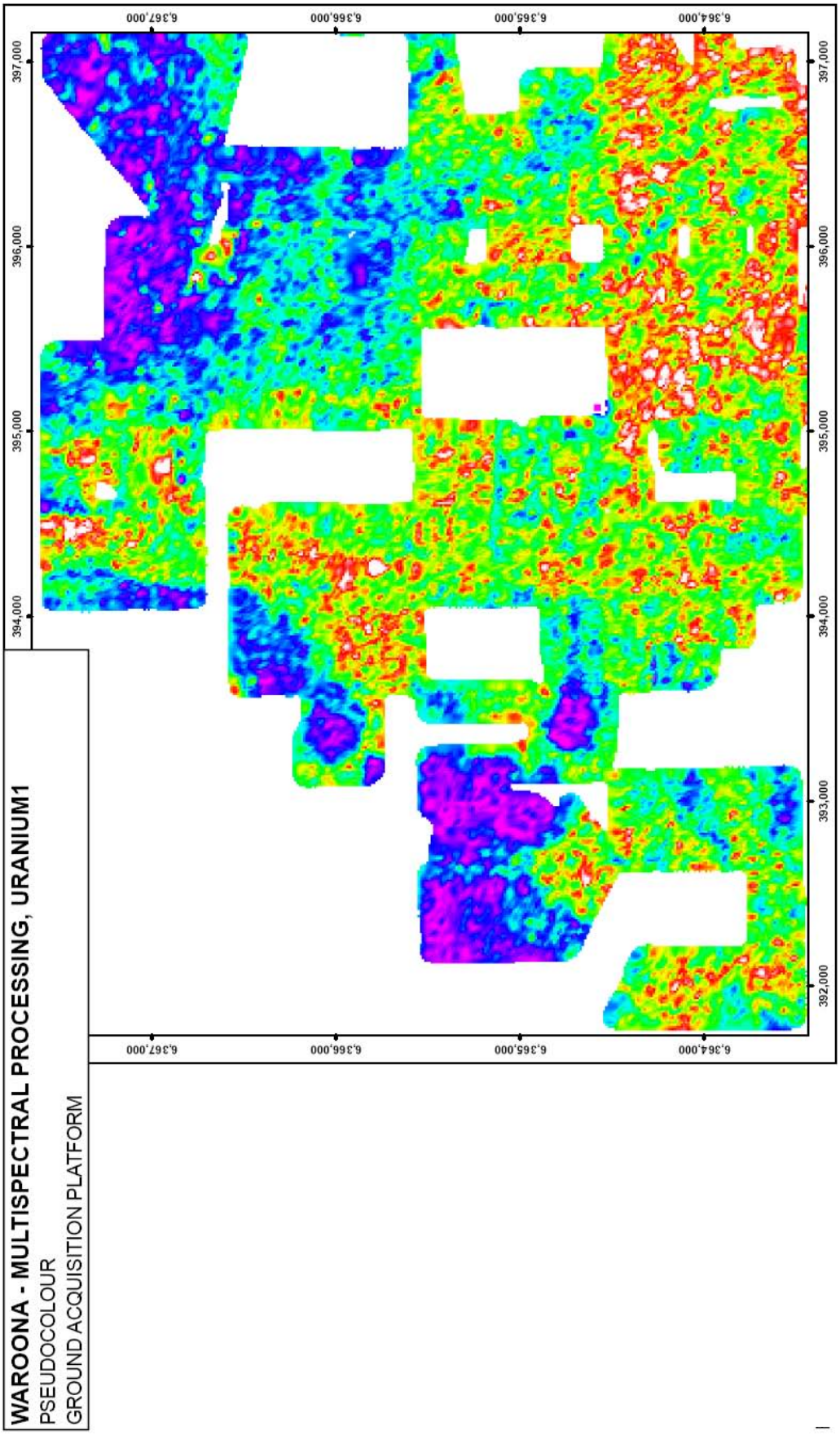


**Figure C.5.13. Uranium 1 multispectral processed, NASVD spectral smoothing, pseudocolour image, Waroona, ground platform.**

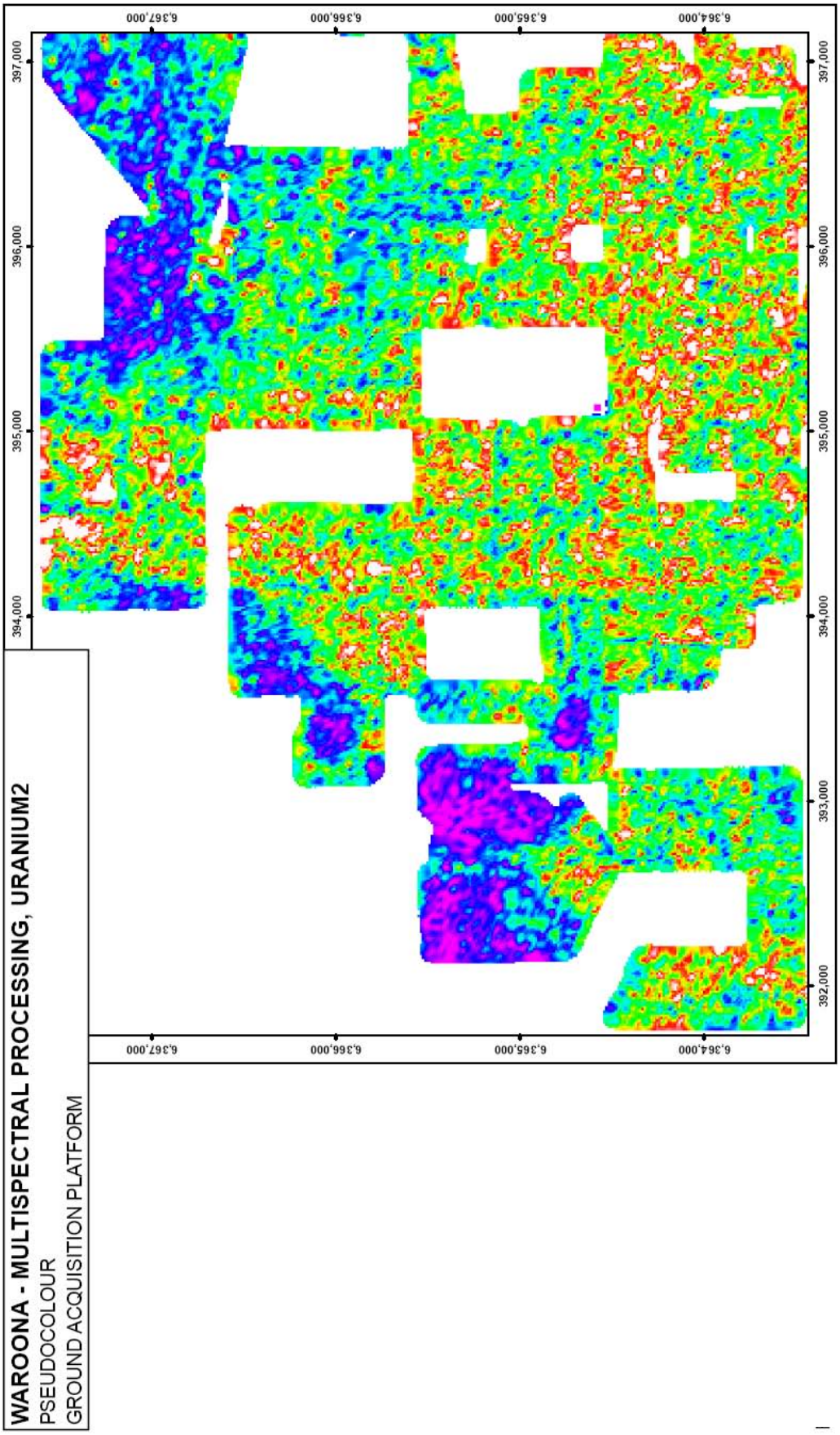


**Figure C.5.14. Uranium 2 multispectral processed, NASVD spectral smoothing, pseudocolour image, Waroona, ground platform.**

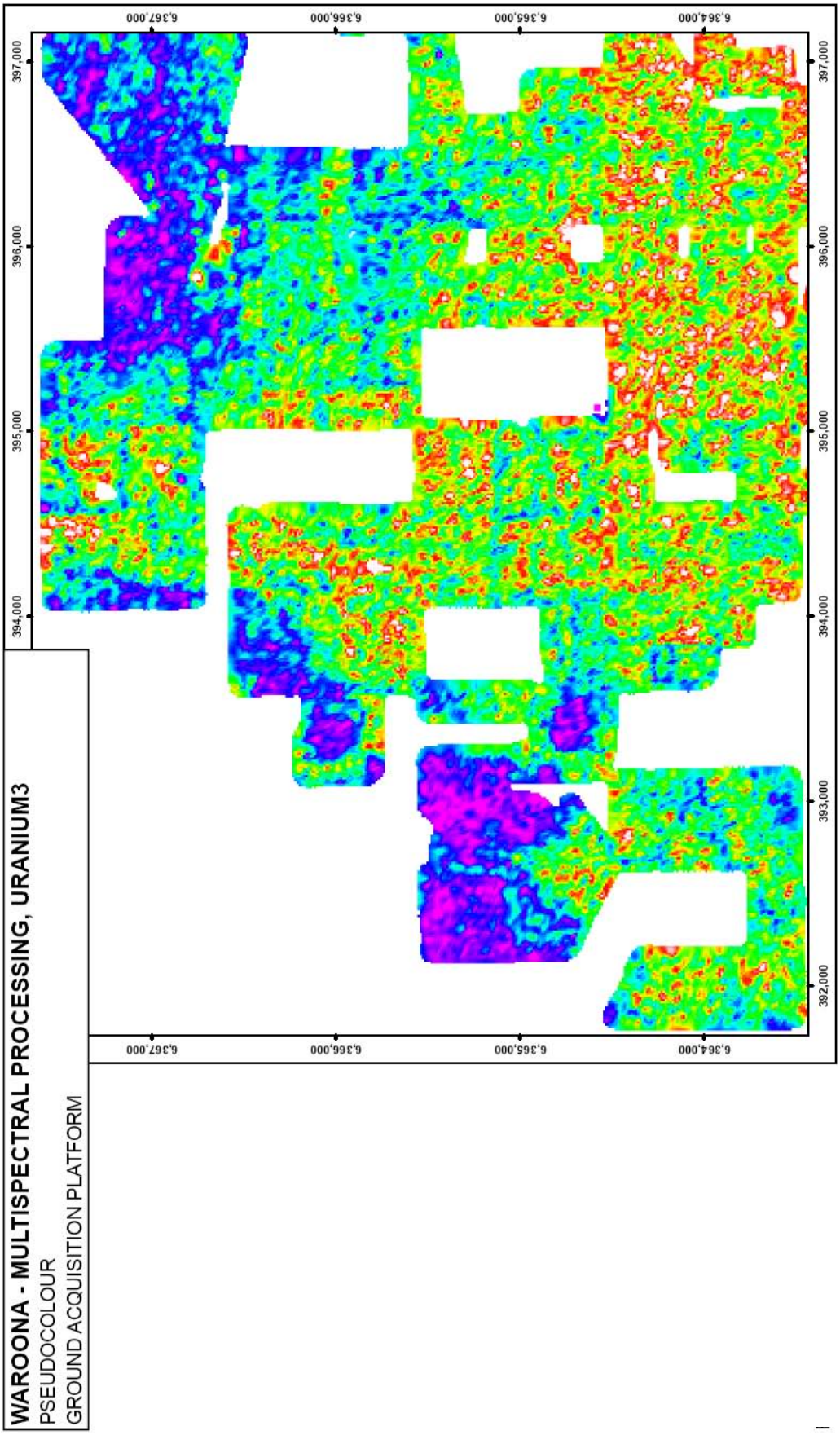


**Figure C.5.15. Uranium 3 multispectral processed, NASVD spectral smoothing, pseudocolour image, Waroona, ground platform.**

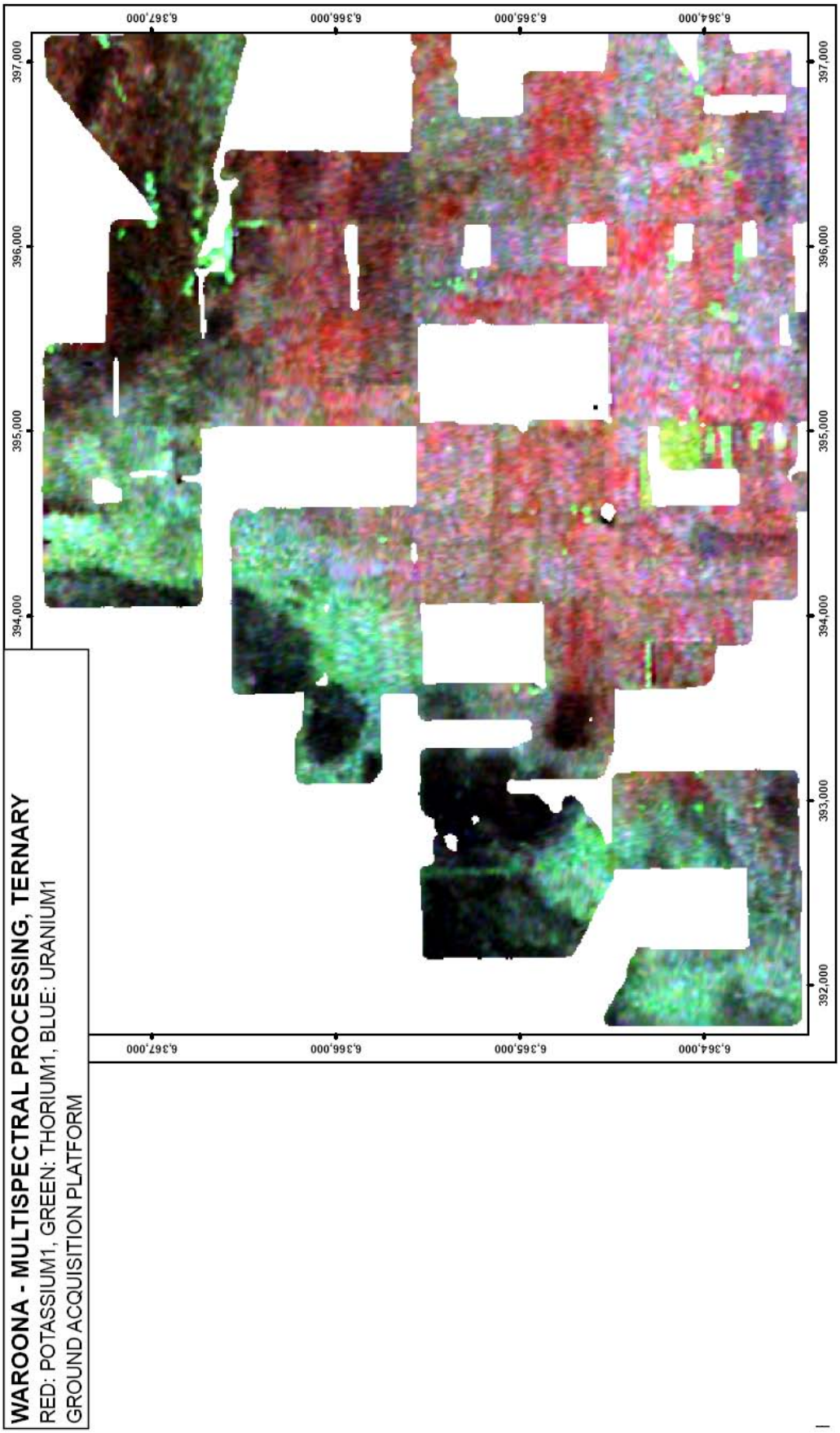


**Figure C.5.16. Ternary multispectral processed, NASVD spectral smoothing, ternary image, Waroona, ground platform.**


**Figure C.5.17. Uranium ternary multispectral processed, NASVD spectral smoothing, ternary image, Waroona, ground platform.**

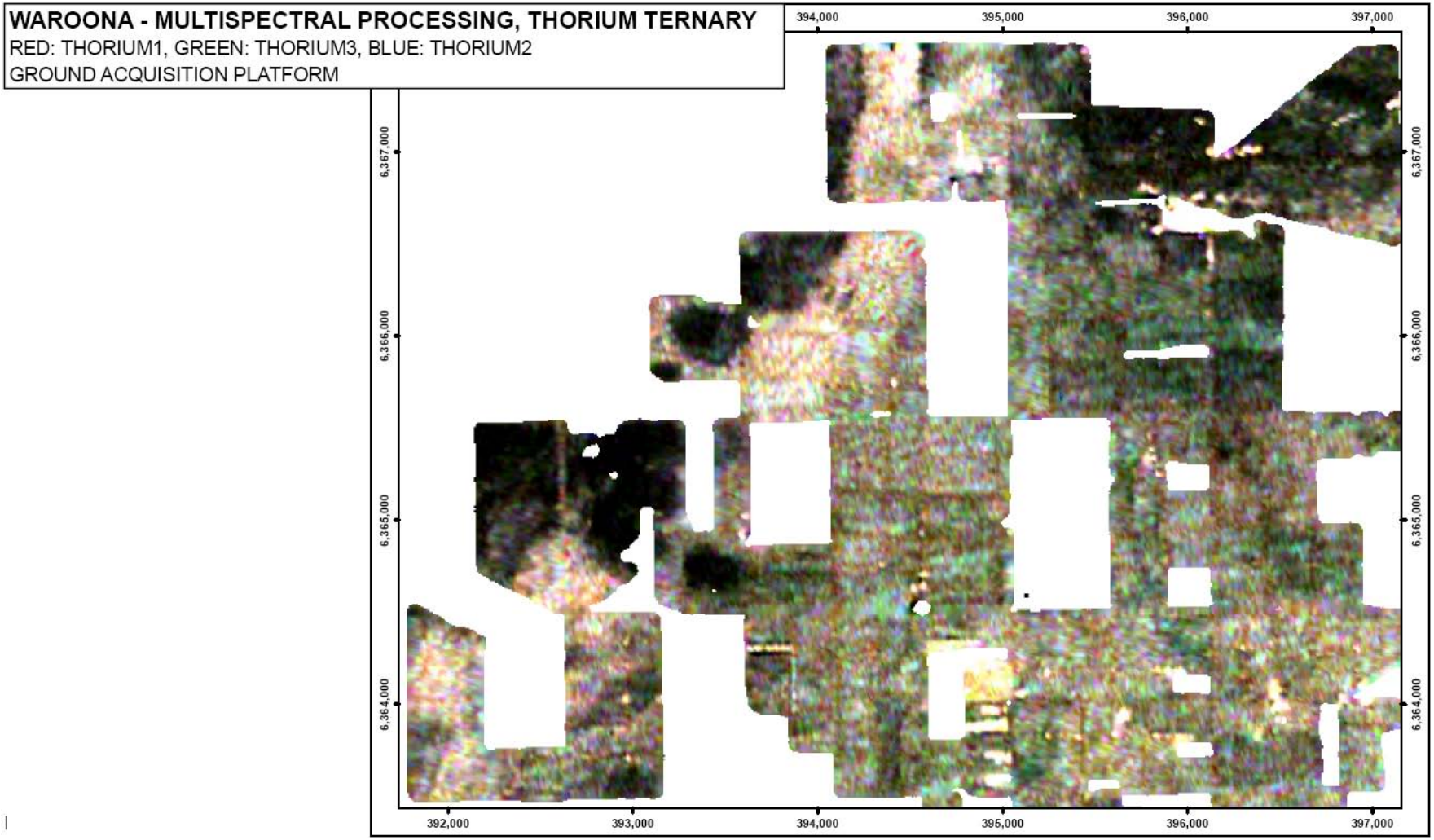


**Figure C.5.18. Thorium ternary multispectral processed, NASVD spectral smoothing, ternary image, Waroona, ground platform.**

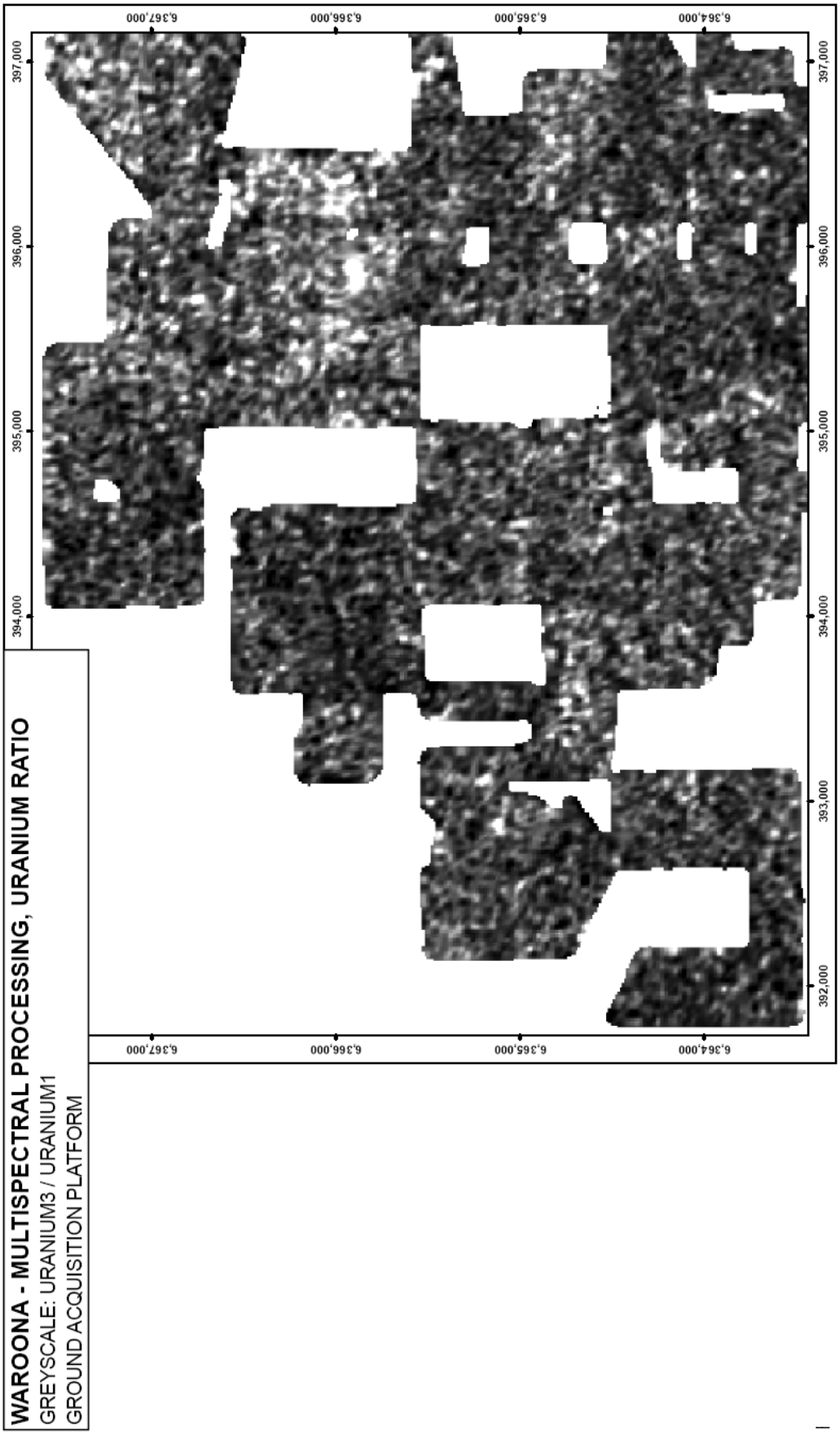


**Figure C.5.19. Uranium ratio multispectral processed, NASVD spectral smoothing, greyscale image, Waroona, ground platform.**

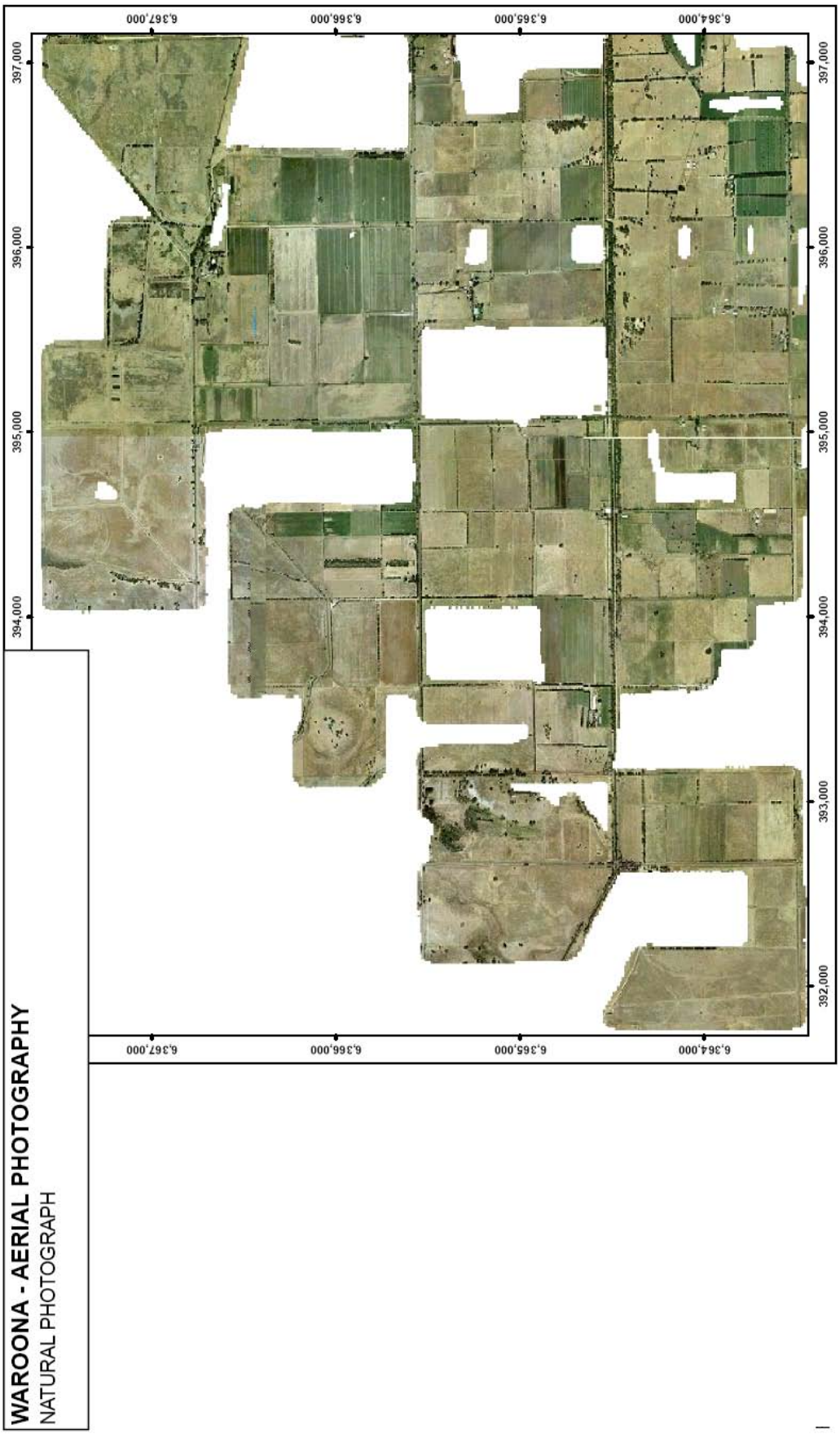


**Figure C.5.20. Natural colour aerial photo, Waroona, ground platform survey area.**

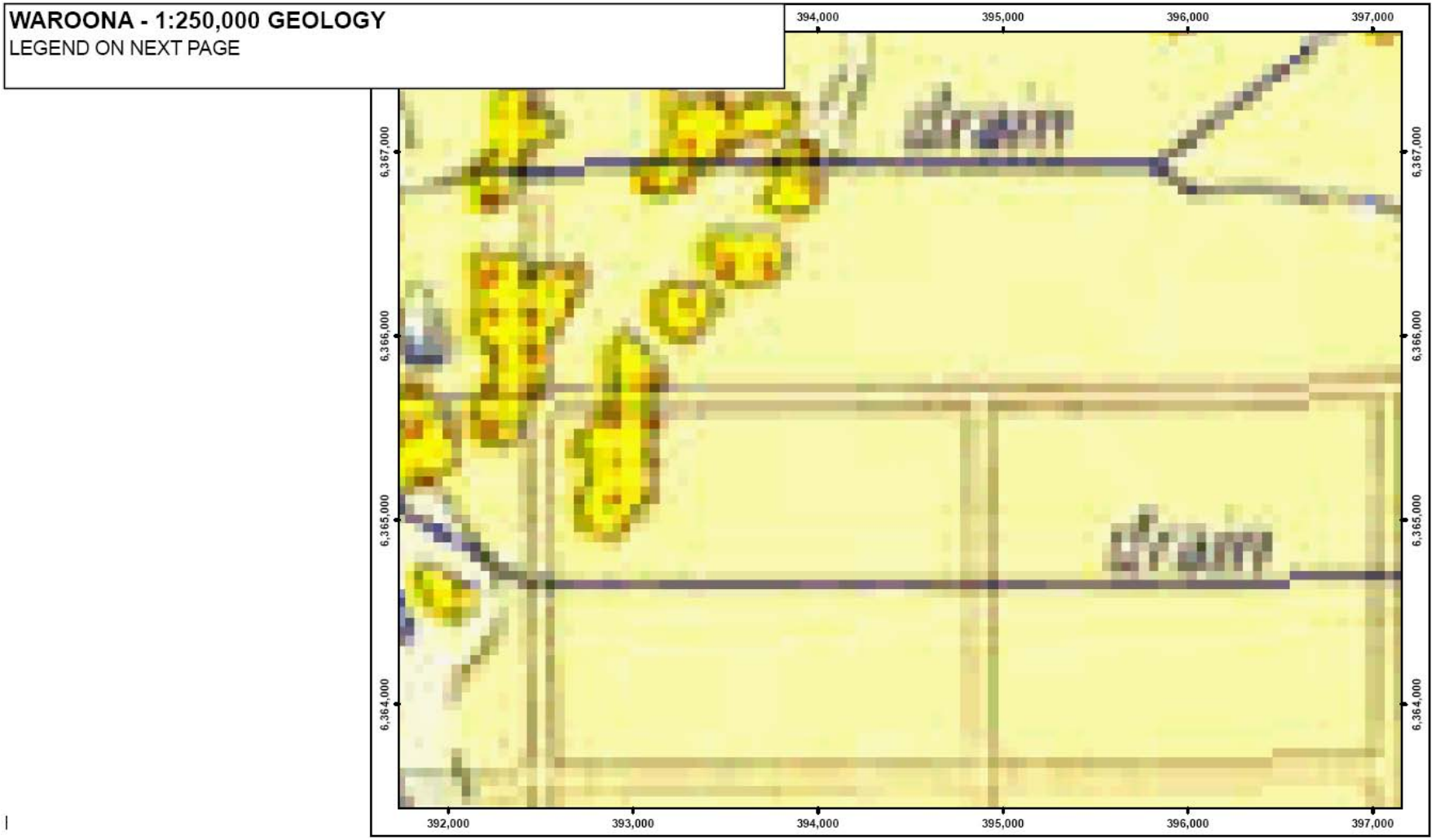


**Figure C.5.21. 1:250,000 geology for Waroona, ground platform survey area (from Low *et al.*, 1980).**

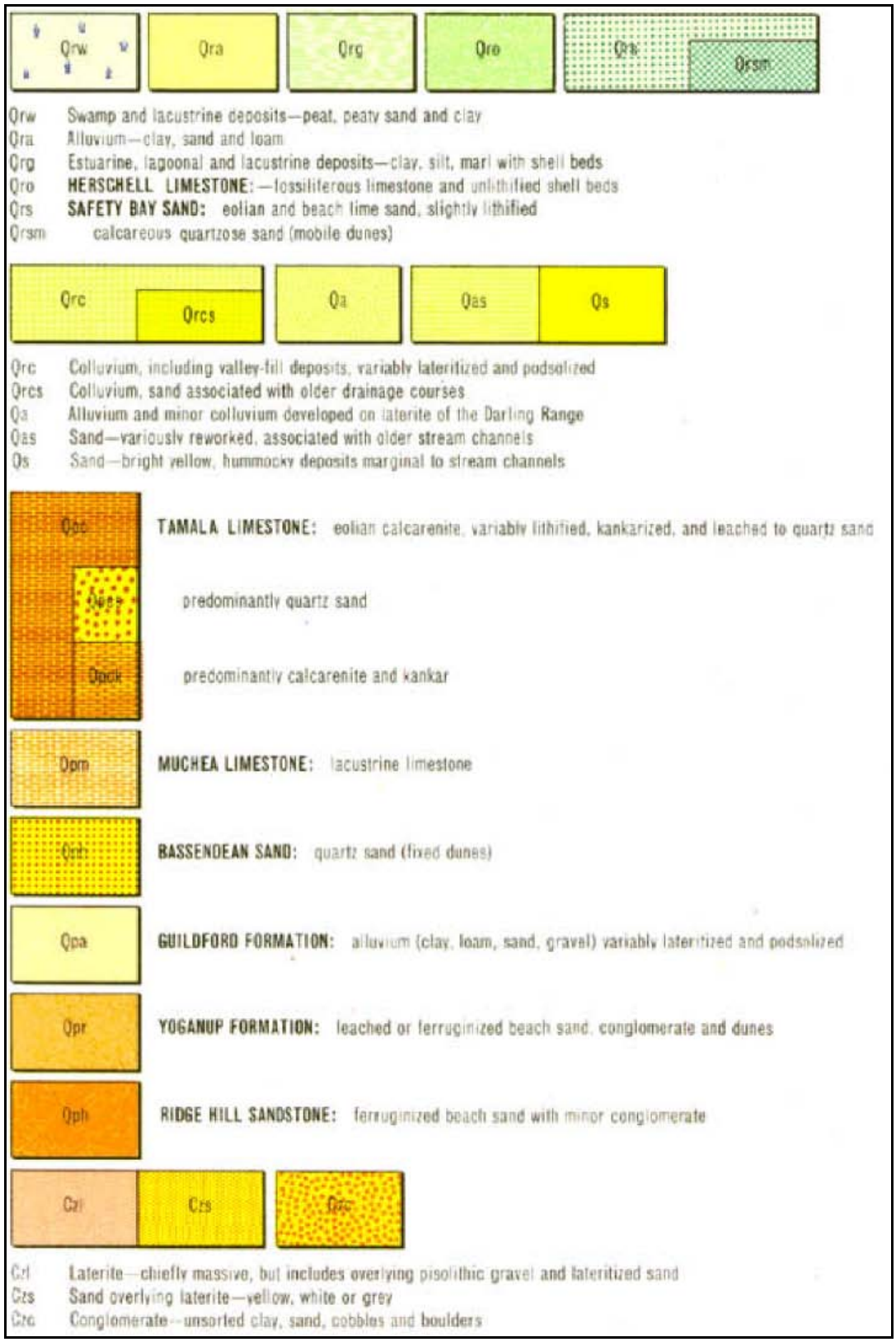


**Figure C.5.21 cont'd. 1:250,000 geology legend for Waroona, ground platform survey area (from Low *et al.*, 1980).**

# Appendix D:  Case Study 3 - Comparison of airborne and ground radiometric line data

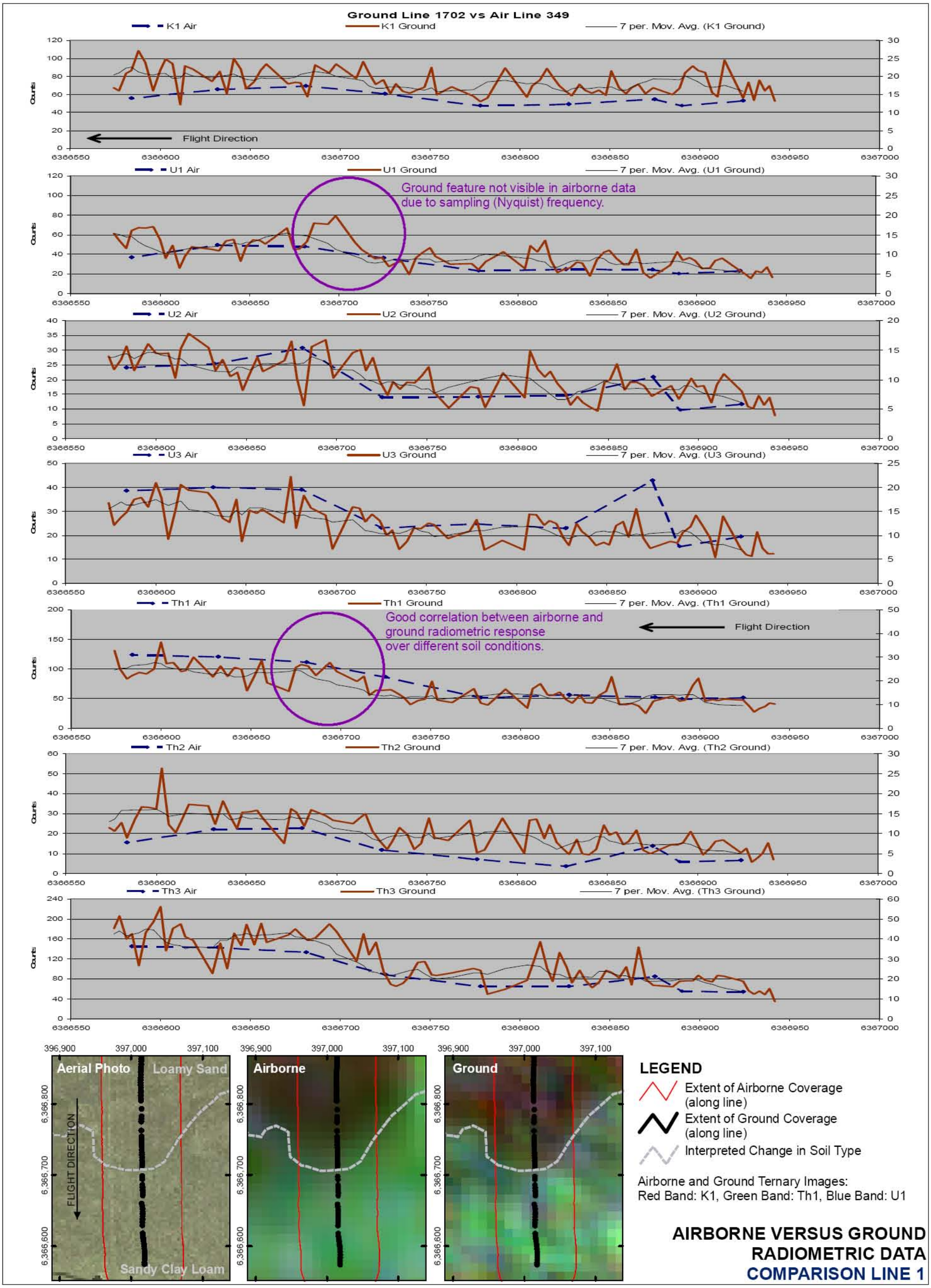


**Figure D.1. Comparison 1 of airborne and ground radiometric line data, Waroona, Western Australia.**

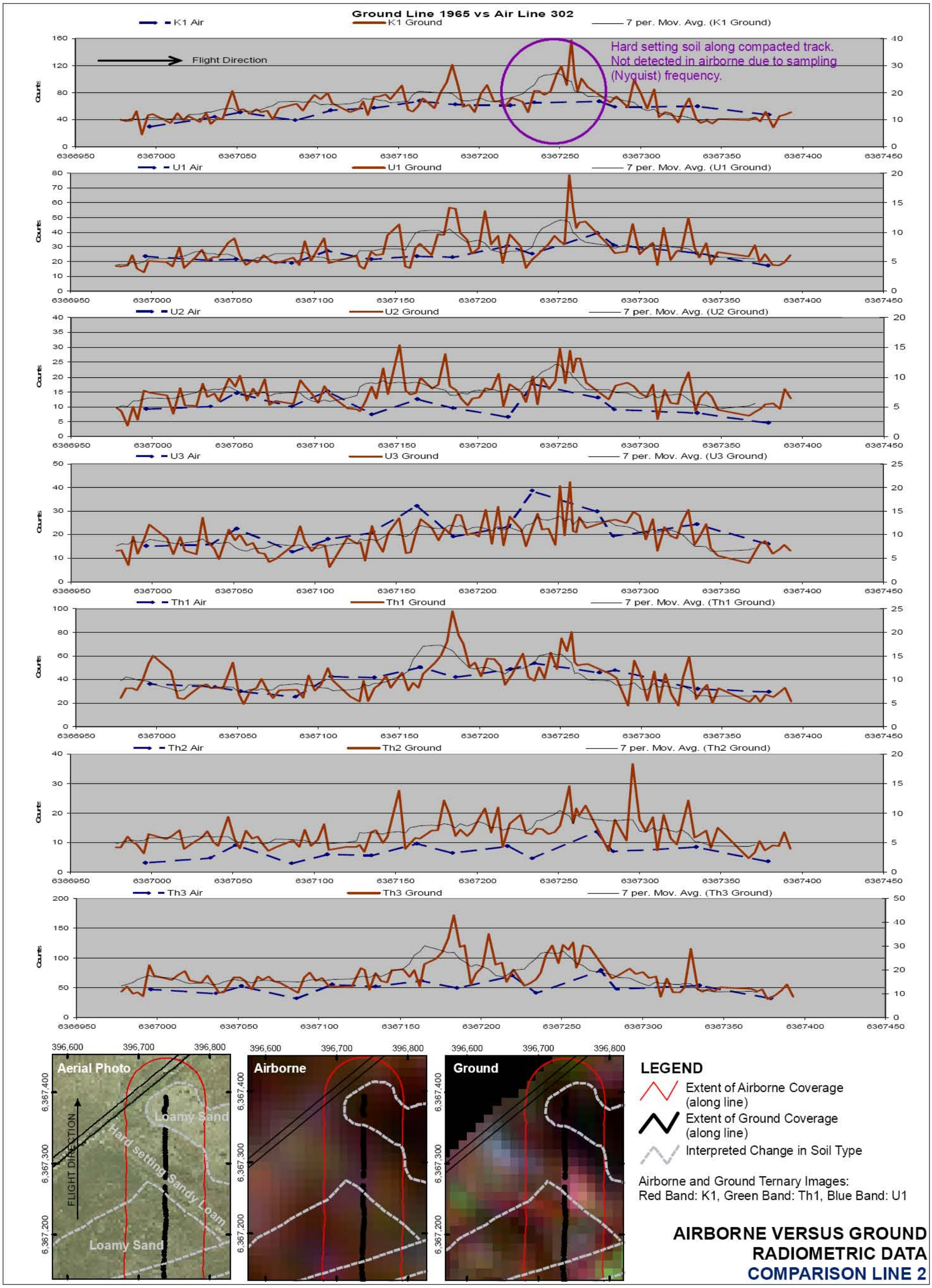


**Figure D.2. Comparison 2 of airborne and ground radiometric line data, Waroona, Western Australia.**

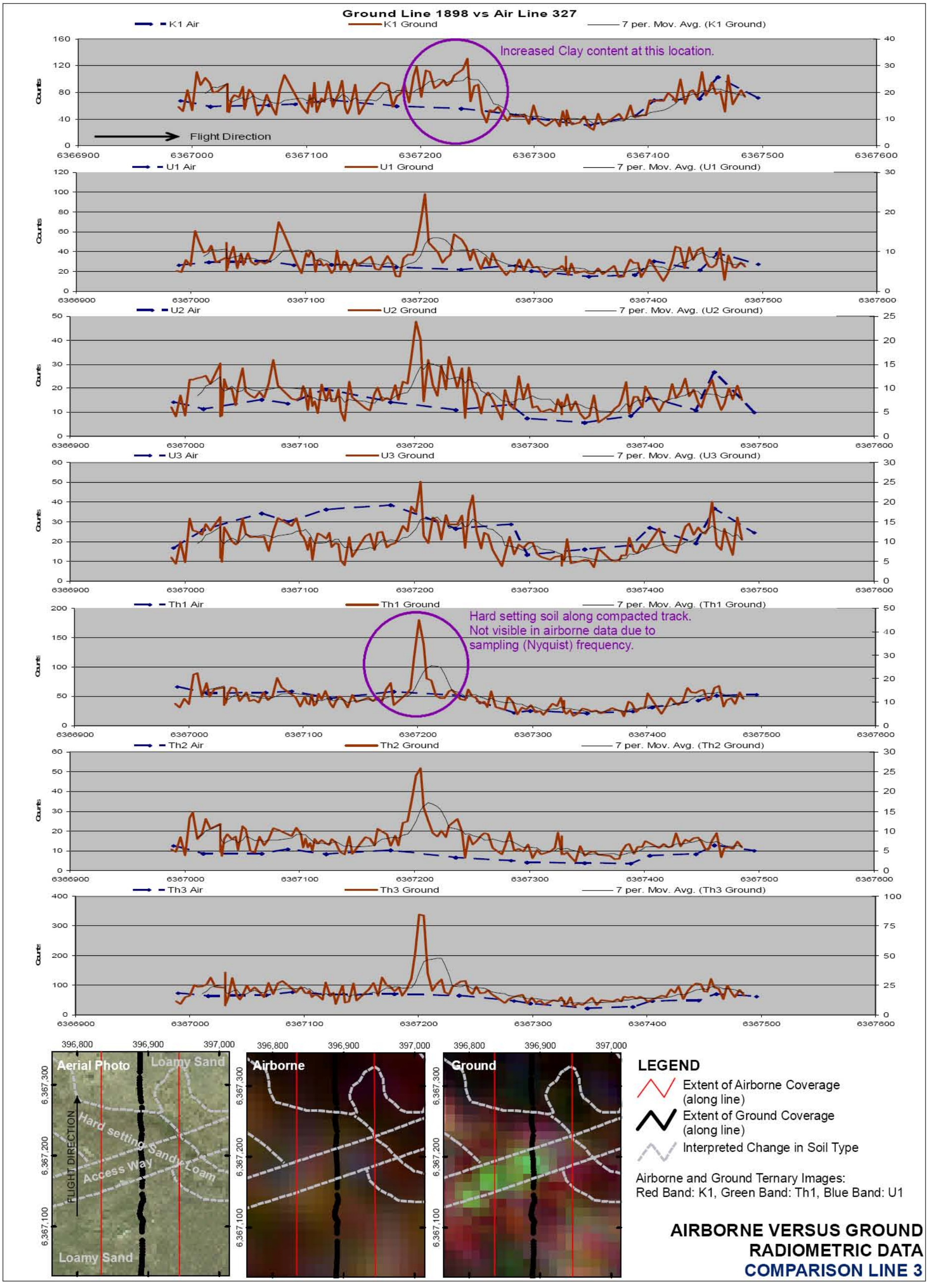


**Figure D.3. Comparison 3 of airborne and ground radiometric line data, Waroona, Western Australia.**

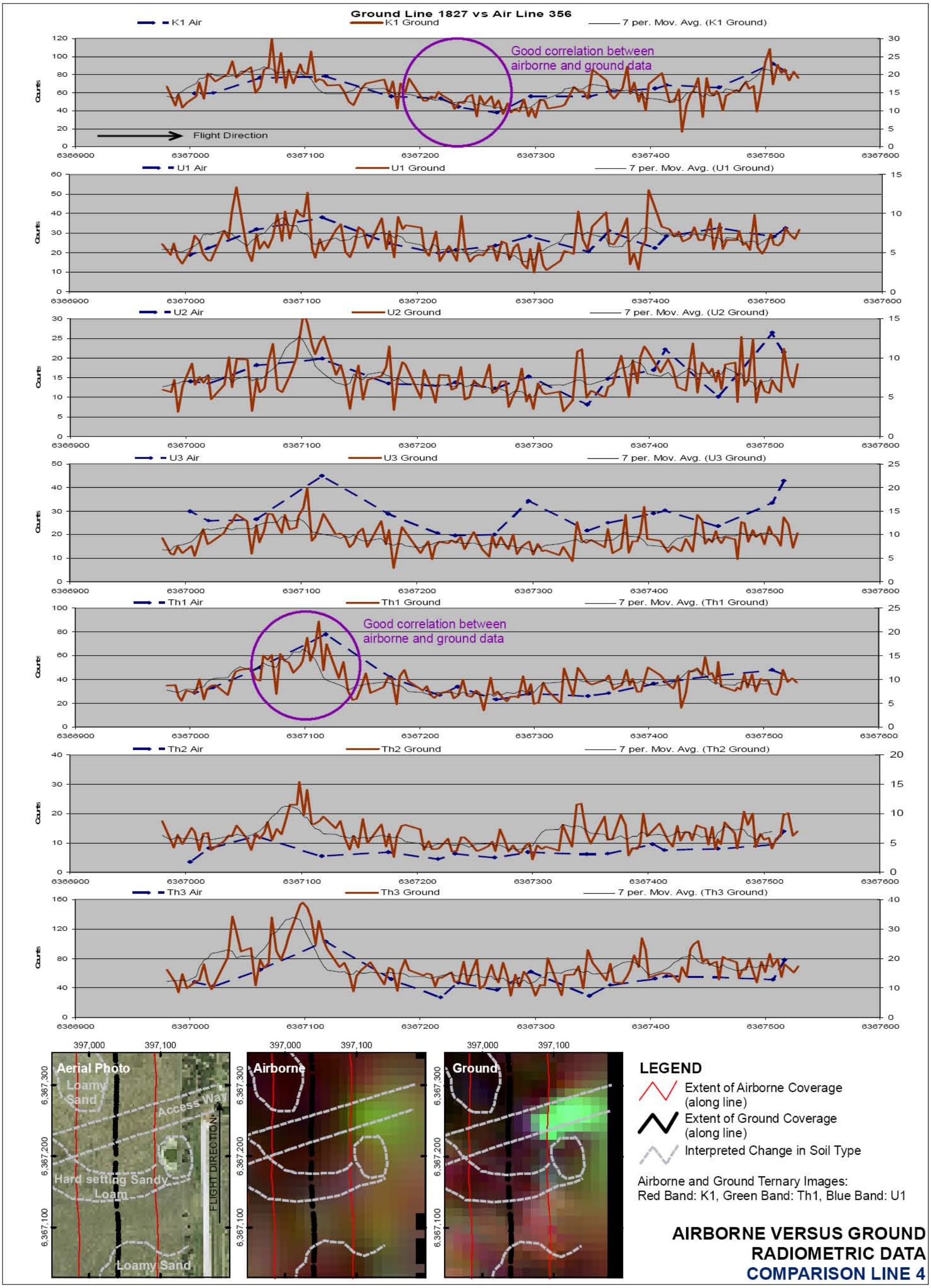


**Figure D.4. Comparison 4 of airborne and ground radiometric line data, Waroona, Western Australia.**

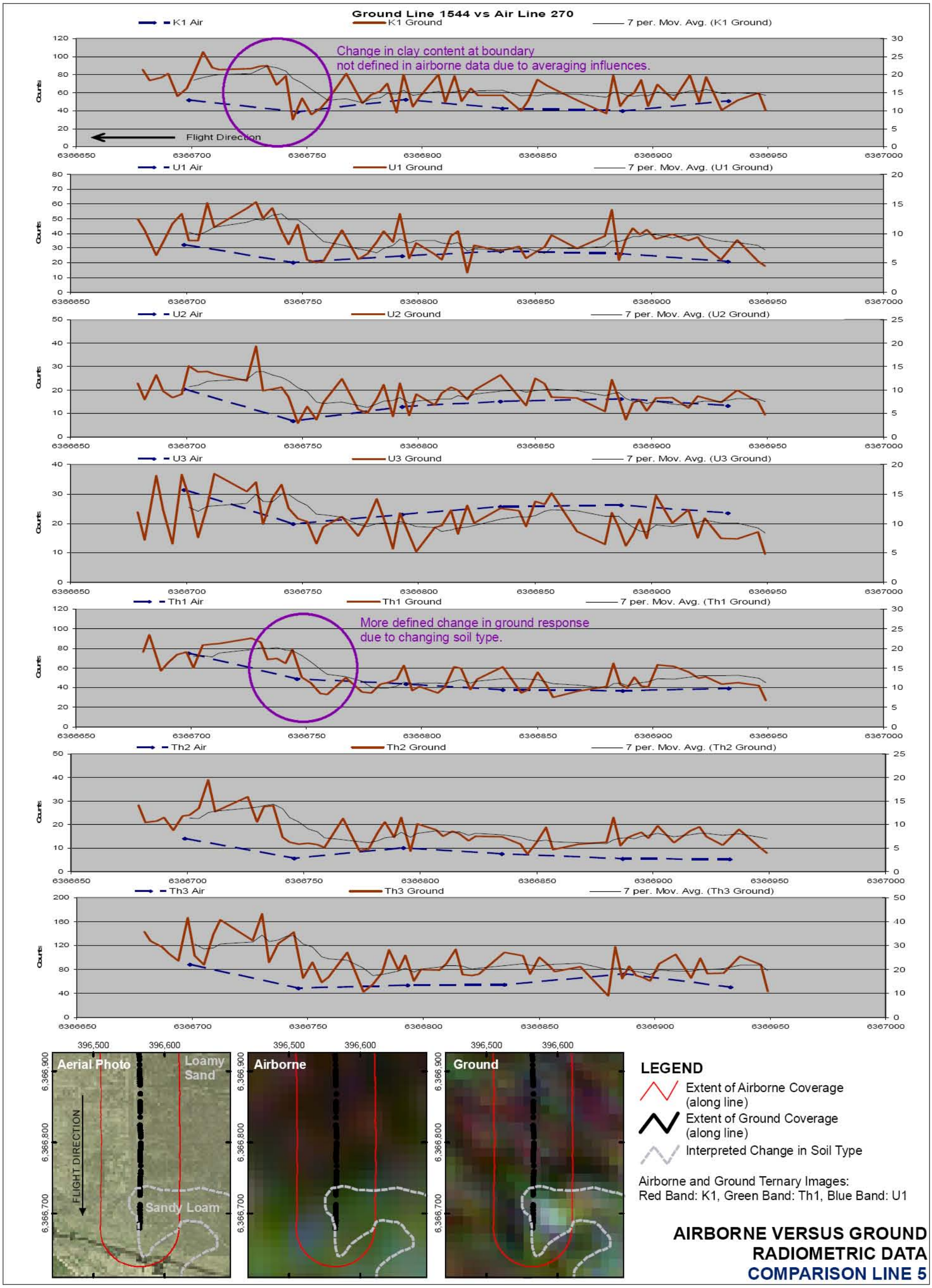


**Figure D.5. Comparison 5 of airborne and ground radiometric line data, Waroona, Western Australia.**

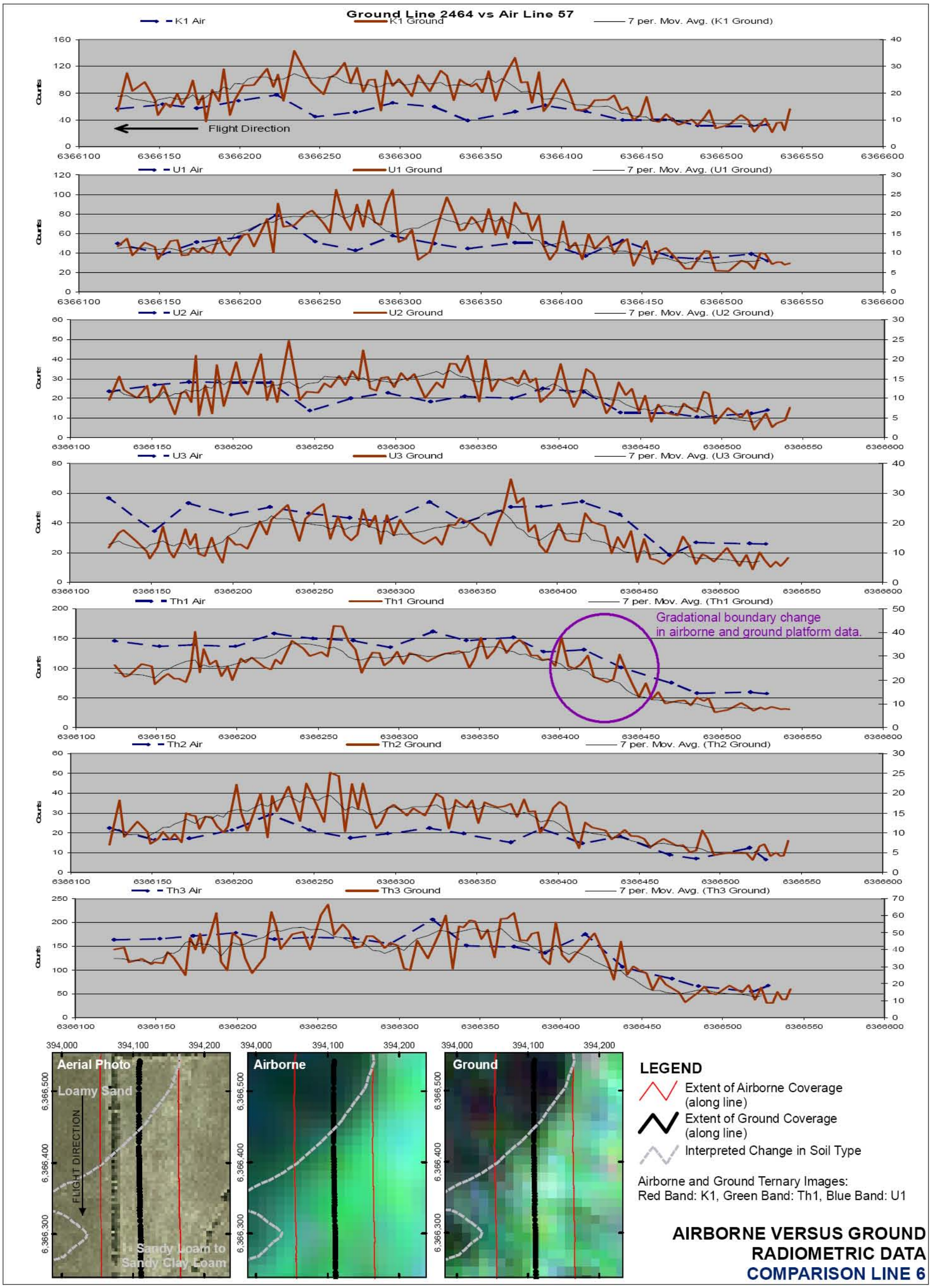


**Figure D.6. Comparison 6 of airborne and ground radiometric line data, Waroona, Western Australia.**

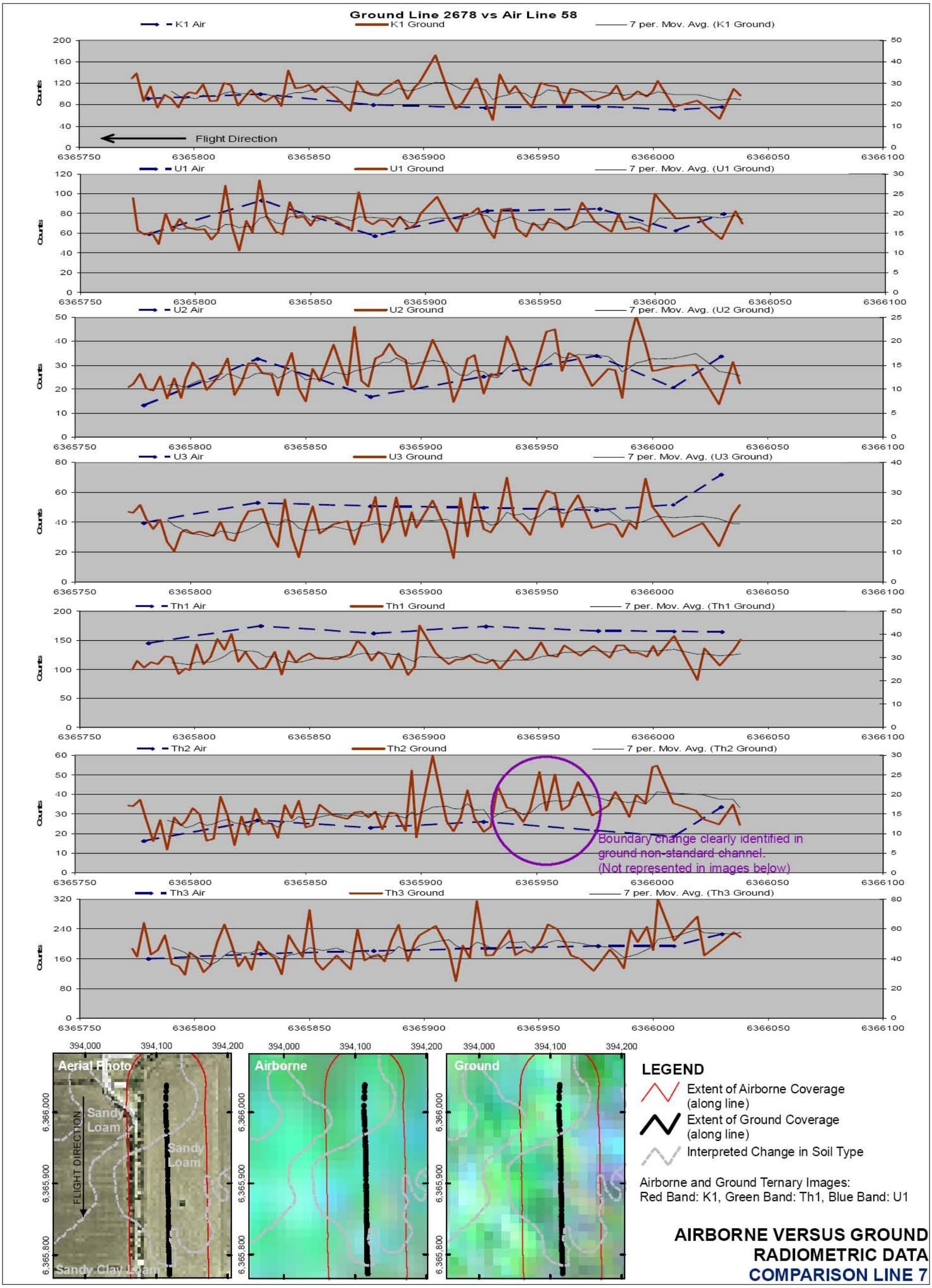


**Figure D.7. Comparison 7 of airborne and ground radiometric line data, Waroona, Western Australia.**

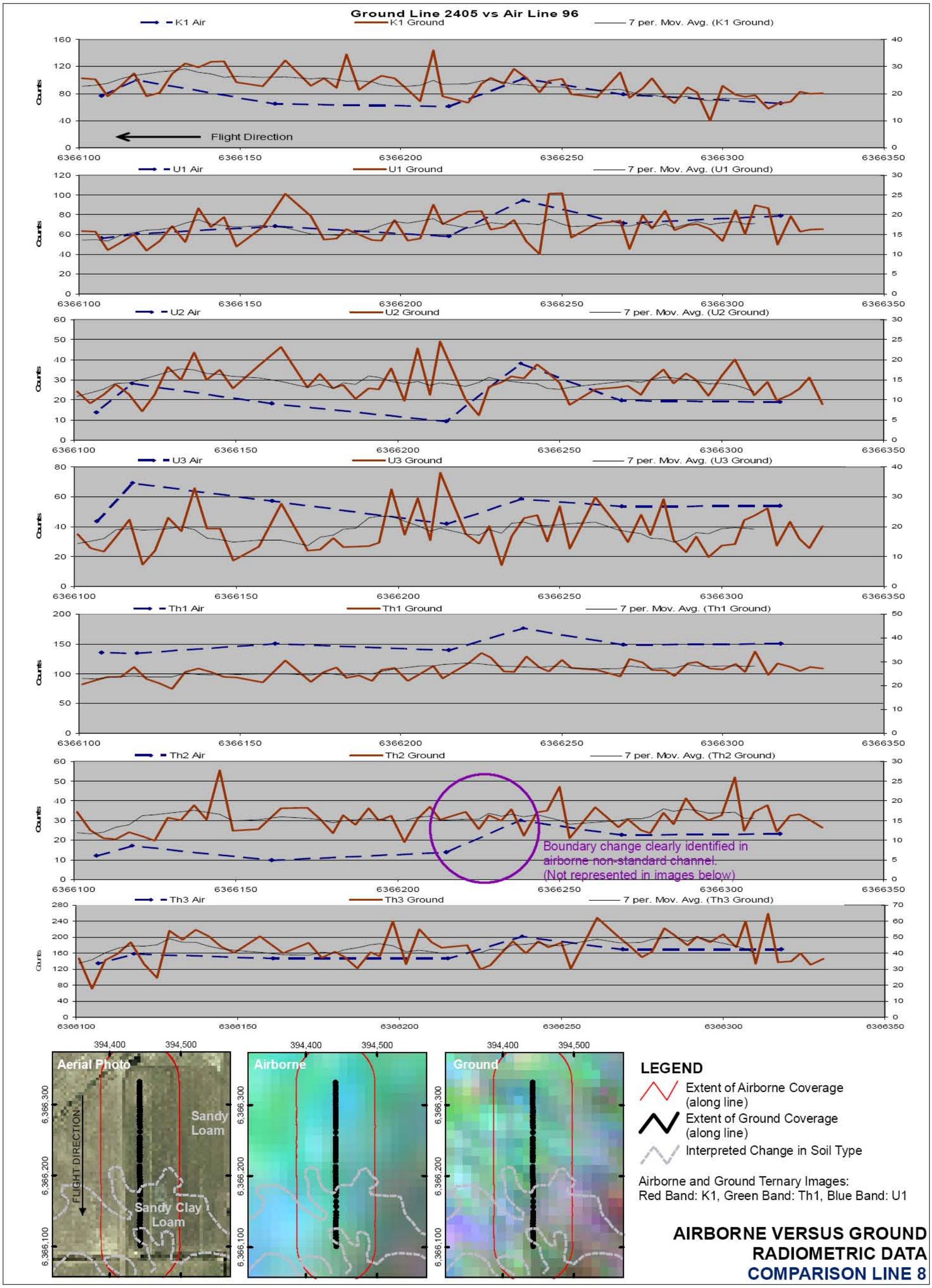


**Figure D.8. Comparison 8 of airborne and ground radiometric line data, Waroona, Western Australia.**

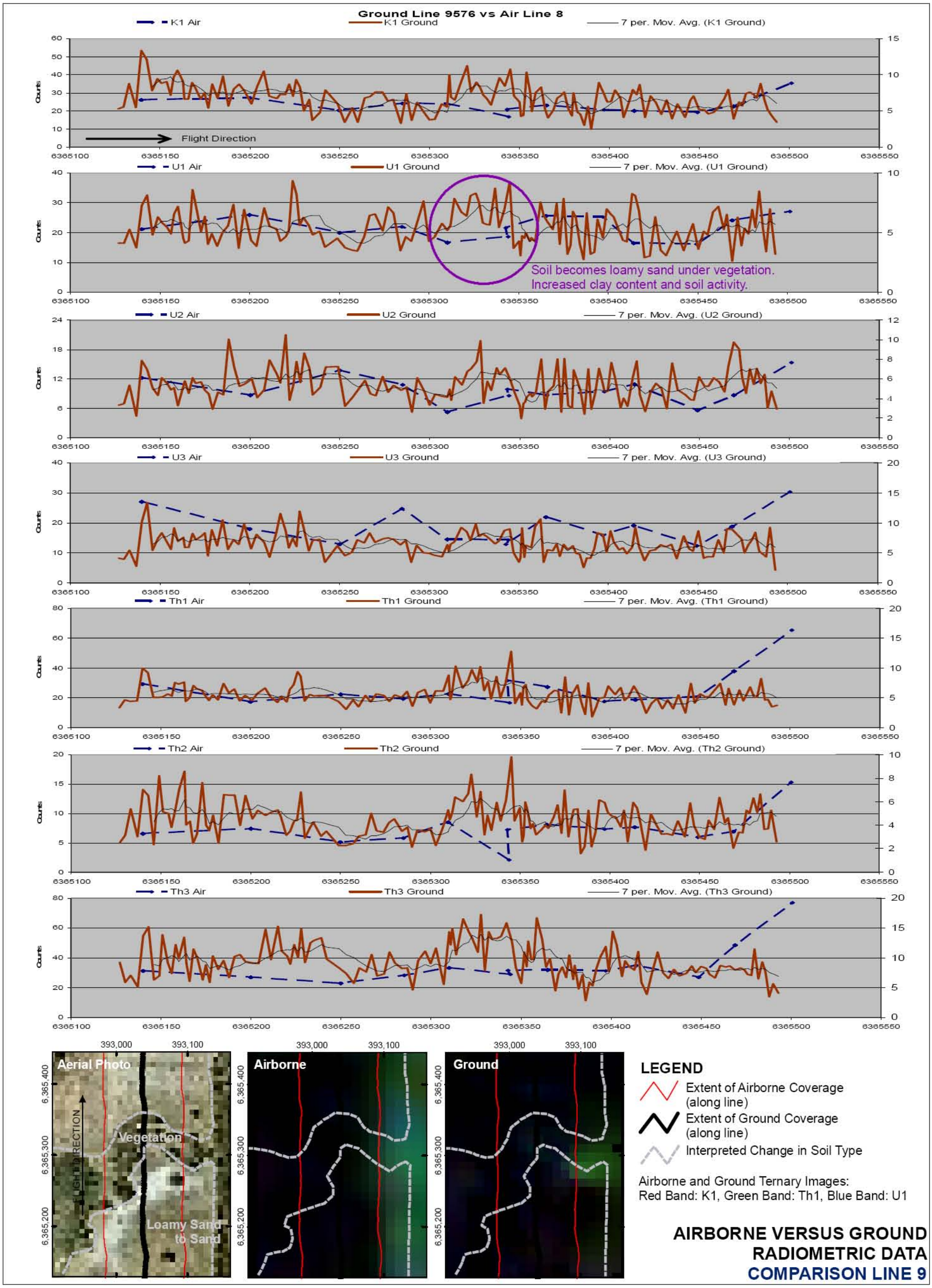


**Figure D.9. Comparison 9 of airborne and ground radiometric line data, Waroona, Western Australia.**

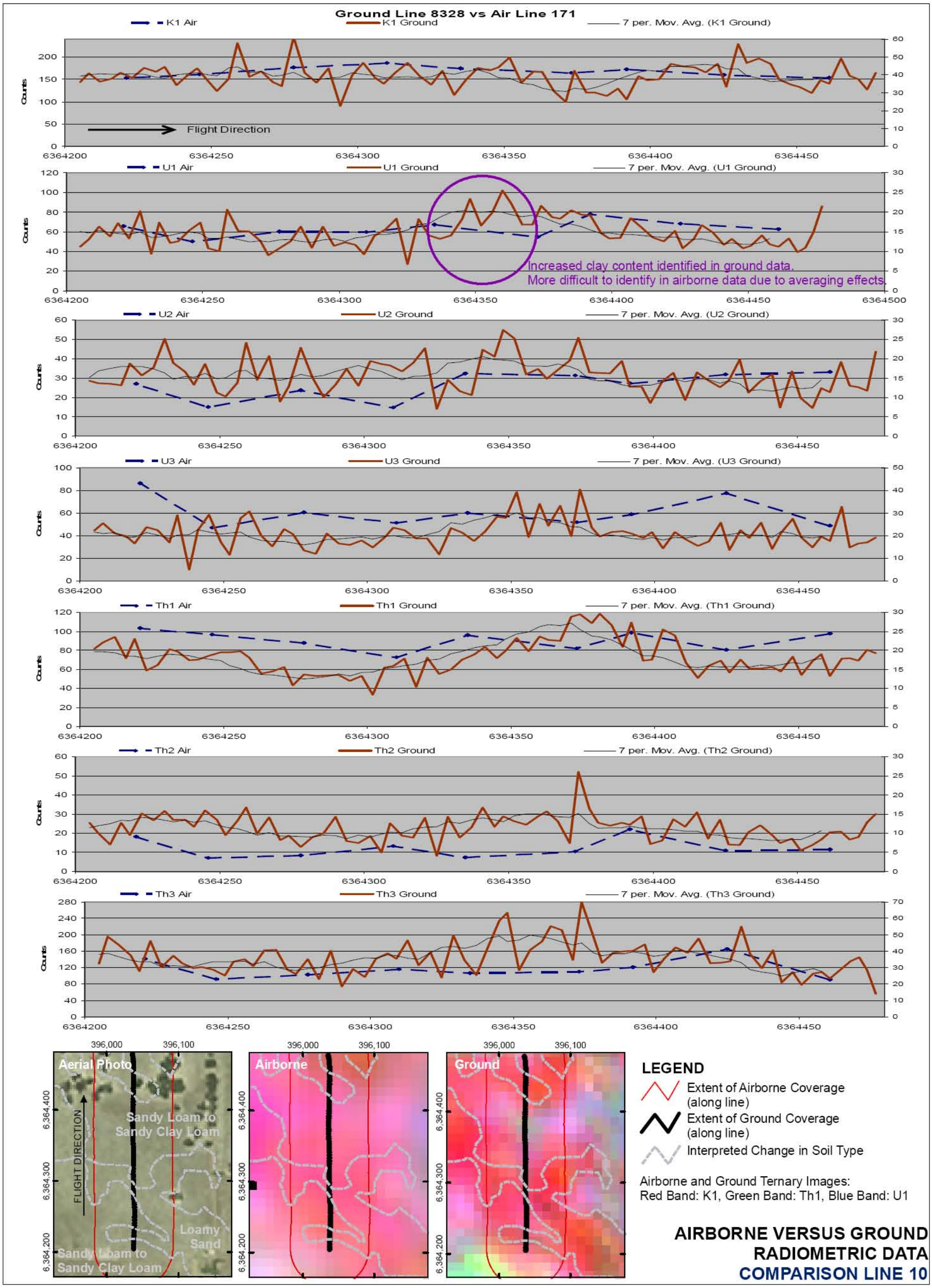


**Figure D.10. Comparison 10 of airborne and ground radiometric line data, Waroona, Western Australia.**

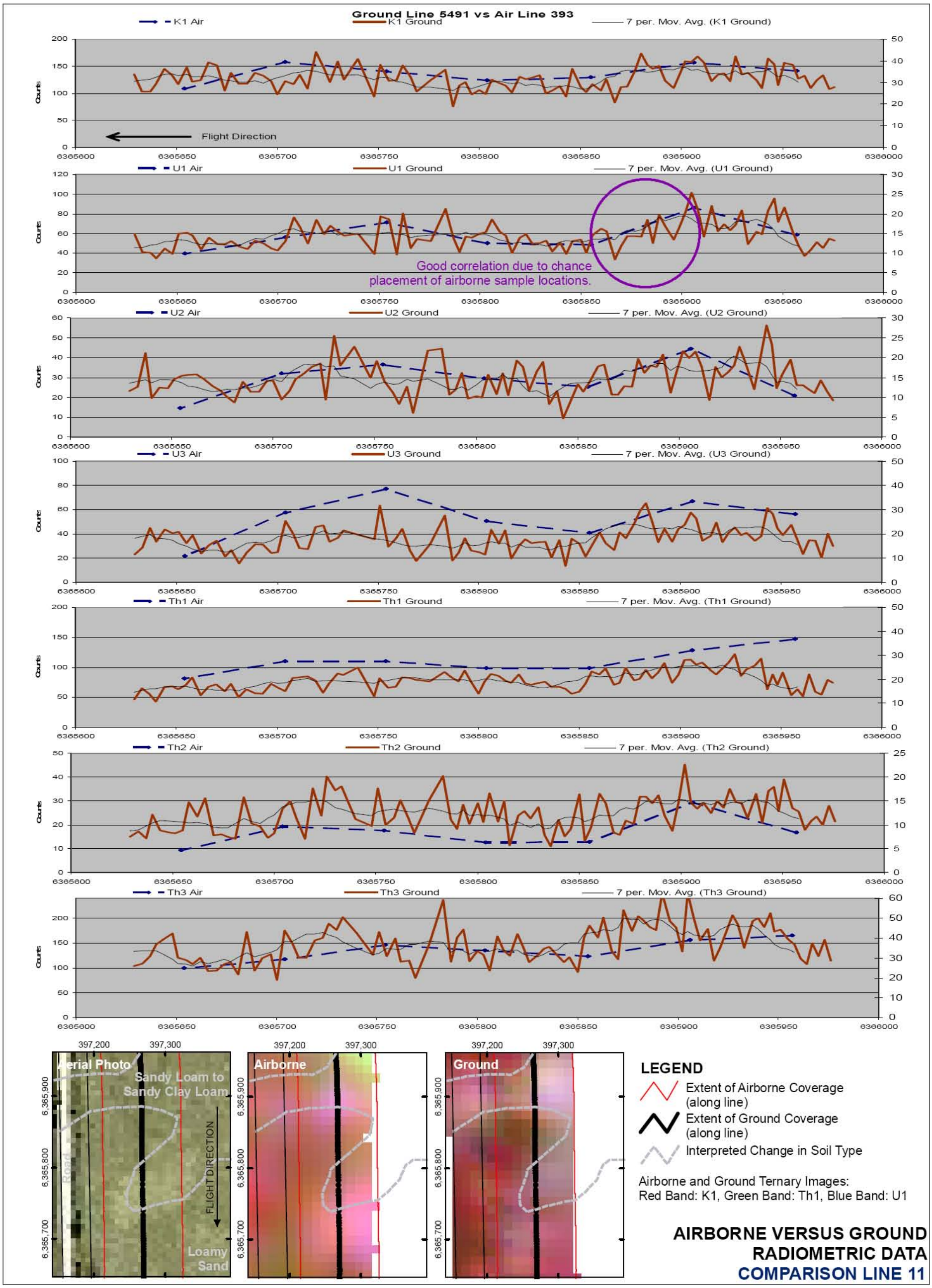


**Figure D.11. Comparison 11 of airborne and ground radiometric line data, Waroona, Western Australia.**

# Appendix E: Waroona ground radiometric data classification results and field sampling photos

## E.1 Summary of soil classification description and classification values

**Table E.1. Soil codes and soil texture descriptions.**

| General soil code | Soil texture | Common reference |
|---|---|---|
| 1 | Clay | Heavy |
| 2 | Sandy clay | |
| 3 | Friable sandy clay | |
| 4 | Clay loam | |
| 5 | Sandy clay loam | |
| 6 | Loam | |
| 7 | Silty Loam | |
| 8 | Sandy Loam | |
| 9 | Loamy sand | |
| 10 | Sand | Light |

**Table E.2. Final soil unit descriptors with contributing unsupervised classification classes and associated field soil codes for Waroona study area.**

| General | Soil Description | GRIDCODE | General Soil Code | | |
|---|---|---|---|---|---|
| | | (class) | A_code | B_code | C_code |
| Qpa | Qpa: Guildford Formation, Clay - Brown sandy clay loam grading to orange sandy clay. Waterlogging evidenced by orange/red mottles at base of profile. | 18 | 5 | 5 | 2 |
| Qpa | Qpa: Guildford Formation, Clay - Dark brown fine sandy loam grading to light brown/light orange sandy clay. Waterlogging evidenced by orange mottles at base of profile. | 19 | 8 | 5 | 2 |
| Qpa | Qpa: Guildford Formation, Clay - Hard setting dark brown sandy loam grading to light brown/light orange sandy clay. Waterlogging evidenced by orange mottles at base of profile. | 13 | 85 | 5 | 2 |
| Qpa | Qpa: Guildford Formation, Clay - Hard setting dark brown sandy loam grading to orange/brown sandy clay loam to orange friable fine sandy clay. Minor waterlogging evidenced by orange colour of soil at base of profile. | 13 | 85 | 5 | 2 |
| | | 17 | 89 | 5 | 3 |
| Qpa | Qpa: Guildford Formation, Clay - Hard setting dark brown sandy loam grading to orange/brown sandy clay. | 26 | 8 | 5 | 2 |
| | | 27 | 8 | 5 | 2 |

| General | Soil Description | GRIDCODE (class) | General Soil Code | | |
|---|---|---|---|---|---|
| | | | A_code | B_code | C_code |
| Qpa | Qpa: Guildford Formation, Clay - Light brown sandy loam grading to light orange sandy clay. | 25 | 8 | 85 | 2 |
| Qpa | Qpa: Guildford Formation, Sand - Dark brown fine loamy sand grading to light brown loamy sand on light brown/yellow sandy clay. Waterlogging evidenced by orange mottles at base of profile. | 4 | 9 | 9 | 2 |
| | | 6 | 9 | 9 | 2 |
| Qpa | Qpa: Guildford Formation, Sand - Dark brown loamy sand grading to brown sandy clay loam on light brown/light orange sandy clay. Waterlogging evidenced by orange mottles at base of profile. | 5 | 9 | 5 | 2 |
| | | 12 | 9 | 58 | 2 |
| Qpa | Qpa: Guildford Formation, Sand - Dark brown sandy loam grading to brown sandy clay loam on light brown/orange sandy clay. Waterlogging evidenced by orange mottles at base of profile. | 20 | 8 | 5 | 2 |
| Qpa | Qpa: Guildford Formation, Sand - Dark brown sandy loam grading to brown sandy clay loam on orange sandy clay loam. Minor waterlogging evidenced by orange colour of soil at base of profile. | 21 | 8 | 5 | 2 |
| Qpa | Qpa: Guildford Formation, Sand - Dark brown sandy loam on brown/orange sandy clay. Waterlogging evidenced by orange mottles at base of profile. | 7 | 8 | 8 | 2 |
| Qph | Qph: Bassendean Sands - Grey loamy sand grading to light brown sandy clay loam. Waterlogging evidenced by orange mottles at base of profile. | 4 | 9 | 9 | 2 |

| General | Soil Description | GRIDCODE | General Soil Code | | |
|---|---|---|---|---|---|
| | | (class) | A_code | B_code | C_code |
| Qph | Qph: Bassendean Sands - Grey loamy sand on light grey sandy clay loam. | 3 | 9 | 9 | 5 |
| Qph | Qph: Bassendean Sands - Grey loamy sand grading to light grey sand. Loamy sand at surface resulting from sustained presence of organic matter. | 1 | 9 | 10 | 10 |
| Qph | Qph: Bassendean Sands - Grey loamy sand grading to light grey/light orange sandy clay loam. Minor waterlogging evidenced by orange colouring at base of profile | 8 | 9 | 9 | 5 |
| Qph | Qph: Bassendean Sands - Grey sand grading to light grey to white loamy sand | 2 | 10 | 10 | 9 |
| Qph | Qph: Bassendean Sands - Grey/brown loamy sand grading to light grey/light brown/orange loamy sand. Waterlogging evidenced by orange mottles at base of profile. | 9 | 9 | 9 | 9 |
| Qpr | Qpr: Yoganup Formation - Grey loamy sand grading to light brown sandy clay loam. Waterlogging evidenced by orange mottles at base of profile. | 3 | 9 | 9 | 5 |
| | | 4 | 9 | 9 | 2 |
| Qpr | Qpr: Yoganup Formation - Grey loamy sand on light grey sandy clay loam. | 2 | 10 | 10 | 9 |
| | | 3 | 9 | 9 | 5 |
| | | 8 | 9 | 9 | 5 |
| Qpr | Qpr: Yoganup Formation - Grey loamy sand grading to light grey sand. Loamy sand at surface resulting from sustained presence of organic matter. | 1 | 9 | 10 | 10 |

| General | Soil Description | GRIDCODE | General Soil Code | | |
|---|---|---|---|---|---|
| | | (class) | A_code | B_code | C_code |
| Qpr | Qpr: Yoganup Formation - Grey loamy sand grading to light grey/light orange sandy clay loam. Minor waterlogging evidenced by orange colouring at base of profile | 8 | 9 | 9 | 5 |
| Qpr | Qpr: Yoganup Formation - Grey sand grading to light grey to white loamy sand | 2 | 10 | 10 | 9 |
| Qpr | Qpr: Yoganup Formation - Grey/brown loamy sand grading to light grey/light brown/orange loamy sand. Waterlogging evidenced by orange mottles at base of profile. | 9 | 9 | 9 | 9 |
| Qrw | Qrw: Swamp and lactustrine - Brown loamy sand grading to brown/orange sandy clay. Waterlogging evidenced by orange mottles at base of profile. | 5 | 9 | 5 | 2 |
| Qrw | Qrw: Swamp and lactustrine - Hard setting dark brown sandy clay loam grading to brown sandy clay. Waterlogging evidenced by orange mottles at base of profile. | 9 | 9 | 9 | 9 |
| | | 10 | 5 | 5 | 2 |
| Qrw | Qrw: Swamp and lactustrine - Hard setting dark browm sandy loam grading to brown/orange sandy clay. Waterlogging evidenced by orange mottles at base of profile. | 11 | 8 | 5 | 2 |
| Qrw | Qrw: Swamp and lacustrine - Hard setting brown sandy clay loam grading to orange fine sandy clay. Significant waterlogging evidenced by strong orange colour of soil and red mottles at base of profile. | 24 | 5 | 5 | 2 |
| Qrw | Qrw: Swamp and lacustrine - Hard setting brown sandy loam grading to dark brown sandy clay. | 16 | 8 | 5 | 2 |

| General | Soil Description | GRIDCODE | General Soil Code | | |
|---|---|---|---|---|---|
| | | (class) | A_code | B_code | C_code |
| Qrw | Qrw: Swamp and lacustrine - Hard setting dark brown sandy clay loam grading to dark brown sandy clay. Significant waterlogging evidenced by orange mottles in central and lower profile horizons. | 15 | 5 | 5 | 2 |
| Qrw | Qrw: Swamp and lacustrine - Hard setting dark brown sandy clay loam grading to orange friable sandy clay. Significant waterlogging evidenced by strong orange colour of soil at base of profile. | 22 | 5 | 5 | 3 |
| Qrw | Qrw: Swamp and lacustrine - Hard setting dark brown sandy loam grading to brown/orange friable sandy clay. Significant waterlogging evidenced by strong orange colour of soil and orange mottles at base of profile. Occasional laterite present. | 23 | 85 | 5 | 2 |
| Qrw | Qrw: Swamp and lacustrine - Hard setting dark brown sandy loam grading to dark brown sandy clay. Significant waterlogging evidenced by orange mottles in central and lower profile horizons. | 14 | 8 | 5 | 2 |
| Road | Road, accessway | 14 | 8 | 5 | 2 |
| | | 15 | 5 | 5 | 2 |
| | | 16 | 8 | 5 | 2 |

## E.2 Radiometric classification results and general soil type

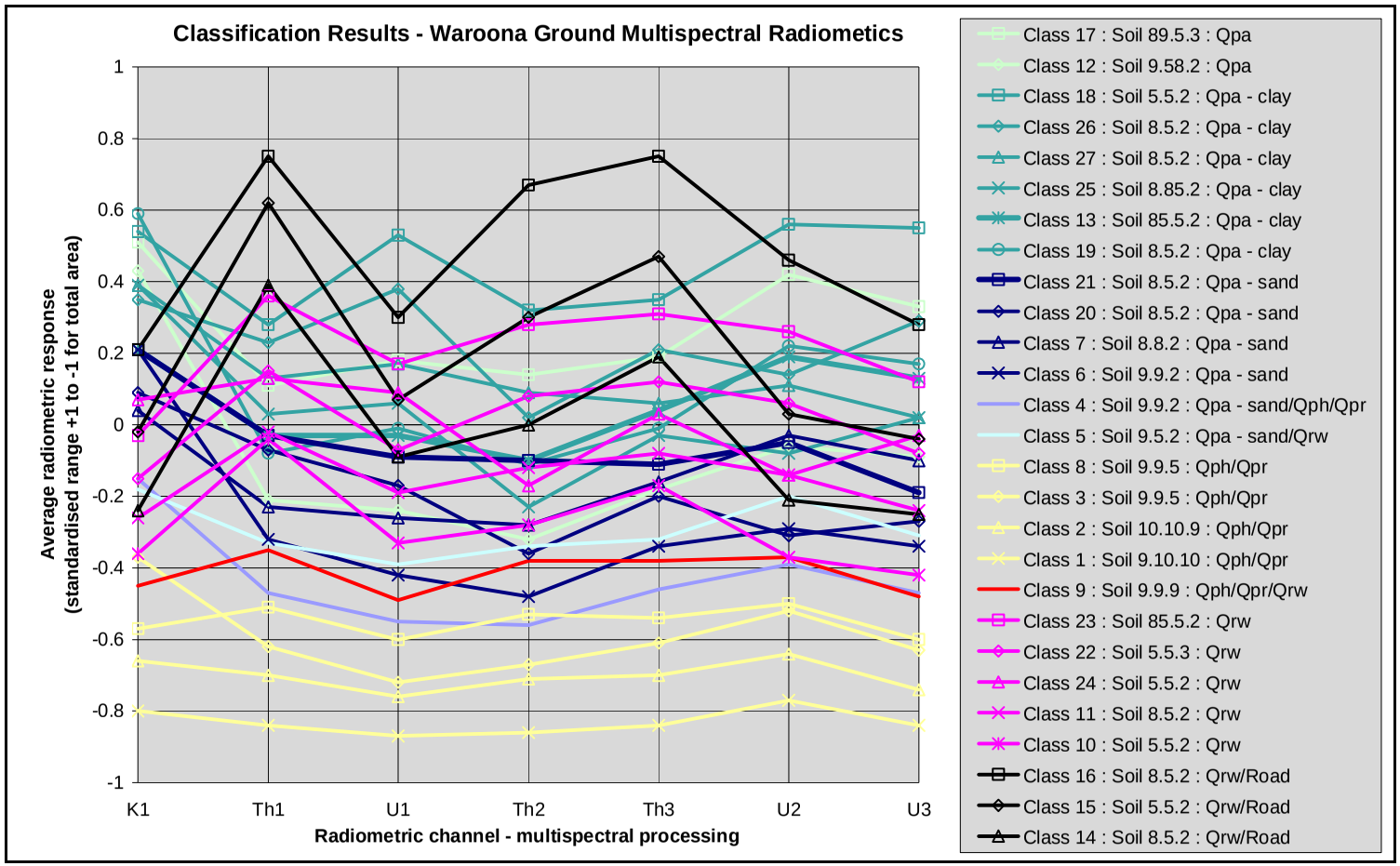


**Figure E.1. Classification results from the unsupervised classification of Waroona ground radiometric multispectral processed data.**

## E.3 Radiometric classification results and associated field sample information with standardised average radiometric classification response.

**Classification Group 1**

**Average Radiometric Response (standardised +1 to -1 range for total area)**

| K1 | Th1 | Th2 | Th3 | U1 | U2 | U3 |
|---|---|---|---|---|---|---|
| -0.8 | -0.84 | -0.86 | -0.84 | -0.87 | -0.77 | -0.84 |

| No Photo Available | Horizon depth | Soil Description | Soil Code |
|---|---|---|---|
| | A (0 to10cm) | Dark Grey Loamy Sand | 9 |
| | B (10 to20cm) | Grey Sand | 10 |
| | C (20 to 40cm) | Orange Grey Sand | 10 |
| 48 | **Comment** | | |

|  | **Horizon depth** | **Soil Description** | **Soil Code** |
|---|---|---|---|
| | A (0 to10cm) | Dark Grey Loamy Sand | 9 |
| | B (10 to20cm) | Grey Sand | 10 |
| | C (20 to 40cm) | Light Grey Sand | 10 |
| 47 | **Comment** | | |

| Horizon depth | Soil Description | Soil Code |
|---|---|---|
| A (0 to10cm) | Grey Sand (organic matter) | 10 |
| B (10 to20cm) | Grey Sand | 10 |
| C (20 to 40cm) | Light Yellow Grey Sand | 10 |
| **Comment** | | |

67



| Horizon depth | Soil Description | Soil Code |
|---|---|---|
| A (0 to10cm) | Grey Sand (organic matter) | 10 |
| B (10 to20cm) | Grey Brown Sand | 10 |
| C (20 to 40cm) | Light Brown Loamy Sand | 9 |
| **Comment** | | |

65



| Horizon depth | Soil Description | Soil Code |
|---|---|---|
| A (0 to10cm) | Grey Loamy Sand | 9 |
| B (10 to20cm) | Dark Grey Loamy Sand | 9 |
| C (20 to 40cm) | Dark Grey Sand | 10 |
| **Comment** | Non wetting | |

109

**Classification Group 2**

**Average Radiometric Response (standardised +1 to -1 range for total area)**

| K1 | Th1 | Th2 | Th3 | U1 | U2 | U3 |
|---|---|---|---|---|---|---|
| -0.66 | -0.7 | -0.71 | -0.7 | -0.76 | -0.64 | -0.74 |

| | Horizon depth | Soil Description | Soil Code |
|---|---|---|---|
|  | A (0 to10cm) | Dark Grey Loamy Sand | 9 |
| | B (10 to20cm) | Dark Grey Loamy Sand | 9 |
| | C (20 to 40cm) | Pale Grey Loamy Sand | 9 |
| 74-p8 | **Comment** | | |
|  | **Horizon depth** | **Soil Description** | **Soil Code** |
| | A (0 to10cm) | Light Grey Sand | 10 |
| | B (10 to20cm) | White Sand | 10 |
| | C (20 to 40cm) | White Sand | 10 |
| 66 | **Comment** | | |

| | Horizon depth | Soil Description | Soil Code |
|---|---|---|---|
|  | A (0 to10cm) | Grey Sand (organic matter) | 10 |
| | B (10 to20cm) | Grey Sand | 10 |
| | C (20 to 40cm) | Light Grey Brown Sand | 10 |
| 72 | **Comment** | | |
|  | **Horizon depth** | **Soil Description** | **Soil Code** |
| | A (0 to10cm) | Grey Sand (organic matter) | 10 |
| | B (10 to20cm) | Grey Brown Sand | 10 |
| | C (20 to 40cm) | Light Brown Loamy Sand | 9 |
| 73 | **Comment** | | |
| **No Photo Available** | **Horizon depth** | **Soil Description** | **Soil Code** |
| | A (0 to10cm) | Grey Loamy Sand | 9 |
| | B (10 to20cm) | Dark Grey Loamy Sand | 9 |
| | C (20 to 40cm) | Dark Grey Loamy Sand | 9 |
| 110 | **Comment** | | |

**Classification Group 4**

**Average Radiometric Response (standardised +1 to -1 range for total area)**

| K1 | Th1 | Th2 | Th3 | U1 | U2 | U3 |
|---|---|---|---|---|---|---|
| -0.15 | -0.47 | -0.56 | -0.46 | -0.55 | -0.39 | -0.47 |

| No Photo Available | Horizon depth | Soil Description | Soil Code |
|---|---|---|---|
| | A (0 to10cm) | Grey Loamy Sand | 10 |
| | B (10 to20cm) | Brown Sandy Loam | 8 |
| | C (20 to 40cm) | Light Brown Sandy Clay with Orange Mottles | 2 |
| 190-p8r3 | **Comment** | | |
|  | **Horizon depth** | **Soil Description** | **Soil Code** |
| | A (0 to10cm) | Grey Brown Loamy Sand | 9 |
| | B (10 to20cm) | Grey Loamy Sand | 9 |
| | C (20 to 40cm) | Orange friable Sandy Clay | 3 |
| 164-p22 | **Comment** | | |

| Horizon depth | Soil Description | Soil Code |
|---|---|---|
| A (0 to10cm) | Grey Loamy Sand | 9 |
| B (10 to20cm) | Grey Loamy Sand | 9 |
| C (20 to 40cm) | Light Orange Fine Sandy Clay with Orange Mottles | 2 |
| **Comment** | | |



166-p23

| Horizon depth | Soil Description | Soil Code |
|---|---|---|
| A (0 to10cm) | Dark Grey Loamy Sand | 9 |
| B (10 to20cm) | Dark Grey Loamy Sand with Orange Mottles | 9 |
| C (20 to 40cm) | Light Brown Fine Sandy Clay Loam with Orange Mottles | 2 |
| **Comment** | | |



196-p27

| Horizon depth | Soil Description | Soil Code |
|---|---|---|
| A (0 to10cm) | Grey Loamy Sand | 9 |
| B (10 to20cm) | Brown Fine Sandy Loam | 8 |
| C (20 to 40cm) | Light Brown Sandy Clay Loam with Orange Mottles | 2 |
| **Comment** | | |



198-p28

**Classification Group 5**

**Average Radiometric Response (standardised +1 to -1 range for total area)**

| K1 | Th1 | Th2 | Th3 | U1 | U2 | U3 |
|---|---|---|---|---|---|---|
| -0.18 | -0.33 | -0.34 | -0.32 | -0.39 | -0.2 | -0.31 |

| No Photo Available | Horizon depth | Soil Description | Soil Code |
|---|---|---|---|
| | A (0 to10cm) | Dark Brown Fine Sandy Loam | 8 |
| | B (10 to20cm) | Dark Brown Sandy Clay Loam | 5 |
| | C (20 to 40cm) | Orange with Dark Orange Mottles Sandy Clay | 2 |
| 30 | **Comment** | | |
|  | **Horizon depth** | **Soil Description** | **Soil Code** |
| | A (0 to10cm) | Brown Loamy Sand | 9 |
| | B (10 to20cm) | Brown Sandy Clay Loam | 5 |
| | C (20 to 40cm) | Orange Fine Sandy Clay with Red Mottles | 2 |
| 162-p21 | **Comment** | | |

| No Photo Available | Horizon depth | Soil Description | Soil Code |
|---|---|---|---|
| | A (0 to10cm) | Brown Grey Sandy Loam | 8 |
| | B (10 to20cm) | Brown Sandy Clay Loam | 5 |
| | C (20 to 40cm) | Brown Sandy Clay with Orange Mottles | 2 |
| 161 | **Comment** | | |
| **No Photo Available** | **Horizon depth** | **Soil Description** | **Soil Code** |
| | A (0 to10cm) | Dark Brown Loamy Sand | 9 |
| | B (10 to20cm) | Dark Brown Sandy Loam | 8 |
| | C (20 to 40cm) | Orange with bright Orange mottles Sandy Clay | 2 |
| 49 | **Comment** | | |
|  | **Horizon depth** | **Soil Description** | **Soil Code** |
| | A (0 to10cm) | Brown Loamy Sand | 9 |
| | B (10 to20cm) | Light Brown Loamy Sand | 9 |
| | C (20 to 40cm) | Grey with Orange Mottles Sandy Clay | 2 |
| 43 | **Comment** | Laterite Nodules in B&C | |

| Horizon depth | Soil Description | Soil Code |
|---|---|---|
| A (0 to10cm) | Brown Loamy Sand | 9 |
| B (10 to20cm) | Red Brown Loamy Sand | 9 |
| C (20 to 40cm) | Light Brown with Orange Mottles Coarse Sandy Clay | 2 |
| **Comment** | | |

112



| Horizon depth | Soil Description | Soil Code |
|---|---|---|
| A (0 to10cm) | Dark Brown Loamy Sand | 9 |
| B (10 to20cm) | Dark Brown Loamy Sand | 9 |
| C (20 to 40cm) | Light Brown Sand | 10 |
| **Comment** | Non wetting | |

96

**No Photo Available**

| Horizon depth | Soil Description | Soil Code |
|---|---|---|
| A (0 to10cm) | Black Loamy Sand | 9 |
| B (10 to20cm) | Dark Grey Sandy Loam | 8 |
| C (20 to 40cm) | Light Grey Brown Light Sandy Clay Loam | 5 |
| **Comment** | | |

78

**Classification Group 6**

**Average Radiometric Response (standardised +1 to -1 range for total area)**

| K1 | Th1 | Th2 | Th3 | U1 | U2 | U3 |
|---|---|---|---|---|---|---|
| 0.21 | -0.32 | -0.48 | -0.34 | -0.42 | -0.39 | -0.34 |

| | Horizon depth | Soil Description | Soil Code |
|---|---|---|---|
|  | A (0 to10cm) | Dark Brown Fine Silty Clay Loam | 5 |
| | B (10 to20cm) | Dark Brown Fine Sandy Clay Loam | 5 |
| | C (20 to 40cm) | Orange with dark Orange Mottles and Laterite nodules friable sandy clay | 3 |
| 33 | **Comment** | | |
|  | **Horizon depth** | **Soil Description** | **Soil Code** |
| | A (0 to10cm) | Dark Grey Loamy Sand | 9 |
| | B (10 to20cm) | Light Brown Loamy Sand | 9 |
| | C (20 to 40cm) | Light Brown Sandy Clay with Orange Mottles at 50 cm. | 2 |
| 202-p17&18 | **Comment** | | |

| Horizon depth | Soil Description | Soil Code |
|---|---|---|
| A (0 to10cm) | Grey Brown Fine Loamy Sand | 9 |
| B (10 to20cm) | Pale Grey Fine Sand | 10 |
| C (20 to 40cm) | Pale Orange with Dark Orange Mottles fine Sandy Clay Loam | 5 |
| **Comment** | | |



35

| Horizon depth | Soil Description | Soil Code |
|---|---|---|
| A (0 to10cm) | Dark Brown Loamy Sand with Laterite nodules to 1cm. | 9 |
| B (10 to20cm) | Dark Brown Loamy Sand with Laterite nodules to 1cm. | 9 |
| C (20 to 40cm) | Yellow with Orange Mottles Sandy Clay | 2 |
| **Comment** | | |



2

| Horizon depth | Soil Description | Soil Code |
|---|---|---|
| A (0 to10cm) | Grey Loamy Fine Sand | 9 |
| B (10 to20cm) | Pale Grey Loamy Fine Sand | 9 |
| C (20 to 40cm) | Yellow with Orange Mottles and Laterite nodules Sandy Clay Loam | 5 |
| **Comment** | | |



5

| Horizon depth | Soil Description | Soil Code |
|---|---|---|
| A (0 to10cm) | Dark Brown Loamy Sand | 9 |
| B (10 to20cm) | Dark Brown Loamy Sand | 9 |
| C (20 to 40cm) | Bright Orange with Faint Mottles Friable Sandy Clay | 3 |

6

| Comment |
|---|
| Disturbed Clay surface layer |

**No Photo Available**

| Horizon depth | Soil Description | Soil Code |
|---|---|---|
| A (0 to10cm) | Dark Brown Loamy Fine Sand | 9 |
| B (10 to20cm) | Yellow Brown fine Sandy Loam | 8 |
| C (20 to 40cm) | Yellow with small Orange mottles fine Sandy Clay | 2 |

18

| Comment |
|---|
| |



| Horizon depth | Soil Description | Soil Code |
|---|---|---|
| A (0 to10cm) | Dark Brown Loamy Sand | 9 |
| B (10 to20cm) | Light Brown Sand | 10 |
| C (20 to 40cm) | Light Brown with Orange mottles Heavy Sandy Clay | 2 |

108

| Comment |
|---|
| |

| No Photo Available | Horizon depth | Soil Description | Soil Code |
|---|---|---|---|
| | A (0 to10cm) | Dark Brown Sandy Loam | 8 |
| | B (10 to20cm) | Light Brown Sand | 10 |
| | C (20 to 40cm) | Pale Brown with Orange mottles Sand | 10 |
| 107 | **Comment** | | |

**Classification Group 7**

**Average Radiometric Response (standardised +1 to -1 range for total area)**

| K1 | Th1 | Th2 | Th3 | U1 | U2 | U3 |
|---|---|---|---|---|---|---|
| 0.04 | -0.23 | -0.28 | -0.16 | -0.26 | -0.03 | -0.1 |

|  | Horizon depth | Soil Description | Soil Code |
|---|---|---|---|
| | A (0 to10cm) | Dark Brown Sandy Loam | 8 |
| | B (10 to20cm) | Brown Sandy Clay Loam | 5 |
| | C (20 to 40cm) | Orange Sandy Clay with Red Mottles | 2 |
| 209-p24 | **Comment** | | |

| | Horizon depth | Soil Description | Soil Code |
|---|---|---|---|
|  | A (0 to10cm) | Dark Grey Loamy Sand | 9 |
| | B (10 to20cm) | Dark Grey Loamy Sand | 8 |
| | C (20 to 40cm) | Brown Sandy Clay with Orange Mottles | 2 |
| 159-p12 | **Comment** | | |

| | Horizon depth | Soil Description | Soil Code |
|---|---|---|---|
|  | A (0 to10cm) | Light Brown Loamy Sand (Much Organic Matter) | 9 |
| | B (10 to20cm) | Pale Brown Loamy Sand | 9 |
| | C (20 to 40cm) | Light Yellow Loamy Sand | 9 |
| 203-p16 | **Comment** | | |

| | Horizon depth | Soil Description | Soil Code |
|---|---|---|---|
|  | A (0 to10cm) | Dark Brown Fine Sandy Loam | 8 |
| | B (10 to20cm) | Dark Brown Fine Sandy Loam | 8 |
| | C (20 to 40cm) | Orange friable Sandy Clay Loam | 5 |
| 36 | **Comment** | | |

| No Photo Available | Horizon depth | Soil Description | Soil Code |
|---|---|---|---|
| | A (0 to10cm) | Dark Brown Sandy Clay Loam | 5 |
| | B (10 to20cm) | Dark Brown Sandy Clay Loam | 5 |
| | C (20 to 40cm) | Light Brown with Orange mottles Loamy Sand | 9 |
| 105 | **Comment** | | |

| No Photo Available | Horizon depth | Soil Description | Soil Code |
|---|---|---|---|
| | A (0 to10cm) | Dark Brown Sandy Clay Loam | 5 |
| | B (10 to20cm) | Dark Brown Heavy Sandy Clay Loam | 5 |
| | C (20 to 40cm) | Light Brown with Orange mottles Clayey Sand | 9 |
| 104 | **Comment** | | |

**Classification Group 8**

**Average Radiometric Response (standardised +1 to -1 range for total area)**

| K1 | Th1 | Th2 | Th3 | U1 | U2 | U3 |
|---|---|---|---|---|---|---|
| -0.57 | -0.51 | -0.53 | -0.54 | -0.6 | -0.5 | -0.6 |

| | Horizon depth | Soil Description | Soil Code |
|---|---|---|---|
|  | A (0 to10cm) | Dark Grey Loamy Sand | 9 |
| | B (10 to20cm) | Grey Loamy Sand | 9 |
| | C (20 to 40cm) | Light Orange Brown Loamy sand some Dark Orange Mottles | 9 |
| 175-p9&10 | **Comment** | | |
|  | **Horizon depth** | **Soil Description** | **Soil Code** |
| | A (0 to10cm) | Grey Loamy Sand | 9 |
| | B (10 to20cm) | Light Grey Loamy Sand | 9 |
| | C (20 to 40cm) | Light Orange Loamy Sand | 9 |
| 176-p7 | **Comment** | | |

| | Horizon depth | Soil Description | Soil Code |
|---|---|---|---|
|  | A (0 to10cm) | Dark Grey Loamy Sand (Organic Matter) | 9 |
| | B (10 to20cm) | Light Brown Very Sandy Clay Loam | 5 |
| | C (20 to 40cm) | Pale Brown Very Sandy Clay Loam | 5 |
| 71 | **Comment** | | |

| | Horizon depth | Soil Description | Soil Code |
|---|---|---|---|
|  | A (0 to10cm) | Grey Loamy Sand | 9 |
| | B (10 to20cm) | Light Grey Loamy Sand | 9 |
| | C (20 to 40cm) | Light Grey Loamy Sand | 9 |
| 111 | **Comment** | | |

| | Horizon depth | Soil Description | Soil Code |
|---|---|---|---|
|  | A (0 to10cm) | Black Loamy Sand | 9 |
| | B (10 to20cm) | Dark Grey Loamy Sand | 9 |
| | C (20 to 40cm) | Light Grey Brown Light Sandy Clay Loam | 5 |
| 76 | **Comment** | | |

**Classification Group 9**

**Average Radiometric Response (standardised +1 to -1 range for total area)**

| K1 | Th1 | Th2 | Th3 | U1 | U2 | U3 |
|---|---|---|---|---|---|---|
| -0.45 | -0.35 | -0.38 | -0.38 | -0.49 | -0.37 | -0.48 |

| | Horizon depth | Soil Description | Soil Code |
|---|---|---|---|
|  | A (0 to10cm) | Grey Loamy Sand | 9 |
| | B (10 to20cm) | Light Brown Loamy Sand | 9 |
| | C (20 to 40cm) | Orange Brown Loamy Clayey Sand | 9 |
| 173-p31 | **Comment** | | |
|  | **Horizon depth** | **Soil Description** | **Soil Code** |
| | A (0 to10cm) | Grey Brown Loamy Sand | 9 |
| | B (10 to20cm) | Grey Loamy Sand | 9 |
| | C (20 to 40cm) | Grey Orange Loamy Sand | 9 |
| 154-p6 | **Comment** | | |

| | Horizon depth | Soil Description | Soil Code |
|---|---|---|---|
|  | A (0 to10cm) | Dark Brown Loamy Sand | 9 |
| | B (10 to20cm) | Light Brown Slightly Clayey Sand | 10 |
| | C (20 to 40cm) | Light Brown with Orange mottles Sandy Clay | 2 |
| 95 | **Comment** | | |

**Classification Group 10**

**Average Radiometric Response (standardised +1 to -1 range for total area)**

| K1 | Th1 | Th2 | Th3 | U1 | U2 | U3 |
|---|---|---|---|---|---|---|
| -0.36 | -0.04 | -0.28 | -0.17 | -0.33 | -0.37 | -0.42 |

| | Horizon depth | Soil Description | Soil Code |
|---|---|---|---|
|  | A (0 to10cm) | Brown Loamy Sand | 9 |
| | B (10 to20cm) | Brown Sandy Loam | 8 |
| | C (20 to 40cm) | Brown Sandy Clay (Orange Mottles) | 2 |
| 172-p33 | **Comment** | | |

| | Horizon depth | Soil Description | Soil Code |
|---|---|---|---|
|  | A (0 to10cm) | Dark Brown Sandy Clay Loam | 5 |
| | B (10 to20cm) | Dark Brown Sandy Clay Loam | 5 |
| | C (20 to 40cm) | Orange Brown Heavy Sandy Clay | 2 |
| 46 | **Comment** | | |

| | Horizon depth | Soil Description | Soil Code |
|---|---|---|---|
|  | A (0 to10cm) | Coarse Sandy Clay Loam | 5 |
| | B (10 to20cm) | Grey with Orange Mottles heavy Sandy Clay | 2 |
| | C (20 to 40cm) | Grey with Orange Mottles heavy Sandy Clay | 2 |
| 92 | **Comment** | Hard Set | |

| | Horizon depth | Soil Description | Soil Code |
|---|---|---|---|
|  | A (0 to10cm) | Dark Grey with Orange Mottles heavy fine Sandy Clay | 2 |
| | B (10 to20cm) | Dark Brown Fine Silty Clay Loam | 5 |
| | C (20 to 40cm) | Dark Brown Fine Silty Loam | 2 |
| 82 | **Comment** | | |

**Classification Group 11**

**Average Radiometric Response (standardised +1 to -1 range for total area)**

| K1 | Th1 | Th2 | Th3 | U1 | U2 | U3 |
|---|---|---|---|---|---|---|
| -0.26 | -0.02 | -0.12 | -0.08 | -0.19 | -0.14 | -0.24 |

| | Horizon depth | Soil Description | Soil Code |
|---|---|---|---|
|  | A (0 to10cm) | Dark Grey Loamy Sand | 9 |
| | B (10 to20cm) | Brown Loamy Sand | 9 |
| | C (20 to 40cm) | Orange Brown Fine Sandy Clay with red mottles | 2 |
| 171-p32 | **Comment** | | |

| | Horizon depth | Soil Description | Soil Code |
|---|---|---|---|
|  | A (0 to10cm) | Brown Sandy Loam | 8 |
| | B (10 to20cm) | Brown Sandy Clay Loam (Orange Mottles) | 5 |
| | C (20 to 40cm) | Brown Sandy Clay (Orange Mottles) | 2 |
| 168-p29&30 | **Comment** | | |

| Horizon depth | Soil Description | Soil Code |
|---|---|---|
| A (0 to10cm) | Brown Sandy Loam (much organic matter) | 8 |
| B (10 to20cm) | Brown Sandy Clay Loam with Orange Mottles | 5 |
| C (20 to 40cm) | Orange Heavy Sandy Clay with Red Mottles | 2 |
| **Comment** | | |

208-p25&26



| Horizon depth | Soil Description | Soil Code |
|---|---|---|
| A (0 to10cm) | Dark Grey Loamy Sand | 9 |
| B (10 to20cm) | Brown Sandy Clay Loam | 5 |
| C (20 to 40cm) | Heavy Grey Sandy Clay with Orange Mottles | 2 |
| **Comment** | | |

158-p11



| Horizon depth | Soil Description | Soil Code |
|---|---|---|
| A (0 to10cm) | Dark Brown Sandy Clay Loam | 5 |
| B (10 to20cm) | Brown Sandy Clay Loam | 5 |
| C (20 to 40cm) | Brown Orange Friable Sandy Clay | 3 |
| **Comment** | | |

155-p7

| Horizon depth | Soil Description | Soil Code |
|---|---|---|
| A (0 to10cm) | Dark Brown Sandy Loam | 8 |
| B (10 to20cm) | Brown Sandy Clay Loam | 5 |
| C (20 to 40cm) | Brown Orange Friable Sandy Clay Loam | 3 |
| **Comment** | | |

157-p9&10

**No Photo Available**

| Horizon depth | Soil Description | Soil Code |
|---|---|---|
| A (0 to10cm) | Dark Red Brown Sandy Clay Loam | 5 |
| B (10 to20cm) | Dark Red Brown Sandy Clay Loam | 5 |
| C (20 to 40cm) | Dark Red Brown Heavy Sandy Clay | 2 |
| **Comment** | | |

44



| Horizon depth | Soil Description | Soil Code |
|---|---|---|
| A (0 to10cm) | Grey with Orange Mottles heavy Sandy Clay | 2 |
| B (10 to20cm) | Grey with Orange Mottles heavy Sandy Clay | 2 |
| C (20 to 40cm) | Grey with Orange mottles Coarse Sandy Clay | 2 |
| **Comment** | Hard set and cracked | |

93

| No Photo Available | | Horizon depth | Soil Description | Soil Code |
|---|---|---|---|---|
| | | A (0 to10cm) | Dark Brown Sandy Loam | 8 |
| | | B (10 to20cm) | Dark Brown with Orange mottles Sandy Clay Loam | 5 |
| | | C (20 to 40cm) | Dark Grey with Orange mottles Heavy Sandy Clay | 2 |
| | 91 | **Comment** | Hard set | |

| | | Horizon depth | Soil Description | Soil Code |
|---|---|---|---|---|
| | | A (0 to10cm) | Dark Brown Loamy Sand | 9 |
| | | B (10 to20cm) | Dark Brown very Sandy Clay Loam | 5 |
| | | C (20 to 40cm) | Dark Brown Heavy Sandy Clay | 2 |
| | 97 | **Comment** | Non wetting | |

**Classification Group 12**

**Average Radiometric Response (standardised +1 to -1 range for total area)**

| K1 | Th1 | Th2 | Th3 | U1 | U2 | U3 |
|---|---|---|---|---|---|---|
| 0.43 | -0.21 | -0.32 | -0.18 | -0.24 | -0.06 | -0.09 |

| No Photo Available | Horizon depth | Soil Description | Soil Code |
|---|---|---|---|
| | A (0 to10cm) | Dark Brown Sandy Loam | 8 |
| | B (10 to20cm) | Orange Brown Sandy Clay Loam | 5 |
| | C (20 to 40cm) | Bright Orange Friable Sandy Clay | 2 |
| 31 | **Comment** | | |
|  | **Horizon depth** | **Soil Description** | **Soil Code** |
| | A (0 to10cm) | Grey Fine Loamy Sand | 9 |
| | B (10 to20cm) | Grey Loamy Sand | 9 |
| | C (20 to 40cm) | Light Brown Sandy Clay with Orange Mottles | 2 |
| 187-p2 | **Comment** | | |

| | Horizon depth | Soil Description | Soil Code |
|---|---|---|---|
|  | A (0 to10cm) | Light Brown Loamy Sand | 9 |
| | B (10 to20cm) | Brown Sandy Loam with Laterite Nodules | 8 |
| | C (20 to 40cm) | Light Brown Fine Sandy Clay with Orange Mottles | 2 |
| 188-p1r3 | **Comment** | | |

| | Horizon depth | Soil Description | Soil Code |
|---|---|---|---|
|  | A (0 to10cm) | Light Brown Fine Loamy Sand | 9 |
| | B (10 to20cm) | Yellow Brown Fine Sandy Clay Loam | 5 |
| | C (20 to 40cm) | Yellow fine Sandy Clay | 2 |
| 11 | **Comment** | | |

| | Horizon depth | Soil Description | Soil Code |
|---|---|---|---|
|  | A (0 to10cm) | Dark Grey Loamy Sand | 9 |
| | B (10 to20cm) | Pale Yellow Sand | 10 |
| | C (20 to 40cm) | Light Orange very Sandy Clay | 2 |
| 27 | **Comment** | | |

204-p19

| Horizon depth | Soil Description | Soil Code |
|---|---|---|
| A (0 to10cm) | Dark Brown Sandy Loam | 8 |
| B (10 to20cm) | Brown Fine Sandy Loam | 8 |
| C (20 to 40cm) | Brown Heavy Sandy Clay with Orange Mottles | 2 |
| **Comment** | | |



9

| Horizon depth | Soil Description | Soil Code |
|---|---|---|
| A (0 to10cm) | Dark Brown Sandy Loam | 8 |
| B (10 to20cm) | Dark Brown Sandy Loam | 8 |
| C (20 to 40cm) | Orange with dark Orange Mottles Fine Sandy Clay | 2 |
| **Comment** | | |

**No Photo Available**

40

| Horizon depth | Soil Description | Soil Code |
|---|---|---|
| A (0 to10cm) | Dark Brown Loamy Sand | 9 |
| B (10 to20cm) | Dark Brown Sandy Clay Loam | 5 |
| C (20 to 40cm) | Orange Sandy Clay | 2 |
| **Comment** | | |

| | Horizon depth | Soil Description | Soil Code |
|---|---|---|---|
| | A (0 to10cm) | Light Brown Loamy Sand | 9 |
| | B (10 to20cm) | Pale Grey/Brown Sand | 10 |
| | C (20 to 40cm) | Light Grey with Orange Mottles Sandy Clay | 2 |
| 7 | **Comment** | | |
| **No Photo Available** | **Horizon depth** | **Soil Description** | **Soil Code** |
| | A (0 to10cm) | Dark Brown Sandy Clay Loam | 5 |
| | B (10 to20cm) | Dark Brown Sandy Clay Loam | 5 |
| | C (20 to 40cm) | Light Orange Brown with Orange Mottles Sandy Clay | 2 |
| 106 | **Comment** | | |
| **No Photo Available** | **Horizon depth** | **Soil Description** | **Soil Code** |
| | A (0 to10cm) | Brown Loamy Sand | 9 |
| | B (10 to20cm) | Light Brown Loamy Sand | 9 |
| | C (20 to 40cm) | Light Orange Grey Coarse Clayey Sand | 9 |
| 98 | **Comment** | | |

**Classification Group 13**

**Average Radiometric Response (standardised +1 to -1 range for total area)**

| K1 | Th1 | Th2 | Th3 | U1 | U2 | U3 |
|---|---|---|---|---|---|---|
| 0.21 | -0.03 | -0.1 | 0.04 | -0.03 | 0.19 | 0.13 |

| | Horizon depth | Soil Description | Soil Code |
|---|---|---|---|
|  | A (0 to10cm) | Brown Sandy Loam | 8 |
| | B (10 to20cm) | Orange Brown Sandy Clay Loam | 5 |
| | C (20 to 40cm) | Orange Sandy Clay with Red Mottles | 2 |
| 194-p35 | **Comment** | | |
|  | **Horizon depth** | **Soil Description** | **Soil Code** |
| | A (0 to10cm) | Dark Brown Sandy Clay Loam | 5 |
| | B (10 to20cm) | Orange Brown Sandy Clay Loam | 5 |
| | C (20 to 40cm) | Brown Sandy Clay with Orange Mottles | 2 |
| 201-p15 | **Comment** | | |

| | Horizon depth | Soil Description | Soil Code |
|---|---|---|---|
|  | A (0 to10cm) | Brown Sandy Clay Loam | 5 |
| | B (10 to20cm) | Brown Heavy Sandy Clay with Orange Mottles | 2 |
| | C (20 to 40cm) | Light Brown Sandy Clay with Orange Mottles | 2 |
| 199-p13 | **Comment** | | |

| | Horizon depth | Soil Description | Soil Code |
|---|---|---|---|
|  | A (0 to10cm) | Dark Brown Fine Sandy Loam | 8 |
| | B (10 to20cm) | Dark Brown Fine Sandy Clay Loam | 5 |
| | C (20 to 40cm) | Orange with dark Orange Mottles friable Fine Sandy Clay | 3 |
| 4 | **Comment** | | |

| | Horizon depth | Soil Description | Soil Code |
|---|---|---|---|
|  | A (0 to10cm) | Dark Brown Sandy Loam | 8 |
| | B (10 to20cm) | Dark Brown Sandy Clay Loam | 5 |
| | C (20 to 40cm) | Brown with Orange Mottles Coarse Sandy Clay | 2 |
| 8 | **Comment** | C Horizon very hard set | |

| | Horizon depth | Soil Description | Soil Code |
|---|---|---|---|
|  | A (0 to10cm) | Dark Brown Sandy Clay Loam | 5 |
| | B (10 to20cm) | Dark Brown Sandy Clay Loam | 5 |
| | C (20 to 40cm) | Light Brown with Orange mottles Loamy Sand | 9 |
| 103 | **Comment** | | |

| | Horizon depth | Soil Description | Soil Code |
|---|---|---|---|
|  | A (0 to10cm) | Dark Brown Sandy Loam | 8 |
| | B (10 to20cm) | Brown Sandy Clay Loam | 5 |
| | C (20 to 40cm) | Orange Brown with Orange Mottles Sandy Clay | 2 |
| 100 | **Comment** | | |

**Classification Group 14**

**Average Radiometric Response (standardised +1 to -1 range for total area)**

| K1 | Th1 | Th2 | Th3 | U1 | U2 | U3 |
|---|---|---|---|---|---|---|
| -0.24 | 0.39 | 0 | 0.19 | -0.09 | -0.21 | -0.25 |

| | Horizon depth | Soil Description | Soil Code |
|---|---|---|---|
|  | A (0 to10cm) | Brown Sandy Loam | 8 |
| | B (10 to20cm) | Brown Sandy Clay Loam + orange mottles | 5 |
| | C (20 to 40cm) | Orange friable Sandy Clay | 3 |
| 153-p5 | **Comment** | | |
| **No Photo Available** | **Horizon depth** | **Soil Description** | **Soil Code** |
| | A (0 to10cm) | Dark Brown Sandy Loam | 8 |
| | B (10 to20cm) | Dark Brown with Orange mottles Sandy Clay Loam | 5 |
| | C (20 to 40cm) | Dark Brown with Orange mottles Sandy Clay | 2 |
| 83 | **Comment** | Hard set | |

| Horizon depth | Soil Description | Soil Code |
|---|---|---|
| A (0 to10cm) | Dark Red Brown Sandy Clay Loam | 5 |
| B (10 to20cm) | Dark Red Brown Sandy Clay Loam | 5 |
| C (20 to 40cm) | Dark Brown with Orange Mottles Heavy Sandy Clay | 2 |
| **Comment** | | |

113



| Horizon depth | Soil Description | Soil Code |
|---|---|---|
| A (0 to10cm) | Dark Brown with Orange mottles Sandy Clay | 2 |
| B (10 to20cm) | Dark Brown heavy Sandy Clay | 2 |
| C (20 to 40cm) | Dark Brown heavy Sandy Clay | 2 |
| **Comment** | Hard set and cracked | |

80

**Classification Group 15**

**Average Radiometric Response (standardised +1 to -1 range for total area)**

| K1 | Th1 | Th2 | Th3 | U1 | U2 | U3 |
|---|---|---|---|---|---|---|
| -0.02 | 0.62 | 0.3 | 0.47 | 0.07 | 0.03 | -0.04 |

| | Horizon depth | Soil Description | Soil Code |
|---|---|---|---|
|  | A (0 to10cm) | Brown Sandy Clay Loam | 5 |
| | B (10 to20cm) | Brown Sandy Clay Loam (heavier) + orange mottles | 5 |
| | C (20 to 40cm) | Orange friable Sandy Clay | 3 |
| 152-p1 | **Comment** | | |
|  | **Horizon depth** | **Soil Description** | **Soil Code** |
| | A (0 to10cm) | Orange Brown Sandy Clay Loam (organic matter) | 5 |
| | B (10 to20cm) | Orange Brown with bright Orange Mottles Heavy Sandy Clay | 5 |
| | C (20 to 40cm) | Grey Brown with bright Orange Mottles Heavy Sandy Clay | 2 |
| 68 | **Comment** | | |

| | Horizon depth | Soil Description | Soil Code |
|---|---|---|---|
|  | A (0 to10cm) | Dark Brown Sandy Loam (organic matter) | 8 |
| | B (10 to20cm) | Dark Brown with Orange Mottles Heavy Sandy Clay Loam | 5 |
| | C (20 to 40cm) | Dark Brown Heavy Sandy Clay Loam | 5 |
| 70 | **Comment** | Hard set | |

| | Horizon depth | Soil Description | Soil Code |
|---|---|---|---|
|  | A (0 to10cm) | Dark Brown Sandy Loam | 8 |
| | B (10 to20cm) | Dark Brown with Orange mottles Sandy Clay Loam | 2 |
| | C (20 to 40cm) | Dark Brown with Orange mottles Sandy Clay | 2 |
| 85 | **Comment** | Hard set | |

| | Horizon depth | Soil Description | Soil Code |
|---|---|---|---|
|  | A (0 to10cm) | Dark Brown Fine Sandy Silty Clay | 3 |
| | B (10 to20cm) | Grey very heavy Sandy Clay | 2 |
| | C (20 to 40cm) | Dark Grey heavy fine Sandy Clay | 2 |
| 89 | **Comment** | | |

| | Horizon depth | Soil Description | Soil Code |
|---|---|---|---|
|  | A (0 to10cm) | Dark Brown Sandy Clay Loam | 5 |
| | B (10 to20cm) | Dark Grey with Orange mottles Sandy Clay | 2 |
| | C (20 to 40cm) | Grey very heavy Sandy Clay | 2 |
| 79 | **Comment** | Hard set and cracked | |

**Classification Group 16**

**Average Radiometric Response (standardised +1 to -1 range for total area)**

| K1 | Th1 | Th2 | Th3 | U1 | U2 | U3 |
|---|---|---|---|---|---|---|
| 0.21 | 0.75 | 0.67 | 0.75 | 0.3 | 0.46 | 0.28 |

| | Horizon depth | Soil Description | Soil Code |
|---|---|---|---|
|  | A (0 to10cm) | Brown Sandy Clay Loam | 5 |
| | B (10 to20cm) | Brown Sandy Clay Loam (heavier) + orange mottles | 5 |
| | C (20 to 40cm) | Orange friable Sandy Clay | 3 |
| 150-pS-1 | **Comment** | | |

| | Horizon depth | Soil Description | Soil Code |
|---|---|---|---|
|  | A (0 to10cm) | Dark Brown Clay Loam (minor sand grit) | 4 |

| | Horizon depth | Soil Description | Soil Code |
|---|---|---|---|
| | B (10 to20cm) | Dark Brown with orange mottles Clay Loam (minor sand grit) | 4 |
| | C (20 to 40cm) | Dark Grey Heavy Sandy Clay | 2 |
| 69 | **Comment** | | |
| **No Photo Available** | **Horizon depth** | **Soil Description** | **Soil Code** |
| | A (0 to10cm) | Dark Brown Sandy Loam | 8 |
| | B (10 to20cm) | Dark Brown Sandy Clay Loam | 5 |
| | C (20 to 40cm) | Dark Brown Sandy Clay | 2 |
| 84 | **Comment** | Hard set | |
|  | **Horizon depth** | **Soil Description** | **Soil Code** |
| | A (0 to10cm) | Brown Sandy Loam | 8 |
| | B (10 to20cm) | Dark Red Brown Sandy Clay Loam with small Laterite nodules | 5 |
| | C (20 to 40cm) | Grey Heavy Sandy Clay | 2 |
| 90 | **Comment** | Hard set and cracked | |

**Classification Group 17**

**Average Radiometric Response (standardised +1 to -1 range for total area)**

| K1 | Th1 | Th2 | Th3 | U1 | U2 | U3 |
|---|---|---|---|---|---|---|
| 0.51 | 0.11 | 0.14 | 0.19 | 0.18 | 0.42 | 0.33 |

| | Horizon depth | Soil Description | Soil Code |
|---|---|---|---|
|  | A (0 to10cm) | Dark Brown Sandy Loam | 8 |
| | B (10 to20cm) | Orange Brown Sandy Clay Loam | 5 |
| | C (20 to 40cm) | Bright Orange Fine Sandy Clay (friable) | 2 |
| 212-p20&21 | **Comment** | | |
|  | **Horizon depth** | **Soil Description** | **Soil Code** |
| | A (0 to10cm) | Dark Red Brown Fine Loamy Sand | 9 |
| | B (10 to20cm) | Orange Brown Fine Sandy Clay Loam | 5 |
| | C (20 to 40cm) | Orange friable Fine Sandy Clay | 2 |
| 39 | **Comment** | Hard set & Cracked | |

**Classification Group 18**

**Average Radiometric Response (standardised +1 to -1 range for total area)**

| K1 | Th1 | Th2 | Th3 | U1 | U2 | U3 |
|---|---|---|---|---|---|---|
| 0.54 | 0.28 | 0.32 | 0.35 | 0.53 | 0.56 | 0.55 |

| | Horizon depth | Soil Description | Soil Code |
|---|---|---|---|
|  | A (0 to10cm) | Light Brown Sandy Loam | 8 |
| | B (10 to20cm) | Brown Sandy Clay Loam | 5 |
| | C (20 to 40cm) | Orange Fine Sandy Clay with Red Mottles | 2 |
| 195-p32 | **Comment** | | |
| **No Photo Available** | **Horizon depth** | **Soil Description** | **Soil Code** |
| | A (0 to10cm) | Brown Sandy Clay Loam | 5 |
| | B (10 to20cm) | Brown Sandy Clay Loam (heavier) + orange mottles | 5 |
| | C (20 to 40cm) | Orange friable Sandy Clay | 3 |
| 151 | **Comment** | | |

| | Horizon depth | Soil Description | Soil Code |
|---|---|---|---|
|  | A (0 to10cm) | Brown Fine Sandy Clay Loam | 5 |
| | B (10 to20cm) | Brown Clay Loam | 4 |
| | C (20 to 40cm) | Light Orange Brown with Orange Mottles Sandy Clay | 2 |
| 10 | **Comment** | | |

**Classification Group 19**

**Average Radiometric Response (standardised +1 to -1 range for total area)**

| K1 | Th1 | Th2 | Th3 | U1 | U2 | U3 |
|---|---|---|---|---|---|---|
| 0.59 | -0.08 | -0.11 | -0.01 | -0.01 | 0.22 | 0.17 |

| | Horizon depth | Soil Description | Soil Code |
|---|---|---|---|
|  | A (0 to10cm) | Dark Brown Fine Silty Loam | 7 |
| | B (10 to20cm) | Dark Brown Fine Sandy Loam | 8 |
| | C (20 to 40cm) | Orange friable Fine Sandy Clay Loam | 5 |
| 32 | **Comment** | | |

| Horizon depth | Soil Description | Soil Code |
|---|---|---|
| A (0 to10cm) | Grey Fine Loamy Sand | 9 |
| B (10 to20cm) | Light Brown Sandy Clay Loam | 5 |
| C (20 to 40cm) | Bright Orange Fine Sandy Clay with Red Mottles | 2 |
| **Comment** | | |



189-p38

| Horizon depth | Soil Description | Soil Code |
|---|---|---|
| A (0 to10cm) | Light Brown Sandy Loam | 8 |
| B (10 to20cm) | Brown Sandy Clay Loam | 5 |
| C (20 to 40cm) | Light Brown Sandy Clay with Orange Mottles at more than 50 cm | 2 |
| **Comment** | | |



193-p34

| Horizon depth | Soil Description | Soil Code |
|---|---|---|
| A (0 to10cm) | Light Grey Fine Loamy Sand | 9 |
| B (10 to20cm) | Light Brown Sandy Loam | 8 |
| C (20 to 40cm) | Light Brown Sandy Clay with Orange Mottles | 2 |
| **Comment** | | |



213-p33

| Horizon depth | Soil Description | Soil Code |
|---|---|---|
| A (0 to10cm) | Dark Brown Fine Sandy Clay Loam | 5 |
| B (10 to20cm) | Orange Brown Sandy Clay Loam | 5 |
| C (20 to 40cm) | Orange with faint dark Orange Mottles Sandy Clay | 2 |
| **Comment** | | |

16



| Horizon depth | Soil Description | Soil Code |
|---|---|---|
| A (0 to10cm) | Dark Brown Fine Sandy Loam | 8 |
| B (10 to20cm) | Dark Brown Fine Sandy Clay Loam | 5 |
| C (20 to 40cm) | Orange with dark Orange Mottles Fine Sandy Clay | 2 |
| **Comment** | | |

37

**No Photo Available**

| Horizon depth | Soil Description | Soil Code |
|---|---|---|
| A (0 to10cm) | Dark Brown Sandy Loam | 8 |
| B (10 to20cm) | Dark Brown Sandy Clay Loam | 5 |
| C (20 to 40cm) | Light Orange Brown with Orange Mottles Coarse Sandy Clay | 2 |
| **Comment** | | |

99

**Classification Group 20**

**Average Radiometric Response (standardised +1 to -1 range for total area)**

| K1 | Th1 | Th2 | Th3 | U1 | U2 | U3 |
|---|---|---|---|---|---|---|
| 0.09 | -0.07 | -0.36 | -0.2 | -0.17 | -0.31 | -0.27 |

| | | | |
|---|---|---|---|
|  | **Horizon depth** | **Soil Description** | **Soil Code** |
| | A (0 to10cm) | Dark Brown Fine Sandy Loam | 8 |
| | B (10 to20cm) | Dark Brown Fine Sandy Clay Loam | 5 |
| | C (20 to 40cm) | Light Brown Fine Sandy Clay | 2 |
| 12 | **Comment** | | |
|  | **Horizon depth** | **Soil Description** | **Soil Code** |
| | A (0 to10cm) | Brown Sandy Loam | 8 |
| | B (10 to20cm) | Orange Brown Sandy Clay Loam | 5 |
| | C (20 to 40cm) | Orange Fine Sandy Clay with Red Mottles | 2 |
| 186-p34&35 | **Comment** | | |

| | Horizon depth | Soil Description | Soil Code |
|---|---|---|---|
|  | A (0 to10cm) | Brown Fine Sandy Loam | 8 |
| | B (10 to20cm) | Brown Fine Sandy Clay Loam | 5 |
| | C (20 to 40cm) | Light Brown with Orange Mottles fine Sandy Clay | 2 |
| 13 | **Comment** | | |

| | Horizon depth | Soil Description | Soil Code |
|---|---|---|---|
|  | A (0 to10cm) | Dark Brown Sandy Loam | 8 |
| | B (10 to20cm) | Dark Brown Sandy Clay Loam | 5 |
| | C (20 to 40cm) | Orange Yellow Friable Clay | 3 |
| 26 | **Comment** | | |

| | Horizon depth | Soil Description | Soil Code |
|---|---|---|---|
|  | A (0 to10cm) | Dark Brown Sandy Loam | 8 |
| | B (10 to20cm) | Light Brown Sandy Clay Loam with Orange Mottles | 5 |
| | C (20 to 40cm) | Light Brown Heavy Sandy Clay with Orange Mottles | 2 |
| 206-p30 | **Comment** | | |

| | Horizon depth | Soil Description | Soil Code |
|---|---|---|---|
|  | A (0 to10cm) | Dark Brown Loamy Sand | 9 |
| | B (10 to20cm) | Pale Brown Loamy Sand with Laterite nodules | 9 |
| | C (20 to 40cm) | Pale yellow Clay Sand with Laterite nodules | 9 |
| 20 | **Comment** | | |

**Classification Group 21**

**Average Radiometric Response (standardised +1 to -1 range for total area)**

| K1 | Th1 | Th2 | Th3 | U1 | U2 | U3 |
|---|---|---|---|---|---|---|
| 0.21 | -0.03 | -0.1 | -0.11 | -0.09 | -0.05 | -0.19 |

| | Horizon depth | Soil Description | Soil Code |
|---|---|---|---|
|  | A (0 to10cm) | Dark Brown Loam | 6 |
| | B (10 to20cm) | Dark Brown with orange mottles Sandy Clay Loam | 5 |
| | C (20 to 40cm) | Orange Brown with orange mottles Heavy Sandy Clay | 2 |
| 29 | **Comment** | | |

192-p36

| Horizon depth | Soil Description | Soil Code |
|---|---|---|
| A (0 to10cm) | Brown Sandy Loam | 8 |
| B (10 to20cm) | Brown Sandy Clay Loam | 5 |
| C (20 to 40cm) | Orange Sandy Clay with Red Mottles and laterite nodules | 2 |
| **Comment** | | |

**No Photo Available**

| Horizon depth | Soil Description | Soil Code |
|---|---|---|
| A (0 to10cm) | Dark Brown Sandy Clay Loam | 5 |
| B (10 to20cm) | Dark Brown Sandy Clay Loam | 5 |
| C (20 to 40cm) | Dark Brown Heavy Sandy Clay Loam | 5 |
| **Comment** | | |

102

**Classification Group 22**

**Average Radiometric Response (standardised +1 to -1 range for total area)**

| K1 | Th1 | Th2 | Th3 | U1 | U2 | U3 |
|---|---|---|---|---|---|---|
| -0.15 | 0.15 | 0.08 | 0.12 | -0.07 | 0.06 | -0.08 |

| | Horizon depth | Soil Description | Soil Code |
|---|---|---|---|
|  | A (0 to10cm) | Cracking Dark Brown Sandy Clay Loam | 5 |
| | B (10 to20cm) | Brown Sandy Clay Loam | 5 |
| | C (20 to 40cm) | Brown Orange Friable Sandy Clay | 3 |
| 156-p8 | **Comment** | | |

**Classification Group 23**

**Average Radiometric Response (standardised +1 to -1 range for total area)**

| K1 | Th1 | Th2 | Th3 | U1 | U2 | U3 |
|---|---|---|---|---|---|---|
| -0.03 | 0.36 | 0.28 | 0.31 | 0.17 | 0.26 | 0.12 |

| | Horizon depth | Soil Description | Soil Code |
|---|---|---|---|
|  | A (0 to10cm) | Brown Sandy Loam | 8 |
| | B (10 to20cm) | Brown Sandy Clay Loam (Orange Mottles) | 5 |
| | C (20 to 40cm) | Orange Fine Sandy Clay | 2 |
| 167-p28 | **Comment** | | |
|  | **Horizon depth** | **Soil Description** | **Soil Code** |
| | A (0 to10cm) | Dark Brown Sandy Loam | 8 |
| | B (10 to20cm) | Orange Brown Sandy Clay Loam | 5 |
| | C (20 to 40cm) | Orange Fine Sandy Clay with red mottles | 2 |
| 170-p26 | **Comment** | | |

| No Photo Available | Horizon depth | Soil Description | Soil Code |
|---|---|---|---|
| | A (0 to10cm) | Dark Brown Sandy Clay Loam with Laterite Nodules | 5 |
| | B (10 to20cm) | Dark Brown Fine Sandy Clay Loam with Laterite Nodules | 5 |
| | C (20 to 40cm) | Dark Brown Clay Loam with Laterite nodules | 4 |
| 86 | **Comment** | Hard set and cracked | |
|  | **Horizon depth** | **Soil Description** | **Soil Code** |
| | A (0 to10cm) | Dark Brown Sandy Clay Loam with Laterite Nodules | 5 |
| | B (10 to20cm) | Dark Brown Fine Sandy Clay Loam with Laterite Nodules | 5 |
| | C (20 to 40cm) | Dark Brown Clay Loam with Laterite nodules | 4 |
| 87 | **Comment** | Hard set and cracked | |
|  | **Horizon depth** | **Soil Description** | **Soil Code** |
| | A (0 to10cm) | Dark Brown Fine Silty Loam | 7 |
| | B (10 to20cm) | Dark Brown Fine Silty Clay Loam | 5 |
| | C (20 to 40cm) | Dark Grey with Orange mottles Heavy fine Sandy Clay | 2 |
| 81 | **Comment** | | |

**Classification Group 24**

**Average Radiometric Response (standardised +1 to -1 range for total area)**

| K1 | Th1 | Th2 | Th3 | U1 | U2 | U3 |
|---|---|---|---|---|---|---|
| 0.07 | 0.13 | -0.17 | 0.03 | 0.09 | -0.14 | -0.03 |

| | Horizon depth | Soil Description | Soil Code |
|---|---|---|---|
|  | A (0 to10cm) | Brown Sandy Clay Loam | 5 |
| | B (10 to20cm) | Orange Brown Fine Sandy Clay Loam | 5 |
| | C (20 to 40cm) | Orange Fine Sandy Clay with Red Mottles | 2 |
| 191-p37 | **Comment** | | |
|  | **Horizon depth** | **Soil Description** | **Soil Code** |
| | A (0 to10cm) | Dark Brown Loamy Sand | 9 |
| | B (10 to20cm) | Dark Brown Loamy Sand | 9 |
| | C (20 to 40cm) | Brown with Dark Orange Mottles heavy Sandy Clay | 2 |
| 19 | **Comment** | | |

**Classification Group 25**

**Average Radiometric Response (standardised +1 to -1 range for total area)**

| K1 | Th1 | Th2 | Th3 | U1 | U2 | U3 |
|---|---|---|---|---|---|---|
| 0.39 | 0.03 | -0.23 | -0.03 | 0.06 | -0.08 | 0.02 |

| | Horizon depth | Soil Description | Soil Code |
|---|---|---|---|
|  | A (0 to10cm) | Light Brown Sandy Loam | 8 |
| | B (10 to20cm) | Brown Sandy Loam | 8 |
| | C (20 to 40cm) | Light Brown Sandy Clay with Orange Mottles | 2 |
| 205-p31 | **Comment** | | |
|  | **Horizon depth** | **Soil Description** | **Soil Code** |
| | A (0 to10cm) | Brown Sandy Loam | 8 |
| | B (10 to20cm) | Orange Brown fine Sandy Clay Loam | 5 |
| | C (20 to 40cm) | Light Orange with faint Orange mottles fine Sandy Clay | 2 |
| 15 | **Comment** | | |

| | Horizon depth | Soil Description | Soil Code |
|---|---|---|---|
|  | A (0 to10cm) | Light Brown Sandy Loam | 8 |
| | B (10 to20cm) | Orange Brown Sandy Clay Loam | 5 |
| | C (20 to 40cm) | Bright Orange Fine Sandy Clay (friable) | 3 |
| 211-p22 | **Comment** | | |

| | Horizon depth | Soil Description | Soil Code |
|---|---|---|---|
|  | A (0 to10cm) | Light Brown Loamy fine Sand | 9 |
| | B (10 to20cm) | Light Brown Loamy fine Sand | 9 |
| | C (20 to 40cm) | Light Yellow Loamy Fine Sand | 9 |
| 17 | **Comment** | | |

| | Horizon depth | Soil Description | Soil Code |
|---|---|---|---|
|  | A (0 to10cm) | Dark Brown Fine Sandy Loam | 8 |
| | B (10 to20cm) | Yellow Brown Fine Sandy Loam | 8 |
| | C (20 to 40cm) | Dark Yellow Fine Sandy Clay | 2 |
| 3 | **Comment** | | |

**Classification Group 26**

**Average Radiometric Response (standardised +1 to -1 range for total area)**

| K1 | Th1 | Th2 | Th3 | U1 | U2 | U3 |
|---|---|---|---|---|---|---|
| 0.35 | 0.23 | 0.2 | 0.21 | 0.38 | 0.14 | 0.29 |

| | Horizon depth | Soil Description | Soil Code |
|---|---|---|---|
|  | A (0 to10cm) | Dark Brown Fine Sandy Clay Loam | 5 |
| | B (10 to20cm) | Brown with Orange Mottles Sandy Clay Loam | 5 |
| | C (20 to 40cm) | Orange with dark Orange Mottles Heavy Sandy Clay | 2 |
| 38 | **Comment** | | |

**Classification Group 27**

**Average Radiometric Response (standardised +1 to -1 range for total area)**

| K1 | Th1 | Th2 | Th3 | U1 | U2 | U3 |
|---|---|---|---|---|---|---|
| 0.39 | 0.13 | 0.09 | 0.06 | 0.17 | 0.11 | 0.02 |

| | Horizon depth | Soil Description | Soil Code |
|---|---|---|---|
|  | A (0 to10cm) | Brown Fine Sandy Loam | 8 |
| | B (10 to20cm) | Dark Brown Fine Sandy Clay Loam | 5 |
| | C (20 to 40cm) | Bright Orange Fine Sandy Clay (friable) | 3 |
| 210-p23 | **Comment** | | |
|  | **Horizon depth** | **Soil Description** | **Soil Code** |
| | A (0 to10cm) | Brown Sandy Loam | 8 |
| | B (10 to20cm) | Orange Brown Sandy Clay Loam | 5 |
| | C (20 to 40cm) | Orange Brown Sandy Clay | 2 |
| 28 | **Comment** | Hard set | |

| Horizon depth | Soil Description | Soil Code |
|---|---|---|
| A (0 to10cm) | Dark Brown Sandy Loam | 8 |
| B (10 to20cm) | Dark Brown Sandy Loam | 8 |
| C (20 to 40cm) | Yellow Brown with Orange Mottles Fine Sandy Clay | 2 |
| 1 | **Comment** | |

**No Photo Available**

| Horizon depth | Soil Description | Soil Code |
|---|---|---|
| A (0 to10cm) | Dark Brown Sandy Loam | 8 |
| B (10 to20cm) | Orange Brown Sandy Clay Loam | 5 |
| C (20 to 40cm) | Orange Brown Sandy Clay | 2 |
| 101 | **Comment** | |

# References


Adams, F., and R. Dams, 1970, Applied gamma-ray spectrometry: Pergamon Press.

Adams, J. A. S., and P. Gasparini, 1970, Gamma-ray spectrometry of rocks: Elsevier publishing company.

Allyson, J. D., and D. C. W. Sanderson, 1998, Monte Carlo simulation of Environmental Airborne Gamma-Spectrometry: Journal of Environmental Radioactivity, **38**, 259–282.

Anderson-Mayes, A. M., 1999, Enhancing the interpretation of multi-variate airborne geophysical data for dryland salinity studies: PhD thesis, University of Queensland.

Baranov, V. L. and N. G. Morozova, 1973, The behaviour of natural radionuclides in soil, *in* V. M. Klechkovskii et al., eds., Radioecology: Halsted Press, 3-29.

Baxter, J. L., and S. L. Lipple, ed., 1985, Perenjori 1:250,000 Geological Series: Geological Survey of Western Australia.

Bierwirth, P., 1996, Investigation of airborne gamma-ray images as a rapid mapping tool for soil and land degradation, Wagga Wagga, NSW, Record 1996/22: Australian Geological Survey Organisation.

Bierwirth, P., S.Hardy, P. Wilson, S. Philip, D. Smith, I. Heiner, and M. Grundy, 1996, Radio Ga-Ga integrating gamma-radiometrics into landscape modelling of soils attributes; results of an ACLEP exchange: ACLEP newsletter, **5**, no. 3, 15-18.

Billings, S. D., 1998, Geophysical aspects of soil mapping using airborne gamma-ray spectrometry: Ph.D. thesis, University of Sydney.

Billings, S. D., and J. Hovgaard, 1999, Modelling detector response in airborne gamma-ray spectrometry: Geophysics, **64**, 1378–1392.

Billings, S. D., B. R. S. Minty, and G. N. Newsam, 2003, Spatial resolution and deconvolution of airborne gamma-ray spectrometry: Geophysics, **68**, 1257-1266.

Calleja, B. M., 2001, Soil mapping using high resolution radiometrics: Honours dissertation, Curtin University of Technology.

Chin, J., ed. 1986, Kellerberrin 1:250,000 Geological Series: Geological Survey of Western Australia.

Clark, R. B., J. S. Duval, and J. A. S. Adams, 1972, Computer simulation of an airborne gamma ray spectrometer: Journal of Geophysical Research., **77**, no. 17, 3021–3031.

Cook, S. E., R. J. Corner, G. Grealish, P. E. Gessler, and C. J. Chartres, 1996a, A rule based system to map soil properties: Journal of the Soil Science Society of America, **60**, 1893–1900.

Cook, S. E., R. J. Corner, P. R. Groves, and G. J. Grealish, 1996b, Use of airborne gamma-radiometric data for soil mapping: Australian Journal of Soil Research; **34**, 183–194.

Cooper, S., N. Crossely, D. Cummins, G. Drysdale, R. Denham, P. Galloway, T. Lacey, H. Lauk, J. Smith, and J. Wayland, 2001, Elashgin focus catchment report: Department of Agriculture and Food, Government of Western Australia.

Cruvinel, P. E., and F. A. Balogun, 2006, [Compton scattering tomography for agricultural measurements]: Engenharia Agrícola, **26**, 151-160.

Darnley, A. G. and M. Fleet, 1968, Evaluation of airborne gamma-ray spectrometry in the Bancroft and Elliott Lake areas of Ontario, Canada: Proceedings of the fifth International Symposium on Remote Sensing Environment, Expanded Abstracts, 833-853.

Darnley, A. G. and R. L. Grasty, 1971, Mapping from the air by gamma-ray spectrometry, *in* R. W. Boyle, ed., Geochemical Exploration: Canadian Institute of Mining and Metallurgy, **11**, 485-500.

de Lange, P. W., 1959, The radiometric analysis of naturally leached uranium and thorium ore samples: Comparison of different methods: Journal of the South African Institute of Mining and Metallurgy, **60**, 640-656.

Dickson, B. L., and K. M. Scott, 1997, Interpretation of aerial gamma-ray surveys – adding the geochemical factors: AGSO Journal of Australian Geology and Geophysics, **17**, no.2, 187-200.

Dickson, B. L., and G. Taylor, 2000, Maximum noise fraction method reveals detail in aerial gamma-ray surveys: Exploration Geophysics, **31**, 73-77.

Donahue, R. L., R. W. Miller, and J. C. Shickluna, 1983, An introduction to soils and plant growth: Prentice Hall Inc.

Drury, S., 1993, Image Interpretation in Geology: Blackwell Science.

Foote, R. S., 1968, Application of airborne gamma-radiation measurements to pedologic mapping: Proceedings of the fifth International Symposium on Remote Sensing Environment, Expanded Abstracts, 585-587.

Garrels, R. M., and C. L. Christ, 1964, Solutions, minerals and equilibria: Harper and Row.

GeoAg Pty Ltd, 2004, Rapid soil mapping land capability assessment of Harvey Irrigation Area: GeoAg Pty Ltd.

George, R. J., 1998, Evaluation of airborne geophysics for catchment management, Toolibin Western Australia: National Airborne Geophysics Project, Agriculture, Fisheries and Forestry, National Dryland Salinity Program.

Grasty, R. L., and Minty, B. R. S., 1995, A guide to the technical specifications for airborne gamma-ray surveys: Australian Geological Survey Organisation.

Green, A. A., M. Berman, P. Switzer, and M. D. Craig, 1988, A transformation for ordering multispectral data in terms of image quality with implications for noise removal: IEEE Transactions on Geoscience and Remote Sensing, **26**, no. 1, 65–74.

Gulyakin, I. V., and E. V. Yudintseva, 1960, [The entrance into plants and accumulation in the yield of some radioactive products of division]: Izvestiya Akademii Nauk SSSR, Seriya Biologicheskaya, **6**, 874-885.

Gunn, P. J., 1978, Inversion of airborne radiometric data: Geophysics, **43**, 133-142.

Harriss, R. C., and J. A. S. Adams, 1965, Geochemical and mineralogical studies on the weathering of granite rocks: American Journal of Science, **264**, 146-173.

Heath, R. L., 1964, Scintillation spectrometry, Gamma ray spectrum catalogue, Report IDO–16880: United States Atomic Energy Commission.

Hem, J., 1985, Study and interpretation of the chemical characteristics of natural water, Water-supply Paper 2254: United States Geological Survey.

Hoogteijling, P. J., and G. J. Sizou, 1948, Radioactivity and grain size of soil: Physica, **14**, 65-72.

Hovgaard, J., and R. L. Grasty, 1997, Reducing statistical noise in airborne gamma-ray data through spectral component analysis: Proceedings of Exploration 97: Fourth Decennial Conference on Mineral Exploration, Expanded Abstract, 753–764.

IAEA, 2003, Guidelines for radioelement mapping using gamma ray spectrometry data, technical report series, no. 1363: International Atomic Energy Agency.

Isbell, R. F., 1997, The Australian Soil Classification, Australian Soil and Land Survey Handbook: CSIRO Publishing.

Kiss, J. J., E. De Jong, and J. R. Bettany, 1988, The distribution of natural radionuclides in native soils of southern Saskatchewan: Canadian Journal of Environmental Quality, **17**, 437-445.

Langmuir, D., and J. S. Herman, 1980, The mobility of thorium in natural waters at low temperatures: Geochimica et Cosmochimica Acta, **44**, 1753-1766.

Lawrie, K. C., T. J. Munday, D. L. Dent, D. L. Gibson, R. C. Brodie, J. R. Wilford, N. S. Reilly, R. A. Chan, and P. Baker, 2000, A geological systems approach to understanding the processes involved in land and water salinisation - The Gilmore project area, central-west New South Wales: AGSO Research Newsletter, **52**, 13-32.

Lee, J. B., A. S. Woodyatt, and M. Berman, 1990, Enhancement of high spectral resolution remote-sensing data by a noise-adjusted principal components transform: IEEE Transactions on Geoscience and Remote Sensing, **28**, no.3, 295-304.

Leeper, G. W., and N. C. Uren, 1993, Soil Science: an introduction: Melbourne University Press.

Low, G. H., D. C. Lowry, and R. W. Lake, 1980, Pinjarra 1:250,000 Geological Series: Geological Survey of Western Australia.

Mahon D. C. and R. W. Mathewes, 1983, Uptake of naturally occurring radioisotopes by vegetation in a region of high radioactivity: Canadian of Soil Science, **63**, 281-290.

Marchesi Sociats, J. M., 1948, [Potassium fertilizers in tomato cultivation]: Madrid.

Marsden, E., and C. Watson-Munro, 1944, Radioactivity of New Zealand soils and rocks: New Zealand Journal of Science and Technology, **26B**, 99–114.

Marshall, T. J., 1947, Mechanical composition of soil in relation to field descriptions of texture, Bulletin No. 224: Council for Scientific and Industrial Research.

Martz, L. W., and E. de Jong, 1987, Using cesium-137 to assess. the variability of net soil erosion and its association with topography in Canadian Prairie landscape: CATENA **14**, 439-451.

Martz, L. W., and E. de Jong, 1988, CATCH: a Fortran Program for Measuring Catchment Area from Digital Elevation Models: Computers and Geosciences, **14**, 627-640.

Martz, L. W., and E. de Jong, 1990, Natural radionuclides in the soils of a small agricultural basin in the Canadian prairies and their associations with topography, soil properties and erosion: CATENA **17**, 85-96.

Miller, J. R., and R. F. Reitemeier, 1957, Rate of leaching of radio-strontium through soils by simulated rain and irrigation waters, Resource Report No. 300: United States Department of Agriculture.

Miller, R. W., and R. L. Donahue, 1990, Soils: An Introduction to Soils and Plant Growth: Prentice-Hall Inc.

Minty, B. R. S., 1997, The fundamentals of airborne gamma-ray spectrometry: Journal of Australian Geology and Geophysics, **17**, 39-50.

Minty, B. R. S., 1998, Multichannel models for the estimation of radon background in airborne gamma-ray spectrometry: Geophysics, **63**, 1986-1996.

Minty, B. R. S., P. McFadden, and B. L. N. Kennett, 1998, Multichannel processing for airborne gamma-ray spectrometry: Geophysics, **63**, 1971-1985.

Minty, B. R. S., and J. Hovgaard, 2001, Spectral methods for reducing noise in gamma ray spectrometry: Presented at the 15th Geophysical Conference, Australian Society of Exploration Geophysicists.

Moore, G., ed., 1998, Soil Guide: A handbook for understanding and managing agricultural soils, Bulletin 4343: Department of Agriculture Western Australia.

O'Dea, J., and M. Dowdall, 1999, Spatial Analysis of Natural Radionuclides in Peat overlying a lithological contact in County Donegal, Ireland: Journal of Environmental Radioactivity, **44**, 107-117.

Pracilio, G., G. J. Street, P. Nallan Chakravartula, J. R. Angeloni, D. Sattel, M. Owers, and R. Lane, 1998, Airborne geophysical surveys to assist planning for salinity control 3, Lake Toolibin SALTMAP survey interpretation report: World Geoscience Corporation.

Pracilio, G., M. L Adams, and K. R. J. Smettem, 2003, Use of airborne gamma radiometric data for soil property and crop biomass assessment, northern dryland agricultural region, Western Australia, *in* J. V. Stafford and A. Werner, eds., Precision Agriculture '03, Proceedings of the 4th European Conference: Wageningen Academic Publishers, 551-557.

Purvis, A. E. and F. J. Buckmeier, 1969, Comparison of airborne spectral gamma radiation data with field verification measurements: Proceedings of the sixth International Symposium on Remote Sensing Environment, Expanded Abstracts, 553-564.

Schoknecht, N. R., ed., 2001, Soil Groups of Western Australia, Technical Report 193: Department of Agriculture and Food, Government of Western Australia.

Sherrif, R. E., 2002, Encyclopedic dictionary of applied geophysics: Society of Exploration Geophysics.

Sizou, G. J., and P. J. Hoogteijling, 1947, Radioactivity and granular composition of soil: Physica, **13**, 517-528.

Somasiri, S., S. Y. Yee, and P.M. Huang, 1971, Influence of certain pedogenic factors on potassium reserves of selected Canadian Prairie soils: Soil Science Society of America Proceedings, **35,** 500-505.

Spies, B., and P. Woodgate, 2005, Salinity mapping methods in the Australian context: Natural Resource Management Ministerial Council, Land and Water Australia.

Street, G. J., ed., 2004, Geospatial data for natural resource management short course: Australian Society of Exploration Geophysicists.

Talibudeen, O., 1964, Natural radioactivity in soils: Soils and Fertilizers, **27**, 347-359.

Taylor, G., and R. A. Eggleton, 2001, Regolith geology and geomorphology: Wiley.

Taylor, M., K. Smettem, G. Pracilio, and W. Verboom, 2002, Relationships between soil properties and high resolution radiometrics, central eastern Wheatbelt, Western Australia: Exploration Geophysics, **33**, 95-102.

Trener, G. B., and M. A. Scaramucci, 1948, Soil radioactivity of the surrounding Merano and of Lurisia (Cuneo): Ricerca Scientifica, **18**, 756-760.

Watkins, K. P., I. M. Tyler, and A. H. Hickman, 1986, Cue 1:250,000 Geological Series: Geological Survey of Western Australia.

Webmineral, 2006, Mineralogy Database, http://www.webmineral.com, accessed 27 January 2006.

Wilford, J. R., 1992, Regolith mapping using integrated Landsat TM imagery and high resolution gamma-ray spectrometric imagery – Cape York Peninsula, Record 1992/78: Bureau of Mineral Resources.

Wilford, J. R., 1995, Airborne gamma ray spectrometry as a tool for assessing relative landscape activity and weathering development of regolith, including soils: AGSO Research Newsletter, **22**, 12-14.

Wilford, J. R., P. N. Bierwirth, and M. A. Craig, 1997, Application of airborne gamma-ray spectrometry in soil/regolith mapping and applied geomorphology: AGSO Journal of Australian Geology and Geophysics, **17,** 201-216.